Final Report 2000-32

Research

High-Strength Concrete Prestressed Bridge Girders:

Long Term and Flexural Behavior

Technical Report Documentation Page

1. Report No.	2.	3. Recipients Accession No.
MN/RC - 2000-32		

4. Title and Subtitle	5. Report Date
HIGH-STRENGTH CONCRETE PRESTRESSED BRIDGE GIRDERS: Long Term and Flexural Behavior	November 2000 6.

7. Author(s)	8. Performing Organization Report No.
Theresa M. Ahlborn Catherine E. French Carol K. Shield	

9. Performing Organization Name and Address	10. Project/Task/Work Unit No.
University of Minnesota, Dept. of Civil Engineering 500 Pillsbury Drive, S.E. Minneapolis, MN 55455	11. Contract (C) or Grant (G) No. c) 69098 wo) 83

12. Sponsoring Organization Name and Address	13. Type of Report and Period Covered
Minnesota Department of Transportation 395 John Ireland Boulevard Mail Stop 330 St. Paul, Minnesota 55155	Final Report 2000 14. Sponsoring Agency Code

15. Supplementary Notes

16. Abstract (Limit: 200 words)

This project involved the construction of two long-span, high-strength composite prestressed bridge girders to investigate their structural behavior and the adequacy of American Association of State Highway and Transportation Officials (AASHTO) 1993 provisions for their design. The scope of the research included examining prestress losses, transfer length, cyclic load response, and ultimate flexural strength.

The research revealed that prestress losses could not be determined solely from strain gage instrumentation. Foil strain gages attached to the strand cannot measure losses caused by relaxation and drift over time. Vibrating wire strain gages embedded in the concrete cannot account for losses in the prestressing strand before the concrete hardens. Researchers used vibrating wire gage data to measure the prestress losses incurred since the time of strand release. To back-calculate the losses that occur before release, researchers used total prestress losses determined from flexural cracking and crack reopening loads. The measured prestress losses were found to be much higher than those predicted by analytical methods.

Prestress losses predicted by AASHTO not only ignore concrete stress before release but also overestimate the high-strength concrete modulus, leading to lower initial losses, and overpredict the creep and shrinkage, leading to higher long-term losses.

17. Document Analysis/Descriptors	18. Availability Statement
prestressed bridge girders flexural strength high strength concrete	No restrictions. Document available from: National Technical Information Services, Springfield, Virginia 22161

19. Security Class (this report)	20. Security Class (this page)	21. No. of Pages	22. Price
Unclassified	Unclassified	390	

HIGH-STRENGTH CONCRETE PRESTRESSED BRIDGE GIRDERS:
Long Term and Flexural Behavior

Final Report

Prepared by

Theresa M. Ahlborn
Catherine E. French
Carol K. Shield

Department of Civil Engineering
University of Minnesota

November 2000

Published by

Minnesota Department of Transportation
Office of Research Administration
200 Ford Building Mail Stop 330
117 University Avenue
St. Paul, Minnesota 55117

ACKNOWLEDGEMENTS

The work on this project has been jointly conducted under the sponsorship of the Minnesota Department of Transportation (Mn/DOT), Minnesota Prestress Association (MNPA), University of Minnesota Center for Transportation Studies (CTS), Precast/Prestressed Concrete Institute (PCI), and the National Science Foundation Grant No. NSF/GER-9023596-02.

Appreciation is expressed to those members who served on the Mn/DOT Technical Activity Panel. Their support and expertise was of the highest contributions. Appreciation is also acknowledged for the generous donations of material, equipment and technical expertise by Elk River Concrete Products, Union Wire & Rope, W.R. Grace & Co., Simcote Inc., Lefebvre & Sons Trucking, Truck/Crane Services Inc., Golden Rigging Inc., Carl Borg Inc., Atlas Foundation Co., Progressive Contractors Inc., Midspec Inc., C.S. McCrossan Inc, LaMetti & Sons and A-1 Hydraulics.

The authors wish to express their appreciation to several colleagues that helped in the many phases of this project, including the following: Jeff Kielb, Paul Bergson, Dave Cumming, Eric Leagjold, Mike Sondag.

TABLE OF CONTENTS

LIST OF TABLES

LIST OF FIGURES

NOTATION

a	=	distance from support to load point location
a, b	=	constants
AASHTO	=	American Association of State Highway Transportation Officials
ACI	=	American Concrete Institute
A_g	=	gross area of concrete section
A_{net}	=	net area of concrete section
A_{ps}	=	total area of prestressing steel
ASTM	=	American Standard for Testing and Materials
b	=	width of compression face
c, $c_{1,2,3}$	=	distance from the neutral axis of the cross section to the fiber of interest
c_a	=	total camber after crack closure including the camber due to dead load, prestress, and crack closure
c_e	=	expected camber
$c_{e\text{-}na}$	=	segment height for the fiber arc at the neutral axis
cgs	=	distance from the neutral axis of the cross section to the center of gravity of strands
CR	=	creep component of prestress losses
C_t	=	creep coefficient at a given time, t
$c_{tr\text{-}comp}$	=	distance from the composite section neutral axis to the point of interest
C_u	=	ultimate creep coefficient
d_b	=	strand diameter
DL	=	Dead Loads
d_p	=	distance from extreme fiber in compression to prestress centroid
e	=	eccentricity of the prestressing strand centroid from the neutral axis of the cross section
E_c	=	modulus of elasticity of concrete; modulus of concrete at 28 days
E_{ci}	=	initial modulus of elasticity of concrete at the time the force is applied
e_{gross}	=	eccentricity of the prestressing steel in the gross concrete section
e_{net}	=	eccentricity of the prestressing steel in the net concrete section
E_s	=	modulus of elasticity of steel
ES	=	elastic shortening component of prestress loss

f'_c	=	compressive strength of concrete
$f'_{c,28}$	=	28-day compressive strength of concrete
$f'_{c,t}$	=	compressive strength of concrete at time t
f'_{ci}	=	initial concrete compressive strength
f_c	=	concrete compressive stress at a strain ε; net compressive stress at prestress centroid at time t_1, taking into the change in applied load and loss of prestress
f_{cds}	=	compressive stress at the *cgs* due to all dead loads except those accounted for at the time of prestressing; compressive stress at the level of the prestressing steel due to all dead loads except those accounted for at the time of prestressing
$f_{cgs@t1}$	=	prestress at level of strand centroid, at time t_1
f_{cir}, f_{cr}	=	compressive stress due to prestressing force acting immediately after the force is applied minus the stress due to all dead loads at that time
f_{ct}	=	splitting tensile strength of concrete
f_{pi}	=	the initial after seating strand stress
$f_{ps,after\text{-}release}$	=	stress in the strand after release
f_{py}	=	yield stress, generally assumed to be $0.90f_{pu}$
f_{pu}	=	ultimate strength of strand
f_r	=	modulus of rupture of concrete
f_{st}	=	stress in prestressing steel at time t_1
h	=	total girder depth
HSC	=	high strength concrete
I	=	Impact Factor; moment of inertia
$I_{1,2,3}$	=	moment of inertia of the cross section when loads are applied
I_g	=	gross moment of inertia of concrete section
I_{net}	=	moment of inertia of the net concrete section
$I_{tr}, I_{tr\text{-}comp}$	=	moment of inertia of the transformed composite section
k, kip	=	one thousand pounds
K	=	stiffness
K_{ca}	=	age of loading correction factor
K_{ch}	=	relative humidity correction factor

K_{cir}, K_{cr}, K_{es}, K_{sh} = correction factors for pretensioned members

K_{cs}, K_{ss} = size and shape correction factors

L = specimen length

L/d = length-to-deflection ratio

LL = Live Loads

$Loss$ = loss of prestress to time of interest, expressed in percent

M = bending moment

$M_{2,3}$ = moment due to self weight and externally applied loads

MCF = moist cure factor

M_g = moment due to gross self weight of member and any additional permanent loads at the time of prestressing

M_{sw} = girder self-weight

N = number of fatigue cycles

NSC = normal strength concrete

P = maximum applied load indicated by the testing machine; total force of the prestressing strands, including losses

$P_{after\text{-}release}$ = force in the prestressing strand after release

PCI = Precast/Prestressed Concrete Institute

PCR = portion of ultimate creep

P_i = initial prestress force, after seating and before release

PSH = portion of ultimate shrinkage

psi = pounds per square inch

$r_{a\text{-}crack}$ = radius of curvature at the crack depth

$r_{e\text{-}na}$ = radius of curvature for the fiber arc at the neutral axis

$relax, RET$ = relaxation of prestressing steel, component of prestress losses

RH = mean ambient relative humidity in percent

S = average girder spacing

$s_{a\text{-}crack}$ = arc length after crack closure at the crack tips

$s_{e\text{-}crack}$ = arc length at the tip of the crack

$s_{e\text{-}na}$ = arc length for the fiber arc at the neutral axis

$s_{e\text{-}top}$ = expected length of the top fiber of the girder

SI = metric International System of units

S_r	=	stress range
SCF, SSF	=	size and shape correction factors
SH	=	shrinkage component of prestress losses
t	=	time from placing concrete
t	=	time in days at end of time interval
t_1	=	time in days at beginning of interval, ≥ 1/24 days
t_2	=	time in days at end of time interval
UCR	=	ultimate creep of concrete, dependent on curing condition
USC	=	U.S. Customary units
USH	=	ultimate shrinkage of concrete for normal weight concrete, dependent on curing
V/S	=	volume to surface area ratio of member
w	=	amount of water
w_c	=	dry unit weight of concrete at the time of test
x	=	distance from support to the point of deflection of interest
z_{crack}	=	depth of the crack as measured from the top of the girder
z_{na}	=	depth of the neutral axis from the top of the girder
Δh	=	change in height
Δp	=	change in pressure
ΔT	=	change in temperature
Δ_{top}	=	change in length of the top arc fiber
Δ_{bot}	=	change in length of the bottom arc fiber
$\Delta\sigma_{relax,t\text{-}release}$	=	strand stress relaxation between the time of release to the time of interest
α, β	=	constants
β_1	=	$0.85 - 0.05(f'_c - 4) \geq 0.65$
ε_c	=	concrete compressive strain
ε_o	=	concrete strain at maximum compressive stress
ε_s	=	steel strain
$\varepsilon_{sh,t}$	=	shrinkage strain at a given time, t
$\varepsilon_{sh,u}, \varepsilon_{su}$	=	ultimate shrinkage strain

ε_u	=	ultimate compressive strain of concrete
$\varepsilon_{vw,after\text{-}release}$	=	the vibrating wire strain gage reading as recorded immediately after release
$\varepsilon_{vw,t}$	=	the vibrating wire strain gage reading at the time of interest, t
ϕ	=	strength reduction factor
γ_p	=	0.40 for $f_{py}/f_{pu} \leq 0.85$
λ	=	unit weight of fluid
σ_c	=	concrete stress at the fiber of interest
$\sigma_{c,after\text{-}release}$	=	concrete cross section after release
θ_a	=	central angle after crack closure
θ_e	=	expected central angle
ω, ω'	=	non-prestressed tensile and compressive reinforcement

Executive Summary

Two long-span high-strength composite prestressed bridge girders were constructed to investigate their structural behavior and the adequacy of American Association of State Highway and Transportation Officials (AASHTO) 1993 provisions for their design. The scope of this research included investigation of prestress losses, transfer length, cyclic load response and ultimate flexural strength. The non-composite span to depth ratio was 35 for the 45 in. deep girders. Twenty-eight day concrete compressive strengths exceeded 11,000 psi for the girders and 4,500 psi for the composite decks.

It was found that prestress losses could not be determined solely from strain gage instrumentation. Foil strain gages attached to the strand cannot measure losses due to relaxation and drift over time. Vibrating wire strain gages embedded in the concrete cannot account for losses in the prestressing strand before the concrete hardens. The vibrating wire gage data were used to measure the prestress losses incurred since the time of strand release. To back-calculate the losses incurred prior to release, total prestress losses determined from flexural cracking and crack reopening loads were used. The measured prestress losses were found to be much higher than those predicted by analytical methods. The major source of the difference was attributed to the higher experimentally-determined initial losses. The analytical methods did not account for the existence of tensile stresses in the concrete prior to release.

Prestress losses predicted by AASHTO not only ignore concrete stress prior to release but also overestimate the high strength concrete modulus (leading to lower initial losses) and overpredict the creep and shrinkage (leading to higher long term losses).

The AASHTO relationship for transfer length was found to be conservative for large diameter prestressing strands (0.6 in.) spaced at 2 in. on center. Load – deflection responses to simulated cyclic HS25 truck load and overload levels were predictable, and no stiffness degradation was noted after more than 2.4 million cycles. Ultimate flexural strength, controlled by the normal strength deck, was conservatively predicted by AASHTO design specifications.

CHAPTER 1 INTRODUCTION

1.1 Background

The use of prestressed concrete bridges in the United States has increased dramatically in the past five decades (Dunker and Rabbat, 1990a, 1990b). In addition, the concrete design strength has steadily increased in prestressed bridge girder construction over the years. For example, standard concrete mix design strengths for prestressed bridge girders built for the Minnesota Department of Transportation (Mn/DOT) have increased over 50 percent in the past decade. These higher concrete strengths are being produced with little difficulty from readily available materials. To achieve further economy, it is likely that these design strengths will continue to increase.

The use of high strength concrete (HSC) as a feasible construction material has been discussed for many years. As early as 1932, engineers speculated that the use of high strength concrete could lead to cost savings, especially in long-span construction (Towles, 1932). Towles was comparing concrete design compressive strengths of 5000 to 7000 psi (34.5 to 48 MPa), a maximum practical limit for the time.

High strength concrete research by Klieger (1957) was conducted to provide high early strength concrete. Based on this research, he concluded that careful quality control and low water-cement ratios were required to obtain high quality high early strength concrete. He was able to produce 28-day compressive strengths of 7500 to 8500 psi (52 to 59 MPa).

Achieving high concrete strengths appears to be somewhat regionally dependent. In the Minneapolis - St. Paul area, continued use of high strength concrete has shown that design compressive strengths on the order of 10,000 to 14,000 psi (69 to 97 MPa) are readily produced through the use of additives, such as silica fume and fly ash. Workability of the low water-cement ratio concrete is attained through high-range water reducers, also known as superplasticizers. In Seattle, compressive strengths of 19,000 psi (131 MPa) have been achieved, while in New York strengths have exceeded 21,000 psi (145 MPa) (Godfrey, 1987). Breen (1990) has reported that in the laboratory, researchers have produced 29,000 psi (200 MPa) concrete.

High strength concrete has been used by prestressed concrete producers for many years. Producers use high early strength concrete to minimize casting bed turn around time. In the

manufacturing process, formwork can be removed and high strength concrete members prestressed within an 18-24 hour time period, allowing for the forms to be reused daily. However, few designers take advantage of this additional concrete compressive strength.

In 1970, the use of high strength concrete was applied to bridges. The Willows Creek Bridge in Ontario, Canada was the first bridge reported to use high strength concrete in design and construction (Burgess et al., 1970). The five span structure was 787 ft. (240 m) long and consisted of 50 precast post-tensioned concrete T-beams with a cast-in-place deck slab. The project demonstrated that a workable mix design could be produced with readily available materials to obtain a minimum compressive strength of 6000 psi (41.4 MPa).

The design strength of concrete has steadily increased in bridge construction over the years. In just the past decade, standard concrete mix designs for bridges built under the Minnesota Department of Transportation (Mn/DOT) jurisdiction have gone from 4500 to 7000 psi (31 to 48 MPa), with some design exceptions allowing for 8000 psi (55 MPa). Keeping pace with other prestressed/precast applications and to achieve further economy, the bridge industry will most likely continue to increase these strengths.

Current design provisions of the American Concrete Institute (ACI) and the American Association of State Highway Transportation Officials, Inc. (AASHTO) are based on empirical relationships developed from isolated tests of specimens with concrete compressive strengths on the order of 5000 to 8000 psi (34.5 to 55 MPa). The scarcity of empirical data for higher strength concrete has led to limits on the maximum compressive stress of 10,000 psi (69 MPa) to be used for shear and development length provisions in design codes such as ACI 318-95. A limited number of recent tests indicate that relationships for transfer and development length of strands in high strength concrete (HSC), as well as prestress losses with time, vary from relationships based on tests of normal strength concrete specimens. These property changes directly affect the prestress losses and serviceability of prestressed concrete members.

High strength concrete offers many advantages to prestressed bridge girders including enabling increased span lengths and/or wider girder spacings. For a fixed bridge cross section, HSC can be used to increase span lengths. Shallower HSC sections can be used in place of normal strength concrete members of the same length enabling greater bridge underclearances or lower bridge embankments. Alternatively, placing HSC girders at a wider spacing enables fewer

girder lines per constant width bridge. Fewer required girders lead to lower fabrication, transportation and erection costs.

The viability of HSC prestressed girders is not only dependent on reliably achieving higher concrete strengths, but also on the amount and type of prestressing strand which can be placed in the cross section. In the construction of prestressed girders to be used at wider spacings, the compressive strength at the time of release tends to control the girder design because the girder self-weight is a small fraction of the load it will be subjected to in service. Consequently a large amount of prestressing force must be "stored" in the girder until it is placed in the field at which time it will carry an additional dead load and the live load.

To achieve the full benefit of high strength concrete, larger diameter (0.6 in. [15.2 mm]) and possibly higher strength strands (300 ksi [2070 MPa]) should be incorporated in the prestressed sections. The current use of 0.5 in. (12.7 mm) diameter 270 ksi (1860 MPa) strand quickly limits the achievable girder spans and spacings.

1.2 Objective and Scope

1.2.1 General

This study was developed to investigate the feasibility of using high strength concrete in the design and construction of prestressed concrete bridge girders. Although the definition of high strength concrete varies throughout the country, it is defined here as a concrete compressive strength between 7,000 and 15,000 psi (48 and 103 MPa). The lower limit corresponds to the maximum concrete strength specified in Minnesota for prestressed girders. The upper limit represents the current practical maximum strength that can be produced with locally available materials (Mokhtarzadeh, 1996).

The study was limited to the consideration of high strength concrete prestressed bridge girders that become composite with a normal strength concrete deck. Only non-skew, simple span bridges were considered. The composite decks were assumed to be placed using unshored construction. Low relaxation strands were the only strands considered because they have become the industry standard. The 15th edition of the American Association of State Highway and Transportation Officials (AASHTO) *Standard Specifications for Highway Bridges* (1993) was used as the design guide.

1.2.2 Test Programs

Due to the lack of information available on high strength concrete and its use in prestressed bridge girders, a comprehensive program was devised to address both issues. The entire research program consisted of two primary phases: high strength concrete materials research, design implications of high strength prestressed bridge girders, and behavior of high strength prestressed bridge girders. The materials research was conducted by others at the University of Minnesota to determine the effect of varying parameters on the mechanical properties of HSC produced from locally available materials. Results of mechanical properties and durability of high strength concrete were documented by Mokhtarzadeh (1996) and Kreisel (1996), respectively.

This report specifically addresses the remaining phase of the comprehensive program mentioned: design implications and behavior of high strength prestressed concrete bridge girders. Results regarding the shear behavior of HSC prestressed girders is addressed in a companion report by Cumming (1997). The primary objective of these two phases was to determine the adequacy of the present AASHTO specifications for designing prestressed bridge girders with high strength concrete.

A parametric study was performed to determine the viability and design implications of using high strength concrete for Minnesota Department of Transportation (Mn/DOT) prestressed concrete bridge girders. A computer program, SPAN (Leap Software, 1990), was used to determine the required number of strands and strand pattern as a function of maximum span length a given set of loading parameters and while varying the concrete strengths and transverse girder spacings. The study indicated that it is feasible to design with HSC up to 12,000 psi (83 MPa) in conjunction with using 0.6 inch (15.2 mm) diameter 270 ksi (1860 MPa) low-relaxation strands.

A comprehensive testing program was devised and included monitoring two full-size girders for several years after fabrication to investigate HSC effects on prestress losses and long term deflection. The girders were subjected to a series of cyclic and static load tests and tests to ultimate in flexure to investigate serviceability and ultimate strength behavior. The results have been correlated with information obtained from companion material tests, as well as comparison to other relevant research.

1.3 Organization of the Study

Chapter Two contains a literature review relevant to the behavior of high strength concrete and the testing of high strength prestressed bridge girders. Chapter Three reviews the feasibility of using high strength concrete in Minnesota prestressed concrete girders through a parametric study. Chapter Four discusses the issues behind the design of the two composite test girders.

Chapter Five describes the test setup, including the loading frame and data acquisition system used during testing. Chapter Six describes the general properties (material and geometric) of the girders and the properties assumed in the numerical modeling. Chapter Seven reports the initial and time-dependent response of the girders (i.e., at the time of prestressing strand release and response of the girders over time without considering load testing).

Beginning with Chapters Eight and Nine, the response of the girders under static load, cyclic load and initial flexural crack testing is presented. Chapter Ten discusses the results of ultimate flexural load testing for both girders. Chapter Eleven presents a geometric compatibility theory to explain the effects of Girder II pre-release cracking on behavior. Chapter Twelve concludes the report with conclusions and recommendations for using high strength concrete in prestressed bridge girders

CHAPTER 2 REVIEW OF PREVIOUS INVESTIGATIONS

2.1 Introduction

The use of high strength concrete in bridge applications is expected to produce more economical designs by allowing for increased span lengths, shallower sections, fewer girders for a given span, or a combination of the three. Several researchers have investigated and reported these advantages of using high strength concrete. This chapter reviews the benefits and cost effectiveness of using high strength concrete for prestressed concrete bridge girders. General concepts of specific material properties are discussed, as well as previous tests of high strength concrete prestressed girders and some of the available numerical modeling methods.

2.1.1 Benefits of High Strength Concrete for Prestressed Bridge Girders

Research sponsored by the U.S. Department of Transportation in the early 1980's (Carpenter et al., 1980; Jobse, 1987) compared two prestressed concrete designs of a 150 ft. (46 m) simple span bridge to show the greater load carrying capabilities of high strength concrete girders. Both designs used a bridge width of 36 ft. (11 m), HS20-44 loading, a bulb tee section, and a composite normal strength deck. The first design comprised nine girders with 6000 psi (41.4 MPa) concrete. The second design used four girders of 10,000 psi (69 MPa) concrete. In spite of the additional thickness of the deck (5.5 versus 6.5 in. [140 versus 170 mm]) needed for the greater transverse span among the four high strength girders, the advantage of using high strength concrete was quite clear through the overall material quantity savings.

Similar results have been discussed by Castrodale et al. (1988b). For a prestressed composite bridge with a span of 115 ft. (35 m), a width of 36 ft. (11 m), and a normal strength concrete deck, the required number of AASHTO-PCI Type IV girders was reduced from nine 6000 psi (41.4 MPa) girders to four 10,000 psi (69 MPa) girders. They concluded that use of high strength concrete also resulted in a reduction of the total number of strands required. Again, an increased deck thickness was needed to span the larger transverse distance between the high strength girders. However, the overall dead load was reduced. The use of fewer girders for a given span and bridge width leads to reduced fabrication and erection time, as well as material savings and reduced shipping and erection costs.

Another benefit of high strength concrete in bridge applications investigated by Castrodale et al. (1988b) and speculated by others (Breen, 1990; Carpenter et al., 1980; Jobse, 1987; Rabbat

and Russell, 1982; Towles, 1932) was that an increase in concrete strength leads to longer maximum spans. For a constant cross section (an AASHTO-PCI Type IV girder in Castrodale's study), constant girder spacing, loading and deck thickness, a span of about 108 ft. (33 m) for a 6000 psi (41.4 MPa) girder could be increased to about 137 ft. (42 m) for a 12,000 psi (83 MPa) girder. This increase in span length can lead to a reduction in the number of piers and supports required for multiple span bridges and improved traffic safety. (It should be noted here that a maximum span limit exists due to the lateral stability of these longer members, and is discussed further in Section 2.6.5.)

Another possible benefit identified by Carpenter (1980) and Castrodale et al. (1988b) is that for a constant span width, shallower high strength concrete members could be used in place of deeper normal strength concrete members, which could improve clearances at highway crossings or results in a reduction of embankment costs.

2.1.2 Cost Effectiveness

The cost effectiveness of using high strength concrete has been debated by many over the years. Although the benefits of using high strength concrete include a saving in material quantities, the cost of producing high strength concrete is higher than normal strength concrete. This is mainly due to the increased aggregate and silica fume cost and use of superplasticizer.

A recent study by Adelman and Cousins (1990) compared the cost effectiveness of high strength concrete girder sections to confirm the results of Castrodale et al. (1988b) as previously discussed, that an increase in compressive strength and stiffness can result in increased transverse girder spacings and/or larger span lengths. Concrete strengths of 11,500 psi (79 MPa) were considered. Using Louisiana unit costs, an average cost difference was determined to be $0.54/ft. ($1.77/m) less for normal than high strength concrete girders, including strands, material, and fabrication. An average cost per foot for each girder type was then determined based on in place costs for the superstructure, including transportation and erection costs. These costs were then applied to a case study to determine what the superstructure savings would have been if high strength concrete had been used.

A typical LDOTD (Louisiana Department of Transportation and Development) interstate bridge was considered for the case study. The bridge was three span (120 ft. [36.5 m] for each span) with a width of 42.8 ft. (13 m). Seven Type IV-Mod normal strength concrete girders

(6000 psi [41.4 MPa]) resulted in a total superstructure cost of $876/ft. ($2875/m) while the use of six Type IV-Mod high strength concrete girders (10,000 psi [69 MPa]) resulted in a total superstructure cost of $828/ft. ($2720/m). For this bridge, a savings of more than 5.5% or $17,000 would have been achieved. Depending on the design conditions, the savings for using high strength concrete girders could substantially increase.

2.1.3 Optimized Sections

In the early application of prestressed concrete for bridge applications, each contractor had a slightly different girder shape. Standardization of these sections took place in the 1950's and early 1960's by AASHTO and was developed for use with normal strength concretes below 5000 psi (34.5 MPa) (Castrodale, 1988b; Rabbat and Russell, 1982). Realization of the full potential of high strength concrete must therefore include considerations for girder sections that most readily benefit from the use of high strength concrete.

In the early 1980's, Rabbat and Russell (1982) investigated current AASHTO girders in excess of 80 ft. (24.5 m) for structural efficiency when used in high strength concrete applications. Although the design strength was limited to 7000 psi (48 MPa), they noted that the designer's goal should be to use a section that has the highest section modulus with the least area. Conversely, for a given sectional area, the highest section modulus is desirable. They concluded that the most economical bridges for spans between 70 and 130 ft. (21.3 to 39.6 m) are constructed from prestressed bridge girders, although AASHTO girders are not the most structurally efficient for use with high strength concrete when compared to other state standard sections. (Minnesota sections were not compared in the study.)

Studies conducted at the University of Texas at Austin (Castrodale et al., 1988b; Hartmann et al., 1988) compared selected AASHTO girder sections to Texas girder sections and reviewed their effectiveness for high strength concretes on the order of 12,000 psi (83 MPa). Results prompted the researchers to propose new sections that would take advantage of the high strength concrete. The proposed sections typically had less area with a higher section modulus, making for a slightly deeper section.

2.2 Behavior of Concrete

Researchers have revealed that high strength concrete mechanical properties depend on the aggregate, admixtures and the water-cementitious material ratio. The concrete relies on each of

the ingredients independently and their interaction, similar to normal strength concrete. However, high strength concrete properties have been found to behave differently than normal strength. A review of high strength concrete mechanical properties and their variation from normal strength follows.

2.2.1 Compressive Strength over Time

Normal strength concrete increases in strength rapidly over the first few weeks after casting, then continues to increase at a slower rate. High strength concrete behaves similarly, but at different strength increase rates. Many factors affect the compressive strength gain over time. These include, but are not limited to, the fineness of cement (Type I versus Type III), the curing procedure (moist, heat or steam cured), and the reduction of water-to-cementitious materials ratio for high strength concretes. Several forms of the age-strength relationship have been proposed, including logarithmic functions and hyperbolic functions. The hyperbolic function recommended by ACI Committee 209 (1992) is listed in Eqn. (2.1) and has generally been adopted. The equations are valid for both U.S.C. and SI units as long as units are consistent for $f'_{c,t}$ and $f'_{c,28}$.

$$f'_{c,t} / f'_{c,28} = t/(a+bt), \tag{2.1}$$

where

$f'_{c,t}$ = compressive strength of concrete at time t,

t = time from placing concrete (days),

$f'_{c,28}$ = 28-day compressive strength of concrete,

a, b = constants.

ACI Committee 209 (1992), based on an extensive study by Branson and Christianson (1971), recommended equations for Type I and III cement, and moist and steam cured concretes. The Branson and Christianson report used data from six studies, resulting in a total of 88 specimens, up to 350 days old. Recommendations were for normal weight, sand-lightweight and all lightweight concretes. Concrete strengths were limited to 7000 psi (48 MPa). Values for the constants a and b were found to range from 0.50 to 9.25 and 0.67 to 0.98, respectively. The following relationships are recommended for normal strength concrete based on steam-cured condition and cement type.

Steam-cured concrete, Type I cement:

$$f'_{c,t} / f'_{c,28} = t/(1.00 + 0.95t) \quad (2.2)$$

Steam-cured concrete, Type III cement:

$$f'_{c,t} / f'_{c,28} = t/(0.70 + 0.98t) \quad (2.3)$$

All of the data used to derive these formulas were within 20% of the predicted values. The base of these equations was the 28-day strength. It was shown that steam curing and Type III cement strongly influenced the early age strength, hence the flatness of the strength-time curve (Eqn. 2.3) when plotted.

Mokhtarzadeh (1996) studied the effect of cement type, the curing, and the content of cementitious material on the strength gain with time for higher strength concretes. The testing program varied the method of curing, amount of cementitious material, type and brand of cement, gradation and type of coarse aggregate, and amount of fly ash and silica fume. Concrete strengths ranged from 7000 to 15000 psi [48 to 103 MPa]. A heat-cure method was used in place of the steam-cure process throughout his study to provide a more realistic curing environment. The following general equations resulted from the extensive study.

Heat-cured concrete, Type III cement, all mixes:

$$f'_{c,t} / f'_{c,28} = t/(0.21 + 1.00t). \quad (2.4)$$

Heat-cured concrete, Type III cement, reference mixes:

$$f'_{c,t} / f'_{c,28} = t/(0.28 + 0.99t). \quad (2.5)$$

Heat-cured concrete, Type III cement, silica fume mixes:

$$f'_{c,t} / f'_{c,28} = t/(0.17 + 1.00t). \quad (2.6)$$

The constant a (of Eqn. 2.1) decreased for cases involving high strength concrete, while the constant b remained relatively unchanged. This indicates that higher concrete strengths gain initial strength at a faster rate than the lower strength counterparts but level off at approximately the same rate after 28-days.

2.2.2 Stress-Strain Curve and Modulus of Elasticity

The instantaneous compressive stress-strain relationship of concrete depends on so many factors that it is difficult to accurately estimate the relationship for a particular concrete from its constituents and curing conditions. Several empirical expressions representing complete compressive stress-strain curves have been proposed and are well documented by Suttikan

(1978). The most common model, proposed by Hognestad (1955), and a recently published model for higher concrete compressive strengths are discussed.

The equation proposed by Hognestad (1955) is composed of a second-degree parabolic ascending branch (Eqn. 2.7) and a linear descending branch (Eqn. 2.8).

For $0 \geq \varepsilon \geq \varepsilon_o$:

$$f_c = f_c'\left(\frac{2\varepsilon}{\varepsilon_o} - \left(\frac{\varepsilon}{\varepsilon_o}\right)^2\right), \tag{2.7}$$

For $\varepsilon_o \geq \varepsilon \geq \varepsilon_u$:

$$f_c = f_c'\left[\frac{\varepsilon_u - 0.85\varepsilon_o - 0.15\varepsilon}{\varepsilon_u - \varepsilon_o}\right], \tag{2.8}$$

where

ε = concrete compressive strain

f_c = concrete compressive stress at a strain ε

f'_c = maximum compressive stress in concrete stress-strain curve

ε_o = concrete strain at maximum compressive stress

ε_u = ultimate compressive strain of concrete.

The modulus of elasticity is the "ratio of normal stress to corresponding strain for tensile or compressive stresses below the proportional limit of the material" (ACI 318-95, 1995). High strength concrete acts like a true composite. Therefore the modulus of elasticity is dependent on the stiffness of both the cement paste and aggregates (ACI Committee 363, 1984). There have been many investigations of the relationship between the modulus of elasticity and the compressive strength of concrete. Mokhtarzadeh (1996) thoroughly documented many of the published relationships. Listed are a few of the more commonly used relationships in this study.

ACI Building Code 318-95 (1995) and Pauw (1960) used data from seven sources which included many aggregate types and concrete strengths to define modulus of elasticity. The tested concrete had strengths of 6500 psi (45 MPa) or less. Pauw recognized that lightweight concretes exhibited lower moduli to compressive strength ratio than normal-weight concrete, weighing from 90 to 155 lb/ft^3 (1440 to 2480 kg/m^3).

$$E_c = 33 w_c^{1.5} (f'_c)^{0.5}, \text{ USC} \tag{2.9}$$

$$E_c = 0.043\, w_c^{1.5} (f'_c)^{0.5}, \text{ SI} \tag{2.10}$$

where

E_c = modulus of elasticity of concrete (psi, MPa)

w_c = dry unit weight of concrete at the time of test (lb/ft^3, kg/m^3)

f'_c = compressive strength of concrete (psi, MPa).

These equations use the dry unit weight of the concrete to account for the differences in aggregate properties.

ACI Committee 363 (1984) and Carrasquillo et al. (1981) studied how high strength concrete affects the modulus of elasticity to compressive strength relationship. They determined that the ACI 318 equation overestimates modulus of elasticity for high strength concrete. Carrasquillo et al. explained that the overestimation was due to the mortar-aggregate composite activity in higher strength concretes. As the strength of the mortar increases, the compressive strength increases correspondingly because mortar strength typically controls the compressive strength. Both the mortar and aggregate stiffness affect the modulus of elasticity, therefore when only the mortar is stiffer, the modulus of elasticity does not increase proportionally with the compressive strength.

The researchers used the data from their study as well as data from other investigators to define high strength concrete properties. The concrete compressive strengths ranged from 4570 to 11,100 psi (32 to 77 MPa). Carrasquillo et al. recommended the following equation which was adopted by ACI Committee 363.

$$E_c = \left[40{,}000\sqrt{f'_c} + 1.0\times10^6\right]\left(\frac{w_c}{145}\right)^{1.5}, \text{ USC} \tag{2.11}$$

$$E_c = \left[3320\sqrt{f'_c} + 6900\right]\left(\frac{w_c}{2320}\right)^{1.5}, \text{ SI} \tag{2.12}$$

where

E_c = modulus of elasticity of concrete (psi, MPa)

w_c = dry unit weight of concrete at the time of test (lb/ft^3, kg/m^3)

f'_c = compressive strength of concrete (psi, MPa).

The researchers recommended using this equation for 3000 to 12,000 psi (21 to 83 MPa) compressive strength concrete.

2.2.3 Splitting Tensile Strength

The splitting tensile test, or Brazilian split cylinder test, is one of three ways to measure the tensile strength in concrete, two of which are discussed here. The modulus of rupture is discussed in the following section. The splitting tensile test applies a compressive load to diametrically opposite sides of a horizontally placed cylinder. This test causes a compressive force in the direction the testing machine applies the load and perpendicular tensile stress at the middle of the cylinder. The equation from ASTM C 496-90 used to solve for the splitting tensile strength from the maximum load is

$$f_{ct} = \frac{2P}{\pi L d} \tag{2.13}$$

where

f_{ct} = splitting tensile strength of concrete

P = maximum applied load indicated by the testing machine

L = specimen length

d = diameter of the specimen.

ACI Building Code 318-95 (1995) provides an approximate equation for the splitting tensile strength of concrete given the concrete compressive strength as shown in the following equations. This equation is only used for normal weight concrete,

$$f_{ct} = 6.7(f_c)^{0.5}, \text{USC} \tag{2.14}$$

$$f_{ct} = 0.56(f_c)^{0.5}, \text{SI} \tag{2.15}$$

where

f_{ct} = splitting tensile strength (psi, MPa)

f_c = compressive strength of concrete (psi, MPa).

ACI Committee 363 (1984) and Carrasquillo et al. (1981) reported a splitting tensile strength equation for high strength concrete. Carrasquillo et al. derived the equation from data accumulated from 4 x 8 in. (102 x 203 mm) cylinders made with crushed limestone or glacial gravel,

$$f_{ct} = 7.4(f_c)^{0.5}, \text{USC} \tag{2.16}$$

$$f_{ct} = 0.59(f_c)^{0.5}, \text{SI} \tag{2.17}$$

where

f_{ct} = splitting tensile strength (psi, MPa)

f_c = compressive strength of concrete (psi, MPa).

This equation is recommended for 3000 to 12,000 psi (21 to 83 MPa) compressive strength concrete.

Mokhtarzadeh (1996) developed a relationship using a regression analysis model. He tested 314, 6 x 12 in. (152 x 305-mm) cylinders ranging in strength from approximately 7000 to 15,000 psi (48 to 103 MPa). The cylinders contained five types of coarse aggregates consisting of two river gravels, two limestones, and a granite. Concretes incorporated silica fume, fly ash, combinations of silica fume and fly ash, and were either moist- or heat-cured. Only the heat cured results are reported here.

Heat-cured concrete:

$$f_{ct} = 3.63(f_c)^{0.57}, \text{USC} \tag{2.18}$$

$$f_{ct} = 0.42(f_c)^{0.57}, \text{SI} \tag{2.19}$$

where

f_{ct} = splitting tensile strength (psi, MPa)

f_c = compressive strength of concrete (psi, MPa).

Mokhtarzadeh (1996) concluded that the ACI 318 equation for the prediction of splitting tensile strength is applicable to high strength concretes. In fact, when forcing his data to the 0.5 exponential form, the coefficients were 6.77 and 6.47 for moist-cured and heat-cured data respectively, compared with 6.7 as suggested by ACI 318 (1995).

2.2.4 Modulus of Rupture

The modulus of rupture (MOR) test is a second way to indirectly measure the tensile strength of concrete. Although the flexural strength is not a true material property, as it is dependent on the specimen dimensions and loading configuration, the standard third point MOR test is frequently assumed to provide an indication of tensile strength. It is not as accurate as the split cylinder test because it measures when complete failure occurs, when the first crack opens. These occur at different times because of the nonlinearity of the concrete stress-strain curve, and because stress and strain is a function of depth for flexure. Therefore these results tend to be higher than the splitting tensile strength (McNeely and Lash, 1963). Raphel (1984)

recommended multiplying the modulus of rupture by 0.75 to get the actual tensile strength of the concrete.

ASTM C 78-94 provides the following equation to calculate the modulus of rupture from the maximum load of the third point bending test,

$$f_r = \frac{Mc}{I} \tag{2.20}$$

where

f_r = modulus of rupture

$M = pa = (P/2)\ (L/3) = (PL/6)$ maximum bending moment; a constant moment region exists across the middle third of the beam

$c = (d/2)$ distance from the centroid to the point of maximum strain

$I = bh^3/12$ moment of inertia

P = maximum applied load indicated by the testing machine

L = span length

d = depth of specimen

b = width of specimen.

After substitution into the flexure equation (Eqn. 2.20), the following equation, found in ASTM C 78-94, results. The terms are as defined previously,

$$f_r = \frac{PL}{bd^2}. \tag{2.21}$$

There have been many researchers who have investigated the concrete modulus of rupture and compressive strength relationship. Investigators have published many more relationships, too many to list here. Therefore, listed are the commonly used equations for predicting the modulus of rupture for both normal and high strength concrete.

ACI Building Code 318-95 (1995) provides an approximation for the modulus of rupture, generally defined for normal strength concretes, given the compressive strength as

$$f_r = 7.5(f'_c)^{0.5}, \text{ USC} \tag{2.22}$$

$$f_r = 0.62(f'_c)^{0.5}, \text{ SI} \tag{2.23}$$

where

f_r = modulus of rupture (psi, MPa)

f'_c = concrete compressive strength (psi, MPa).

ACI Committee 363 (1984) and Carrasquillo et al. (1981) looked at the modulus of rupture relationship for 3000 to 12,000 psi (21 to 83 MPa) concrete. After examining the data from third-point loading on 4 x 4 x 14 in. (102 x 102 x 356 mm) beams made from limestone aggregate, Carrasquillo et al. derived the following equation.

$$f_r = 11.5(f'_c)^{0.5}, \text{USC} \tag{2.24}$$

$$f_r = 0.94(f'_c)^{0.5}, \text{SI} \tag{2.25}$$

where

f_r = modulus of rupture (psi, MPa)

f'_c = concrete compressive strength (psi, MPa).

Mokhtarzadeh (1996) tested 280 6 x 6 x 24 in. (150 x 150 x 610 mm) beams ranging in strength from approximately 7000 to 15,000 psi (48 to 103 MPa) and cast from the same mixes as the splitting tensile strength test. The following empirical relationships for predicting the average flexural strength (f_r) of heat cured high strength concrete from its compressive strength (f_c) were determined.

Heat-cured concrete:

$$f_r = 23.57(f_c)^{0.40}, \text{USC} \tag{2.26}$$

$$f_r = 1.19(f_c)^{0.40}, \text{SI} \tag{2.27}$$

where

f_r = flexural strength (psi, MPa)

f_c = compressive strength of concrete (psi, MPa).

Mokhtarzadeh (1996) also compared his data to the ACI form by forcing his data to the 0.5 exponential power. He concluded that the ACI 363 (1984) equation for the prediction of flexural strength was applicable to moist-cured high strength concretes, but suggested a coefficient of 9.3 for heat-cured high strength concretes.

2.2.5 Creep and Shrinkage Effects

Time-dependent effects of concrete can greatly influence the level of prestress force in prestressed concrete members. As creep and shrinkage of concrete occurs, a loss of prestress causes a flexural member to decrease in stiffness causing an increase in deflection. With continued shrinkage, members may crack under service conditions when restrained. The creep

and drying shrinkage of high strength concrete have been known to vary from that of normal strength concrete. Research conducted on high strength concrete has shown that both the creep coefficient and rate of shrinkage may decrease for increased concrete strengths (Perenchio and Klieger, 1978; Samdi et al., 1987; Paulson et al., 1991). Although, ACI Committee 363 (1984) states that shrinkage for high strength concrete is similar to that of normal strength concrete and long-term creep strains are expected to be the same because higher strength concretes are subjected to higher stresses. Relationships for creep and shrinkage in general terms as well as those more commonly used relationships developed for normal and high strength concretes follow.

Creep is defined as the time dependent change in strain (deformation) due to a sustained stress. It is generally expressed in the following nonlinear form,

$$C_t = \frac{t^{\beta}}{\alpha + t^{\beta}} C_u , \tag{2.28}$$

where

C_t = creep coefficient at a given time, t

α,β = constants

C_u = ultimate creep coefficient.

Shrinkage, in this report, refers to the change in volume of a concrete member due to drying. It is also expressed generally in a nonlinear form as follows,

$$\varepsilon_{sh,t} = \frac{t}{\alpha + t} \varepsilon_{sh,u} , \tag{2.29}$$

where

$\varepsilon_{sh,t}$ = shrinkage strain at a given time, t

α = constant, dependent on curing condition

$\varepsilon_{sh,u}$ = ultimate shrinkage strain.

Creep and shrinkage effects caused by deviations from "standard conditions" are accounted for through a series of correction factors. These correction factors are for variations in humidity greater than 40%, age at time of loading dependent on curing conditions, thickness of members greater than 6 in. (150 mm) and slumps of concrete greater than 4 in. (100 mm). ACI Committee 209 (1992) reports that concrete creep prediction for any given time, t, is generally expressed as follows, with the terms as defined previously

$$C_t = \frac{t^{0.6}}{10 + t^{0.6}} C_u \left(\prod_{i-1}^{n} k_i \right). \tag{2.30}$$

Correction factors include k_{rh} (relative humidity), k_{age} (age at time of loading), k_{size} (member size adjustment), and k_{slump} (high slump factor) and are documented in the ACI 209 reference. The equation was developed for normal strength concretes ranging in compressive strength from 3000 to 7000 psi (21 to 48 MPa). A typical value for the ultimate creep coefficient, C_u, is suggested to be 2.35 for normal strength concrete. When applying a correction factor for a relative humidity of 70%, the ultimate creep coefficient is 1.88.

ACI Committee 209 (1992) also reports that shrinkage of concrete at any given time, t, varies for moist-cured and steam-cured concrete. The shrinkage function is generally expressed as follows, with the terms as defined previously.

Moist-cured concrete, after 7 days,

$$\varepsilon_{sh,t} = \frac{t}{35 + t} \varepsilon_u \left(\prod_{i=1}^{n} k_i \right). \tag{2.31}$$

The average suggested value for ε_u is 800 $x10^{-6}$. When applying a correction factor for a relative humidity of 70%, the ultimate suggested strain is 560 με.

Steam-cured concrete, after 1-3 days,

$$\varepsilon_{sh,t} = \frac{t}{55 + t} \varepsilon_{sh,u} \left(\prod_{i=1}^{n} k_i \right). \tag{2.32}$$

The average suggested value for $\varepsilon_{sh,u}$ is 730 $x10^{-6}$. Again, when adjusting for a relative humidity of 70%, the ultimate suggested strain is 510 με.

Nilson (1985) reported that the ultimate creep coefficient for high strength concrete is much lower than that of normal strength concretes. His base for normalizing was 3000 psi (21 MPa) concrete. Relationships followed the ACI 209 recommendation, and parameters were used for normal strength concrete such that ultimate creep coefficients could be compared. As shown in Table 2.1, the ultimate creep coefficient for high strength concrete was almost half of that for normal strength concrete.

Table 2.1 Creep Coefficients for Varying Concrete Strengths

Material	f'_c (psi)	C_{CU}	$C_{CU}/C_{CU,3000}$
Low Strength	3000	3.1	1.00
	4000	2.9	0.94
	6000	2.4	0.77
	8000	2.0	0.65
High Strength	10000	1.6	0.52

Mokhtarzadeh (1996) considered creep behavior of high strength concrete mixes of four aggregate combinations and ranging in strength from 7000 to 15,000 psi (48 to 103 MPa). Creep specimens were maintained at a relative humidity of 50%. Heat-cured specimens were loaded to 60% of their one day strength at one day, while moist-cured specimens were loaded at 28-days to 45% of their 28-day compressive strength. Following the same nonlinear equation form, he used a regression analysis with his data to produce the following result for high strength concrete with the terms defined previously.

Limestone reference mix:

$$C_t = \frac{t^{0.40}}{18.47 + t^{0.40}}[2.28]. \tag{2.33}$$

Rounded gravel with silica fume:

$$C_t = \frac{t^{0.56}}{7.87 + t^{0.56}}[2.45]. \tag{2.34}$$

Mokhtarzadeh (1996) also considered shrinkage behavior of mixes corresponding to the creep tests. Following the same nonlinear equation form, he used a nonlinear regression analysis with his data to produce the following result for high strength concrete,

$$\varepsilon_{sh,t} = \frac{t}{65 + t}[530\mu\varepsilon]. \tag{2.35}$$

2.3 Behavior of Mild Steel

Mild steel reinforcement includes deformed reinforcing bars, epoxy coated bars, plain and deformed wires and welded wire fabric. Grades of steel are based on minimum tensile yield strength and include 40, 60, and 75 ksi [300, 420, and 520 MPa]. Creep and relaxation of mild steel reinforcement are of small magnitude and hence such time-dependent effects are typically

ignored in design. The static behavior of mild steel reinforcement is generally idealized as elastic-perfectly plastic in both tension and compression. The modulus of elasticity is usually assumed to be 29,000 ksi [200 GPa].

2.4 Behavior of High Strength Prestressing Strand

The importance of using high strength steel in prestressed concrete is to take advantage of a material with superior qualities while using smaller quantities of steel at a larger eccentricity. Strands are available in either Grade 250, 270 or 300 ksi (1730, 1860 or 2070 MPa) based on the ultimate tensile strength and either stress-relieved or low-relaxation. Seven-wire low-relaxation strands are most commonly used. It has been observed that prestressing steels offer substantially higher strengths than mild steel reinforcing steels at lower ultimate strain levels. A typical modulus of elasticity value for all grades of prestressing strand, independent of the manufacturing process, is 28,800 ksi (200 GPa).

2.4.1 Fatigue of Prestressing Strand

Fatigue is the process of deterioration of the material mechanical properties due to fluctuating stresses, such as those induced by repetitive live load applications on a highway structure. The resistance of the material is often described by an *S-N* curve, where *S* represents the stress range in the material and *N* the number of cycles to failure, also known as fatigue life. Below a certain stress range, termed the endurance limit, materials will not fail, independent of the number of cycles.

ACI Committee 215 (1992) was charged to study fatigue in concrete structures. They recommended a maximum stress range of $0.12f_{pu}$ for prestressing strands, where f_{pu} is the ultimate tensile strength of the strand. For a Grade 270 strand, this range limit would be 32 ksi (220 MPa). This limit is substantially higher than stress range values observed in uncracked prestressed members. However, if cracking does occur or is allowed, this limitation may become critical.

Paulson et al. (1983) reviewed several cyclic strand tests on isolated elements and completed additional tests as well. The researchers developed a lower bound *S-N* relationship for prestressing strands. Specimens were tested under stress ranges from 22 to 81 ksi (150 to 560 MPa) for minimum stress levels from 75 to 165 ksi (520 to 1140 MPa). Although in prestressed concrete the minimum steel stress is relatively high (50 to 60 percent of ultimate), it did not have

enough of a significant influence on the fatigue life of the strand to warrant inclusion in the *S-N* relationship. The relationship that was developed follows,

$$Log(N) = 11.0 - 0.5Log(S_r), \tag{2.36}$$

where

N = number of fatigue cycles

S_r = stress range (ksi, MPa).

Based on typical stress ranges induced in prestressed members under repetitive loads (usually less than 10 to 15 ksi), the researchers recommended a reasonable fatigue limit stress of 20 ksi (135 MPa).

2.4.2 Relaxation of Prestressing Strand

Relaxation is the loss of stress in a strand maintained under a constant temperature and strain. This loss varies with time and initial stress. Relaxation losses in prestressing steels are generally negligible for stresses less than 50 percent of ultimate strength. However, losses increase rapidly with an increase in stress and decrease over time. Relaxation depends on the type and grade of steel, namely stress-relieved or low-relaxation type and Grade 250 or Grade 270. Because the stated research program herein worked only with low-relaxation strands in the test girders, the following discussion is limited to low-relaxation strands.

Magura et al. (1964) conducted an extensive investigation of the relaxation properties of prestressing wires. Based on their results, the PCI Committee on Prestress Losses (1975) recommended the following relationship to predict the loss of prestress (*relax*) due to relaxation over the time interval t_1 to t.

Low-relaxation prestressing steel:

$$relax = f_{st}\left[\frac{\log(24t) - \log(24t_1)}{45}\left(\frac{f_{st}}{f_{py}} - 0.55\right)\right], \tag{2.37}$$

in which

$f_{st} / f_{py} \geq 0.55$

where

t_1 = time in days at beginning of interval, ≥ 1/24 days

t = time in days at end of time interval

f_{st} = stress in prestressing steel at time t_1 (psi, MPa)

f_{py} = yield stress (psi, MPa), generally assumed to be $0.90f_{pu}$.

Low relaxation strands are much more popular in prestress applications, as they tend to relax only 25 percent of that for stress-relieved strands.

The predictive equation is the most commonly used in computing prestress relaxation losses and best fit to test data (Magura et al., 1964). Section 2.5.2 of this report contains further information on methods for estimating total prestress losses.

2.5 Prestressed Concrete Behavior

Prestressed concrete construction utilizes two main structural materials: high strength prestressing strands and concrete, taking advantage of the superior qualities of each material. Concrete exhibits excellent compressive properties and very poor tensile properties. Prestressing strands have excellent tensile properties. However, because they are long slender elements, they behave poorly in compression due to buckling. Additionally, the following discussion is limited to a first-order Euler-Bernoulli flexural beam analysis. Prestressed beams are long slender elements in which higher-order shear and torsional effects, including warping, are very small and can be neglected.

Prestressed concrete, employs prestressed steel within the concrete to resist internal tensile stresses occurring through the member cross section. The steel is pretensioned to induce compressive stresses in the concrete. By lowering the centroid of the prestressing steel from the centroid of the concrete section, the resulting eccentricity of the prestress force causes the member to camber upwards and further adds compression in the bottom. In order to cause bottom fiber cracking in the prestressed concrete cross section, the external loads must overcome the internal moment and precompression caused by the prestressing steel and the tensile strength of the concrete. Without the prestress force or internal moment to resist such external forces, the plain (nonprestressed) concrete member will crack under lower applied moments. Therefore, prestressed concrete members are often considered superior to nonprestressed members.

When designing prestressed concrete members, the internal stresses are limited such that externally applied loads do not induce stresses beyond the specified limits. The AASHTO Bridge Specifications (1996) has set these limits as follows.

Stress Limits at the Time of Release (temporary stresses before losses due to creep and shrinkage):

Compressive stresses are limited to $0.60f'_{ci}$ for pretensioned members, where f'_{ci} is the initial concrete compressive strength at the time of release. Tensile stresses have variable limits. In precompressed tensile zones, no limits are set. However, in other tension areas where bonded reinforcement is not provided, the tensile stresses are limited to 200 psi or $3\sqrt{f'_{ci}}$. In areas where this tensile limit is exceeded, bonded reinforcement must be provided such that the maximum tensile stress does not exceed $7.5\sqrt{f'_{ci}}$.

Stress Limits at Service Load Conditions (after losses have occurred):

Compressive stresses are limited to $0.40f'_c$, where f'_c is the concrete compressive strength at 28 days. Again, the tensile stresses are limited depending on variable conditions. For members with bonded reinforcement (including the prestressing steel itself), the tensile stress is limited to $6\sqrt{f'_c}$, but reduced in half for severe corrosive exposure. In areas without bonded reinforcement, the tensile stresses are limited to zero.

2.5.1 Basic Principles of Flexure

Estimating the flexural stresses in a prestressed concrete member is required for design. Typically, a method known as the force-in-the-tendon approach is used for such estimations. This approach separately determines the stresses due to the prestressing force and then adds the stresses due to external actions. The standard concrete stress formula for the force-in-tendon approach is as follows (tension is positive),

$$\sigma = \frac{-P}{A_1} + \frac{-Pec_1}{I_1} + \frac{M_2 c_2}{I_2} + \frac{M_3 c_3}{I_3}, \tag{2.38}$$

where

σ = concrete stress at the fiber of interest

P = total force of the prestressing strands, including losses

A_1 = area of concrete

e = eccentricity of the prestressing strand centroid from the neutral axis of the cross section (positive down)

$c_{1,2,3}$ = distance from the neutral axis of the cross section to the fiber of interest (positive down)

$I_{1,2,3}$ = moment of inertia of the cross section when loads are applied

$M_{2,3}$ = moment due to self weight and externally applied loads.

Although this formulation appears simple and straightforward, several authors of leading textbooks on prestressed concrete have conflicting definitions of the terms used for geometric section properties, A and I (Collins and Mitchell, 1991; Libby, 1990; Lin and Burns, 1981; Naaman, 1982; Nilson, 1987). The subscripts ($_{1,2,3}$) refer to the method of computing geometric properties. Geometric properties can be listed in three categories: gross, net, and transformed. Methods of calculating the three categories of geometric properties are discussed in detail in Section 6.3. What follows is a discussion of these textbook authors' conflicting definitions as applied to the force-in-tendon formulation, resulting in three methods for concrete stress determination: design, transformed and alternative (net).

Naaman (1982) discusses stress determination for prestressed and post-tensioned flexural members. When using the force-in-tendon approach for pretensioned members, geometric section properties used are those of the gross area, while net area properties are used with post-tensioned members. He states that although this is practical, depending on the problem at hand and whether it is a preliminary or final design, either gross or net may be used. However, no detailed explanation or example problems are presented. For non-flexural tension members, he suggests using net properties for terms incorporating the prestress force (subscript 1 in Eqn. 2.38) and transformed properties for applied moment terms (subscripts 2 and 3).

Lin and Burns (1981) discuss two methods for determining stresses in prestressed members: an exact theoretical solution and an approximate solution. The exact theoretical solution uses transformed section properties for all terms in the force-in-tendon formulation, separating noncomposite and composite properties for respective loadings. To determine the most exact stress at any point along the length of the beam, transformed properties are computed at each point to account for draping of strands. This approach uses the seating force prior to release, not the force after losses due to elastic shortening. The authors agree that this exact approach is seldom followed in practice. Rather, the gross or net section is considered. They report that in most cases the error is negligible. An example problem for a prestressed member is illustrated, resulting in less than one percent difference between the exact theoretical solution with transformed properties (and the seating force) and the approximate solution with gross section

properties (and the force after seating). In addition, they noted that any losses that occur on post-tensioned bonded tendons take place on the transformed section as a whole.

Libby (1990) discussed the use of the effective beam cross section. He stated the following:

> "When the prestressing force is applied (at transfer) to pretension a concrete member that does not contain nonprestressed flexural reinforcement, the deformation of the concrete is a function of its net section properties because the concrete alone is compressed by the tensile force in the prestressing steel. ...the prestressing steel shortens and does not assist the concrete in resisting the prestressing force. The net section is defined as the section that results when the area occupied by the tendons (or ducts in the case of post-tensioning) is deducted from the gross section. Because the pre-tensioned reinforcement is bonded to the concrete, when there is a change of strain in the concrete at the level of the prestressed reinforcement after the transfer of the force to the concrete, there must be a corresponding and equal change of strain in the steel. Therefore, when external loads, other than the dead load of the beam, which is acting at the time of prestressing are applied, the deformation of the member is a function of the transformed net section, which can be defined as the section that results when the area of the bonded reinforcement (prestressed and nonprestressed) is transformed into an elastically equivalent area of concrete, with the area of concrete displaced by the reinforcement taken into account. ... In normal pretensioning practice, the effect of the transformed section is small, and little is normally gained by taking these effects into account...."

Libby's illustrative example problem compares stresses due to prestressing based on the gross section with those based on the net section. The ratio of the area of prestressing steel to gross concrete area was 0.76%. Only a slight increase (1.6%) in stresses was noted for the net section over that of the gross section.

Nilson (1987) discussed the calculation of section properties used in determining elastic flexural stresses. He clearly stated the following:

> "for pretensioned construction, the transformed section should be used, in theory, for all calculations. However, the difference in properties of the gross and transformed sections is usually small, permitting calculations to be based on the gross cross section."

Therefore, when using Eqn. (2.38), Nilson recommends that all geometric properties (with subscripts $_{1,2,3}$) be based on the transformed section. However, no consideration is given to the prestressing reinforcement ratio of the section. Nilson also commented that the net section was only considered in post-tensioned construction where tendons passed through ducts of considerable size. Once the tendons were grouted, the transformed section should be used and the gross section may be satisfactory as well.

Collins and Mitchell (1991) have yet another version for applying the force-in-tendon formulation. Their interpretation was presented as follows:

> "If the force in the tendon has been estimated, the stresses in the concrete due to the prestressing can be calculated. These self-equilibrating prestressing stresses are added to the stresses due to external loads to find the total concrete stresses. It is important to recognize that when calculating the self-equilibrating concrete stresses by this 'force-in-the-tendon' approach, the tendon area must be neglected in determining the section properties. When calculating the concrete stresses due to external loads the transformed area of the tendon may be accounted for if the tendon is bonded to the concrete. ... To simplify the calculation of stresses, the gross section properties are often used in determining both the self-equilibrating stresses due to prestress and the stresses due to external loads. This procedure can be unconservative for unbonded, post-tensioned construction if the area of the ducts forms a significant portion of the cross section. For bonded construction, using the gross section properties will be conservative. ..."

Therefore, when using the Collins and Mitchell version, the subscripts 1 and 2 in Eqn. (2.38) refer to geometric properties based on the net section for the force and self-weight moment terms, and subscript 3 refers to the transformed section properties for use with externally applied moment terms.

While each of these textbook authors have defined their own interpretation of the force-in-tendon formulation, they each have differing opinions leaving gaps in the approach. It may still be unclear as to which section properties are used when computing stresses. Summarizing, some specify gross section properties throughout, some suggest transformed section properties throughout, and yet some state a combination of transformed and net section properties should be used. However, most do agree that for the purpose of design, computing stresses based on the

gross section is adequate. Not addressed by each author was the effect that the amount of prestressing reinforcement had on section properties. When computing stresses for analysis, the most accurate estimation is desired and the gross section may not be sufficient. In the case of high strength concrete used in prestressed beams, the reinforcement ratio increases as more steel is placed in the section to equilibrate higher concrete compressive stresses. Reinforcement ratios in normal strength concrete beams are on the order of 0.3 to 0.9 %, where high strength beams can easily exceed 1.5 to 1.8%. For the purpose of this report, three interpretations of the force-in-tendon formulation are discussed, the design method, transformed method, and alternate (net) method.

2.5.1.1 Design Method

Most leading authorities agree that for the purpose of design, the force-in-tendon formulation can be based on the gross cross section. Gross section properties are based on a total cross-sectional area of concrete for both the noncomposite and composite member. When computing the composite section properties, the deck concrete is transformed into an equivalent girder concrete area with the deck centroid remaining as it was prior to transformation. Prestressing steel and mild steel reinforcement are neglected in the determination of gross properties. This procedure is often used because it is simple and gives conservative results.

The standard stress formula from the force-in-tendon approach (Eqn. 2.38), as applied to a composite prestressed member similar to the test girders presented in this report, with tension positive, becomes:

$$\sigma_{design} = \frac{-P}{A_g} + \frac{-Pec_{g,nc}}{I_{g,nc}} + \frac{M_{sw}c_{g,nc}}{I_{g,nc}} + \frac{M_{nc}c_{g,nc}}{I_{g,nc}} + \frac{M_c c_{g,c}}{I_{g,c}}, \qquad (2.39)$$

where σ_{design} is the concrete stress at the fiber of interest and terms remaining were previously defined in Eqn. (2.38). The subscripts 1,2,3 from Eqn. (2.38) have been replaced with gross cross-sectional properties of the noncomposite and composite section, subscripts *nc* and *c*, respectively. M_{nc} is the total moment due to externally applied loads on the noncomposite section, and M_{sw} is the girder self-weight. And finally, M_c is the total moment due to externally applied loads on the composite section.

2.5.1.2 Transformed Method

Transformed section properties can be used to estimate stresses in a prestressed concrete member. The gross concrete area less the total steel area plus the total transformed steel area produces the transformed section. The composite section incorporates the transformation of the deck concrete. The stress formula is similar to the (gross) design method with the exception that all gross properties are replaced with transformed properties (subscript *tr*). The formulation incorporates the noncomposite and composite cross section and becomes:

$$\sigma = \frac{-P}{A_{tr,nc}} + \frac{-Pec_{tr,nc}}{I_{tr,nc}} + \frac{M_{sw}c_{tr,nc}}{I_{tr,nc}} + \frac{M_{nc}c_{tr,nc}}{I_{tr,nc}} + \frac{M_{c}c_{tr,c}}{I_{tr,c}}. \qquad (2.40)$$

As with the design method using gross section properties (Section 2.5.1.1), the moment due to externally applied loads on the noncomposite member, M_{nc}, and the girder dead weight, M_{sw}. Although it is not difficult to transform section properties for this formulation, it is imperative that an accurate estimation of the modular ratio (between the concrete and the prestressing steel) is made. For cross sections that are highly reinforced, the difference between (gross) design method and transformed method may not be negligible. Additionally, to be most accurate, the force P must be the seating force before any losses due to elastic shortening have occurred. This method is not acceptable for computing long term losses because only the initial force prior to elastic shortening is used. Updating the force at various time steps and using transformed section properties will not produce accurate estimations.

2.5.1.3 Alternate (Net) Method

An alternate method is presented here which incorporates a combination of using net section properties and transformed section properties. Determining transformed properties is discussed previously. Net section properties are computed similar to the gross section properties with the exception that the prestressing steel area has been removed from the gross section. The noncomposite section has a net area equal to the gross area less the area of prestressing steel. Applying the section properties accordingly, the stress formulation from Eqn. (2.38) for the alternate method becomes:

$$\sigma = \frac{-P}{A_{net,nc}} + \frac{-Pec_{net,nc}}{I_{net,nc}} + \frac{M_{sw}c_{net,nc}}{I_{net,nc}} + \frac{M_{nc}c_{tr,nc}}{I_{tr,nc}} + \frac{M_{c}c_{tr,c}}{I_{tr,c}} \qquad (2.41)$$

where the variables have been previously defined with the following exceptions. The net section properties (denoted by the subscript *net*) are used only for the noncomposite section on which the prestressing force and self-weight moment act. The prestress force P is the force in the strands after release. The moments due to externally applied loads acting on the noncomposite and composite sections remain unchanged. Collins and Mitchell (1991) and Libby (1990) state that the dead weight, M_{sw}, is acting at the time when the prestressing force is applied, hence the net section must be used. Therefore, if the self-weight is included in the computation of elastic shortening and relaxation (initial) losses, the net section is to be used. Lin and Burns (1981) and Nilson (1987) imply that the concrete is bonded to the strands at the time of prestressing force application and therefore, the transformed section is acting to resist the self weight of the member. In other words, if the self-weight is not included in computing the initial losses, the transformed section should be used. In either case, the noncomposite transformed section resists the self-weight of the composite deck.

2.5.2 Prestress Losses

While prestressed concrete has many advantages, the most significant disadvantage is associated with time dependent effects. Creep and shrinkage of concrete combined with relaxation of the steel reduce the effective prestress in the steel over time. This reduction of stress results in what is more commonly called "prestress losses." The losses are interdependent such that an alteration of stress due to concrete creep simultaneously causes an alteration of rate of steel relaxation. Additionally, shrinkage is taking place at the same time. An overestimation of prestress losses in design may cause excessive camber, while an underestimation in design may result in member cracking under service loads.

Several methods are available for predicting prestress losses, although very little information is available on losses in high strength concrete. Methods assume normal strength concrete behavior and include four components for prestress losses: elastic shortening, creep, shrinkage, and relaxation. Lump sum predictions are accepted in bridge design, as long as reasonable design assumptions are made. AASHTO Bridge Standards (1996) and the PCI Design Handbook (1992) follow simplified acceptable methods. The PCI Committee on Prestress Losses (1975) has recommendations available for estimating prestress losses on a time step basis. Naaman (1982) also has documented a detailed time step method for prestress loss estimation.

Each of these four methods are discussed. The discussion is limited to pretensioned construction using low relaxation prestressing strands and heat curing of normal weight concrete.

2.5.2.1 AASHTO Method

The AASHTO Bridge Design Manual (1993) uses a simplified method to estimate prestress losses. Total losses, Δf_s, are equal to the summation of losses due to elastic shortening, ES, creep of concrete, CR_c, shrinkage of concrete, SH, and steel relaxation, CR_s. Losses are typically computed on a lump sum basis at the following time steps: release, 28-days, deck casting and long term. The following relationships are used to compute each component.

Elastic Shortening, ES:

$$ES = f_{cir}\left(\frac{E_s}{E_{ci}}\right), \tag{2.42}$$

where

f_{cir} = compressive stress at the *cgs* due to prestressing force acting immediately after the force is applied minus the stress due to all dead loads at that time, computed at the section or sections of maximum moment (psi)

E_s = modulus of elasticity of the steel, which AASHTO assumes to be 28×10^6 (psi)

E_{ci} = modulus of elasticity of the concrete at the time the force is applied (psi).

Creep of Concrete, CR_c:

$$CR_c = 12 f_{cir} - 7 f_{cds}, \tag{2.43}$$

where

f_{cds} = compressive stress at the *cgs* due to all dead loads except those accounted for at the time of prestressing (psi).

Shrinkage of Concrete, SH:

$$SH = 17{,}000 - 150RH, \tag{2.44}$$

where

RH = mean ambient relative humidity in percent.

Steel Relaxation, CR_s: (Low-relaxation prestressing steel)

$$CR_s = 5{,}000 - 0.10ES - 0.05(SH + CR_s). \tag{2.45}$$

The total change in strand stress is estimated as the summation of these four loss components, ($\Delta f_{ps} = ES + CR_c + SH + CR_s$). Prestress losses are then computed as the change in strand stress relative to the initial tensioning stress, f_{pi}.

2.5.2.2 PCI Design Handbook Method

The PCI Design Handbook (1992) uses the following method to estimate the total prestress change, *TL*, or change in strand stress, Δf_{ps}. The estimation is based on the report of a task group sponsored by ACI-ASCE Committee 423, Prestressed Concrete.

Elastic Shortening, *ES*:

$$ES = K_{es} f_{cir} \left(\frac{E_s}{E_{ci}} \right), \tag{2.46}$$

where

K_{es} = 1.0 for pretensioned members

E_s = modulus of elasticity of the steel, stated to be about 28.5×10^6 psi

E_{ci} = modulus of elasticity of the concrete, at the time the force is applied (psi).

f_{cir} = net compressive stress due to prestressing force acting at the centroid of the prestressing steel immediately after the prestress is applied (psi)

such that

$$f_{cir} = K_{cir} \left(\frac{P_i}{A_g} \right) - \frac{M_g e}{I_g}, \tag{2.47}$$

and

K_{cir} = 0.9 for pretensioned members

P_i = initial prestress force (after seating and before release)

e = eccentricity of centroid of prestressing steel with respect to the centroid of the concrete cross section

A_g = gross area of concrete section

I_g = gross moment of inertia of concrete section

M_g = moment due to self weight of member and any additional permanent loads at the time of prestressing.

Creep of Concrete, *CR*:

$$CR = K_{cr}\left(\frac{E_s}{E_c}\right)\left(f_{cir} - f_{cds}\right), \tag{2.48}$$

where

K_{cr} = 2.0 for pretensioned members

E_c = modulus of concrete at 28 days

f_{cds} = compressive stress at the level of the prestressing steel due to all dead loads except those accounted for at the time of prestressing (psi).

Shrinkage of Concrete, *SH*:

$$SH = \left(8.2\times10^{-6}\right)K_{sh}E_s\left(1-0.06\frac{V}{S}\right)\left(100-RH\right), \tag{2.49}$$

where

K_{sh} = 1.0 for pretensioned members

V/S = volume to surface area ratio of member

RH = mean ambient relative humidity in percent.

Steel Relaxation, *RE*:

$$RE = [K_{re} - J(SH + CR + ES)]C\,, \tag{2.50}$$

for Grade 270 Low-relaxation prestressing steel where

K_{re} = 5000

J = 0.040

C = a constant based on the ratio of initial prestress to ultimate strength of strands (PCI Handbook). For example: if initially tensioned to 75% of ultimate, C=1.0; if initially tensioned to 69% of ultimate, C=0.70.

The total change in strand stress, *TL*, as this method refers to it, is estimated as the summation of these four loss components, ($TL = \Delta f_{ps} = ES + CR + SH + RE$). Prestress losses are then computed as the change in strand stress relative to the initial tensioning stress, f_{pi}.

2.5.2.3 PCI Committee on Prestress Losses Method

The PCI Committee on Prestress Losses (1975) recommends the following method for predicting losses on a time step basis. Total stress changes, *TL*, (also Δf_{ps}) are equal to the summation of strand stress changes due to elastic shortening, *ES*, creep of concrete, *CR*,

shrinkage of concrete, *SH*, and steel relaxation, *RET*. The report is based on US customary units, and therefore only those are given here. The following relationships are recommended to compute each component.

Elastic Shortening, *ES*:

$$ES = f_{cr}\left(\frac{E_s}{E_{ci}}\right), \tag{2.51}$$

where

f_{cr} = compressive stress due to prestressing force acting immediately after the force is applied minus the stress due to all dead loads at that time (psi)

E_s = modulus of elasticity of the steel (psi)

E_{ci} = modulus of elasticity of the concrete at the time the force is applied (psi).

Creep of Concrete, *CR*:

$$CR = (UCR)(SCF)(MCF)(PCR)(f_c) \tag{2.52}$$

where

$UCR = 95 - 20E_c/10^6 \geq 11$, for normal weight heat-cured concrete

SCF = size and shape of member factor

MCF = age at prestress and length of moist cure factor

$PCR = (AUC)_t - (AUC)_{t1}$ = portion of ultimate creep over the time interval t_1 to t, in which AUC is the estimated variation of creep with time

f_c = net compressive stress at prestress centroid at time t_1, taking into the change in applied load and loss of prestress in the previous interval (psi).

The variables *SCF*, *MCF*, *AUC*, and *PCR* are listed in tables of the reference (PCI Committee on Prestress Losses, 1975) such that linear interpolation can be used to account for variations in the parameters.

Shrinkage of Concrete, *SH*:

$$SH = (USH)(SSF)(PSH) \tag{2.53}$$

where

$USH = 27{,}000 - 3000E_c/10^6 \geq 12{,}000$, ultimate shrinkage of concrete for normal weight concrete, independent of curing (psi)

SSF = size and shape factor, given in reference for linear interpolation

$PSH = (AUS)_t - (AUS)_{t1}$ = portion of ultimate shrinkage over the time interval t_1 to t, in which AUS is the estimated variation of shrinkage with time.

Steel Relaxation, *RET*: (Low-relaxation prestressing steel)

$$RET = f_{st}\left[\frac{\log(24t)-\log(24t_1)}{45}\left(\frac{f_{st}}{f_{py}}-0.55\right)\right], \tag{2.54}$$

with parameters as previously introduced in Eqn. (2.37). The total change in strand stress, *TL*, as this method refers to it, is estimated as the summation of these four loss components, ($TL = \Delta f_{ps} = ES + CR + SH + RET$). Prestress losses are then computed as the change in strand stress relative to the initial tensioning stress, f_{pi}. The PCI Committee recommendations include several example problems for computing prestress losses.

2.5.2.4 Naaman's Time Step Method

Naaman's time step method (Naaman, 1982) is a much more refined model, using the most accurate relationships available for predicting each prestress loss component.

Elastic shortening, *ES*:

$$ES = f_{cir}\left(\frac{E_s}{E_{ci}}\right), \tag{2.55}$$

where parameters were previously defined for Eqn. (2.42).

Although this estimation appears to be the same as the simplified methods, an iterative method is used to approximate the shortening. When the prestressing force is applied, member shortening occurs causing a reduced force, which in turn is a smaller force being applied. The stress due to initial shortening is approximated using the Eqn. (2.55). Subtracting this stress from the initial tensioning stress, and subtracting any loss due to steel relaxation, gives a first approximation of the strand stress. This stress is then converted to a strand force by multiplying by the total area of prestressing steel. Next, the reduced force is used to approximate a new concrete stress using the definition of f_{cir} (Eqn. 2.42). This new concrete stress is multiplied by the modular ratio (E_s/E_{ci}) to compute a new elastic shortening loss. The process is repeated until convergence is achieved, usually in two to three iterations.

Creep of Concrete, *CR*:

Using the relationship for creep of concrete as suggested by ACI Committee 209 (1992), the creep at any time, t, is computed. This equation has been adapted to the time step method by computing the creep over a time interval.

$$CR = \left[\frac{t_2^{\beta}}{\alpha + t_2^{\beta}} - \frac{t_1^{\beta}}{\alpha + t_1^{\beta}}\right] C_u K_{ch} K_{ca} K_{cs} \left[f_{cgs@t1}\left(\frac{E_s}{E_c}\right)\right] \tag{2.56}$$

where

t_1, t_2 = time at beginning and end of time step, respectively

α = 10 for NSC, variable for HSC

β = 0.6 for NSC, variable for HSC

C_u = ultimate creep coefficient, equals 2.35 for normal strength concrete

K_{ch} = relative humidity correction factor

K_{ca} = age of loading correction factor

K_{cs} = shape correction factor

$f_{cgs@t1}$ = prestress at level of strand centroid, at time t_1

E_s = modulus of elasticity of prestressing steel

E_c = modulus of elasticity of concrete at 28 days.

Shrinkage of Concrete, *SH*:

$$SH = 0.157 E_s \varepsilon_{su} K_{sh} K_{ss} \ln\left(\frac{t_2}{t_1}\right), \tag{2.57}$$

where

ε_{su} = ultimate shrinkage strain of concrete

K_{sh} = relative humidity correction factor

K_{ss} = size and shape correction factor.

t_1 = time in days at beginning of interval, $\geq$ 2.08 days

t_2 = time in days at end of time interval, not more than 1214 days (in which 1214 days is considered equivalent to end of service life).

A simple linear relationship between water content and ultimate shrinkage strain is often used in practice,

$$\varepsilon_{su} = \left[2 + \frac{11}{230}(w - 220)\right] 10^{-4}. \tag{2.58}$$

The term w defines the amount of water, in pcy.

Steel Relaxation, Δf_{pR} :

Modified from PCI Committee on Prestress Losses (1975), the following relationship is used for computing low-relaxation prestressing steel loss,

$$\Delta f_{pR} = \frac{f_{ps@t1}}{45}\left(\frac{f_{ps@t1}}{f_{py}} - 0.55\right)\log\left(\frac{t_2}{t_1}\right), \tag{2.59}$$

where parameters were previously defined in Eqn. (2.37).

2.6 Prestressed Concrete Girder Related Research

With the accelerated use of high strength concrete, concerns have arisen regarding the applicability of current bridge design codes. A study conducted by Castrodale et al. (1988b) reviewed both AASHTO and ACI codes for application to high strength concrete based on very limited test data and analytical studies. Although by no means a complete review, the study drew attention to several areas of concern. These concerns included: transfer and development length of strands in high strength concrete girders, prestress losses, camber and deflection limits, flexural behavior of members, and stability of longer span girders. A review of each issue along with code relationships and related studies are discussed.

2.6.1 Transfer and Development Length

Transfer length is defined as the length in which the prestress force is transferred from the strands to the concrete, beginning at a zero concrete force at the end of the member and ending at the end of the transfer zone. Two relationships are commonly used in prestressed concrete design to predict the transfer length of a given diameter prestressing strand. AASHTO (1996) defines the transfer length, L_t, in terms of the strand diameter, d_b, as:

$$L_t = 50 d_b . \tag{2.60}$$

ACI 318 (1995) defines transfer length in terms of strand diameter, d_b, and the effective prestress force, f_{se}, after all losses, as:

$$L_t = \frac{f_{se}}{3} d_b . \tag{2.61}$$

The benefits of high strength concrete can only be fully achieved by placing more prestressing force into the member, typically through the use of larger strands. In 1988, the

Federal Highway Administration (FHWA) issued a moratorium disallowing the use of 0.6 in. (15.2 mm) diameter prestressing strands and introduced a factor of 1.6 on the AASHTO and ACI expressions for development length of smaller diameter strands. The notice was issued due to a lack of experimental research regarding transfer and development length and the use of the larger diameter strand on the typical two inch spacing for prestressed bridge applications. Because of the continued interest to produce high strength concrete girders, several research programs were conducted.

The objective of the research conducted by Deatherage and Burdette (1991) was to investigate transfer and development length of prestressing strands in concrete beams, as well as lateral spacing requirements of the strand. Several strand diameters were considered (including 0.6 in. strand [15.2 mm]), two strand surface conditions (mill and weathered) and two center-to-center lateral spacings (2 in. and 1.75 in. [50.8 mm and 44.5 mm]). For the 5000 psi (34 MPa) concrete mix used, results indicated that the transfer length of strands on 2 in. (50.8 mm) spacings was longer than current AASHTO or ACI codes predict. The specimen with 1.75 in. (44.5 mm) spacing showed lower transfer length. However, the latter specimen contained weathered strand (a more realistic situation), thereby improving the strand bond characteristics. Development length results were within 10 percent of AASHTO/ACI predictions, independent of strand surface condition or lateral spacing.

Research conducted by Russell and Burns (1993) sought to determine the transfer and development length of both 0.5 and 0.6 in. (12.7 and 15.2 mm) diameter strand and the influence of lateral spacing. The study indicated that high concrete strengths at release resulted in shorter transfer lengths, although concrete strength was not a main variable and ranged only from 5,000 to 7,700 psi (34 to 53 MPa). Transfer lengths were 41.6 in. (1057 mm) for single-strand and 42.1 in. (1070 mm) for 3- and 5-strand rectangular specimens and AASHTO type (22 in., 560 mm deep) girders with 2 in. (50.8 mm) center-to-center strand spacing. No splitting cracks were observed for 0.6 in. (15.2 mm) strand on 2 in. (50.8 mm) lateral spacing, and a larger spacing of 2.25 in. (57.2 mm) had no effect on transfer length. A transfer length relationship was suggested in the same form as the ACI 318 (1995) relationship,

$$L_t = \frac{f_{se}}{2} d_b . \qquad (2.62)$$

Mitchell, et al. (1993) specifically studied the influence of high strength concrete and strand diameter on transfer and development length. Concrete strengths ranged from 4,500 to 12,900 psi (31 to 89 MPa) and strand sizes included 3/8, 1/2, and 0.62 in. (9.5, 12.7, and 15.7 mm) diameter. It was shown that an increase in concrete compressive strength at the time of strand release resulted in a reduction of transfer length. Transfer lengths for single strand rectangular specimens (7.9 x 9.8 in. [200 x 250 mm]) ranged from 17.1 to 34.3 in. (435 to 872 mm) for concrete strengths up to 9500 psi (65 MPa). An increase in concrete strength also resulted in a reduction of the strand development length due to a reduction in the flexural bond length. Design expressions for transfer length were proposed which took into account the concrete compressive strength at the time of force transfer and in service. The diameter of the strand appeared to have no additional influence than is currently accounted for in design provisions. From the research, Mitchell suggested a transfer length, L_t, of

$$L_t = 0.33 f_{pi} d_b \sqrt{\frac{3}{f'_{ci}}}, \tag{2.63}$$

where

f_{pi} = the initial after seating strand stress, psi

f'_{ci} = initial concrete compressive strength, psi

d_b = strand diameter, in.

The Mitchell study varied from the current study in two ways. The Mitchell study used the slope-intercept method for determining transfer length and a gradual release method was employed for detensioning the strands. Both of these variations can result in shorter transfer lengths.

The previously mentioned research programs, as well as others that were initiated as a result of the FHWA moratorium, often resulted in conflicting design recommendations for transfer and development length of prestressing strands. In an attempt to reconcile some of the differences, the FHWA (Buckner, 1994, 1995) conducted an independent review of recent research. The expression recommended for transfer length was similar to the ACI 318 relationship, with the exception of using f_{si} in place of f_{se}, such that

$$L_t = \frac{f_{si}}{3} d_b, \tag{2.64}$$

where f_{si} is the strand stress at the end of the transfer zone immediately after release. Buckner reports that the use of the term f_{si} is more rational considering that the transfer length is established at release of the prestress and does not significantly change with time. Recommendations apply to prestressed members with normal weight concrete having a minimum release strength of 3500 psi (24.2 MPa) or higher, a specified compressive strength of 5000 psi (34.5 MPa) or higher, and for Grade 270, seven-wire, low-relaxation, uncoated prestressing strands.

2.6.2 Prestress Losses

Prestress losses are the time dependent effects associated with prestressed concrete behavior and may vary for high strength concrete applications. Material behavior of high strength concrete and how it differs from that of normal strength concrete was discussed in Section 2.2. Several methods for estimating prestress losses were reviewed in Section 2.5.2. These procedures were developed using data from low to normal strength concrete under normal service conditions. The PCI Design Handbook (1992) notes that for designs varying from normal (i.e. high strength concrete), more complex and detailed analyses may be necessary. Prominent research groups have recorded prestress losses in high strength prestressed concrete girders. Specific details and results of the tests are given in Section 2.6.4 while discussing each prestressed girder research program as a whole.

2.6.3 Camber and Deflection Limitations

Estimating camber and deflection of precast prestressed members is complex due to the interaction of prestress losses, loadings, and concrete strength gain with time. Calculations consider prestressing effects, dead load, live load, erection loads, creep and shrinkage of concrete, and steel relaxation. The initial camber is defined as an upward deflection due to the eccentricity of the prestressing force at the time of prestress transfer less the downward deflection due to the self weight of the member. It should be noted that the PCI Design Handbook (1992) states that prestressed members are not designed for a specified camber or deflection, rather only their inherent existence is specified. Serviceability deflection limits are specified for steel girders to indirectly account for fatigue in the AASHTO code (1996). Prestressed concrete girders have no such limits, however it is general practice to stay within the

limits as defined for steel girders. The span-to-deflection limit of 800 is used as a typical rule-of-thumb guideline.

Martin (1977) discussed a rational method of estimation using multipliers to predict camber and deflection at erection and final (end of service life). Suggested multipliers for prestressed concrete beams both with and without composite topping are listed in Table 2.2. Section 4.6 of the PCI Design Handbook (1992) uses these multipliers in example calculations to estimate camber and deflection, similar to the method used in this study. Because these multipliers were based on general experience from use of normal strength concrete, they may inadequately predict camber and deflection of precast prestressed members using high strength concrete. Little information is currently available for estimating camber and deflections of prestressed high strength concrete members.

Table 2.2 Suggested Multipliers for Estimating Long-term Camber and Deflections

	Without Composite Topping	With Composite Topping
At Erection:		
(1) Deflection (downward) component - apply to the elastic deflection due to the member weight at release of prestress.	1.85	1.85
(2) Camber (upward) component - apply to the elastic camber due to prestress at time of release of prestress.	1.8	1.8
At Final:		
(3) Deflection (downward) component - apply to deflection calculated in (1).	2.7	2.4
(4) Camber (upward) component - apply to camber calculated in (2).	2.45	2.2
(5) Deflection (downward) - apply to elastic deflection due to superimposed dead load only.	3	3
(6) Deflection (downward) - apply to elastic deflection caused by the composite topping.	--	2.3

Kelly, Bradberry and Breen (1988) field instrumented eight 127 ft (38.7 m) long prestressed AASHTO Type IV bridge girders. Four of the girders were in one bridge, while the remaining four were in a second bridge. The girders were instrumented at the time of casting and monitored for three years following. Two of the girders in each bridge were instrumented to measure concrete surface strains, prestressing strand strains, internal concrete temperatures, and camber or deflection. The remaining girders were instrumented to measure only concrete surface

strains and camber. The 28-day concrete compressive strength for the mix was 8620 psi (59.4 MPa). Tests were made to determine the concrete modulus, and creep and shrinkage of the concrete. Some of the conclusions of this study were as follows:

1. The AASHTO equation for predicting the elastic modulus of concrete should not be used for predicting deflections of high strength concrete members (f'c > 9000 psi, 62.1 MPa). It was recommended that the following relationship for the concrete modulus of elasticity be used in lieu of the one presently proposed by AASHTO:

$$E_c = 40{,}000\sqrt{f_c'} + 1.5\times10^{-6}\ psi. \qquad (2.65)$$

2. Elastic camber and deflection of high strength concrete girders can be accurately predicted using moment area equations if actual concrete strengths are known and used.
3. The rate of concrete strength gain, the concrete creep coefficient, the relative humidity, the age of concrete at release, and the construction schedule significantly affected the time-dependent camber or deflection of a girder.

A camber study of Mn/DOT prestressed bridge girders was conducted by Woolf (1998) to investigate the relationship between predicted and measured girder cambers. Three camber prediction methods were used for comparison: the PCI Multiplier Method reviewed previously, a time-step approach recommended by Branson (1971), and a computer program "CRACK" proposed by Ghali (1991). Although high strength girders were not considered in the study, it was concluded that careful modeling of material properties was required to predict accurate cambers. Camber was most influenced by the actual prestress force in each girder, however girders cast on the same bed and of the same concrete mix could produce initial camber differences of 2 to 10%. Camber was not significantly influenced by the prestress modulus of elasticity or the weight of the girder, but was more sensitive to changes in the initial jacking force, concrete modulus of elasticity and ultimate creep coefficient. The PCI Method gave reasonable long-term camber results compared with the more detailed methods considered.

2.6.4 Recent Pertinent Research of Prestressed Girders

Behavior of prestressed concrete girders encompasses time-dependent behavior as well as response to all types of load testing. This section contains a brief summary of selected recent experimental research regarding high strength concrete used in prestressed highway bridges. Construction Technology Laboratory (CTL) in conjunction with Tulane University and the

University of Texas at Austin have performed a significant amount of research into the use of high strength concrete in highway structures.

Reese (1983)

Fatigue strength is rarely directly considered in the design of prestressed concrete structures. No failures of prestressed concrete girders in service due to structural fatigue are known to exist in the United States (Reese, 1983). The fatigue life of cracked prestressed concrete girders is primarily a function of strand cyclic stress range. Once a flexural member cracks, prestressing strands and reinforcing bars, if present, must provide the internal tensile resistance. The failure mode is generally by progressive fatigue or fracture of the prestressing strand's individual wires.

Reese (1983) provides a comprehensive review of seventeen flexural fatigue test programs. Strand stress ranges or information to adequately determine strand stress ranges was provided in only six of the programs. In order to obtain more accurate fatigue information, three full-size Texas Type C prestressed concrete bridge girders were fabricated and tested. The 50 ft (15.2 m) long beams used 0.5 in (12.7 mm) diameter Gr. 270 prestressing strands. Concrete strengths ranged from 5350 to 6350 psi (37 to 44 MPa) for the test girders. Each girder had a 77 in. (2.0 m) wide deck slab that was 7.75 in. (197 mm) thick.

Maximum fatigue loads corresponded to nominal concrete tensile stresses of $7.25\sqrt{f'_c}$ to $10.5\sqrt{f'_c}$, producing strand stress ranges from 24.2 to 32.5 ksi (165 to 225 MPa) which resulted in fatigue failures after 595,000 to 1,480,000 cycles. The strand stress ranges in the test specimens were approximately 20 percent higher under dynamic loading than readings taken at identical loads during intermittent static tests. Reese concluded that the use of dynamic load and impact factors during design should be used to account for this additional range.

Overman, Breen and Frank (Report 300-2F, 1984)

The results of this study indicate that 1977 AASHTO indirect design criteria for flexural fatigue strength of pretensioned concrete girders through limitation of the nominal tensile stress in the precompressed tensile zone will not ensure adequate fatigue life. For the eleven full scale girders tested, split cylinder strengths of approximately $6.5\sqrt{f'_c}$ were a more realistic predictor in determining cracking stresses than those indicated by the modulus of rupture of $7.5\sqrt{f'_c}$. The maximum girder concrete strength tested was 7100 psi (49 MPa). It was found that pretensioned concrete bridge girders without well-distributed, confined passive reinforcement which were actually subjected to loads producing nominal tensile stresses of $6\sqrt{f'_c}$ could fail as a result of

fatigue of prestressing strands at less than 3 million cycles. The tests indicated extremely detrimental effects of occasional modest overload cycles and the marked influence of strand stress ranges due to excessive prestress losses. The authors noted a cracked section stiffness index (EI) of approximately 20 percent of the uncracked value can conservatively be used to estimate deflections due to loads above the zero tension load.

Castrodale, et al. (Report 381-3, 1988a)

In this research project, Castrodale, Burns and Kreger (1988a) examined the stress transfer characteristics of 0.5 in. (13 mm) diameter low-relaxation strand in normal and high strength concrete specimen. In addition, two one-third scale Type IV girder specimens were fabricated with 12,000 psi (83 MPa) concrete and tested in flexure to evaluate current design provisions and analysis techniques. They concluded the following:

1. The 1984 AASHTO expression for estimating transfer length was conservative for high strength concrete.
2. The maximum usable concrete strain to failure was lower for high strength concrete than for normal strength concrete.
3. Placement of high strength concrete in narrow congested sections is possible through the use of high-range water reducers (superplasticizers).

Castrodale, et al. (Report 381-4F, 1988b)

Researchers performed a review of the AASHTO and ACI Codes, current practices, previous tests, and recent literature to determine the safety and efficiency of using high strength concrete in prestressed bridge girders. Selected girder cross sections were reviewed to determine the sensitivity of different design parameters and to determine the effectiveness of those cross sections with the use of high strength concrete. Some of their findings include:

1. The AASHTO and ACI simplified flexural design approach for strength appears to provide good, conservative estimates of the capacity.
2. Current expressions for determining strand stress at ultimate appear to be adequate.
3. Further study should be conducted to determine the effects that concrete strength has on all aspects of design, including lateral stability, fatigue, cracking, and deflections.

Bruce et al. (1994)

The objective of this investigation was to evaluate the feasibility of using high strength concrete in the design and construction of highway bridges. Four full-size prestressed bulb-tee

girders were fabricated and tested as a part of the program. Early-age flexure and shear strength tests were conducted on two bulb-tee specimens. The third specimen was used for evaluation of long-term static load behavior followed by late-age flexural strength test. The fourth specimen was subjected to a fatigue test followed by a flexural strength test. The specimens were 54-in. (1.4 m) deep bulb-tee sections with a 6 in. (152 mm) thick web. Each girder specimen was 70 ft (21 m) long and had a design 28-day compressive strength of 10,000 psi (69 MPa). Prior to testing, three of the four bulb-tee specimens had a 9.5 in. (240 mm) thick and 10 ft (3 m) wide deck added.

The high strength girders performed adequately with respect to the design requirements of the AASHTO Standard Specifications for Highway Bridges (1996). Transfer lengths were consistently less than predicted. Girder camber/deflection measurements, made under various loading conditions up to and including the design service load, were reasonably consistent with deflections calculated using conventional methods. Early age losses due to elastic shortening were in reasonable agreement with predictions, and measured prestress losses at 28-days were significantly less than values calculated using AASHTO provisions and recommendations of the PCI Committee on Prestress Losses (1975). AASHTO equations for calculating flexural cracking moment, concrete flexural shear strength, and flexural strength provided a conservative prediction of the girder specimen flexural properties.

It was concluded that the provisions of AASHTO were conservatively applicable for members with concrete compressive strengths up to 10,000 psi (69 MPa). Results of the program demonstrated several potential benefits of utilizing high strength concrete for highway bridge structures including larger girder spacing and lower prestress losses. Therefore, the use of high strength concrete for highway bridges was recommended. However, no insight was given to the use high strength girders for very long spans where factors such as creep may significantly influence behavior.

2.6.5 Stability

With the use of higher strength concretes to increase the span length of girders comes the concern of lateral stability. Today, manufacturers are capable of producing longer span lengths. However, these lengths are typically limited by the mode of transportation and allowable gross vehicle weight rather than design restrictions and stability concerns.

In 1971, Anderson (1971a, 1971b) noted that lateral stability of long beams lifted by cranes could be substantially improved by locating the lifting loops away from the ends and closer to the center of the beam. Further study in the late 1980's by Imper and Laszlo (1987) noted that shortening the handling span was extremely difficult without exceeding the maximum allowable fiber stresses. They suggested other options including increasing the concrete strength. This would increase the modulus of elasticity of the concrete, thereby increasing the beam stiffness. They also noted that bracing the member to increase the weak axis moment of inertia would be effective. This has been most commonly used in the past.

Castrodale et al. (1988b) compared several girder cross sections for lateral stability of hanging beams (i.e. beams lifted by cranes) and concluded the following. Eccentricity of the lifting points has a significant effect on lateral stability of girders and must be considered in design. The use of high strength concrete (to 12,000 psi [83 MPa]) was most effective when used to increase capacity for a given span rather than to increase the maximum lifting span. Sections with greater weak-axis moments of inertia were most stable.

Mast (1989) noted that lateral buckling of the type described by Timoshenko (1961) is seldom critical in a concrete beam, but rather stability of long span concrete girders can be considered as a rolling issue. He generalized that when a beam is lifted, a combination of the initial imperfections (alignment) and the eccentricity of the lifting hooks may cause the beam to tilt. This in turn causes the beam to bend and deflect progressively about the weak axis. As the section becomes cracked, the phenomenon increases rapidly. This phenomenon may occur even with a slight lifting. The beam may or may not stabilize itself, and could lead to failure due to bending about the weak axis.

Mast developed the basic theory of roll flexibility for prestressed concrete girders. By showing that the torsional stiffness of concrete I-beams with flanges and web thicknesses greater than 6 in. (150 mm) was much larger than the roll stiffness, the problem reduced from a buckling problem to a simple bending and equilibrium problem. Hence, a simple method for analysis of lateral stability of hanging beams was developed. The method was applicable to all concrete strengths provided accurate estimations were made for the concrete material properties and prestress force. The 4th Edition of the PCI Design Handbook (1992) has included Mast's theory of roll flexibility in the consideration of stability during handling.

Mast also discussed several practices for increasing stability. Those practices include raising the roll axis of the concrete member by providing a yoke above it and adding material to the bottom flange to lower the section center of gravity to increase the weak axis moment of inertia. However, modifying the cross section was typically not an option with standard bridge girder sections.

2.7 Numerical Modeling of Composite Girders

Successful designs require accurate predictions of deformations and stresses during all stages of construction and service. An accurate tool is helpful for optimizing designs for efficiency and economy. This is especially true for higher concrete strengths used to obtain longer members. There is software available to allow the engineer to optimize a design within AASHTO requirements. Other tools are available to predict losses, stress ranges, crack patterns, and deflection. Design tools, as well as analytical tools used for comparison of predicted behavior to actual field data, are briefly discussed.

2.7.1 Program SPAN

SPAN (Leap Software, 1990) was developed specifically for the engineering community. It is a design program for simply-supported pretensioned concrete bridge girders. The program selects the strand pattern for a given cross section and span length based on AASHTO Specifications. Prestress losses, camber and stresses along the length of the beam are tabulated for a predetermined construction sequence. User friendliness allows the engineer to quickly optimize the design using several layout options (i.e. girder spacings and sizes).

The analysis used in computing losses, camber and stresses is simple and straightforward. Losses are based on the simplified AASHTO method, reviewed in *Section 2.5.2*. The moment-area method of analysis is used to determine initial camber. Long-term camber predictions are based on the PCI Multiplier Method (Section 2.6.3). The force-in-tendon approach is used for determining stresses, and is based on gross cross-sectional properties. Prestressing strand material properties are predefined by selecting a grade and size of strand. Design compressive strengths at release and 28-days are required as input and the modulus of elasticity relationship is based on ACI 318 (1995). However, no modifications can be made for high strength concrete material properties such as changes to the modulus of elasticity or ultimate creep characteristics,

although this program is one of the most generally accepted programs available for current bridge design.

2.7.2 Program Pbeam

Suttikan's *Pbeam* program (1978) was developed at the University of Texas at Austin for analysis of initial and time dependent responses for partially or fully prestressed concrete members. It accounts for the nonlinearity and the time-dependent effects of the materials including creep, shrinkage, stress relaxation and strength. Members can have any cross section, composite or noncomposite deck action, and can be subjected to various loading conditions to simulate actual construction sequences and load histories.

The following assumptions and limitations, as stated directly by Suttikan (1978) were made in the development of the program.

"1. Beams are straight in their original positions and are of cross-sectional shape having one axis of symmetry.
2. Bernoulli's hypothesis holds, i.e. strain increment distributions vary linearly through the depths of the beams.
3. The deformations (strains and curvatures) are small although the displacements (horizontal, vertical, and rotational) can be any size.
4. Shear deformation is negligible.
5. No out of plane movement is considered, i.e. it is assumed that no lateral or local buckling occurs.
6. Only statically applied loads in the plane passing through the axis of symmetry of the cross section are considered.
7. Material properties in the beams can be represented by the uniaxial behaviors of those materials.
8. Equilibrium equations are written in the deformed state.
9. Soil and other restraints can be represented by sets of linear or nonlinear springs."

A discrete element method was used to analyze instantaneous responses and a step-by-step method was used to determine the time-dependent responses. A rigid piston with an axial spring, two rotational springs, and two rigid end blocks (developed by Suttikan) defined the mechanical

model used throughout. The beam was idealized as a straight line passing through its centroid and then modeled by a series of mechanical models connecting end to end at nodal points. The program was shown to predict behavior of several beams within reasonable accuracy of field data.

Several options were available for defining stress-strain curves and time dependent effects. Internally generated models were provided, or an option was available to input experimental values as user-defined models. This was possible by inputting discrete points to define piecewise linear relationships for all material properties. Results using the user-defined models for high strength concrete could be compared with results generated from normal strength concrete relationships. Output results included forces, concrete and steel strains, and displacements at various heights through the member and along the length for any given time-step. Assumptions and geometric considerations of the test girders in this project are discussed in Section 6.4. Results from *Pbeam* are provided for each girder (Chapters Seven through Ten).

CHAPTER 3 FEASIBILITY OF HIGH STRENGTH CONCRETE BRIDGE GIRDERS

3.1..Introduction to the Parametric Study

Several factors influence the design and behavior of prestressed concrete bridge girders when using higher concrete strengths. The geometric shape of the member, strand size and grade, the design concrete strength, and related properties are key factors in determining maximum girder span lengths and transverse spacings. A parametric study to investigate the effects of these factors and to determine the viability of using high strength concrete for Minnesota prestressed bridge girders was performed and is presented. A typical bridge width and slab thickness was assumed for consistency in design. Bridge dimensions, girder dimensions and properties, concrete properties, strand properties, and design loading assumptions are discussed.

A computer program, SPAN (Leap Software, 1990), was used to determine the number and location of prestressing strands required for a given span. The strand pattern and supplemental reinforcing was chosen to satisfy allowable stresses at all locations along the girder. The maximum span length, required number of strands, and strand pattern were determined as a function of a given set of loading parameters while the concrete strengths and transverse girder spacings were varied. Ultimate capacity and the cracking load, as well as horizontal and vertical shear, were computed to verify the acceptance of a final design for each combination. Based on these results, curves were generated to show the effect of several variables. The methodology of the computer analysis and the results are discussed.

3.2 Assumptions of the Parametric Study

3.2.1 Bridge Data

This study concentrated on simple span, non-skewed, prestressed concrete girder bridges. A typical bridge cross section is shown in Figure 3.1. An overall bridge width of 52 ft. (16 m) was used with a roadway width of 48 ft. (15 m) to accommodate four 12 ft. (3.7 m) traffic lanes. Transverse girder spacings were varied at 4, 7, 10 and 12 ft. (1.2, 2.1, 3.1, and 3.7 m). The respective number of beam lines for the cross sections was 13, 8, 5, and 5. The composite bridge deck was assumed to have a constant thickness of 7 in. (180 mm) plus a 2 in. (51 mm) wearing

course and a 1 in. (25 mm) haunch above each girder. Unshored construction was assumed for the cast-in-place deck.

3.2.2 Girder and Deck Data

Five standard Minnesota Department of Transportation (Mn/DOT) bridge girder shapes were investigated, including the 45M, 54M, 63I, 72I, and 81I. The number in each title signifies the noncomposite girder height in inches. A typical girder cross section with a 4 ft. (1.2 m) composite deck is illustrated in Figure 3.2. Each girder has a top width of 30 in. (760 mm), a bottom width of 26 in. (660 mm), a web thickness of 6 in. (150 mm), and a varying web height 20.5 in. (520 mm) less than the overall noncomposite height. Noncomposite section properties as used by Mn/DOT personnel in the design of bridges are tabulated in Table 3.1. Composite section properties are dependent on transverse girder spacing, albeit the overall composite height was always the noncomposite girder height plus a 1 in. (25 mm) haunch plus a 9 in. (230 mm) total deck thickness independent of transverse spacing. Only interior girders were investigated; no fascia beams or exterior girders were considered.

Table 3.1 Noncomposite Section Properties Used in Parametric Study

Mn/DOT Girder	45M	54M	63I	72I	81I
Height, in. [mm]	45 [1143]	54 [1370]	63 [1600]	72 [1830]	81 [2060]
Area, in^2 [m^2]	624 [0.403]	678 [0.437]	729 [0.473]	783 [0.505]	837 [0.540]
Weight, plf [kN/m]	672 [9.89]	730 [10.7]	785 [11.6]	843 [12.4]	901 [13.3]
Height to the neutral axis from bottom, in. [mm]	22.34 [567]	26.75 [679]	31.10 [790]	35.50 [902]	39.90 [1010]
I, in^4 [m^4]	167,048 [0.070]	265,828 [0.111]	390,160 [0.162]	545,520 [0.227]	731,966 [0.305]
S_b, in^3 [m^3]	7476 [0.123]	9937 [0.163]	12545 [0.206]	15358 [0.252]	18345 [0.301]

Reference: Mn/DOT Bridge Design Manual, 1991

Design spans were considered in 1 ft. (3.1 m) increments. Typically, the end of beam to the centerline of bearing distance is 7.5 in. (190 mm). Therefore, the overall (release) span was the design span plus 1.25 ft. (380 mm).

A standard Mn/DOT deck was used throughout this parametric study. The slab thickness was 7 in. (180 mm) topped by a 2 in. (51 mm) wearing course. A 1 in. (25 mm) haunch was placed over the girder with a width equal to that of the girder top flange (30 in. [760 mm]). In

actual bridges, the haunch thickness typically varies over the length of the girder with each bridge design to account for camber variations between girders. However, the haunch thickness was held constant for the purpose of this study.

3.2.3 Material Data

Four materials were used for the basis of this parametric study: concrete used in the noncomposite girder, concrete used for the composite deck, mild steel reinforcement and the prestressing steel. Properties assumed for each material are presented.

3.2.3.1 Concrete Girder Properties - Parametric Study

Twenty-eight day concrete compressive strengths investigated for the girders ranged from 7000 psi (48 MPa) to a maximum of 15,000 psi (103 MPa). The 7000 psi (48 MPa) minimum was chosen to be consistent with the concrete strength typically specified for current Minnesota prestressed concrete bridge girders. Intermediate concrete strengths considered were 10,000 and 12,000 psi (69 and 83 MPa).

Material properties used in current design practice are based on data available for normal strength concrete ($f'_c < 8000$ psi). Properties that vary for high strength concrete were reviewed in Section 2.2. Expressions for high strength concrete material properties were incorporated into the parametric study to investigate their effects on design. These expressions, how they were varied and their effects on design are discussed in the sections which follow.

A few relationships that remained unchanged were the ratio of release strength to 28-day compressive strength, allowable stresses, and the assumed unit weight of concrete. A release compressive strength at 18 hours was assumed to be 85 percent of the 28-day compressive strength under a relative humidity of 75% and was limited to a maximum of 10,000 psi (69 MPa) at 18 hours. Note, however, the companion materials study at the University of Minnesota (Mokhtarzadeh, 1996) determined that 18-24 hour compressive strengths maintained the 85% f'_c relationship for high strength concrete and strengths could exceed 10,000 psi (69 MPa) in less than 24 hours using materials that were readily available in Minnesota. Concrete tensile and compressive stress allowables, at both release and 28-days, were determined in accordance with the AASHTO Specifications (1993) and were reviewed in Section 2.5. A concrete weight of 155 pcf (2480 kg/m^3) was assumed for the girder in accordance with the Mn/DOT Prestressed Girder Program (Bridge Design Manual, 1991, Section 5-392.502).

3.2.3.2 Concrete Deck Properties - Parametric Study

A concrete deck design strength of 4000 psi (28 MPa) in accordance with Mn/DOT standards was assumed for the benchmark. Concrete deck strengths of 7000 and 10,000 psi (48 and 69 MPa) were used in a few cases to investigate the effect of deck strength. Material property relationships for normal strength concrete were used for deck strengths less than 10,000 psi (69 MPa). High strength concrete relationships as reviewed in Section 2.2 were used for the higher deck strength. The deck was assumed to be 150 pcf (2400 kg/m^3) normal weight concrete. Lightweight concrete was not considered in this study.

3.2.3.3 Prestressing Strand and Reinforcing Steel Properties - Parametric Study

To allow for the maximum girder span with the least number of strands, 0.6 in. (15.2 mm) diameter Grade 270 ksi (1860 MPa) low-relaxation type strands were used for the majority of this study. For comparison purposes, 0.5 in. (12.7 mm) diameter strands and Grade 300 ksi (2070 MPa) low-relaxation type strands were also considered. The initial prestress force was taken as 75% of the ultimate strength. Basic transfer length was calculated at 50 times the strand diameter. Basic development lengths were calculated in accordance with the AASHTO Specifications (1993, Eqn. 9-32) using transfer and development length multipliers of 1.0 and 1.6 for bonded lengths, respectively. Strand geometric and material properties are listed in Table 3.2.

Table 3.2 Prestressing Strand Properties Used in Parametric Study

Strand Geometric Properties		
Strand Diameter, in. [mm]	0.50 [12.7]	0.60 [15.2]
Strand Area, in^2 [mm^2]	0.153 [99]	0.215 [139]
Basic Transfer Length, in. [mm]	25 [635]	30 [762]
Basic Development Length, in. [mm]	Eqn. 9-32	Eqn. 9-32
Strand Material Properties [1]		
Ultimate Strength, f'_s ksi [MPa]	270 [1860]	300 [2070]
Initial Prestress, 75% f'_s ksi [MPa]	203 [1395]	225 [1550]
Modulus of Elasticity, E_s ksi [MPa]	28,000 [193,000]	28,000 [193,000]

[1] Strand material properties are independent of strand diameter.

Prestressing strands were placed in the section as either straight strands or strands that were draped at 40% of the length to the end of each member. Bundling and shielding of strands were

not considered in this study because they are uncommon practices in Minnesota prestressed bridge girders.

Mild steel reinforcing was assumed to be Grade 60 for both tension and shear. Standard Mn/DOT details required four No. 8 bars (1 in. diameter [25 mm]) to be placed in the top flange of every girder for the entire length. The modulus of elasticity for the mild steel reinforcement was assumed to be 29,000 ksi (200 GPa).

3.2.4 Design Aids

Analysis and design followed guidelines as specified in the following codes and manuals:

- ACI 318 Building Code Requirements for Reinforced Concrete and Commentary, 1995
- AASHTO Standard Specifications for Highway Bridges, Fifteenth Edition, 1993
- Mn/DOT Bridge Design Manual, 1991 update
- Mn/DOT Bridge Details Manual, 1991 update
- Mn/DOT Bridge Standard Plans Manual, 1991 update
- Mn/DOT Standard Specification for Construction, 1988 edition.

Loadings used in the design of the prestressed bridge girders were grouped into two areas: loads acting on the noncomposite section and loads acting on the composite section. A discussion of what types of loads were included in each category and the assumed values of each load type follows.

Noncomposite loading includes the self weight of the girder, the prestress force induced through the strands, and any additional loads up to the time at which the deck has cured such that it can resist loads. The self weight of girders included in this study were listed in Table 3.1. The prestress force is dependent on the number and type of strands used, and subject to prestress losses. The girders in this study were assumed to be placed in a bridge using unshored construction techniques. Therefore, diaphragm loads and the bridge deck were also considered noncomposite loads. Diaphragm loads were not changed for each transverse spacing, rather the following loads, as typically used in design, were used. To simulate the load due to diaphragm placement prior to deck placement, a superimposed dead load (SDL) of 20 plf (290 N/m) was applied to girders assumed spaced at 4 and 7 ft. (1.2 and 2.1 m) on centers. Similarly, an SDL of 30 plf (440 N/m) was applied to girders assumed spaced at 10 and 12 ft. (3.0 and 3.7 m). An

SDL was also applied to simulate the bridge deck self weight based on dimensions discussed in Section 3.2.2.

Loading on the composite section included all superimposed dead loads (SDL) and live loads occurring after deck placement and curing. The SDL on the composite section (after deck placement and curing) was assumed to include the following:

- 25 psf (1.2 kPa) to simulate a 2 in. (50 mm) low slump (nonstructural) wearing course
- 17 psf (0.8 kPa) to simulate an allowable for a future wearing course and a guard rail load: 1/3 of the load to first interior girder for transverse girder spacings of 4 ft. and 7 ft., 2 of load for 10 and 12 ft. spacings. A typical J-rail (guard rail) barrier load was assumed.

The total superimposed dead loads for the composite girders are tabulated in Table 3.3.

Table 3.3 Design Loads for Variable Transverse Girder Spacings

GIRDER SPACING:	4 ft.	7 ft.	10 ft.	12 ft.
SDL on noncomposite	20 plf + self wt + prestress + deck wt	20 plf + self wt + prestress + deck wt	30 plf + self wt + prestress + deck wt	30 plf + self wt + prestress + deck wt
SDL on composite	25 psf + future all + rail load = 303 plf	= 429 plf	= 623 plf	= 707 plf
Live Load	HS-25 & Military	HS-25 & Military	HS-25 & Military	HS-25 & Military

All span lengths discussed in this study were designed to carry the HS-25 standard truck and lane loading. Spans were also checked for military loading, although this loading generally governs simply supported spans of 40 ft. (12.2 m) or less and was not a controlling factor in this study. Distribution of wheel loads, the impact factor, and loading combinations were calculated in accordance with AASHTO Specifications (1993) and for completeness are listed.

Distribution of Wheel Loads, *D.F.*:

(Prestressed concrete girders, bridge of two or more traffic lanes, per wheel)

$$D.F. = \frac{S}{5.5}, \tag{3.1}$$

where S = average girder spacing.

Impact Factor, I:

$$I = \frac{50}{(L+125)} \leq 0.30, \tag{3.2}$$

where

L = length of span in feet.

Loading Combinations:

Service Load Design:

$$Group1 = 1.0x[1.0(DL)+1.0(LL+I)], \tag{3.3}$$

Load Factor Design:

$$Group1 = 1.3x[1.0(DL)+1.67(LL+I)], \tag{3.4}$$

where

DL = Dead Loads

LL = Live Loads

I = Impact Factor.

3.2.5 Prestress Losses

Total losses are a stress loss in the prestressing strands due to a combination of creep and shrinkage of concrete, elastic shortening of the member, and steel relaxation of the strands. Losses due to elastic shortening, creep and shrinkage may change from expected when used in conjunction with high strength concrete instead of normal strength concrete. ACI Committee 363 (1984) states that shrinkage for high strength concrete is similar to that of normal strength concrete and creep is expected to be the same because higher strength concretes are subjected to higher stresses. The parametric study benchmark determined losses for elastic shortening, shrinkage and creep of concrete based on the AASHTO Specifications (1993). Losses for steel relaxation were computed in accordance with the PCI Design Handbook (1992). These methods were reviewed in Section 2.5.2.

3.3 Design Methodology of the Parametric Study

The computer program SPAN, developed by LEAP Software, Inc. (1990) was used to design the girders in this phase of the study. Based on user defined loads, transverse girder spacing, and a given girder cross section, the number of prestressing strands and a strand pattern was

determined for a given length, such that stresses along the beam were within allowable limits. Flexure and shear stresses were checked at release (18 hours), final (all service loads applied), and ultimate capacity. The minimum practical length was taken as the larger of a span of 80 ft. (24.5 m) or a span that required at least 12 strands.

The standard Mn/DOT template for strand placement was used, starting at 2 in. (50.8 mm) from bottom moving up in 2 in. (50.8 mm) layers: 3 rows of 12 strands, 1 row of 6 strands, additional rows of 2 strands in the web to a maximum of 3 in. (76 mm) below the top of the girder. A minimum number of strands were determined for a given length such that midspan stresses were within allowable stress limits at both release and final. Strands within the web were draped to reduce end stresses where needed, Figure 3.3(a). If draping was found to be inadequate in maintaining end stresses within allowable concrete stress limits, three alternatives were considered.

First, if only the tensile stresses at the top of the girder were exceeded, tension steel was added, Figure 3.3(b). The Mn/DOT standard detail requires four No. 8 bars placed in the top flange of the girder, independent of cross-sectional stresses. However, tensile stresses must still be within allowable limits as specified in AASHTO for maximum tension with bonded reinforcement (see Section 2.5). If allowable stresses were still not met, the second option was to vary the strand pattern allowing for more strands higher in the web at midspan so that more strands could be draped, Figure 3.3(c). The third and final option was to add additional strands in the web for draping, but care was taken so midspan compressive stresses were not exceeded, Figure 3.3(d). Strands were always added in pairs symmetrical about the centerline of the section to avoid minor axis bending.

Once allowable stress limits for service loads were met at the midspan and ends for both release and final conditions, stresses were calculated and compared with allowable limits at tenth points along the girder, at the hold down points ($0.4L$), at $H/2$ (L is the span length and H is the overall member depth), and at the prestress transfer point. Ultimate capacity was determined, as well as horizontal and vertical shear values at service and ultimate limit states. Cracking load criterion was also checked. Camber and deflection computations were calculated at release (18 hours), erection (28 days) and final (end of service life). Only after all the above requirements were met (i.e., allowable stresses, ultimate flexural and shear capacities, and cracking load) was the section said to be in a final design state.

For each of the girder cross sections, maximum lengths for varying concrete strength were determined. A coarse mesh procedure was initially used in which the number of strands required for a given cross section and spacing were determined for span lengths in 10 ft. (3.0 m) increments until the span length was such that allowable concrete stress limits could not be met. A fine mesh procedure was then used by reducing the "over-stressed" span length by a one foot increment until a maximum span length was determined. The final section was then chosen when the allowable stresses along the entire length of the girder (investigated at one-tenth points) were met for a given strand pattern.

3.4 Results of the Parametric Study

The parametric study was separated into two components. The first component served as a benchmark. In this case, several parameters were investigated to reveal the response of increasing concrete strength on design. Current design standards were assumed for the benchmark case. That is, normal strength concrete relationships remained unchanged as the concrete strength was increased. The second portion of the parametric study included the effect of changing not only the concrete strength, but also changing the relationships that might accompany high strength concrete.

Using the basic assumptions and design methodology discussed previously, five Mn/DOT girder sections were investigated using two strand sizes, two strand grades, four transverse girder spacings, and several concrete strengths. By tabulating the number of strands required for a given length, curves were generated to show the effect of these variables. The results are discussed.

3.4.1 Effect of Strand Size

The 0.6 in. (15.2 mm) diameter strand has a 40% greater area and therefore a 40% greater capacity than the 0.5 in. (12.7 mm) diameter strand. This is a valuable property when used in conjunction with high strength concrete. In order to determine the validity of using 0.6 in. (15.2 mm) strands with high strength concrete, a comparison was made to the 0.5 in. (12.7 mm) strand in design.

With a constant transverse girder spacing of 7 ft. (2.1 m) assumed, Mn/DOT 45M girder designs using the two strand sizes and concrete strengths of 7 and 10 ksi (48 and 69 MPa) are presented in Figure (3.4a). The design span length is plotted against the number of Grade 270

low-relaxation (LL) strands required. For a girder concrete strength of 7 ksi (48 MPa), 22- 0.5 in., Gr. 270k-LL (12.7 mm, Gr. 1860 MPa-LL) strands were required for a span length of 70 ft. (21 m). As the span length was increased for the 7 ksi (48 MPa) girder strength, the number of strands required also increased. Strands were added in pairs, resulting in curves that were not necessarily smooth. A maximum span of 92 ft. (28 m) could be obtained by using 42 of the 0.5 in., Gr. 270k-LL strands. Adding more strands caused allowable compressive stresses at midspan under final conditions to be exceeded. Similar strand/span length combinations are currently used in Minnesota. As anticipated, more 0.5 in. (12.7 mm) strands were required than 0.6 in. strands for a given span length; 22 – 0.5 in. strands at a span of 70 ft. (21 m) versus 16-0.6 in. (15.2 mm) strands. Also, as expected, this was true for both concrete strengths investigated, and was typical of all girder sizes considered independent of transverse girder spacing.

Figures (3.4b) to (3.4e) show that as the size of the girder increased from 54M to 81I, the advantage of using 0.6 in. (15.2 mm) strand in combination with higher strength concrete on the order of 10,000 psi (69 MPa) was the increased span length. Also shown in these figures was the verification that less of the larger diameter strands are required for a given span length than of the small diameter strands. Therefore, this study further concentrated on the use of 0.6 in. (15.2 mm) strands in conjunction with high strength concrete.

Also noted on these figures is the template capacity of 56 strands limited by the fixed anchorage of the prestressing bed. This is the typical limit at Minnesota prestressing plants, and is independent of the strand size.

3.4.2 Strand Grade

Efficiency of the overall cross section is of concern when trying to incorporate both higher strength strands and concrete. Two grades (strengths) of strands are available for prestressing applications, Grade 270 ksi and Grade 300 ksi (1860 and 2070 MPa). Typically for bridge applications the Grade 270 ksi-LL type strand has been used.

A comparison was made for 0.6 in. (15.2 mm) strands of Gr. 270 and Gr. 300 (1860 and 2070 MPa). Assuming a transverse girder spacing of 7 ft. (2.1 m), Figure 3.5a shows the design span with respect to the number of 0.6 in. (15.2 mm) strands for the Mn/DOT 45M girder. For both concrete strengths considered, 7000 and 10000 psi (48 and 69 MPa), little to no gain in

maximum length was achieved using the higher strand strength. And only a savings of 1 to 2 pairs of strands was seen at any given length.

Other girder sizes (54M-81I) are presented in Figures 3.5b-e and show similar results. However, as the girder size increases, the efficiency of using the stronger strand decreases as does the maximum achievable span. This was because strands must be added in pairs, in which the stronger strand had a much higher force. As the girder size increased, so did the eccentricity of the prestressing force. The larger eccentricity and higher force combined to apply a higher internal moment and caused allowable stress limits to be exceeded. Therefore, the lower strength strand (Gr. 270) was most efficient in the deep (larger) sections when concrete strengths above 10,000 psi (69 MPa) were used.

After discussions with local designers and fabricators, it was decided that the Gr. 300 ksi (2070 MPa) strand would have limited use with current prestressing equipment. Additionally, the strand was not readily available because of manufacturing problems. Therefore, concentration was placed on achieving longer spans with the more widely accepted Gr. 270 (1860 MPa) strand.

3.4.3 Girder Size

The size of a girder which can be used for a specified span length is directly related to the strength of concrete used. Figure 3.6a plots the number of 0.6 in. Gr. 270k-LL (15.2 mm, Gr. 1860 MPa-LL) strands required for a specified length for all five girder sizes at a given transverse girder spacing of 4 ft. (1.2 m). A shallower section can be used in place of a larger one under certain circumstances. For example, if a 145 ft. (44 m) girder is needed for a bridge site, a Mn/DOT-72I would be required to achieve this span using normal strength concrete. However, by increasing the concrete strength to just 10,000 psi (69 MPa) and increasing the number of strands, the section can be replaced by a Mn/DOT 54M and results in a 18 in. (460 mm) reduction of overall height. This can lead to lower embankments for a constant under-clearance height, or greater under-clearance heights for constant roadway elevations.

Considering only the 4 ft. (1.2 m) girder spacing in Figure 3.6a, further increases in concrete strength above 10,000 psi (83 MPa) resulted in only slight increases in span length. For the very high concrete strengths on the order of 15,000 psi (103 MPa), little to no gain in length was achieved. This small span increase was attributed to the limitation of the area of prestressing

steel available. Adding more and more pairs of strands was less and less effective as the center of gravity (*cgs*) of the prestressing strands continued to rise in the section. Adding any additional pairs of strands became ineffective in attempting to increase the span length because allowable stress limits were exceeded. This trend of increasing concrete strength with no benefit in a length increase was consistent for wider transverse girder spacings, Figures 3.6b-d. The data show that the number of strands required for achieving the maximum span increased rapidly, giving a steep rise in the slope of each plot. This effect appeared especially pronounced in the wider spaced girder designs (discussed in Section 3.4.4).

At a constant span length, the deeper girder requires fewer strands to resist the same load as a shallower girder. This is due to the location of strands being further from the center of gravity of the strands (*cgs*) in the deeper girder allowing for more flexural load resistance. Figures 3.6b-d show the same type of plot for these girders with transverse girder spacings of 7, 10, and 12 ft. (2.3, 3.0, and 3.7 m).

For a constant number of strands, the deeper girders achieved longer lengths than the shallower girders. For example, thirty-six 0.6 in. (15.2 mm) strands in a 63I girder with 10,000 psi (69 MPa) concrete could reach 150 ft. (46 m) at a 4 ft. (1.2 m) spacing, while the same pattern and concrete strength could allow an 81I to achieve a 170 ft. (52 m) length. This again was due to the strand location being further from the center of gravity in the deeper girder allowing for the prestress force to resist a larger moment induced in the longer span under the same applied load.

As with previous figures in this chapter, the template capacity of 56 strands is noted. This was the limit at Minnesota prestressing plants, and was independent of the strand size. The capacity of prestressing beds must also be considered. Generally prestressing strands are tensioned to 75% of their ultimate strength, (i.e., 203 ksi (1390 MPa) for a Gr. 270 ksi (1860 MPa) strand. The prestressing beds had a capacity of two million pounds. Therefore the limit for the total number of 0.6 in. strands tensioned to this level was 46. Hence, the bed capacity limit of 46 strands was also noted on the figures.

3.4.4 Transverse Girder Spacing

The transverse girder spacing was defined as the distance between the centerline of two girders placed along side of each other for the length of the bridge. Figure 3.7a illustrates a 45M

girder at three transverse girder spacings of 4, 7, and 10 ft. (1.2, 2.13, and 3.05 m) and two concrete strengths of 7000 and 10000 psi (48 and 69 MPa). Figures 3.7b-e illustrate similarly plots for girder sizes 54M - 81I.

For a specific girder cross section at any given length, the narrower spaced girders required fewer strands than the wider spaced girders. This was due to a smaller percentage of superimposed dead and live load being distributed to the narrowly spaced girders. The high ratio of applied loads to dead load for the wider spaced girders requires more strands and in turn gives a reduced effectiveness of additional steel being placed higher and higher in the cross section. Overall however, the increased concrete strength was of little benefit to increasing the maximum span length for a given spacing as seen by the curves rapid rise.

At lengths lower than the maximum, an increased concrete strength can result in fewer girder lines being used for a specific project. From Figure 3.7a, a 100 ft. (30 m) Mn/DOT 45M spaced at 4 ft. (1.2 m) would not increase in length or see a strand reduction by increasing the concrete strength from 7000 to 10,000 psi (31 to 69 MPa). However, the increase in concrete strength along with a 38% increase in the number of strands (from 22 to 36) could result in the girders being placed at a 7 ft. (2.1 m) transverse spacing for the 100 ft. (30 m) span, providing a more efficient bridge design with fewer girders.

3.4.5 Maximum Span Lengths

The maximum span for each girder at a given concrete strength and girder spacing was determined based on allowable stress and ultimate strength design criteria. Figures 3.8a-d show the maximum spans for all five girder sizes versus concrete strength at a constant girder spacing. Increasing the concrete strength from 7000 to 10,000 psi (48 to 69 MPa) gave increased maximum span lengths of approximately 20-35%.

As the concrete strength was increased above 10,000 psi (69 MPa), the maximum attainable spans continue to rise for some transverse spacings, but at a lesser rate, shown by the graphs leveling out. For girders spaced 4 ft. (1.2 m) apart, virtually no length gain was achieved for concrete strengths above 10,000 psi (69 MPa), i.e., a level plot. At wider spacings of 7, 10, and 12 ft. (2.1, 3.7 and 6.1 m), maximum achievable lengths level out at approximately 12,000 psi (83 MPa). The use of high strength concrete is most practical when coupled with an increase in prestress force applied to the section. The amount of prestress force applied to the section is

most effective when it is positioned with a large eccentricity. This can be accomplished by increasing either the reinforcement area (using larger diameter strands, 0.6 in. rather than 0.5 in.) or the grade of reinforcement (Gr. 300 rather than Gr. 270). The effectiveness of increasing the concrete compressive strength eventually decreases as the amount of reinforcement increases because the eccentricity of the additional reinforcement reduces (as the possible reinforcement locations fill up in the template) thereby decreasing its flexural effectiveness. Therefore, a limit of 12,000 psi (83 MPa) concrete strength used in conjunction with the 0.6 in. Gr. 270-LL (15.2 mm, Gr. 1840-LL) prestressing strands is recommended for use with the Mn/DOT girder shapes investigated.

Figures 3.9a-d show the maximum spans versus girder spacing at constant concrete strengths. These figures confirm that larger shapes can achieve longer spans with the same concrete strength, although not shown here was the increase in number of strands from girder to girder that was required to achieve such lengths. However, also shown was the fact that the narrower the girder spacing, the longer the maximum achievable span was. This was due to smaller percentages of superimposed dead loads and live loads being distributed to the narrowly spaced girders. This was also seen in Figures 3.7a-e.

3.4.6 Governing Stresses

To investigate the governing concrete stress of a girder design, the number of strands must be held constant and the span length increased until one or more of the stress limits are exceeded, similar to the fine mesh procedure discussed in Section 3.3. For intermediate span lengths, a coarse mesh procedure was used and only the required number of strands were determined for a given length. The fine mesh procedure was used to determine the maximum span length, and therefore the governing concrete stress could be investigated only at the maximum span lengths. For the Mn/DOT girders and span lengths investigated, the ultimate moment or shear capacity was not a governing factor.

The release strength was expected to govern the design of the wider spaced girders because the final design load to dead load ratio was high. This indicates that a large amount of stress must be stored in the section at the time of release so that loads under final conditions would not cause failure. The percentage of loads due to the self weight of the girder increases with

decreased girder spacings, and consequently stress limits under final conditions were expected to govern the design for closely spaced girders (i.e., 4 ft. [1.2 m]).

The maximum span is generally defined by the convergence of more than one limiting stress condition. Governing stress categories have been defined as tabulated in Table 3.4. The limiting stress is noted as compression or tension limit. The service state (at the time of release or final conditions with all service loads applied) and the location along the girder length at which the stress limit was exceeded is also noted. Figures 3.10a-d show the governing stresses for each maximum span length investigated.

Table 3.4 Governing Stress Categories

Category	Compression / Tension	Service Condition	Location in Girder
CRE	Compression	Release	End
CRH	Compression	Release	Harp Points
TFCL	Tension	Final	Centerline
CFCL	Compression	Final	Centerline

The design of 7000 and 10,000 psi (48 and 69 MPa) girders at their maximum span length and 4 ft. (1.2 m) transverse spacing was governed by the 28-day compressive stress at midspan under final conditions (CFCL), Figure 3.10a. Any increase in length would result in exceeding the allowable compression stress (at harp points). However, as the strength of the girder increased to 12,000 psi (83 MPa), the state of governing stress changed. The compression stress was no longer the limiting factor because of the increased allowable stress, but rather the tension stress was the limit. This was due to the fact that the tensile limit increased at a slower rate than the compressive limit, i.e., the tensile limit increases by the square root of the compressive strength while the allowable compressive stress was directly proportional to compressive strength. The trend at very high strengths (15,000 psi [104 MPa]) showed compression at the harp points at release (CRH) began to govern simultaneously with tension at the centerline under final conditions (TFCL), even though there was little benefit in increasing the maximum span at very high strengths (Section 3.4.5).

For girders spaced at 7, 10, and 12 ft. (2.1, 3.1, and 3.7 m), maximum spans were governed simultaneously by allowable compressive stresses at the time of release located at the harp points (CRH) and tension under final conditions at midspan (TFCL), Figures 3.10b-d. When the harp

point was changed from the 40% points to a single location at midspan, compression stress limits at release were exceeded at the 40% points. Varying the release strength above a practical limit of 10,000 psi (69 MPa), with 40% harp points, would not allow for increased span lengths because the tensile stresses at midspan under final conditions were nearly maximized. Increasing the 28-day compressive strengths to higher ranges (10,000 psi and above) did not generally change the governing design stress for the wider spaced girders.

For the case of CRE (compression at release at the ends), end stresses governing in the girder indicated that not enough strands were available for draping to reduce end stresses, even with pattern rearrangement. Therefore, the length must be shortened or debonding of the strands must be used. This case only occurred on two occasions and no trend can be concluded.

3.5 A Normal to High Strength Concrete Design Comparison

The use of high strength concrete girders spaced wider than girders of normal strength concrete for a constant span will reduce the number of beam lines and decrease the total number of strands required for a typical bridge. Figure 3.11 illustrates this with a Mn/DOT 81I at a constant span length of 160 ft. (49 m).

The data show a 7000 psi (48 MPa) girder at a 4 ft. (1.2 m) spacing required 32 (0.6 in., Gr. 270k-LL [15.7 mm, 1860 MPa]) strands. Using the 52 ft. (16 m) bridge width, 13 girders with a total of 416 strands would be required. A 7000 psi (48 MPa) girder with a transverse spacing of 7 ft. (2.1 m) could not achieve the 160 ft. (49 m) length, therefore the concrete strength of the girder had to be increased. At 10,000 psi (69 MPa), girders spaced at 7 ft. (2.1 m) required 48 (0.6 in. [15.7 mm]) strands each, for a total of 364 strands in 8 girders. This is a significant reduction in both strands and number of girders for only a moderate increase in concrete strength.

This example shows economic savings resulting from a lower number of strands and girders required, as well as less installation time, will most likely outweigh the additional costs incurred from using higher strength concrete. Additional bridge projects may show savings and each individual project can be quickly analyzed this way through use of graphs presented in this chapter.

CHAPTER 4 DESIGN OF THE TWO TEST SPECIMENS

4.1 Test Girders

Two composite high strength prestressed bridge girders were designed, constructed, and tested to investigate the structural behavior of sections incorporating high strength concrete. The design parameters chosen (i.e., strand size, maximum span length, assumed transverse girder spacing) were based on the results of the parametric study. The girder variables included in the study comprised the concrete mix design, stirrup anchorage details, and end strand patterns (strand draping versus debonding).

4.1.1 Strand Size

The parametric study showed the viability of high strength concrete prestressed girders was dependent on the amount and strength of the prestressing strand, which can be placed in the cross section. To achieve the full benefit of high strength concrete, larger diameter (0.6 in. [15.2 mm]) strands should be incorporated in the prestressed sections. This enables larger prestress force to be placed low in the cross section, leading to greater strand effectiveness (greater eccentricity). The current use of 0.5 in. (12.7 mm) diameter 270 ksi (1860 MPa) strand quickly limits the achievable girder spans and spacings through limiting the number of strands that can be placed in the cross section. Although a 0.6 in. (15.2 mm) 300 ksi (2070 MPa) low relaxation strand would give more available force per strand than the 270 ksi (1860 MPa) strand, it is not widely accepted in the bridge girder industry because it is not readily available and jacking equipment is not easily accessible. Therefore, the 0.6 in. (15.2 mm) diameter 270 ksi (1860 MPa) low-relaxation strand was chosen for design of the test girders.

4.1.2 Transverse Girder Spacing

Governing stresses and their effect on transverse girder spacing were also taken into consideration. Girder design can be governed by the concrete strength required at the time of release or at service. Closely spaced girders can achieve longer span lengths than widely spaced girders because narrowly spaced girders carry a smaller proportion of the bridge dead and live loads. The girder self-weight is a substantial portion of the maximum load the closely spaced girders are required to carry. Consequently, less force is required to be stored in the section at the time of release and the service strength controls the design of narrower spaced girders. For

more widely spaced girders, which require high strength achievement at release, it may be more economical to let the girder sit on the precasting bed for a longer period of time to achieve higher release strengths rather than increasing the high early compressive strength at release.

A target design governed by service strength was selected to more efficiently utilize the benefits of high strength concrete. Hence, a narrow transverse girder spacing of 4 ft. (1.2 m) on center was chosen to maximize the girder span length. The 4 ft. spacing represented a practical minimum, leaving a gap of 18 in. (0.46 m) between girder flanges to facilitate deck forms and diaphragm placement.

4.1.3 Design Loads

Design loads were grouped in two categories: noncomposite section loads and those loads acting on the composite section. Noncomposite loads included the prestress force, self weight of the girder, and loads due to diaphragm placement and the deck. To simulate diaphragms and deck forms, a superimposed uniform dead load of 20 plf (290 N/m) was applied in design. The monolithic deck dead weight was also applied.

Composite loads included a 25 psf (1.2 kPa) low slump wearing course, 17 psf (0.8 kPa) future wearing course allowable, and a guard rail load. The design of the composite section also included an HS25-44 highway truck loading and the AASHTO military load. These loads were documented by Kielb (1994). Loading combinations and wheel load distributions were applied using the same method as in the parametric study (Section 3.2.4).

4.1.4 Girder Size, Length, Required Concrete Strength, and Reinforcement

A standard size Mn/DOT 45M I-girder was selected for testing, as it was the smallest girder size typically used for overpass and interstate bridge construction in Minnesota. Additionally, current prestress bed capacities at the precast facility would not be exceeded and testing facilities and equipment would be maximized. The 45 in. (1140 mm) deep girders were designed to maximize the span length on a 4 ft. (1.2 m) girder spacing. To determine the required concrete strength and reinforcement to achieve the maximum attainable length, an analysis was performed with SPAN (Leap Software, 1990) in accordance with the AASHTO Specifications (1993).

From the parametric study, to maximize the span length, a 28-day concrete compressive strength of 10,500 psi (72 MPa) was found to be required with forty-six 0.6 in. (15.2 mm) diameter 270 ksi (1860 MPa) low-relaxation strands to reinforce the section. The maximized

span length of 132 ft. - 9 in. (40.5 m) represents more than a 30 percent increase in the maximum span length currently achieved using conventional 7,000 psi (48 MPa) concrete fabricated with 0.5 in. (12.7 mm) diameter 270 ksi (1860 MPa) strands. A composite deck was designed based on Mn/DOT standard specifications. The test girder dimensions are illustrated in Figure 4.1.

4.1.5 Girder Mix Designs and Design Strength

The objective of a companion study at the University of Minnesota was to investigate properties of high strength concrete made with locally available materials (Mokhtarzadeh, 1996). Laboratory tests showed that local aggregates could be used to achieve high strength concretes. Limestone aggregates provided mixes with the highest strengths without the use of microsilica. Mixes with glacial gravel aggregates reached similar strengths with the addition of microsilica. Rounded glacial gravel is currently the standard aggregate specified by Mn/DOT, and limestone is disallowed for prestress concrete use based on its high absorption. In an effort to better understand the effect of aggregate on the behavior of HSC prestressed girders, it was planned that one girder (Girder I) be cast with a limestone aggregate mix and the other (Girder II) with a glacial gravel mix incorporating 7.5% microsilica (replacement by weight of cement).

The concrete mix for Girder I consisted of Type III Portland cement, sand, crushed limestone aggregate, and a superplasticizer. The mix had an average water/cementitious material ratio of 0.32. The mix for Girder II also used Type III Portland cement, sand and superplasticizer. However, rounded glacial gravel aggregate with 7.5% microsilica was used instead of limestone. Girder II mix had an average water/cementitious material ratio of 0.36. Quantities of both mixes are listed in Table 4.1. Both mixes showed good workability and consolidation during placement, and no modifications were made to the standard construction techniques followed by the precast manufacturer. Mix quantities for the normal strength composite deck are discussed in Section 4.2.1.

The 28-day nominal design compressive strength of the noncomposite test girders was specified as 10,500 psi (72 MPa). The nominal design release strength was assumed to be 85% of that at 28-days, or 8925 psi (62 MPa) and was a required minimum to meet allowable stresses at release.

Table 4.1 Concrete Mix Design for Test Girders

	GIRDER I - Limestone	GIRDER II - Glacial Gravel with microsilica
Type III Portland Cement	750 pcy [440 kg/m^3]	695 pcy [410 kg/m^3]
Fine Aggregate	1330 pcy [790 kg/m^3]	1290 pcy [770 kg/m^3]
Limestone ($^5/_8$" maximum aggregate size)	1970 pcy [440 kg/m^3]	-
Glacial Gravel ($^3/_4$" maximum aggregate size)	-	1880 pcy [1120 kg/m^3]
Superplasticizer	150 oz/yd^3 [5.6 kg/m^3]	123.3 oz/yd^3 [4.6 kg/m^3]
Microsilica	-	56 pcy [33 kg/m^3]
Water/cementitious material ratio	0.32	0.36

4.1.6 Debonding and Draping of Strands

The strand pattern for the two composite test girders was based on a 2 in.-on-center template. The required strand pattern for the test girders at midspan is shown in Figure 4.2.

At the ends of the girder, stresses due to self weight are negligible (or go to zero). The eccentricity of the prestress force at the ends can cause tension cracks in the top and crushing in the bottom of the girder. To reduce the end stresses due to the eccentric force, one of two means is typically employed: reducing the eccentricity or decreasing the force. The eccentricity can be reduced by draping strands at the end. To decrease the force, strands can be debonded in the end region. A recommended limit of 25 percent debonding results in draping/debonding combinations (PCI Design Handbook, 1992). Currently, Mn/DOT does not use strand debonding to reduce end stresses in prestressed girders because of corrosion concerns. To investigate the effect of debonding on girder behavior, three ends utilized a 4-draped/8-debonded combination. In one end of one girder 12 draped strands were used to control end stresses for comparison to the draped/debonded combination. Figures 4.3 and 4.4 depict the end strand patterns for draped and debonded strands, respectively, used in the test girders.

4.1.7 Mild Steel Reinforcement Details

Mild steel reinforcement was used for two main reasons in the girders. First, stirrups were provided for shear resistance. And second, tension reinforcement was provided in the top flange.

Proper anchorage of stirrups is of concern when girder design is governed by shear. If a shear crack occurs in the web, the stirrup must be able to fully develop strength to resist crack

opening. The current Mn/DOT epoxy-coated stirrup is a "U-shaped" stirrup. It was suspected that the "U" stirrup may not provide sufficient anchorage to develop the bar force. Therefore, two shear stirrup details were investigated. One detail employed the typical Mn/DOT "U" stirrup; the other incorporated a "modified U" stirrup configuration with leg extensions for better anchorage. All bars were epoxy coated.

Tension steel provided in the top flange of each girder consisted of four No. 8 bars. The bars were Grade 60 and not epoxy coated. Each bar ran the length of the girder, with splices provided in accordance with AASHTO design specifications. Details of the mild steel reinforcement are reprinted here from Kielb (1994) in Figures 4.5 through 4.7. The three figures show an elevation view, a cross-sectional view and all bar details.

4.1.8 Test Girder Variables Summarized

The variables mentioned (aggregate, draping/debonding combinations, and stirrup configuration) were combined in an attempt to maximize information obtained from the two test girders. Figure 4.8 depicts the two noncomposite test girders and their respective variables. Comparing ends IA and IB, the aggregate (concrete mix) and strand patterns remained constant and the stirrup configuration varied (A Mn/DOT "U", B-D modified "U"). Ends IB and IIC have the same strand pattern and stirrup configuration, but varied in aggregate (I limestone, II glacial gravel with microsilica). Ends IIC and IID have the same stirrup details and aggregate, but the strand pattern varied from debonded on end IIC to draped on IID.

4.2 Composite Deck

Results of the parametric study indicated that using a high strength concrete deck to match the strength of the girder was of little benefit to increasing the maximum achievable span (less than 1%). In addition, it was believed that high strength concrete deck placement may prove to be a difficult field operation. Therefore, it was decided to maintain the standard 3Y33 deck mix currently used by Mn/DOT.

4.2.1 Deck Mix Design and Design Strength

The concrete mix used in the composite deck of both girders consisted of Type I Portland cement, sand, glacial gravel, and air entraining agent. The mix had an average water/cementitious material ratio of 0.42. An air entraining agent was added to provide a total

air content of 5.5% ±1.5%. Design mix quantities are listed in Table 4.2. The mix showed good workability and consolidation during placement, and no modifications were made to the standard construction techniques as would be followed by the field contractor. Actual batch information, including location of pour from each truck, are given in Kielb (1994).

Table 4.2 Concrete Mix Design for the Composite Deck

	Mn/DOT 3Y33 Mix
Type I Portland Cement	640 pcy [380 kg/m^3]
Fine Aggregate (sand)	1195 pcy [710 kg/m^3]
Glacial Gravel ($^3/_4$" max)	1810 pcy [1070 kg/m^3]
Air Entraining Agent	6.4 oz/yd^3 [0.24 kg/m^3]
Water/cementitious material ratio	0.42

The 28-day nominal compressive strength of the composite deck was specified as 4000 psi (28 MPa).

4.2.2 Composite Deck Details

Construction of the deck was performed to simulate actual field methods. Unshored construction was used to place the composite deck by bracing form work off of each girder. Decks are usually poured in two lifts: a 7 in. (180 mm) structural deck is placed directly over the girder, and a 2 in. (50 mm) low slump wearing course is placed at a later time for roadway durability. For ease of construction in the testing facility, the deck was cast in a monolithic pour totaling 9 in. (230 mm). Dimensions of the composite deck were shown in Figure 4.1. Because a "one lift pour" was used for deck construction, the composite girder was expected to behave slightly differently than using a "two lift pour". In the case of the "two lift pour", only the 7 in. (180 mm) deck is carried by the noncomposite section, and the 2 in. (50 mm) wearing course is carried by the composite section. By casting a 9 in. (230 mm) monolithic deck, the entire weight of the deck was carried by the noncomposite section. Design calculations predicted the difference in deflection due to deck casting as small (less than 1%) and deflection differences due to loading on the composite section were negligible.

All mild steel reinforcement used in the decks was epoxy coated, Grade 60, No. 4 bars. Longitudinal reinforcement (running along the length of the beam) was provided to meet Mn/DOT Bridge Design Manual Specifications (1991) and was placed in the top and bottom of

the deck. Cover requirements were in accordance with the specifications with the following exception: a 3 in. (76 mm) cover was used for top reinforcement, to simulate the field cover including the low slump wearing course. Typically transverse reinforcement (running perpendicular to the length of the beam) is designed to carry slab loads spanning adjacent girders, predetermined by Mn/DOT standard specifications. In this case however, the composite decks of the two test girders were independent of each other. Therefore, transverse reinforcement was designed to meet minimum ACI 318 (1995) temperature and shrinkage requirements because the composite deck was only 48 in. (1220 mm) wide. The overhanging flanges of the deck on either side of the girder did not warrant transverse flexural reinforcement. Reinforcing details of the composite deck are shown in Figure 4.9.

4.3 Additional Design Assumptions

The actual design of the girders was performed in accordance with AASHTO Specifications (1993), which was the standard that the Minnesota Department of Transportation had adopted. Design assumptions and requirements followed those used in the parametric study and previously discussed in Section 3.2.4. Assumptions specifically used in the design of the test girders are discussed.

4.3.1 Prestress Losses

For the purpose of initial design, total prestress losses were estimated as losses due to elastic shortening, steel relaxation, and creep and shrinkage. Losses due to creep and shrinkage of concrete and elastic shortening were computed in accordance with AASHTO Specifications (1993). The PCI Method (PCI Design Handbook, 1992) was used to estimate the loss due to the prestressing steel relaxation at the time of release. Losses due to the prestressing steel relaxation under final conditions were calculated in accordance with AASHTO 9.16.2.1.4.

Nominal losses for design of the two test girders were predicted to be 10.2 % at release and 35.8 % under final service conditions (AASHTO, 1996). Sample calculations were provided by Kielb (1994) in an appendix. Note under design conditions and assumptions, both girders were expected to behave the same.

4.3.2 Girder Stability

Handling of long span girders was of great concern. Therefore, lift hooks were placed in the girder to ensure stability during handling. Placement was dictated by not exceeding allowable stress limits while assuming a small rotation about the roll axis in accordance with PCI stability criteria (PCI Design Handbook, 1992). A factor of safety of 2.0 governed for the hook locations of 9 ft. (2.7 m) from each end. A double lift hook arrangement was used to accommodate construction equipment. Therefore, hooks were placed at 8 and 10 ft. (2.4 and 3.0 m) from each end of the girder. No stability problems were encountered during handling.

4.4 Fabrication and Instrumentation of the Girder Specimens

4.4.1 Fabrication

Fabrication of the two test girders began on August 5, 1993 at Elk River Concrete Products prestressing plant in Elk River, Minnesota. Actual construction was performed by both Elk River Concrete Products employees and University of Minnesota personnel. Standard construction techniques were employed throughout the construction process. A detailed description of the fabrication was documented by Kielb (1994) and a copy of the field log during construction is included in Appendix F of the same reference. A summary of the construction timeline is given in Table 4.3. A brief description is presented for completeness. Additional timelines involving load testing to cracking and ultimate flexural strength are presented in Chapters Eight through Ten.

The construction of the test girders can be summarized in the following sequence. First, the prestressing strands were laid in the bed and lightly pretensioned (to approximately 4 kips each) for ease of strain gage placement on the strands. Mild steel reinforcement (stirrups and top flange longitudinal reinforcement) was placed. Additional instrumentation, including vibrating wire and PML-type gages, was installed before the girder formwork was positioned. Prestressing strands were fully tensioned on August 6, 1993. Because both girders were constructed on the same prestressing bed, strands in both girders were tensioned to the same level.

Formwork was installed on August 9, 1993 prior to concrete placement. Concrete was mixed at the plant batch station. Each girder contained approximately 7.0 cy (2.3 m^3) batches. Although both girders were cast on the same bed, Girder I was cast approximately 1.0 hour prior

to casting Girder II. The girders were vibrated by means of form vibrators as well as hand-held vibrators. The top surface was intentionally roughened by brooming. Immediately following casting, and tarpaulins were placed over the formwork. Only heat of hydration from each girder was used during the curing period, no additional heat or steam curing was incorporated.

Table 4.3 Construction Timeline Summary

Date	Time since casting (days)	Event
August 5, 1993	-	Instrumentation Installation Began at Prestress Plant
August 6, 1993	-	Tensioning of Prestressing Strands
August 9, 1993; 1:00-2:00 pm 2:00-3:00 pm	- -	Casting of Concrete - Girder I Casting of Concrete - Girder II
August 10, 1993; 8:30 am 12:30 pm	- -	Formwork Removed - Girder II Formwork Removed - Girder I
August 10, 1993; 2:30 pm	1.0	Release of Prestressing Strands
August 11, 1993; 9:30 am 11:30 am	2.0	Move from bed to prep area - Girder II Move from bed to prep area - Girder I
October 18, 1993	60	Transport to Testing Facility
February 25, 1994	201	Placement of Composite Deck
August 23, 1994	378	First Static Load Test - Girder I
June 27, 1995	690	First Static Load Test - Girder II

Stripping of the formwork began shortly after each girder reached the required release strength on August 10, 1993. As shown in Table 4.3, Girder II form removal began 17.5 hours after casting Girder II; whereas Girder I form removal began at 22.5 hours after casting. A total of 6.0 hours elapsed between the form removal for Girder II (2 hours for Girder I) and the time at which the strands were simultaneously flame cut at each end of the girders. Pre-release cracks (described in detail in Section 11.1) were observed to develop in Girder II between the time of formwork removal and strands release. The cracks were noted to completely close immediately upon strand release. The following day, the girders were relocated to a storage site in the prestressing yard until moved to the test site approximately 60 days later.

Both girders were transported to an off-campus testing facility in October of 1993. No stability problems or additional cracks were observed due to transportation. Deck formwork placement began shortly after the girders were located in the testing facility. At the time the

decks were cast, the interior laboratory temperature was well below the Mn/DOT specified minimum for casting concrete. Therefore, a temporary tent was constructed over the girders and deck formwork such that heaters placed under the girders would be evenly heated to a temperature of 75°F over three days. The tent was removed for approximately 5 hours while the deck was cast. The composite deck was cast on each girder individually on February 25, 1994 using unshored construction. After completion of casting, the temporary tent was reinstalled to prevent heat loss for 5 days.

4.4.2 Girder Instrumentation

Instrumentation included strain gages applied to the strands and transverse reinforcement, embedded concrete strain gages and vibrating wire strain gages, DEMEC (DEtachable MEChanical) gages and displacement transducers. The instrumentation was located in both the girder and the deck to optimize the information on prestress losses, long-term deflections, and transfer length of strands. Detailed figures of instrumentation along with actual placement locations are found in Kielb (1994).

A total of nine of the forty-six strands were instrumented with strain gages to investigate tensioning and transfer length. The pairs of debonded strands were instrumented at 15, 22, and 30 in. (380, 560 and 760 mm) from the end of their respective sheath points. Harping of the draped strands was at 0.40L (40% of the member length) from each end. At 0.45L and midspan of the girders, strands were instrumented to obtain data regarding the strain along the length of the strands at the time of prestress, and stress ranges in the strands during fatigue tests.

Sixty DEMEC gages spaced 6 in. (150 mm) on center were applied to the surface of the concrete at the end regions of the beam to measure the external concrete strains to investigate transfer lengths. Vibrating wire gages, located at 0.45L and midspan, were used to investigate the change in concrete strain over time due to creep, shrinkage and other environmental effects. Additionally, vibrating wire gages were used to determine strain distributions through the girder height during flexural load testing. Embedded single-axis concrete gages were also placed at *0.2L*, *0.3L* and midspan in the girders to investigate the depth distribution of concrete compressive stress during the flexure tests.

Deck instrumentation consisted of embedded concrete gages to investigate depth distribution of strain along the length of the member. Vibrating wire gages were placed to maximize

information on compression stress distribution during the flexure tests. Full documentation of instrumentation labeling and actual locations was included in Kielb (1994).

CHAPTER 5 TEST SETUP

5.1 Loading Frame System

Three components comprised the loading frame system: the reaction blocks that served as the supports, the loading frame itself including bracing of the frame, and independent bracing of the test girders. Each of these components is discussed separately.

5.1.1 Support Reaction Blocks

The two girders were supported on reinforced concrete pedestals to provide a 5 ft. (1.5 m) vertical clearance to the laboratory floor. The four pedestals (one at each end of each girder) were fabricated to accommodate large end rotations and vertical centerline deflections expected during ultimate flexural testing. Each reaction block was designed to resist the reaction load by bearing against the slab-on-grade concrete floor. No additional anchorage to the floor system was used. The blocks were individually cast in place and details of their construction are discussed by Kielb (1994).

Neoprene bearing pads are typically used in bridge construction between the girder sole plate and the support. However, in an effort to reduce the end deflections during load testing, the test girders were supported on steel rollers. Each roller was 3-1/8 in. (80 mm) in diameter and rested on a steel plate embedded into the concrete reaction block. During periodic static loading, cyclic loading and flexural crack testing, each girder was simply supported such that one end was fixed against rolling but free to rotate while the other was completely free to roll and rotate. To accomplish this, one roller was welded to the embedded steel plate (but not welded to the girder) and the other roller was simply set in place with no welding used. For the ultimate flexural tests, welds were broken allowing each roller to be free. This was intended to allow each end of the girder to move equally relative to the hydraulic jack locations such that shear forces in the jacks would be reduced, rather than forcing movement entirely to one end of the girder and possibly damaging equipment. When the weld was removed from the roller, it left a small edge on the roller resulting in a slight inequality of free rotation between the two ends of the girder. However, the release was deemed adequate to protect the accumulation of shearing forces in the jacks.

5.1.2 Loading Frame

Periodic static and cyclic load testing of each girder were performed using two point loads. As shown in Figure 5.1, the load point locations each included a load frame and hydraulic actuator, and were located at 40% of the length from the girder end supports corresponding to the strand harps points. The load frames were placed on the concrete floor and bolted to soil anchors using transfer plates. Information including the load frame configuration, sizes of members, and connection details of the load frame used during static and cyclic load testing, and the soil anchors are described in Chapter Eight of Kielb (1994). For completeness, a brief summary is given.

Below grade helical type soil anchors were installed with a minimum capacity of 75 kips per anchor to provide uplift resistance for the load frames. Anchors were connected to the load column base plates through transfer plates by two methods: using either a Dywidag thread bar or high strength threaded rods. Both methods are illustrated and documented by Kielb (1994).

Each load frame consisted of several structural steel pieces as shown in Figure 5.2. From the floor, two 5 ft. (1.5 m) stub columns were topped with two 15 ft. (4.6 m) loading columns. The two columns were tied together near the top with a 4 ft. (1.2 m) wide loading tube. From the loading tube, a hydraulic actuator with a bottom spreader beam was hung to apply the load directly to the test girder. The actuator was braced in the plane of the load frame using threaded stabilizing bars. The top surface of the test girder at the location of the load frame was grouted to ensure a level, uniform contact surface between the spreader beam and the girder composite deck. Connections within the load frame were bolted in all cases. Cross bracing between the two load frames was not used in the initial static and cyclic load tests; hence each load frame system was independent of the other.

The same load frame system was used for ultimate flexural testing with the following exceptions. A pipe jack replaced the hydraulic actuators used for the cyclic and periodic static testing, see Section 5.2.1 and 5.2.3. A clevis pin load cell was placed between the spreader beams and the pipe jacks. Each jack was braced for sidesway by connecting it to a 4 ft. (1.2 m) side tube, which in turn was connected to the respective loading columns. A general schematic of the load frame is illustrated in Figure 5.3. The two load frames were tied together using cable and turnbuckle (C&T) systems. The frames were cross braced together in the horizontal and vertical planes using a total of four C&Ts. The horizontal C&Ts were located at the level of the

loading tubes. The vertical C&Ts were connected from the bottom of the stub columns diagonally to the top of the loading tube. Turnbuckles were tightened to stiffen the overall loading system and to prevent twisting of the frames.

5.1.3 Bracing of the Test Girders

During periodic static load testing, cyclic loading, and initial flexural crack testing, the test girders were unbraced. Although design requirements typically include diaphragms placed at third points along the length of the girder, it was believed that the loading jacks could be placed such that the load would be applied directly through the vertical axis of symmetry of the girder, and no bracing would be required along the length of the girder. (Tiltmeters placed perpendicular to the longitudinal beam axis at midspan indicated no measurable out-of-plane motion.) In addition, the girder ends were unbraced. The free rollers were visually positioned perpendicular to the girder length when the girders were initially placed. For both girder cases, the free end roller self-corrected its position and slightly turned itself to be perpendicular to the girder.

A similar technique was used for the ultimate flexural testing. Placing the loading jacks directly over the girder vertical axis of symmetry prevented the girder from twisting under the load. No bracing was required along the girder length. However, each end of the girder was chained to its respective reaction block to prevent uplift of the girder end due to the energy release at the time of failure. Using a double chain system rated for 25,000 lbs. (110 kN) of vertical lift, the chains were threaded through TS4x6x1/4 tubes placed directly above the support and chained back through reaction block lifting loops on each side of the girder. The chain system was hand tightened so as not to inhibit free rotation of the girder ends. Photos illustrating the end chaining system used during ultimate flexural testing are shown in Figures 5.4 and 5.5.

5.2 Testing Equipment

The testing equipment for cyclic load and periodic static load testing varied from both the flexural crack testing and ultimate flexural testing equipment. The respective equipment is described, as well as the data acquisition system and software used. Methods of data reduction are also discussed.

5.2.1 Periodic Static Load and Cyclic Load Testing

The loading equipment for the periodic static and cyclic load tests for each girder consisted of a hydraulic pump, hydraulic actuators, and controllers, all manufactured by MTS Corporation. The hydraulic power for the actuators was supplied by a 21 gpm (80 LPM) pump. The pump was a closed loop system, operating at 3000 psi (21 MPa) and utilizing a water-based heat exchanger to cool the hydraulic fluid. The fluid was driven through a high pressure line to a central accumulator where the hydraulic lines for the two actuators (one per load frame) were connected in parallel to the fluid circuit.

Each hydraulic actuator was fatigue rated for 35 kips (240 kN) and had a total stroke range of 10 in. (250 mm). Both actuators were servo-controlled and capable of operating in either load or displacement control. Actuator locations (load points) on each girder were listed in Figure 5.1. In this project, the hydraulic actuators were used in load control in an effort to maintain the required HS25 truck load (as discussed in Section 8.1). Each actuator received its independent command signal through an MTS 406 controller.

An MTS 410 Function Generator was used to provide the load control command for testing. For cyclic load testing, an inverted haversine function was used. Static load testing was performed using a ramp function. Initial testing was performed where one actuator was distinguished as the "master" and was given a direct input signal from the ramp function generator via the actuator controller. The second actuator was "slaved" to the first such that the input signal to the second actuator controller was taken as the output from the first "master" controller. This resulted in significant vibrations in the girder at low cyclic load levels. Therefore, both actuators were converted to "master" mode by feeding each actuator controller the signal directly from the function generator. An MTS 464 Data Display unit could visually monitor the load and displacement of each actuator. Testing procedures, along with commanded load levels for each type of test are discussed in more detail in Section 8.1 and 8.2 of this document.

5.2.2 Flexural Crack Testing

The loading equipment used for cyclic and periodic static load testing was also used for flexural crack testing with the following exception. An additional dead load was attached to each girder because the 35 kip (240 kN) actuators alone did not have sufficient capacity to crack

the sections. A dead load in the form of concrete weights and a stabilizing tube frame was obtained from a local contractor and had a total weight of 35.0 kips (156 kN). The concrete weights and steel stabilizing frame were rolled beneath the girder and jacked up into position for chaining. Once the dead load was hung from the girder using chains and binders, the positioning jacks were removed. A photo of the additional dead load and how it was hung from the test girder during each crack test is shown in Figure 5.6. The chain locations for the concrete weights hung from each girder are shown in Figure 5.7 and listed in Table 5.1. The respective moments induced by the hanging dead load were linearly distributed between point loads and are listed in Table 5.1 for several locations of interest. Variation of the induced moments between girders was due to unintentional differences in placement of the hanging weights. Once the dead load was hanging in place, static testing up to the cracking load began immediately using a ramp function for the hydraulic actuators as mentioned in Section 5.2.1.

Table 5.1 Moments Induced by Hanging Dead Load during Crack Testing

	Girder I	Girder II
Distance from midspan to chain, in. (m) †		
d_1	60 (1.5)	78 (2.0)
d_2	60 (1.5)	66 (1.7)
Moments induced due to Dead Load, in-k (kN-m) †		
end IA/IIC	0 (0)	0 (0)
Load Point IA/IIC	11240 (1270)	11410 (1290)
Hanging Load, pt. G	13070 (1480)	12840 (1450)
cL (midspan)	13070 (1480)	12850 (1450)
Hanging Load, pt. H	13070 (1480)	12860 (1450)
Load Point IB/IID	11330 (1280)	11200 (1270)
end IB/IID	0 (0)	0 (0)

† Distances and locations are noted in Figure 5.7.

5.2.3 Ultimate Flexural Testing

An initial estimation using internal equilibrium of the maximum load required to break each girder during ultimate flexural testing was on the order of 190 kips (850 kN) per load point. Equipment was obtained through a local contractor to perform the testing. Two single acting hydraulic pipe jacks were connected to the load frame as shown previously in Figure 5.3. A clevis pin load cell rated at 200 kips (890 kN) was placed in line with the jack and spreader beam

to determine the applied load at each pipe jack location. A gasoline-powered pump provided hydraulic pressure up to a maximum of 6000 psi (41 MPa). Hydraulic fluid was driven through one high pressure line to a hydraulic splitter, which allowed the two jacks to be operated in parallel. Control of the jacks was only available through manual adjustment of a pressure regulator placed in line prior to reaching the splitter. Each jack had a piston area of approximately 8 $in.^2$ (5200 mm^2) and when in operation had a total estimated capacity of 300 kips (1330 kN) and a stroke of 48 in. (1.2 m). A transducer was placed in line with the regulator to measure line pressure, which in turn was used to verify the applied load for each jack by comparing to the load cell readings.

5.2.4 Data Acquisition System

Data was acquired using two basic methods. The first method was through manually recording data, while the second method utilized an electronic recording system. Manually recorded data included monitoring of P3500 strain indicator boxes for strand strain changes during fabrication, a survey dumpy level for changes in girder camber over time, a GEOKON readout box for thermistors and vibrating wire gage values (when the electronic recording system was not available), and a Whittemore dial gage for changes in strain at DEMEC point locations.

Data that was electronically recorded required the use of the Megadac 3016AC Data Acquisition System manufactured by OPTIM Electronics, Figure 5.8. The system was used during fabrication of the test girders and throughout the life of the girders, including static, cyclic and ultimate flexural testing. Operating on AC power, the system had 512 kilobytes of internal memory and a data sampling rate of up to 25,000 samples per second, depending on the number of channels to be sampled. Two AC3884-VW1K boards were installed to record up to 16 channels of vibrating wire gages (eight channels for thermistors and eight for strain). A total of 56 channels were available for low level (strain gage) signals with quarter bridge completion and signal conditioning. An additional 24 channels were capable of monitoring high-level voltage signals from instruments such as displacement transducers, load cells, pressure transducers, and LDVTs with external signal conditioning. The system also provided an adjustable excitation voltage of 0-15 volts DC, which was necessary for powering tiltmeters and DCDTs. Data was transferred to a personal computer via an IEEE-488 interface.

5.2.5 Software

The OPTIM Megadac system mentioned previously was controlled via TCS (Test Control Software) Version 5.1 supplied with the system. The software enabled independent channel configuration including card gain, post gain, conversion from resistance, voltage or frequency to engineering units. Alarm functions to detect power supply failures and excessive strain readings were also options available through the software.

Data reduction included use of spreadsheets for plotting curves such as stress-strain, load-deflection and prestress losses with time. In the case of manual data acquisition, such as reading P3500 strain indicator boxes, strand slip dial indicators or camber via surveying equipment, data was entered into spreadsheet software and reduced accordingly. When data from more than one source was available to obtain a specific quantity, such as prestress forces or deflections at midspan, an attempt was made to reconcile any differences in readings in order to obtain the best estimate for the quantity.

5.3 External Instrumentation

Instrumentation external to the composite test girders and used during static and cyclic load testing, as well as flexural cracking and ultimate testing is discussed. Instrumentation internal to the girders was previously discussed in Section 4.4.2.

5.3.1 Deflection

A number of devices were used to measure deflection. A survey level was used to remotely monitor camber from the time of fabrication. Initially, camber was measured at the 1/4 points [32.9 ft. (10 m)] along the girder length until just prior to transportation of the girders to the testing facility. The measurements were then taken at the 1/8 points [16.5 ft. (5 m)]. After approximately 580 days, it was noticed that Girder II appeared to have a "gull wing" shape, so camber measurements were taken at 2 ft. (0.6 m) increments along the girder length for both girders to better define the profile. LVDTs were used to measure vertical deflection at several points along the length of the girder during periodic static and cyclic load testing. In particular, deflections were measured from the underside of the bottom flange at midspan and 40% length points (directly below the load points).

During initial flexural crack testing, hanging the dead load required the midspan LVDT to be attached to the top surface of the deck. A system was devised to hang the 10 in. (254 mm)

LVDT from a roof joist directly over midspan. Due to the short duration of crack testing, the relative movement of the roof system under environmental conditions (rain, sleet, and snow) could be neglected.

Ultimate flexural testing presented the problem of large deflections with no opportunity to reset the "small range" LDVTs during testing. One LVDT with a total travel of 10 in. (254 mm) was hung from the roof joist as during initial flexural crack testing to measure the midspan deflection of the top of the composite girder. However, deflections up to 48 in. (1.2 m) could be achieved by the loading jacks. Hence, a pressure transducer system was designed and constructed to measure these large deflections. Gallon-sized containers filled with plumbing antifreeze were placed on top of the composite deck at the midspan and 40% of length points. The fluid was then routed from the containers to pressure transducers approximately 6 ft. (2.8 m) below. The following relationship was used to determine the change in height (girder deflection under a load) of the girder from the change in pressure at the level of the transducers,

$$\Delta p = \gamma \Delta h \tag{5.1}$$

where

Δp = change in pressure, psi (MPa)

γ = unit weight of fluid, 0.0368 lbs/in^3 (1020 kg/m^3)

Δh = change in height, in (m).

Although the pressure transducer deflection measuring method showed noise in the data due to sloshing of fluid in the containers, a general trend of deflection could be determined within ±0.5 in. (±13 mm) over the total range of 48 in. (1.2 m). Figure 5.9 illustrates the placement of these deflection devices during ultimate flexural testing. Figure 5.10 shows a photo of the two deflection devices used at midspan; the LVDT is in the foreground and hangs from above, and the gallon-sized fluid container is shown stabilized by a wooden frame.

5.3.2 Rotation and Twist

During periodic static and initial crack testing, the rotation of each girder was measured using full bridge tiltmeters. The tiltmeters were Model 880 manufactured by Applied Geomechanics and had a total tilt range of ±0.5 degree. Four tiltmeters per girder were used to monitor longitudinal bending rotation along the girder length. One tiltmeter was located at each end directly above the supports, one was located at 35% of the length from the free support end

and the fourth was located at 45% of the length from the free support. All tiltmeters were located within 0.5 in. of the neutral axis of the composite girder. In addition to tiltmeters, end rotation of each girder at the free roller support due to longitudinal bending was monitored by two LVDTs; one placed 1 in. (25 mm) below the top edge of the composite deck and the other was located 0.5 in. (13 mm) above of the bottom of the girder. Figure 5.11 shows the two (top and bottom) LVDTs in position at the end of Girder I.

Twist of each girder during loading was measured by two methods. The first method was to place a tiltmeter perpendicular to the girder length at midspan. During periodic static and initial crack testing, any twist of the girder could then be recorded electronically via the data acquisition system. Secondly, a spring loaded LVDT with a stainless steel rounded tip was also placed perpendicular to the girder length at midspan. The spring loaded LVDT measured displacement between an external reference frame and a steel plate epoxied to the girder bottom flange. This second method was used as a check for static and crack testing while it was the only method available for detection of girder twist during cyclic testing. Due to the time required for stability of the signal from the tiltmeters (approximately one second), they could be read only during periodic static load and flexural crack testing, not during cyclic testing. In general, both methods indicated negligible twist.

5.3.3 Crack Initiation and Reopening

The girders were monitored for cracking under service load conditions. During these tests, acoustic emission (AE) monitoring was employed to determine when the member reached its cracking and crack reopening load. The AE monitoring equipment consisted of three parts, AE transducers, pre-amplifiers, and an AE signal monitor, all manufactured by Dunegan/Endevco Corporation. The transducers were piezoelectric resonant devices with frequency sensitivities between 200 kHz and 1 MHz and resonant frequencies of either 490 or 290 kHz. Four AE transducers were placed on the bottom surface of each girder, centered across the width of the girder, in an attempt to crudely source locate crack initiation. Transducer locations along the girder length are illustrated in Figure 5.12. The pre-amplifiers had approximately flat frequency responses from 50 kHz to 2 MHz and were equipped with 50 kHz high pass filters.

The AE monitor, Dunegan/Endevco model DE8000, was capable of monitoring multiple AE transducers and is shown in Figure 5.13. The monitor did not digitize the AE signal waveform,

but rather performed analog signal feature extraction (i.e., peak amplitudes, signal duration). The minimum signal thresholds for the AE monitor were established experimentally by gradually lowering the threshold setting for each individual channel until spurious signals were recorded while the beam was in an unloaded state. The thresholds were then increased by 2 decibels (dB) to eliminate these spurious signals. This threshold value was then accepted if no spurious signals were recorded for one hour. In this way the ability of the monitor to capture all significant AE event signals was maximized.

In an effort to accurately determine the crack reopening load, two LVDTs with a range of ±0.1 in. (±2.5 mm) each were used during static and cyclic load testing after the initial crack test. In the case of Girder I, the two LVDTs were placed on the underside of the bottom flange. One LVDT was placed over the first visual crack while the second was positioned next to the crack. For the case of Girder II, LVDTs were initially located similarly to those in Girder I, over and near the first visual crack that appeared on the underside of the bottom flange. The LVDTs were then relocated to determine reopening load levels for the cracks opening on the vertical side face of the bottom flange.

CHAPTER 6 PROPERTIES OF GIRDER SPECIMENS I and II

6.1 Introduction

This chapter presents an overview of the material and geometric properties of the noncomposite and composite test girders. Material properties were determined from tests conducted on actual materials used in the girder construction, except where noted. Both material and geometric properties listed here were used in the analytical portions of the study, Chapters Seven through Eleven.

6.2 Test Girder Material Properties

6.2.1 Noncomposite Girder Concrete Properties

Mechanical properties of the girder concrete were measured at several times throughout the project duration. Properties tested and their respective ASTM Standard Test Methods are discussed. Plastic molds were used for all 6 x 12 in. (150 x 300 mm) cylinders, including those used for compressive strength, modulus of elasticity and splitting tensile strength. Steel molds [6 x 6 x 24 in. (150 x 150 x 610 mm)] were used for modulus of rupture specimens. PVC molds with DEMEC point inserts were used for the 4 x 11 in. (100 x 280 mm) creep and shrinkage specimens. A high strength sulfur-based capping compound was used when measuring compressive strength and modulus of elasticity.

All material property test specimens were made at the time of girder casting and initially cured with the girders. Each girder contained seven batches of concrete, which are documented by location within the girder and actual mix content in Appendix C of Kielb (1994). Samples were taken randomly from the batches. The girder manufacturer cast concrete cylinders using two methods: ASTM Standards and the Sure-Cure® system. Cylinders cured by the Sure-Cure® system were cured at the same temperature as the girder as monitored by temperature probes on the girder formwork. Cylinders were cast and cured at the Elk River Plant to ASTM standards. Additionally, cylinders cast for long term testing at the University of Minnesota (UMN) Laboratory were not cured according to ASTM standards. These cylinders were placed next to the girder formwork and covered with tarps, causing lower cure temperatures and resulting in lower initial strengths. However, cylinder strengths converged with results from the Elk River

Plant over time. Following removal of the tarps at 24 hours, UMN concrete specimens were transported to the UMN Lab.

Material properties given in Tables 6.1 - 6.5 for the time period within 24 hours of casting were determined from the manufacturer's samples using the Sure-Cure® and Materials Laboratory at Elk River as noted. Material properties measured at later times were determined from samples tested at the UMN Laboratory.

6.2.1.1 Concrete Compressive Strength

The required girder concrete compressive strengths were 8925 psi (61.5 MPa) at release and 10,500 psi (72.4 MPa) at 28-days. To insure that these strengths would be achieved, the target nominal mix design strength was 12,000 psi (83 MPa) at 28 days. Strengths measured prior to release and at 28 days were above the required design strengths. Required and measured concrete compressive strengths are given in Table 6.1. All cylinders were tested for compressive strength in accordance with the ASTM C 39 Test Method (1992). Measured strengths are reported to the nearest 100 psi (0.1 MPa) of the sample mean. With the exception of the first f'_c compressive strength test results at release (within 24 hours), all reported data were based on tests of three or more cylinders from a minimum of two batches and were within the ASTM acceptable range of results for three or more specimens tested by a single operator in a laboratory condition (i.e., 7.8% of the sample mean). The tests performed to determine the time each girder could be released was based on the first single cylinder compressive strength to surpass the design release strength, as is typical of the prestressed concrete industry. For the case of Girder I, the first reading was taken from the third of three cylinders tested, and for Girder II, the reading was based on the first of three cylinders tested.

Starting at 21 hours after casting, the limestone girder had a mean strength of 9300 psi, which increased to 12,100 psi at 28 days. The glacial gravel girder started at a higher mean release strength of 10,400 psi at 14 hours and reached a stable strength of 11,100 psi by 28 days. At later ages, measured concrete compressive strengths were higher for the girder cast with limestone aggregate than for the girder cast with rounded glacial gravel and microsilica. The decrease in strength for both girders at 200 days is best explained by the testing facility location as previously discussed. For the purpose of analysis, the 28-day compressive strength was used unless otherwise noted.

Table 6.1 Test Girder Concrete Compressive Strength

	Required Nominal Strength	Girder I - Limestone	Girder II- Glacial Gravel with microsilica
Concrete Compressive Strength, f'_c (ksi [MPa])			
within 24 hours	8925 [61.5]	9300 ^{ER} [64.1] (21 hrs)	10,400 ^{SC} [71.9] (14 hrs)
7 days	-	11,400 ^{ER} [78.5]	11,000 ^{ER} [75.7]
28 days	10,500 [72.4]	12,100 ^{ER} [83.4]	11,100 ^{ER} [76.5]
200 days	-	11,600 ^{UMN} [80.1]	10,800 ^{UMN} [75.7]
480 days	-	12,600 ^{UMN} [86.9]	11,100 ^{UMN} [76.5]

$^{SC, ER, UMN}$ Testing facilities: Sure Cure® System at Elk River, Elk River Prestress Plant Materials Laboratory, University of Minnesota Structures Laboratory, respectively.

6.2.1.2 Modulus of Elasticity

To determine the concrete static modulus of elasticity, E_c, 6 x 12 in. (150 x 300 mm) cylinders were tested using a compressometer according to ASTM C 469 (1990). Measured values for Girders I and II are given in Table 6.2. Each value represents the average of two tested cylinders from one batch. Cylinders cast from the three batches of concrete used in the center region of each girder were used for testing at the three given times. Predicted values were calculated according to the ACI Building Code 318-95 (1995) for normal strength concrete and ACI Committee 363 (1984) for high strength concrete using corresponding compressive strengths from Table 6.1. Curing conditions varied for the cylinders used to measure E_c and f'_c at 1 and 28 days. Corresponding f'_c values for 1-day moduli tests performed at the University were 8420 and 8740 psi (33.2 and 60.3 GPa) for Girders I and II, respectively. Similarly, corresponding 28-day strengths for the moduli tests were 10870 and 9650 psi (42.9 and 38.0 GPa) for the two respective girders. However, the tabulated compressive strengths from the Elk River Material Lab were used to determine the predicted moduli.

As can be seen, the measured moduli were consistently lower than either ACI equation predicted. Recalling that the ACI 318 relationship was based on low to normal strength concrete, a larger deviation was expected than using the ACI 363 relationship as shown. ACI 363 was a much better predictor of the elastic modulus, although measured moduli at 28 days for Girders I and II were 4810 and 4800 ksi, respectively, nearly 25% less than predicted, mostly likely due to curing conditions discussed previously.

Table 6.2 Modulus of Elasticity of Concrete in Test Girders

		Expected from Design	Girder I - Limestone	Girder II- Glacial
Modulus of Elasticity, E_c (ksi [GPa])				
1 day	Measured	-	4380 [30.2]	4750 [32.8]
		$f'_c = 8925$ psi	$f'_c = 9300$ psi	$f'_c = 10{,}400$ psi
	ACI 318 †	6020 [41.5]	6140 [42.4]	6500 [44.8]
	ACI 363 ‡	5280 [36.4]	5370 [37.0]	5610 [38.7]
28 days				
	Measured	-	4810 [33.2]	4800 [33.1]
		$f'_c = 10{,}500$ psi	$f'_c = 12{,}100$ psi	$f'_c = 11{,}100$ psi
	ACI 318 †	6530 [45.0]	7000 [48.3]	6710 [46.3]
	ACI 363 ‡	5640 [38.9]	5970 [41.2]	5760 [39.8]
480 days				
	Measured	-	4680 [32.3]	4800 [33.1]

† Predicted by ACI 318 (1995): $E_c = 33w^{1.5}(f'_c)^{0.5}$ where $w = 155$ lb/ft^3

‡ Predicted by ACI 363 (1984): $E_c = [40{,}000(f'_c)^{0.5} + 10^6)]*(w/145)^{1.5}$

6.2.1.3 Cracking Strength

The cracking strength of the girder concrete was evaluated using two standard methods: splitting tensile strength and modulus of rupture tests. Splitting tensile strength tests were conducted on 6 x 12 in. (150 x 300 mm) cylinders (ASTM C 496) at a loading rate of 17000 lb. (75.5 kN) per minute. Modulus of rupture tests were conducted on 6 x 6 x 24 in. (150 x 150 x 600 mm) beams at a loading rate of 1800 lb. (8 kN) per minute and under simple beam third-point flexural loading conditions (ASTM C 78). These rates corresponded to a stress increase of 150 psi (1.03 MPa) per minute, and were within the ASTM specified loading rate ranges of 100-200 psi (0.69 to 1.38 MPa) per minute for splitting tensile tests and 125-175 psi (0.86 to 1.21 MPa) per minute for modulus of rupture testing.

Specimens were tested at 28 days. A total of six cylinders chosen randomly from four batches of concrete in each girder were used for splitting tensile tests, and three beam specimens from the center batch (#3) of each girder were used for modulus of rupture testing. Based on the formulations discussed in Sections 2.2.3 and 2.2.4, maximum loads and specimen dimensions were used to determine the splitting tensile strength and modulus of rupture. Measured values from each test are listed in Table 6.3 for both girders.

When designing prestressed concrete members, tensile limits are implemented to avoid cracking of the concrete at two distinct times: at the time of release (when no time-dependent losses have occurred) and under service conditions (after losses have occurred). Therefore, comparison values are also listed for these two limit states in Table 6.3. According to the AASHTO Bridge Specifications (1993), the allowable tensile limit permitted at the time of release is $7.5\sqrt{f'_{ci}}$ (based on the nominal concrete compressive strength at release time), while the limit after losses have occurred is $6.0\sqrt{f'_c}$ (based on 28-day nominal compressive strength). In both girders, and independent of the test performed, the measured cracking strength was higher than either AASHTO limit state. This indicates the AASHTO limit states based on normal strength concrete are conservative for the high strength concrete used in this study. For the purpose of the analysis in this study, the measured modulus of rupture was used as the cracking strength.

Table 6.3 Cracking Strength of Concrete in Test Girders

	Expected from Design	Girder I – Limestone	Girder II- Glacial Gravel with microsilica
Modulus of Rupture, f_r (psi [MPa])			
28 days Measured	-	950 ± 41 [6.6 ± 0.3]	750 ± 68 [5.2 ± 0.5]
ACI 363 (Eqn. 2.24)	-	1260 [8.7]	1210 [8.3]
Mokhtarzadeh (Eqn. 2.26)	-	1010 [7.0]	980 [6.7]
Tensile Strength Split Cylinder, f_t (psi [MPa])			
28 days Measured	-	1070 ± 146 [7.4 ± 1.0]	1110± 94 [7.7 ± 0.6]
ACI 363 (Eqn. 2.16)	-	830 [5.7]	790 [5.4]
Mokhtarzadeh (Eqn. 2.18)	-	770 [5.3]	730 [5.0]
Comparative AASHTO Limit States (psi [MPa])			
	f'_{ci} = 8925 psi	f'_{ci} = 9300 psi	f'_{ci} = 10,400 psi
7.5 $\sqrt{f'_{ci}}$ - release	710 [4.9]	720 [5.0]	770 [5.3]
	f'_c = 10,500 psi	f'_c = 12,100 psi	f'_c = 11,100 psi
6 $\sqrt{f'_c}$ - 28 days	620 [4.2]	660 [4.6]	630 [4.4]

6.2.1.4 Creep and Shrinkage of Concrete

To investigate creep and (drying) shrinkage characteristics of the high strength concrete used, specimens were made on-site at the time of production of the two prestressed girders. Specimens

were 4 x 11 in. (100 x 280 mm) cylinders, stored under the curing tarps with the girders for the first 18 hours. Four specimens in total were cast for these tests: one from each girder for creep testing and one from each girder for shrinkage testing. The cylinders were then transported to the University of Minnesota structural engineering creep testing laboratory where they were stored at 72±4°F and 50±5% relative humidity. Creep and shrinkage strains were measured from three sets of Whittemore gage points spaced equidistantly around the perimeter, forming three 8 in. (200 mm) gage lines along the height of each cylinder.

The two creep specimens (one from each girder mix) were placed in series (one stacked on top of the other) in a creep-load testing frame and loaded to a level of 5150 psi (35.5 MPa) at an age of 24 hours to simulate actual release time. This load level represented 60% of the average one-day compressive strength of the mixes and was maintained for a period of 380 days. In comparison, this load level was 43% and 46% of the measured 28-day compressive strengths for Girders I and II, respectively. Strains from companion shrinkage specimens were deducted from the measured strains of the creep frame specimen to isolate the creep strains. The ends of the shrinkage specimens were sealed with epoxy coating to provide the same exposed surface area as that of the creep specimens. Length change and weight change were also recorded for a period of one year for the shrinkage cylinders.

The creep and shrinkage data collected from this project were analyzed using a nonlinear regression. Two curves for creep and two curves for shrinkage were modeled using the generalized forms given in Section 2.2.5. The results of each model are discussed.

Discussion of Creep of the Girder Concrete

ACI Committee 209 (1992) reported that creep of concrete at any given time, t, may generally be expressed as follows:

$$C_t = \frac{t^b}{a + t^b} C_u \left(\prod_{i=1}^{n} k_i \right), \tag{6.1}$$

where C_t is the creep coefficient at a given time, t, a and b are constants of 10 and 0.6, respectively, C_u is the ultimate creep coefficient and k is a series of correction factors. This formulation was developed for "standard conditions," and correction factors are applied for more specific cases. The test data was collected at a relative humidity of 50%. Because the girders were housed in a similar environment as the companion specimens, the relative humidity

correction factor, k_{RH}, was taken as 1.0. All remaining correction factors (older ages at loading, air content, member size and slumps more than 4 in. (102 mm)), were taken as 1.0.

Creep strains may be expressed in a similar form shown. Correction factors apply to this relationship just as they did for the creep-time relationship for conditions that vary from "standard".

$$\varepsilon_t = \frac{t^b}{a+t^b}\varepsilon_u\left(\prod_{i=1}^{n} k_i\right) \tag{6.2}$$

where ε_t is the creep strain at any given time, t, a and b are constants defined previously, and ε_u is the ultimate creep strain.

Using the predefined constants of 10 and 0.6 from the ACI 209 (1992), a "forced" creep relationship was developed to describe the measured data. A "fitted" curve was also developed in which case the constants (a and b) were defined to best fit the data. In this way, an ultimate creep coefficient and ultimate creep strains for each girder could be determined for both "forced" and "fitted" cases. In Table 6.4, the creep parameters (defined in Eqns. (6.1) and (6.2)) for the "forced" and "fitted" curves are listed for the concrete in each girder.

Table 6.4 Creep Data of Concrete in Test Girders

	Girder I - Limestone		Girder II- Glacial Gravel with microsilica	
	Forced Curve [1]	Fitted Curve	Forced Curve [1]	Fitted Curve
a	10	17.3	10	18.5
b	0.6	0.38	0.6	0.39
C_u	1.04	2.40	1.24	2.89
ε_u (x10^{-6})	1030	2370	1310	3071

[1]ACI Committee 209 (1992) relationship.

Figures 6.1 and 6.2 illustrate the forced and fitted curve functions along with the recorded data for Girders I and II, respectively. As expected, the fitted curve slightly better represents the measured data than the forced curve over the period of time that creep was measured on the cylinders. However, when the curves are extrapolated out past one year, it is found that the rate of creep for the fitted curve is much lower than that for the forced curve. After two years, only 41% of the ultimate creep has occurred for the fitted curve, whereas 86% has occurred for the forced curve. The difference is even more dramatic after 50 years, when the fitted curve predicts that only 71% of the ultimate creep has been experienced, compared to 97% for the forced curve.

Because of the very slow rate of creep predicted by the fitted curve, the parameters associated with forced curve are used in the program *Pbeam* in Section 7.4.4. High strength concrete is expected to creep less, resulting in a lower C_u value. Consistent with this expectation and as shown in Table 6.4, the forced C_u was lower than 2.35 for both girders. The parameters in the "fitted" cases compare well with high strength concrete results reported by Mokhtarzadeh (1996) and documented in Eqns. (2.33) and (2.34).

Discussion of Shrinkage of the Girder Concrete

ACI Committee 209 (1992) also reported a standard function for shrinkage at any time after age 1-3 days for steam-cured concrete, expressed as:

$$\varepsilon_{sh,t} = \frac{t}{\alpha + t}\varepsilon_{sh,u}\left(\prod_{i=1}^{n} k_i\right), \tag{6.3}$$

where $\varepsilon_{sh,t}$ is the shrinkage strain at any given time, t, α is 55 for steam-cured concrete loaded at ages 1-3 days, $\varepsilon_{sh,u}$ is the ultimate shrinkage strain, and k represents a series of correction factors. As with the creep-time function, all correction factors (older ages at loading, air content, member size and slumps more than 4 in. (102 mm)), were taken as 1.0.

The test girder cylinder data resulted in ultimate shrinkage strains shown in Table 6.5. 'Forced Curve' refers to ultimate shrinkage strains that were determined by forcing the data to the ACI 209 shrinkage relationship for steam cured concrete. 'Fitted Curve' is a best fit model of the data for both parameters.

Table 6.5 Shrinkage Data of Concrete in Test Girders

	Girder I – Limestone		Girder II- Glacial Gravel with microsilica	
	Forced Curve [1]	Fitted Curve	Forced Curve [1]	Fitted Curve
α	55	375	55	147
$\varepsilon_{sh,u}$ ($x10^{-6}$)	-105	-226	-150	-202

[1] ACI Committee 209 (1992) relationship.

For comparison purposes, $\varepsilon_{sh,u}$ for normal strength concrete is -730 $x10^{-6}$ when using the forced curve constant. High strength concrete is expected to shrink less due to the lower water content of the mix, resulting in a lower $\varepsilon_{sh,u}$ value. Consistent with this expectation and as shown in Table 6.5, $\varepsilon_{sh,u}$ for the forced case was lower than the typical NSC value.

Figures 6.3 and 6.4 are provided for easier visualization when comparing the forced and fitted shrinkage functions to the recorded shrinkage data of Girders I and II, respectively. Although the "forced" and "fitted" curves show deviation from the data at early and late stages, respectively, the fitted curve better represents the measured data at later ages than the forced curve. A different equation form may be in order for the best fit data to truly be a 'best fit', however for the purpose of this study, the generalized ACI 209 form was preserved.

Shrinkage of high strength concrete reported by Mokhtarzadeh (1996) specified the data best fit a form where α was equal to 65 and the ultimate shrinkage strain was equal to -530$\mu\varepsilon$ (Eqn. 2.35). Measurements from the girder concrete recorded shrinkage data much lower than this, indicating a possible source for error when computing prestress losses at later ages. Therefore, the Mokhtarzadeh parameters are used as a modification to measured properties when estimating prestress losses using the program *Pbeam* in Section 7.4.4.

6.2.2 Mild Steel Reinforcement

All mild steel reinforcement used in the girders and decks was Grade 60. Epoxy-coated No. 4 bars were used for slab reinforcement and girder stirrups, with the exception of four epoxy-coated No. 6 stirrups at each end of the girders to resist bursting. Four No. 8 bars (not epoxy-coated) ran longitudinally in the top flange of the girder along the entire length. Tensile tests were performed on three samples of each specimen type of the No. 4 bars to determine yield and ultimate strength, and are reported in Kielb (1994). Results of the tensile tests from individual specimen types, as well as the average of the three specimen types, are tabulated in Table 6.6. In addition, the average measured areas of the rebars are tabulated. A generalized stress-strain curve is shown in Figure 6.5. A modulus of elasticity of 29,000 ksi (200 GPa) was assumed.

Table 6.6 Mild Steel Reinforcement Tensile Test Results

Nominal Design Material Properties			
	Nominal Area (in^2 [mm^2])	Yield Stress, F_y (ksi [MPa])	Ultimate Stress, F_u (ksi [MPa])
No. 4 bar - Grade 60	0.200 [129]	60.0 [415]	90.0 [620]
Material Test Results			
Specimen Type	Measured Area (in^2 [mm^2])	Yield Stress, F_y (ksi [MPa])	Ultimate Stress, F_u (ksi [MPa])
No. 4 Slab rebar	0.185 [119]	75.0 [515]	121 [835]
No. 4 Modified U Stirrup	0.180 [116]	72.7 [500]	116 [800]
No. 4 Mn/DOT U Stirrup	0.185 [119]	75.0 [515]	119 [820]
Average of 3 Specimen:	0.183 [118]	74.3 [510]	119 [820]

6.2.3 Prestressing Strand Properties

The 0.6 in. (15.3 mm) diameter Grade 270 ksi (1860 MPa) low-relaxation prestressing strand was manufactured and donated by Union Wire Rope, Kansas City, Missouri. A generalized load-strain curve of the strand was provided in the mill test report supplied by the manufacturer and is documented in Kielb (1994). Additional information provided by the manufacturer included the measured diameter and area, yield strength, modulus of elasticity and ultimate strand strength. This information is listed in Table 6.7 along with the nominal values originally used in design of the test girders. Laboratory tests (documented by Kielb, 1994) were used to supplement the manufacturer information and are also listed in Table 6.7. These laboratory tests are briefly discussed. With the exception of strand area, the measured and manufacturer recorded results were relatively close to the property values used in the test girder design.

Laboratory tests were performed by University of Minnesota researchers at the Minnesota Department of Transportation Materials Research Center to measure the five material properties. The average cross-sectional area was determined by weighing and measuring lengths of strand and then computing the area by assuming the unit weight of steel to be 490 pcf (7850 kg/m^3). The strand diameter was determined by measuring the center wire and one outside wire of one seven-wire strand sample per roll (two total) using a ±0.0001 in. (0.0025 mm) micrometer. The strand area was the summation of the center wire area and six times the outside wire area. The two strand samples used to determine cross-sectional area had the same recorded area.

Table 6.7 Prestressing Strand Test Results

0.6" ϕ - Grade 270 ksi (Kielb, 1994)

	Nominal	Manufacturer Recorded	Measured
Diameter, in [mm]	0.600 [15.2]	0.600 [15.2]	0.614 [15.6]
Area, in^2 [mm^2]	0.215 [139]	0.228 [147]	0.228 [147]
Modulus of Elasticity, ksi [MPa]	28,500 [196,500]	28,800 [198,600]	29,100 [200,700] † 29,890 [206,200] ‡
Yield stress, f_{py}, ksi [MPa]	243 [1670]	247 [1700]	239 [1650]
Ultimate stress, f_{pu}, ksi [MPa]	270 [1860]	267 [1840]	269 [1860]

† Obtained from strain gages on single strands.
‡ Obtained from extensometer data.

A standard tensile test was performed on ten samples to determine the yield and ultimate loads, which were then converted to yield and ultimate stresses based on the measured area. The yield stress, f_{py}, was 239±2.5 ksi (1650±17 MPa) and the ultimate stress, f_{pu}, was 269±1.0 ksi (1860±6.9 MPa). A generalized stress-strain curve for the prestressing strand in tension is shown in Figure 6.6.

Modulus of elasticity measurements were also recorded during the yield and ultimate load tests for six of the ten samples using two methods. First, an "apparent" modulus was determined to be 29,100±200 ksi (200,700±1400 MPa) using strand strain gage data from gages oriented along the helix angle on the outside of one wire (of the seven-wire strand). Second, the overall modulus of elasticity was determined using extensometer data; yielding a value 29,890±2680 ksi (206,200±18,500 MPa). The difference between the two moduli is that strand gage data gives a relative modulus for the single wire that the gage was placed on. In addition, the outside wire on which the gage was placed experienced both torsion and extension. The modulus obtained from gage data is appropriate to use for translating the girder strand strain gage data to stresses. This procedure was used to determine the strand tensioning levels and strand stress ranges from measured strains observed under loads. The modulus determined from the extensometer data represents an overall modulus from all seven wires of the prestressing strand. This value is appropriate for determining transformed section properties, deflections, and cracking loads. However, during testing, the data recorded using the extensometer showed significant scatter, possibly indicating slip of the extensometer or incorrect testing procedure (noted by the high standard deviation). Due to this scatter, the modulus of elasticity as determined by the

manufacturer (28,800 ksi) was used for computing transformed sections, deflections and cracking loads in place of the measured extensometer modulus.

The rolls of prestressing strand were covered and stored outdoors at the prestressing yard for approximately one week before use. Once the strands were laid in the prestressing bed, they remained unprotected for five days until concrete pouring. The strand surface condition appeared free of oil and had a light surface rust prior to girder casting.

6.2.4 Composite Deck Concrete Properties

A standard Mn/DOT 3Y33 mix was specified for the deck with a nominal required strength of 4000 psi (27.6 MPa). Nominal required and/or predicted properties are tabulated in Table 6.8 along with measured property values. Material tests included concrete compressive strength, modulus of elasticity, modulus of rupture and splitting tensile strength. Tests were conducted in accordance with ASTM Standards as stated previously for girder material tests. Creep and shrinkage specimens were not prepared for the deck concrete. For the purpose of analysis, normal strength concrete values of C_u=2.35 and $\varepsilon_{sh,u}$=730 $\mu\varepsilon$ were used for the ultimate creep coefficient and ultimate shrinkage strain, respectively.

Table 6.8 Material Properties of Concrete in Deck

Test Type	Nominal	Measured	Predicted[1]
Compressive Strength, f'_c (psi [MPa])			
7 days	-	5090 [35.1]	-
28 days	4000 [27.6]	5860 [40.4]	$f'_c = 5860$ psi
Modulus of Elasticity, E_c (ksi [GPa])			
28 days	3830 [26.5] †	3990 [28.6]	4640 [32.0] †
Modulus of Rupture, f_r (psi [MPa])			
28 days	474 [3.3] ‡	632 [4.4]	574 [4.0] ‡
Splitting Tensile Strength, f_t (psi [MPa])			
28 days	423 [2.9] *	514 [3.5]	512 [3.5] *

[1]Predicted properties were based on the measured compressive strength (as opposed to the nominal compressive strength) at 28 days for the respective relationship.
† ACI 318 (1995): $E_c = 33w^{1.5}(f'_c)^{0.5}$ where w = 150 lb./ft^3
‡ AASHTO (1996): $f_r = 7.5\sqrt{f'_c}$
* ACI 318 (1995): $f_t = 6.7\sqrt{f'_c}$.

All material test results for the concrete deck exceeded those used in the initial design of the composite girders. A measured compressive strength of 5860 psi (40.4 MPa) surpassed the

nominal design strength by 45%. The measured modulus was greater than the nominal modulus of elasticity, E_c, based on the nominal design strength; however, the measured modulus was 14% less than that predicted using the measured compressive strength and the ACI 318 (1995) relation for E_c. Similarly, comparing the nominal modulus of rupture, f_r, which was based on the nominal design strength, to the measured modulus results in the measured modulus being greater than predicted by 33%. Using the measured compressive strength to predict f_r with the AASHTO relationship for the nonprestressed composite deck results in a value of 574 psi (4.0 MPa), indicating the AASHTO limit for cracking strength of normal strength concrete was conservative for the composite deck concrete. The nominal splitting tensile strength, f_t, was lower than measured. The predicted splitting tensile strength based on measured compressive strengths was nearly equal to that measured.

6.3 Girder Specimen Geometric Properties

Geometric properties of the girder can be calculated in various ways so as to give different levels of accuracy in analysis of behavior. Properties assumed in design are often more conservative than those used in analysis and are often estimated during the design process. Geometric section properties are computed by three methods: gross, net, and transformed. Depending on the method chosen for computing such properties, predicted stresses can vary significantly. Flexural stresses predicted by the force-in-tendon approach using the different methods were discussed in Section 2.5.1. A detailed discussion of how to compute geometric properties by these three methods is presented.

6.3.1 Section Property Definitions

Geometric section properties are necessary for determining flexural stresses and deflections. Properties include cross-sectional area, moment of inertia (with respect to the axis of bending), and neutral axis location. Properties can be computed for both the noncomposite and composite member cross sections.

Gross section properties are based on the total cross-sectional area of concrete for both the noncomposite and composite members. When computing the composite section properties, the deck concrete is transformed into an equivalent girder concrete area with the deck centroid remaining as it was prior to transformation. The centroid of the composite section is then shifted from the noncomposite section, accounting for the addition of the deck. Prestressing steel and

mild steel reinforcement are neglected in the determination of gross properties. The most common geometric section definition used in design is that of the gross section.

Net section properties are computed similarly with the exception that the prestressing steel area has been removed from the gross section, hence changing all three basic properties: cross-sectional area, moment of inertia and location of the neutral axis. The noncomposite section has a net area equal to the gross area less the area of prestressing steel. The remaining two properties are then calculated based on this net section. Typically, the net section properties are used only for the noncomposite section on which the prestressing force acts. As with the gross section properties, the presence of the mild steel reinforcement is neglected.

Transformed section properties are also commonly used as an estimation of actual geometric properties for analysis. The gross concrete area less the total steel (prestress and mild reinforcement) plus the total steel transformed to an equivalent area of concrete produces the transformed section. The composite section incorporates the transformed deck concrete. The mild steel reinforcement refers only to the steel in the compression flange of the girder and not that of the deck. Reinforcing in the deck is minimal and shown to have little effect on section properties.

The following subscript notation is used to distinguish among these properties. Gross, net and transformed properties are labeled with the subscripts *g*, *net*, and *tr*, respectively. In addition, noncomposite properties, *nc*, are differentiated from composite properties, *c*.

6.3.2 Computed Geometric Section Properties

Different geometric properties were used appropriate to the project phase (i.e., design, data reduction, analysis). Gross section properties were used in design.. During analysis, gross, net and transformed properties were used and noted as such. This was done because the large amount of prestressing steel in the section can have a great effect on the geometric properties. Computed properties (area, moment of inertia and neutral axis location from the bottom fiber; A, I, and y_b, respectively) are listed for Girders I and II in Table 6.9. The difference between the two girders was not their geometry, but rather the concrete modulus of elasticity used for the modular ratio in calculations of transformed section properties. In addition, the reported properties for transformed noncomposite and composite sections are based on the modulus of elasticity of the prestressing strand as determined by the manufacturer (see Section 6.2.3).

Table 6.9 Geometric Section Properties

Noncomposite Section Properties	Design	Girder I	Girder II
Gross Section Properties			
$A_{g,nc}$, cross-sectional area, in^2	624	623	623
$I_{g,nc}$, moment of inertia, in^4	167,048	166,600	166,600
$y_{b\text{-}g,nc}$, location of neutral axis, from bottom, in	22.34	22.38	22.38
$e_{g,nc}$, eccentricity of prestressing strands at midspan, in	16.95	16.99	16.99
Net Section Properties			
$A_{net,nc}$, cross-sectional area, in^2	na	613	613
$I_{net,nc}$, moment of inertia, in^4	na	163,400	163,400
$y_{b\text{-}net,nc}$, location of neutral axis, from bottom, in	na	22.67	22.67
$e_{net,nc}$, eccentricity of prestressing strands at midspan, in	na	17.28	17.28
Transformed Section Properties			
$A_{tr,nc}$, cross-sectional area, in^2	na	691	691
$I_{tr,nc}$, moment of inertia, in^4	na	188,200	188,300
$y_{b\text{-}tr,nc}$, location of neutral axis, from bottom, in	na	21.56	21.56
$e_{tr,nc}$, eccentricity of prestressing strands at midspan, in	na	16.17	16.17
Composite Section Properties			
Gross Section Properties			
$A_{g,c}$, cross-sectional area, in^2	895	971	971
$I_{g,c}$, moment of inertia, in^4	315,600	356,400	356,700
$y_{b\text{-}g,c}$, location of neutral axis, from bottom, in	30.77	32.34	32.35
$e_{g,c}$, eccentricity of prestressing strands at midspan, in	25.41	26.95	26.96
Transformed Section Properties			
$A_{tr,c}$, cross-sectional area, in^2	na	1083	1084
$I_{tr,c}$, moment of inertia, in^4	na	395,800	396,200
$y_{b\text{-}tr,c}$, location of neutral axis, from bottom, in	na	31.91	31.92
$e_{tr,c}$, eccentricity of prestressing strands at midspan, in	na	26.52	26.53

6.3.3 Weight per Lineal Foot

The weight of the test girder was assumed for initial design on a per lineal foot basis. The noncomposite girder self weight for design was 672 plf (9.81 kN/m) which was calculated

from the gross girder area (624 in^2 [402 m^2]) and the assumed concrete density of 155 pcf (2480 kg/m^3) (Mn/DOT Bridge Design Manual, 1991, §5-392.502). The composite girder self weight included the additional weight of 481 plf (7.02 kN/m) due to the deck, which was calculated from the gross deck area (462 in^2 [300 m^2]) and the assumed concrete density of 150 pcf (2400 kg/m^3). This resulted in a total composite design weight of 1150 plf (16.8 kN/m). These assumed design weights do not account for the volume of steel in the section, but rather are based solely on gross concrete area. Assumed design weights are tabulated in Table 6.10.

Table 6.10 Test Girders Self-weight

Weights in plf [kN/m]	Design	Girder I	Girder II
Noncomposite girder [1]	672 [9.81]	710 [10.4]	716 [10.4]
Deck weight[1]	481 [7.02]	479 [6.99]	479 [6.99]
Composite test section (girder + deck)	1150 [16.8]	1190 [17.4]	1200 [17.5]

[1]Weights of the noncomposite girder, deck, and composite cross sections listed for Girders I and II include the weight of prestressing and mild steel reinforcement.

Actual girder self weights varied for each test girder due to the weight differences of each concrete mix. The weight of concrete for each girder and the deck was determined by the average weight of six cylinders from each concrete mix. The concrete weights were then multiplied by the volume of each cylinder and resulted in the following densities: Girder I - limestone aggregate, 152 pcf (2430 kg/m); Girder II - glacial gravel with microsilica, 153 pcf (2450 kg/m); deck, 147 pcf (2350 kg/m). Using the as-built dimensions of the deck (for average width and depth), and replacing the density of concrete by the density of mild steel reinforcement actually in the section, a weight per foot of the noncomposite and composite girders was determined. These final weights are tabulated in Table 6.10. As shown, the noncomposite and composite girder weights were both higher than anticipated. This was due to the large amount of prestressing steel in the sections, because steel has a density 3.33 times that of concrete.

In addition, an average unit weight of each noncomposite girder was calculated to include the weight of the prestressing and mild steel reinforcement. Taking the noncomposite weight per foot and dividing by the gross girder area (624 in^2 [402 m^2]), the following densities result. Girder I had an average unit weight of 164 pcf (2620 kg/m) while Girder II had an average unit weight of 165 pcf (2640 kg/m). These unit weights compared well with the Mn/DOT standard of 165 pcf (2640 kg/m).

6.4 *Pbeam* Model Properties

The analytical program *Pbeam*, developed by Suttikan (1978), was used in this study for comparison of measured data to initial and time dependent responses of the prestressed concrete test girders. Basic assumptions of the program are reviewed in Section 2.7.2. Several options were available to account for linear and nonlinear responses of the concrete and steel materials, and to define the geometric and time line models. The options and specific models used in this study are discussed. Experimentally determined material properties were used to define a model for each girder. A generalized HSC model was defined for each girder that incorporated results from a study on the mechanical behavior of high strength concrete (Mokhtarzadeh, 1996). Units of psi, inches and days are used throughout. Data input files are given in Appendices A through D for each model.

6.4.1 Girder Concrete Model

The *Pbeam* high strength concrete model included a stress-strain relationship, creep, shrinkage and aging functions. The parameters for each relationship are summarized in Table 6.11 for Using Measured Properties and Modified Shrinkage Model of each girder. Each relationship and respective parameters of the models are reviewed for completeness.

Table 6.11 Pbeam Model Parameters

Property/Parameter	Girder I		Girder II	
	Using Measured Properties	Modified Shrinkage Model	Using Measured Properties	Modified Shrinkage Model
28-day strength, f'_c (measured)	12,100 psi		11,110 psi	
Elastic moduli, E_c	4810 ksi		4800 ksi	
Creep, a =	0.6		0.6	
b =	10.0		10.0	
C_u =	1.04		1.24	
Shrinkage, α =	375.0	65.0	147.0	65.0
$\varepsilon_{sh,u}$ =	-226 $\mu\varepsilon$	-530 $\mu\varepsilon$	-202 $\mu\varepsilon$	-530 $\mu\varepsilon$
Age function, a =	0.21		0.02	
b =	0.99		1.00	

The stress-strain relationship for high strength concrete (HSC) has been shown to differ from the Hognestad model for normal strength concrete (ACI 363 1984; Mokhtarzadeh 1996). The *Pbeam* program requires a user input curve of up to 12 points to define the stress-strain

relationship when not using the default model. A complete stress-strain curve for each mix was not measured. Therefore, a modified stress-strain model was determined for each HSC mix using the measured 28-day modulus of elasticity, E_c, and the 28-day ultimate compressive strength, f'_c, as summarized in Table 6.11. The compressive strain corresponding to f'_c was assumed to be 2500 με (Wee et al.,1996). The generalized HSC stress-strain model for each girder was based on the measured 28-day ultimate compressive strength. However, the elastic modulus for Girder I (limestone) was computed using the ACI 363 relationship which was found to be a lower bound for the heat-cured limestone reference mix with Type III cement by Mokhtarzadeh (1996). The study found the ACI 318 moduli relationship to be the lower bound for heat-cured rounded glacial gravel mixes with microsilica and Type III cement, most closely matching the Girder II mix, hence the ACI 318 equation was used for Girder II. A best guess approximation was used to define the remaining portions of the curve for each mix. The model using measured properties and the generalized stress-strain relationships for Girders I and II are shown in Figures 6.7 and 6.8, respectively.

Creep and shrinkage models were developed from recorded data for each girder mix, and reported in Section 6.2.1.4. The general forms of ACI 209 (1992) creep and shrinkage relationships for normal strength concrete were preserved. The best-fit models for creep and shrinkage are summarized in Tables 6.4 and 6.5. A creep recovery ratio of 0.70 was assumed for both girder mixes. Mokhtarzadeh reported shrinkage parameters for all heat-cured high strength concrete specimens, independent of aggregate and these parameters, listed in Table 6.11, were used for the Modified Shrinkage Model.

High strength concrete mixes used in this study resulted in high-early compressive strengths, therefore the default age function, based on ACI 209 (1992), was modified for each girder model (using measured properties and generalized HSC models) based on measured compressive strengths and elastic moduli at 1, 7 and 28 days. The age relationship followed the form

$$\frac{(f_c')_t}{(f_c')_{28}} = \frac{t}{a+bt} \tag{6.4}$$

where $(f_c')_t$ is the concrete compressive strength at a given time, t, and $(f_c')_{28}$ is the measured 28-day compressive strength. The age function parameters, a and b, that best matched time-dependent strengths and moduli for the two girders are listed in Table 6.11.

The unit weight of concrete was measured and reported in Section 6.3.3 (Girder I = 152 pcf (2430 kg/m^3), Girder II = 153 pcf (2450 kg/m^3)) and did not vary between the two high strength concrete models.

6.4.2 Deck Concrete Model

The stress-strain relationship for the composite deck concrete model was chosen to be the program default based on the Hognestad model for normal strength concrete (Suttikan, 1978, Figure 2.5). The model incorporated the measured concrete strength and modulus at 28 days as reported in Section 6.2.4. Measured creep and shrinkage data were not available on the deck concrete mix, so the default parameters were used. Both functions were based on ACI 209 (1992) relationships for normal strength concrete in a moist-cured condition. Using an ultimate creep coefficient of 2.35 and an ultimate shrinkage strain of –551 after application of correction factors for relative humidity at 50%, deck thickness (0.888), slump of 4 in., cement content (0.98), fine aggregate content (39.6%) and 4% air content.

The age function was not used for the deck concrete because loads were not applied to the composite deck until after reaching the 28-day compressive strength and no measured data was available. The unit weight of concrete used for the deck was measured as 147 pcf (2350 kg/m^3).

6.4.3 Reinforcing and Prestressing Steel

Idealized tension and compression curves from the generalized tensile relationships shown previously in Figures 6.5 and 6.6 were used for the mild steel and prestress reinforcement. The material model used for the mild steel reinforcement was an elastic perfectly-plastic model, user input as a bilinear function defined by three points, assuming symmetry for tension and compression. The prestressing steel model was also user input and defined by 12 points on the stress-strain curve, assuming symmetry for tension and compression. Measured yield and ultimate stress and strain values were used for both models. Both materials had a unit weight of 490 pcf. The material models used no age, creep or shrinkage functions. The PCI Committee on Losses (1975) relaxation function for low-relaxation prestressing steel was included only for the prestress reinforcement model, although adjusted to accommodate the construction time line as discussed.

6.4.4 Geometric Composite Girder Definition

The cross section of the composite girder was discretized to compute stresses, strains and deflections of fibers at all levels. The discretization of the composite girder at the midspan was developed to match the transformed area, center of gravity and transformed moment of inertia. The composite girder was divided height wise into nine concrete layers closely matching the actual girder shape. The noncomposite girder was defined by seven of the layers and the deck made up the two remaining layers. Each concrete layer was then divided height wise into subsections such that strains were computed through the girder height at increments equal to or less than one inch (25 mm). Mild steel reinforcing in the deck and top flange of the noncomposite girder was included as individual layers. Each pair of draped strands was defined as a linear piece-wise layer that allowed for a changing height along the girder length. Debonding of strands on three of the four ends was also accounted for by allowing pairs of strands to transfer force to the girder at the debonded strand locations. The span was divided into 28 length wise elements, the maximum that *Pbeam* could accommodate with the number of layers used to describe the cross section.

6.4.5 Time Line for Model

The time line for the *Pbeam* model was chosen to be as close to the actual time line of the girder histories as possible. However, program constraints did not allow for prestressing strand relaxation to begin until the time of casting. Because the prestressing strands were tensioned 3 days prior to concrete casting, a relaxation loss of 1.9 ksi (13.1 MPa) was subtracted from the initial prestressing strand stress. However, the relaxation function parameters of a=45 and b=0.55 were not modified. Changing the initial prestressing without changing the relaxation parameters lead to slightly overpredicted relaxation losses. However, these losses were very small compared to the losses due to creep and shrinkage. The remaining complete girder history was input as a part of the program to check stress and deflection levels at the following times: release (24 hours), moving in the precasting yard (3-7 days), 28 days, deck placement (200 days), HS25 load testing (Girder I at 500 days, Girder II at 687 days), first crack test (Girder I at 593 days, Girder II at 721 days), and ultimate flexural testing (Girder I at 860 days, Girder II at 840 days). Data input files for the two girders using measured properties are given in Appendices A and B.

Results from the *Pbeam* input files are compared with measured values and other predictions. Prestress losses and camber results are summarized and discussed in Sections 7.4.4 and 7.6.2, respectively. Additionally, Chapter Ten compares ultimate capacities of each girder as predicted by *Pbeam* with measured values.

CHAPTER 7 TIME DEPENDENT RESPONSE OF GIRDERS

7.1 Introduction

This chapter presents the time-dependent behavior of the test girders. Early age behavior (defined as the first 14 days of girder life) includes prestressing strand tensioning level and relaxation prior to release, transfer length, initial prestress losses, camber, and cracking due to manufacturing and release. Long term time dependent behavior includes prestress losses and camber changes over the life of each girder (i.e., to the end of ultimate flexural strength tests; Girder I life was 860 days, Girder II life was 840 days). Material properties used in this chapter were documented in Chapter Six, unless otherwise noted.

7.2 Tensioning Level

Prestressing strands were specified to be tensioned to 75% of their ultimate strength ($0.75 f_{pu}$) after seating losses. Using a nominal strand area of 0.215 in^2 (140 mm^2) for the forty-six strands, a nominal initial tension level was specified to be 2003 kips (8910 kN). Strands were initially pretensioned to approximately 10% of f_{pu} to untangle the strands such that instrumentation could be installed and mild steel reinforcement could be placed. Upon completion of those tasks and prior to formwork placement, a hydraulic jack pulled each strand to its specified tensioning level. The girders were constructed in series (on the same prestressing bed) such that strands were tensioned to the same level in both girders. Table 7.1 summarizes several time steps at and around the time of tensioning, and the corresponding stress level induced. Calculations discussed in this section were based on the measured strand area of 0.228 in^2 (147 mm^2), an ultimate strand strength of f_{pu} = 269 ksi (1860 MPa) and an apparent modulus of elasticity of the prestressing strand, based on strain gage data, of 29,100 ksi (200,700 MPa) from Section 6.2.3.

As mentioned previously, the task of preloading strands was performed only for convenience of separating strands so that additional instrumentation could be applied without cable twisting or gage damage. The initial preload strain was recorded by four gages on four different strands. Three of the four gages measured an average of 440 με with a standard deviation of 30 με. This corresponded to a stress of 12.8 ± 0.9 ksi (88.3 ± 6.2 MPa) or 5% f_{pu}. The remaining gage was damaged by twisting of the strands. Preloading the strands to a level of less than 55% f_{pu} results in negligible relaxation (Naaman, 1982).

Table 7.1 Strand Tensioning and Release Summary

Time Line	Method of Obtaining Measurement	f_{ps}, strand stress level, ksi	$\%f_{pu}$ ultimate tensile	$\% f_{pi}$ initial tension[1]
Preload, (Day 1)	Strand strain gages, ε_s = 440 με	12.8	-	-
Before Seating, (2)	Hydraulic jack, P = 44.5 kips	195	72.6%	-
After Seating, (2)	Strand strain gages, ε_s = 6585 με	191.6	71.3%	100%
Elastic Shortening :		Change in strand stress, ksi		$\% f_{pi}$
Release –GI, (6)	Strand strain gages [2], Δ = 807 με	23.5	-	12.3%
Release –GII, (6)	Strand strain gages [2], Δ = 708 με	20.6	-	10.7%

[1] Initial tension base value begins after seating of the strands.
[2]Gage readings normalized to center of gravity of strands at midspan.

Measurements of full strand tensioning were recorded with 88 additional gages applied to the preloaded strands. Before seating the strands against the bulkheads, strands were tensioned to 44 kips (200 kN) based on the calibrated dial gage of the hydraulic jack. This corresponded to a "before seating" stress of 195 ksi (1350 MPa) or 72.6% f_{pu}. An "after seating" stress was determined from the total 92 strain gages installed on the strands and monitored throughout the tensioning process. Eighty-three percent of the gages survived the tensioning process and indicated that the strands were tensioned to an absolute strain level of 6585 :, (including the preload strain). This corresponded to a stress of 191.6 ksi (1320 MPa), or 71.3% f_{pu} "after seating", with a standard deviation of 5.8 ksi (40 MPa). The "after seating" stress was defined throughout the analysis as the measured initial tensile strand stress (100% initial tensioning level, f_{pi}). Seating is the level after which losses in the strand begin to occur.

Strand strain gage data were also recorded immediately before and after release to give an indication of the elastic shortening component of prestress losses. Girder I data was recorded from eight gages in the midspan region (center 13 ft [4 m]) and measured a strain reduction of 807 ± 44 με. This change resulted in a strain at release corresponding to a prestress loss of 23.5 ksi (162 MPa), 12.3% of the initial tensioning level, f_{pi}, due to elastic shortening only. Girder II data was also collected from eight gages in the midspan region and measured a strain change of 708 ± 101 με. A prestress loss due to elastic shortening of 20.6 ksi (142 MPa) was computed, 10.7% from the initial tensioning level.

7.3 Girder Cracking

Three types of cracking were observed during the early phase of construction of the girders (from the time forms were removed to the time strand release was finalized). Vertical "pre-release" cracks were observed to develop in Girder II about one hour prior to strand release. After strand release, the pre-release cracks were no longer visible, but cracking in the bottom flange of all four ends was observed. Also after release, web cracking was noted in Girder End IID containing the fully draped strand pattern. Crack observations were categorized as prior to and after release, and are discussed.

7.3.1 Pre-release Cracks (Girder II)

In cases where a prestressed girder is slow in achieving the required release strength, it is typically left on the precasting bed for a longer period of time before strand release. This occurred in the study with Girder I. Because both girders were cast on the same bed, Girder II had to remain unreleased on the bed (even though it had already reached the required release strength) until Girder I could be released. Formwork for Girder II was removed and it was forced to sit on the bed without being released until the release strength of Girder I was achieved.

Girder I, the limestone concrete mix, had been cast first approximately 1.0 hour prior to the casting of Girder II. Girder II was the first to achieve its nominal release strength at an age of 14 hours. Form removal of Girder II began three hours later to facilitate attachment of DEMEC points to the girder surface for transfer length measurements. The forms on Girder I were removed at an age of 22 hours, although Girder I did not achieve its release strength until a half-hour later.

A total of 6.0 hours elapsed between the time the forms were removed from Girder II and release (2 hours for Girder I). During this time, pre-release cracks were observed to develop in Girder II (no cracking was seen in Girder I). A total of fifteen vertical cracks were observed along the length of the girder, concentrated within the middle 40% of the span length. The vertical cracks extended from the top flange toward the bottom flange.

A list of the crack locations and depths (from the top flange and downward) is given in Table 7.2. Eleven of the cracks extended approximately 34 in. (864 mm) deep (nearly to the bottom flange). Four of the cracks were less than 7 in. (175 mm) deep. Crack widths were estimated to be on the order of 0.005 to 0.025 in. (0.13 to 0.64 mm). Two of the deeper cracks (highlighted

with a black marker in the photograph) are shown in Figure 7.1. The photograph was taken prior to release.

The source of the pre-release cracks was attributed to the thermal and shrinkage effects experienced by Girder II after form removal. The girder deformations were restrained by the prestressing strands (not yet released), the hold down points, and friction between the girder and the bed. These deformations initiated the pre-release cracks in the girder starting at the top flange and going into the web. Similar pre-release cracks have been observed in other studies of high strength prestressed girders (Roller, 1993).

Table 7.2 Vertical Pre-Release Crack Locations (Girder II)

Location from End II-C (ft [m])	Crack Depth on West Side of Beam (in. [mm])	Crack Depth on East Side of Beam (in. [mm])	Average Crack Depth (in. [mm])
32.8 [10.0]	40.0 [1015]	34.0 [865]	37.0 [940]
34.0 [10.4]	6.75 [170]	6.75 [170]	6.75 [170]
34.2 [10.5]	42.0 [1065]	31.0 [785]	36.5 [925]
39.5 [12.0]	44.0 [1120]	31.0 [785]	37.5 [955]
41.0 [12.5]	8.00 [205]	0.00 [0]	4.0 [100]
54.3 [16.6]	40.0 [1015]	29.0 [735]	34.5 [875]
58.7 [17.9]	8.00 [205]	0.00 [0]	4.0 [100]
59.7 [18.2]	32.0 [815]	30.0 [760]	31.0 [785]
63.0 [19.2]	30.0 [760]	26.0 [660]	28.0 [710]
65.5 [20.0]	42.0 [1065]	32.0 [815]	37.0 [940]
66.0 [20.3]	0.0 [0]	6.75 [170]	3.38 [85]
69.5 [21.1]	41.5 [1055]	28.0 [710]	34.8 [885]
76.3 [23.2]	43.0 [1090]	37.5 [955]	40.3 [1020]
87.3 [26.6]	32.0 [815]	30.0 [760]	31.0 [785]
95.0 [28.9]	28.0 [710]	28.0 [710]	28.0 [710]

Prestressing strands were flame cut to release the girders from the prestressing bed. Upon strand release, the vertical cracks in the girder closed completely. If not for the lines drawn on Girder II to identify the initial pre-release crack locations, there was no indication the girder had been initially damaged.

7.3.2 Bottom Flange End Cracking Due to Release

After the strands were flame cut to release the girders from the prestressing bed, one to two cracks were observed to develop in the bottom flange of each end of the girders. End cracking for Girder I - End A is shown in Figure 7.2. Crack patterns in the bottom flange of the remaining three ends were very similar. Plant personnel commented that cracking of this nature was common and most likely caused from the detensioning pattern. Subsequent research performed by Kannel (1997a, 1997b) confirmed the end cracking may result from the strand release methodology. In that study, cracks were eliminated by changing the strand cutting pattern and debonding some strands in the end region.

7.3.3 Web Cracking Due to Release (Girder II)

In addition to the bottom flange cracking observed in End IID, web cracking was noted. The web crack locations (highlighted by black marker) are shown in Figure 7.3. One crack, observed to form during release, ran from the intersection of the web and top flange down toward the bottom flange at approximately a 45-degree angle. The crack was evident from both sides of the girder, although it was a hairline crack. A series of short cracks, 3 to 6 in. (75 to 150 mm) in length each and totaling 3.5 ft (1.1 m), also formed at release along the web to top flange interface on both sides of the girder. Within four days, additional cracking was noted between the two original crack locations. However, crack growth stabilized and no additional cracking in the end was observed.

End IID, the only end observed to develop web cracks, was the only end with 12 draped strands; the other three ends used a strand pattern combination of 4 draped and 8 debonded strands. The fully draped pattern had been used in the past by the prestress manufacturer with no web damage. However, the larger diameter strand used for these test girders (0.6 in. [15.2 mm]) placed a 40% larger force in the web than the standard smaller diameter strands (0.5 in. [12.7 mm]), even though the individual design strand stress of $75\%f_{pu}$ was the same. No modifications, including the addition of end blocks or changing of the center-to-center strand spacing, had been made to the web to accommodate the larger force. Therefore, the draped/debonded strand combination is recommended for use to eliminate web cracking in the 6 in. (152 mm) web of the Mn/DOT girder sections with the larger diameter strand placed at 2 in. (50.8 mm) centers.

7.4 Prestress Losses

Prestress losses, or time-dependent decreases in strand stress, occur instantaneously due to elastic shortening at release and over time due to steel relaxation, and creep and shrinkage of concrete. The components generating the prestress losses are interdependent, leading to the complex nature of predicting prestress losses and determining the state of stress in a member at any given time. The force in the prestressing strands continuously decreases until such time when the losses stabilize; the majority of the losses occur within the first 6 to 12 months of the member life (Naaman, 1982).

A comprehensive review of the force-in-tendon approach used in determining the concrete stress in the cross section at the time of interest was discussed in Section 2.5. Several interpretations were discussed for applying the force-in-tendon approach based on varying definitions of geometric section properties. When discussing design losses (the change in the strand force P with respect to the initial strand force P_i over time), the concrete stress was computed from Eqn. (2.39) based on gross geometric properties. The alternate method for determining the concrete stress (Eqn. 2.41), in which stress equilibrating loads are based on net section properties, was used for better accuracy when comparing predicted to measured values, and its use is discussed in further detail in Section 7.4.1.

Design losses using gross section and nominal material properties were computed in Section 4.3.3. Losses were calculated to be 10.2% at release and 35.8% under final service conditions. Using design assumptions, both girders were expected to behave the same.

7.4.1 Measured Release Losses

The determination of prestress losses at any given time must incorporate all stress loss components of the strand from the time of tensioning. Foil-type gages were placed directly on the prestressing strands to determine the initial tensioning level (Section 7.2). Concrete embedded vibrating wire gages were installed in each girder near the center of gravity of strands (*cgs*) to determine the concrete strain change. Details regarding the vibrating wire gages and how they were used to determine prestress losses are discussed.

Data were recorded from concrete embedded vibrating wire gages installed near the center of gravity of the strands (*cgs*) to monitor the change in concrete strain with time. One gage was installed along the length at each of the following locations: $0.45L$, $0.50L$, and $0.55L$, to give

release and long-term strain changes. Prestress losses were defined as the loss in strand stress at the level of the *cgs* at any given time relative to the initial tensioning stress. Placement of each gage was offset (height wise) from the location of the center of gravity of the prestressing strands. The offset distance for each gage was less than 0.75 in. (20 mm). Because the offset distance was small relative to the distance between the *cgs* and the neutral axis, no gage height adjustment was made. The vibrating wire gage strain data were directly interpreted as concrete strain readings at the *cgs*.

The concrete stress immediately after release can be expressed as the change in strain as recorded from the vibrating wire gages ($\Delta\varepsilon_{vw\text{-}release}$) multiplied by the concrete modulus at the time of release, E_{ci}, plus any stress existing in the concrete immediately before release (e.g., due to restrained shrinkage or thermal strains) such that

$$\sigma_{c,after-rel} = \Delta\sigma_{c@rel} + \sigma_{c,before-rel} = \left(\Delta\varepsilon_{vw-release} E_{ci}\right) + \sigma_{c,before-rel}. \qquad (7.1)$$

From Eqn. (2.41), the concrete stress in the cross section after release, $\sigma_{c,after\text{-}rel}$, at the level of the *cgs* (using the sign convention of tension positive) is

$$\sigma_{c,after-rel} = \frac{-P_{after-rel}}{A_{net}} + \frac{-P_{after-rel} e_{net}^{\,2}}{I_{net}} + \frac{M_{sw} e_{net}}{I_{net}}, \qquad (7.2)$$

where

$P_{after\text{-}rel}$ = force in the prestressing strand after release,

A_{net}, I_{net} and e_{net} = net geometric section properties (see Table 6.9)

M_{sw} = girder self-weight moment at midspan (see Table 6.10).

Setting Eqn. (7.1) equal to Eqn. (7.2) and solving for the force in the strand after release results in

$$P_{after-release} = \left[\frac{1}{1/A_{net} + e_{net}^2/I_{net}}\right]\left(\frac{M_{sw} e_{net}}{I_{net}} - \left(\Delta\varepsilon_{vw-release} E_{ci}\right) - \sigma_{before-release}\right). \qquad (7.3)$$

The stress in the strand after release, $f_{ps,after\text{-}release}$, can be computed based on the total area of prestress, A_{ps},

$$f_{ps,after-release} = \frac{P_{after-release}}{A_{ps}}. \qquad (7.4)$$

The initial loss of stress in the prestressing strand can then be computed as the change in strand stress from the time of initial tensioning, f_{pi}, to the strand stress immediately after release relative to the initial strand stress,

$$\%Loss_{initial} = \left(\frac{f_{pi} - f_{ps,after-release}}{f_{pi}} \right) 100 . \qquad (7.5)$$

The initial tensioning stress, f_{pi}, was determined from foil gages placed directly on the strands and was reported as 191.6 ksi (1320 MPa) in Table 7.1. By determining the difference in strand stress relative to the initial tensioning level, any stress relaxation that occurred in the strand prior to release is included. Additionally, any changes in steel stress due to temperature changes between the time of tensioning and the time the concrete bonds to the steel is included, as well as any other sources of losses.

Between the time the concrete bonds to the steel and immediately prior to release, concrete stresses may exist in a girder because the prestress steel in the bed restrains the concrete as shrinkage occurs and because temperature effects result from the differences in coefficients of thermal expansion between the concrete and steel. Concrete shrinkage causes unrestrained concrete to contract, but because the free length prestress steel in the precasting bed restrains the shortening, the concrete incurs tensile stresses. Also, as the temperature increases due to the heat of hydration during curing, the steel within the concrete wants to expand to a greater degree than the concrete (the coefficient of thermal expansion is greater for steel than concrete). Once the two materials are bonded, the increased temperature will cause tensile stresses in the concrete while reducing the steel stress. These tensile stresses in the concrete (prior to release) reduce the prestress force (Eqn. 7.3).

The level of concrete stress in each test girder was not known prior to release. Therefore, to determine the losses using this method, lower and upper bounds were assumed. As a lower bound, the concrete stress before release was set equal to zero (from Eqn. 7.1, $\sigma_{c,before-rel} = 0$), which is the typical design assumption, and the average initial prestress loss from the vibrating wire gages in each girder was computed. The lower bound prestress loss immediately after release in Girder I was 15.5% and in Girder II was 18.6%. Figures 7.4 and 7.5 show the lower bound prestress losses from all gages for Girders I and II, respectively, for the first 10 days after casting.

An upper bound was also considered to investigate the effect that concrete stress existing in the girders prior to release (from Eqn. 7.1, $\sigma_{c,before\text{-}rel} \neq 0$) may have had on losses. Because concrete tensile strength tests were not performed at the time of release, the maximum tensile strain in the concrete was estimated as the 28-day cracking strength. Using this modulus of rupture value as an upper bound for estimating prestress losses was justifiable because both researchers and precast manufacturers have reported cracking in girders prior to release. Cracking prior to release was also observed in one of the two test girders used in this study (Section 7.3.1). Based on this assumption for $\sigma_{c,before\text{-}rel}$, upper bound initial prestress losses were computed to be 29.1% and 29.3% for Girders I and II. Although these computed losses are significantly larger that those reported as lower bound initial losses, they should be considered only as an upper bound because stresses in the concrete were not known prior to release.

7.4.2 Measured Long Term Losses

To determine long term prestress losses (the loss of strand stress over time), perfect bond between the steel and the concrete, and between the concrete and the gage, was assumed such that the concrete strain change at the *cgs* was equal to the steel strain change at the *cgs*, which was equal to the gage strain change. Because the vibrating wire strain gage was embedded in concrete, the strain readings recorded after release incorporated changes due to creep and shrinkage of the concrete. Any stress relaxation of the prestressing strand occurring after release was not included because relaxation is defined as a loss in steel stress at a constant strain; thus strain gages cannot detect relaxation. However, using a theoretical relationship of relaxation with respect to time (PCI Committee on Prestress Losses, 1975) relaxation losses were superimposed on total losses at any given time by using incremental time steps and updating the stress in the strands to the time of interest.

The change in strand stress over time with reference to 'after release' (time t less time of release) was computed as

$$\Delta\sigma_{s,(t-release)} = \left[\left(\varepsilon_{vw,t} - \varepsilon_{vw,after-release}\right)E_s\right] + \Delta\sigma_{relax(t-release)}, \qquad (7.6)$$

where

$\varepsilon_{vw,t}$ = the vibrating wire strain gage reading at the time of interest, t

$\varepsilon_{vw,after\text{-}release}$ = the vibrating wire strain gage reading as recorded immediately after release,

E_s = modulus of elasticity of the prestressing steel, (28,800) ksi,

$\Delta\sigma_{relax,t\text{-}release}$ = strand stress relaxation between the time of release to the time of interest.

Because the stress loss due to relaxation was not measured, the relationship from Eqn. (2.37) (PCI Committee on Prestress Losses, 1975) was used to estimate stress relaxation that occurred in the girders. The strands were tensioned four days prior to release. Using the PCI relationship, relaxation was estimated to be 2.1 ksi (14.7 MPa) over the four days and was inherent in the initial loss as reported previously. Relaxation losses beyond release to later times of interest were small because the majority of relaxation occurred within 4 days after tensioning. By 28 days, relaxation was estimated to have increased over and above relaxation prior to release by 0.27 ksi (0.2% loss) and by the time of crack testing it was estimated to have increased by 0.60 ksi (0.3% loss) from the time of release.

Based on the assumptions, long term prestress losses were computed relative to the initial tensioning stress, f_{pi}, as

$$\%Loss_{Long-term} = \left[\frac{f_{ps,after-release} - \Delta\sigma_{s(t-release)}}{f_{pi}} 100\right] + \%Loss_{initial}, \qquad (7.7)$$

where $f_{ps,after\text{-}release}$ was defined in Eqn. (7.4), $\Delta\sigma_{s(t\text{-}release)}$ was defined in Eqn. (7.6) and the $\%Loss_{initial}$ was defined in Eqn. (7.5).

Long term losses were computed for each girder using initial losses of 15.5% and 18.6% for Girder I and II, respectively, as computed in Section 7.4.1 with the assumption that concrete stress before release was equal to zero (i.e., lower bound initial losses). Measured losses as recorded by the vibrating wire gages at selected time steps are tabulated in Table 7.3.

Table 7.3 Measured Lower Bound Losses[1]

	Girder I - Limestone	Girder II - Glacial Gravel
Initial at release	15.5%	18.6%
28 days	21.6%	22.2%
Deck Casting	23.9%	23.3%
Crack Testing	26.6%	25.8%
Ultimate Flexural Test	27.2%	26.3%

[1] Losses tabulated assume the concrete stress before release was zero (i.e., lower bound losses).

As with initial release losses, the effect that any concrete stress that existed in each girder prior to release was investigated. Superposition of this effect can be used for long term losses. Assuming the concrete stress before release was a maximum of the 28-day measured modulus of rupture, long term losses reported in Table 7.3 would increase by a maximum of 13.6% for Girder I and 10.7% for Girder II. This effect and its potential influence on cracking loads are discussed further in Sections 8.3 and 9.3 for Girders I and II, respectively.

Figures 7.6 and 7.7 illustrate the change in prestress losses for the life of each test girder (maximum 860 days) and do not include superposition of relaxation losses which were on the order of 0.3% loss. Losses appear to have a rapid increase during the first 100 days before stabilizing. Deck placement occurred at 200 days. The strand stress change due to weight of the deck was subtracted from the total strand stress after deck placement because losses do not include this component, only the effect that this component has on creep of the non-composite girder concrete. Load testing (static and fatigue) that occurred during the time period from 375 to 700 days appeared to have little effect on prestress losses.

7.4.3 Measured Temperature

Internal girder concrete temperatures were monitored with the vibrating wire gages from the time of concrete casting. The temperature variations in Girders I and II are shown in Figures 7.8 and 7.9 from the time of casting to 8.8 days. The time denoted by full days (0.0, 1.0, 2.0, etc.) corresponded to 12:00 p.m. (noon) for that given day. The temperature monitoring began in the 95°F (35°C) range in the hot sunlight the day of casting before dropping to 85°F (29°C) once the formwork was in place. The heat of hydration process increased the temperature of the concrete almost immediately after casting. Cooling began at 0.5 days (midnight) after casting. Formwork was stripped at about 1.2 days after casting noted by the decrease in cooling at 112°F (44°C). The girder reached ambient temperature by late evening at 1.8 days (about 10:00 p.m.). The daily ambient temperature was observed to vary 10 to 20°F (5 to 10°C) in any 24-hour period during the first 8.8 days. After that time, temperature was monitored less frequently.

The figures show that curing under their own heat of hydration, the girders reached maximum curing temperatures of 152 and 156°F (67 and 69°C), for Girders I and II, respectively. This was within the PCI maximum recommended curing temperature of 190°F (88°C) (*PCI Design Handbook*, 1992).

Once inside the testing facility at a girder age of 60 days, daily temperature variations were minimized as the girders were protected from the elements, including direct sunlight. Although the testing facility was unheated, temperature changes were gradual and temperature gradients through the member were negligible.

A change in temperature can cause a material to change its dimension. As the temperature increases, a material generally expands. The expansion of a homogeneous and isotropic material is linearly related to its coefficient of thermal expansion. In the case of prestressed girders, where two materials exist together in one system, and whereas the coefficients of thermal expansion of the two materials are not equal, equilibrium and compatibility must be maintained as temperature changes occur. Changes in temperature in the prestressed girder directly affect the stress in the strands. To investigate the influence of thermal strains on prestress losses, the following simplifications were assumed:

1. a block of concrete is prestressed with a single strand at the centroid,
2. no thermal gradient exists, i.e., temperature changes are constant through the depth of the concrete,
3. creep and shrinkage of concrete are neglected,
4. stress relaxation of the prestress is neglected, and
5. two arbitrary times are chosen as t_1 and t_2, where both times are after release.

At time t_1, the temperature of the girder is T_1. At some later time, t_2, the temperature of the girder is T_2. By ignoring all other sources of losses, the change in prestressing force due to this change in temperature will be investigated.

The change of prestress force, ΔP, over any given time increment after release due solely to a change in temperature, ΔT, can be solved through the use of constitutive equations, compatibility and equilibrium for concrete and prestressing steel. Assume the strain in the concrete at time t_1 is given by

$$\varepsilon_{c1} = \frac{-P_1}{E_c A_c}, \tag{7.8}$$

and the strain in the prestressing strand is given by

$$\varepsilon_{s1} = \frac{P_1}{E_s A_s}, \tag{7.9}$$

where

P_1 = force in the prestress strand at time t_3,

A_c and E_c = area and modulus of net concrete section, and

A_s and E_s = area and modulus of the prestressing steel.

As the temperature increases by some quantity (T_2-T_1), the concrete and steel strains at some later time t_2 become

$$\varepsilon_{c2} = \frac{-P_2}{E_c A_c} + \alpha_c (T_2 - T_1), \tag{7.10}$$

and

$$\varepsilon_{s2} = \frac{P_2}{E_s A_s} + \alpha_s (T_2 - T_1), \tag{7.11}$$

where

P_2 = force in prestress at time t_2,

α_c and α_σ = coefficient of thermal expansion for the concrete and steel, respectively.

From strain compatibility, the change in concrete strain between times t_1 and t_2 must be equal to the change in steel strain over the same time period,

$$\Delta\varepsilon_c = \varepsilon_{c2} - \varepsilon_{c1} = \Delta\varepsilon_s = \varepsilon_{s2} - \varepsilon_{s1}. \tag{7.12}$$

Substituting Eqns. (7.8-11) into (7.12) and rearranging to solve for the change in prestress force, ΔP, results in

$$\Delta P = P_2 - P_1 = -(\alpha_s - \alpha_c)(T_2 - T_1)\frac{A_s E_s A_c E_c}{A_s E_s + A_c E_c}. \tag{7.13}$$

Due to the inequality of thermal coefficients between the concrete and the steel, a negative temperature change, $T_2 < T_1$, would cause an increase in the strand force and would appear to lower the prestress losses. This effect is shown in Figures 7.4 and 7.5. As the daily temperature varies, the prestress losses oscillate. The overall increasing monotonic slope about which the losses fluctuate is due to the changing prestress losses caused from creep and shrinkage of concrete and steel relaxation.

The effect of temperature changes on prestress losses was considered using the coefficient of thermal expansion for each material. The coefficient of thermal expansion of concrete, α_c, varies with the aggregate used. The range for normal weight concrete is 5.0 to 7.0 x 10^{-6} /°F (8.5 to 12.6 x 10^{-6} /°C) depending on the aggregate and amount of natural sand (*PCI Design Handbook*,

1992). For mixes most closely representing materials used in the test girders, concrete thermal expansion coefficients may range as low as 2.0 to 5.7 x 10^{-6} /°F (4.3 to 10.3 x 10^{-6} /°C), (ACI 209, 1992). Material data were not recorded for the test girder concrete coefficients of thermal expansion. For design, a coefficient of 6.0 x 10^{-6} /°F (10.0 x 10^{-6} /°C) is frequently used.

To determine the relative influence of temperature changes on the prestressed concrete system (after release), two cases were considered using Eqn. (7.13). Because the relationship assumes that prestressing is placed at the centroid of the concrete section and not offset at some eccentricity, the following comparisons are shown only as general trends. First, assuming an extreme temperature drop of 200°F (110°C), the prestressing force in this case would increase by 27.7 kips (125 kN), which is equivalent to a reduction of 1.1% in prestress loss. Second, a more realistic temperature change of 50°F (28°C) was considered. Realizing an ambient temperature of 75°F was recorded when the strands were first tensioned, a 50°F change would easily encompass the temperature range undergone by the girders (25°F to 100°F). This case would result in a prestress loss of ±0.3%. However, temperature variations are not normally included as a component of predicted prestress losses, i.e., predicted prestress losses assume a constant temperature. Therefore, due to the anticipated low variation in prestress loss at realistic temperature changes as shown by the general trends above, and due to the actual coefficient of thermal expansion for the concrete not being measured, the prestress losses after release were not adjusted for variations in temperature. Additionally, the initial reference point, the temperature at which the gage, concrete and steel bonded, was not known.

7.4.4 Predicted Prestress Losses

Several methods for predicting prestress losses are available for comparison to measured data. These methods were previously discussed in Section 2.6.3. Four of the methods (a time-step approach, PCI Committee (1975), PCI Design Handbook (1992), and AASHTO (1996)) were used as predictors of initial and long-term prestress losses for each test girder assuming nominal design properties from ACI 318. In addition, losses were calculated using the time step approach based on high strength material properties. Using the same parameters as presented in Section 2.2 and in Table 6.11, Table 7.4 lists the assumed material properties for the Nominal Design Model and the HSC Nominal Model. Although Mokhtarzadeh (1996) suggests a single set of parameters for shrinkage of HSC, no such general suggestion is given for creep. For the

purposes of this report, the HSC design case creep is given as the lower bound from Mokhtarzadeh's work (C_u = 0.94). As an upper bound, the ultimate creep coefficient make be taken as that for NSC (C_u = 2.35).

Table 7.4 Assumed Properties for Predicted Design Losses

Property/Parameter	Nominal Design Case Using NSC Relationships	Nominal HSC Design Case
Nominal Compressive Strength Release, f'_{ci} 28-days, f'_c	8,925 psi 10,500 psi	8,925 psi 10,500 psi
Elastic modulus Release, E_{ci} 28-days, E_c	6016 ksi † 6525 ksi	4780 ksi ‡ 5100 ksi
Creep, a = b = C_u =	0.60+ 10.0 2.35	0.60* 10.0 0.94
Shrinkage, α = $\varepsilon_{sh,u}$ =	55.0+ 780 με	65.0 * 530 $\mu\varepsilon$

†ACI 318 (1995).
‡ACI 363 (1984).
+ACI 209 (1992).
*Mokhtarzadeh (1996).

The measured losses and predicted results of each method are compared for several time steps of interest [initial, 28-day, deck casting at 200 days, initial crack test (Girder I - 598 days, Girder II - 727 days), and ultimate testing for each girder (GI - 840 days, GII - 860 days)] in Table 7.5. (Table 7.6 compares measured losses with those predicted by analytical methods using measured material properties). Comparisons are discussed.

Measured Losses versus Time Step Cases

The Time Step method was used to predict losses based on nominal material properties determined from both normal strength (NSC) and high strength concrete (HSC) relationships. The results are listed in Table 7.5 as "Time Step Nominal Design Case" and "Time Step HSC Nominal Case." The actual design process would not have accounted for the casting sequence in which relaxation of the strand stress occurred for four days prior to release. Therefore, stress relaxation was estimated to begin 24 hours prior to release, as commonly assumed in current engineering practice.

Table 7.5 Predicted Design Losses

	Measured [1]		Time Step Nominal Design Case [2]	Time Step HSC Nominal Case [3]	PCI Comm.[2] (1975)	PCI Handbook (1992) [2]	AASHTO (1996) [2]
	Girder I	Girder II					
Initial	15.5%	18.6%	11.2%	13.8%	10.6%	9.9%	10.2%
28-days	21.6%	22.2%	22.9%	20.1%	19.7%	*	*
Deck casting	23.9%	23.3%	33.2%	26.6%	25.8%		
Crack Testing	26.6%	25.8%	35.9%	28.6%	28.8%		
Ultimate Flexure	27.2%	26.3%	36.4%	29.0%	28.8%		
Final Service	-	-	38.1%	30.4%	33.1%	26.6%	35.8%

[1] Lower bound measured losses from vibrating wire gages embedded in each girder (See Table 7.3).
[2] Predictions using nominal design values with NSC relationships (See Table 7.4).
[3] Predictions using nominal design values with HSC relationships (See Table 7.4).
* PCI Handbook and AASHTO use lump sum predictors for initial and final service conditions with no intermediate time steps.

When comparing the two predictive methods, initial losses were much higher for the high strength concrete model because the initial concrete modulus was significantly lower than that of the normal strength model. With a lower concrete modulus, predicted elastic shortening (strand stress loss) at release is increased. As time continued, the effect of the reduced creep and shrinkage of high strength concrete was reflected as lower relative losses. By 28 days, the high strength model consistently predicted lower losses, as expected.

In the case of Girder I, the use of nominal high strength design properties to predict losses via the time step method was a much better predictor of lower bound measured losses than normal strength properties. Considering the measured loss has an inherent stress relaxation loss of 1.1% at the time of release due to the unforeseen casting sequence not accounted for in the predictive methods, the initial predicted losses using the time step method may be closer to initial lower bound measured losses than they initially appear. Had the design stage accounted for the strand stress relaxation loss prior to release, predicted initial losses using high strength concrete parameters and including relaxation would be within 0.7% of the measured initial loss. Lower bound long term measured losses tended to be below both normal and high strength models predictions. If the HSC creep model was based on an upper bound for creep losses (C_u = 2.35), then the long term losses would have been significantly larger (approximately 9%) for times from deck casting to final service.

For the Girder II "Time Step Cases," predicted losses in Table 7.5 were the same as Girder I because the nominal design properties were the same for both girders. The two test girders were expected to behave similarly. The only variable expected to cause a difference in losses was the concrete mix, which is not accounted for in this predictive method other than by the predicted concrete moduli which had the same nominal value. The measured lower bound initial loss in Girder II was much higher than both normal and high strength concrete models predicted, although closer to the high strength model as expected because of the lower concrete modulus computed from high strength models. By superposition of the 1.1% relaxation loss at release in the predictive methods, the measured lower bound initial loss was 3.7% higher than the high strength nominal case predicted. Lower bound measured long term losses of Girder II were less than the lower bound measured losses in Girder I and less than predicted using the Time-Step method, indicating that the pre-release concrete stress in Girder II was much higher than in Girder I. Implications of the pre-release cracking observed in Girder II on losses and general behavior is discussed in Chapter Eleven.

7.4.4.2 Measured Losses versus Commonly Used Design Loss Predictors

Prestressed concrete design often incorporates loss estimations based on simplified lump-sum methods such as those presented in the PCI Design Handbook (1992) and by AASHTO (1996). A more complex estimation is available using the method suggested by the PCI Committee on Prestress Losses (1975). All three methods for predicting prestress losses are commonly used in current engineering design, and were tabulated in Table 7.5 for comparison to lower bound measured losses. Nominal design properties with normal strength concrete relationships (Table 7.4) were used for predicting losses, and because both girders were designed the same, predicted losses were identical for the girders.

In the case of each predictive method for both girders, the predicted initial losses were less than the lower bound measured losses by 4.9 to 8.7% because the methods were based on normal strength concrete relationships (reviewed in Section 2.5.2), the modulus of elasticity was overpredicted for high strength concrete. The larger modulus causes lower predicted elastic shortening losses at release (i.e., lower initial losses).

The lump-sum methods predict losses at final service conditions. While the girders were tested to ultimate flexure at an average age of 850 days, it is difficult to compare the last

measured losses to the final predicted losses. The long term predicted losses include creep and shrinkage based on normal strength concrete relationships. Previous research has shown that normal strength concrete tends to creep and shrink more than high strength concrete (Mokhtarzadeh, 1996). Therefore, it would be expected that the predictive methods would result in greater losses at final conditions than what might be measured. In the PCI Committee method (1975) that was also based on normal strength concrete material properties, the predicted losses at the final service condition were greater than the lower bound measured losses.

To compare lower bound measured losses at intermediate time steps with a commonly used method, losses were predicted using the PCI Committee method (1975). For both girders, the initial predicted losses were less than the lower bound measured losses, as discussed previously. By 28 days, when creep and shrinkage tend to influence losses to a greater degree, predicted losses were less than lower bound measured losses for both Girders I and II. Because NSC relationships were used for creep and shrinkage, it was expected that predicted losses would be higher than the lower bound measured losses. However, because the lower bound measured losses at release were higher than predicted, the effect of accelerated creep and shrinkage had not yet been overcome. Comparing the relative difference of measured losses to predicted losses between release and 28-days, the difference in the predictive method is larger as expected. By the time of the ultimate flexural tests, losses were predicted to be 1.6% higher than lower bound measured losses for Girder I and 2.5% higher than lower bound measured losses for Girder II. Because commonly-used loss predictors are based on normal strength concrete material property relationships, they cannot be expected to accurately predict losses in prestressed concrete girders manufactured with high strength concrete.

7.4.4.3 Analytical Methods of Predicting Losses

The comparisons with predictive losses were based on design assumptions. To better compare the measured losses to predicted losses, two analytical methods (the modified Time Step Method and the program *Pbeam*) were used for each girder considering two concrete models (using measured properties and measured properties with modified shrinkage). The assumptions and results of each model are discussed for both girders and results are tabulated with measured losses in Table 7.6. Discussion of the model differences follows the comparison of the lower bound measured losses to predicted losses of the models.

Table 7.6 Predicted Analytical Losses Using Measured Properties

	Measured [1]	Time Step Using Modified Shrinkage [3]	*Pbeam*	
			Using Measured Properties [2]	Using Modified Shrinkage [3]
Girder I:				
Initial	15.5%	14.9%	14.4%	14.4%
28-days	21.6%	21.8%	19.6%	21.2%
Deck casting	23.9%	28.8%	23.3%	26.9%
Crack Testing	26.6%	30.8%	23.8%	27.5%
Ultimate Flexure	27.2%	31.2%	24.3%	28.0%
Final Service	-	32.6%	25.9%	29.0%
Girder II:				
Initial	18.6%	13.8%	13.4%	13.4%
28-days	22.2%	21.2%	19.1%	20.7%
Deck casting	23.3%	28.5%	23.3%	26.4%
Crack Testing	25.8%	30.9%	23.3%	26.9%
Ultimate Flexure	26.3%	31.1%	23.3%	26.9%
Final Service	-	32.6%	24.8%	28.5%

[1] Lower bound measured losses from vibrating wire gages embedded in each girder (See Table 7.3).
[2] Measured material properties (See Table 6.11).
[3] Modified shrinkage coefficients from HSC Design model (See Table 6.11).

7.4.4.4 Measured Losses versus Time Step Case

The "Time Step Using Modified Shrinkage" case from Table 7.6 represents a reasonable estimation of prestress losses based on measured material properties from each girder. The method is a modified version of Naaman's Time Step Approach (1982). Measured material properties consistent with Naaman's method include the measured concrete elastic moduli at known time steps (at 1-day and 28-days), prestressing ultimate strength (for relaxation curves), and strand elastic modulus and strand yield stress as obtained from the manufacturer. The "Time Step Using Modified Shrinkage" case differs from Naaman's Time Step Approach in the following ways. The concrete creep and shrinkage relationships suggested by Naaman have been replaced with relationships using 'forced' curves from measured creep and the shrinkage curve suggested by Mokharzadeh (1996) for each test girder (Section 6.2.1.4). The concrete stress computed at the beginning of each time step is based on gross geometric section properties for Naaman's method while the modified method used herein is based on net geometric section

properties for a more accurate estimation. In addition, the initial strand stress immediately before release in the modified method accounts for three days of relaxation prior to girder casting by using a continuous time line starting at strand tensioning.

Predicted losses for Girder I from the "Time Step Using Modified Shrinkage" case were reasonably close when compared with lower bound measured losses from Girder I. The initial predicted loss was 0.6% less. The long-term predicted losses were not as close to the measured lower bound losses, typically overpredicting the measured losses by 4.9%. Much of this difference is because the time-step method does not account for shrinkage or creep of the deck concrete. It only considers the effect of the weight of the deck on the concrete stress at the cgs. Girder II predictions using the Time Step Method with measured properties were less than the lower bound measured losses at early times, and then were higher at later times. The initial predicted losses were 4.8% less than lower bound measured losses. By 28 days, Girder II predicted losses were less than the lower bound measured losses by 1.0 %. With increasing age, the lower bound measured losses were lower than predicted by 4.8 to 5.2%. The difference in Time-Step prestress losses between the two girders at release (14.9% and 13.8%) was caused by the difference in initial measured concrete modulus.

7.4.4.5 Measured Losses versus Pbeam Cases

The "*Pbeam* Using Measured Material Properties" case refers to the type of concrete model used for the girder, including concrete aging, creep, shrinkage, elastic modulus, and ultimate compressive strength as determined from measured material properties. This model, along with the assumptions used to define the other material properties (deck concrete, mild steel reinforcement, and prestress strand) and the section geometry were discussed previously in Section 6.4. Girder concrete parameters are listed in Table 6.11.

Predicted initial losses using the *Pbeam* method were less than the lower bound measured losses for both girders. As with other predictive methods, *Pbeam* did not account for losses due to thermal changes (i.e., actual initial losses are influenced from differences in between concrete and steel thermal expansion coefficients, and temperatures vary over the girder life). Additionally, *Pbeam* assumes the concrete stress prior to release was zero, as assumed for lower bound losses. The initial loss for Girder I was underestimated by 1.1% when compared with the lower bound initial measured loss. Girder II initial loss was also underestimated by *Pbeam*, as it

was using the Time-Step Method, by 5.2%. The *Pbeam* case using measured material properties with modified shrinkage properties predicted that the losses in Girder I remained less than lower bound measured losses early in the Girder history, but then predicted larger losses than measured, ranging from -3% to 1.1%. Girder II predicted losses were underestimated by *Pbeam* at 28-days by 1.5% and were slightly overpredicted at later ages. Differences between the two analytical methods (Time-Step and *Pbeam*), as well as differences between the two girders are discussed.

Differences in the Time-Step method and the *Pbeam* program at release are discussed for Girder I. Both methods incorporated the initial measured concrete elastic modulus. The main difference between the two methods at release was the girder geometry. *Pbeam* could not perfectly model the sloping portions of the flanges, hence the concrete area and moment of inertia were not identical to those of the test girders. Also, the *Pbeam* output resolution of the strand stress is 1 ksi (0.6% loss). At later times differences between the two methods appear because the time-step method only relies on the concrete stress at the cgs and assume plane sections remain plane. The time-step method did not account for any creep or shrinkage in the deck. No change was observed in the prestress losses for Girder II when adjusting the strand placement at the *cgs* because the change was within the resolution of the output. *Pbeam* is a fiber based model, so the restrictions that plane sections remain plane is removed, and *Pbeam* could account for shrinkage and creep of the deck, however these parameters were not measured, so typical NWC values were assumed for the deck. With this in mind, the difference in losses between the Time-Step and *Pbeam* methods is accountable.

To investigate the measured shrinkage properties, a *Pbeam* analysis was also performed using the measured shrinkage properties. As discussed in Section 6.2.14, the measured shrinkage of cylinders from girder concrete were considerably lower than predicted using the high strength concrete relationship proposed by Mokhtarzadeh (1996) and presented in Table 6.11. Additionally, shrinkage data presented in Figures 6.3 and 6.4 did not compare well with typical shrinkage models. When the measured shrinkage parameters were used, *Pbeam* results indicated lower long term losses than the "Modified Shrinkage Properties" shrinkage model. As expected, shrinkage had no effect on predicted release losses as no shrinkage had taken place in the *Pbeam* model. *Pbeam* predicted losses with the HSC shrinkage model were 1.6% higher than those calculated with *Pbeam* using measured properties (21.2 compared to 19.6%) for

Girder I by 28-days. Girder I losses were also higher over time, as expected, and were equally as high as the non-modified shrinkage model was low when compared to measured lower bound losses. The lower bound measured losses used for comparison were determined by assuming the concrete stress before release was equal to zero. If concrete stresses prior to release did exist, the measured losses would increase and be closer to the *Pbeam* predictions using the modified shrinkage model.

Additional comparisons can be made for Girder II in the context that the modified HSC shrinkage model had no effect on initial losses reported for the *Pbeam* case using measured material properties. Increased shrinkage as predicted by *Pbeam* with the HSC model for Girder II (Table 6.11) resulted in increased losses as expected when compared with the *Pbeam* case using measured material properties. However, the effects of pre-release cracking in Girder II must be considered. A detailed review of the pre-release cracking and its effect on Girder II long-term behavior and prestress losses are given in Chapter Eleven.

7.5 Transfer Length

At the time of the test girder design, an FHWA moratorium (1988) was in effect which stated that 0.6 in. (15.2 mm) diameter prestressing strands were not to be used on 2.0 in. centers without further investigation. As the test girder designs became finalized, the opportunity to obtain transfer length data on 0.6 in. diameter strands on 2 in. centers in full scale high-strength concrete prestressed girders became an objectives. As noted in Section 4.1.1, the use of larger strand area was required to take full advantage of the high strength concrete.

7.5.1 Measured Transfer Length

Instrumentation used to investigate transfer length included surface-embedded DEMEC gages and vibrating wire gages embedded in the concrete. The intention of gage placement was to capture the point of full force transfer along the length of the girder. DEMEC points were embedded longitudinally at 6.0 in. (152 mm) centers starting at 2 to 3 in. (51 to 76 mm) from the end and continuing 4 ft (1.2 m) beyond the last debonded strand, for a total of 24 ft (7.3 m) from the end. For the end configuration without debonding, DEMEC points were embedded for a total distance of 4 ft (1.2 m). DEMEC points were located height-wise as closely as possible to the center of gravity of the strands (*cgs*), while staying horizontal on the vertical face of the bottom flange. Although the *cgs* varied in the end region from 8.21 to 5.39 in. (209 to 137 mm)

due to strand draping and debonding, the DEMEC points were located at a constant height of 5.2 in. (132 mm) above the bottom flange. All ends included one vibrating wire gage located at 15.5 to 16.8 in. (394 to 427 mm) from the end and between 5.25 and 5.75 in. (133 to 146 mm) height-wise from the bottom face. Extreme steel congestion in the bottom flange end region caused the vibrating wire gage data to be unreliable. Results from the DEMEC points are discussed.

DEMEC points were read using a Whittemore dial gage. Due to the number of points to be read and the time involved with the manual approach used for reading, only one reading per 6 in. (152 mm) length was recorded at any given time. The difference in readings before and after release gave a length change. A strain was then determined by dividing the length change by the original length. As the strain increased from zero at the end of the member to a maximum value, the transfer length could be defined. However, with the data scatter that is inherent with the measuring process, two other strain averaging methods were used for determining transfer length from the recorded strain.

Transfer lengths were determined graphically from the measured experimental DEMEC data using methods proposed by Russell and Burns (1993, Report 1210-5F) and Cousins et al. (1993). In the "95% Average Maximum Strain Method" proposed by Russell and Burns, strain readings were first smoothed by averaging the data over three gage lengths to reduce anomalies in the data. The average maximum strain was determined by computing the numerical average of the smoothed strains contained within the strain plateau. The intersection of a line corresponding with 95% of the average smoothed strain data and the smoothed strain profile represented the transfer length. Figures 7.10a-d illustrate the results from this method for both girders, Ends IA through IID. Using this procedure, transfer lengths in the range of 20.4 to 28.5 in. (518 to 725 mm) were obtained for the four girder ends.

The "Final Average Method" employed by Cousins et al. (1993) eliminated data points outside of the range of one standard deviation from the averaged strain plateau. The average strain of the remaining data points was then determined, and the transfer length was defined as the intersection of the final average strain and the data. Figures 7.11a-d illustrate the results from this method for both girders, Ends IA through IID. The results obtained with this method were very similar to those obtained using the 95% Average Maximum Strain Method and ranged from 22.4 to 28.8 in. (569 to 732 mm).

Table 7.7 summarizes transfer length estimations for the four girder ends using the two numerical approaches described previously. In addition, the average transfer lengths of the two methods are reported. The measured transfer length referred to herein for each girder is the average of results for both ends.

Table 7.7 Measured Transfer Length Summary

Graphical Methods Using Measured Surface Strain Data	Girder - End [in. (mm)]			
	I-A	I-B	II-C	II-D
95% Average Maximum Strain Method	27.6 (701)	28.5 (725)	22.4 (570) †	22.2 (565)
Final Average Method	27.4 (696)	22.4 (569)	24.8 (630)	28.8 (732)
AVERAGE of Methods	27.5 (699)	25.5 (647)	23.6 (600)	25.5 (650)
Measured Transfer Length‡	*26.5 (673)*		*24.6 (624)*	

† A spuriously high data point was omitted which indicated a transfer length of 14.8 in. (376 mm).
‡ Measured Transfer Length was the average of the two methods for each girder, and is used throughout except where noted.

It should be noted that reported transfer lengths are for straight strands that were fully bonded in the section. The transfer length change due to the small percentage of additional force (less than 5% of the total force) provided by the debonded strands bonding beyond the point of sheathing was not separable and hence neglected. Reported transfer lengths are therefore only for the initial force transfer into the end of the girder. Spacing of DEMEC gages along the draped strands was too large for an accurate determination of transfer length of draped strands to be obtained.

7.5.2 Predicted Transfer Length

The two most common transfer length predictors, AASHTO (1996) and ACI 318 (1995), were used for comparison to measured transfer length data. Additionally, the current FHWA recommendation (Buckner, 1995) was also compared. All three relationships were reviewed in Section 2.6.1. Listed in Table 7.8 are transfer lengths from each relationship. Nominal design transfer lengths were based on a nominal strand diameter of 0.60 in. (15.3 mm), nominal tensioning level of 75% f_{pu} [202.5 ksi (1400 MPa)], and initial and final prestress losses as predicted by the PCI Committee on Prestress Losses (1971). Predicted transfer lengths incorporating the measured properties from the individual girders are also listed. These properties included a measured strand diameter of 0.614 in. (15.6 mm), measured initial tensioning level of 191.6 ksi (1320 MPa), and lower bound measured initial losses for each

respective girder (see Table 7.3) for the FHWA method. Final losses for the ACI 318 method were taken as the lower bound losses measured at the time of ultimate flexural testing.

Table 7.8 Predicted Transfer Length Summary

Method for Prediction	Nominal in. (mm)	Girder I in. (mm)	Girder II in. (mm)
AASHTO [1]	30.0 (760)	30.7 (780)	30.7 (780)
ACI 318 [2]	25.6 (650)	28.6 (725)	28.9 (735)
FHWA [3]	34.3 (870)	33.1 (840)	31.9 (810)
Measured [4]	-	*26.5 (673)*	*24.6 (624)*

[1] AASHTO (1996): $L_t = 50\ d_b$
[2] ACI 318 (1995): $L_t = (f_{se}\ d_b)/3$
[3] FHWA (Buckner, 1995): $L_t = (f_{si}\ d_b)/3$
[4] Measured transfer length as reported in Table 7.7.

When compared with measured transfer lengths, all three relationships (AASHTO, ACI 318 and FHWA) predicted longer transfer lengths for the individual girders. This indicates the relationships conservatively predicted the transfer length of 0.6 in. (15.3 mm) diameter Grade 270 ksi (1860 MPa) low-relaxation strands embedded in the high strength concrete test girders and placed on 2 in. (50.8 mm) centers. The AASHTO equation was a reasonable predictor, especially in the case of Girder I, and was independent of the prestress losses in the section. The FHWA equation would seem to be the most logical predictor because it was based on initial losses. However, it is the ACI 318 relationship, based on final lower bound measured losses, that appears to be the most accurate when compared to measured transfer lengths in both girders.

7.5.3 Surface Strain Comparisons

Surface strain data was used to verify predicted strain distributions in the girder end regions. Data from DEMEC points was initially used to determine the transfer length in the first few feet of the girder. However, in three of the four girder ends, DEMEC points were embedded up to 20 ft. (6 m) beyond the transfer zone in hopes of capturing the transfer zone of the debonded strands. Although the transfer zone of the debonded strands interior of the girder could not be defined due to the coarse spacing of the DEMEC points and the small increase in force due to the bonding of the strands relative to the total force, the surface strain data was useful in comparing to predicted strain distributions from each girder end.

Figure 7.12a shows the strain that was measured on Girder I, End A from the DEMEC surface gages at release. Superimposed on the figure is the calculated strain distribution induced by the prestress force and self-weight obtained from the flexural relationship of the force-in-the-tendon approach (previously introduced in Section 2.5.1),

$$\varepsilon = \frac{\sigma}{E_{ci}} = \frac{1}{E_{ci}}\left[\frac{-P}{A} + \frac{-Pec}{I} + \frac{Mc}{I}\right], \tag{7.14}$$

where E_{ci} was the modulus of elasticity of concrete at release and the remaining parameters, previously defined in Eqn. (2.38), are discussed.

The *Nominal Design Case* displayed on Figure 7.12a is the calculated strain along the length of the girder determined using nominal design properties of the girder. These properties included gross geometric section properties, an effective prestress level of $75\%f_{pu}$ less initial prestress losses as predicted by the PCI Committee on Prestress Losses (1971), and the ACI 318 (1995) predicted concrete modulus. The calculated strains were also based on the AASHTO assumed transfer length of $50\ d_b$ (where d_b is the strand diameter).

The *Predicted Case* illustrated on Figure 7.12a is the calculated strain along the length of the girder determined using measured material properties and net geometric section properties of the girder. Measured material properties included an effective prestress level of $71.3\%f_{pu}$ (Table 7.1) less initial measured prestress losses (Table 7.3), the measured concrete modulus at release (Table 6.2), and the average measured transfer length (Table 7.6). Similar measured and calculated strain distributions are shown in Figures 7.12b through 7.12d for girder ends IB, IIC, and IID, respectively.

The shallow dips in the calculated strains reflect the effect of the gravity load causing a decrease in the concrete compression strain at the level of the strands. The slight increases are caused by the initiation of bonding pairs of debonded strands along the length of the girder. The increases appear minor due to the small percentage of debonded strands becoming bonded versus the total bonded strands already in the cross section.

In all four ends, the calculated nominal strain was much lower than the actual data indicated. The nominal concrete modulus at release was much higher than measured, causing the prediction to be lower. Strains predicted using measured properties and losses computed from vibrating wire gages assuming zero concrete stress before release compared well with measured strains.

Girder I indicated somewhat higher strains near the end than predicted, but leveled out once into the girder length (Figures 7.12a and 7.12b). A similar trend was expected in Girder II End C where the same strand draping/debonding combination was used as in Girder I, however the predicted strains were lower than measured (Figure 7.12c). Predicted strains in End II-D (Figure 7.12d) appeared accurate. DEMEC points were placed 5.2 in. (130 mm) above the bottom flange and height location was accounted for in computed strains. DEMEC point data also included the localized effect of force concentration in the bottom flange of the girder, perhaps explaining the few large peaks and difference between calculated and measured strains in the initial transfer zone.

7.6 Camber

Camber is defined as the deflection of the center relative to a straight line between the ends of a prestressed concrete member referenced as positive upward. At any given time, the upward component of deflection can be calculated from the effective prestress force which is offset from the neutral axis by an eccentricity, *e*. The downward component of deflection is due to the self weight of the girder and any additional loads. Superposition of these deflections results in the camber of the member.

7.6.1 Measured Camber

Camber was monitored for both girders beginning at the time of strand release. Figure 7.13 illustrates centerline cambers observed during the first 10 days after girder casting. Long-term centerline camber for each girder is shown in Figure 7.14 until the time of ultimate flexural testing (Girder I was 860 days, Girder II was 840 days). Table 7.9 summarizes the measured camber at specific times for the two girders.

Camber was first measured with the girders still on the precasting bed, using a 1/16 in. graduated scale to measure the vertical distance between the bed and girder bottom. After each girder had been lifted from the bed and immediately set back down (lift/set), camber was remeasured. Girder I had a measured (on-bed) camber of 4.76 in. (121 mm) which increased to 4.84 in. (122 mm) the next morning and continued to increase to 5.47 in. (139 mm) after lifting the girder from the bed and setting it back down. Girder II had a measured (on-bed) camber of 3.86 in. (98 mm) which decreased to 3.74 in. (95 mm) by morning before increasing to 4.06 in. (103 mm) after lifting and setting the girder back down. The "true" camber lay between these

values. Friction between the precasting bed and the girder tends to reduce the initial on-bed camber and increase the lift/set camber measurement. Therefore, the on-bed and lift/set cambers were averaged to result in the measured initial camber used throughout this report and listed in Table 7.9.

Table 7.9 Measured Camber Summary

Event	Time from Release	Girder I - Limestone	Girder II - GG w/ microsilica
Initial Camber			
"On-bed"	0.5 hour	4.76 in. [121 mm]	3.86 in. [98 mm]
Next morning	15 hours	4.84 [122]	3.74 [95]
Lift/set	20 hours	5.47 [139]	4.06 [103]
Initial Camber	*averaged* [1]	*5.12 [130]*	*3.96 [101]*
Long-term Camber			
Move to Prep Area in Yard	24 hours	6.34 [161]	4.92 [125]
Day 3	2 days	6.44 [166]	5.00 [127]
Day 4	3 days	6.63 [168]	5.16 [131]
Day 28	28 days	7.64 [194]	5.49 [139]
Transport to Test Facility	67 days - *before* 70 days - *after*	7.80 [198] 7.76 [197]	5.53 [140] 5.59 [142]
Deck Casting	3 days - *before* 200 days – *before* 201 days – *after* 5 days - *after*	7.38 [187] 7.07 [180] 4.49 [114] 3.62 [92]	5.00 [127] 4.88 [124] 2.13 [54] 1.26 [32]
First Crack Testing	GI = 598 days GII = 727 days	3.41 [86]	0.93 [24]
Ultimate Flexure Testing	GI = 860 days GII = 840 days	3.41 [86]	1.04 [26]

[1] Average of "on-bed" and lift/set cambers to account for bed friction.

Once the girders were moved from the bed to the prep area in the prestressing yard, the support conditions changed. Instead of being supported at each end, supports were located 2 ft. (0.6 m) in from the ends causing an increase in camber. Measurements were taken using a dumpy surveying level and a ±0.01 in. rod. Both girders experienced a 24% increase in initial camber due to handling and placement. Girder I camber measured 6.34 in. (161 mm) and Girder II camber measured 4.92 in. (125 mm) by the time both girders were one day old.

Continued monitoring of the girder cambers showed increasing upward deflections until an age of 28 to 30 days at which time they stabilized. The camber was unaffected at an age of 67 to

70 days, corresponding to the time the girders were transported to the testing facility and placed on supports 7.5 in. (191 mm) from each end. Measurements indicated the girder camber decreased by 0.04 in (1 mm) for Girder I and increased by 0.06 in. (1.5 mm) for Girder II due to transporting and new placement. Deck casting affected the camber of each test girder in that once the decks were cast, an immediate camber decrease was noted due to the unshored construction. Girder I showed a 2.58 in. (66 mm) deflection change and Girder II decreased by 2.75 in. (70 mm). Comparisons of measured cambers to predicted cambers are made in Section 7.6.2.

Measured long-term cambers for Girder I stabilized and appeared not to be hampered by static, cracking and cyclic load testing (age 300 to 670 days). An overall low camber was measured at an age of 690 days and was 2.99 in. (76 mm), see Figure 7.14. Some camber recovery was noted after all static and fatigue load testing was halted. A final camber measurement of 3.41 in. (86 mm) was recorded before testing to flexural failure.

Measured long-term cambers for Girder II stabilized after deck casting and began to decrease when load testing started at 690 days, shown in Figure 7.14. The girder took on a "gull-wing" shape and a low measured camber of 0.69 in. (18 mm) was recorded at an age of 766 days, corresponding to the last day of load testing. The camber then increased to 1.04 in (26 mm) just prior to the ultimate flexural failure test. Chapter Eleven discusses the effects of pre-release cracks in Girder II on the measured camber.

Deflected Shape without Load

Camber measurements were originally taken at quarter points along the girder lengths. At an age of 70 days, the measurement locations were refined to eighth points. The timing of the procedure change was the day after the girders were transported to the testing warehouse. When Girder II visually appeared to have a "gull wing" deflected shape, the measurement locations were further refined to 2 ft. (0.6 m) increments. (The "gull wing" shape is seen when the center region of the girder becomes level or has a change in curvature, i.e., a negative camber while the end regions show a positive camber.) At this time, the girders were 630 days old when refinements began and both had experienced placement of a composite deck at an age of 200 days. All static and cyclic load testing had been completed on Girder I, and no load testing had started on Girder II.

Figures 7.15 and 7.16 show the cambered shapes of the two test girders. The shapes are not meant to show a precise and smooth curve, but rather the general curvature of each girder from end to end. The camber was measured with reference to the bottom flange. As a result, roughness of the bottom concrete surface (the girders were not surface prepared to smooth out all air voids) caused the observed distortion of the curves with data measured at 2 ft (0.6 m) increments.

The deflected shapes are shown for several events. Both figures show the camber at initial conditions (average of lift/set camber measured at quarter points off of the precasting bed), 70 days (the day after transporting the girders to the test facility and first measured at eighth points), 630 days (first measured at 2 ft. increments), after completion of cyclic load testing (age 767 days), and the final deflected shape. It is evident that Girder I camber was symmetrical and showed little change in shape over time. Girder II, although symmetrical, was nearing flat when the first camber profile was taken at 2 ft. increments. Although the centerline camber decreased over time, the deflected shape remained relatively unchanged. The difference of strand pattern combinations in Girder II ends appeared to have no effect on the overall deflected shape as noted by the symmetry.

7.6.2 Predicted Camber

Camber predictions were computed using three methods. The first method, the PCI Multiplier Method *(PCI Design Handbook*, 1992), is the most common method chosen by design engineers to predict camber and was reviewed in Section 2.6.3. Deflections due to the prestress force were computed using superposition of Cases 3 and 5, Design Aid 11.1.4 (*PCI Design Handbook*, 1992) to account for draped and debonded straight strands. Second, the Moment-Area Method of deformation analysis was used to determine the initial deflection. Long term camber predictions were not made with the moment-area method because creep and shrinkage effects, which directly influence camber over time, cannot be accounted for directly through the strand stress. And third, camber predictions were determined using the analytical program *Pbeam* with material properties defined in Section 7.4.2.

Predictions were based on both nominal and measured properties for the first two of three methods and are tabulated in Table 7.10. A nominal design case was calculated for the PCI Multiplier and Moment-Area methods using nominal material properties and gross geometric

design properties for each girder. Nominal losses predicted by the Time-Step Method recommended by the PCI Committee on Losses (1975) were used for computing camber, see Table 7.6. Camber was also predicted for each method using measured material properties and measured lower bound losses (Table 7.7). Predictions were for unloaded service conditions in which only the member self-weight (girder and deck) and effective prestress force acted to produce the total camber (columns titled Girder I and Girder II in Table 7.10). Net section properties were used for the applied prestress force and the girder self-weight while the deck self-weight was applied to the transformed non-composite section. For the Girder I cases (nominal and with measured properties), the camber was computed using the draped/debonded strand pattern found in the test girder. For the Girder II cases, the camber was computed from the average camber predicted using a draped/debonded strand pattern and a fully draped strand pattern to simulate the actual unsymmetrical end conditions of Girder II. The average camber using this procedure was ±0.25 in. (±6 mm).

The PCI Multiplier method predicted nominal initial cambers of 4.50 and 4.34 in. (114 and 110 mm) for Girders I and II, respectively. Differences between the two girders reflect the difference in the end region strand patterns. Using the same method and measured material properties including lower bound initial losses, initial cambers were computed to be 5.49 in. (139 mm) for Girder I and 4.92 in. (125 mm) for Girder II. Girder I had a measured initial (averaged) camber of 5.12 in. (131 mm) and Girder II had 3.96 in. (101 mm) initial camber. The PCI predicted camber using lower bound measured losses for Girder I was 6.7% higher than the observed camber. In the case of Girder II, the PCI predicted camber using lower bound measured losses was 20% higher than observed. Using upper bound measured losses, cambers of 3.96 in.(101 mm) and 4.15 in. (105 mm) were predicted for Girders I and II, respectively, using the PCI Multiplier method. As stated in Section 7.4.2, it is believed that using lower bound losses (assuming the concrete stress prior to release was zero) confirmed more accurately the actual losses in Girder I, whereas upper bound losses were most likely more accurate for Girder II. Using the initial measured cambers reported in Table 7.10, initial losses were back calculated to be 18.9% and 31.9% for Girders I and II, respectively. The back calculated value for Girder I fell between the upper and lower bound measured losses (15.5-29.1%), indicating that some concrete stress probably existed in the section. The value for Girder II however was above the upper bound measured loss (29.3%), indicating that concrete stress would had have to

exceed the concrete cracking strength. Because this was not possible, it is believed that pre-release cracking in Girder II greatly influenced its behavior. The cracking and effect on behavior is discussed in detail in Chapter Eleven. Therefore, the PCI method for predicting camber at initial conditions was adequate when measured material properties (including initial losses) were known.

Table 7.10 Predicted Camber Summary

	Girder I			Girder II		
	Measured	Nominal Design [1]	With Measured Properties[2]	Measured	Nominal Design [1]	With Measured Properties[2]
PCI Multiplier Method, in. [mm]						
Initial Camber	*5.12 [130]*	4.50 [114]	5.49 [139]	*3.96 [107]*	4.34 [110]	4.92 [125]
Before Deck (200 days)*	*7.38 [187]*	7.86 [200]	9.53 [242]	*5.00 [127]*	7.59 [193]	8.53 [217]
After Deck (201 days)*	*3.62 [92]*	4.78 [121]	5.84 [148]	*1.26 [32]*	4.50 [114]	4.82 [123]
Final Service Conditions	NC[3]	1.87 [47]	1.53 [139]	NC[3]	1.53 [39]	1.01 [26]
Moment-Area Method						
Initial Camber	*5.12 [130]*	4.23 [107]	5.17 [131]	*3.96 [107]*	4.20 [107]	4.72 [120]
Pbeam Using Measured Properties with Modified Shrinkage						
Initial Camber	*5.12 [130]*	NC[3]	5.69 [144]	*3.96 [107]*	NC[3]	5.07 [129]
28-days	*7.64 [194]*	-	7.24 [184]	*5.49 [139]*	-	6.72 [171]
Before Deck (200 days)[4]	*7.38 [187]*	-	7.95 [202]	*5.00 [127]*	-	7.45 [189]
After Deck (201 days)[4]	*3.62 [92]*	-	4.36 [111]	*1.26 [32]*	-	3.82 [97]
Crack Testing	*3.41 [86]*	-	1.74 [44]	*0.93 [24]*	-	0.94 [24]
Ultimate Flexural Tests	*3.41 [86]*	-	1.75 [44]	*1.04 [26]*	-	0.95 [24]
Final Service Condition	NC[3]	-	2.03 [52]	NC[3]	-	1.22 [31]

[1] Nominal Design Case predicts camber with nominal material properties and gross geometric design properties.
[2] Predictions for each girder used measured material properties and lower bound measured losses.
[3] Not Considered.
[4] Measured deck casting measurements are reported for 3 days before and 5 days after deck casting for comparison to predictions where the effects of temperature changes on camber due to girder heating are reduced.

Initial cambers predicted by the Moment-Area Method are nearly identical for the nominal design case. The slight decrease is due to the inclusions of a tapered prestress force in the transfer zone. The differences viewed between the PCI Multiplier and moment-area methods for each case reflects the ability of the moment-area method to incorporate the variation in stress due to the transfer length in the debonded and end regions. For each girder, camber was computed

via the moment-area method using both nominal and measured properties. The nominal AASHTO transfer length of 30 in. (762 mm) was used for the nominal moment-area cases. Measured transfer lengths were used for determining the predicted cambers of the two test girders with measured properties. Nominal predictions were 17.4% lower than measured for Girder I and 5.7% higher than measured for Girder II. When using measured properties and lower bound measured losses, this method predicted camber 0.9% higher than measured for Girder I and 19.2% higher for Girder II. As with the PCI Multiplier method and recalling that pre-release cracking in Girder II most likely influenced camber measurements, the moment-area method for predicting camber at initial conditions was adequate when measured material properties (including initial losses) were known.

Initial camber using the *Pbeam* analytical program was computed for each girder using measured material properties. Although it might be expected that the *Pbeam* method would predict accurate deflections at initial conditions, the reader is reminded that this method does not adequately account for force transfer into the girder over any finite length. Therefore, the initial cambers as predicted by *Pbeam* are higher than measured because more force in the girder produces higher camber predictions. *Pbeam* predicted cambers 11.1 and 28.0% higher than measured for Girders I and II, respectively.

The relative camber change due to deck casting was computed using the PCI Multiplier and *Pbeam* methods. In predicting cambers for the two test girders using the PCI Multiplier method, the deck weight was applied to the transformed non-composite section. The computed elastic deflections were 3.08 and 3.09 in. (78.2 and 78.5 mm) for the nominal design cases of the two girders. Using measured material properties, Girder I had a predicted change of 3.69 in. (93.7 mm) while Girder II had a predicted change of 3.70 in. (94.0 mm). The *Pbeam* program predicted relative deflection changes of 3.59 and 3.63 in. (91.2 and 92.2 mm) in Girders I and II, respectively, due to casting of the deck.

When comparing the deck casting camber predictions to measured camber changes, the thermal gradient in each girder must be considered. The girders had been heated three days prior to casting of the deck to ensure meeting the Mn/DOT requirement of 65° F minimum girder temperature at the time of deck casting (Kielb, 1994). Gages installed through the height of each noncomposite girder in the midspan regions indicated that the temperature in the girder prior to deck casting was uniform through the depth. After deck casting, however, the heat of hydration

from the deck caused a thermal gradient in the noncomposite girder. Gages indicated that this thermal gradient had disappeared five days after casting. Therefore, when comparing predicted camber changes to measured camber changes, measured changes were considered between 3 days prior to 5 days after deck casting. In this way, the relative camber changes were 3.76 and 3.74 in. (95.5 and 95.0 mm) for Girders I and II, respectively (Table 7.9). Hence, camber changes due to deck casting were underestimated by 1.9 and 1.1% for the two girders using the PCI Multiplier method with measured properties. The *Pbeam* results were similarly close, underestimating the change by 4.5% and 2.9 % for Girders I and II, respectively. The closeness of the predictions to the measured changes indicates that the measured material properties and assumptions used herein for deck casting were accurate.

The final measured camber of each girder was taken immediately before testing to ultimate flexure. Although the final service cambers (assumed at 50 years) were computed for each girder using the PCI Multiplier and *Pbeam* methods (and listed in Table 7.10), no comparisons to measured cambers can be made. However, measured cambers before ultimate testing can be compared with *Pbeam* predictions corresponding to the simulated girder age at ultimate. Girder I had a measured camber of 3.41 in. (86.6 mm) at ultimate testing compared with 1.75 in. (44.5 mm) as predicted by *Pbeam*, a 49% decrease from measured. Girder II, however, measured 1.04 in. (26 mm) at ultimate but was predicted to have a camber of 0.95 in. (24.1 mm), a 9% decrease from measured. Using the *Pbeam* parameters with the measured shrinkage as defined in Section 7.4.2, camber predictions were higher and increased differences by nearly one half for Girder I. Results for Girder II were more significant and Chapter Eleven discusses the effects of pre-release cracks on measured camber.

7.7 AASHTO Stress Limit Comparisons

When designing prestressed concrete members, internal stresses are limited such that externally applied loads do not induce stresses beyond the specified limits. The current AASHTO Bridge Specifications (1996) has set limits for concrete compressive and tensile stresses at the time of release and under service load conditions. Limits were reviewed in Section 2.5 and are tabulated in Table 7.11. The nominal concrete strengths used to determine the predicted stress limits for the nominal design case are noted in the table. Compressive and

tensile limits are included for each girder based on measured release and 28-day concrete strengths.

Table 7.11 AASHTO Stress Limit Comparison

	Nominal Design	Girder I Limit	Girder I Measured	Girder II Limit	Girder II Measured
At Release, f'_{ci}	*8925 psi* ‡	*9300 psi*	-	*10400 psi*	-
Compression, *$0.6f'_{ci}$*, ksi	-5.36 †	-5.58	-4.04	-6.24	-4.16
Tensile, *$7.5\sqrt{f'_{ci}}$*, ksi	+0.709	+0.733	NA	+0.765	NA
At Service Loads, f'_c	*10,500 psi*	*12,100 psi*	-	*11,100 psi*	-
Compression, *$0.4f'_c$*, ksi	-4.20	-4.84	-3.61	-4.44	-3.59
Tensile, *$6\sqrt{f'_c}$*, ksi	+0.615	+0.660	NA	+0.632	NA

† Sign convention: tension is positive.
‡ 1 ksi = 6.895 MPa.

Measured stress levels were determined for release and service load conditions at midspan. At release, measured top and bottom fiber stresses were computed using measured lower bound losses at release and the basic flexural stress equation (Eqn. 2.41) with net section properties and the measured girder self-weight. Measured extreme fiber stresses at release for both girders listed in Table 7.11.

At the time of release, limits for each girder were higher than nominal design, simply because of higher than expected measured release strengths. For both girders, the stress distribution through the girder depth was entirely compressive as expected when compared with predictions using measured material properties. No tensile stresses were assumed. Measured compressive stresses at the bottom fiber at release were well within AASHTO limits using either nominal or measured strengths.

Total concrete stresses at service load conditions were determined from superposition of the state of stress through the composite girder due to losses without external load and the induced service stress due to external loading (from Chapters Eight and Nine). The state of stress was defined using the prestressing force less the average measured lower bound losses during load testing in conjunction with the basic flexural stress equation (Eqn. 2.41). Stress changes induced at the top and bottom fibers of the prestressed non-composite member under service conditions are reported in Sections 8.2.3 and 9.2.3 for Girders I and II, respectively. Top and bottom fiber stresses are tabulated for each girder for comparison with AASHTO stress limits. Under the

service condition (externally loaded to 'Preload + 100% HS25'), Girder I showed total top and bottom fiber stresses of -3.53 and -0.84 ksi (-24.3 and -5.8 MPa) compression. Girder II showed total top and bottom fiber stresses of -3.59 and -1.17 ksi (MPa) compression, respectively. Top fiber stresses noted in Table 7.11 are for the top fiber of the noncomposite girder, consistent with AASHTO limit criteria.

Under service load conditions, the limits for each girder were higher than nominal due to higher measured compressive strengths. Measured compressive stresses in the top fiber of the girder flange of the composite girders were within AASHTO limits, independent of nominal or measured concrete strength. Under service conditions, and accounting for lower bound measured prestress losses, neither girder had reached the tensile limits at the bottom fiber, indicating the girders were initially uncracked under service loads.

CHAPTER 8 LOAD TESTING OF COMPOSITE GIRDER I

8.1 General Load Testing of the Composite Girder

Load testing of the composite girders included static tests to truck levels and overload conditions, cyclic load testing to the same levels, flexural crack testing above overload conditions, and an ultimate flexural test. The detailed loading history for Girder I is given in Appendix C. A summarized load history is shown in Figure 8.1. Results of the load testing are given in this chapter for Girder I and in the following chapter for Girder II. The intent of this section on general load testing is to discuss the nominal load levels (i.e., the terms *preload, truck load level* and *overload condition*), the nominal load history, and the general load testing procedure for both girders.

8.1.1 Nominal Load Levels

Design of bridge girders is based on a standard *truck load level.* The standard HS25 design truck is used in the State of Minnesota and was used for the test girder design. The HS25 truck consists of a tractor and semi-trailer with a total of three axles. The front axle carries 10 kips (45 kN) while the rear two axles carry 40 kips (180 kN) each. Front and rear axle spacings of 14 ft. (4.3 m) governed the design. AASHTO Specifications (1996, see Section 4.3.1) require a distribution factor of 0.727 per axle to be applied for design with two or more lanes of traffic. An impact factor of 1.195 was also applied to the truck load. In order to determine the maximum effect of a moving vehicle on the shear and bending stresses in the girders, the shear and moment envelopes were developed by calculating the effect of placing the HS25 truck at the following critical sections: at *H/2* from the ends (where *H* is the height of the noncomposite member) and at tenth points along the girder length (at every *0.1L*).

In the girder tests, the *truck load level* was defined by a four point loading configuration (with load points at *0.4L* from each end and two supports) used to induce the same midspan stresses as the design truck. The maximum midspan moment that the above design truck load would induce, including the effect of the distribution and impact factors, was calculated to be 11,400 in-k (1290 kN-m). An applied load of 18 kips (80 kN) at each load point was required to induce the equivalent stress for the truck load level at midspan.

An *overload condition* represented 125% of the HS25 truck load level, or 1.25 times the wheel loads defined previously. The same distribution and impact factors applied to the

overload condition. The 125% level was defined from reviewing Weigh-In-Motion (WIM) data provided by Mn/DOT. Although loads to 138% HS25 had been recorded, it was rare. The 125% level was more representative of repeated overload conditions. The maximum moment induced at midspan by the overload condition was calculated to be 14,200 in-k (1600 kN-m). Using the same approach, the four point loading configuration required 22.5 kips (100 kN) per load point to induce an equivalent midspan stress for the overload condition.

A *preload* was applied to the test girder prior to truck or overload levels. The preload represented design levels for a superimposed dead load consisting of an equivalent diaphragm load on the non-composite section and a guard rail barrier load and future wearing course on the composite section. The diaphragm load of 18 plf (0.26 kN/m) was expected to induce a bottom fiber stress of 53 psi (.365 Pa) on the transformed noncomposite section. The guard rail load of 135 plf (2.3 kN/m) and 17 psf (0.82 Pa) allowable future wearing course load were expected to induce a bottom fiber stress of 424 psi on the transformed composite section. The bottom fiber stress was assumed additive and to achieve a bottom fiber stress of 477 psi, a load of 9.39 kips (42 kN) per load point was required. An actual applied load of 9.25 kips (41 kN) per load point was used as the preload level to accommodate equipment limitations under the total load combination of preload plus overload.

Table 8.1 lists the test level and corresponding design condition. Also, tabulated is the load per actuator required to induce the design condition stress at midspan of the member. The cumulative load per actuator for the design truck load and the overload condition includes the preload.

Table 8.1 Nominal Load Levels

Test Level	Design Condition	Midspan Moment (in-k [kN-m])	Load per Actuator (k [kN])	Cumulative Load per Actuator (k [kN])
Preload	Guard rail and wearing course	5840 [660]	9.25 [41]	9.25 [41]
Design Truck Load	HS25 AASHTO Design Truck	11,360 [1280]	18.0 [80]	27.25 [120]
Overload Condition	125% HS25 Truck	14,200 [1600]	22.5 [100]	31.75 [140]

8.1.2 Nominal Load History

Load testing was performed on each composite girder in an effort to simulate stresses imposed by the HS25 design truck and overload condition. A nominal load history was defined

to incorporate 70 years of traffic on an uncracked member. Mn/DOT WIM data over a two-year time period was extrapolated to show that on a typical overpass bridge in the Minneapolis-St. Paul metropolitan area, approximately 1,000,000 truck loading events would occur in 70 years. Similarly, 80,000 overload events were expected to occur in the 70-year life of the bridge. It was also decided to test the girders after crack testing for a minimum additional amount equal to half of the number of HS25 and overload truck load cycles applied before crack testing.

Cyclic testing was performed at a loading rate of 0.75 Hz for HS25 truck loads and 0.65 Hz for the overload condition. These loading rates corresponded to 15.4 days of continuous testing for 1,000,000 cycles of HS25 load and 2.13 days for 80,000 cycles of the overload condition. The numbers of cycles, listed in Table 8.2, represent the minimum number of cycles that were applied to the test girders. Also, tabulated is the cyclic load range per actuator required to induce design stresses at midspan into the test girder.

Table 8.2 Nominal Load History

Order of Testing	Minimum Number of Cycles	Load Range per Actuator (k [kN])
70 years at HS25	1,000,000	9.25 - 27.25 [41 - 120]
70 years at 125% HS25	80,000	9.25 - 31.75 [41 - 140]
Postcracked at HS25	500,000	9.25 - 27.25 [41 - 120]
Postcracked at 125% HS25	40,000	9.25 - 31.75 [41 - 140]

8.1.3 Load Test Procedure

In general, load testing was performed by first loading the girder to the specified preload simulating the superimposed design dead load on the composite section. Chapter Five has complete information on the test setup, including the loading system configuration and instrumentation. With the preload applied, static testing included "holds" at load levels where significant data was collected and "ramp loading" at a rate of one kip per 14.3 seconds. The hold and ramp patterns were repeated until the desired load level was achieved. Unloading was performed in a similar manner. Load steps were typically on the order of two to five kips between "holds." For cyclic testing, the same preload was applied on which haversine cyclic testing was superimposed.

Figure 8.1 summarizes the type and order of load testing performed for Girder I. Static testing was performed prior to any cyclic testing, intermittently during cyclic testing, and at the

completion of cyclic testing to document any stiffness changes that might indicate damage incurred during testing. Low level periodic static and cyclic testing for equipment check-out began at a girder age of 300 days. The first static load test to the full HS25 truck load on Girder I was performed at an age of 378 days. Cyclic testing began shortly thereafter. Testing was halted for four months (age 450 to 580 days) due to cold temperature conditions. Flexural cracking tests were performed statically (age 593 days), followed by static crack reopening tests. Additional cyclic and intermediate static tests were performed prior to the ultimate flexural test. The last static test was performed at an age of 670 days, prior to the ultimate flexure test at 860 days.

A detailed loading history of Girder I is documented in Appendix C. Included in the appendix listing is the name and type of test performed, date, loading rate (static and cyclic), TCS software test name, the number of cycles performed, the name of the spreadsheet containing the original imported ASCII data, and the mode of test control (Master or Slave, Deflection or Load, and Actuator A or B).

8.2 Periodic Static and Cyclic Load Test Results

Girder I was tested according to the summarized schedule in Table 8.3. The test name corresponds to the total testing history presented in Appendix C. Results from the intermittent static testing are documented and indicate that no damage was induced into the test girder due to cyclic loading equivalent to nearly 150 actual years of service load levels.

Table 8.3 Load Cycles on Girder I

TEST NAME [†]	Number of Load Cycles at Given Load Levels				Cumulative Cycles
	0.5 preload + 100% HS25 [‡]	0.5 preload + 125% HS25 [‡]	Preload + 100% HS25	Preload + 125% HS25	
075HZ100	10,000				10,000
065HZ125		10,000			20,000
70YR	1,010,000				1,030,000
70YR125		120,000			1,150,000
04HZ125				80,000	1,230,000
POSTCRK1			700,000		1,930,000
POSTCRK2				100,000	2,030,000
POSTCRK3				400,000	2,430,000
TOTALS:	1,020,000	130,000	700,000	580,000	**2,430,000**
Nominal:	*1,000,000*	*80,000*	*500,000*	*40,000*	*1,620,000*

[†] Test name referenced from Appendix C.
[‡] Initial testing applied 0.5 preload until equipment repairs were completed to accommodate higher levels.

8.2.1 Composite Girder Stiffness (Load-Deflection Response)

The composite test girder was subjected to static testing resulting in a load-deflection response. Selected tests of standard truck loading and overload levels at significant load history steps, as well as the girder stiffness, are summarized in Table 8.4. The static test name corresponds to the total testing history presented in Appendix C and is summarized in Figure 8.1.

Table 8.4 Static Test Summary of Girder I

	Test Name [†]	Static Load Level	Stiffness, k/in [kN/m]	r^2
Initial static test	Truck 3 [‡]	100% HS25	14.0 [2450]	0.9998
After 10^6 cycles	Truck 8	125% HS25	14.5 [2530]	0.9998
Pre-crack, 1.2x 10^6 cycles	Truck 11	125% HS25	14.6 [2550]	0.9998
Post-crack	Crk2	125% HS25	14.1 [2460]	1.0000
Post-crack, 2x 10^6 cycles	Truck 13	125% HS25	14.1 [2460]	0.9998
Post-crack, 2.4x 10^6 cycles	Truck 17	125% HS25	14.3 [2500]	0.9999
Measured Average Stiffness	*HS25 Truck*		*14.2 k/in*	-

[†] Corresponds to load history documented in Appendix C.
[‡] Static testing prior to test Truck 11 (last test before crack testing) may have been recorded without proper grounding.

Measured Stiffness

The stiffness is a measure of load per unit deflection. To determine the stiffness of the girder during each static load test, the average applied load (of the two actuators) was plotted versus centerline deflection, as seen in Figure 8.2. Also shown is the predicted stiffness, discussed. Nominal truck load and overload levels are noted.

For completeness, a few points of clarification regarding Figure 8.2 are needed. First, each test showed some initial equipment seating during full contact with the girder and preload application resulting in each curve starting at a slightly different deflection for the preload (±0.10 in.). Therefore, the data plotted is the actual data less a shift along the x-axis such that the initial starting displacements overlay one another. The actuator load was not adjusted. In this way, the data is preserved while allowing for visual ease in comparing the stiffness. Second, while only the results of five static tests are shown at various time-steps throughout the fatigue testing program, additional static testing performance was consistent with those represented here. And third, the average actuator load is plotted because the two actuator loads never differed by more than 0.25 kips (1.1 kN). The larger differences were seen at the high end of loading when the difference was 1.6% of the total load.

Table 8.4 lists the test name for each of the data sets shown in Figure 8.2, the maximum static load applied during that test, and the measured stiffness. A linear regression was performed on each data set (load versus deflection for each test name) without forcing a zero intercept. The linear slope was then taken as the stiffness, in units of kips per inch. The correlation coefficient, r^2, is also tabulated to give an indication of correlation in the data, with a perfect correlation having an r^2 value equal to one. As Table 8.4 shows, the stiffness of the girder was unaffected by continued cyclic loading and static crack testing. The tabulated measured average stiffness was the average of the five tests summarized. In this way, each test was weighted equally; otherwise data sets with more data points would have been weighted heavier.

Predicted Stiffness

Stiffness can be predicted using the following method. Assuming the loading condition to be a simple beam with two equal concentrated loads symmetrically placed on the beam, elastic theory predicts the following deflection, Δ:

$$\Delta = \frac{Pa}{24E_c I_{tr}}\left(3La - 3a^2 - x^2\right), \tag{8.1}$$

where P is the load applied at each load point, L is the center-to-center support length, a is the distance from support to load point location, x is the distance from support to point of interest, E_c is the concrete modulus of elasticity, and I_{tr} is the moment of inertia of the transformed composite section. This relationship holds true when $a \leq x \leq (L-a)$. Rearranging terms to get P/Δ gives a direct relationship for the stiffness, K.

$$K = \frac{P}{\Delta} = \frac{24E_c I_{tr}}{a}\left[\frac{1}{3La - 3a^2 - x^2}\right], \tag{8.2}$$

Predictions incorporated the following constants:

L = 1578 in.(40 m)

a = 632 in. (16 m)

x = 789 in. (20 m), to midspan.

Predicted stiffnesses are tabulated in Table 8.5 along with the average measured stiffness. Recalling that the design composite section included a total 9 in. (230 mm) thick deck (structural deck plus wearing course), a nominal design stiffness for the composite member was computed using the gross moment of inertia transformed to the girder modulus (315,600 in^4) and the nominal ACI 318 (1995) concrete modulus (6525 ksi) based on a nominal compressive strength of 10,500 psi. 'Predicted - Girder I' stiffness was based on the 28-day measured concrete modulus (4810 ksi) and the transformed moment of inertia of the composite section (396,000 in^4).

Table 8.5 Predicted Stiffness, Deflection, and *L/d* Ratio for Girder I

	Stiffness, k/in [kN/m]	Deflection at HS25, in. [mm]	Span-to-defl, *L/d*, ratio
Measured Average	*14.2 [2490]*	*1.27 [32]*	*1250*
Nominal Design	16.7 [2920]	1.08 [27]	1465
Predicted - Girder I	15.5 [2710]	1.16 [29]	1360
Predicted - overestimate E_c by 10%	16.4 [2870]	1.10 [28]	1430
Predicted - underestimate E_c by 10%	14.7 [2570]	1.23 [31]	1290

The predicted stiffness shown in Figure 8.2 is based on the measured modulus and transformed composite section properties (Predicted - Girder I). The start point at the applied

preload has been shifted for easier visual comparison in the same fashion as stated previously for the raw data.

Both the nominal design case and the predicted case using measured properties indicated stiffer sections were expected than measured. A 15% stiffer section was expected from nominal estimates while measured properties predicted a 9% stiffer section. Using the stiffness relationship in Eqn. (8.2), the discrepancy and the effect of changing the stiffness terms, $E_c I_{tr}$, was analyzed. The length parameters were not varied between measured and predicted.

If the concrete modulus were overpredicted by 10% (e.g., E_c = 5290 ksi) the composite transformed moment of inertia would decrease (e.g., I_{tr} = 379,500 in^4) resulting in a higher stiffness of 16.4 k/in (2870 kN/m). Conversely, underpredicting the modulus by 10% (e.g., E_c = 4330 ksi, I_{tr} = 416,000 in^4) resulted in a predicted stiffness of 14.7 k/in (2570 kN/m). This would indicate that a lower modulus might correctly predict the girder stiffness. Girder I had a measured concrete modulus of 4680 ksi (32.3 GPa) at 480 days, approximately midway through the static and cyclic load testing period compared to E_c at 28-days of 4810 ksi (33.2 GPa). With the 2.7% decrease in measured modulus and a corresponding I_{tr} = 396,600 in^4, a stiffness of 15.0 k/in (2950 kN/m) was expected, a 5.6% difference from what was measured.

Also listed in Table 8.5 is the expected deflection due to an HS25 truck (at P =18 kips) resulting from the corresponding stiffness, K. The span-to-deflection (L/d) ratio is often used as a measure of stiffness, and although prestressed concrete has no code limitation for this value, the limit of 800 is used as a typical rule-of-thumb guideline from steel bridge girder construction (AASHTO, 1996). As evident from the table, the span-to-deflection ratio for measured and predicted stiffness was well within this rule-of-thumb guideline. The predicted deflection and L/d ratios were higher than the measured values for the same reasons the stiffness was lower, as stated previously.

8.2.2..Strand Strain and Stress Ranges

A concern with prestressed concrete bridge girders is that of strand fracture resulting from fatigue. Strand fracture would significantly reduce the load carrying capacity of the member, and could potentially cause failure of the structure. Prestressing strands were instrumented to give an indication of the strain level in the strands corresponding to truck loads and overloads. Of the 18 gages installed on the bottom three rows of strands in the constant moment region, a

total of six gages remained in operation throughout the static tests and provided useful data for determining the induced stress change during loading conditions. One gage was located in strand row 3 (six inches up from the girder bottom fiber), one gage was located in strand row 2 (four inches up) and the remaining four gages were located in strand row 1 (two inches up). The center of gravity of the midspan strand pattern was at 5.39 in. (137 mm) above the bottom fiber.

Measured Strand Strains

The change in strain induced in the bottom row of strands during truck loading and overload conditions (excluding any preload strains) is tabulated in Table 8.6 for the time steps introduced in Section 8.2.1. The bottom row of strands was selected for presentation because they undergo the highest change in stress under load, and there was redundancy in that more than one gage supplied data at this level. Additionally, the foil gages were applied to one wire in a strand and are therefore converted to stress using the measured modulus [E_s of 29,100 ksi (200 GPa)] when compared with predicted stress changes. Static testing did not always include a "hold" at load levels equal to the exact preload plus truck load or overload. Therefore a strain-to-load conversion was determined from a linear regression of each data set (load versus strain data collected from each gage of every test name) without forcing a zero intercept. Regression analyses resulted in r^2 values in the range of 0.963 to 0.999. The conversion, or slope of the regressed strain-load data relationship, is listed showing an overall average of 7.55 ±0.55 με/kip.

Table 8.6 Measured Strand Strain and Stress Ranges - Girder I

	Strain-to-Load conversion (με/kip)	HS25 Truck Loading		Overload Truck	
		ΔStrain (με) †	ΔStrand Stress (ksi)	ΔStrain (με)	ΔStrand Stress (ksi)
Initial Static Test	6.81	123 ‡	3.57	153 ‡	4.46
After 10^6 fatigue cycles	6.57	118	3.44	148	4.30
Precrack, 1.2x 10^6 cycles	7.85	141	4.11	177	5.14
Post-crack	8.62	155	4.52	194	5.65
Post-crack, 2x 10^6 cycles	7.76	140	4.07	175	5.08
Post-crack, 2.4x 10^6 cycles	7.71	139	4.04	174	5.05
Average of Tests	*7.55 ±0.75 με/kip*	*136 ±13.5 με*	*3.96 ±0.39 ksi*	*170 ±16.9 με*	*4.95 ±0.49 ksi*

† All strain and stress data given for the bottom row of strands, 2 in. (50 mm) from bottom of the girder.
‡ Sign convention: tension is positive.

The strain-to-load conversion factor was used to determine the expected strain change from the measured data at truck load and overload levels by multiplying the factor by 18 and 22.5 kips (80 and 100 kN), respectively. For two of the six tests shown that had "holds" within 0.1 kips (0.4 kN) of the truck and overload levels, any agreement with actual measured strains and strain changes obtained from the strain-to-load conversion was within 1%, indicating this procedure was reasonable. Gages from the two remaining rows indicated strain changes less than the bottom row of strands, as expected due to their reduced eccentricity.

Figure 8.3 illustrates strain data collected for Girder I by the bottom row of strands. For each test shown, the average strain reading of the four gages (in strand row 1) was plotted relative to the average actuator load. The initial static test and test after one million cycles, shown in the figure as outlined symbols, may have been recorded without proper grounding. This is seen by the deviation of data (for the earlier two tests) from the remaining tests, and by their lower strain-to-load conversion factors (slopes) listed in Table 8.6. The dashed line plotted on Figure 8.3 is the result of the strain-to-load regression analysis for the 'Precrack Test with 1.2 Million Cycles', and is shown to correlate well with the remaining data.

A direct conversion to stress change due to loading was made by multiplying the strain change with the measured apparent strand modulus of elasticity (as measured from strain gages applied directly to strand samples), 29,100 ksi (200,700 MPa). Table 8.6 shows that continued load testing and fatigue cycles produced no evident damage to the strands, as there was not a noticeable increase in stress change over time. Further discussion will refer to the measured stress change in the bottom row of strands under truck loading as 4.0 ksi (27.3 MPa) and 5.0 ksi (34.1 MPa) for overload conditions.

Predicted Strand Strain

The stress through the depth of the girder and at the level of strand rows was easily predicted by linear elastic theory,

$$\Delta\sigma = \frac{\Delta Mc}{I} = \frac{(\Delta Pa)c}{I}, \tag{8.3}$$

where $\Delta\sigma$ is the stress from ΔM, the moment induced due to the symmetrical load change ΔP at a distance a from the support, c is the distance from the neutral axis to the height at which the stress is calculated (the bottom row of strands for this case), and I is the moment of inertia of the

composite section. Load points were nearly symmetrically placed for Girder I load tests (within 5 in. or 0.3% of the total length), as noted in Figure 5.1.

Table 8.7 lists the predicted stress changes for HS25 truck loading and overload conditions at the bottom row of strands. Load levels of 18 and 22.5 kips (80 and 100 kN) were used for the respective loading conditions, giving predicted stress ranges from preload to peak conditions. A nominal value for I (i.e., I_{gross}) was used to predict the nominal design case. $I_{transformed}$ of the composite section was used to give a more accurate estimate of predicted stress changes, and are listed as 'Predicted - Girder I'.

Table 8.7 Predicted Strand Strain and Stress Ranges - Girder I

	HS25 Truck Loading		Overload Truck	
	ΔStrain (με)[†]	ΔStrand Stress (ksi) [†]	ΔStrain (με)	ΔStrand Stress (ksi)
Measured Average Range	*136* [‡]	*3.96*	*170*	*4.95*
Nominal Design Case	-	4.53	-	5.67
Predicted - Girder I	-	5.12	-	6.49
ACI 215 (1992) *Uncracked Stress Range Limit* *Cracked Stress Range Limit*	--	 *32 ksi* *11 ksi*	--	 *32 ksi* *11 ksi*
Paulson et al. Stress Range Limit	-	*20 ksi*	-	*20 ksi*

[†] All strain and stress data given for the bottom row of strands, 2 in. (50 mm) from bottom of the girder.
[‡] Sign convention: tension is positive. Measured strains expected to be different from predicted due to gage orientation on strands for measured case.

Predicted and measured stress ranges were low when compared with fatigue limits. ACI Committee 215 (1992) recommended a maximum stress range of 0.12 f_{pu} for uncracked prestressed sections and $0.04f_{pu}$ for cracked sections. For the test girders with an ultimate measured strand strength, f_{pu}, of 269 ksi (1850 MPa), these stress range limits would be 32 ksi (220 MPa) and 11 ksi (76 MPa) for the uncracked and cracked sections, respectively. These limits are substantially higher than the stress ranges induced in the test girder during overload conditions, which was within the uncracked state. Paulson et al. (1983) recommended a reasonable fatigue stress limit of 20 ksi for strands in prestressed members subjected to repetitive loading. Again, Paulson's limit is much higher than the strand stress ranges recorded by the girders.

In all cases tabulated, the measured and predicted strand stress levels were much lower than damaging levels. The large self-weight of the composite member relative to superimposed loads,

in closely spaced long span girders, only allows for low live load induced stresses. For this girder, design truck loads and overload conditions were not expected to induce damage. Girders located at a wider spacing would be expected to have increased stress ranges because the widely spaced girders would carry a greater proportion of live load.

8.2.3..Concrete Strains and Stresses

Concrete strains were measured with vibrating wire gages through the depth of the girder, resulting in strain data for both tensile and compressive stress levels. Strains were recorded from seven vibrating wire gages at various heights within the constant moment region for the preload, HS25 truck level and overload tests. Gage locations from bottom were noted as: two gages at 2.5 in. (64 mm), two at 4.75 in. (121 mm), one at 5.0 in. (127 mm), one at 42.5 in. (1080 mm), and one at 49.5 in. (1260 mm). Load step "holds" did not always coincide with exact load levels of the preload plus truck or overload. Therefore, in an attempt to preserve the variability within the data, a linear interpolation of the raw data was used between the two closest load steps to obtain strains at the prescribed load levels for each gage. A load versus strain plot is shown in Figure 8.4 for the five bottom flange gages for the static test "Pre-crack, after 1.2 million cycles." Strains were not recorded at the 'Preload + HS25' load level of 27.25 kips for this static test and therefore were linearly interpolated, as shown in the figure as the outlined symbols. The apparent scatter at the origin indicates the actual data collection start point and the data was not adjusted.

To determine the strain distribution due to the applied loading through the height of the cross section, a strain versus height comparison was made for the two load combinations of interest: 'Preload + HS25', and 'Preload + Overload'. It can be seen in Figure 8.4 that at any constant load level, three of the gages in the bottom flange placed farthest from the bottom fiber have lower tensile strains than the two gages placed closer to the bottom, as expected. Gages in the top flange and deck showed the same trend in that the gage closest to the top fiber had the highest compressive strain under the applied loading.

Figure 8.5 shows the strain change at varying heights through the cross section for the two load combinations. At each gage height, the recorded strain change of all static tests performed for the two load combinations are marked. Gages placed at 2.5 in. (64 mm) from the bottom show higher tensile strain changes than gages higher in the cross section.

Of interest were the concrete compressive and tensile stresses at the extreme fibers. A linear regression of the data (strain versus depth of the section, as shown in Figure 8.5) was performed for each test at the truck load level and overload condition to obtain the strains at the extreme fibers. All values of r^2 were greater than 0.995.

The outlined symbol in Figure 8.5 indicates the neutral axis location, where strain in the cross section is zero. The extreme fiber strains and corresponding stresses under service and overload conditions determined from linear regression of strain data are discussed in the next section. Figure 8.5 is especially important to the following discussion of concrete strains.

8.2.3.1 Concrete Tensile Stresses and Strains

Measured Strains

The critical tensile strains in concrete under four point loading occurred at the bottom fiber of the girder. However, the concrete embedment gages could only be placed within two to five inches of the bottom fiber. Therefore, using the linear regression equations from measured strain versus gage height data for each summary test (as discussed previously), the strain change at the bottom fiber was determined from recorded data for the two load combinations: 'Preload + HS25' and 'Preload + Overload'. The preload strain changes were separated from the combinations for ease in later comparison to measured strand stress ranges by proportioning the applied loads.

The bottom fiber strain ranges due to preload, HS25 truck and overload conditions are listed in Table 8.8 for the summary load tests with the exception of "Post-crack, 2x 10^6 cycles" case during which data from the vibrating wire gages were not recorded. Also, tabulated are the corresponding stress ranges, and the overall measured averages for the bottom fiber of each case. A direct conversion to stress change was made by multiplying the measured 28-day concrete modulus of elasticity, 4810 ksi (33.2 MPa) by the measured strain change. The average computed bottom fiber strains and stresses reported in Table 8.8 are referred to herein as the *measured average bottom fiber strain/stress.* Pre-crack and post-crack tests were both considered in the averaging because no stiffness degradation was noted (see Table 8.4).

Measured concrete strains showed no degradation over time due to continued cyclic load testing. Strain changes recorded prior to cracking the girder were similar to those recorded in the post-crack condition. Although post-crack loads did exceed crack reopening loads, as discussed

in Section 8.3.1.1, the level of cracking that occurred during service loads was relatively small and did not cause a stiffness change.

Table 8.8 Measured Concrete Tensile Strain and Stress Ranges - Girder I

	Preload Level		HS25 Truck Load		Overload Truck	
	Δ Strain (με) †	Δ Concrete Stress (ksi)	Δ Strain (με)	Δ Concrete Stress (ksi)	Δ Strain (με)	Δ Concrete Stress (ksi)
Initial static test	89.0 ‡	0.43	173.2	0.83	215.9	1.04
After 10^6 fatigue cycles	86.3	0.42	168.0	0.81	200.9	0.97
Pre-crack, 1.2x 10^6 cycles	83.3	0.40	162.0	0.78	204.8	0.99
Post-crack	91.7	0.44	178.5	0.86	224.7	1.08
Post-crack, 2x 10^6 cycles	88.8	0.43	172.8	0.83	218.0	1.05
Post-crack, 2.4x 10^6 cycles	Concrete tensile strain data not recorded					
Measured average	*87.8 ±3.2 με*	*0.42 ±0.02 ksi*	*170.9 ±6.2 με*	*0.82 ±0.03 ksi*	*212.8 ±9.8 με*	*1.02 ±0.05 ksi*

† All strain and stress data given for the *bottom fiber* of the concrete girder.
‡ Sign convention: tension is positive.

Predicted Concrete Tensile Stresses and Strains

Concrete stresses in the extreme bottom fiber were predicted in a similar manner to strand stresses using Eqn. (8.3). Concrete stress predictions for preload, HS25 truck loading and overload conditions are listed in Table 8.9 along with the measured average bottom fiber strain and stress ranges. A nominal value for I (i.e., I_{gross}) were used to predict the nominal design case. $I_{transformed}$ of the composite section were used to give a more accurate estimation of predicted bottom fiber stresses, and are listed under "Predicted - Girder I."

The nominal design case had a 35% increase in concrete stress because of the overestimated nominal concrete modulus for all load cases listed in Table 8.9. The nominal concrete modulus was predicted from ACI 318 (1995), originally derived from normal strength concrete data. Using measured properties, the predicted case was 10% greater in stress range for the three load cases. Considering the concrete modulus, E_c, to be a variable if $I_{transformed}$ used in predicting the stress change from Eqn. (8.3), a 10% decrease in E_c resulted in predicted stress changes nearly identical to those stress changes computed from measured data. Predicted strains for the two load combinations ("Preload + HS25" and "Preload + Overload") were computed through the section depth using the measured modulus and transformed composite properties, and are plotted

on Figure 8.5 to show the closeness of the data to the prediction. The levels of tension measured in the bottom fiber due to load testing were close to those predicted using the measured concrete modulus and transformed composite section properties and within the data scatter.

Table 8.9 Predicted Bottom Fiber Concrete Stress Ranges - Girder I

	Preload Level		HS25 Truck Load		Overload Level	
	Δ Strain ($\mu\varepsilon$) [†]	Δ Concrete Stress (ksi)	Δ Strain ($\mu\varepsilon$)	Δ Concrete Stress (ksi)	Δ Strain ($\mu\varepsilon$)	Δ Concrete Stress (ksi)
Measured Average	*87.8* [‡]	*0.42*	*170.9*	*0.82*	*212.8*	*1.02*
Nominal Design Case	-	0.57	-	1.11	-	1.39
Predicted - Girder I	-	0.47	-	0.91	-	1.14
Predicted - overestimate E_c 10%	-	0.48	-	0.94	-	1.17
Predicted - underestimate E_c 10%	-	0.45	-	0.89	-	1.11

[†] All concrete tensile strain and stress ranges given for the *bottom fiber* of the girder.
[‡] Sign convention: tension is positive.

Although stress ranges during loading are of interest, it is the overall level of tension in the bottom fiber of the girder during service loads that is limited by AASHTO (1996). From the measured prestress loss information presented in Section 7.4 and the service stress ranges above, the overall tension level in the girder under service loads can be calculated. Using a prestress force less the measured lower bound prestress loss value of 26.6% (the average lower bound measured loss during the load testing period) and the girder self weight and deck weight in the flexural stress equation (Eqn. 2.41), the bottom fiber concrete stress was calculated to be at a state of –1.96 ksi compression, prior to load application. The measured concrete tensile stress at the bottom fiber due to the load combination of preload and HS25 truck load was +1.24 ksi (8.55 MPa). Superimposing the two stresses, the state of stress at the bottom fiber of Girder I was -0.72 ksi compression. Similarly, the preload plus overload condition would place the bottom fiber in a state of compression at -0.52 ksi. The stress levels were used in Section 7.9 to compare with AASHTO stress limits under service load conditions.

8.2.3.2 Comparison of Strand and Concrete Data for Tension

Concrete strain ranges determined from vibrating wire gages due to superimposed loads can also be used for verification of the prestressing strand strain ranges induced during load testing. Using the regressed strain-to-height data from the previous section, the strain range due to HS25

truck loading was determined at 2 in. (50 mm) from the bottom, at the level of the bottom row of strands. The concrete gages (vibrating wire gages) showed strain ranges at the bottom row level were on the order of 151 to 167 με, with an average of 160 με for HS25 truck loading. Perfect bond between the strands and the concrete is assumed, such that concrete strain equals steel strain. To determine the strand stress range, the strain ranges were multiplied by the strand modulus, E_s, of 28,800 ksi (198.6 GPa), which resulted in strand stress ranges of 4.34 to 4.81 ksi (29.9 to 33.2 MPa), with an average of 4.61 ksi (31.8 MPa). Similarly, for overload conditions, an averaged measured strain range of 199 με was recorded, resulting in an average stress range 5.73 ksi (39.5 MPa).

The foil gages installed directly on the bottom row of prestressing strands, however, indicated lower stress ranges with averages being 3.96 and 4.95 ksi (27.3 and 34.1 MPa) for the HS25 truck and overload conditions, respectively (see Table 8.6). In other words, the concrete gages showed average stress increases of 16.4% and 15.8% over the strand gages for the two load conditions. In either case (concrete or strand gages), consequential damage to the prestressing strands would not be expected at these low stress ranges.

The possible reasons for the differences in measured stress ranges between the two gage types were considered. All gages used in this comparison were located at midspan. The six vibrating wire gages were embedded at various depths through the cross section to give a full strain distribution. The linearly regressed concrete gage strain-to-height data was used to determine strain at any depth in the girder. The four foil strand gages were applied directly to the strands in the bottom strand row [2 in. (50 mm) from girder bottom] to measure strand strain. Recalling that the strand gage was meant to represent an average strain in all the wires of the strand, it in fact was installed on only one wire. Differences were seen between the measured strand modulus of elasticity when determined by the strand strain gages and the strand modulus determined by the manufacturer using an extensometer. Additionally, orientation variation in the strand foil gages was noted as the gages were aligned with the axis of the strand wire to which they were applied, not with the axial strand alignment. The vibrating wire gages may have also been oriented off from the axial alignment of the girder, they provided a generalized strain distribution, rather than a local strain as the strand gages did. It is believed that the strand foil gages would therefore be a better representor of strain and stress ranges due to superimposed

loads because localized effects can influence the stress range applied and strand gages tend to account for these effects.

8.2.3.3 Concrete Compressive Data

Measured Strains

Under the superimposed loading conditions considered, the composite test girder undergoes compression above the level of the composite neutral axis. Compressive strains in the deck and top flange of the girder at the midspan location were recorded by two gage types, vibrating wire gages and PML-type gages, for the two load combinations: 'Preload + HS25,' and 'Preload + Overload.' Static load tests, previously given in Table 8.4, are used here for comparison except for the tests for which PML-type or vibrating wire gages were not recorded ('Post-crack, 1.2 million cycles' and 'Post-crack 2.4 million cycles').

Each test recorded midspan strain changes from seven PML gages at various heights in the cross section. One PML gage was located at midspan (and vertically along the centriodal axis) at each of the following heights: 25.5, 35, 38, 41, 43.5, 48.5 and 51.5 in. (650, 890, 965, 1040, 1105, 1230, and 1310 mm). The two top gages were located in the composite deck. Load step "holds" did not always coincide with exact load levels of the preload plus truck or overload. Therefore, in an attempt to preserve the variability within the data, a linear interpolation of the raw data was used between the two closest load steps to obtain strains at the prescribed load levels for each gage. A load versus strain change plot is shown in Figure 8.6 for the seven top flange and deck gages for the static test 'Pre-crack, 1.2 million cycles.' Strain changes were not recorded at the 'Preload + HS25' load level of 27.25 kips for this static test and therefore were interpolated, as shown by the hollow symbols in Figure 8.6. Gages located above the composite neutral axis location (at 31.9 in. from bottom) showed compressive strain changes, as expected, while the remaining gage below the neutral axis indicated a tensile strain change. The strain distribution through the composite member depth is shown in Figure 8.7 for the PML recorded strain changes due to the load combination of 'Preload + HS25.'

Compressive strain changes through the composite girder depth recorded by the vibrating wire gages were determined from the same linear regression (strain-to-height relationship at the two load combinations) analysis used for tensile strain changes. Superimposed on Figure 8.7 is the regressed vibrating wire gage data for the 'Preload + HS25' load combination (short dashed

line). The general shape of the PML Gage recorded strain changes-to-applied loads is reasonably close to what the vibrating wire gages recorded. All data is zeroed to the beginning of the given load test. The predicted case shown in the figure was based on Eqn. (2.41) and is the same as that shown in Figure 8.5 as the "Preload + HS25" Load Case.

Similar results were found for load-to-strain behavior recorded by PML Gages at the load combination level of 'Preload + Overload'. Figure 8.8 shows the strain change distribution through the depth of the composite section for the higher load case. Consistent with observations from the lighter load case, superimposed vibrating wire gage data showed reasonably close strain changes to those of the PML Gages.

The differences in compressive strain data between the two gage types at the top gage height [51.5 in. (1310 mm)] can be attributed to a shrinkage crack at midspan in the deck. Along the length of the girder, the crack was located within 4 inches of the vibrating wire gage and immediately next to the PML-type gage. The crack, although no depth extent is known, could cause lower strain in the adjacent PML gage because the crack would have to close before picking up the load (strain). Comparatively, the vibrating wire gage further away (along the span length) would not see the local effect of the crack and would carry a more representative strain. In fact, with both gages located at the same depth of 3.5 in. (90 mm) from the deck top, the vibrating wire gage had a strain 1.7% higher than predicted, while the PML gage was on the order of 19.3% lower due to the presence of the deck shrinkage crack for the 'Preload + HS25' load combination. Similarly for the overload condition, the vibrating wire gage was 3.1% higher and the PML gage was 17.1% lower than predicted.

Using linear regression on the data, strain ranges from vibrating wire gage data due to preload, HS25 truck and overload conditions are listed in Table 8.10 for two compressive locations of interest: top fiber of the prestressed girder flange at the girder-to-deck interface [45 in. (1140 mm) above bottom] and top fiber of the overall composite member [55 in. (1400 mm) above bottom]. Also, tabulated in Table 8.10 are the corresponding stress ranges obtained by multiplying the measured concrete vibrating wire gage strain changes by the measured 28-day concrete modulus of elasticity. A measured girder modulus of 4810 ksi (33.2 GPa) was used to convert to stress for the top fiber of the prestressed (noncomposite) member and a measured deck modulus of 3990 ksi (28.6 GPa) was used for stress conversion at the top of the composite deck.

The average computed fiber strains and stresses reported in Table 8.10 are referred to herein as the *measured average strains and stresses.*

Table 8.10 Measured Concrete Compressive Strain and Stress Ranges - Girder I

	Preload Level		HS25 Truck Load		Overload Truck	
	Δ Strain (με) †	Δ Concrete Stress (ksi)	Δ Strain (με) †	Δ Concrete Stress (ksi)	Δ Strain (με) †	Δ Concrete Stress (ksi)
Top fiber of prestressed girder flange (45 in. from bottom)						
Initial static test	-44.9 ‡	-0.22	-87.4	-0.42	-109	-0.52
After 10^6 fatigue cycles	-44.7	-0.21	-86.9	-0.42	-106.6	-0.51
Pre-crack, after 1.2x 10^6 cycles	-39.8	-0.19	-77.5	-0.37	-97.8	-0.47
Post-crack	-37.8	-0.18	-73.6	-0.35	-91.7	-0.44
Post-crack with 2x 10^6 cycles *	-40.1	-0.19	-78.1	-0.39	-96.8	-0.46
Measured average (top of prestressed member)	*-41.5 ±3.2 με*	*-0.20 ±0.02 ksi*	*-80.7 ±6.2 με*	*-0.39 ±0.03 ksi*	*-100. ±7.2 με*	*-0.48 ±0.03 ksi*
Top fiber of deck (55 in. from bottom)						
Initial static test	-74.6	-0.36	-145	-0.58	-181	-0.72
After 10^6 fatigue cycles	-73.8	-0.36	-144	-0.57	-175	-0.70
Pre-crack, 1.2x 10^6 cycles	-67.2	-0.32	-131	-0.52	-165	-0.66
Post-crack	-66.6	-0.32	-130	-0.52	-162	-0.65
Post-crack, 2x 10^6 cycles	-68.8	-0.33	-134	-0.53	-167	-0.67
Measured average (top of composite member)	*-70.2 ±3.8 με*	*-0.34 ±0.02 ksi*	*-137 ±7.3 με*	*-0.55 ±0.03 ksi*	*-170 ±3.2 με*	*-0.68 ±0.02 ksi*

† All strain data from vibrating wire gages.
‡ Sign convention: tension is positive.
* Concrete compressive strain data not recorded beyond test: 'Post-crack with 2x 10^6 cycles.'

The overall level of compression in the top fiber of the prestressed girder flange during service loads is limited by AASHTO (1996). From the measured prestress loss information presented in Section 7.4 and the service stress ranges, the overall compression level at the girder-to-deck interface can be calculated. Using a prestress force less the measured lower bound prestress loss value of 26.6% (the average lower bound measured loss during the load testing period) and the girder self weight and deck weight in the flexural stress equation (Eqn. 2.41), the top fiber concrete stress of the precast girder flange was calculated to be -3.02 ksi (20.4 MPa) compression, prior to load application. The change in measured concrete compressive stress at the top fiber of the prestressed girder flange due to the load combination of preload and HS25

truck load was -0.59 ksi (4.1 MPa). Superimposing the two stresses, the overall state of stress at the top fiber of the prestressed member was -3.61 ksi compression. Similarly, the preload plus overload condition would place the top fiber of the girder flange in a state of compression at -3.70 ksi. The stress levels are used in Section 7.9 to compare with AASHTO stress limits under service load conditions.

Predicted Strains

The concrete stress predictions for preload, HS25 truck loading and overload conditions are listed in Table 8.11 along with the measured average fiber strains and stresses from Table 8.10 for each load case. Predicted stress changes were determined from elastic theory, Eqn. (8.3). A nominal value I (i.e., I_{gross}) was used to predict the nominal design case. A nominal girder modulus of 6525 ksi (45.0 MPa) was used for the top fiber of the prestressed member, and a nominal deck modulus of 3830 ksi (26.5 MPa) was used for the top fiber of the composite member. Measured values of E_c at 28-days [4810 ksi (33.1 MPa) for the girder and 3990 ksi (28.6 MPa) for the deck] were used to determine $I_{transformed}$ in Eqn. (8.3) to provide a more accurate estimation of predicted fiber stress and strain changes due to the superimposed loads for comparison, and are listed under >Predicted - Girder I=. The 'Predicted – Girder I' strains are shown plotted in Figures 8.5, 8.7, 8.8 and 8.9.

Table 8.11 Predicted Concrete Compressive Strain and Stress Ranges - Girder I

	Preload Level		HS25 Truck Load		Overload Level	
	Δ Strain (με) [1]	Δ Concrete Stress (ksi)	Δ Strain (με)	Δ Concrete Stress (ksi)	Δ Strain (με)	Δ Concrete Stress (ksi)
Top fiber of girder flange						
Measured Average	*-41.5 με*	*-0.20 ksi*	*-80.7 με*	*-0.39 ksi*	*-100 με*	*-0.48 ksi*
Nominal Design Case	-	-0.26	-	-0.51	-	-0.63
Predicted - Girder I	-39.5	-0.19	-76.8	-0.37	-96.0	-0.46
Top fiber of deck						
Measured Average	*-70.2 με*	*-0.34 ksi*	*-137 με*	*-0.55 ksi*	*-170 με*	*-0.68 ksi*
Nominal Design Case	-	-0.26	-	-0.51	-	-0.64
Predicted - Girder I	-70.1	-0.34	-136	-0.54	-171	-0.68

[1] Sign convention: tension is positive.

Nominal stresses in the prestressed girder portion of the composite member were much higher than measured (30% higher), due to the overestimation of the nominal high strength concrete modulus determined from a normal strength relationship which is also reflected in the moment of inertia being too high. Predicted strain and stress changes were comparable to the measured strain and stress changes (the difference was at most 5% lower than measured and more commonly less than 2% different). The stresses were directly related to the modulus of elasticity assumed for the concrete, E_c. The measured average and 'Predicted – Girder I' stresses were similar because the same E_c was assumed, whereas a nominal E_c was used for the nominal design case which led to the higher predicted nominal design case stresses.

Data was also recorded for a series of PML Gages located at 30% of the length from each end support (outside of the constant moment region). Gage placement was through the vertical axis of the cross section at various heights. Figure 8.9 shows the predicted linear strain distribution through the section depth at *0.3L* due to the 'Preload + HS25' load combination. Data was recorded on End IA at two gage heights [38 and 44 in. (965 and 1115 mm)] and on End IB at three gage heights [38.5, 44.3, and 51.5 in. (980, 1125, and 1310 mm)] for the four static summary tests. The predicted strain distribution from the applied load is shown using elastic theory, Eqn. (8.3), to determine the stress change multiplied by the measured concrete modulus and with actual actuator point load placements, a, as shown in Figure 5.1 and transformed composite section properties.

The data appears reasonable for both end locations. Similar trends of increasing compression with increasing distance from the neutral axis were seen at other load steps, including the 'Preload + Overload' condition. The lower compressive strain readings in the composite deck were similar to those observed at midspan and can again be attributed to a shrinkage crack in the deck at the gage location on End IB. Along the length of the girder, the crack was located within 3 inches of the PML Gages. The crack, although no depth extent is known, could cause the PML gage next to it to read lower, because the crack would have to close before picking up the load (strain). The gage, located at a depth of 3.5 in. (90 mm) from the deck top, had a strain reading 15% lower than predicted for the 'Preload + HS25' load combination due to the presence of the deck shrinkage crack (Figure 8.7). For the 'Preload + Overload' combination shown in Figure 8.8, the PML gage in the deck read 7% lower than predicted, indicating that the crack may have closed at higher load levels.

8.2.3.4 Neutral Axis Location

The vibrating wire gages through the section depth were also used to verify the neutral axis location of the composite section. As shown in Figure 8.5, the predicted neutral axis location was 31.9 in. (810 mm) from the bottom of the girder based on the centroid of the transformed composite section. A linear regression of all the vibrating wire gage data (strain versus gage height) indicated the neutral axis was located relatively close, at a location of 30.6 in. (775 mm).

The strain distribution through the centerline axis at midspan of the test girder was also shown in Figure 8.7 for the embedded PML concrete gages. Although only one gage was placed below the predicted neutral axis location, a linear regression analysis of it and the three gages above it indicated the neutral axis was located at 31.6 in. (800 mm) for both load combinations (r^2 values were never less than 0.983). The strain data recorded by the PML gages correlated better with the predicted neutral axis location than the vibrating wire gage data.

A decrease in neutral axis location (measured from the bottom fiber) relative to the predicted (assumed) position would cause the girder to undergo lower tensile strains in the bottom fiber during loading than would be predicted, as well as higher compressive strains than would be predicted in the top portion of the test girder. The vibrating wire gage tensile data were very close to the predicted values, while one set of compressive strain data (from the PML gages) was lower and one set higher (from the vibrating wire gages) than the predicted values. The differences in compressive data from the two gage types were discussed in Section 8.2.3.

8.2.4 Out-of-Plane Deflection

The composite test girder was not braced laterally along its length during load testing, as described in Section 5.1.3. A sidesway deflection system was devised to determine the lateral motion experienced by the test girder during load testing. The bottom flange showed consistent out-of-plane lateral motion on the order of 0.05 to 0.10 in. (1.3 to 2.5 mm) during load testing. For comparison purposes, a maximum downward deflection of 1.54 in. (39 mm) was recorded during maximum overload conditions of a static load test.

There were two possible reasons for this sidesway motion. First, the loading ram could have been placed such that it was not perfectly symmetrical about the centerline vertical axis of the composite girder. Second, if the strands were not perfectly aligned within the forms during manufacturing, or if the formwork itself was not perfectly symmetrical, the girder may not have

been manufactured absolutely symmetrically. The noncomposite girder showed no signs of instability during transportation or handling, although the magnitude of lateral movement was not recorded during those times. In either case, the level of lateral movement recorded during loading was very small and in no way reflected degradation of the composite test girder or loading system.

8.3 Flexural Cracking Load Test Results

Flexural crack testing was performed to determine both the initial cracking load and the load required to reopen the cracks. Results from crack testing were expected to verify the measured losses from vibrating wire concrete embedment gages. Crack testing required a superimposed dead load (sdl) to be hung from the girder with an additional load application from the hydraulic actuators. Details of the test setup and procedures were discussed in Section 5.2.2. Instrumentation specific to crack testing was discussed in Section 5.3.3. Acoustic emissions (AE) monitoring equipment was used to detect and approximately locate crack initiation while visual inspection was used to precisely identify each crack location. Table 8.12 lists the initial crack test as well as subsequent crack reopening tests along with the timeline, test name and comments pertinent to each test.

Table 8.12 Summary of Crack Testing for Girder I

	Time line	Test Name [1]	Other comments
Initial Crack Test	After 1.2 million load cycles	CRACK1 - Loop 1	Apply dead load and load beyond cracking, no unload data, following static test TRUCK11.
Reopen 1 Test	Post-crack, 1.2 million load cycles	CRACK2 - Loop 1	Load and unload truck test, apply dead weight, load beyond cracking, and unload.
Reopen 2 Test	Post-crack, 2 million load cycles	CRACK3 - Loop 1	Apply dead load and load to beyond cracking, no unload data, following static test TRUCK13.
Reopen 3	Post-crack after 2 million load cycles	CRACK4 - Loop 1	Apply dead load, load beyond cracking, unload, following static test CRACK3.
Reopen 4		CRACK4 - Loop 2	
Reopen 5		CRACK4 - Loop 3	

[1] Corresponds to testing name noted in Appendix C - Load History.

8.3.1 Cracking Load and Crack Locations

The initial flexural cracking test for Girder I occurred at an age of 593 days on March 27, 1995 (approximately 1 year and 7.5 months after casting). The girder had been subjected to 1.2 million load cycles and eleven intermittent static truck tests prior to crack testing (Figure 8.1). Immediately prior to crack testing, a static test was performed to a load level equivalent to the 'Preload + HS25' load combination. No damage was detected prior to the initial crack test in the form of loss of stiffness, crack initiation via AE, visual cracking or otherwise.

8.3.1.1 Measured Initial Cracking and Reopening Loads

The total load applied during the initial flexural crack test was the hanging dead load plus the average actuator load of 33.4 kips (149 kN) at each actuator location. The two actuators never differed in load by more than 0.25 kips (1.1 kN). Visual crack data recorded during the initial crack test is tabulated in Table 8.13. The table lists a total of 24 cracks which were visually observed to develop during the initial flexural crack test. The cracks are listed in order of location from End A. The order of crack formation is noted. The first three visual cracks (B-BF-9, 10, and 11) appeared at locations of 71.5, 72.8, and 74.4 ft. (21.8, 22.2, and 22.7 m) from End A and at the load step '28 kips (125 kN) per actuator plus the hanging superimposed dead load' (28k+sdl). The crack name notation refers to the end on which the crack occurred (A or B), the location within the cross section where the crack first initiated (BF= bottom flange, W= web, TF= top flange), and the crack order number from each respective end.

As crack testing continued, further cracking was induced, leading to a total of 24 cracks. Cracks typically ran across the bottom face of the flange and up 4 to 6 in. (100 to 150 mm) on each side of the bottom flange (approximately to the center of gravity of strands at 5.39 in., [137 mm]). The crack location distances noted were overall distances from the girder end and include the overhang distance of 7.5 in. (191 mm) at the support. Also, tabulated is the computed total applied moment *at each crack location* at the time of crack formation. This total moment includes the effect of the hanging superimposed dead load as well as the actual load from each actuator. The order of crack formation is listed, where the numbering increases from load step to load step and the lowest cracking moment at each load step begins alphanumerically. Load steps were targeted at 2.0 kip (8.9 kN) intervals, resulting in a moment resolution of 1250 in-k (141 kN-m) at midspan per load step.

Table 8.13 Initial Flexural Cracking Loads and Locations for Girder I

Crack Name	Distance from A	Cracking Load †	Cracking Moment (in-k) ‡	Formation Order
Actuator Load Point at End A: 52.9 ft.				
A-BF-1	53.4 ft. *	32k + sdl	31,500	3d
A-BF-2	54.5	33.4k + sdl	32,525	4c
A-BF-3	55.7	33.4k + sdl	32,790	4d
A-BF-4	57.2	32k + sdl	32,320	3g
A-BF-5	58.2	30k + sdl	31,265	2a
A-BF-6	60.2	32k + sdl	32,970	3i
A-BF-7	61.2	30k + sdl	31,910	2b
Chain from superimposed dead load: 61.38 ft. (5 ft. offset of midspan)				
A-BF-8	62.6	32k + sdl	33,225	3j
A-BF-9	63.9	32k + sdl	33,230	3k
A-BF-10	65.6	32k + sdl	33,230	3l
Midspan: 66.38 ft.				
B-BF-14	67.4	32k + sdl	33,235	3m
B-BF-13	69.1	32k + sdl	33,235	3n
B-BF-12	70.2	32k + sdl	33,235	3o
Chain from superimposed dead load: 71.38 ft. (5 ft. offset of midspan)				
B-BF-11††	71.5	28k + sdl	30,690	1c
B-BF-10††	72.8	28k + sdl	30,400	1b
B-BF-9††	74.4	28k + sdl	30,070	1a
B-BF-8	75.6	32k + sdl	32,350	3h
B-BF-7	77.1	32k + sdl	32,015	3f
B-BF-6	78.3	32k + sdl	31,770	3e
Actuator Load Point at End B: 79.5 ft.				
B-BF-5	79.8	32k + sdl	31,340	3c
B-BF-4	80.9	32k + sdl	30,710	3b
B-BF-3	82.4	33.4k + sdl	30,622	4b
B-BF-2	83.7	32k + sdl	29,030	3a
B-BF-1	85.0	33.4k + sdl	29,050	4a

† Crack load corresponds to load step during visual inspection.
‡ Moment as computed at the location of each crack, corresponding with visual cracking load.
†† Designates the first three visual cracks.
* Metric conversions are: 1 ft. = 0.3048 m, 1 kip = 4.4482 kN, 1 in-k = 0.1130 kN-m.

During the initial crack test, the AE system detected crack initiation at a load level of '21 kips per actuator plus the hanging superimposed dead load' (21k +sdl), with a resolution of ±2 k. Zoned source location was used due to the high dissipation of the concrete, which yielded source location accuracy to within only two to three feet (0.6 to 0.9 m). Therefore, the AE system was most useful for informing the researchers when and approximately where to look for a crack. No cracks were visually noted prior to the detection of AE signals.

The load levels and moments for both AE and visual inspection during the initial crack test as well as subsequent crack reopening tests are listed in Table 8.14. The first visual crack was B-BF-9, occurring at the load step (28k + sdl), and a moment level of 30070 in-k (3400 kN-m) at the crack location of 74.4 ft. (22.7 m) from End A. Because the dead load was hung at locations between the actuators, a constant applied moment region existed only between the dead load points. The moment due to applied loads outside of this region (where the first cracks occurred) varied linearly between the load points. Therefore, the moments listed in Table 8.14 for AE and visual cracking have been computed using the actual load readings from each actuator plus the hanging superimposed dead load. First, the moment *at the location of crack* B-BF-9 is listed. And second, the *midspan* moment using the same given load level is listed.

Table 8.14 Measured Flexural Cracking Load and Reopening Loads for Girder I

Test Name	AE Crack Load [1]	AE Crack Moment (in-k) [2]		Visual Crack Load [1]	Visual Crack Moment (in-k) [2]	
		At crack location [3]	At midspan		At crack location [3]	At midspan
Initial Crack	21k[4] + sdl	25,650*	26,280	28k + sdl	30,070	30,700
Reopen 1	14k + sdl	21,250	21,890	16k + sdl	22,520	23,150
Reopen 2	15k + sdl	21,870	22,510			
Reopen 3	15k + sdl	21,870	22,510			
Reopen 4	-	-	-	16k + sdl	22,520	23,150
Reopen 5	-	-	-			

[1] Load designation is the load applied by the actuator (in kips) which was in addition to the superimposed dead load provided by the hanging concrete blocks.
[2] Metric conversion: 1 in-k = 0.1130 kN-m.
[3] Moment as computed at the location of the first crack B-BF-9 and corresponding to the crack load.
[4] Resolution of data was ±2.0 kips (± 1250 in-k).
* Moment includes hanging dead load and applied actuator load effects.

For each flexural crack test (initial and reopening) listed in Table 8.14, the AE system detected crack reopening prior to the visual observation for the first three reopening tests after

initial cracking. Cracks B-BF-9, -10, and -11, the first cracks to form initially, were consistently the first cracks to reopen. The decrease in load from initial cracking to crack reopening was expected, as less load is required to reopen a preexisting crack because the load no longer needs to overcome the tensile strength capacity of the concrete. The increase in load level (e.g., Reopen 2 and 3 versus Reopen 1) for subsequent crack reopening tests using AE is explained as follows. Acoustic emissions are mostly a product of crack growth and partially a product of the opening and closing of a crack. As the crack was cycled through opening and closing at the same load level, the crack stabilized such that there was no crack growth and a reduction in AE signals was noted. Furthermore, the interior crack surface begins to smooth leading to a subsequent reduction of AE signals at the same load level. Consequently, a larger load is needed to produce the equivalent level of AE signals. By the fourth and fifth crack reopening test, the required load for AE signals is larger than the original cracking load, indicating that AE was best used for initial crack detection and the first few reopening cycles for crack growth. Although tests Reopen 4 and Reopen 5 indicated an AE reopening load of 17 and 27 kips plus superimposed dead load, respectively, the information should not be used as a comparison for the reasons stated previously. Therefore, a dash (-) is shown in Table 8.14 for these two tests. The visual crack reopening loads were consistent as anticipated.

During the crack reopening tests, no additional crack formations were seen and noticeable crack growth was limited. The existing cracks appeared to grow one to three inches (25 to 75 mm) during Reopen Test 1, due to the increased applied stress from the same moment applied in load control to a reduced section modulus. Continued reopening tests showed no additional growth of preexisting cracks. The maximum load reached during the initial crack test was also the maximum load of all crack reopening tests. Measured displacements at crack openings, as determined by LVDTs placed across cracks during reopening tests, are discussed in Section 8.3.1.3.

8.3.1.2 Measured Load - Deflection Response

The load-deflection response for static testing up to the 'Preload + Overload' condition was presented in Section 8.2.1, and showed no degradation due to continued load cycles through 2.4 million cycles. Static testing performed before and after crack testing showed no degradation for this load range to 125% HS25 (below crack reopening loads). However, static testing above the

cracking moment (up to 250% HS25) did show a change in the moment-deflection response of the composite girder.

Moment-deflection response is used for discussions of flexural crack testing rather than load-deflection response because crack testing required hanging a superimposed dead load in combination with a load application via the hydraulic actuators. Because the dead load was hung at locations between the actuators, the loads generate different moments due to different application points. It is clearer to superimpose the moments. The superimposed hanging dead load and actuator loads result in a constant moment region only between the dead load hanging points (without regard to the girder self-weight). Further detail on actual symmetrical load application locations was given in Section 5.2.2.

The moment-deflection response of the initial flexural crack test for Girder I is given in Figure 8.10. The applied moment at midspan is plotted relative to the midspan deflection. Notation is included to indicate when the AE system first detected crack initiation and when the first visual crack appeared based on the midspan moment at the time of detection (see Table 8.14). A static test to 'Preload + HS25' was performed immediately prior to crack testing and results are shown in the figure for stiffness comparison. Closer inspection of the relationship between the data and the straight dashed line shows that the stiffness did not begin to degrade from its initial slope until about 22,000 in-k (2490 kN-m), just before the AE system recorded events.

Similarly, the moment-deflection responses of the crack reopening tests are superimposed on the initial crack test response and are illustrated in Figure 8.11. As expected, a decrease in stiffness was observed with the damaged section after passing crack reopening. The moment-deflection response for the crack reopening test diverges from linear at a lower moment than observed for the initial crack opening test, corresponding with the AE and visual reopening load level trends tabulated previously in Table 8.14. Reopen Tests 1, 2, and 3 follow the same loading path indicating that once the girder is in a cracked state and reloaded to the same level, it maintains its relative stiffness. With closer inspection of the data, the moment-deflection curves of the first three reopen tests began to deviate from a straight line at about 17000 in-k (1920 kN-m), or at a load level of about '6.4 kips plus the superimposed dead load' (6.4k + sdl). The moment-deflection response indicates that crack reopening occurred at approximately the same

load level as determined by crack width gages (discussed in Section 8.3.1.3) and well before AE and visual crack reopening.

A convergence of the moment-deflection curves for the initial crack test and the reopening tests was observed at a moment level of about 32,000 in-k (3620 kN-m). This was expected because once the initial crack had formed, the tensile capacity of the concrete had been overcome. Crack reopening tests did not require the load to overcome the tensile capacity of the concrete (because it was already cracked). Consequently the moment-deflection response of the crack reopening tests on the composite girder all followed the same path and eventually intersected the initial crack test response.

Also, indicated in Figure 8.11 is a shift for Reopen tests 4 and 5. This phenomenon is most likely due to creep of the girder under sustained load during the testing period. These last two tests were performed as loops 2 and 3 of a single test day where the dead load was left hanging on the composite test girder for 4 hours. The slope of each of these last two curves appears to be offset and parallel from the straight line and is not significantly different from the reopening tests where creep was not an issue.

8.3.1.3 Measured Bottom Flange Crack Width Displacements

After Reopening Test 1 and prior to Reopen 2, two LVDTs were placed on the underside of the bottom flange of the damaged girder (longitudinally along the girder length and perpendicular to the flexural cracks) in an effort to accurately determine the load level at which the cracks reopened. Both LVDTs had an overall travel range of 0.10 in. (2.5 mm) with an accuracy of ±0.0001 in. (0.0025 mm). The first gage was placed directly *over* crack B-BF-9 on the bottom flange in the longitudinal direction of the beam and below the vertical axis of symmetry. The second gage was placed *near* the crack, approximately 2 in. (50 mm) away toward the supported end and 2 in. (50 mm) off the vertical axis. The LVDT displacement recorded at each gage location includes the displacement due to crack opening as well as any concrete deformation occurring between the LVDT anchor points.

A plot of the applied midspan moment versus the crack width opening is shown in Figure 8.12 for the static truck test prior to Reopen 2 test, as well as for Reopen 2 itself. In the legend, *over* refers to the gage placed over the crack and *near* refers to the gage offset from the crack. The typical service range of induced moment is shown as a reference. Both gages show

consistency (i.e. they remained parallel) in opening while the load applied caused the bottom fiber of the girder to change from compression to tension. As the applied midspan moment increased above 16,000 in-k (1810 kN-m), the gage *over* the crack showed an abrupt increase in displacement, noted by the sharp bend and decrease in slope, and the crack began to open. The gage *near* the crack showed the displacement stabilized, such that additional strain was no longer distributed to the concrete *near* the crack (the deformation was concentrated in the crack).

The measured displacements shown in Figure 8.12 indicate concentrated deformations taking place at the crack near the high end of the typical service range, corresponding to a load level of '6k + sdl' or an applied midspan moment of 16,500 in-k (1865 kN-m). The AE monitoring system exhibited crack reopening events at a higher load level of '15k +sdl', although the crack did not visually reopen until a load level of '16k +sdl.'

Additional data was recorded during subsequent reopening tests and are superimposed in Figure 8.13. The gages were consistent in that the relative shape of each curve remained in tact. The slight lateral shifts in data from test to test were expected with the level of system noise involved. This data implied that continued cycling of the test girder through truck load levels and overload conditions showed no change in the load (moment) level at which the crack opened or in the relative width of the opening at any given load level.

8.3.1.4 Predicted Initial Cracking Load

Predicted flexural cracking loads and corresponding cracking stresses were compared to those observed. Table 8.15 lists the initial measured (AE and visual) cracking load along with the predicted loads for four cases of losses: nominal, measured, Time-Step predicted losses, and *Pbeam* predicted losses. Using the following relationship, the predicted actuator load per point could be back-calculated from the actuator moment required to cause the bottom fiber stress to reach the modulus of rupture,

$$\sigma = \left[-\frac{P_{eff}}{A_{nc}} - \frac{P_{eff} e_{nc} c_{nc}}{I_{nc}} + \frac{M_{sw} c_{nc}}{I_{nc}} \right] + \frac{M_{deck} c_{nc}}{I_{nc}} + \frac{M_{(sdl+actuator)} c_c}{I_c}. \qquad (8.4)$$

The predicted nominal design case assumed the tensile stress to crack the section was equal to the nominal modulus of rupture $7.5\sqrt{f'_c}$= or 769 psi. In addition, design material and gross geometric properties (A, e, c, I and M) were used for the noncomposite ($_{nc}$) and composite ($_c$) section properties. Predicted nominal losses of 28.8% estimated from the PCI Committee on

Prestress Losses (1975) at the time of crack testing (Section 7.4.2) were used to define the nominal effective strand force, P_{eff}. This led to a predicted total applied midspan moment of 23,460 in-k (2650 kN-m), or an actuator moment of 10,620 in-k (1200 kN-m), required to achieve the nominal cracking stress. With the applied four-point loading configuration, a load of '16.5 kips plus the superimposed hanging dead load' would be needed to reach the nominal modulus of rupture, as listed in Table 8.15.

Table 8.15 Predicted Initial Cracking Load for Girder I

	Load Level (Actuator + Superimposed)	Applied Midspan Cracking Moment (in-k)	Cracking Stress (ksi) †	Cracking Stress Level ($x\sqrt{f_c'}$)
AE Initial Crack‡	*21k + sdl*	*26,300 (25650 ‡)*	*+0.16 (-0.04 ‡)*	~0‡
Visual Initial Crack	*28k + sdl*	*30,710 (30070‡)*	*+0.51 (+0.43 ‡)*	$3.6\sqrt{f_c'}$‡
Nominal Design Case	16.5k + sdl	23,460	+0.769	$7.5\sqrt{f_c'}$
Predicted - Girder I *				
Measured Losses, 26.6%	36.7k + sdl	36,190	+0.951	$8.6\sqrt{f_c'}$
Time-Step Losses, 32.4%	30.0k + sdl	31,970		
Pbeam Losses, 27.5%	35.7k + sdl	35,560		

† Sign convention: tension is positive.

‡ Computed at the location of the first visual crack, B-BF-9, as opposed to midspan.

* Assumed losses at crack testing summarized in Table 7.5. Lower bound losses assume zero concrete stress prior to release.

The best fit predictions, listed under 'Predicted - Girder I' in Table 8.15, for cracking moments were based on the 28-day measured cracking stress of 951 psi. Using lower bound measured average losses of 26.6% (assuming concrete stress prior to release was zero), net section properties for the four geometric properties in the bracketed terms of Eqn (8.4), and transformed noncomposite and composite section properties, respectively, for the remaining terms in Eqn. (8.4), a total applied midspan cracking moment of 36,190 in-k (4090 kN-m) was computed. This gave a predicted cracking moment of 23,320 in-k (2620 kN-m) due to the actuators alone, or a total predicted load level of '36.7 kips per actuator plus the superimposed dead load' (36.7k +sdl). Using the same previously defined geometric properties and the losses as predicted by the Time-Step method at the time of crack testing (Section 7.4.2), the predicted cracking load would have been approximately the same, at '27.4k + sdl'. Output results using the *Pbeam* program with measured material properties with modified shrinkage predicted the cracking load to be even higher yet, at '35.7k + sdl'. In all cases, predicted cracking loads

indicate losses must be higher than lower bound measured losses. Further discussion of losses based solely on measured initial crack and reopening loads is included in Section 8.3.1.6.

8.3.1.5 Predicted Crack Reopening Load

The crack reopening load, also known as the load when the bottom fiber reaches zero tension, was compared to predictions tabulated in Table 8.16. The same assumptions were applied for predicting the nominal design and predicted cases of crack reopening as assumed for the initial cracking load comparison, with the following exception. The crack reopening load is computed when the level of bottom fiber stress is equal to zero. Also tabulated for comparison are the crack reopening load as detected by the AE monitoring system and visual inspection (see Table 8.14) and the LVDTs placed to monitor crack widths during the reopening tests (Section 8.3.1.3).

Table 8.16 Predicted Crack Reopening Load for Girder I

	Load Level (Actuator + Superimposed)	Crack Reopening Moment (in-k) †
Bottom Flange Crack Reopen As recorded from LVDTs ‡	*6k + sdl*	*16,850*
AE Reopen	*14k + sdl*	*21,900 (21,250 *)*
Visual Reopen	*16k + sdl*	*23,150 (22,520 *)*
Nominal Design Case	4.3k + sdl	15,780
Predicted - Girder I		
Measured Losses, 26.6%	17.9k + sdl	24,350
Time-Step Losses, 32.4%	11.2k + sdl	20,130
Pbeam Losses, 27.5%	16.2k + sdl	23,280

† Metric conversion: 1 in-k = 0.1130 kN-m.
‡ Italicized text indicates measured values.
* Moment computed at location of the first crack, B-BF-9, as opposed to midspan.

The nominal design case conservatively predicted much lower reopening loads than measured. The predicted reopening moment using lower bound measured losses and material properties was 5.2% greater than the moment recorded as the first visual crack reopened and nearly 45% higher than the moment level when LVDTs placed across the crack on the bottom flange detected crack opening. Predicted reopening moments using the Time-Step and *Pbeam* losses were on the same order of moments predicted using lower bound measured losses because of the similar losses used from the other methods.

8.3.1.6 Discussion of Cracking Loads

Table 8.15 lists the measured load and moment level results from the AE and visual inspection of first crack formation (at crack B-BF-9). With the measured AE and visual applied initial cracking moments 27% and 15%, respectively, less than predicted using lower bound measured losses of 26.6%, attention was given to finding a probable cause for the discrepancy. Two variables had a large effect on the estimated cracking loads from Eqn. (8.4): the assumed modulus of rupture and prestress losses. The influence of each variable is reviewed.

Because the modulus of rupture was measured at 28-days rather than at crack testing, it was a source of possible error in predicting the cracking loads. The midspan cracking stress corresponding to the measured cracking loads was back-calculated and compared with the measured modulus of rupture. The stress was computed from Eqn. (8.4) using a measured lower bound prestress loss of 26.6% to determine the effective prestress force, net section properties for the first three bracketed terms, and transformed section properties for the noncomposite and composite remaining terms. A stress level of +0.141 ksi (tension) was computed at the load level that AE monitoring detected crack formation. The bottom of the girder was computed to be at a state of stress of +0.498 ksi (tension) when the first visual crack appeared. The 28-day measured modulus of rupture for Girder I was 0.950± 0.040 ksi (Table 6.3). Because the midspan cracking stress level under the actual loading condition at the first appearance was computed to be only half of the measured modulus of rupture, it is unlikely that an error in measuring cracking stress could be the only reason for the high predicted cracking loads.

Measured cracking loads were used to estimate prestress losses for comparison to the lower bound measured losses determined from vibrating wire gages embedded in the concrete. The measured lower bound loss used in predicting initial and crack reopening loads in Section 8.3.1.4 and 8.3.1.5 was 26.6% (Section 7.4.1) and is shown italicized in Table 8.17. Estimated prestress losses were back-calculated from the measured applied cracking moment using Eqn. (8.4). The strand force P was calculated by assuming the bottom fiber concrete stress at cracking was equal to the measured concrete modulus of rupture while the actual applied moment was taken into consideration. Knowing the force P and the strand area, A_{ps}, losses were computed relative to the initial tensioning stress. Losses at the time of crack testing were back-calculated to be 36.4% using the AE crack detection moment level and 32.0% using the moment level when the first visual crack was noticed. Estimated losses are also listed in Table 8.17. Losses were also back-

calculated using the applied moment when bottom flange LVDTs recorded crack reopening (Table 8.16) in conjunction with a zero tension stress in place of the measured rupture modulus. In this way, losses were computed to be 34.1% for the measured crack width case. When using AE and visual reopening moments for the case of the bottom fiber stress at zero, losses were computed to be 29.1% and 27.8%, respectively.

Table 8.17 Estimated Losses from Cracking Tests of Girder I

	Load Level (Actuator + Superimposed)	Estimated Prestress Loss at Crack Testing	Estimated $\sigma_{c,\ before\text{-}rel}$
		Measured *Lower Bound: 26.6%* † *Upper Bound: 40.2%* ‡	*0 ksi* *0.950 ksi*
Initial Crack Testing assuming $\sigma_{bottom\ fiber} = 0.95$ ksi			
AE Initial Crack	21k + sdl	36.4%	0.69 ksi
Visual Initial Crack	28k + sdl	32.0%	0.38
Crack Reopening Testing assuming $\sigma_{bottom\ fiber} = 0.0$ ksi			
Bottom Flange Crack Reopen	6k + sdl	34.1%	0.53
AE Reopen	14k + sdl	29.1%	0.18
Visual Reopen	16k + sdl	27.8%	0.09

† Measured lower bound losses determined from vibrating wire gages (Table 7.5) assume zero concrete stress before release (Section 7.4.2).

‡ Measured upper bound losses assume concrete stress before release equal to the measured modulus of rupture at 28 days.

Confidence may be best placed in the losses estimated from the crack reopening tests using the bottom flange crack data (34.1%). It was known that the bottom fiber stress was zero at crack reopening and data clearly showed the load (or moment) level at which crack reopening was detected (Figure 8.13). In addition, assuming the measured modulus of rupture was accurate, confidence can also be placed in the results from the initial testing as recorded by AE (36.4%) because of the girders virgin state. In either case, the consistency between the estimated losses was extremely high even though both estimated measures were determined independently.

When compared with lower and upper bound measured losses from vibrating wire gages, the estimated losses from initial crack testing and reopening tests were reasonable. The lower bound measured losses assumed that the concrete stress in the section was zero at the time of release (Section 7.4.2). The upper bound measured losses assumed the concrete stress prior to release was equal to the 28-day measured modulus of rupture, and were 13.6% higher than lower bound

losses, or 40.2% at crack testing. The losses determined from crack testing were used to estimate the stress in the concrete prior to release ($\sigma_{c,before\text{-}rel}$) using the relationships developed in Eqns. (7.1-7.6). The estimated concrete stresses before release for the two cases with most confidence (AE during initial crack testing and LVDT data at crack reopening) was 0.69 and 0.53 ksi (4.8 and 4.1 MPa), respectively, and are listed in Table 8.17. None of the estimates indicated that the tensile capacity of the girder was exceeded, confirming observations that no cracking existed in Girder I prior to release.

Using losses estimated from LVDT gages placed across bottom flange cracks at crack testing, initial and long term losses were estimated. The difference between lower bound measured losses and losses estimated from LVDT data (7.5%) at crack testing was superimposed on the initial and long term lower bound losses to determine a 'best-guess' estimate of losses assuming the concrete stress prior to release was equal to 0.53 ksi (4.2 MPa). Long term 'best guess' estimates of measured losses are listed in Table 8.18 along with lower and upper bound losses.

Table 8.18 Best Guess - Estimated Losses for Girder I

	Lower Bound Measured Losses[1]	Estimated Prestress Loss from LVDT Data taken at Crack Testing	Upper Bound Measured Losses[2]
Initial Loss	15.5%	23.0%	29.1%
28-days	21.6%	29.1%	35.2%
Deck Casting	23.9%	31.4%	37.5%
Crack Testing	26.6%	34.1%	40.2%
Ultimate Flexural Test	27.2%	34.7%	40.8%

[1] Measured lower bound losses determined from vibrating wire gages (Table 7.5) assume zero concrete stress before release (Section 7.4.2).

[2] Measured upper bound losses assume concrete stress before release equal to the measured modulus of rupture at 28 days.

8.3.2 Strand Strain and Stress Ranges

The same six strand gages that provided useful data during the intermittent static test at truck load and overload conditions (see Section 8.2.2) were informative during the flexural cracking and reopening tests. Table 8.19 lists the six gage names, their respective location from End A, and height from the bottom of the girder. Also tabulated is the nearest flexural crack, the distance to nearest crack, and the load level when the crack formed. All of the gages, except

gage FIAC15 located at midspan, were located outside of the constant moment region, but within the actuator load points. Four of the six gages were located within an inch of crack B-BF-10, one of the first three cracks to form, at 72.8 ft. (22.2 m) from End IA.

Table 8.19 Strand Strain Gage Information for Initial Crack Test - Girder I

Gage Name[1]	Distance from End A (ft)	Gage Height from bottom of girder (in)	Nearest Flexural Crack	Distance to Nearest Flexural Crack (in)	Load Level at Crack Formation (k+sdl)
FIA35	59.50	6.0	A-BF-6	8.5	32k+sdl
FIAC15	66.35	2.0	A-BF-10	9.0	32k+sdl
FIB19	72.80	2.0	B-BF-10	< 1.0	28k+sdl
FIB15	72.85	2.0	B-BF-10	< 1.0	28k+sdl
FIB25	72.90	4.0	B-BF-10	< 1.0	28k+sdl
FIB12	73.00	2.0	B-BF-10	2.0	28k+sdl

[1]Corresponds to Appendix D in Kielb (1994).

The moment-stress relationship for each of the six gages is portrayed in Figure 8.14 for the initial flexural crack test. Each gage had nearly 100 strain readings averaged at each hold point. The average stress value was determined from the average strain multiplied by the apparent modulus as measured from gage data (29,100 ksi, 201 GPa). It is plotted relative to the moment on the *y*-axis, which is the actual applied moment at the location of the gage, accounting for actual actuator loads and placement as well as the hanging dead load location (not including self-weight). The standard deviation of each gage at any given data point was very low (<5 με) with the exception of gage FIB12. Its standard deviation was nearly 20 times higher (100 με), as shown by the jagged curve rather than the smooth curves of the remaining gages. Although the standard deviation was high during this test, the gage still provided useful information regarding the general trend of stress in the strand. The predicted stress for the bottom row of strands is also shown on the figure for comparison. Stress was predicted using measured material properties including a strand modulus of 28,800 ksi (199 GPa), and transformed composite section properties.

Each of the four gages that were located within an inch from the first crack show a significant jump in stress just prior to visual crack detection (the applied moments at these gage locations were on the order of 28,000 to 30,000 in-k). This corresponds to a flexural cracking load range of '25 to 27 kips per actuator plus the superimposed dead load'. The two remaining

gages (FIA35 and FIAC15) were 8.5 to 9 inches away from cracks that formed at later load steps. Neither of these two gages showed a significant jump in stress at the visual crack level, as expected. The horizontal shift shown for all gages at approximately the 30,000 in-k level was caused from load redistribution and further cracking as the load level was held for nearly one half hour while the girder was inspected for additional cracks. It is interesting to note that the only gage at midspan and within the constant moment region (FIAC15) indicated a decrease in stress at the hold level, perhaps signifying stress redistribution away from the first cracks.

The same data was collected for the six gages during the flexural crack reopening tests. Figure 8.15 shows the moment-to-stress relationship for gage FIB15 during precrack, initial crack and crack reopening tests. This figure is similar to the composite girder moment-deflection response in that once the girder was cracked subsequent loadings after cracking followed a flatter slope due to the reduced section upon crack reopening. The jump in stress at the initial crack test is pronounced here, as tests of the cracked girder show smooth transitions during loading. The curves (initial and all reopen tests) converged beyond the initial visual cracking moment, and near the maximum applied moment level, as expected and confirmed from the same characteristic of the moment-deflection response. The remaining gages not shown here produced similar graphs and results.

8.3.3 Concrete Strain and Stress Ranges

Two types of gages were used to record concrete strain data. As with the static test results presented in Section 8.2.3, vibrating wire gages and embedded concrete PML gages were used. Vibrating wire gages placed through the depth at midspan provided both compressive and tensile data during flexural crack load testing. In this section, concrete tensile stresses are compared with stresses determined from strand gage data (Section 8.3.2). Concrete compressive strains in the deck and top flange were also recorded during flexural crack load testing by PML gages and are compared with vibrating wire gages.

Vibrating wire gage data (midspan moment versus strain) recorded during the precrack static test to 125% HS25 and the initial flexural crack test are shown in Figure 8.16. The typical service range up to 100% HS25 load is also noted for reference. Precrack test results are plotted with a solid line, and the initial flexural crack test is plotted with a dashed line. Data recorded thereafter was limited, with only the second crack reopening test recording vibrating wire gage

data at occasional load steps, shown in the figure as hollow symbols. The gages located in the deck and top flange [51.5 and 42.5 in. (1310 and 1080 mm)] show compressive strain changes as expected under the loading scenario, while strains recorded in the bottom flange indicated tensile changes in strain.

The strain distribution through the midspan cross section is illustrated in Figure 8.17 for several load steps of interest. The 'Preload + HS25' load combination was recorded during the pre-crack static truck test and is linear, as expected from previous static test results documented in Section 8.2.3 and Figure 8.5. Also shown is the predicted strain distribution for the 'Preload + HS25' load combination based on the actual moment induced and transformed composite section properties.

The distribution remained linear until just prior to AE crack detection at the load step '20k +sdl' at which time the lowest gage in the bottom flange showed a reduction in tensile strain. As the load level increased, so did the amount the bottom tensile strains dropped off. The three remaining gages continued to behave linearly, even at higher load steps. This behavior would be expected as cracking occurred, considering gage and cracking locations. All gages were located at midspan. The lowest gage, embedded at 2.5 in. (64 mm) above bottom, was well below the center of gravity of the strands (*cgs*) of 5.39 in. (137 mm). The next gage up, at 4.75 in. (120 mm), was nearly aligned with the *cgs* such that surrounding concrete would experience the strain without crack influence because the crack depth did not extend that far. Gages in the top flange and deck do not experience the localized effect from cracking that is experienced by the bottom flange gages. Even though first cracks formed 5.1 to 8.0 ft. (1.6 to 2.4 m) away from midspan, the bottom fibers at midspan experienced some strain change, as shown in the figure at the 'Visual Crack, 28k +sdl' load step. By the maximum load step of '34k +sdl', cracks had formed at 9.3 and 12.2 in. (236 and 310 mm) on either side of the midspan gages. The greater reduced tensile strain at the bottom gage is an artifact of the closer cracks. After cracking, the strain was no longer linearly distributed down to the bottom fibers. Had the gages been located exactly at a crack, the concrete strain would have been reduced to zero.

Stress ranges at the level of the *cgs* from vibrating wire gages can be compared with stress ranges from gages placed directly on the strands due to crack testing. The stress range of 12.0 ksi at the *cgs* of the strands determined from a vibrating wire strain of 418 με multiplied by the strand modulus of 28,800 ksi (199 GPa) when the first visual crack appeared, whereas the strain

was computed from the linear regression of vibrating wire strain versus gage height for the top three gages shown in Figure 8.17. Only one strand gage at midspan collected data for comparison, although it was located at 2.0 in. (50.8 mm) from the bottom. It recorded a strain of 513 just prior to cracking and 493 με immediately after the first crack appeared. Corresponding stress ranges of 14.9 and 14.3 ksi, respectively, were determined using the apparent strand modulus of 29,100 ksi (201 GPa). While it is difficult to conclude strongly based on the results of one gage, the two methods for determining stress change due to superimposed loading are within reason.

Concrete compressive and tensile strains were also recorded by seven concrete embedded PML gages located through the girder cross section at midspan. Figure 8.18 shows a graph of the moment versus strain results of the seven PML gages at varying heights for the initial flexural crack test. The typical service range is noted for comparison to show that the moment-strain relationship was linear to well above this range. Strains at all gage heights begin to show nonlinearity at about 25,500 in-k (2880 kN-m), or at a load level of '20k +sdl', and corresponding to immediately before AE monitoring began recording initial crack events.

The PML strain distribution through the depth of the midspan cross section is shown in Figure 8.19 for the pre-crack truck test, AE and Visual Crack Load levels, and crack reopening tests 2 and 3. (Data was not recorded for the Reopen 1 test.) The 'Preload + HS25' pre-crack test results were similar to the intermittent static truck test results shown in Figure 8.7 and discussed in Section 8.2.3. The 'Predicted' distribution at the 'Preload + HS25' load level was based on the nominal moment for this load combination and transformed composite section properties.

8.3.4 Out-of-Plane Deflection

As previously discussed in Section 8.2.4, the test girder was not braced laterally along its length during load testing, including flexural crack testing. The sidesway deflection system devised for static and fatigue loading was also used during crack testing to provide insight into how much lateral motion the test girder experienced during load testing. The bottom flange showed consistent out-of-plane motion on the order of 0.10 in. (2.5 mm) for vertical deflections as high as 4.1 in. (104 mm). The two possible reasons for this sidesway motion discussed in Section 8.2.4 are applicable here as well. Most notably is the fact that this out-of-plane motion

was very small relative to the length and longitudinal deflection of the girder, and can be considered negligible. Flexural crack testing did not cause any instability conditions in the test girder.

CHAPTER 9 LOAD TESTING OF COMPOSITE GIRDER II

9.1 General Load Testing of Composite Girder

Load testing of the composite girders included static tests to truck levels and overload conditions, cyclic load testing to the same levels, flexural crack testing above overload conditions, and an ultimate flexural test. The detailed loading history for Girder II is given in Appendix D. A summarized load history is shown in Figure 9.1 for Girder II. Results of the tests are given in this chapter for Girder II. The nominal load levels (i.e., the terms *preload, truck load level* and *overload condition*), the nominal load history, and the general load testing procedure for both girders was given in Section 8.1.

9.1.1 Nominal Load Levels

Design of the test girders is based on a standard HS25 design truck used in the State of Minnesota. The *truck load level*, *overload condition* and *preload* levels were defined in Section 8.1. Table 9.1 lists the test level and corresponding design condition used for testing the girders. Also, tabulated is the load per actuator required to induce the design condition stress at midspan of the member. The cumulative load per actuator for the design truck load and the overload condition includes the preload.

Table 9.1 Nominal Load Levels

Test Level	Design Condition	Midspan Moment (in-k [kN-m])	Load per Actuator (k [kN])	Cumulative Load per Actuator (k [kN])
Preload	Guard-rail and wearing course	5840 [660]	9.25 [41]	9.25 [41]
Design Truck Load	HS25 AASHTO Design Truck	11,360 [1280]	18.0 [80]	27.25 [120]
Overload Condition	125% HS25 Truck	14,200 [1600]	22.5 [100]	31.75 [140]

9.1.2 Nominal Load History

A nominal load history was defined to incorporate 70 years of traffic on an uncracked member. Testing of Girder II was nominally defined to be the same as testing of Girder I. Therefore, 1,000,000 truck loading events were defined to occur in 70 years. Similarly, 80,000 overload events were determined to occur in the 70-year life of the bridge. It was also decided to test the cracked girders for half of the truck load cycles.

The numbers of cyclic events, listed in Table 9.2, were chosen to represent the minimum number of cycles to be induced into the test girders. Also, tabulated is the cyclic load range per actuator required to induce design stresses at midspan into the test girder.

Table 9.2 Nominal Load History

Order of Testing	Minimum Number of Cycles	Load Range per Actuator (k [kN])
70 years at HS25	1,000,000	9.25 - 27.25 [41 - 120]
70 years at 125% HS25	80,000	9.25 - 31.75 [41 - 140]
Post-cracked at HS25	500,000	9.25 - 27.25 [41 - 120]
Post-cracked at 125% HS25	40,000	9.25 - 31.75 [41 - 140]

9.1.3 Load Test Procedure

Figure 9.1 summarizes the type and order of load testing performed for Girder II. Static testing was performed prior to any cyclic testing, intermittently during cyclic testing, and at the completion of cyclic testing to document any stiffness changes that might indicate damage incurred during testing. The first static load test to the full HS25 truck load level on Girder II was performed at an age of 690 days. Cyclic testing began shortly thereafter. Flexural cracking tests were performed statically followed by static crack reopening tests. Additional cyclic and intermediate static tests were performed prior to the ultimate flexural test. The last static test was performed at an age of 840 days, prior to the ultimate failure test at 850 days. A detailed loading history of Girder II is documented in Appendix D.

9.2 Periodic Static and Cyclic Load Test Results

Girder II was tested according to the summarized schedule in Table 9.3. The test name corresponds to the total testing history presented in Appendix D. Results from the intermittent static testing are documented and indicate that no damage was induced into the test girder due to cyclic loading equivalent to nearly 150 years of actual service load levels.

Table 9.3 Load Cycles on Girder II

TEST NAME	Number of Load Cycles at Given Load Levels			Cumulative Cycles
	Low Level (6 to 10 kips)	Preload + 100% HS25 (9 to 27 kips)	Preload + 125% HS25 (9 to 32 kips)	
DYNAMP	10,000			10,000
70YR100		1,000,000		1,010,000
70YR125			100,000	1,110,000
POSTCR20		1,000,000		2,110,000
POSTCR21			1,100,000	3,210,000
TOTALS:	10,000	2,000,000	1,200,000	**3,210,000**
Nominal:	-	*1,000,000 + 500,000*	*80,000 + 40,000*	*1,620,000*

9.2.1 Composite Girder Stiffness (Load-Deflection Response)

The composite test girder was subjected to static testing resulting in a measured load-deflection response. Selected tests of standard truck loading and overload levels at significant load history steps, as well as the girder stiffness, are summarized in Table 9.4. The static test name corresponds to the total testing history presented in Appendix D and is summarized in Figure 9.1.

Table 9.4 Static Test Summary of Girder II

	Test Name †	Static Load Level	Stiffness, k/in [kN/m]	r^2
Initial - first static test	Truck 21 ‡	125% HS25	13.4 [2350]	0.9998
Pre-crack, 10^6 load cycles	Truck 24	125% HS25	13.7 [2400]	0.9994
Post-crack,10^6 load cycles	Truck 26	125% HS25	13.3 [2320]	0.9998
Post-crack, 2x 10^6 cycles	Truck 29	125% HS25	13.5 [2360]	0.9997
Post-crack, 3x 10^6 cycles	Truck 31	125% HS25	13.7 [2400]	0.9999
Measured Average Stiffness	*HS25 Truck*		*13.5 k/in*	-

† Corresponds to load history documented in Appendix D.

‡ Static testing prior to test Truck 11 (last test before crack testing) may have been recorded without proper grounding.

Measured Stiffness

The stiffness is a measure of load per unit deflection. To determine the stiffness of the girder during each static load test, the average applied load (of the two actuators) was plotted versus

centerline deflection, as seen in Figure 9.2. Also shown is the predicted stiffness. Nominal truck load and overload levels are noted.

For completeness, a few points of clarification regarding Figure 9.2 are needed. First, each test showed some initial equipment seating during full contact with the girder and preload application resulting in each curve starting at a slightly different deflection for the preload (±0.10 in.). Therefore, the data plotted is the actual data including a shift along the x-axis such that the initial starting points overlay one another. The actuator load was not adjusted. In this way, the data is preserved while allowing for visual ease in comparing the stiffness. Second, while only the results of five static tests are shown at various time-steps throughout the fatigue testing program, additional static testing performance was consistent with those represented here. And third, the average actuator load is plotted because the two actuator loads never differed by more than 0.25 kips (1.1 kN). The larger differences were seen at the high end of loading when the difference was 1.6% of the total load.

Table 9.4 lists the test name for each of the data sets shown in Figure 9.2, the maximum static load applied during that test, and the measured stiffness. A linear regression was performed on each data set (load versus deflection for each test name). A detailed discussion on analysis was provided in Section 8.2. As Table 9.4 clearly shows, the stiffness of the girder was unaffected by continued cyclic loading and static crack testing. The tabulated measured stiffness was the average of the five tests summarized. In this way, each test was weighted equally; otherwise data sets with more data points would have been weighted heavier.

Predicted Stiffness

Stiffness can be predicted using the method previously presented in Section 8.2.1. A direct relationship for stiffness, K, was established as (P/Δ) (the applied load to deflection ratio) and given in Eqn. (8.2). Predictions for Girder II incorporated the following constants:

L = 1578 in.(40 m)

a = 632 in. (16 m)

x = 789 in. (20 m), to midspan.

Predicted stiffnesses are tabulated in Table 9.5 along with the average measured stiffness. Recalling that the design composite section included a total 9 in. (230 mm) thick deck (structural deck plus wearing course), a nominal design stiffness for the composite member was computed using the gross moment of inertia transformed to the girder modulus (315,600 in^4) and the

nominal ACI 318 (1995) concrete modulus (6530 ksi). 'Predicted - Girder II' stiffness was based on the 28-day measured concrete modulus (4800 ksi) and the transformed moment of inertia of the composite section including reinforcement (396,200 in^4).

Table 9.5 Predicted Stiffness, Deflection, and *L/d* Ratio for Girder II

	Stiffness, k/in [kN/m]	Deflection at HS25, in. [mm]	Span-to-defl, *L/d*, ratio
Measured Average	*13.5 [2360]*	*1.27 [32]*	*1250*
Nominal Design	16.7 [2920]	1.08 [27]	1465
Predicted - Girder II	15.5 [2710]	1.16 [29]	1360
Predicted - overestimate E_c by 10%	16.4 [2870]	1.10 [28]	1430
Predicted - underestimate E_c by 10%	14.7 [2570]	1.23 [31]	1290

The predicted stiffness shown in Figure 9.2 was based on the measured modulus and transformed composite section properties (Predicted - Girder II). The start point at the applied preload has been shifted for easier visual comparison in the same fashion as stated previously for the raw data.

Both the nominal design case and the predicted case using measured properties indicated stiffer sections were expected than measured. A 19% stiffer section was expected from nominal estimates while measured properties predicted a 13% stiffer section. Using the stiffness relationship in Eqn. (8.2), the discrepancy and the effect of changing the stiffness terms, $E_c I_{tr}$, was analyzed. The length parameters were not varied between measured and predicted.

If the concrete modulus were overpredicted by 10% (e.g., E_c = 5290 ksi) the composite transformed moment of inertia would decrease (e.g., I_{tr} = 379,500 in^4) resulting in a higher stiffness of 16.4 k/in (2870 kN/m). Conversely, underpredicting the modulus by 10% (e.g., E_c = 4330 ksi, I_{tr} = 416,000 in^4) resulted in a predicted stiffness of 14.7 k/in (2570 kN/m). This would indicate that a lower modulus might correctly predict the girder stiffness. However, Girder II had a measured concrete modulus of 4800 ksi (33.1 GPa) at 480 days, approximately midway through the static and cyclic load testing period compared, which was equal to E_c at 28-days. Additionally, measured camber changes due to deck casting, as noted in Section 7.6.2, were within 2% of predicted using measured material properties, indicating that the measured concrete modulus was accurate.

Also listed in Table 9.5 is the expected deflection due to an HS25 truck (at P =18 kips) resulting from the corresponding stiffness, K. The span-to-deflection (L/d) ratio is often used as a measure of stiffness, and although prestressed concrete has no code limitation for this value, the limit of 800 is used as a typical rule-of-thumb guideline from steel bridge girder construction (AASHTO, 1996). As evident from the table, the span-to-deflection ratio for measured and predicted stiffness was well within this rule-of-thumb guideline. The predicted deflection and L/d ratios were higher than the measured values for the same reasons the stiffness was lower, as stated previously.

9.2.2 Strand Strain and Stress Ranges

A concern with prestressed concrete bridge girders is that of strand fracture resulting from fatigue. Strand fracture would significantly reduce the load carrying capacity of the member and could potentially cause failure. Prestressing strands were instrumented to give an indication of the strain level in the strands corresponding to truck loads and overloads. Of the 18 gages installed on the bottom three rows of strands in the constant moment region, a total of twelve gages remained in operation throughout the static tests and provided useful data for determining the induced stress changes during loading conditions. One gage was located in strand row 3 (six inches up from the girder bottom fiber), two gage was located in strand row 2 (four inches up) and the remaining eight gages were located in strand row 1 (two inches up). The center of gravity of the midspan strand pattern was at 5.39 in. (137 mm) above the bottom fiber.

Measured Strand Strains

The change in strain induced in the bottom row of strands during truck loading and overload conditions (excluding any preload strains) is tabulated in Table 9.6 for the time steps introduced in Section 9.2.1. The bottom row of strands was selected for presentation because they undergo the highest change in stress under load, and there was redundancy in that more than one gage supplied data at this level. Static testing did not always include a 'hold' at load levels equal to the exact preload plus truck load or overload. Therefore a strain-to-load conversion was determined from a linear regression of each data set (load versus strain data collected from each gage of every test name) without forcing a zero intercept. Regression analyses resulted in r^2 values in the range of 0.963 to 0.999. The conversion, or slope of the regressed strain-load data relationship, is listed showing an overall average of 7.55 ±0.55 με /kip.

Table 9.6 Measured Strand Strain and Stress Ranges - Girder II

	Strain-to-Load conversion (με /k)	HS25 Truck Loading		Overload Truck	
		Δ Strain (με) †	Δ Strand Stress (ksi)	Δ Strain (με)	Δ Strand Stress (ksi)
Initial Static Test	7.59	137 ‡	3.98	171 ‡	4.97
Pre-crack, 10^6 load cycles	6.78	122	3.55	152	4.43
Post-crack, 10^6 cycles	7.70	139	4.04	173	5.04
Post-crack, 2x 10^6 cycles	7.47	134	3.91	168	4.89
Post-crack, 3x 10^6 cycles	7.90	142	4.14	178	5.17
Average of Tests	*7.49 ±0.43 με /k*	*135 ±7.7 με*	*3.92 ±0.22 ksi*	*169 ±9.7 με*	*4.90 ±0.28 ksi*

† All strain and stress data given for the bottom row of strands, 2 in. (50 mm) from bottom of the girder.
‡ Sign convention: tension is positive.

The strain-to-load conversion factor was used to determine the expected strain change from the measured data at truck load and overload levels by multiplying the factor by 18 and 22.5 kips (80 and 100 kN), respectively. Gages from the two remaining rows indicated strain changes were less than the bottom row of strands, due to their reduced eccentricity.

Figure 9.3 illustrates strain data collected for Girder II by the bottom row of strands. For each test shown, the average strain reading of the eight working gages is plotted relative to the average actuator load. The dashed line plotted on Figure 9.3 is the result of the strain-to-load regression analysis for the 'Pre-crack Test, 1.0 Million Cycles,' and is shown to correlate well with the remaining data.

A direct conversion to stress change due to loading was made by multiplying strain change with the measured apparent strand modulus of elasticity (as measured from strain gages applied directly to strand samples), 29,100 ksi (200,700 MPa). Table 9.6 shows that continued load testing and fatigue cycles produced no evident damage to the strands, as there was not a noticeable increase in stress changes over time. Further discussion will refer to the measured stress change in the bottom row of strands of Girder II under truck loading as 3.92 ksi (27.0 MPa) and 4.90 ksi (33.8 MPa) for overload conditions.

Predicted Strand Strain

The stress through the depth of the girder and at the level of strand rows was easily predicted by linear elastic theory, such that the stress change, $\Delta\sigma$, was given in Eqn. (8.3). Table 9.7 lists

the predicted stress changes for HS25 truck loading and overload conditions at the bottom row of strands. Load levels of 18 and 22.5 kips (80 and 100 kN) were used for the repetitive loading conditions, giving predicted stress ranges from preload to peak conditions. A nominal value for I (e.g., I_{gross}) were used to predict the nominal design case. $I_{transformed}$ of the composite section was used to give a more accurate estimate of predicted stress changes, and is listed as 'Predicted - Girder II'. The measured average strain and stress ranges from data listed in Table 9.6 are included for comparison.

Table 9.7 Predicted Strand Strain and Stress Ranges - Girder II

	HS25 Truck Loading		Overload Truck	
	Δ Strain (με) †	Δ Strand Stress (ksi) †	Δ Strain (με)	Δ Strand Stress (ksi)
Measured Average Range	*135* ‡	*3.92*	*169*	*4.92*
Nominal Design Case	-	4.53	-	5.67
Predicted - Girder II	179	5.21	223	6.49
ACI 215 (1992)				
Uncracked Stress Range Limit	-	*32 ksi*	-	*32 ksi*
Cracked Stress Range Limit	-	*11 ksi*	-	*11 ksi*
Paulson et al. Stress Range Limit	-	*20 ksi*	-	*20 ksi*

† All strain and stress data are given for the bottom row of strands, 2 in. (50 mm) from bottom of the girder.
‡ Sign convention: tension is positive. Measured strains were expected to be different from predicted strains due to gage orientation on strands for measured case.

Predicted and measured stress ranges were low when compared with fatigue limits. ACI Committee 215 (1992) recommended a maximum stress range of 0.12 f_{pu} for uncracked prestressed sections and $0.04f_{pu}$ for cracked sections. For the test girders with an ultimate measured strand strength, f_{pu}, of 269 ksi (1850 MPa), these stress range limits would be 32 ksi (220 MPa) and 11 ksi (76 MPa) for the uncracked and cracked sections, respectively. These limits are substantially higher than the stress ranges induced in the test girder during overload conditions, which was within the 'uncracked state'. Paulson et al. (1983) recommended a reasonable fatigue stress limit of 20 ksi for strands in prestressed members subjected to repetitive loading. Again, Paulson's limit is much higher than the strand stress ranges recorded by the girders.

In all cases tabulated, the measured and predicted strand stress levels were much lower than damaging levels. The large self-weight of the composite member relative to superimposed loads, in closely spaced long span girders, only allows for low live load induced stresses. For this

girder, design truck loads and overload conditions were not expected to induce damage. Girders located at a wider spacing would be expected to have increased stress ranges because the widely spaced girders would carry a greater proportion of live load.

9.2.3 Concrete Strains and Stresses

Concrete strains were measured with vibrating wire gages through the depth of the girder, resulting in strain data for both tensile and compressive stress levels. Strains were recorded from seven vibrating wire gages at various heights in the constant moment region for the preload, HS25 truck level and overload conditions. Gage locations from bottom were noted as: two gages at 2.25 in. (57 mm), one at 2.5 in. (64 mm), one at 5.25 in. (133 mm), two at 5.5 in. (140 mm), and one at 42.25 in. (1070 mm).

A load versus strain plot is shown in Figure 9.4 for the six bottom flange gages for the static test 'Pre-crack, 1.0 Million Cycles.' The typical service range, as induced by the actuators, is noted for reference. Gages located higher in the bottom flange (5.25 to 5.50 in. up) experienced lower strain ranges during load testing than gages located lower in the section (2.25 to 2.5 in.), as expected. Both gages located at *0.45L* along the length experienced relative lower strain ranges than strands at midspan or *0.55L*, indicating that the girder cross section at *0.45L* was exposed to lower stresses during load testing than either midspan or *0.55L*.

To determine the strain distribution due to the applied loading through the height of the cross section, a strain versus height comparison was made for the two load combinations of interest: 'Preload + HS25', and 'Preload + Overload'. Figure 9.5 shows the strain distribution at varying heights through the cross section for the two load combinations. At each gage height, the recorded strain change of all static tests performed for the two load combinations are marked. Gages placed at 2.25 and 2.5 in. (57 and 64 mm) from the bottom show higher tensile strain changes than gages higher in the cross section, as expected.

Of interest are concrete compressive and tensile stresses at the extreme fibers, discussed in detail in the following sections. A linear regression of the data (strain versus depth of the section, as shown in Figure 9.5) was performed for each test at the truck load level and overload condition to obtain the strains at the extreme fiber. All values of r^2 were greater than 0.993. The hollow symbol in Figure 9.5 indicates the neutral axis location, where strain in the cross section is zero. The extreme fiber strains and corresponding stresses under service and overload

conditions determined from linear regression of strain data are discussed in the following sections.

9.2.3.1 Concrete Tensile Strains

Measured Strains

The critical tensile strains in concrete under four point loading occurred at the bottom fiber of the girder. However, the concrete embedment gages could only be placed within two to five inches of the bottom fiber. Therefore, using the linear regression equations from measured strain versus gage height data for each summary test (as discussed previously), the strain change at the bottom fiber was determined from recorded data for the two load combinations: 'Preload + HS25' and 'Preload + Overload'. Strains from these combinations were used to determine stresses at the extreme fibers under service and overload conditions.

The bottom fiber strain ranges due to preload, HS25 truck and overload conditions are listed in Table 9.8 for the summary load tests with the exception of 'Post-crack, 2x 10^6 cycles' case during which data from the vibrating wire gages were not recorded. Also, tabulated are the corresponding stress ranges, and the overall measured averages for the bottom fiber of each case. A direct conversion to stress change was made by multiplying the measured 28-day concrete modulus of elasticity, 4800 ksi (33.1 MPa) by the measured strain change. The data was regressed and used to determine the *equivalent* bottom fiber strain or stress change that the girder would see. The average computed bottom fiber strains and stresses reported in Table 9.8 are referred to herein as the *measured average bottom fiber strain/stress*.

Measured concrete strains showed no degradation over time due to continued cyclic load testing. Strain changes recorded prior to cracking the girder were similar to those recorded in the post-crack condition even though the post-crack loads exceeded crack reopening loads (Section 9.3.1.5).

Table 9.8 Measured Concrete Tensile Strain and Stress Ranges - Girder II

	Preload Level		HS25 Truck Load		Overload Truck	
	Δ Strain (με) †	Δ Concrete Stress (ksi)	Δ Strain (με)	Δ Concrete Stress (ksi)	Δ Strain (με)	Δ Concrete Stress (ksi)
Initial static test	92.5 ‡	0.44	180	0.86	225	1.08
Pre-crack, 10^6 load cycles	91.8	0.44	179	0.86	223	1.07
Post-crack, 10^6 cycles	95.4	0.46	186	0.89	233	1.12
Post-crack, 2x 10^6 cycles	94.3	0.45	184	0.88	230	1.10
Post-crack, 3x 10^6 cycles	93.5	0.45	182	0.87	229	1.10
Measured average	*93.5 ±1.4 με*	*0.45 ±0.01 ksi*	*182 ±2.8 με*	*0.87 ±0.01 ksi*	*228 ±3.9 με*	*1.09 ±0.02 ksi*

† All strain and stress data given for the *bottom fiber* of the concrete girder.
‡ Sign convention: tension is positive.

Predicted Concrete Tensile Stresses and Strains

Concrete stresses in the extreme bottom fiber were predicted in a similar manner to strand stresses using Eqn. (8.3). Concrete stress predictions for preload, HS25 truck loading and overload conditions are listed in Table 9.9 along with the measured average bottom fiber strain and stress ranges. A nominal values for I (e.g., I_{gross}) was used to predict the nominal design case. $I_{transformed}$ of the composite section was used to give a more accurate estimation of predicted bottom fiber stresses, and are listed under 'Predicted - Girder II.' Dividing the predicted stress changes by nominal or measured concrete modulus, E_c, respectively, results in the nominal and predicted concrete strain changes due to the static load levels.

Table 9.9 Predicted Bottom Fiber Concrete Strain and Stress Ranges - Girder II

	Preload Level		HS25 Truck Load		Overload Level	
	Δ Strain (με) †	Δ Concrete Stress (ksi)	Δ Strain (με)	Δ Concrete Stress (ksi)	Δ Strain (με)	Δ Concrete Stress (ksi)
Measured Average	*93.5‡*	*0.45*	*182*	*0.87*	*228*	*1.09*
Nominal Design Case	-	0.57	-	1.11	-	1.39
Predicted - Girder II	-	0.47	-	0.92	-	1.14
Predicted - overestimate E_c 10%	-	0.43	-	0.85	-	1.06
Predicted - underestimate E_c 10%	-	0.51	-	0.99	-	1.23

† All concrete tensile strain and stress ranges are given for the *bottom fiber* of the girder.
‡ Sign convention: tension is positive.

The nominal design case had a 35% increase in concrete stress because of the overestimated nominal concrete modulus, based on NSC relationships from ACI 318 (1995). Predicted stresses for the three load cases were computed through the section depth using the manufacturer measured modulus and transformed composite properties, and are plotted on Figure 9.5 to show the closeness of the data to the prediction. The levels of tension measured in the bottom fiber due to load testing were close to those predicted using the measured concrete modulus and transformed composite section properties.

Although stress ranges during loading are of interest, it is the overall level of tension in the bottom fiber of the girder during service loads that is limited by AASHTO (1996). From the measured prestress loss information presented in Section 7.4 and the service stress ranges, the overall tension level in the girder under service loads can be calculated. Using a prestress force less the measured lower bound prestress loss value of 25.8% (the average measured lower bound loss during the load testing period) and the girder self weight and deck weight in the flexural stress equation (Eqn. 2.41), the bottom fiber concrete stress was calculated to be at a state –2.01 ksi compression, prior to load application. The measured concrete tensile stress at the bottom fiber due to the load combination of preload and HS25 truck load was +1.24 ksi (8.55 MPa). Superimposing the two stresses, the state of stress at the bottom fiber of Girder I was –0.77 ksi compression. Similarly, the preload plus overload condition would place the bottom fiber in a state of compression at -0.57 ksi. The stress levels were used in Section 7.9 to compare with AASHTO stress limits under service load conditions.

9.2.3.2 Comparison of Strand and Concrete Data for Tension

Concrete strain ranges determined from vibrating wire gages due to superimposed loads can also be used for verification of the prestressing strand strain ranges induced during load testing. Using the regressed strain-to-height data from the previous section, the strain range due to HS25 truck loading was determined at 2 in. (50 mm) from the bottom, at the level of the bottom row of strands. The concrete gages (vibrating wire gages) showed strain ranges at the bottom row level were on the order of 166 to 173 με, with an average of 170 με for HS25 truck loading. Perfect bond between the strands and the concrete is assumed, such that concrete strain equals steel strain. To determine the strand stress range, the strain ranges were multiplied by the strand modulus, E_s, of 28,800 ksi (198.6 GPa), which resulted in strand stress ranges of 4.79 to 4.98 ksi

(33.0 to 34.3 MPa), with an average of 4.88 ksi (33.6 MPa). Similarly, for overload conditions, an averaged measured strain range of 213 με was recorded, resulting in an average stress range 6.13 ksi (42.3 MPa).

The foil gages installed directly on the prestressing strands, however, indicated lower stress ranges with averages being 3.92 and 4.92 ksi (27.0 and 33.9 MPa) for the HS25 truck and overload conditions, respectively (see Table 9.6). In other words, the concrete gages showed average stress increases of 19.6% and 19.7% over the strand gages for the two load conditions. In either case (concrete or strand gages), consequential damage to the prestressing strands would not be expected at these low stress ranges.

The possible reasons for the differences in measured stress ranges between the two gage types were considered. All gages used in this comparison were located at midspan. The six vibrating wire gages were embedded at various depths through the cross section to give a full strain distribution. The linearly regressed concrete gage strain-to-height data was used to determine strain at any depth in the girder. The eight foil strand gages were applied directly to the strands in the bottom strand row [2 in. (50 mm) from girder bottom] to measure strand strain. Recalling that the strand gage was meant to represent an average strain in all the wires of the strand, it in fact is installed on only one wire. Differences were seen between the measured strand modulus of elasticity when determined by the strand strain gages and the strand modulus determined by the manufacturer using an extensometer. Additionally, orientation variation in the strand foil gages was noted as the gages were aligned with the axis of the strand wire to which they were applied, not with the axial strand alignment. The vibrating wire gages may have also been oriented off from the axial alignment of the girder, they provided a generalized strain distribution, rather than a local strain as the strand gages did. It is believed that the strand foil gages would therefore be a better representor of strain and stress ranges due to superimposed loads because localized effects can influence the stress range applied and strand gages tend to account for these effects.

9.2.3.3 Concrete Compressive Data

Measured Strains

Under the superimposed loading conditions considered, the composite test girder undergoes compression above the level of the composite neutral axis. Compressive strains in the deck and

top flange of the girder at the midspan location were recorded by two gage types, vibrating wire gages and PML-type gages, for the two load combinations: 'Preload + HS25,' and 'Preload + Overload.' Static load tests, previously given in Table 9.4, are used here for comparison.

Each test recorded midspan strain changes from seven PML gages at various heights in the cross section. One PML gage was located at midspan (and vertically along the centriodal axis) at each of the following heights: 25, 35.5, 38, 41, 43.5, 48.5 and 51.5 in. (635, 900, 965, 1040, 1105, 1230, and 1310 mm). A load versus strain plot is shown in Figure 9.6 for the seven top flange and deck gages for the static test 'Pre-crack, 1.0 Million cycles.' Gages located above the composite neutral axis location showed compressive strain changes, as expected, while the remaining gage below the neutral axis indicated a tensile strain change. The strain distribution through the composite member depth is shown in Figure 9.7 for the PML recorded strain changes due to the load combination of 'Preload + HS25.' Consistency within the data indicates no member degradation with continued load cycles.

Compressive strain changes through the composite girder depth recorded by the vibrating wire gages were determined from the same linear regression (strain-to-height relationship at the two load combinations) analysis used for tensile strain changes. Superimposed on Figure 9.7 is the regressed vibrating wire gage data for the 'Preload + HS25' load combination. Similar results were found for load-to-strain behavior recorded by PML Gages at the load combination level of 'Preload + Overload'. Figure 9.8 shows the strain change distribution through the depth of the composite section for the higher load case. As expected from the lighter load case, superimposed vibrating wire gage data showed reasonably close strain changes to that of the PML gages.

The strain changes measured by the top deck PML gage (51.5 in., [1310 mm]) lag behind those measured 3 in. (76 mm) lower, opposite of predicted, and can be attributed to a shrinkage crack at midspan in the deck. From the beginning of testing the gage, as seen in Figure 9.6, does not record strain like the remaining gages. This indicates that the shrinkage crack in the top of the deck, and located within 3 in. (76 mm) of the gage, is closing. The crack, although no depth extent is known, could cause the PML gage next to it to read lower, because the crack would have to close before picking up the load (strain). As the crack closes completely, the load-strain slope becomes the most flat of all gages, as would be expected for the highest gage in the cross section. It appears that the deck shrinkage crack closes at an average actuator load of 12.5 kips

(56 kN), or at a level just above the preload amount and equal to approximately 20% of the HS25 truck load level.

Using linear regression, strain ranges from vibrating wire gage data due to preload, HS25 truck and overload conditions are listed in Table 9.10 for two compressive locations of interest: top fiber of the prestressed girder flange at the girder-to-deck interface [45 in. (1140 mm) above bottom] and top fiber of the overall composite member [55 in. (1400 mm) above bottom]. Also, tabulated in Table 9.10 are the corresponding stress ranges, obtained by multiplying the measured concrete vibrating wire gage strain changes by the measured 28-day concrete modulus of elasticity. A measured girder modulus of 4800 ksi (33.1 GPa) was used to convert to stress for the top fiber of the prestressed (noncomposite) member and a measured deck modulus of 3990 ksi (28.6 GPa) was used for stress conversion at the top of the composite deck. The average computed fiber strains and stresses reported in Table 9.10 are referred to herein as the *measured average strain and stresses.*

Table 9.10 Measured Concrete Compressive Strain and Stress Ranges - Girder II

	Preload Level		HS25 Truck Load		Overload Truck	
	Δ Strain (με) †	Δ Concrete Stress (ksi)	Δ Strain (με) †	Δ Concrete Stress (ksi)	Δ Strain (με) †	Δ Concrete Stress (ksi)
Top fiber of prestressed (non-composite) member (45 in. from bottom)						
Initial static test	-49.4 ‡	-0.24	-96.1	-0.46	-111	-0.53
Pre-crack, with 10^6 load cycles	-51.2	-0.25	-99.6	-0.48	-123	-0.59
Post-crack with 10^6 load cycles	-51.4	-0.25	-100.	-0.48	-113	-0.54
Post-crack with 2x 10^6 cycles	-51.0	-0.24	-99.3	-0.48	-114	-0.54
Post-crack with 3x 10^6 cycles	-47.1	-0.23	-91.6	-0.44	-113	-0.54
Measured average (top of prestressed member)	*-50.0 ±1.8 με*	*-0.24 ±0.01 ksi*	*-97.3 ±3.6 με*	*-0.47 ±0.02 ksi*	*-115 ±4.7 με*	*-0.55 ±0.02 ksi*
Top fiber of deck (55 in. from bottom)						
Initial static test	-80.9	-0.32	-157	-0.63	-186	-0.74
Pre-crack, with 10^6 load cycles	-83.0	-0.33	-162	-0.64	-200	-0.80
Post-crack with 10^6 load cycles	-84.0	-0.34	-163	-0.65	-190	-0.76
Post-crack with 2x 10^6 cycles	-83.3	-0.33	-162	-0.65	-190	-0.76
Post-crack with 3x 10^6 cycles	-78.3	-0.31	-152	-0.61	-190	-0.75
Measured average (top of composite member)	*-81.9 ±2.3 με*	*-0.33 ±0.01 ksi*	*-150 ±4.5 με*	*-0.64 ±0.02 ksi*	*-191 ±5.2 με*	*-0.76 ±0.02 ksi*

† All strain data from vibrating wire gages.
‡ Sign convention: tension is positive.

Predicted Strains

The concrete strain and stress predictions for preload, HS25 truck loading and overload conditions are listed in Table 9.11 along with the measured average fiber strains and stresses from Table 9.10 for each load case. Predicted stress changes were determined from elastic theory, Eqn. (9.3). A nominal values for I (e.g., I_{gross}) was used to predict the nominal design case. A nominal girder modulus of 6525 ksi (45.0 MPa) was used for the top fiber of the prestressed member, and a nominal deck modulus of 3830 ksi (26.5 MPa) was used for the top fiber of the composite member. Measured values of E_c at 28-days [4800 ksi (33.1 MPa) for the girder and 3990 ksi (28.6 MPa) for the deck] and $I_{transformed}$ of the noncomposite section were

used to provide a more accurate estimation of predicted fiber strain changes due to the superimposed loads for comparison, and are listed under 'Predicted - Girder II'.

Table 9.11 Predicted Concrete Compressive Strain and Stress Ranges - Girder II

	Preload Level		HS25 Truck Load		Overload Level	
	Δ Strain (με) †	Δ Concrete Stress (ksi)	Δ Strain (με)	Δ Concrete Stress (ksi)	Δ Strain (με)	Δ Concrete Stress (ksi)
Top fiber of prestressed (non-composite) member						
Measured Average	*-50.0 με*	*-0.24 ksi*	*-96.1 με*	*-0.46 ksi*	*-111 με*	*-0.53 ksi*
Nominal Design Case	-	-0.26	-	-0.51	-	-0.63
Predicted - Girder II	-39.5	-0.19	-76.8	-0.37	-96.0	-0.46
Top fiber of composite member						
Measured Average	*-81.9 με*	*-0.33 ksi*	*-159 με*	*-0.64 ksi*	*-191 με*	*-0.76 ksi*
Nominal Design Case	-	-0.26	-1	-0.51	-	-0.64
Predicted - Girder II	-70.7	-0.28	-138	-0.55	-172	-0.69

† Sign convention: tension is positive.

Nominal concrete compressive stress changes in the prestressed girder portion of the composite member were much closer than measured (up to 15% higher), due to the overestimation of the nominal high strength concrete modulus determined from a normal strength relationship. The predicted case using measured properties shows that expected stress changes are 14% to 21% lower than measured at the top of the girder flange, and 10% to 14% lower than measured at the top of the deck.

Data was also recorded for a series of PML Gages located at 30% of the length from each end support (outside of the constant moment region). Gage placement was through the vertical axis of the cross-section at various heights. Figure 9.9 shows the predicted linear strain distribution through the section depth at *0.3L* due to the 'Preload + HS25' load combination. Data was recorded on End IIC at three gage heights [38, 44 in. and 51.5 (965, 1115, and 1310 mm)] and on End IID at two gage heights [38, and 44 in. (980, and 1125 mm)] for the five static summary tests. The predicted strain distribution determined from the stress distribution of the applied loading is shown using elastic theory, Eqn. (8.3), with actual actuator point load placements, *a*, of 630 in. (16.0 m) and transformed composite section properties. The data appears reasonably close to the predicted strains for both ends. Similar trends of increasing

compression with increasing distance from the neutral axis were seen at other load steps, including the 'Preload + Overload' condition.

9.2.3.4 Neutral Axis Location

The vibrating wire gages through the section depth were also used to verify the neutral axis location of the composite section. As shown in Figure 9.5, the predicted neutral axis location was 31.9 in. (810 mm) from the bottom of the girder. The prediction was based on Eqn. (8.3) using the measured moduli to determine $I_{transformed}$ of the composite section. A linear regression of all the vibrating wire gage data (strain versus gage height) indicated the neutral axis was located 2.0 in. (50 mm) lower at 29.9 in. (760 mm).

The strain distribution through the centerline axis at midspan of the test girder was also shown in Figure 9.7 for the embedded PML concrete gages. Although only one gage was placed below the predicted neutral axis location, a linear regression analysis of it and the three gages above it indicated the neutral axis was located at 31.5 in. (800 mm) for both load combinations (r^2 values were never less than 0.987). The strain data recorded by the PML gages and used to determine the neutral axis more closely matches the predicted neutral axis location than the vibrating wire gage data. The PML gage data was recorded at a lesser distance from the neutral axis than the vibrating wire gage data allowing for localized effects to be accounted for, and most likely resulting in a more accurate estimation of the neutral axis location.

A decrease in neutral axis location (measured from the bottom fiber) relative to the predicted (assumed) position would cause the girder to undergo lower tensile strains in the bottom fiber during loading than would be predicted, as well as higher compressive strains than would be predicted in the top portion of the test girder. The vibrating wire gage tensile data were very close to the predicted values, while one set of compressive data (from the PML gages) was lower and one set higher (from the vibrating wire gages) than the predicted values. The differences in compressive strain data from the two gage types were discussed in Section 9.2.3.

9.2.4 Out-of-Plane Deflection

The composite test girder was not braced laterally along its length during load testing, as described in Section 5.1.3. A sidesway deflection system was devised to determine the lateral motion experienced by the test girder during load testing. The bottom flange showed consistent out-of-plane lateral motion on the order of 0.05 to 0.10 in. (1.3 to 2.5 mm) during load testing.

For comparison purposes, a maximum downward deflection of 1.54 in. (39 mm) was recorded during maximum overload conditions of a static load test.

There were two possible reasons for this sidesway motion. First, the loading ram could have been placed such that it was not perfectly symmetrically about the centerline vertical axis of the composite girder. Second, if the strands were not perfectly aligned within the forms during manufacturing, or if the formwork itself was not perfectly symmetrical, the girder may not have been manufactured absolutely symmetrically. In either case, the level of lateral movement recorded during loading was very small and in no way reflected degradation of the composite test girder or loading system.

9.3 Flexural Cracking Load Test Results

Flexural crack testing was performed to determine both the initial cracking load and the load required to reopen the cracks. As discussed in Section 8.3, cracking load results were also expected to verify the measured prestress losses. Crack testing required a superimposed dead load (sdl) to be hung from the girder with an additional load application from the hydraulic actuators. Details of the test setup and procedures were discussed in Section 5.2.2. Instrumentation specific to crack testing was discussed in Section 5.3.3. Acoustic emissions (AE) monitoring equipment was used to detect and approximately locate crack initiation while visual inspection was used to precisely identify each crack location. Table 9.12 lists the initial crack test as well as subsequent crack reopening tests along with the timeline, test name and comments pertinent to each test.

Table 9.12 Summary of Crack Testing for Girder II

	Time line	Test Name[1]	Other comments
Initial Crack	After 1.1 million cycles of fatigue	CRACK20 - Loop 1	Following static test TRUCK25, includes dead weight hanging load.
Reopen 1	Post-crack with 1.1 million cycles of fatigue	CRACK21 - Loop 1	Three full load/unload cycles at the static loading rate was performed once the hanging dead load was applied.
Reopen 2		CRACK21 - Loop 2	
Reopen 3		CRACK21 - Loop 3	

[1] Corresponds to testing name noted in Appendix III - Load History.

9.3.1 Cracking Load and Crack Locations

The initial flexural cracking test for Girder II occurred at an age of 725 days on August 3, 1995 (approximately 2 years from casting). The girder had been subjected to 1.1 million load

cycles and five intermittent static truck tests prior to crack testing (Figure 9.1). Immediately prior to crack testing, a static test was performed to a load level equivalent to the 'Preload + HS25' load combination. No damage was detected prior to the initial crack test in the form of loss of stiffness, crack initiation via AE, visual cracking or otherwise.

9.3.1.1 Measured Initial Crack and Reopening Loads

The total load applied during the initial flexural crack test was the hanging dead load plus the average actuator load of 33.4 kips (149 kN) at each actuator location. The two actuators never differed in load by more than 0.25 kips (1.1 kN). Visual crack data recorded during the initial crack test is tabulated in Table 9.13. The cracks are listed in order of location from End C. The order of crack formation is noted. The first six visual cracks (C-BF-12, 13, 14, 15, 17 and D-BF-17) appeared at locations of 58.3, 59.8, 60.9, 62.2, 63.8, and 68.0 ft. (17.8, 18.2, 18.6, 19.0, 19.4, and 20.7 m) from End C and at the load step '18 kips (80 kN) per actuator plus the hanging superimposed dead load' (18k+sdl). The crack name notation refers to the end on which the crack occurred (C or D), the location within the cross section where the crack first initiated (BF= bottom flange, W= web, TF= top flange), and the number of the crack from its respective end. All of these initial cracks appeared on only one side of the girder and were 8-10 inches long. The formation was such that approximately half of the crack was located on the vertical side face of the bottom flange, and the crack continued up to the top surface of the bottom flange.

Table 9.13 Initial Flexural Cracking Loads and Locations for Girder II

Crack Name	Distance from C	Cracking Load †	Cracking Moment (in-k) ‡	Formation Order
C-BF-1	45.0 ft. *	28k + sdl	24,565	20
C-BF-2	46.2	28k + sdl	25,230	22
C-BF-3	47.6	28k + sdl	26,005	24
C-BF-4	49.0	28k + sdl	26,765	25
C-BF-5	52.3	28k + sdl	27,460	27
C-BF-6	51.8	28k + sdl	28,330	29
C-BF-7	53.0	28k + sdl	28,982	31
Actuator Load Point at End C: 53.3 ft.				
C-BF-8	54.3	26k + sdl	28,010	14
C-BF-9^{+}	55.3	26k + sdl	28,225	15
C-BF-10	55.7	26k + sdl	28,315	16
C-BF-11	57.2	28k + sdl	29,920	32
C-BF-12 ††	58.3	18k + sdl	23,855	1
C-BF-13 ††	59.8	18k + sdl	24,160	2
Chain from superimposed dead load:59.88 ft. (78 in. offset of midspan)				
C-BF-14 ††	60.9	18k + sdl	24,190	3
C-BF-15 ††	62.2	18k + sdl	24,190	4
C-BF-16^{+}	63.0	30k + sdl	31,735	35
C-BF-17 ††	63.8	18k + sdl	24,195	5
C-BF-18	64.92	28k + sdl	30,515	33
C-BF-19 $^{+}$	65.7	24k + sdl	27,985	9
Midspan: 66.38 ft.				
D-BF-17 $^{+}$ ††	68.0	18k + sdl	24,200	6
D-BF-16	69.3	24k + sdl	27,990	10
D-BF-15	70.9	26k + sdl	29,250	19
D-BF-14^{+}	71.5	24k + sdl	27,995	11
Chain from superimposed dead load: 71.88 ft. (5.5 ft. offset of midspan)				
D-BF-13	72.3	26k + sdl	29,170	18
D-BF-12	73.7	26k + sdl	28,870	17
D-BF-11	74.9	24k + sdl	27,345	8
D-BF-10	76.1	24k + sdl	27,100	7
D-BF-9	77.5	26k + sdl	28,060	13
D-BF-8	79.1	26k + sdl	27,705	12
Actuator Load Point at End D: 79.6 ft.				
D-BF-7	80.2	28k + sdl	28,580	30
D-BF-6	81.6	28k + sdl	27,800	28
D-BF-5	83.1	28k + sdl	26,975	26
D-BF-4	84.4	30k + sdl	27,355	34
D-BF-3	85.8	28k + sdl	25,510	23
D-BF-2^{+}	86.9	28k + sdl	24,865	21
D-BF-1^{+}	88.3	32k + sdl	26,605	36

† Crack load corresponds to load step during visual inspection.
‡ Moment as computed at the location of each crack, corresponding with visual cracking load.
†† Designates the first six visual cracks.
* Metric conversions are: 1 ft. = 0.3048 m, 1 kip = 4.4482 kN, 1 in-k = 0.1130 kN-m.
$^{+}$ Designates cracks that occurred on one side only.

As crack testing continued, further cracking was induced, leading to a total of 36 cracks. Cracks typically ran from across the bottom face of the flange and up 4-6 in. (100-150 mm) on each side of the bottom flange (approximately to the center of gravity of strands at 5.39 in. [137 mm]). Only one crack, D-BF-10, extended further and penetrated the web by 3.5 in. (89 mm) on each side of the test girder. The crack location distances noted were overall distances from the girder end and include the overhang distance of 7.5 in. (191 mm) at the support. Also, tabulated is the computed total applied moment *at each crack location* at the time of crack formation. This total moment includes the effect of the hanging superimposed dead load as well as the *actual* load from each actuator. The order of crack formation is listed, where the numbering increases from the lowest cracking moment at each load step. Load steps were targeted at 2.0 kip (8.9 kN) intervals, resulting in a moment resolution of 1250 in-k (141 kN-m) at midspan per load step.

During the initial crack test, the AE system detected crack initiation at a load level of '14 kips per actuator plus the hanging superimposed dead load' (14k +sdl). Zoned source location was used due to the high dissipation of the concrete, which yielded source location accurate to within only two to three feet (0.6 to 0.9 m). Therefore, the AE system was most useful for informing the researchers when and approximately where to look for a crack. No cracks were visually noted prior to the detection of AE signals.

The load levels and moments for both AE and visual inspection during the initial crack test as well as subsequent crack reopening tests are listed in Table 9.14. The first visual crack was C-BF-12, occurring at the load step (18k + sdl), and a moment level of 23,855 in-k (2700 kN-m) at the crack location of 58.3 ft. (17.8 m) from End C. Because the dead load was hung at locations between the actuators, a constant applied moment region existed only between the dead load points. The moment due to applied loads outside of this region (where the first cracks occurred) varied linearly. The moments listed in Table 9.14 for AE and visual cracking have been computed using the actual load readings from each actuator plus the hanging superimposed dead load. First, the moment *at the location of crack* C-BF-12 is listed. And second, the *midspan* moment using the same given load level is listed.

For each flexural crack test (initial and reopening) listed in Table 9.14, the AE system detected crack reopening prior to the visual observation. The first six cracks to initially form were consistently the first cracks to reopen. The decrease in load from initial cracking to crack reopening was expected, as less load is required to reopen a preexisting crack because the load

no longer needs to overcome the tensile strength capacity of the concrete. The visual crack reopening loads were consistent as anticipated.

Table 9.14 Flexural Cracking Load and Reopening Loads for Girder II

Test Name	AE Crack Load †	AE Crack Moment (in-k) +		Visual Crack Load †	Visual Crack Moment (in-k) +	
		At crack location ‡	At midspan		At crack location ‡	At midspan
Initial Crack	14k + sdl	21,340	21,680	18k + sdl	23,850	24,200
Reopen 1	6k + sdl	16,290	16,640	10k + sdl	18,820	19,160
Reopen 2						
Reopen 3						

† Load designation is the load applied by the actuator (in kips) which was in addition to the superimposed dead load provided by the hanging concrete blocks.
‡ Moment as computed at the location of the first crack C-BF-12 and corresponding to the crack load.
+ Metric conversion: 1 in-k = 0.1130 kN-m.

During the crack reopening tests, no additional crack formations were seen and noticeable crack growth was limited. Fifty percent of existing cracks appeared to grow three to five inches (75 to 125 mm) during Reopen Test 1, due to the increased applied stress from the same moment applied to a reduced section modulus. Reopen Test 2 showed an increase of 1-3 inches on 18% of the cracks, while Reopen Test 3 showed no additional growth of pre-existing cracks.

9.3.1.2 Measured Load - Deflection Response

The load-deflection response for static testing up to the 'Preload + Overload' condition was presented in Section 9.2.1, and showed no stiffness degradation due to continued load cycles through 3.2 million cycles. Static testing performed before and after crack testing showed no stiffness degradation for this load range to 125% HS25 (below crack reopening loads). However, static testing above the crack reopening moment (up to 250% HS25) did show a change in the moment-deflection response of the composite girder.

Moment-deflection response is used for discussions of flexural crack testing rather than load-deflection response because crack testing required hanging a superimposed dead load in combination with a load application via the hydraulic actuators. Because the dead load was hung at locations between the actuators, the loads generate different moments due to different application points. It is clearer to superimpose the moments. The superimposed hanging dead load and actuator loads result in a constant moment region only between the dead load hanging

points (without regard to the girder self-weight). Further detail on actual (nearly symmetric) load application locations was given in Section 5.2.2.

The moment-deflection response of the initial flexural crack test for Girder II is given in Figure 9.10. The applied moment at midspan is plotted relative to the midspan deflection. Notation is included to indicate when the AE system first detected crack initiation and when the first visual crack appeared based on the midspan moment at the time of detection (see Table 9.14). A static test to 'Preload + HS25' was performed immediately prior to crack testing and results are shown in the figure for stiffness comparison. Closer inspection of the relationship between the data and the straight dashed line shows that the stiffness did not begin to degrade from its initial slope until about 21,500 in-k (2430 kN-m), just before the AE system recorded events.

Similarly, the moment-deflection responses of the crack reopening tests are superimposed on the initial crack test response and are illustrated in Figure 9.11. As expected, a decrease in stiffness was observed with the damaged section after crack reopening. The moment-deflection response for the crack reopening test diverges from linear at a lower moment than observed for the initial crack opening test, corresponding with the AE and visual reopening load level trends tabulated previously in Table 9.14, leading to a decrease in stiffness after crack reopening. Reopen Tests 1, 2, and 3 follow the same loading path indicating that once the girder is in a cracked state and reloaded to the same level, it maintains its relative stiffness. With closer inspection of the data, the moment-deflection curves of the three reopen tests began to deviate from a straight line at about 17,900 to 19,200 in-k (2020 to 2170 kN-m), or at a load level of about '8 to 10 kips plus the superimposed dead load' (8k to 10k + sdl). The moment-deflection response indicates that crack reopening occurred just prior to AE and well before visual crack reopening.

A convergence of the moment-deflection curves for the initial crack test and the reopening tests would be expected because once the initial crack has formed, the tensile capacity of the concrete has been overcome. Crack reopening tests did not require load to overcome the tensile capacity of the concrete (because it was already cracked). Consequently, the moment-deflection response of the composite girder crack reopening tests all followed the same path and eventually intersected the initial crack test response. However, all reopening tests tend to follow the same general moment-deflection path indicating the section was previously cracked. The effects of

pre-release shrinkage cracks on the behavior of Girder II are discussed in detail in Chapter Eleven.

Also, indicated in Figure 9.11 is a shift for Reopen Tests 2 and 3. This phenomenon is most likely due to creep of the concrete under sustained load during the testing period. These last two tests were performed as loops 2 and 3 of a single test day where the dead load was left hanging on the composite test girder for 4 hours. The slope of each of these last two curves appears to deviate from the straight line at a level of '10k + sdl' (19200 in-k) and is not significantly different from the reopening tests where creep was not an issue.

9.3.1.3 Measured Bottom Flange Crack Width Displacements

After the initial crack test and prior to Reopen 1, two LVDTs were placed on the underside of the bottom flange of the damaged girder in an effort to accurately determine the load level at which cracks reopened. Crack D-BF-11 on the bottom flange was gauged in the *over* and *near* manner described in Section 8.3.1.3. The LVDT displacement recorded at each gage location is referred to as the *crack width displacement*, and includes any displacement above the gage due to crack opening as well as any concrete strain occurring between the LVDT anchor points.

A plot of the applied midspan moment versus the crack width opening is shown in Figure 9.12 for the static truck test prior to Reopen Test 1, as well as for Reopen 1 itself. In the legend, *over* refers to the gage placed over the crack while *near* refers to the gage offset from the crack. The typical service range of induced moment is shown as a reference. Both gages show consistency (i.e., they remained parallel) in opening while the load applied caused the bottom fiber of the girder to change from compression to tension. As the applied midspan moment increased above 12,800 in-k (1450 kN-m), the gage *over* the crack showed an abrupt increase in displacement, noted by the bend and decrease in slope, and the crack began to open. The gage *near* the crack showed the displacement stabilized, such that additional strain was no longer distributed to the concrete *near* the crack (the deformation was concentrated in the crack).

The measured displacements shown in Figure 9.12 indicate concentrated deformations taking place at the crack near the high end of the typical service range, corresponding to a load level of '0k + sdl' or an applied midspan moment of 12800 in-k (1865 kN-m). The AE monitoring system exhibited crack reopening events at a higher load level of '14k +sdl', although the AE system was located nearly eight feet away. The crack did not visually open until a load level of

'18k +sdl' corresponding to a displacement of nearly twice the recorded displacement. The initial visual crack level is noted on the figure for reference.

Additional data was recorded during subsequent reopen tests and are superimposed in Figure 9.13. The gages were consistent in that the relative shape of each curve remained in tact. This data implies that continued cycling of the test girder through truck load levels and overload conditions showed no change in the load (moment) level at which the crack opened or in the relative width of the opening at any given load level.

The first six cracks to originally form on the side of the bottom flange between 58 and 68 ft. from end C appeared to reopen during normal cyclic truck load levels. Therefore, side flange crack C-BF-12 [58.3 ft. (17.8 m) from end C] was instrumented with an LVDT over the crack. A second LVDT remained over bottom flange crack D-BF-11 [74.9 ft. (22.8 m)]. The two crack width displacement results are shown in Figure 9.14 for intermittent static tests during the post-crack cyclic testing period. Assuming the two cracks behave the same, the side flange crack does appear to open within the 'Typical Service Range' for the HS25 truck load, although no stiffness change was observed in the service load range (Section 9.2.1).

9.3.1.4 Predicted Initial Cracking Load

Predicted flexural cracking loads and corresponding cracking stresses were compared to those observed. Table 9.15 lists the initial measured (AE and visual) cracking load along with the predicted loads for several cases: nominal losses, measured lower bound losses, Time-Step predicted losses and *Pbeam* predicted losses. Using the relationship from Eqn. (8.4), the predicted actuator load per point could be back-calculated from the actuator moment required to achieve the desired tensile stress. The predicted nominal design case assumptions were discussed in Section 8.3.1.4. Predicted losses of 28.8% estimated from the PCI Committee on Prestress Losses (1975) at the time of crack testing (Table 7.5) were used to define the nominal effective strand force, P_{eff} for the nominal design case. This lead to a predicted total applied midspan moment of 23,240 in-k (2620 kN-m), or an actuator moment of 10,340 in-k (1170 kN-m) required to achieve the nominal cracking stress. With the applied four point loading configuration, a load of '16.5 kips plus the superimposed hanging dead load' would be needed to reach the nominal modulus of rupture, as listed in Table 9.15. [Note: The difference in the

nominal cracking load between Girders I and II, as compared with Table 8.15, is due to the placement of the superimposed dead load, discussed in Section 5.2.2.]

Predictions listed as 'Predicted - Girder II' in Table 9.15 for cracking moments were based on the 28-day measured cracking stress of 747 psi. Using measured average lower bound losses of 25.8% (assuming the concrete stress prior to release is zero), net section properties for the three bracketed terms of Eqn. (8.4), and transformed noncomposite and composite section properties for the remaining terms in Eqn. (8.4), a total applied midspan cracking moment of 34,080 in-k (4130 kN-m) was computed. This lead to a predicted cracking moment of 21,300 in-k (2560 kN-m) due to the actuators alone, or a total predicted load level of '33.7 kips per actuator plus the superimposed dead load' (33.7k +sdl).

Table 9.15 Predicted Initial Cracking Load for Girder II

	Load Level (Actuator + Superimposed)	Applied Midspan Cracking Moment (in-k)	Cracking Stress † (ksi)	Cracking Stress Level ($x\sqrt{f_c'}$)
AE Initial Crack ‡	*14k + sdl*	*21,670 (21340‡)*	*+0.01 (-0.80‡)*	~0
Visual Initial Crack	*18k + sdl*	*24,190 (23850‡)*	*+0.21 (-0.60‡)*	$2.0\sqrt{f_c'}$
Nominal Design Case	16.5k + sdl	23,240	+0.769	$7.5\sqrt{f_c'}_c$
Predicted - Girder II +				
Measured Losses, 25.8%	33.7k + sdl	34,080	+0.747	$7.1\sqrt{f_c'}$
Time-Step Losses, 30.9%	26.0k + sdl	29,230		
Pbeam Losses, 26.9%	32.4k + sdl	33,260		

† Sign convention: tension is positive.
‡ Computed at the location of the first visual crack, C-BF-12, as opposed to midspan.
+ Assumed losses at crack testing summarized in Table 7.5.

Using the previously defined geometric properties and the losses as predicted by the Time-Step method at the time of crack testing (Section 7.4.2), the predicted cracking load would have been lower, at '26.0k + sdl', as expected. Output results using the *Pbeam* program predicted the cracking load in the same range, at '32.4k + sdl'. Predicted cracking loads indicate losses must be higher than lower bound measured losses. Also, effects of pre-release cracks are believed to have strongly influenced the cracking load because the actual measured cracking load was less than 50% of predicted. Further discussion of losses based solely on measured initial crack and reopening loads is included in Section 9.3.1.6 and the effects of pre-release cracks are discussed in Chapter Eleven.

9.3.1.5 Predicted Crack Reopening Loads

The crack reopening load, also known as the load when the bottom fiber reaches zero tension, was compared to predictions tabulated in Table 9.16. The same assumptions are applied for predicting the nominal design and predicted cases of crack reopening as assumed for the initial cracking load comparison, with the following exception. The crack reopening load is computed when the level of bottom fiber stress is equal to zero. Hence, the strain in the bottom fiber is also zero when the crack first reopens. Also tabulated for comparison are the measured crack reopening loads as detected by the AE monitoring system, visual inspection (see Table 9.14) and the LVDTs placed to monitor crack widths during the reopening tests (Section 9.3.1.3).

Table 9.16 Predicted Crack Reopening Load for Girder II

	Load Level (Actuator + Superimposed)	Crack Reopening Moment[+] (in-k) [†]
Bottom Flange Crack Reopen As recorded by LVDTs [‡]	*0 k + sdl*	*12,850*
AE Reopen	*6k + sdl*	*16,640 (16,290[‡])*
Visual Reopen	*10k + sdl*	*19,160 (18,820[‡])*
Nominal Design Case	4.0k + sdl	15,370
Predicted - Girder II Measured Losses, 25.8% Time-Step Losses, 30.9% *Pbeam* Losses, 26.9%	19.0k + sdl 11.3k + sdl 17.1k + sdl	24,820 19,970 23,620

[†] Metric conversion: 1 in-k = 0.1130 kN-m.
[‡] Italicized text indicates measured values.
[+] Moment computed at location of the first crack, C-BF-12, as opposed to midspan.

The measured reopening load and moment as determined from the bottom flange crack width opening data is also listed. As expected, predicted and measured reopening loads were lower than initial cracking loads, as the tension stress in the bottom fiber no longer exists. The nominal design case conservatively predicted much lower reopening loads than measured. The predicted reopening moment using lower bound measured losses and material properties was 29% greater than the moment recorded as the first visual crack reopened and 93% higher than the moment at the level when bottom flange gages detected crack opening.

9.3.1.6 Discussion of Cracking Loads

Table 9.15 listed the measured load and measured moment level results from the AE and visual inspection of first crack formation (at crack C-BF-12). With the measured AE and visual

cracking moments 57% and 41% respectively less than predicted, attention was given to finding a probable cause for the discrepancy, as performed for Girder I in Section 8.3.1. Two variables had a large effect on the estimated cracking loads from Eqn. (8.4): the assumed modulus of rupture and prestress losses. The influence of each variable is reviewed. In addition, the effects of pre-release shrinkage cracks formed in Girder II during fabrication are discussed in Chapter Eleven.

Because the modulus of rupture was measured at 28-days rather than at crack testing, it was a source of possible error in predicting the cracking loads. To investigate this effect, the midspan bottom fiber cracking stress corresponding to the measured cracking loads was back-calculated compared with the measured modulus of rupture. The stress was computed from Eqn. (8.4) using a measured lower bound prestress loss of 25.8% to determine the effective prestress force, net section properties for the first three bracketed terms, and transformed section properties for the noncomposite and composite remaining terms. A stress level of -0.26 ksi (compression) was computed at the load level that AE monitoring detected crack formation. The bottom of the girder was computed to be at a state of stress of -0.05 ksi (compression) when the first visual crack appeared. Both stress levels were computed at the location of the first crack, accounting for lower self-weight and applied moments offset from midspan of the simply supported beam. The measured 28-day modulus of rupture for Girder II was 0.750±0.068 ksi (Table 6.3). Because cracking stress levels predicted the bottom concrete fibers to still be in compression when cracking first appeared, it is unlikely that an error in measuring cracking stress from test cylinders was the only reason for the high predicted cracking loads.

Measured cracking loads were used to estimate the prestress losses for comparison to lower bound measured losses determined from vibrating wire gages embedded in the concrete. Estimated losses were back-calculated from the measured applied cracking moment and are shown in Table 9.17 using Eqn. (8.4). The strand force P was calculated for by assuming the bottom fiber concrete stress at cracking was equal to the measured modulus of rupture while the actual applied moment was taken into consideration. Knowing the force P and the strand area, A_{ps}, losses were computed relative to the initial tensioning stress. Losses at the time of crack tests were back-calculated to be 43.6% at AE crack detection and 41.1% at the moment level when the first visual crack was noticed. Losses were also back-calculated using the applied moment when bottom flange LVDTs recorded opening (Table 9.16) in conjunction with a zero

tension stress in place of the measured rupture modulus. In this way, losses were computed to be 43.2% for the measured crack width case. When using AE and visual reopening moments for the case of the bottom fiber stress at zero, losses were computed to be 39.4% and 36.9%, respectively.

Table 9.17 Estimated Losses from Cracking Tests of Girder II

	Load Level (Actuator + Superimposed)	Estimated Prestress Loss at Crack Testing	Estimated $\sigma_{c,\ before\text{-}rel}$
		Measured *Lower Bound: 25.8%* † *Upper Bound: 36.5%* ‡	*0.0 ksi* *0.750 ksi*
Initial Crack Testing assuming $\sigma_{bottom\ fiber} = f_r = 0.750$ ksi			
AE Initial Crack	14k + sdl	43.6%	1.23 ksi
Visual Initial Crack	18k + sdl	41.1%	1.06 ksi
Crack Reopening Testing assuming $\sigma_{bottom\ fiber} = 0.0$ ksi			
Bottom Flange Crack Reopen	0k + sdl	43.2%	1.21 ksi
AE Reopen	6k + sdl	39.4%	0.94 ksi
Visual Reopen	10k + sdl	36.9%	0.77 ksi

† Measured lower bound losses determined from vibrating wire gages (Table 7.5) assume zero concrete stress before release (Section 7.4.2).

‡ Measured upper bound losses assume concrete stress before release equal to the measured modulus of rupture.

Confidence may be best placed in the losses estimated from the crack reopening tests using the bottom flange crack data (43.2%). It was known that the bottom fiber stress was zero at crack reopening and data clearly showed the load (or moment) level at which crack reopening was detected (Figure 9.13). In addition, assuming the measured modulus of rupture was exactly accurate, confidence can also be placed in the results from the initial testing as recorded by AE (43.6%) because of the girders virgin state. In either case, the consistency between the estimated losses was extremely high even though both estimated measures were determined independently.

When compared with lower and upper bound measured losses from vibrating wire gages, the estimated losses from initial crack testing and reopening tests were on the high end, and exceeded the upper bound measured losses. The lower bound measured losses assume the concrete stress in the section was zero at the time of release (Section 7.4.2). The upper bound measured losses assume the concrete stress prior to release was equal to the 28-day modulus of rupture. Upper bound losses were 10.7% higher than lower bound, and were 36.5% at the time

of crack testing. The losses estimated from crack testing were used to estimate the stress in the concrete prior to release ($\sigma_{c,\ before\text{-}rel}$) using the relationships developed in Eqns. (7.1-7.6). The estimated concrete stresses before release for the two cases with most confidence (AE during initial crack testing and LVDT data at crack reopening) were listed in Table 9.17 and were from 1.21 to 1.23 ksi (8.3 to 8.5 MPa), respectively. All five cases estimated the concrete stress before release to be greater than the measured modulus of rupture, indicating that the girder was cracked prior to release.

Using losses estimated from LVDT gages placed across bottom flange cracks at crack testing, initial and long term losses were estimated and are listed in Table 9.18. However, this assumed the concrete stress prior to release was greater than cracking. Therefore, long term 'best guess' estimates of measured losses are listed as the upper bound losses in Table 9.18, assuming the concrete stress prior to release was equal to the modulus of rupture. Cracking was observed in Girder II prior to release (Section 7.3.1) and the additional influence of the pre-release cracking on losses is further discussed in Chapter Eleven.

Table 9.18 Best Guess - Estimated Losses for Girder II

	Lower Bound Measured Losses†	Estimated Prestress Loss from LVDT Data taken at Crack Testing	Upper Bound Measured Losses‡
Initial Loss	18.6%	36.0%	29.3%
28-days	22.2%	39.6%	32.9%
Deck Casting	23.3%	40.7%	34.0%
Crack Testing	25.8%	43.2%	36.5%
Ultimate Flexural Test	26.3%	43.7%	37.0%

† Measured lower bound losses determined from vibrating wire gages (Table 7.5) assume zero concrete stress before release (Section 7.4.2).

‡ Measured upper bound losses assume concrete stress before release equal to the measured modulus of rupture at 28 days.

9.3.2 Strand Strain and Stress Ranges

The same twelve gages that provided useful data during the intermittent static test at truck load and overload conditions (see Section 9.2.2) were informative during the flexural cracking and reopening tests. Table 9.19 lists the gage names, their respective location from End C, and height from the bottom of the girder. Also tabulated is the nearest flexural crack, the distance to nearest crack, and the load level when the crack formed. Eight of the gages, were located outside

of the constant moment region, but within the actuator load points. The remaining gages were located at midspan. Four of the gages were located within 2 in. (50 mm) of crack C-BF-13, one of the first cracks to form, at 59.8 ft. (18.2 m) from End IIC.

Table 9.19 Strand Strain Gage Information for Initial Crack Test - Girder II

Gage Name †	Distance from End C (ft.)	Gage Height from bottom of girder (in.)	Nearest Flexural Crack	Distance to Nearest Flexural Crack (in.)	Load Level at Crack Formation (k+sdl)
FIIC19	59.70	2	C-BF-13	1.5	18k + sdl
FIIC15	59.75	2	C-BF-13	<1.0	18k + sdl
FIIC25	59.75	4	C-BF-13	<1.0	18k + sdl
FIIC35	59.75	6	C-BF-13	<1.0	18k + sdl
FIIC12	60.20	2	C-BF-14	5.0	18k + sdl
FIIDC12	66.20	2	C-BF-19	6.0	24k + sdl
FIIDC17	66.25	2	C-BF-19	6.5	24k + sdl
FIIDC25	66.45	4	C-BF-19	9.0	24k + sdl
FIIDC35	66.45	6	C-BF-19	9.0	24k + sdl
FIID15	72.85	2	D-BF-13	6.5	26k + sdl
FIID17	72.95	2	D-BF-13	7.8	26k + sdl
FIID19	72.95	2	D-BF-13	7.8	26k + sdl

† Corresponds to Appendix D in Kielb (1994).

The moment-stress change relationship for each of the eight gages located on the bottom row of strands is portrayed in Figure 9.15 for the initial flexural crack test. Each gage had nearly 100 readings averaged at each hold point. The average stress value was determined from the average strain multiplied by the apparent strand modulus (29,100, ksi, 201 GPa). It is plotted relative to the moment on the *y*-axis, which is the actual applied moment at the location of the gage, accounting for actual actuator readings and placement as well as the hanging dead load location (not including self-weight). The standard deviation of each gage at any given data point was very low (<5 με). The predicted stress at midspan for the bottom row of strands is also shown on the figure for comparison. Stress change was predicted using measured material properties including a strand modulus of 28,800 ksi (199 GPa), and transformed composite section properties.

The moment-strand stress change relationship for two gages located in each strand Row 2 and 3 is portrayed in Figure 9.16 for the initial flexural crack test. As with gages located in Row

1, each gage had nearly 100 readings averaged at each hold point. This average stress value is plotted relative the applied moment at the gage location. The predicted stress at midspan for the two rows of strands are also shown on the figure for comparison.

One of the four gages that was located within 2 in. of the first crack (FIIC19 in Row 1) shows a jump in strain just after visual crack detection (the applied moment at this gage location was on the order of 25,000 in-k). This corresponds to a applied load of '19 kips per actuator plus the superimposed dead load'. The remaining gage in Row 1 (FIIC15) did not show a jump in strain at the visual crack level, as expected. The two remaining gages (one each in Rows 2 and 3) near the first crack did not show jumps, nor was it expected as the rows are much closer to the centroid of the strands and would not be as greatly effected by the hairline cracks forming at the bottom of the girder.

The same data was collected for the twelve gages during the flexural crack reopening tests. Figure 9.17 shows the moment-to-stress relationship for gage FIIC15 during precrack, initial crack, and reopening tests. The predicted stress shown was computed at the gage location along the girder length and at the height of the gage (Row 1), 2 in. (50 mm) up from bottom. This figure is similar to the composite girder moment-deflection response in that once the girder was cracked subsequent loadings followed a flatter slope due to the reduced section stiffness upon crack reopening. The curves (initial and all reopen tests) show some signs of convergence beyond the initial visual cracking moment, and near the maximum applied moment level, as expected. However, the curvature difference between initial testing and reopening crack tests is small and confirms results shown in the moment-deflection response, and indicates a pre-cracked section. The remaining gages not shown here produced similar graphs and results.

9.3.3 Concrete Strain and Stress Ranges

Two types of gages were used to record concrete strain data. As with the static test results presented in Section 9.2.3, vibrating wire gages and embedded concrete PML gages were used. Vibrating wire gages placed through the depth at midspan provided both compressive and tensile data during flexural crack load testing. Concrete tensile strains are compared with strains recorded by strand gages (Section 9.3.2). Concrete compressive strains in the deck and top flange were also recorded during flexural crack load testing by PML gages and are compared with vibrating wire gages below.

Vibrating wire gage data (midspan moment versus strain) recorded during the precrack static test to 125% HS25 (solid lines) and the initial flexural crack test (dashed lines) are shown in Figure 9.18. The typical service range up to 100% HS25 load is also noted for reference. Data was collected at two kip load steps after the superimposed dead load was hung from the test girder. Data recorded thereafter was limited, with only the second crack reopening test recording vibrating wire gage data at occasional load steps, shown in the figure as hollow symbols. The gage located in the top flange [42.5 in. (1080 mm)] show compressive strain changes as expected under the loading scenario, while strains recorded in the bottom flange indicate tensile changes in strain.

The strain distribution through the midspan cross section is illustrated in Figure 9.19 for several load steps of interest. The 'Preload + HS25' load combination was recorded during the pre-crack static truck test and is linear, as expected from previous static test results documented in Section 9.1.3 and Figure 9.5. Also shown is the predicted strain distribution for the 'Preload + HS25' load combination based on the actual moment induced and transformed composite section properties. The distribution of measured strains through the cross section remained linear, even to the maximum load level of '30k +sdl' ,or 32,000 in-k (3620 kN-m).

Stress ranges at the level of the *cgs* from vibrating wire gages can be compared with stress ranges from gages placed directly on the strands during crack testing. The stress range of 9.7 ksi at the *cgs* of the strands was determined from a vibrating wire gage strain of 337 με multiplied by a strand modulus of 28,800 ksi (199 GPa) when the first visual crack appeared, whereas the strain computed from the regressed relationship of vibrating wire strain versus gage height for the top three gages shown in Figure 9.19. Four strand gages at midspan collected data for comparison, two were located in Strand Row 1 at 2.0 in. (50.8 mm) from the bottom, one in Row 2 at 4 in. (102 mm) up and one in Row 3 at 6 in. (152 mm) up. The two lowest gages recorded an average stress range of 9.8 ksi corresponding to a strain of 337 με (±9 με), while the Row 2 and 3 gages experienced stress range levels of 9.6 and 8.9 ksi (strain levels of 330 and 307 με). While it is difficult to conclude strongly based on the results of such few gages, the two methods for determining strain change due to superimposed loading are within reason.

Concrete compressive and tensile strains were also recorded by seven concrete embedded PML gages located through the girder cross section at midspan. Figure 9.20 shows a graph of the moment versus strain results of the seven gages at varying heights for the initial flexural

crack test. The typical service range is noted for comparison to show that the moment-strain relationship was not linear through the entire range for gages located above the neutral axis. Strains at all gage heights begin to show non-linearity at about 15,000 in-k (2880 kN-m), or at a load level of '8k +sdl', and corresponding to immediately before AE monitoring began recording initial crack events.

The strain distribution through the depth of the midspan cross section is shown in Figure 9.21 for the pre-crack truck test, AE and Visual Crack Load levels, and crack reopening tests 1, 2 and 3. The 'Preload + HS25' pre-crack truck test results were similar to the intermittent static truck test results shown in Figure 9.7 and discussed in Section 9.2.3. The 'Predicted' distribution at the 'Preload + HS25' load level was based on the nominal moment for this load combination and transformed composite section properties.

As expected, gages placed above the neutral axis showed compression induced from the applied loading, and the gage below the neutral axis showed tension. The first visual crack was detected at a midspan moment of 24,200 in-k (2730 kN-m), at the same time that the gage directly above the neutral axis [35.5 in. (900 mm)] began to shift toward lower compression (Figure 9.20), indicating a neutral axis shift at the time of cracking. In Figure 9.21, the neutral axis had shifted from 31.9 in. (810 mm) at the 'Preload + HS25' load step to 32.5 in. (826 mm) at the 'First Visual Crack' load level.

9.3.4 Out-of-Plane Deflection

As previously discussed in Section 9.2.3, the test girder was not braced laterally along its length during load testing, including flexural crack testing. The sidesway deflection system devised for static and fatigue loading was also used during crack testing to provide insight into how much lateral motion the test girder saw during load testing. The bottom flange showed consistent out-of-plane motion on the order of 0.10 in. (2.5 mm) for vertical deflections as high as 4.1 in. (104 mm). The two possible reasons for this sidesway motion discussed in Section 9.2.4 are applicable here as well. Most notably was the fact that this out-of-plane motion is very small relative to the length and longitudinal deflection of the girder, and can be considered neligible. Flexural crack testing did not cause any instability conditions in the test girder.

CHAPTER 10 ULTIMATE FLEXURAL STRENGTH

10.1 Introduction

Each composite girder was load tested to determine its ultimate flexural strength. General load testing discussed in Chapter Five includes complete information on the ultimate test setup, including the loading system configuration and instrumentation for load and deflection. Ultimate tests were performed on each girder at ages of 860 and 840 days, respectively, for Girders I and II. Both girders showed a substantial amount of ductility. Eventually the girders exhibited an explosive failure due to the anticipated compression failure of the normal strength concrete deck. A general overview is presented for each ultimate flexural failure test. Measured ultimate strengths are compared with predicted strengths using the ACI/AASHTO and strain compatibility methods.

General Behavior

Each girder was individually tested to ultimate flexural failure by applying two point loads for a four point loading configuration. Initially loaded statically to about 32,000 in-k (3620 kN-m) of applied moment at centerline, each girder was then unloaded to 10,000 in-k (1130 kN-m) before being reloaded to ultimate to compare load-deflection data obtained during low level flexural load testing (Chapters Eight and Nine). Load steps in 20 kip (90 kN) increments were maintained until significant deflection was noted, at which time load steps were reduced to approximately 5 kips (22 kN) each. Each ultimate failure test took approximately three hours and ended with the deck concrete crushing and buckling of the longitudinal reinforcement.

Girder I

Photographs were taken before, during and after the testing of each girder. Figure 10.1 shows Girder I in the "before" ultimate testing position from End IB and viewing the length. Chains used to hold the girder to the reaction block can be seen in the foreground. The center region, where failure was expected, was well lit. Nearly 4 ft. (3.2 m) of clearance existed between the bottom of the girder and the laboratory floor. Timber beams were placed below the girder to absorb the impact of the girder as it was expected to drop to the floor during ultimate collapse.

In addition to photographs, each test was videotaped. Footage from Girder I recorded the failure at the heavily damaged region in increments of $1/30^{th}$ of a second. Figures 10.2 to 10.5

are actual video frames. Figure 10.2 is the frame immediately before any evidence of failure was noted. A wire was strung from end to end of the girder and a deflection-measuring page (shown in the middle of the figure) was hung from the wire. When the test first began, the top of the bottom flange of the girder was even with the wire at centerline and top of deflection-measuring page. As testing progressed, the girder deflected downward. A deflection of about 30 inches (760 mm) is seen in the figure, as the level of the web-to-top flange interface is well below the horizontal wire.

Vertical flexure cracks in the girder midspan were marked at load step 'holds' and can be seen in the figure. The first cracks were visually observed to reopen at a moment of 1940 ft-k (23,300 in-k, 220 kN-m). Crack reopening tests from Chapter Eight stated the initial crack reopening level was 23,150 in-k (1930 ft-k, Table 8.14) at midspan, correlating well with the ultimate test measurements. Flexural cracks occurred initially at even increments of about 16 in. (400 mm), consistent with the stirrup spacing in the midspan region. At a midspan moment level of 2620 ft-k (295 kN-m), cracks had progressed between the load points to a height of eight inches, (i.e., to the top of the bottom flange). The first crack in the web at centerline appeared at 3120 ft-k (250 kN-m). By 4140 ft-k (465 kN-m), the entire constant moment region was cracked well into the web. Vertical flexural cracks appeared evenly spaced between the existing cracks, at a spacing of about 8 in. (200 mm). In addition, cracking began outside of the load points. The cracking pattern showed the cracks to fork at the top of the web in the constant moment region at the top flange interface under an approximate level of 4830 ft-k (545 kN-m), or 92 kips per actuator. Outside of the load points, flexure-shear cracks developed to beyond the quarter points at this load level.

The first signs of deck crushing are shown in Figure 10.3, $1/30^{th}$ of a second after Figure 10.2 was recorded. Cracks began to appear to the immediate left of the wooden frame on the top of the deck. Failure progressed quickly and $2/30^{th}$ of a second later (Figure 10.4) the deck exploded off the composite girder. As the girder dropped (note the level of the horizontal wire), the bottom flange-to-web interface showed signs of severe cracking due to the significant stress concentration of the prestress strands in the bottom flange. The remaining portion of the deck crushed, causing the web region to blow out as seen in Figure 10.5, $4/30^{th}$ seconds later. After the dust had cleared, closer inspection revealed buckling of the longitudinal bars in the deck and top flange of the girder, Figure 10.6. Damage at the bottom flange-to-web interface was even

more significant, as it appeared the impact of the girder hitting the timber beams caused diagonal shear cracks to form in the midspan region.

Each girder end had been chained to its respective reaction block prior to testing. Upon the explosive failure, the girder ends lifted the reaction blocks on each end as the midspan region deflected and hit the timber beams. The video footage from ultimate testing of Girder I showed End A lifted the reaction block off the laboratory floor.

Photos of Girder I following ultimate testing are shown in Figures 10.7 to 10.11 as Girder I rests on the timber shoring after deflecting more than 30 in. (760 mm) and dropping another 15 in. (380 mm). An overview of the midspan area is shown in Figure 10.8, although the entire length of the test specimen would not fit into the photo frame. Ultimate failure of Girder I occurred at midspan, as shown. A closer view of the midspan damaged region is seen in Figure 10.9. Compression failure is noted by the buckling of reinforcement in the deck and top flange. The bottom flange shattered on impact after failure, exposing the prestressing strands. Significant cracking at the web-to-bottom flange interface was an artifact of high impact as a result of girder failure. An even closer view of the blown out region between the two center stirrups (approximately 2 ft.) is shown in Figure 10.10. Epoxy coated reinforcement was clean, with little to no adhesion of the concrete remaining.

Girder II

Ultimate flexure testing of Girder II occurred prior to Girder I. Video footage from Girder II was limited and did not capture the actual failure location. The first visual crack occurred at a moment level of 1680 ft-k (20,190 in-k, 190 kN-m). Crack reopening tests from Chapter Nine indicated the initial crack reopening level was 19,160 in-k (1600 ft-k, Table 9.14) at midspan, correlating well with the ultimate test. At a moment level of 2470 ft-k (280 kN-m), flexural cracks extended to the top of the bottom flange between load points. The cracks extended into the web at a moment level of 2910 ft-k (330 kN-m). The cracking pattern showed the cracks to fork at the top of the web in the constant moment region at the top flange interface under an approximate level of 5260 ft-k (590 kN-m), or 100 kips per actuator. Outside of the load points, flexure-shear cracks developed to beyond the quarter points at this load level.

Photos taken after the Girder II ultimate failure test was complete are shown in Figure 10.11 to 10.15. The first photo shows the girder after deflecting 35 in. (890 mm) and dropping another 10 in. (250 mm) before impacting the timber shoring. Figure 10.12 gives an overview of the

failed test specimen. Girder II failed beneath load point D, at *0.4L* from End D, where the moment capacity changes as twelve straight strands became draped. At 0.4L from End C, only four straight strands became draped as strand debonding was used to reduce stresses in the end region rather than by draping alone. The midspan deflection device stabilizer (wood frame in Figure 10.13) was still in place after testing was complete. Significant cracking was seen, as in Girder I, along the length at the web-to-bottom flange interface due to impact of the bottom flange with timber shoring at failure. The load ram is shown extended to the deflected position at failure. Figure 10.14 provides a closer view of the damaged region. An even closer view of the blown out region between two stirrups is shown in Figure 10.15. Fracture of one of the four buckled top flange bars (No. 8) can be seen at the center of the blow out. Fractured longitudinal deck reinforcement is also shown. Prestressing strands were exposed in the shattered bottom flange after impact.

10.2 Measured Ultimate Flexural Strength and Deflection

Load cells at each actuator point recorded the applied load. Pressure transducer readings placed in-line to measure hydraulic pressure for each actuator were converted to load and correlated well with the loads recorded by each actuator load cell. Using the load cell reading and the measured placement of each actuator the moment at each load point was computed.

The ultimate measured moment is the sum of the applied actuator moment and the self-weight moment, and occurred at the midspan of the symmetrically loaded simple-span test girders. The measured ultimate loads and moments for both girders are listed in Table 10.1. Because the ultimate failure location of Girder II was located at *0.4L* from End D, corresponding to the strand harp point and applied load point, the moment measured at this location is also noted.

The ultimate flexural strength is often referred to in terms of the service load, or %HS25 truck load. The failure percentages were computed as follows:

$$\%HS25 = \frac{M_{applied} - M_{preload}}{M_{HS25}} \times 100, \qquad (10.1)$$

where the midspan and load point moments induced by the preload and HS25 truck load were given in Sections 8.1.1 and 9.1.1 for Girders I and II, respectively.

Table 10.1 Measured Ultimate Flexural Loads and Moments

	Girder I	Girder II	Girder II*0.4L - End D* †
Maximum Load – Actuator A/C	132.5 k	134.2 k	-
Maximum Load – Actuator B/D	130.5 k	130.2 k	-
Midspan Moment due to Actuators	6900 ft-k	6950 ft-k	6840 ft-k
%HS25 Truck Load	677% HS25	683% HS25	670% HS25
Self-Weight Moment	2570 ft-k	2580 ft-k	2480 ft-k
M_u - Measured Ultimate Moment	9470 ft-k	9650 ft-k	9320 ft-k

† Moments also computed at *0.4L - End D*, location of ultimate failure in Girder II.

The actuator (total less self weight) moment-deflection response at midspan of Girders I and II are shown in Figures 10.16 and 10.17, respectively. Deflections were measured at each load point, as well as midspan. The deflection plotted with the solid line was taken from the pressure transducer data at midspan with the pressure transducer system described in Section 5.2.3 (to accommodate the full range of expected displacement). A companion LVDT with a limited range of 10 in. (255 mm) was also located at midspan. The LVDT data is superimposed on the plots. Actuator load and deflection data were recorded continuously during loading, and averaged over 100 readings at intermediate load step holds (hollow squares on figures). Because of the large number of data sets collected (approximately 32,000 sets of 12 data channels), data was sampled as the average of every six sets, resulting in one-sixth of the data used for plotting. The *y*-axis plots the actuator applied moment, for comparison with crack testing results. The pressure transducer deflection noise noticeable in the figure was mostly due to instrumentation placement. The converters were inadvertently secured to a load frame column that indicated pull-out during later testing. The noise most likely resulted from initial shaking of the column to which the instrumentation was attached. Additionally, the nature of the pressure transducer measuring system could have contributed to the noise because fluid contained in the buckets atop the girder may have been sloshing. LVDT data correlated well with the average pressure transducer deflection data at the given load steps.

The estimated stiffnesses during ultimate testing are shown as dashed lines in the moment-deflection response (Figures 10.16 and 10.17) and can be compared to the initial measured stiffnesses. Estimated values for Girders I and II were 740 and 720 ft-k/in. (14.1 and 13.7 k/in.), respectively. Measured stiffnesses recorded during initial static testing were 14.2 and 13.5 k/in. for each respective girder (Section 8.2 and 9.2). A secondary slope is drawn on the figures as

well to indicate the reduced stiffness of the cracked section. Estimated secondary stiffnesses were 175 and 161 ft-k/in. (3.33 and 3.06 k/in.) resulting in stiffness reductions of 24.0% and 22.3% for Girders I and II, respectively. This correlates well with the recommended reduced stiffness of 20% EI (Castrodale, 1988b) to be used for estimating the deflections of the cracked section above decompression.

The visual crack reopening width is a small deformation relative to crack widths of a fully cracked section. Therefore, it would be expected that visual crack reopening moments would occur much lower than the corresponding moment of the stiffness change from each ultimate test. For Girder I, a stiffness change estimated from the ultimate moment-deflection response in Figure 10.16 shows significant change in slope at about 2900 ft-k (34,800 in-k, 330 kN-m). The crack reopening load from Girder I occurred much lower, at 23,150 in-k (1930 ft-k, 220 kN-m, Section 8.3). Visual inspection of cracking during testing revealed that cracking extended into the web at a level of 3120 ft-k (250 kN-m) and is shown on Figure 10.16 to occur as the curve becomes nonlinear. Similarly for Girder II, stiffness changed at about 2700 ft-k (32,400 in-k, 305 kN-m) in Figure 10.17 and crack reopening was reported at 19,160 in-k (1600 ft-k, 180 kN-m, Section 9.3). Cracking into the web appeared at 2910 ft-k (330 kN-m) and, like Girder I, occurred as the curve became nonlinear.

Measured deflections at ultimate loads were recorded and are listed in Table 10.2. Gages placed on prestressing strands had a maximum range of 3000 :,. They were not useable for large elongations, and consequently did not perform well during ultimate flexural testing. No information was available regarding ultimate measured strand stresses at failure. In addition, both types of concrete embedment gages (vibrating wire gages and PML gages) were out of range by a deflection of 15 in. (380 mm), less than half of the ultimate deflection, and data could not be reduced to provide useful information regarding ultimate concrete strains in the top flange or deck.

Table 10.2 Measured Ultimate Deflections

Location:	Girder I in. [mm]	Girder II in. [mm]
0.4L from End IA or IIC	28.5 [725]	33.0 [840]
centerline	30.5 [775]	35.4 [900]
0.4L from End IB or IID	28.0 [710]	33.0 [840]

10.3 Predicted Ultimate Flexural Strength

Ultimate flexural capacity can be predicted by several methods, three of which are used discussed for comparison to measured capacities: the ACI or AASHTO method, and the strain compatibility. Predictions were included for the nominal design case using prestress losses predicted by the PCI Committee on Prestress Losses (1974) of 28.8% at the time of ultimate testing. In addition, predictions were determined for each girder using respective measured properties and losses.

10.3.1 ACI/AASHTO Simplified Methods

Design moment strength of flexural members computed by the strength design method of the ACI 318 (1995) and AASHTO (1996) Codes are based on a minimum effective strand stress of 50% f_{pu}. Although the two codes differ in notation, they are duplicate in concept and principles. ACI notation is used for discussion. For members with bonded prestressing tendons, the effective prestress in the strand at ultimate, f_{ps}, is estimated by the following

$$f_{ps} = f_{pu}\left(1 - \frac{\gamma_p}{\beta_1}\left[\rho_p \frac{f_{pu}}{f_c'} + \frac{d}{d_p}\left(\omega - \omega'\right)\right]\right), \tag{10.2}$$

where

$$\rho_p = \frac{A_{ps}}{bd_p}, \tag{10.3}$$

ω and ω' accounts for the non-prestressed tensile and compressive reinforcement,

$\beta_1 = 0.85 - 0.05(f'_c - 4) \geq 0.65$,

$\gamma_p = 0.40$ for $f_{py}/f_{pu} \leq 0.85$,

f'_c = concrete compressive strength of the deck, ksi,

f_{py}, f_{pu} = yield and ultimate strength of strand, ksi,

A_{ps} = total area of prestressing steel, in^2

b = width of compression face, in.

d_p = distance from extreme fiber in compression to prestress centroid.

A ductile under-reinforced section begins failure by excessive elongation of the tensile reinforcement, followed by concrete crushing. Failure by steel fracture prior to concrete failure

is not typically achieved. To be within ductility requirements of the code, the following relationship for the reinforcement ratio index must hold

$$\left[\omega_p + \left(\frac{d}{d_p}\right)(\omega - \omega')\right] \leq 0.36\beta_1, \tag{10.4}$$

where

$$\omega_p = \rho_p \frac{f_{ps}}{f_c'}. \tag{10.5}$$

Once the effective prestress in the strand at ultimate is estimated, force equilibrium is used to determine the neutral axis depth. Internal moment capacity is then computed by summing moments assuming the Whitney stress block distribution for compressive stresses.

Ultimate flexural capacity for the nominal design case was predicted to be 8240 ft-k (930 kN-m) using the ACI simplified method. A corresponding steel stress of 234 ksi (1610 MPa) at failure was estimated. Using measured material properties, and due to the identical deck strengths and midspan strand patterns, Girders I and II had matching predicted capacities of 9300 ft-k (1050 kN-m) with an estimated steel stress of 240 ksi (1650 MPa) at ultimate failure. Capacity predictions, steel failure stresses and ductility limits are tabulated in Table 10.3.

Minimum steel requirements specify the ultimate moment capacity must be 1.2 times greater than the cracking moment of the section such that

$$M_u = \varphi M_n = 1.2 M_{cr}. \tag{10.6}$$

The strength reduction factor, φ, is taken as 1.0 for analysis. The nominal moment capacity was on the order of 6 times the cracking moment for each girder tested.

Table 10.3 Predicted Ultimate Flexural Capacities

	Nominal Design	Girder I midspan	Girder II *0.4L - End D*
M_u - Ultimate Moment Capacity			
Measured	-	*9470 ft-k*	*9320 ft-k*
ACI/AASHTO Predicted	8240 ft-k (930 kN-m)	9300 ft-k (1050 kN-m)	9300 ft-k † (1050 kN-m)
Strain Compatibility Method PCI model ‡	9050 ft-k (1020 kN-m)	10,000 ft-k (1130 kN-m)	10,000 ft-k (1130 kN-m)
Strain Compatibility Method Fitted strand model ¤		9550 ft-k (1080 kN-m)	9570 ft-k (1080 kN-m)
f_{ps} - *Ultimate Strand Stress*			
Measured	-	-	-
ACI/AASHTO Predicted	234.4 ksi (1620 MPa)	240.4 ksi (1650 MPa)	240.4 ksi (1650 MPa)
Strain Compatibility Method PCI model ‡	261.3 ksi (1800 MPa)	262.4 ksi (1810 MPa)	262.4 ksi (1810 MPa)
Strain Compatibility Method Fitted strand model ¤	-	248.0 ksi (1710 MPa)	248.7 ksi (1710 MPa)
Ductility Check at Ultimate Conditions			
ACI/AASHTO Predicted $\gamma_p \leq 0.36\,\beta_1$	$\omega_p = 0.24$ $0.36\,\beta_1 = 0.31$ ductility ok	$\omega_p = 0.18$ $0.36\,\beta_1 = 0.27$ ductility ok	$\omega_p = 0.18$ $0.36\,\beta_1 = 0.27$ ductility ok
Strain Compatibility Method $c/d_p \leq 0.36/\beta_1$	$c/d_p = 0.33$ $0.36/\beta_1 = 0.42$ ductility ok	$c/d_p = 0.31$ $0.36/\beta_1 = 0.48$ ductility ok	$c/d_p = 0.31$ $0.36/\beta_1 = 0.48$ ductility ok

† Moments computed at *0.4L - End D*, location of ultimate failure.
‡ Prestressing stress-strain model from PCI Design Aid 11.2.5 (PCI Design Handbook, 1994).
¤ Prestressing stress-strain model fitted from measured modulus and yield.

10.3.2 Strain Compatibility Method

The ACI approach to determining the ultimate flexural strength of a member may underestimate the strength of beams with high percentages of reinforcement and, for more accurate evaluations of their strength, the strain compatibility and equilibrium method can be used (ACI 318, 1995). When the value of flexural moment is beyond the service load and cracking moment, a prestressed concrete beam starts to behave like a reinforced concrete beam. The ultimate flexural theory from reinforced concrete and its underlying principles are applicable to prestressed concrete. The total strain in the prestressing steel is determined as the load

approaches the ultimate limit state. Force equilibrium is maintained assuming Whitney's rectangular stress block to determine the depth of the neutral axis and the resulting moment capacity.

The total strand strain at ultimate beam failure includes three components. The first strain component, ε_1, is due to the effective prestress, f_{pe}, at the time of testing, using losses either estimated or measured, such that

$$\varepsilon_1 = \varepsilon_{pe} = \frac{f_{pe}}{E_s} = \frac{\left(1 - \frac{\%loss}{100}\right) f_{pi}}{E_s}, \tag{10.7}$$

where E_s is the modulus of the prestressing steel. The second component, ε_2, is the strain required to achieve decompression of the concrete at the centroid of the steel,

$$\varepsilon_2 = \varepsilon_{decomp} = \frac{P_e}{A_c E_c}\left(1 + \frac{e^2}{r^2}\right) = \frac{f_{pe} A_{ps}}{A_c E_c}\left(1 + \frac{e^2}{r^2}\right). \tag{10.8}$$

The additional strain increment, ε_3, due to loading above the decompression load as the load approaches ultimate can be computed from a linear strain distribution where the maximum compressive strain in the extreme compression fiber is $\varepsilon_c = 0.003$ and

$$\varepsilon_3 = \varepsilon_c\left(\frac{d_p - c}{c}\right), \tag{10.9}$$

where c is the depth of the neutral axis. The total strain at the steel centroid at ultimate failure then becomes:

$$\varepsilon_{ps} = \varepsilon_1 + \varepsilon_2 + \varepsilon_3. \tag{10.10}$$

A trial and error solution for ε_{ps} was obtained to determine f_{ps}. The corresponding stress f_{ps} at the predicted nominal strength was obtained from the PCI Design Handbook (1994) Design Aid 11.2.5. For Grade 270 prestressing strands with a nominal modulus of 28,500 ksi (197 GPa), the stress-strain curve can be estimated from the following relationships:

$$f_{ps} = \varepsilon_{ps} E_{ps}, \tag{10.11}$$

for strains less than or equal to 0.0086 and

$$f_{ps} = 270 - \frac{0.04}{\varepsilon_{ps} - 0.007}, \tag{10.12}$$

for strains greater than 0.0086 (PCI Design Handbook, 1994). Flexural capacity can be computed from internal moment summation knowing the ultimate strain at failure and the depth of the neutral axis.

Ultimate flexural capacity for the nominal design case was predicted to be 9050 ft-k (1020 kNm) using the strain compatibility method. A corresponding steel failure stress of 261.3 ksi (1800 MPa) was estimated. Using measured properties, Girders I and II had predicted capacities of 10,000 ft-k (1130 kN-m) with an estimated steel stress of 262.4 ksi (1810 MPa). Predicted capacities and strand failure stresses are tabulated in Table 10.3.

The level of stress estimated at failure is highly sensitive to the stress-strain relationship assumed for the prestressing steel because stresses occur in the highly nonlinear region near and above the yield. Actual stress-strain curves from material tests were not available for the prestressing strands. However, the yield stress at 1% elongation was measured as 239 ksi [1650 MPa] (see Table 6.7, also Kielb 1994). Using the same equation form as the PCI Design Aid 11.2.5 with the measured modulus of 28,800 ksi (199 GPa), a forced yield stress equal to measured at 1% elongation, and visually estimating the nonlinearity begins at an approximate strand stress of 220 ksi, the following relationship was determined for strains greater than or equal to 0.0076 in./in.

$$f_{ps} = f_{pu} - \frac{0.187}{\varepsilon_{ps} - 0.0038}. \qquad (10.13)$$

Using this 'fitted' stress-strain relationship for the strain compatibility method, ultimate moment capacities for Girders I and II were 9570 and 9590 ft-k (1080 and 1080 kN-m), respectively. Corresponding steel failure stresses were 248 and 249 ksi (1710 and 1720 MPa). These predictions are also listed in Table 10.3.

It can be shown that comparable ACI ductility requirements can be preserved with the strain compatibility method when

$$\frac{c}{d_p} = \frac{0.36}{\beta_1}, \qquad (10.14)$$

where c, d_p, and β_1 were defined previously. In all cases using strain compatibility, ductility requirements were maintained and are tabulated in Table 10.3.

10.4 Comparison of Ultimate Flexural Strength

Measured ultimate flexural moment capacities of each test girder are compared with predictions in Table 10.3. The equations in the ACI 318 (1995) Code and AASHTO (1996) Specifications for estimating flexural cracking moment and flexural strength provide excellent predictions of girder ultimate flexural capacity. The predicted capacity for Girder I was within 1.7% of measured, while Girder II was within 0.1%. The use of the strain compatibility method also provided very close estimates. When used with the PCI prestressing steel stress-strain model, the strain compatibility estimates for ultimate strength were within 6.1 % and 8.0% for Girders I and II, respectively. The strain compatibility method used with a more accurate prestressing steel stress-strain relationship provides a very accurate prediction of flexural strength, within 1.0% for Girder I and 2.9% for Girder II.

In all predicted cases, the depth to the neutral axis at ultimate capacity remained near the deck-to-girder interface. Therefore, use of the Whitney stress block assumption appears valid because the concrete in compression was normal strength. The ACI and AASHTO simplified methods for computing ultimate moment capacity have been criticized for not including the effect of higher strength concretes found in the girder of composite sections. However, the neutral axis typically falls within the deck at ultimate failure, thereby not utilizing the additional concrete strength of the high strength girder.

Strand stresses at ultimate beam failure predicted by the methods are compared. The strain compatibility method predicts flexural stresses close to the ultimate strand stress, f_{pu}. While the ACI method predicts lower strand stresses, no comparison can be made to measured strand stresses as data was not available. Predicted ductility values show the girders to be ductile, independent of predictive method. The ductile section showed extreme deflection prior to a compression failure in the deck without strand fracture.

CHAPTER 11 EFFECTS OF PRE-RELEASE CRACKS ON PERFORMANCE

11.1 Introduction

This chapter presents a discussion and hypothesis regarding the affect of initial pre-release cracks observed in Girder II. The two test girders were cast on the same precasting bed such that each girder had the same initial prestress force. Accounting for the differences in mixes by using measured mechanical properties for each girder, predicted behavior was compared with measured behavior in Chapters Eight and Nine. Each girder was expected to behave relative to theoretical predictions. In comparison, Girder II was predicted to have a lower initial camber and a higher flexural cracking moment than Girder I. However, this was not the case. A difference between the girders that was not originally accounted for was the effect of pre-release cracks that occurred in Girder II. A geometric compatibility method was developed to investigate the possible effects that the pre-release cracks might have on girder performance. The method shows promising results for accurately predicting the behavior of a girder subjected to pre-release cracks.

11.1.1 Girder Behavior

As noted in Section 7.3.1, one of the two high strength prestressed concrete bridge girders studied herein developed pre-release cracks prior to strand release. Although both girders were cast on the same bed, Girder I was cast approximately 1.0 hours prior to the casting of Girder II. Girder II achieved its nominal release strength at an age of 14 hours and form removal began at 17 hours. The forms on Girder I were removed at an age of 22 hours, although Girder I did not achieve its release strength until a half hour later.

A total of 6.0 hours elapsed between the time the forms were removed from Girder II and release (2 hours for Girder I). During this time, pre-release cracks developed in Girder II (no cracking was seen in Girder I). A total of fifteen vertical cracks were observed along the length of the girder, concentrated within the middle 40% of the span length. The vertical cracks extended from the top flange toward the bottom flange.

A list of the crack locations and measured depths (from the top flange and downward) on each side of the girder was given in Table 7.2. Crack locations and average depths are summarized in Table 11.1. Eleven of the cracks extended approximately 34 in. (864 mm) deep

(nearly to the bottom flange). Four of the cracks were less than 7 in. (175 mm) deep. In addition, Figure 11.1 sketches the pre-release crack locations.

Table 11.1 Vertical Pre-release Crack Locations and Average Depths (Girder II)

Location from End II-C (ft [m])	Average Crack Depth (in. [mm])
32.8 [10.0]	37.0 [940]
34.0 [10.4]	6.75 [170]
34.2 [10.5]	36.5 [925]
39.5 [12.0]	37.5 [955]
41.0 [12.5]	4.0 [100]
54.3 [16.6]	34.5 [875]
58.7 [17.9]	4.0 [100]
59.7 [18.2]	31.0 [785]
63.0 [19.2]	28.0 [710]
65.5 [20.0]	37.0 [940]
66.0 [20.3]	3.38 [85]
69.5 [21.1]	34.8 [885]
76.3 [23.2]	40.3 [1020]
87.3 [26.6]	31.0 [785]
95.0 [28.9]	28.0 [710]

Prestressing strands were flame cut for release from the prestressing bed. Upon strand release the vertical cracks in the girder closed completely. If not for the lines drawn on Girder II to identify the initial pre-release crack locations, there was no indication the girder had been initially damaged.

11.1.2 Background of Geometric Compatibility Development

Accounting for the differences in the girder material properties and strand patterns at the end of the girders, it was anticipated that the relationship between observed behavior (camber and flexural cracking moment) and predicted behavior would be similar for Girders I and II. Camber was measured with the two test girders still on the bed, and after each girder had been lifted from the bed and immediately set back down (lift/set camber). The "true" initial camber lies between these values. Friction between the precasting bed and the girder tends to reduce the initial on-bed camber and increase the lift/set camber measurement. The predicted camber was based on

measured values of modulus of elasticity and prestressing force, and was discussed in Section 7.6 (see Tables 7.9 and 7.10). Measured and predicted camber values for each girder are re-tabulated in Table 11.2.

Table 11.2 Predicted, Measured and Expected Girder Responses

	Girder I	Girder II	Girder II *Expected*
Initial Camber, in. (mm)			
Measured on-bed camber	4.76 in. [121 mm]	3.86 in. [98 mm]	4.27 in [108 mm]
Measured lift/set camber	5.47 [139]	4.06 [103]	4.90 [125]
Average Measured Camber	*5.12 [130]*	*3.96 [101]*	4.59 [117]
Predicted Initial Camber	5.49 [139]	4.92 [125]	---
Flexural Cracking Moment, including self-weight, ft-k †			
AE Measured	4760	4390	4650
Visual Measured	5130	4600	5010
Predicted Cracking Moment	5580	5450	---
Initial Prestress Losses, %initial tensioning			
Measured Initial Losses	*15.5%*	*18.6%*	15.0%
Predicted Initial Losses	14.4%	13.9%	---

† Cracking moment includes moments due to self-weight and applied loads. Metric conversion: 1 ft-k = 1.355 kN-m.

Midspan flexural cracking moments are also listed in Table 11.1 and include moments due to the combination of self-weight and applied loads, with the self-weight moment of Girders I and II being 2570 ft-k (30,840 in-k, 3480 kN-m) and 2580 ft-k (31,000 in-k, 3500 kN-m) respectively. Measured midspan flexural cracking moments from the applied loads were obtained from acoustic emission monitoring (AE) and through visual observations, and were reported in Sections 8.3 and 9.3 (Tables 8.14 and 9.15) for the two girders (without the self-weight moment). Values for predicted flexural cracking moments were obtained from the flexural stress equation by back-calculating the applied moment needed to cause the bottom fiber to reach a cracking stress level. Assumptions included using the lower bound measured prestress losses to estimate the remaining force in the tendon, calculating the bottom fiber stress due to the prestressing and the self-weight, and using the 28-day modulus of rupture (measured from companion tests) as the cracking stress. Tables 8.15 and 9.16 list the predicted midspan flexural

cracking moments without self weight. The total flexural cracking moment in Table 11.2 includes self-weight.

Lower bound measured and predicted initial prestress losses are also summarized in Table 11.2 for the two test girders. Assumptions and methods of determining prestress losses were documented in Section 7.4 (see Table 7.5). Predicted prestress losses are listed from the '*Pbeam* Method Using Measured Properties' (Table 7.6).

Relative to Girder I, Girder II had approximately the same predicted (total) flexural cracking load; however Girder II was observed to crack at a much lower load than Girder I. Assuming the concrete stress prior to release in each girder was equal to zero, the only other known difference between the girders not taken into account in the predicted response was the presence of pre-release cracks observed in Girder II. Assuming that the relationship between measured and predicted behavior of Girder I was indicative of initially undamaged girder behavior, a calibrated expected response for Girder II was determined:

$$Expected_{II} = \frac{Measured_I}{Predicted_I} Predicted_{II}, \qquad (11.1)$$

where subscripts I and II refer to Girders I and II, respectively. This relationship was used to determine the *expected* response for Girder II had there been no pre-release cracks. The *expected* values for camber and flexural cracking load for Girder II are shown in the last column of Table 11.2. No expected values are shown for Girder I, as this was the girder data used for the calibration. As evident in the tabulation, the measured responses (camber and cracking load) of Girder II were less than the *expected* response.

Because strand release introduces large compressive stresses into the concrete, the initial pre-release cracks often close due to the prestress and girder self-weight. It has been thought that these cracks do not have an effect on girder response and in some cases the cracks are believed to undergo autogenous healing (Meichsner, 1992). In this study, a geometric compatibility theory is developed and presented which indicates pre-release crack closure may affect the stress distribution in the concrete. Figure 11.2 illustrates the stress components immediately after release in a noncomposite prestressed member with pre-release cracks. The prestress causes the bottom fiber to undergo compression while the self-weight induces tension in the bottom fiber. As release occurs, so does crack closure with the crack closing by pivoting about its tip to close. When the crack completely closes, there may be negligible stress above the crack tip, and

measurable stress below the tip. The general concept shown here for the total concrete stress distribution indicates that lower compressive stresses exist in the bottom flange of girders with pre-release cracks.

A geometric compatibility argument is presented in this chapter which describes the effect of the closure of pre-release cracks based on the strain distribution of the girder after release. The closure of the pre-release cracks causes the girder to lose some of its expected camber, and also results in lower compressive strains (and hence stresses) in the bottom fiber of the girder. This reduction in bottom fiber stresses leads to lower flexural cracking loads and lower losses in prestress than for the case of a girder without pre-release cracks.

11.2 Geometric Compatibility Theory

The following section lays out the geometry needed to predict the effect of pre-release crack closure on girder geometry, and hence the girder state of strain and stress. In order to investigate the effect of crack closure, the following simplifications were assumed:

1. the cambered shape of the girder is modeled as an arc of a circle,
2. the pre-release cracks all extend to the same depth, and
3. the pre-release cracks are evenly spaced along the beam.

After strand release, the deformation of the beam can be thought of as the superposition of two deformations: cambering of the beam due to prestressing less the self weight deflection (this results in the *expected* deformation), and bending of the beam to close the pre-release cracks. The first deformation is shown in Figure 11.3. Here the girder cambers by bending about its neutral axis at a depth z_{na}, to obtain the *expected* camber, c_e. The neutral axis length, $s_{e\text{-}na}$, is assumed to be the initial on-bed girder length prior to strand release (initially ignoring elastic shortening). Figure 11.4 shows the standard geometry for the sector and segment of a circle: θ is the central angle, c is the height of the segment, s is the arc length of the segment, and r is the radius of curvature. Applying the geometry of a sector of a circle to the girder in its expected deformation, the relationships between camber, arc length, radius of curvature and central angle can be found as

$$c_{e\text{-}na} = r_{e\text{-}na}\left(1 - \cos\frac{\theta_e}{2}\right), \tag{11.2}$$

and

$$s_{e\text{-}na} = r_{e\text{-}na}\,\theta_e, \tag{11.3}$$

where $c_{e\text{-}na}$, $r_{e\text{-}na}$, and $s_{e\text{-}na}$, are the *expected* values for the segment height (i.e., camber), radius of curvature, and the arc length for the fiber arc at the neutral axis, respectively, and θ_e is the *expected* central angle.

It can be shown that the segment height for the arc of the neutral axis, $c_{e\text{-}na}$, is approximately equal to the segment height for the arc of the bottom fiber of the girder (girder camber, c_e). From Figure 11.5 the following relationship can be obtained

$$c_{e\text{-}na} = c_e + (h - z_{na})\left[1 - \cos\frac{\theta_e}{2}\right], \tag{11.4}$$

where z_{na} is the depth of the neutral axis from the top of the girder and h is the total girder depth. Because the central angle θ is very small (i.e., 0.023 radians in this case), the last term in brackets in Eqn. (11.4) approaches zero. Hence it is a reasonable approximation that the segment height for an arc through any girder depth is equal to the *expected* camber, c_e, and in particular,

$$c_{e\text{-}na} = c_e, \tag{11.5}$$

where $c_{e\text{-}na}$ is the *expected* camber at the neutral axis depth of the uncracked girder.

The relationships given by Eqn. (11.1), (11.2) and (11.4) combine to yield a transcendental equation for θ_e in terms of $c_{e\text{-}na}$ and $s_{e\text{-}na}$, which can be solved numerically for the central angle;

$$c_{e\text{-}na} = \frac{s_{e\text{-}na}}{\theta_e}\left(1 - \cos\frac{\theta_e}{2}\right). \tag{11.6}$$

For example, the central angle, θ_e, for a girder 132 ft-9 in. (40.5 m) long with initial camber of 4.59 in. (117 mm) would be 0.023 radians. The radius of curvature can be found by inverting Eqn. (11.3),

$$r_{e\text{-}na} = \frac{s_{e\text{-}na}}{\theta_e}. \tag{11.7}$$

Once the *expected* radius of curvature and the central angle are found, the *expected* length of the top fiber of the girder, $s_{e\text{-}top}$ can be found,

$$s_{e\text{-}top} = (r_{e\text{-}na} + z_{na})\theta_e, \tag{11.8}$$

where z_{na} is the depth of the neutral axis from the top of the uncracked girder. Similarly, the length of the girder at the depth of the crack tips can be found by the following relationship,

$$s_{e\text{-}crack} = (r_{e\text{-}na} + z_{na} - z_{crack})\theta_e, \tag{11.9}$$

where z_{crack} is the depth of the crack as measured from the top of the girder.

Compression in the top fiber of the beam due to the axial prestress force and the self-weight moment causes the pre-release cracks to close by pivoting about their tips. Because the deformation involves a pivoting of the material about the crack tips, the arc length at the tip of the crack, $s_{e\text{-}crack}$, remains unchanged,

$$s_{a\text{-}crack} = s_{e\text{-}crack}, \tag{11.10}$$

where $s_{a\text{-}crack}$ is the arc length *after* crack closure at the crack tips. Henceforward, subscript a will designate the girder properties *after* pre-release crack closure.

The deformation due to crack closure is superimposed on the *expected* camber deformation. Crack closure shortens the top fiber length by the sum of the lengths of the pre-release crack openings ($\Delta_{top}=\Sigma crack\ width$) and elongates the beam bottom fiber an amount Δ_{bot}, due to pivoting about the crack tip. This deformation causes a reduction in the girder camber. The actual girder shape *after* crack closure is shown in Figure 11.6 with respect to the *expected* girder shape.

The camber measurement following closure of the pre-release cracks can be used to calculate the theoretical pre-release crack widths. By examining the change in top fiber lengths, these theoretical estimates can be compared with the measured pre-release crack widths. To support the theory for this approach, the central angle of the girder shape *after* crack closure (θ_a) is determined using the transcendental equation,

$$c_a = \frac{s_{a\text{-}crack}}{\theta_a}\left(1 - \cos\frac{\theta_a}{2}\right), \tag{11.11}$$

where c_a is the total camber after crack closure and includes the camber due to dead load, prestress, and crack closure.

The radius of curvature at the crack depth ($r_{a\text{-}crack}$) is then found,

$$r_{a\text{-}crack} = \frac{s_{a\text{-}crack}}{\theta_a}. \tag{11.12}$$

These relations are based on the assumption that the girder shape after crack closure can also be represented by the arc of a circle. Once the radius of curvature and the central angle are known, the length of the top fiber can be found,

$$s_{a\text{-}top} = (r_{a\text{-}crack} + z_{crack})\theta_a. \tag{11.13}$$

The shortening of the top arc, Δ_{top}, due to crack closure is the difference between the *expected* top fiber arc length and the top fiber arc length *after* crack closure,

$$\Delta_{top} = s_{e\text{-}top} - s_{a\text{-}top}. \tag{11.14}$$

Dividing the shortening of the top arc, Δ_{top}, by the number of cracks, theoretical pre-release crack widths can be obtained (*Theoretical crack width* = Δ_{top} / *#cracks*). Measured crack widths can then be compared with theoretical crack widths for verification of theory.

Bottom fiber elongations can be computed using two methods. Similar to the procedure given previously, the lengthening of the bottom fiber due to crack closure (Δ_{bot}), can be found. It is also possible to find the bottom fiber elongation by examining the girder end rotation. Figure 11.7 depicts the left girder end rotations due to the initial *expected* camber deformation and the *after* crack closure deformation. The vertical line represents the left girder end prior to release. At release, the girder end rotates counterclockwise about its neutral axis, resulting in the *expected* rotation. Superimposed upon this rotation is the deformation due to crack closure. The girder end rotates clockwise, pivoting about the pre-release crack tip depth to end up in the final actual position *after* crack closure. As shown in the figure, the net result of all the deformations is that the girder top fiber is rotated outward less than expected, and the girder bottom fiber is rotated inward less than expected. In fact, every fiber below the crack tip is longer than it would have been had there been no pre-release cracks. Hence, *after* crack closure, the magnitude of the actual compressive strain is less than the expected strain in fibers below the crack tip depth. The bottom fiber lengthening can be found using similar triangles,

$$\Delta_{bot} = \frac{\Delta_{top}}{z_{crack}}\left(h - z_{crack}\right), \tag{11.15}$$

where Δ_{top} was determined from Eqn. (11.13).

Once this additional lengthening of the bottom fiber is known, the decrease in compressive strain due to crack closure can be found;

$$\Delta\varepsilon_{bot} = \frac{\Delta_{bot}}{L}, \tag{11.16}$$

where L is the on-bed length of the girder, and also equal to the arc length at the depth of the neutral axis, $s_{e\text{-}na}$. This decrease in strain is an average strain reduction over the entire length of the girder, and does not consider any localized effects due to crack closure.

The method developed herein to account for the effects of geometric compatibility was applied to determine crack widths, which would account for the difference between *expected* and measured camber. Average crack openings of 0.0098 in. (0.25 mm) were obtained assuming the average depth of the eleven largest pre-release cracks to be 34 in. (864 mm), an *expected* camber (c_e) of 4.59 in. (117 mm) and a measured camber after crack closure (c_a) of 3.96 in. (101 mm). The measured crack openings were on the order of 0.010 to 0.015 in.(0.25 to 0.38 mm) from visual observations.

Finding the correlation between crack width attributed to geometric compatibility and measured crack widths to be reasonable, the implications of the pre-release crack closure effect were further examined with respect to flexural cracking moments. The initial decrease in bottom fiber strain ($\Delta\varepsilon_{bot}$ = 21.8 με less compressive) from geometric compatibility equation (11.15) indicates that it should take less load (less additional strain) to crack the girder in flexure than would be expected. This agrees with the measured flexural cracking moment of Girder II being less than the *expected* value.

The reduction in bottom fiber strain can be used to calculate the decrease in flexural cracking moment due to the closure of the pre-release cracks,

$$\Delta M = \frac{E_c I_{tr\text{-}comp} \Delta \varepsilon_{bot}}{c_{tr\text{-}comp}} \qquad (11.17)$$

where E_c is the concrete modulus of elasticity, $c_{tr\text{-}comp}$ is the distance from the composite section bottom fiber to the composite neutral axis, and $I_{tr\text{-}comp}$ is the transformed moment of inertia of the composite section. A reduction in bottom fiber strain of 21.8 με would decrease the moment required to crack the girder by 108 ft-k (147 kN-m). This change in expected moment when including geometric effects corresponds to a 2.2% reduction in total centerline moment from the expected moment without geometric effects. The difference between the measured visual cracking moment and the expected visual moment including geometric effects was 6.5% compared with a 8.9% difference between measured visual cracking moments and those expected without considering geometric compatibility. Although this value is small relative to the total cracking moment (self-weight plus applied external loading), it represents a larger change in live load carrying capacity. The change corresponds to a 19.0% reduction in applied centerline moment (live load capacity) relative to the predicted live load capacity, which is still low but in the right direction, compared to the observed difference of 30%. The theory presented

thus far averages the crack closure effect over the entire length of the girder, although as discussed later, the closure of pre-release cracks would be expected to have a localized effect.

11.3 Sensitivity Analysis

The assumptions used in the investigation of geometric compatibility for Girder II were based on "best guess" approximations for the *expected* camber (c_e), measured camber (c_a), crack depth (z_{crack}), and member length at the neutral axis depth ($s_{e\text{-}na}$) (identified as Case 1, the base case, in Table 11.3). A sensitivity analysis of the geometric compatibility theory was conducted to show the effect of reasonable variations in the assumptions on the average crack width, change in bottom fiber strain ($\Delta\varepsilon_{bot}$), and change in cracking load due to pre-release crack closure. These results are included in Table 11.3 as Cases 2-6b.

Table 11.3 Results of Geometric Compatibility Sensitivity Analysis

	Expected Camber c_e (in.)	Actual Camber c_a (in.)	Crack Depth z_{crack} (in.)	*Expected NA Length* $s_{e\text{-}na}$ (in.)	Average Crack Width (in.)	Δ % Loss	$\Delta\varepsilon_{bot}$ (με)	Decrease in Cracking Moment (ft-k)
Case 1	4.59	3.96	34.0	1593	0.0098	-0.17	21.8	108
Case 2	4.59	3.96	34.0	1592	0.0098	-0.17	21.8	108
Case 3a	4.59	3.86	34.0	1593	0.0113	-0.19	25.3	126
Case 3b	4.59	4.06	34.0	1593	0.0082	-0.14	18.4	91
Case 4	4.90	3.96	34.0	1593	0.0146	-0.25	32.6	162
Case 5a	4.59	3.96	10.0	1593	0.0029	-0.88	69.6	346
Case 5b	4.59	3.96	22.3	1593	0.0064	-0.52	45.03	224
Case 6a	4.90	3.96	10.0	1593	0.0043	-1.32	103.8	515
Case 6b	4.90	3.96	22.3	1593	0.0096	-0.77	67.2	334

Case 1: Base case using the best guess approximations for the *expected* camber (c_e), measured camber (c_a), crack depth (z_{crack}) of 34 in. with 11 cracks, and member length at the neutral axis depth ($s_{e\text{-}na}$) of 132.5 ft.

Case 2: Reduction in base case arc length (-1.0 in. [-25 mm]) to account for the change in length due to elastic shortening.

Case 3a: c_a based on the initial *measured* camber (on bed)

Case 3b: c_a based on the initial *measured* camber after girder lift/set

Case 4: Best guess c_e based on *expected* camber after girder lift/set

Case 5a: Pre-release crack depth to top of the web

Case 5b: Pre-release crack depth to the noncomposite neutral axis of the net section

Case 6a: Case 4 with pre-release crack depth to top of the web

Case 6b: Case 4 with pre-release crack depth to the neutral axis.

Beginning with the first variation of the sensitivity analysis, Case 2 shows the effect of variations in member length at the girder neutral axis. In the base case (Case 1), the neutral axis arc length was assumed equal to the initial girder length. In Case 2, the arc length was reduced by 1.0 in. (25 mm) to account for the change in member length at release due to elastic shortening. This case had a negligible effect on the results. Therefore, crack width sizes and changes in cracking moment as explained by geometric compatibility are not affected by small yet reasonable changes in the member length.

Crack widths were also predicted for other variations. Cases 3a and 3b show the effects of variations in initial measured camber (c_a) due to prestressing bed friction. Camber was measured directly off the bed after release (c_a in Case 3a) and again after the girder was lifted and set down with a crane using two pick points (Case 3b). The average of these two cambers was used for the base Case 1. Case 4 shows the effect of changes in the *expected* camber (c_e) corresponding to the *expected* 'lift/set' camber as opposed to the average of 'on-bed' and 'lift/set' for the *expected* camber. Cases 5a and 5b show the effects of variations in assumed crack depth. The base case used an average crack depth (34.0 in. [864 mm]) from the eleven largest cracks observed. This depth represents the distance from the top flange through nearly the entire web. Case 5a represents an average crack depth through the top flange (but not into the web) and Case 5b represents an average crack depth equal to the distance to the noncomposite girder neutral axis. Cases 6a and 6b represent combinations of the assumptions of Cases 4 and 5. The average pre-release crack widths at the top of the girder calculated for all cases fall within a reasonable range 0.003-0.015 in. (0.07-0.37 mm) of the observed crack widths prior to strand release (approximately 0.01 in. [0.25 mm]).

The changes in moment considering geometric effects of pre-release cracked girders are also listed in Table 11.3. Recall Case 1 represents the "best guess" values of the parameters used in the theory. Case 6b represents a reasonable upper bound for the effect of crack closure for the girder under study with respect to the best guess approximation of Case 1, by using the maximum *expected* camber after lift/set in conjunction with a crack depth equal to the distance to the neutral axis from the top fiber. The moment change considering geometric effects for Case 6b corresponds to a 6.7% reduction from the *expected* visual moment (including self-weight), compared with a 2.2% reduction for Case 1. The difference between measured visual cracking moment and the expected visual moment including the geometric effects of Case 6b was 1.7%,

compared to 6.5% for Case 1 considerations and 8.9% for the expected moment without geometric effects. This change also corresponds to a 27% reduction in live load capacity relative to the predicted live load capacity (total flexural cracking moment less the self weight moment) compared with a 30% observed difference. The sensitivity analysis is carried out further to investigate reductions in flexural cracking moments using Cases 1 and 6b of Table 11.3.

Table 11.4 shows a summary of values for average pre-release crack widths and flexural cracking moments for the predicted, measured, *expected* ignoring geometric effects, and *expected* including the geometric effects (for Cases 1 and 6b) cases. The *expected* values considering geometric effects (values after crack closure) are found by applying the change in value (from Table 11.3) to the *expected* values ignoring geometric effects (from Table 11.2). As evident from this table, as applied, the geometric effect model can nearly fully account for the differences between measured and *expected* responses of crack widths and flexural cracking moments, although initial prestress losses were still below those measured.

Table 11.4 Summary of Girder II Responses: Predicted, Measured, Expected, and Expected with geometry effects

	Average Crack Width (in.)	Flexural Cracking Moment (in-k) †		Initial Prestress Loss (%)
		AE ‡	Visual	
Measured	*0.008-0.010*	*4390*	*4600*	*18.6%*
Predicted	0.0	5450		13.9%
Expected Results: with and without Geometric Effects				
Ignoring Geometric Effects	0.0	4650	5010	15.0%
Considering Effects of Case 1	0.0098	4540	4900	14.8%
Considering Effects of Case 6b	0.0096	4320	4680	14.2%

† Flexural Cracking Moments include the self-weight plus externally applied loads.
‡ AE represents Acoustic Emission monitoring.

11.4 Localization of Crack Closure Effect

In applying the geometric effect model, the changes in strain caused by crack closure were averaged over the entire length of the girder. In reality, pre-release crack closure would be expected to cause primarily local changes in strain. Figure 11.8 illustrates this localized phenomenon. A typical crack depth and width are shown at a given location along the girder length. "Before-release" grid lines are denoted as Lines *A-O-A*, *B-B*, and *C-C*, where point *O* is the crack tip. Isolating the effect of crack closure at release from the effects of the prestress and

self-weight, gridlines "after-release" are shown to rotate due to crack closure, becoming Lines *A'-O-A'*, *B'-B'*, and *C'-C'*. Considering these 'after-release' gridlines to be symmetrical, a local strain increase can be seen directly below the crack tip at point *O*. The increase may or may not be large enough to cause cracking at the bottom fiber. Minimal localized differences in the bottom fiber strain are shown at a distance away from the crack, between, for example, points *B* and *C*, and points *B'* and *C'*.

The localized geometric effect due to pre-release crack closure would indicate that initial flexural cracks would occur below the pre-release cracks. This correlated with the initial flexural crack locations observed in the cracking load tests of Girder II which were either directly below or in the vicinity of the pre-release cracks. The location of the flexural cracks, corresponding crack names (Table 9.13) and the distance to the nearest pre-release crack are shown in Table 11.5. Also, listed is the distance to the nearest crack as a function of the girder depth, *h*. All five of the initial flexural cracks were within 0.35*h* of a pre-release crack.

Table 11.5 Initial Flexure Crack and Pre-release Crack Locations

Initial Flexural Crack Location from End C ft. (m)	Flexural Crack Name †	Distance to Nearest Pre-release Crack ‡	
		in. (m)	As a function of girder depth, *h*
53.4 (17.80)	C-BF-12	1.3 (0.40)	0.35*h*
59.7 (18.20)	C-BF-13	0.0 (0.00)	0.00*h*
60.9 (18.57)	C-BF-14	1.2 (0.37)	0.32*h*
62.2 (18.95)	C-BF-15	0.8 (0.25)	0.22*h*
63.8 (19.46)	C-BF-17	0.9 (0.26)	0.23*h*

† Crack Name corresponds to Table 9.13.
‡ Pre-release crack locations noted in Table 7.2.

As a result of the localized nature of the crack closure effect, strain changes would be much greater in the regions directly below the pre-release cracks than the averages calculated in Table 11.3. By assuming that only the area within a distance *h* of the crack (in accordance with St. Venant's Principle) undergoes a strain change, the average change in bottom fiber strain near a crack would be 70.2 με for Case 1 and 334 με for Case 6b. The localization of the strain changes reduces the *expected* cracking moments further. The reduction in cracking moments corresponding to these strains as well as the *expected* cracking moments including the localized effects are listed in Table 11.6. These values indicate that the localized nature of the geometric

effect can account for the differences between the *expected* and measured results, especially in Case 1, where this base case was derived from best-guess approximations.

Table 11.6 Crack Localization Effect on Flexural Cracking Moment

	Reduction on Flexural Cracking Moment due to Localization (ft-k) †	Flexural Cracking Moment with Localized Effect	
		AE (ft-k)	Visual (ft-k)
Measured	---	*4390*	*4600*
Expected Results with Localization Effect			
Ignoring Geometric Effects	---	4650	5010
Considering Effects of Case 1	350	4300	4660
Considering Effects of Case 6b	1075	3575	3935

† Metric Conversion: 1 ft-k = 1.355 kN-m.

11.5 Conclusion

A theory utilizing geometric compatibility was developed to investigate the effects of Girder II pre-release cracks on initial camber and flexural cracking moments. The theory was validated by comparing the theoretical pre-release crack widths to those observed in the field. Closure of the pre-release cracks causes the concrete strains below the crack tips to become less compressive, thereby initiating flexural cracking at a load lower than expected. The theory was developed assuming the crack closure effects are averaged over the length of the girder. Comparing measured camber to expected camber using the geometric compatibility theory, crack widths in the top flange were found to be within reason of those observed on Girder II. However, the pre-release crack closure is more likely to cause local changes in strain below the crack tips. The initiation of the flexural cracks in the vicinity of the pre-release cracks confirms the localized effect. The reduced flexural cracking loads may adversely affect girder performance due to reduced fatigue life (increased strand stress ranges) or reduced strand corrosion protection at the cracks. In the case of the Girder II, the reduced cracking load did not cause the strand stress range under service conditions to exceed the 20 ksi strand stress range limit suggested by Overman, Breen and Frank (1984) for cracked sections.

Pre-release cracks are likely to pose a greater problem for widely-spaced girders for which case the self-weight moment is a smaller percentage of the total moment. Widely-spaced girders tend to have higher required release strengths because of the large amount of prestressing that must be "stored" in them. These girders are more likely to remain on precasting beds for a

longer period of time prior to release to attain higher required release strengths. As a result, they have an increased likelihood of developing pre-release cracks. Also, because the live-load moment is a much larger proportion of the total moment for widely-spaced girders, the imposed live load stress ranges will be larger. In this case, the pre-release cracks may cause the flexural cracking load to be within the live-load range. This would cause much larger local stress ranges in the strands where they cross the flexural crack, perhaps causing a premature fatigue failure.

CHAPTER 12 CONCLUSIONS AND RECOMMENDATIONS

12.1 Introduction

A two phase comprehensive high performance concrete (HPC) program was developed to address bridge design issues. Results of Phase I, mechanical properties and durability of HPC, were documented by Mokhtarzadeh (1996) and Kreisel (1997). Phase II, design implications of high strength prestressed concrete bridge girders and behavior of high strength prestressed concrete bridge girders, are documented herein. Additionally, shear behavior and results of shear tests on the two high strength prestressed concrete bridge girders were reported by Cumming (1997) to complete Phase II. The primary objective of Phase II was to determine the adequacy of the present AASHTO (1996) specifications for designing prestressed concrete bridge girders in Minnesota with HPC.

The study began with an extensive parametric study to better understand limitations of using high strength concrete in Minnesota prestressed bridge girder sections. Based on the results of the parametric study, a section and reinforcement for an experimental study of long-span HPC girders was selected. Tests were conducted on two long-span Mn/DOT 45M girders, fabricated with concrete strengths in excess of 11,100 psi (77 MPa). Short term and long term behavior results are summarized in the following sections. Flexural load testing results during cyclic HS25 truck load, cyclic overloading, cracking, and ultimate load tests are reported. Finally, recommendations for designing prestressed concrete bridge girders with high strength concrete are presented.

12.2 Conclusions of the Parametric Study

The use of high strength concrete in prestressed bridge applications has many benefits. A parametric study documented in Chapter Three was performed to determine the viability of using high strength concrete for Mn/DOT prestressed girders ranging in height from 45 to 81 in. (1.1 to 2.1 m). The Mn/DOT standard during the early stages of development of this research program was to use 0.5 in. Gr. 270 ksi (12.7 mm - Gr. 1860 MPa) low relaxation strands with a maximum 28-day concrete compressive strength of 7000 psi (48 MPa).

The use of 0.6 in. Gr. 270 ksi-LL (15.2 mm - Gr. 1860 MPa) strand was found to be advantageous when considering concrete strengths above 7000 psi (48 MPa). The larger cross-sectional area per strand enabled more effective placement of the prestress force lower in the

cross section, giving way to increased maximum spans lengths. The use of larger diameter strands also permitted a reduction in the total number of required strands.

Strands of the same size but of higher strength (e.g. 300 ksi) would allow for more prestress force to be initially placed in the section, potentially increasing the maximum span length by a larger percentage. These higher strength strands may prove most effective in concrete strengths above 12,000 psi (83 MPa) with release strengths above 10,000 psi (69 MPa). However, certain practical limits must be considered, such as capacity of prestress beds and availability of jacking equipment. The remaining conclusions are drawn on the basis of using the 0.6 in. Gr. 270 ksi-LL (15.2 mm - Gr. 1860 MPa) strand.

An increase in concrete strength can allow for a significant increase in span length. Maximum spans can be increased approximately 20-35% by increasing concrete compressive strengths from 7000 to 10,000 psi (48 to 69 MPa). Higher concrete strengths (greater than 12,000 psi [86 MPa]) provide a smaller percent gain in span length, due to the limitation of number of strands (0.6 in., Gr.270k-LL [15.2 mm - Gr. 1860 MPa]) that can be placed in the section. Concrete strengths above 12,000 psi (83 MPa) showed virtually no benefit in increasing span lengths for the Mn/DOT girder sections investigated.

Increased girder spacings for a given span can also be achieved with HPC. Wider girder spacings translate to fewer required girders for a given structure (e.g., reduced fabrication, transportation, and erection costs). However, for a given span and girder spacing, increasing the concrete strength above about 10,000 psi (69 MPa) does not significantly increase the girder spacings nor reduce the number of strands required for the Minnesota bridge sections considered.

Governing stresses for girder design were investigated at maximum spans. The number of strands required usually represents both a minimum and maximum requirement due to a convergence of more than one limiting stress. Girders spaced closely (4 ft. [1.2 m]) indicate compressive stresses at final conditions govern the design. By increasing the concrete strength, the limiting stresses were changed simultaneously to tension under final service conditions and compression at the time of release at the harp points. Girders spaced wider apart (7, 10 and 12 ft. [2.1, 3.1, 3.7 m]) were typically governed simultaneously by compression at the time of release and tension under final conditions, indicating more efficient use of the section. However, governing stresses in the design of wider spaced girders were not changed by increasing the 28-day concrete strength.

Release strengths on the order of 85% of the 28-day compressive strength have been shown to be attainable (Mokhtarzadeh, 1996). Release strengths were initially limited to 10,000 psi (69 MPa), but laboratory research indicates that strengths higher than 10,000 psi can be achieved in 24 hours or less. Lifting the 10,000 psi limit affects only girders with 28-day compressive strengths above 11,775 psi (81 MPa). It was found that only a slight benefit in increased span was achieved when f'_c > 10,000 psi (69 MPa), and no benefit was seen for f'_c > 12,000 psi (83 MPa). Therefore limiting the release strength to 10,000 psi (69 MPa) when designing Mn/DOT girders seems reasonable.

12.3 Conclusions from the Full Size High-Strength Prestressed Concrete Girders Tests

Two long-span prestressed concrete bridge girders were fabricated with high strength concrete and monitored for behavior. The 132.5 ft. (40 m) girders were Minnesota Type 45M, 45 in. (1140 mm) deep with a 6.0 in. (150 mm) thick web. No end blocks were specified. The 4 ft. (1.2 m) wide composite deck was 9 in. (230 mm) deep with a standard 1.0 in. (25 mm) haunch. Each girder was designed according to AASHTO Standards (1993) and Mn/DOT guidelines (1991). Prestressing reinforcement comprised forty-six 0.6 in. (15.2 mm) Gr. 270 low-relaxation prestressing strands on 2 in. (50 mm) centers. Nominal compressive strengths at release and 28-days were specified to be 8925 and 10,500 psi (62 and 73 MPa), respectively. A normal strength concrete deck was specified to have a 28-day compressive strength of 4000 psi (27.6 MPa), as was typically specified in Minnesota. The girders were tested to investigate short-term and long-term behavior, including prestress losses and camber, cracking loads, response to repeated service loading and overload conditions, and ultimate flexural strength testing.

AASHTO design equations are based on normal strength concrete (NSC) data and nominal design properties. High strength concrete (HSC) properties must be considered to determine their effect on design. Therefore, two issues regarding actual material properties must be addressed. First, how well does using nominal compressive strength correlate with AASHTO design assumptions and relate to actual girder behavior, and second how well do AASHTO models using measured properties predict behavior compared to those predicted using HSC models.

From this study it was found that high strength concrete with compressive strengths above 10,000 psi (69 MPa) could be produced by precasters using regionally available materials. Concrete compressive strengths at 28-days were measured as 12,100 and 11,100 psi (83 and 77 MPa) from companion cylinder tests for Girder I (limestone mix) and Girder II (glacial gravel with microsilica mix), respectively. However, special attention to both material selection and production quality control was required. More stringent quality control procedures may be required than what fabricators are currently accustomed to using.

In addition to the 28-day compressive strength, measured concrete material properties for the girder specimens included initial compressive strength (correlating to the time of release), compressive strengths at 7, 200, and 480 days, initial and 28-day elastic moduli, 28-day modulus of rupture and split tensile tests, and creep and shrinkage for a one year period. Conclusions from material test results are discussed in the context of their effect on prestressed girder design and behavior.

Based on initial and 28-day compressive strength measurements, the ACI 209 (1992) age function for NSC was not accurate. HSC age functions presented by Mokhtarzadeh (1996) correlated well with measured compressive strengths over time and the general rule of thumb that HSC reaches 85% of its 28-day strength in one day (corresponding to release) was adequate. It is imperative to correctly predict the early age strength of a prestressed girder so that release can occur in a timely fashion and cracking at the time of release is avoided.

Modulus of elasticity, E_c, for high strength concrete can vary widely depending on aggregate, cement type, water-cement ratio and curing conditions (Mokhtarzadeh, 1996). The current AASHTO and ACI code equation overpredicts E_c for concrete strengths above 6000-7000 psi (41 to 48 MPa), (Castrodale, 1988b). The ACI 363 (1984) and Mokhtarzadeh (1996) HSC relationships also overpredicted the initial and 28-day moduli of each girder, although the 28-day measured concrete modulus was within the range of data scatter used in developing the HSC relationships.

Lower bound measured early age prestress losses due to elastic shortening and relaxation for Girders I and II were 15.5% and 18.6%, respectively, assuming the concrete stress prior to release was zero. Upper bound initial losses of 25.9% and 29.3% were measured for the two respective girders assuming the maximum concrete stress prior to release was equal to the 28-day modulus of rupture. Initial losses based on nominal properties and NSC relationships predicted

by several methods, including AASHTO (1996), PCI Design Handbook (1992), PCI Committee on Prestress Losses (1975) and the modified Naaman Time-Step Method (Table 7.5), were less than lower bound measured initial losses. Predictive methods assume the concrete stress prior to release is equal to zero. However, tension does exist due to restrained shrinkage and thermal effects resulting from the differences in coefficient of thermal expansion of the steel strand and surrounding concrete.

The effect of using E_c as developed for HSC as opposed to NSC can lead to more accurate loss predictions. Using an overpredicted E_c from AASHTO (1996) or ACI 318 (1995) resulted in a lower change in strand stress due to elastic shortening, i.e., a lower predicted loss than when using more accurate values of E_c. By using an E_c that is lower, as predicted by HSC relationships, the elastic shortening loss is higher and more representative of actual conditions. Predicted initial losses using HSC nominal properties in conjunction with the modified Time-Step Method (Table 7.5) were much closer to the lower bound measured initial losses. Predictions were closest to lower bound measured initial losses when using measured material properties (Table 7.6). Therefore, current code expressions for the modulus of elasticity based on NSC are not sufficient for accurate design of HSC girders.

Lower bound measured long-term prestress losses in the girders were presented in Table 7.5 and compared with predictions by several methods, including AASHTO (1996), PCI Design Handbook (1992), PCI Committee on Prestress Losses (1975) and the modified Naaman Time-Step Method, based on nominal properties and NSC relationships. In all cases, predicted losses were higher than lower bound measured losses after 28-days. It is concluded that the NSC provisions for creep and shrinkage losses are overly conservative for high strength concrete such as that used in the test girders. Measured creep and shrinkage deformations from companion HSC concrete cylinders supported this conclusion. Predicted prestress losses using measured creep and shrinkage properties (Table 7.6) better correlated with the lower bound measured losses.

Differences in measured prestress losses as determined by two methods at the time of flexural crack testing were observed. Losses measured by the embedded vibrating wire strain gages were compared with losses computed from the known cracking loads. Cracking loads were used to determine the strand force at the time of cracking, and hence the prestress loss, whereas crack reopening was determined from gages placed directly over cracks to precisely

determine when bottom fiber concrete tensile strains reached zero. Using this method, losses were 7.7% and 12.0% higher than lower bound losses determined from strain gages for Girders I and II, respectively (Tables 8.17 and 9.17). It was believed that the concrete stress prior to release was non-zero and tensile as explained earlier. Because the value of the concrete stress prior to release was not known, losses determined from cracking tests were most accurate. It was shown that reasonable assumptions of the concrete stress prior to release resulted in losses similar to those determined from crack tests.

AASHTO limit states implemented to avoid cracking of the girder at release and under service conditions based on the modulus of rupture cracking strength of the concrete were found to be conservative. Measured cracking strengths of companion modulus of rupture beams were significantly higher than those predicted by AASHTO (1996) and ACI 318 (1995), and were nearly equal to cracking strengths predicted by ACI 363 (1984) for HSC.

Transfer lengths interpreted from strain readings from all girder ends were consistently less (by approximately 20%) than the transfer length predicted by the AASHTO and ACI relationships. The current FHWA recommended transfer length for 0.6 in. (15.2 mm)-diameter Gr. 270 low-relaxation strands placed on 2 in. (50 mm) centers (Buckner, 1995) also over predicted transfer length by 25%. Therefore, the current transfer length design relationships are conservative.

Behavior of the test girders during transportation and handling was satisfactory. No damage was induced to the girders, and stability provisions according to the PCI Design Handbook (1992) were suitable for the long-span girders with a span length-to-depth ratio of 35.4.

The static response of the girders to design truck loading was favorable. Serviceability testing under HS25 truck and overload (125% HS25) testing showed no stiffness degradation in either girder after being subjected to 1 million cycles in the uncracked state. Static truck load tests conducted after flexural crack testing also showed no effect on girder stiffness at the HS25 and overload levels. These load levels were both less than the visual crack reopening loads for Girder I, but slightly within the service range as detected by crack width gages. Although Girder II flexural cracks appeared to reopen within the service load range, the moment-deflection response and hence stiffness were not affected. Load-deflection response to simulated truck load and overload testing was predictable. The test girders withstood 2.4 to 3.2 million cycles of service overload level loading without failure of serviceability requirements. Both girders

responded with load-to-deflection (L/d) ratios greater than anticipated and well over the rule-of-thumb guideline of $(L/d)_{min} = 800$.

Girder camber (deflection) measurements, made under various serviceability loading conditions up to and including the design service load and an overload condition 25% higher, were reasonably consistent with deflections calculated using "conventional" methods. However, both girders showed a creeping downward deflection during fatigue testing. Camber recovery was seen in both girders after cyclic loading stopped and prior to ultimate flexural failure testing. Measured initial camber for Girder I was well predicted using measured material properties and accounting for the transfer length of the prestress force (Moment-Area Method, Table 7.10). Using measured properties and without the inclusion of transfer length, the PCI Multiplier Method (PCI Design Handbook, 1992) overpredicted camber to a slight degree. Camber predictions based on NSC relationships as a nominal design case were unacceptably low relative to measured, which was a direct effect of the NSC overprediction of concrete modulus. Long term predictions of camber were most accurate when predicted using the *Pbeam* program with measured properties. Camber measurements for Girder II were influenced by pre-release cracking.

It was anticipated that the relationship between the observed and predicted behavior would be similar for both girders. Accounting for the differences in material properties and reinforcing detail, the two girders behaved quite differently when compared to their predicted responses. Girder II had a higher predicted cracking load than Girder I, yet it was observed to crack at a much lower load. Even when the influence of concrete stresses in the girder prior to release was considered, measured upper bound long term losses for Girder II fell short of predictions. Geometric compatibility was used to investigate the effects of the top flange pre-release cracks observed in Girder II on initial camber, initial prestress losses and flexural cracking loads. Comparing measured camber to expected camber using geometric compatibility, crack widths in the top flange were found to be within reason of those observed. Pre-release crack closure was shown to cause concrete strains in the vicinity below the crack tips to become less compressive, thereby causing flexural cracking to initiate at a lower than expected load for Girder II.

The ultimate flexural strengths observed in the study correlated well with the capacities assuming Whitney rectangular stress block assumptions because the normal strength concrete deck was the limiting factor of ultimate strength predictions. The normal strength concrete of the

composite decks eventually precipitated explosive compression failures at the peak flexural loads as expected. The equations in the AASHTO Specifications (1996) for calculating ultimate flexural capacity provide a conservative prediction of ultimate strength when using both nominal and measured material properties by underestimating the capacities. The ultimate flexural capacity of each girder was 2.0% higher than AASHTO and ACI predictions when using measured properties. Again the importance of knowing actual material properties was acknowledged as nominal design properties conservatively underestimated the ultimate strength by 13% for Girder I and 12% for Girder II. The reduced stiffnesses of 24% and 22.3% for Girders I and II, respectively, above the cracking loads correlated well with the recommended reduced stiffness of 20% (Castrodale, 1988b) used for estimating deflections.

12.4 Recommendations

In any experimental program involving a very limited number of tests, it is difficult to draw universal recommendations. However, for the type of girder widely used in the State of Minnesota, when used in conjunction with high strength concrete, the following recommendations seem justified.

1. Current AASHTO design guidelines should be used with great caution when designing high strength concrete prestressed bridge girders. Relationships should be modified to reflect high strength concrete material properties. ACI 363 (1984) predicted modulus of elasticity, creep and shrinkage well.

2. The importance of tight quality control required to manufacture high strength concrete must be understood by fabricators if successful production of high strength concrete prestressed concrete members is anticipated. Precasters should use care in producing concrete strength equal to the specified nominal concrete strength.

3. Concrete with strengths up to 12,000 psi (83 MPa) should be considered for use in prestressed concrete bridge girders by the Minnesota Department of Transportation. Monitoring of such bridges should be performed to determine initial and long term behavior.

4. Further investigation into the level of concrete stress that exists in the girder prior to release is necessary. Methods for predicting prestress losses need to account for concrete stresses in the girder prior to release for accuracy.

5. Further investigation of the effect of pre-release cracks on girder behavior should be considered. Girder fabrication should continue to be monitored for pre-release cracks when using all concrete strengths such that long term observations of in-field conditions can be made.

REFERENCES

ACI Committee 209 (1992). "Prediction of Creep, Shrinkage, and Temperature Effects in Concrete." *ACI SP-27: Designing for the Effects of Creep, Shrinkage, and Temperature in Concrete Structures*, American Concrete Institute (ACI), Detroit, Michigan, 51-93.

ACI Committee 215 (1992). ACI 215R-74/92 "Consideration for Design of Concrete Structures Subjected to Fatigue Loading." *ACI Journal*, 71(3), March, 97-121.

ACI Committee 318 (1995). "Building Code Requirements for Reinforced Concrete and Commentary." *ACI 318-95.* American Concrete Institute (ACI), Detroit, Michigan.

ACI Committee 363 (1984). "State-of-the-Art Report on High-Strength Concrete." *ACI Journal*, 81(4), July-Aug., 364-411.

Adelman, D. and Cousins, T. E. (1981). "Evaluation of the Use of High Strength Concrete Bridge Girders in Louisiana." *PCI Journal*, 35(5), Sept.-Oct., 70-78.

Ahmad, S. H., and Shah, S. P. (1985). "Structural Properties of High Strength Concrete and its Implications for Precast Prestressed Concrete." *PCI Journal*, 30(6), Nov.-Dec., 92-119.

American Association of State Highway Transportation Officials (AASHTO) (1993, 1996). *Standard Specifications for Highway Bridges, 15th Edition*, Washington, D. C.

American Standard for Testing and Materials (1995). *Annual Book of ASTM Standards.* ASTM C 39-94, Test Method for Compressive Strength of Cylindrical Concrete Specimen

ASTM C 78-94, Test Method for Flexural Strength of Concrete (Using Simple Beam with Third-Point Loading)

ASTM C 143-90a, Test Method for Slump of Hydraulic Cement Concrete

ASTM C 192-90a, Practice for Making and Curing Concrete Test Specimens in a Laboratory

ASTM C 231-91b, Test Method for Air Content of Freshly Mixed Concrete by the Pressure Method

ASTM C 469-94, Test Method for Static Modulus of Elasticity and Poisson's Ratio of Concrete in Compression

ASTM C 496-90, Test Method for Splitting Tensile Strength of Cylindrical Concrete Specimens

Anderson, A. R. (1971a). "Lateral Stability of Long Prestressed Concrete Beams." Reader's Comments by Swann, R. A., *PCI Journal*, 16(6), Nov.-Dec., 85-87.

Anderson, A. R. (1971b). "Lateral Stability of Long Prestressed Concrete Beams." *PCI Journal*, 16(3), May-June, 7-9.

Branson, D. E., and Christiason, M. L. (1971). "Time Dependent Concrete Properties Related to Design - Strength and Elastic Properties, Creep, and Shrinkage." *ACI SP-27: Designing for the Effects of Creep, Shrinkage, and Temperature in Concrete Structures*, American Concrete Institute (ACI), Detroit, Michigan, 257-277.

Branson, D. E., and Kripanarayanan, K. M. (1971). "Loss of Prestress, Camber and Deflection of Non-Composite and Composite Prestressed Concrete Structures." *PCI Journal*, 16(5), Sept.-Oct., 22-52.

Breen, John E. (1990). "Prestressed Concrete: The State of the Art in North America." *PCI Journal*, 35(6), Nov.-Dec., 62-67.

Bruce, R. N., Martin, B. T., Russell, H. G., and Roller, J. J. (1994). Feasibility Evaluation of Utilizing High-Strength Concrete in Design and Construction of Highway Bridge Structures. Report FHWA-LA-94-282, Louisiana Transportation Research Center, January.

Buckner, C. D. (1995). "A Review of Strand Development Length for Pretensioned Concrete Members." *PCI Journal*, 40(2), May-June, 84-99.

Buckner, C. D. (1994). An Analysis of Transfer and Development Lengths in Pretensioned Concrete Structures. Report No. FHWA-RD-94-049, Federal Highway Administration, Washington, D. C., December.

Burgess, A. J., Ryell, J., and Bunting, J. (1970). "High Strength Concrete for the Willows Bridge." *Journal of the American Concrete Institute*, Proceedings, 67(8), August, 611-619.

Carpenter, J. E. (1980). "Applications of High Strength Concrete for Highway Bridges," *Public Roads*, 44(2), September, 76-83.

Carrasquillo, R. L., Nilson, A. H., and Slate, F. O., (1981). "Properties of High Strength Concrete Subjected to Short-Term Loads." *ACI Journal, Proceedings*, 78(3), May-June. 171—178. Discussion. *ACI Journal*, 79(2), Mar.-Apr., 162—163.

Castrodale, R. W., Kreger, M. E., and Burns, N. H. (1988a). A Study of Pretensioned High Strength Concrete Girders in Composite Highway Bridges - Laboratory Tests, Research Report 381-3, Center for Transportation Research, University of Texas at Austin.

Castrodale, R. W., Kreger, M. E., and Burns, N. H. (1988b). A Study of Pretensioned High Strength Concrete Girders in Composite Highway Bridges - Design Considerations, Research Report 381-4F, Center for Transportation Research, University of Texas at Austin.

Collins, M. P., and Mitchell, D. (1991). *Prestressed Concrete Structures*, Prentice Hall.

Cousins, T. E., Stallings, J. M. and Simmons, M. B. (1993). Effect of Strand Spacing on Development Length of Prestressing Strand, Final Report submitted to the Alaska Department of Transportation and Public Facilities, Juneau, Alaska, August.

Cumming, D. (1997). "Shear Capacity of High Strength Prestressed Concrete Bridge Girders." Thesis, Master of Science, Department of Civil Engineering, University of Minnesota.

Deatherage, H. J. and Burdette, E. G. (1991). Development Length and Lateral Spacing Requirements of Prestressing Strands for Prestressed Concrete Bridge Products, Transportation Center, University of Tennessee, Knoxville, February.

Dunker, K. F., and Rabbat, B. G. (1990a). "Highway Bridge Type and Performance Patterns." *Concrete International*, 12(8), August, 40-43.

Dunker, K. F., and Rabbat, B. G. (1990b). "Highway Bridge Type and Performance Patterns." *ASCE Journal of Performance of Constructed Facilities*, 4(3), August, 161-173.

Federal Highway Administration (FHWA) (1988). "Prestressing Strand for Pretension Applications - Development Length Revisited." Memorandum, Chief, Bridge Division, Washington D. C., October 26.

Frost, R. J. (1997). "Rational Development of Release Strength Criteria." Thesis, Master of Engineering in Engineering Science, School of Science, Engineering and Technology, Penn State Harrisburg, June.

Ghali, Amin. (1991). "Stress and Strain Analysis in Prestressed Concrete—A Critical Review." *PCI Journal*, Jan.-Feb., 100—105.

Godfrey, K. A. Jr. (1987). "Concrete Strength Record Jumps 36%." *Civil Engineering*, 57(10), October, 82-88.

Hartmann, D. L., Breen, J. E. and Kreger, M. E. (1988). Shear Capacity of High Strength Prestressed Concrete Girders, Research Report 381-2, Center for Transportation Research, University of Texas at Austin.

Hognestad, E., Hanson, N. W., and McHenry, D. (1955). "Concrete Stress Distribution in Ultimate Strength Design." *Journal of the American Concrete Institute*, 27(4), December, 455-479.

Imper, R. R., and Laszlo, G. (1987). "Handling and Shipping of Long Span Bridge Beams." *PCI Journal*, 32(6), Nov.-Dec., 86-101.

Jobse, H. J. (1987). Applications of High Strength Concrete for Highway Bridges, Executive Summary, Concrete Technology Corporation, FHWA/RD-87/079.

Jobse, H. J., and Moustafa, E. S. (1984). "Applications of High Strength Concrete for Highway Bridges." *PCI Journal,* 29(3), May-June, 44-73.

Kannel, J., French, C., and Stolarski, H. (1997a). "Release Methodology of Strands to Reduce End Cracking in Pretension Concrete Girders." *PCI Journal*, 42(1), Jan.-Feb., 42-54.

Kannel, J., French, C., and Stolarski, H. (1997b). Comments by William L. Gamble and Authors. "Release Methodology of Strands to Reduce End Cracking in Pretension Concrete Girders." *PCI Journal*, 42(4), July-Aug., 102-108.

Kelly, D. J., Bradberry, T. E., and Breen, J. E. (1988). Time-Dependent Deflections of Prestressed I-Beams. Research Report 381-1, Center for Transportation Research, University of Texas at Austin.

Kielb, J. A. (1994). "Instrumentation and Fabrication of Two High Strength Concrete Prestressed Bridge Girders." Thesis, Master of Science in Engineering, Department of Civil Engineering, University of Minnesota, December.

Klieger, P. (1957). "Early High-Strength Concrete for Prestressing." *Proceedings*, World Conference on Prestressed Concrete, San Francisco, CA, July, pp. A5.1-A5.14.

Kreisel, R. (1996). "Durability of Non-air-entrained High Strength Concrete." Thesis, Master of Science in Engineering, Department of Civil Engineering, University of Minnesota.

Leap Software (1990). SPAN, Simple-Span Pretensioned Concrete Bridge Girder Design. Ver. 5.0, LEAP Software Inc., Tampa, FL.

Libby, J. R. (1990). *Modern Prestressed Concrete, Design Principles and Construction Methods*, Fourth Edition, Van Nostrand Rienhold, New York.

Lin, T. Y. and Burns, N. H. (1981). *Design of Prestressed Concrete Structures*, Third Edition, John Wiley and Sons, New York.

Magura D. D., Sozen, M. A., and Siess, C. P. (1964). "A Study of Stress Relaxation in Prestressing Reinforcement." *PCI Journal*, 9(2), April, 13-57.

Martin, L. D. and Scott, N. L. (1976). "Development of Prestressing Strand in Pretensioned Members." *ACI Journal*, 73(8), August, 453-456.

Martin, L. D. (1977). "A Rational Method for Estimating Camber and Deflection of Precast Prestressed Members." *PCI Journal*, 22(1), Jan.-Feb., 100-108.

Mast, R. F. (1989). "Lateral Stability of Long Prestressed Concrete Beams, Part 1." *PCI Journal*, 34(1), Jan.-Feb., 34-53.

McNeely, D. J. and Lash, S. D. (1963). "Tensile Strength of Concrete," *ACI Journal, Proceedings*, 60(6), June, 751-761.

Minnesota Department of Transportation Standard Specification for Construction, State of Minnesota, St. Paul, MN, 1988 Edition.

Minnesota Department of Transportation Bridge Details Manual, St. Paul, MN, 1991 Update.

Minnesota Department of Transportation Bridge Design Manual, St. Paul, MN, 1991 Update.

Minnesota Department of Transportation Bridge Standard Plans Manual, St. Paul, MN, 1991 Update.

Mitchell, D., W. D. Cook, A. A. Khan, and T. Tham (1993). "Influence of High Strength Concrete on Transfer and Development Length of Pretensioned Strand." *PCI Journal*, 38(3), May-June, 55-66.

Mokhtarzadeh, A. (1996). "Mechanical Properties of High Strength Concrete." Ph.D. Dissertation, Department of Civil Engineering, University of Minnesota.

Naaman, A. E. (1982). *Prestressed Concrete Analysis and Design, Fundamentals*, McGraw-Hill.

Nawy, E. G. (1996). *Prestressed Concrete, A Fundamental Approach*, Second Edition, Prentice Hall.

Nilson, A. H. (1987). *Design of Prestressed Concrete*, 2nd edition, John Wiley and Sons, New York.

Nilson, A. H. (1985). "Design Implications of Current Research of High-Strength Concrete." *High Strength Concrete, SP-87*, American Concrete Institute, Detroit, p.85-118.

Overman, T. R., Breen, J. E., and Frank, K. H. (1984). Fatigue Behavior of Pretensioned Concrete Girders. Research Report 300-2F, Center for Transportation Research, The University of Texas at Austin.

Paulson, C. Jr., Frank, K. H. and Breen, J. E. (1983). A Fatigue Study of Prestressing Strand. Research Report 300-1, Center for Transportation Research, University of Texas at Austin.

Pauw, A. (1960). "Static Modulus of Elasticity of Concrete as Affected by Density." *ACI Journal*, 32(6), Dec., 679-687.

PCI Committee on Prestress Losses, H. Kent Preston, Chairman. (1975). "Recommendations for Estimating Prestress Losses." *PCI Journal*, 20(4), July-Aug. 44-75.

PCI Design Handbook - Precast and Prestressed Concrete, 4th Edition. (1992). Prestressed Concrete Institute (PCI), Chicago, IL.

Perenchio, W. F. and Klieger, P. (1978). Some Physical Properties of High-Strength Concrete. *Research and Development Bulletin, RD056.01T*, Portland Cement Association.

Power, J. O. (1989). "Readers Comments, Lateral Stability of Long Prestressed Concrete Beams, Part 1, by R. F. Mast." *PCI Journal*, 34(6), Nov.-Dec., 143.

Preston, H. K. (1990). "Handling Prestressed Concrete Strand." *PCI Journal*, 35(6), Nov.-Dec.

Rabbat, B. G., and Russell, H. G. (1982). "Optimized Sections for Precast Prestressed Bridge Girders." *PCI Journal*, 27(4), July-Aug., 88-104.

Raphael, J. M. (1984). "Tensile Strength of Concrete." *ACI Journal*, 18(2), Mar.-Apr., 158-165.

Reese, G. A., (1983). "Fatigue Strength of Prestressed Concrete Girders." Thesis, Master of Science in Engineering, University of Texas at Austin, August.

Russell, B. W. and Burns, N. H. (1993). Design Guidelines for Transfer, Development, and Debonding of Seven Wire Strand in Pretensioned Concrete Girders. Research Report 1210-5F. Center for Transportation Research, University of Texas at Austin.

SAS Institute Inc. (1993). SAS/STAT User's Guide. Version 6, SAS Institute Inc., Cary, North Carolina, 1028 pp.

Shah, S.P. and Ahmad, S.H. (1985). "Structural Properties of High Strength Concrete and its Implications for Precast Prestressed Concrete." *PCI Journal*, 30(6), Nov.-Dec., 92-119.

Suttikan, C. (1978). "A Generalized Solution for Time Dependent Response and Strength of Non-Composite and Composite Prestressed Concrete Beams." Ph.D. Dissertation, University of Texas at Austin, August.

Timoshenko, S. P., and Gere, J. M. (1961). *Theory of Elastic Stability*, Second Edition, McGraw-Hill.

Towles, Thomas T. (1932). "Advantages in the Use of High Strength Concrete." *ACI Journal Proceedings*, 28(9), May, 607-612.

Woolf D. (1995). "Determination of Camber for Prestressed Bridge Girders." Thesis, Department of Civil Engineering, University of Minnesota, December.

Wee, T.H., Chin, M.S., and Mansur, M.A. (1996). "Stress-Strain Relationship of High-Strength Concrete in Compression." *Journal of Materials in Civil Engineering,* 8(2), May, 70-76.

FIGURES

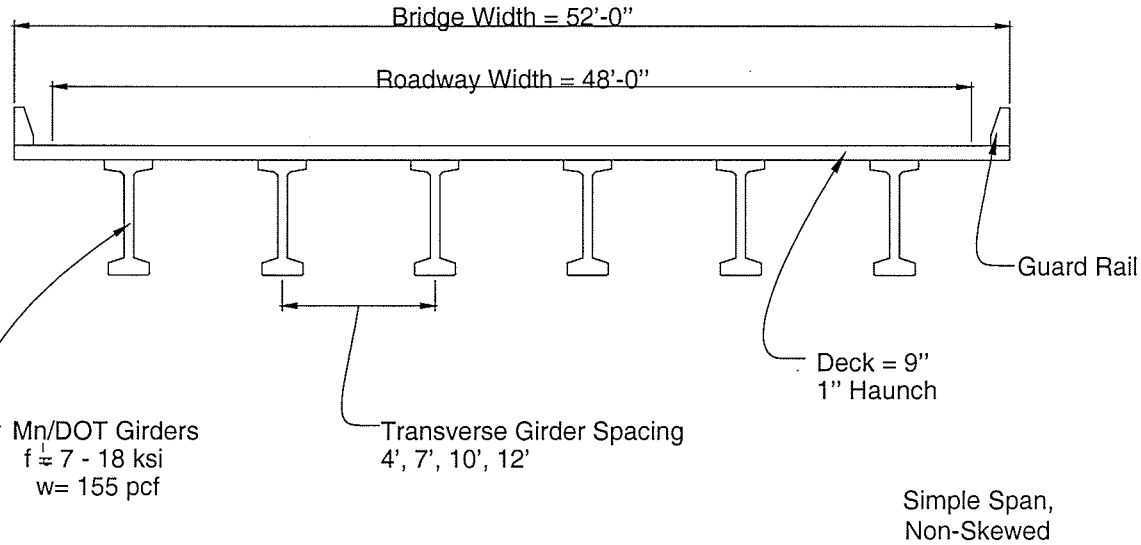

Figure 3.1 Typical Bridge Cross Section

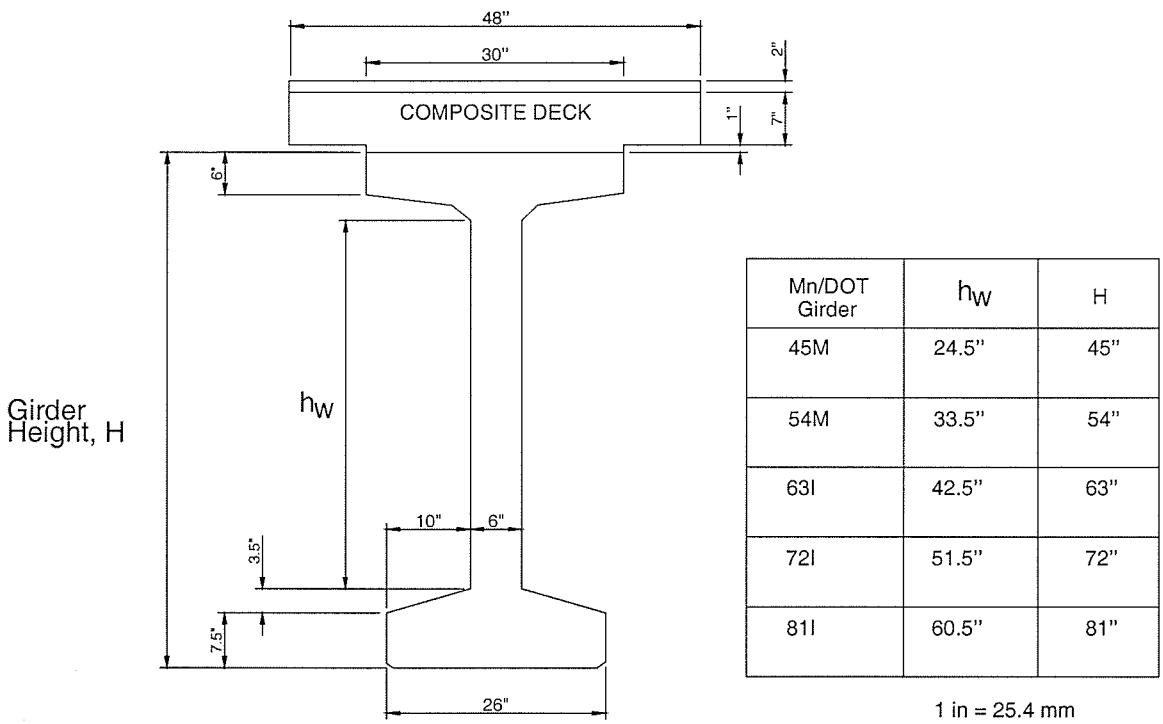

Mn/DOT Girder	h_W	H
45M	24.5"	45"
54M	33.5"	54"
63I	42.5"	63"
72I	51.5"	72"
81I	60.5"	81"

1 in = 25.4 mm

Figure 3.2 Typical Mn/DOT Girder Cross Section

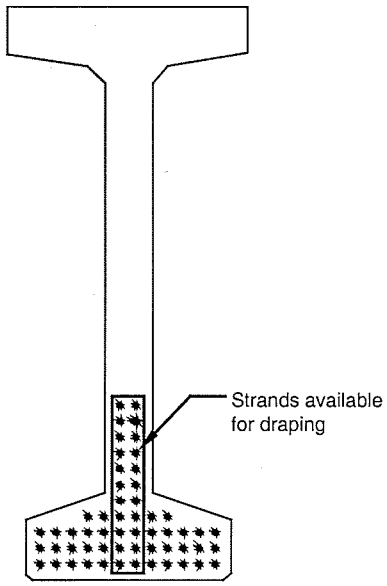

Typical Strand Pattern
Between Drape Points
(a)

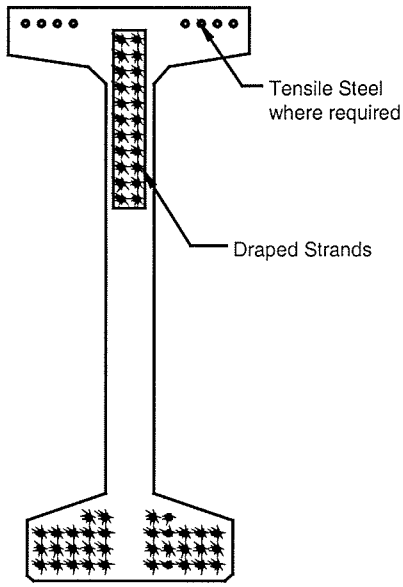

Typical Strand Pattern At End
With Web Strands Draped
(b)

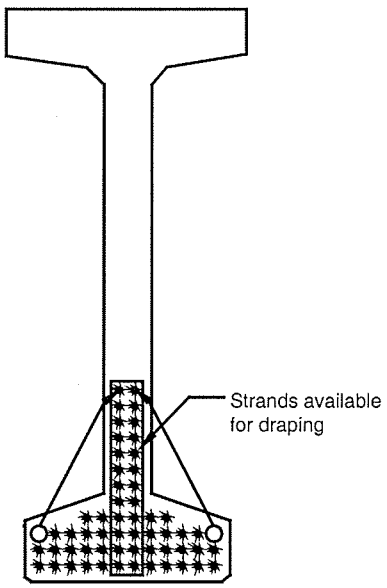

Strand Pattern Varied To
Use More Draped Strands
(c)

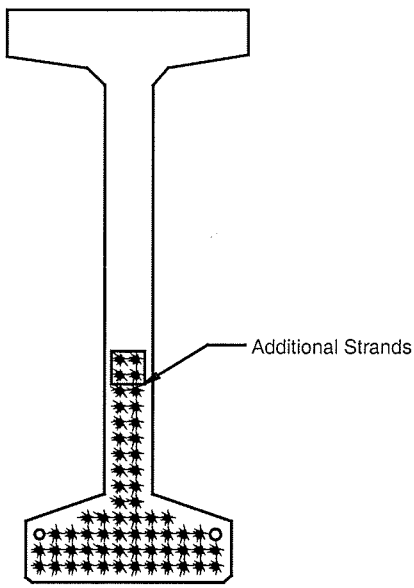

Additional Strands Placed
In Web
(d)

Figure 3.3 Methodology of Strand Placement

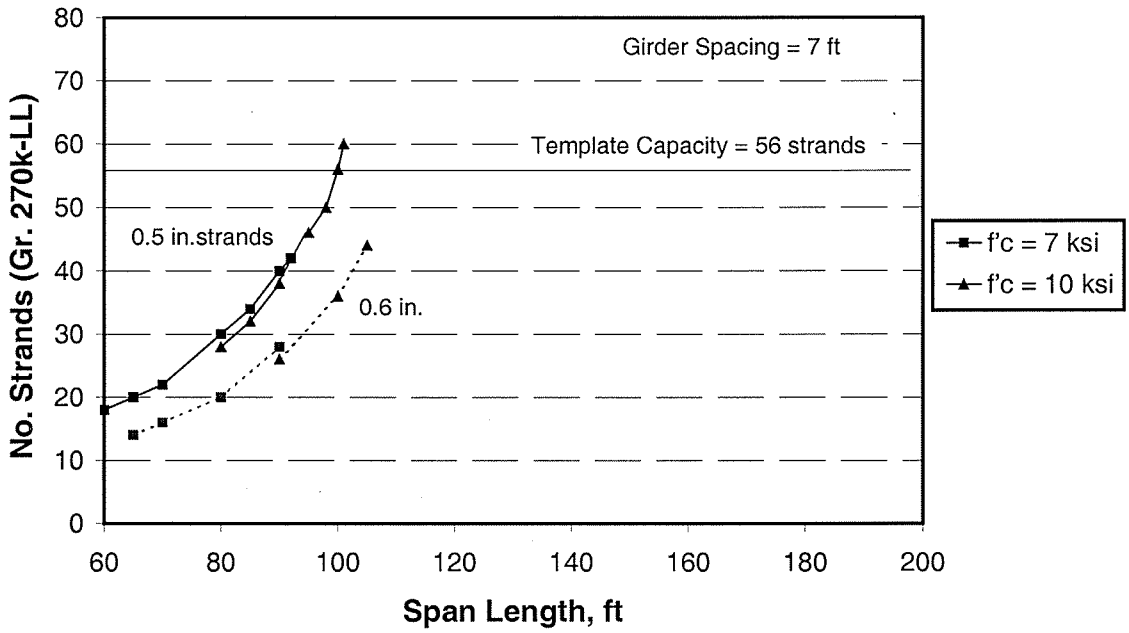

Figure 3.4a Effect of Concrete Strength on Strand Size, Mn/DOT 45M Girders

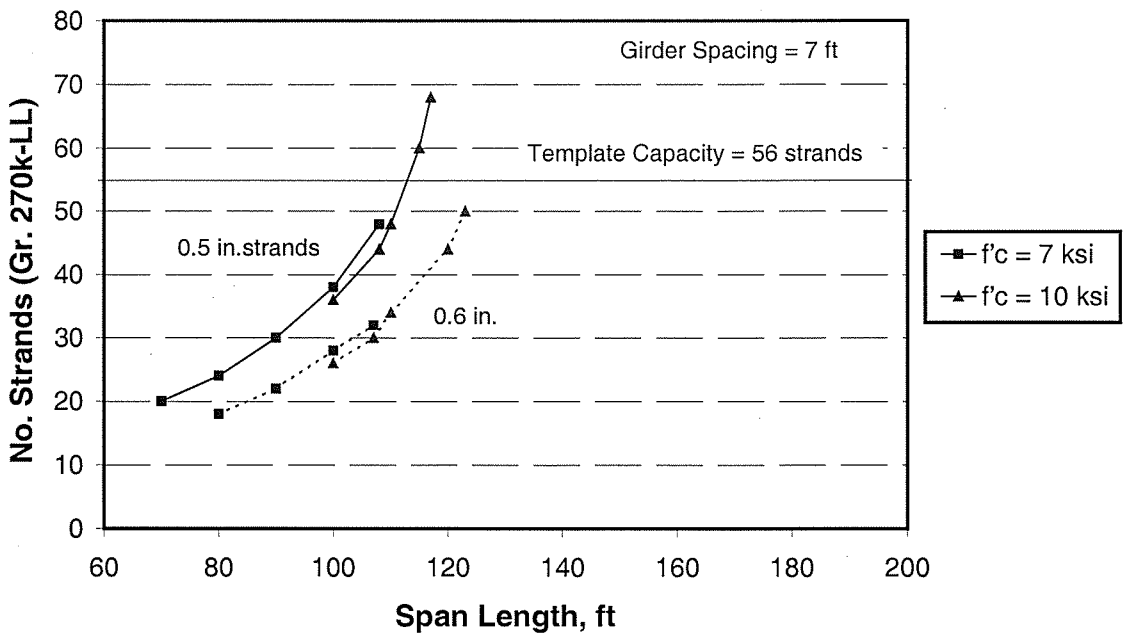

Figure 3.4b Effect of Concrete Strength on Strand Size, Mn/DOT 54M Girders

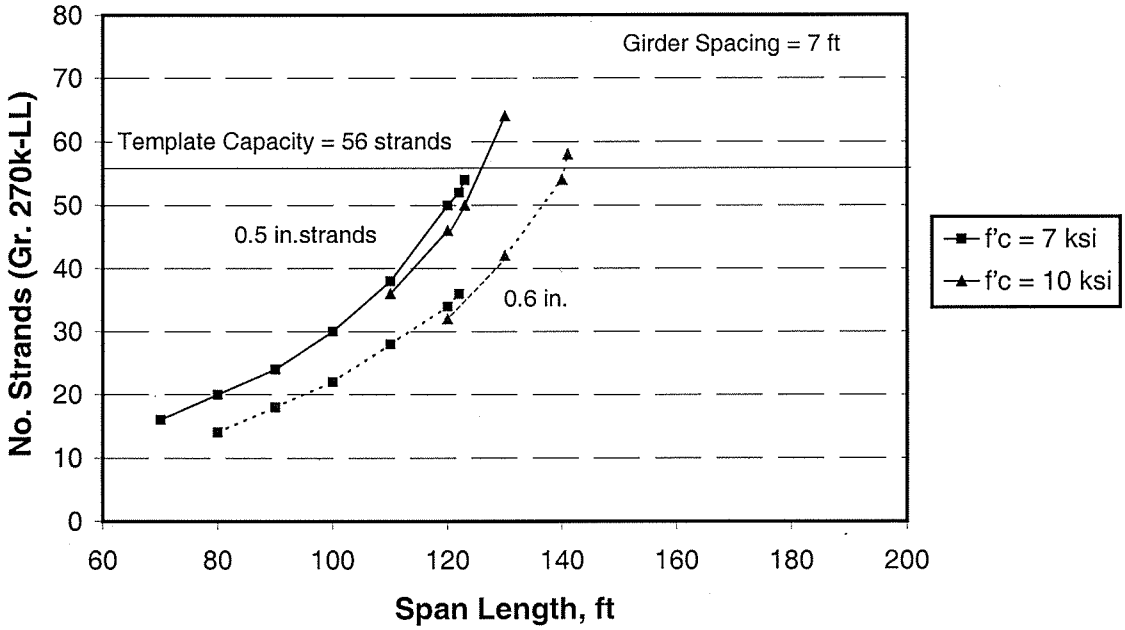

Figure 3.4c Effect of Concrete Strength on Strand Size, Mn/DOT 63I Girders

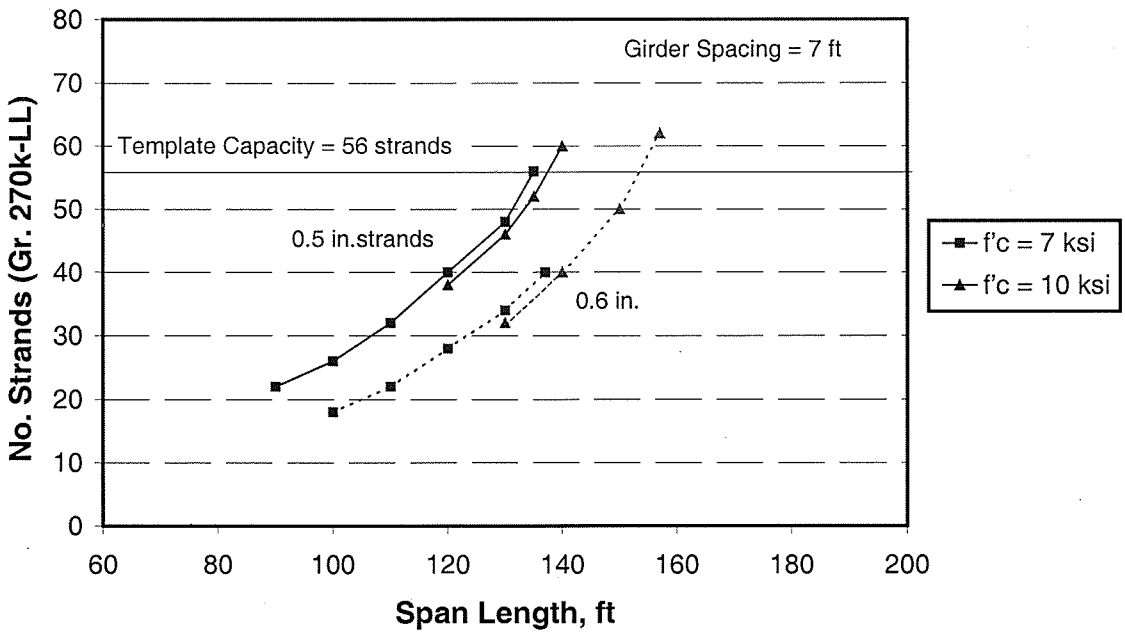

Figure 3.4d Effect of Concrete Strength on Strand Size, Mn/DOT 72I Girders

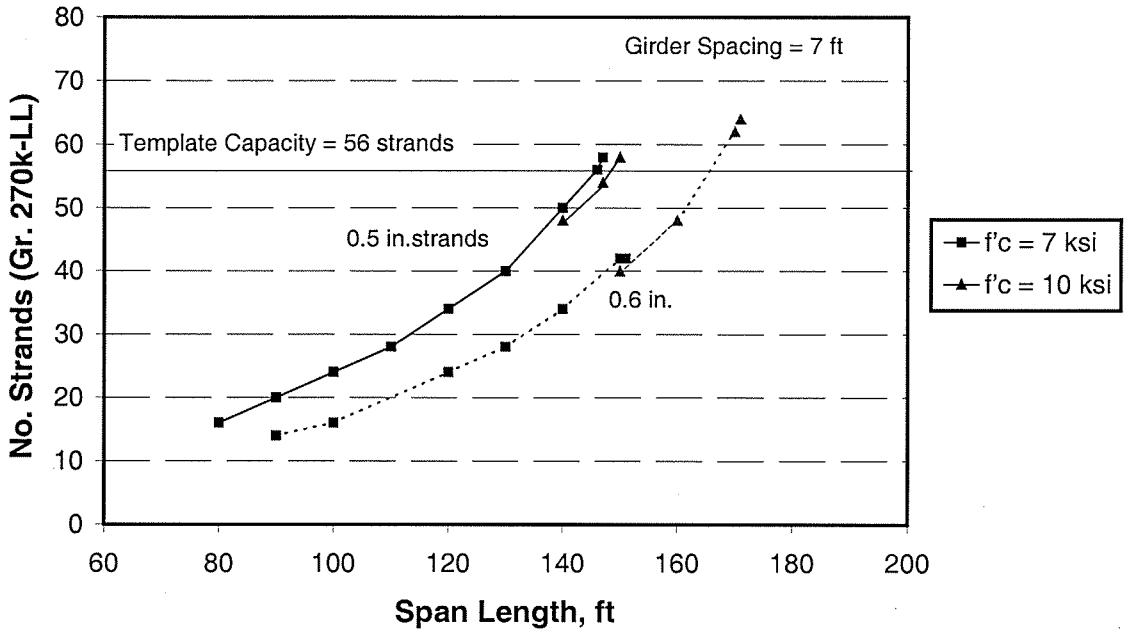

Figure 3.4e Effect of Concrete Strength on Strand Size, Mn/DOT 81I Girders

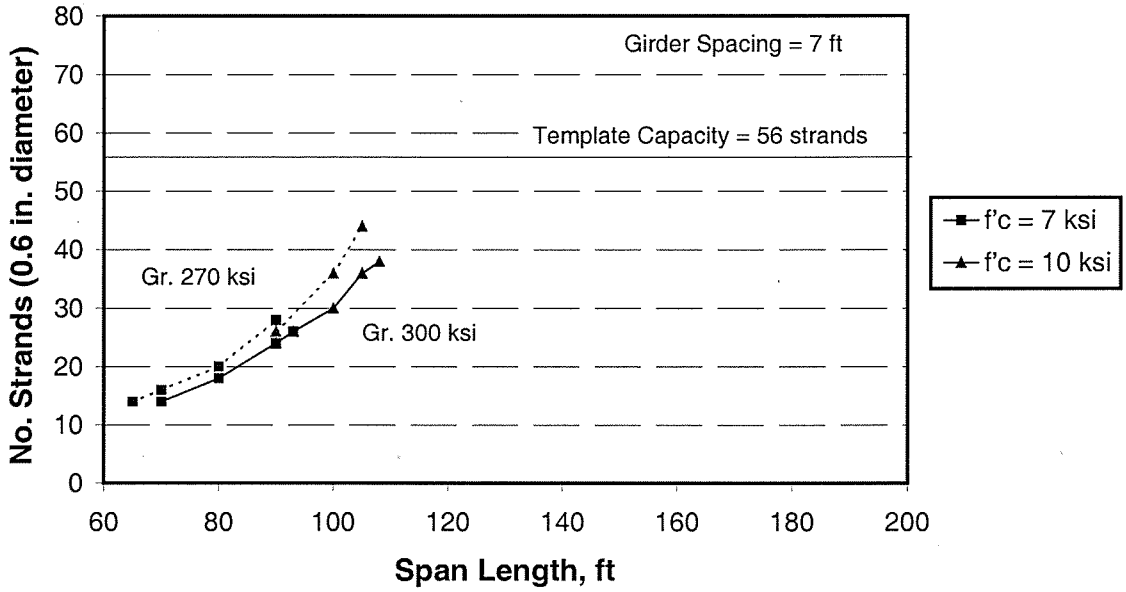

Figure 3.5a Effect of Concrete Strength on Strand Grade, Mn/DOT 45M Girders

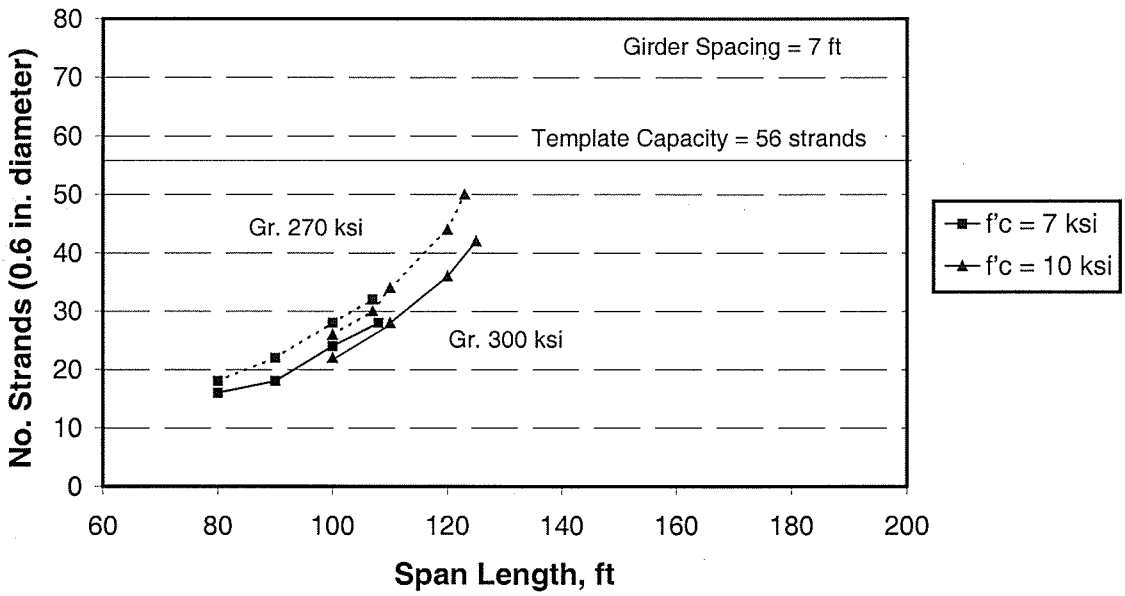

Figure 3.5b Effect of Concrete Strength on Strand Grade, Mn/DOT 54M Girders

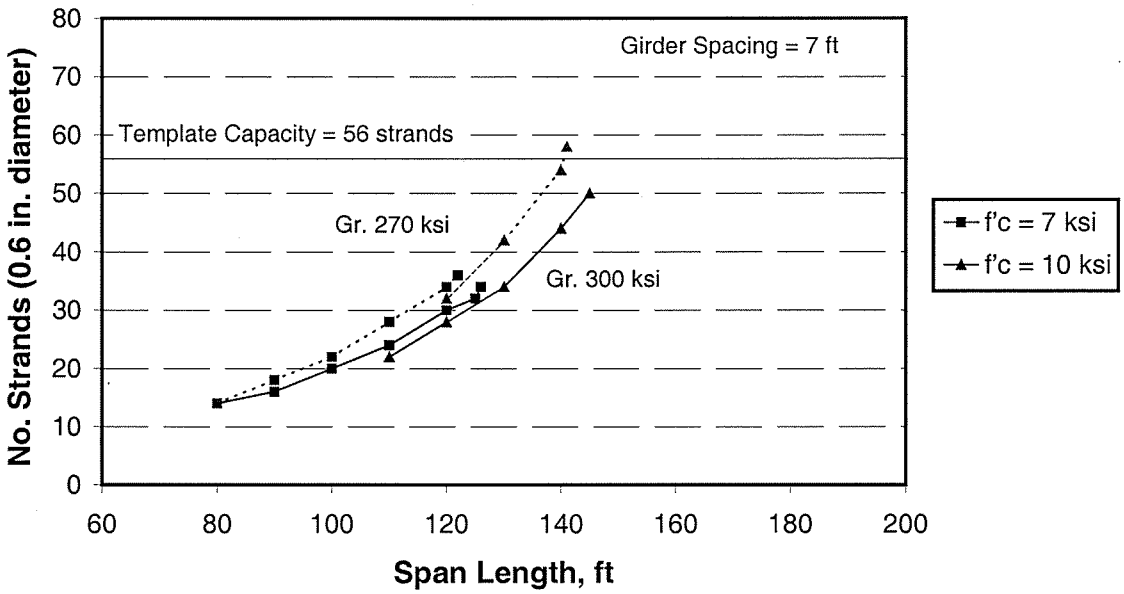

Figure 3.5c Effect of Concrete Strength on Strand Grade, Mn/DOT 63I Girders

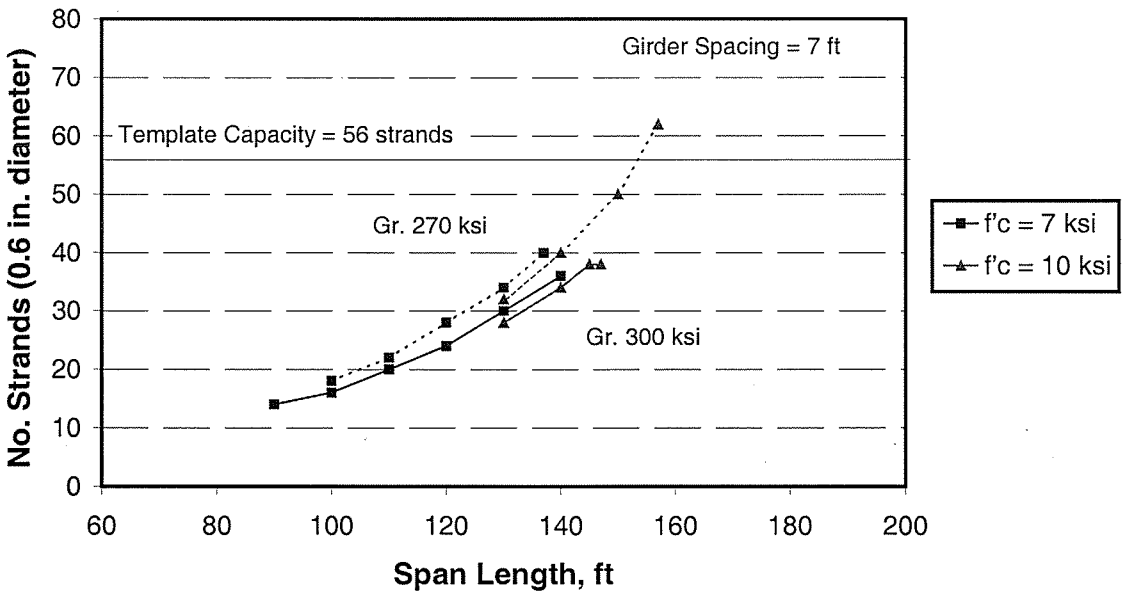

Figure 3.5d Effect of Concrete Strength on Strand Grade, Mn/DOT 72I Girders

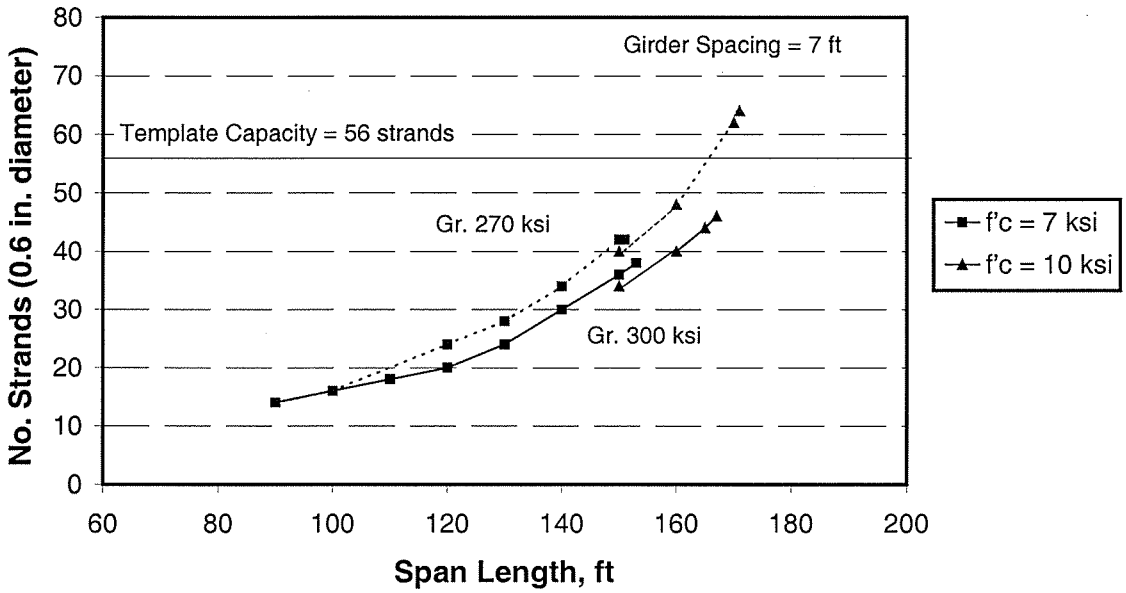

Figure 3.5e Effect of Concrete Strength on Strand Grade, Mn/DOT 81I Girders

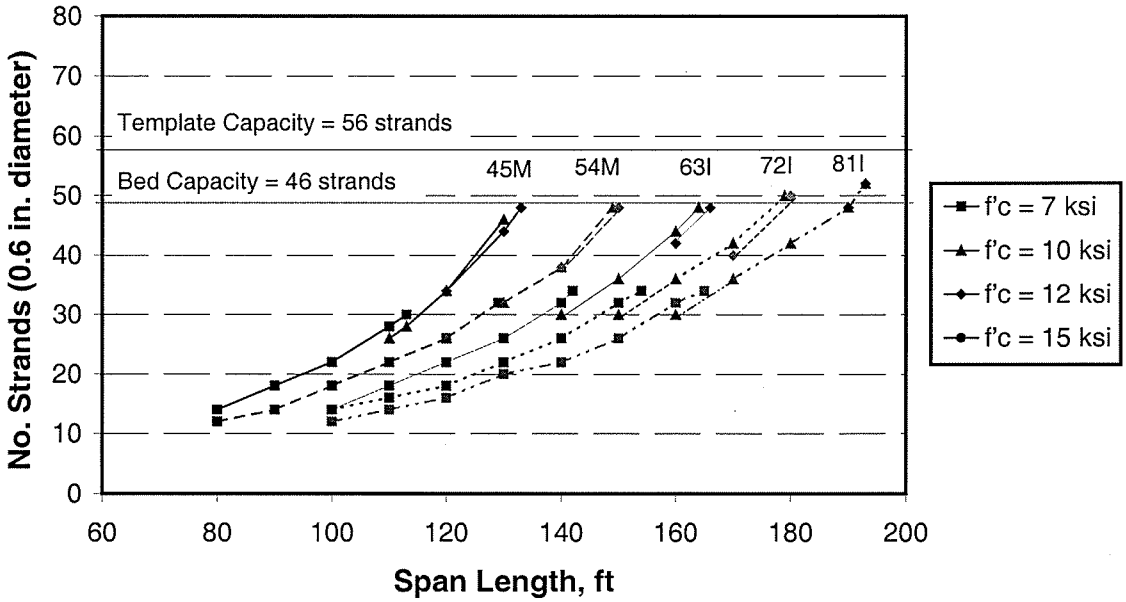

Figure 3.6a Effect of Concrete Strength on Girder Size, Girder Spacing = 4 ft.

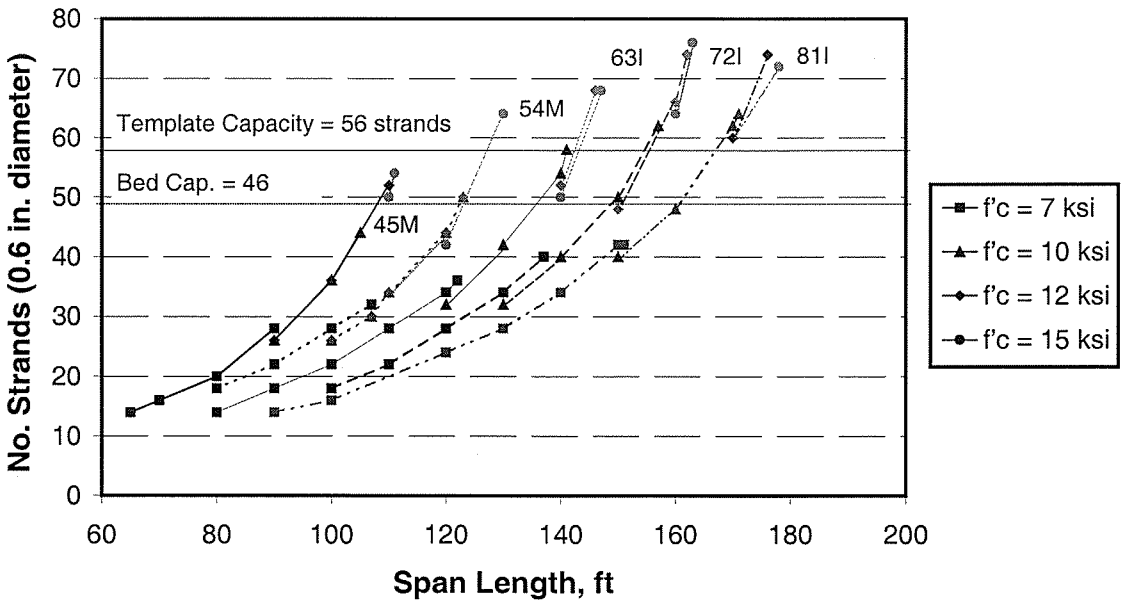

Figure 3.6b Effect of Concrete Strength on Girder Size, Girder Spacing = 7 ft.

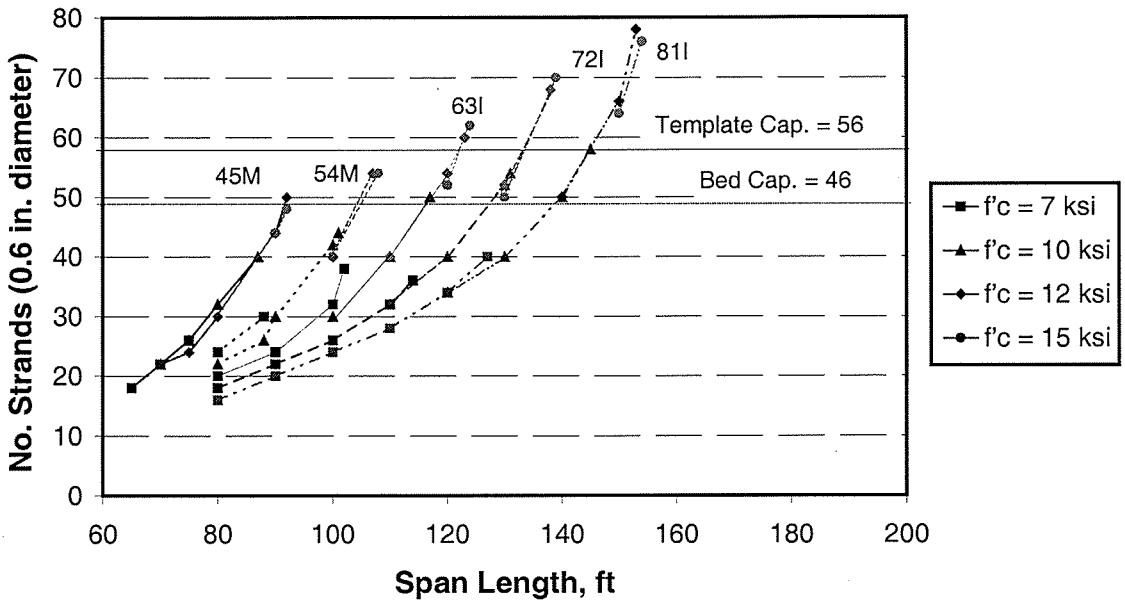

Figure 3.6c Effect of Concrete Strength on Girder Size, Girder Spacing = 10 ft.

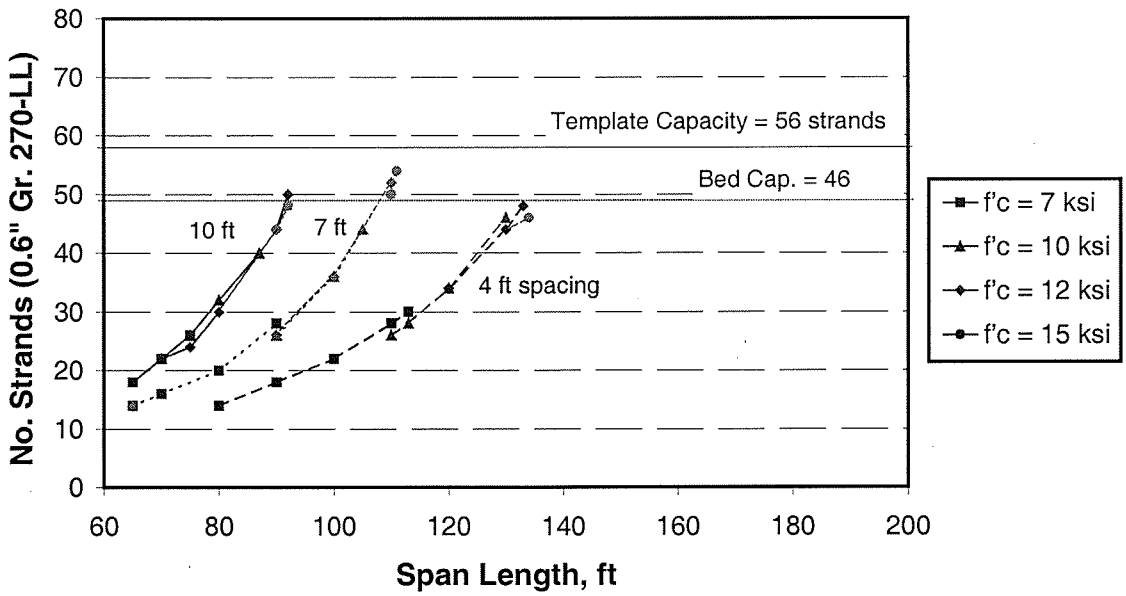

Figure 3.6d Effect of Concrete Strength on Girder Size, Girder Spacing = 12 ft.

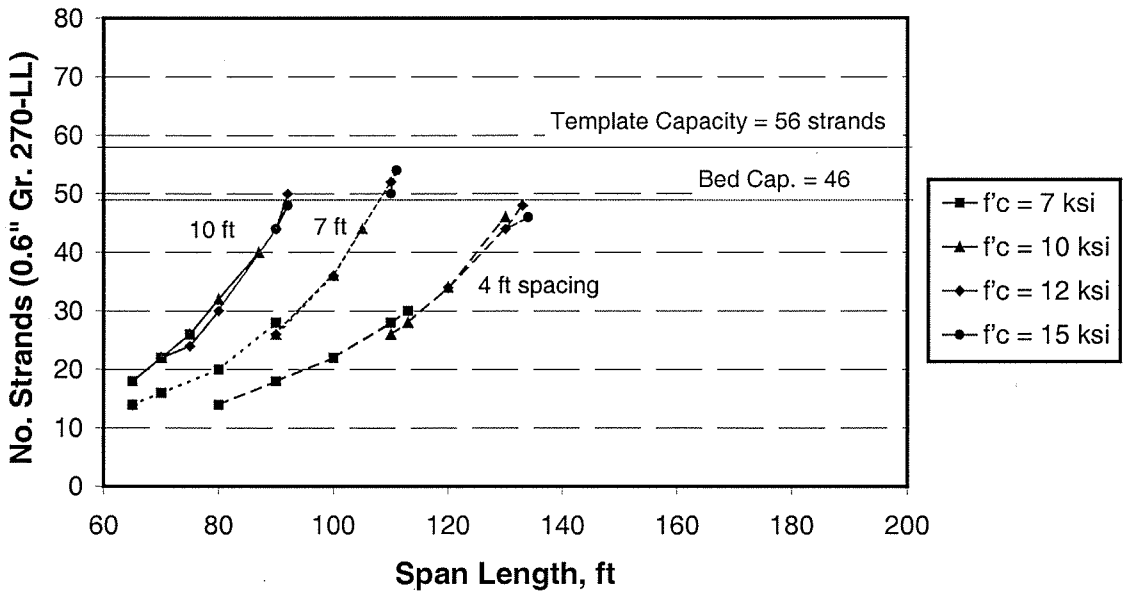

Figure 3.7a Effect of Concrete Strength on Transverse Girder Spacing, Mn/DOT 45M

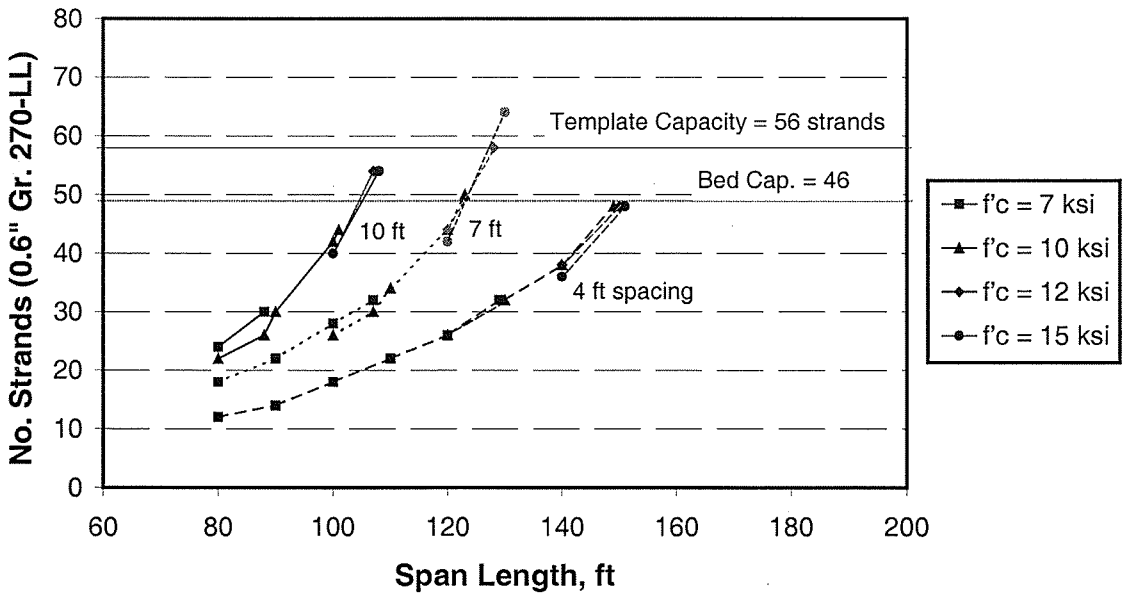

Figure 3.7b Effect of Concrete Strength on Transverse Girder Spacing, Mn/DOT 54 M

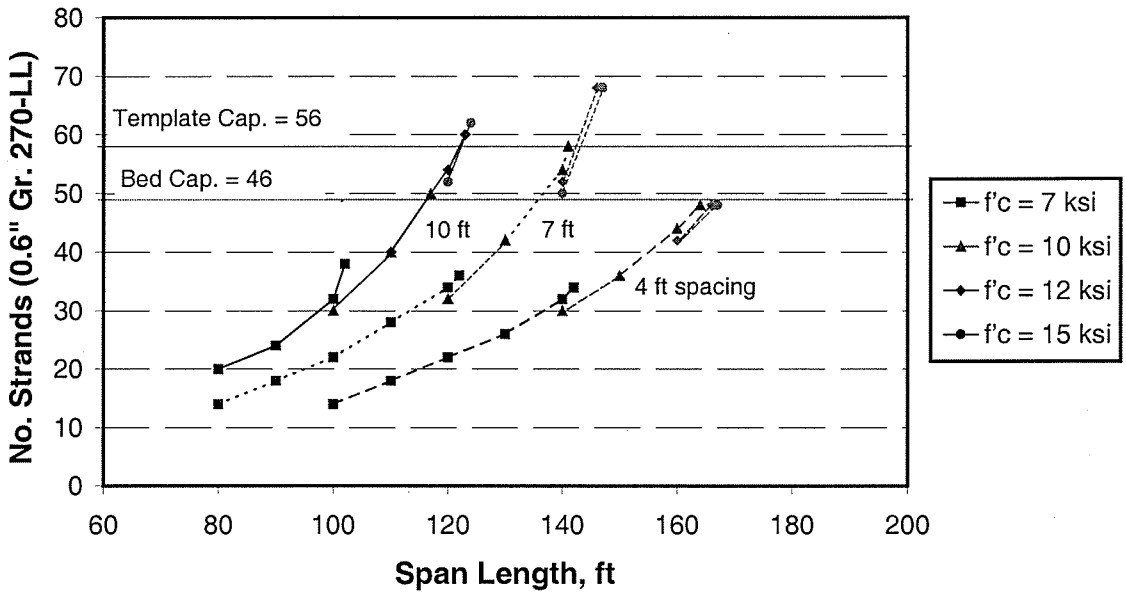

Figure 3.7c Effect of Concrete Strength on Transverse Girder Spacing, Mn/DOT 63I

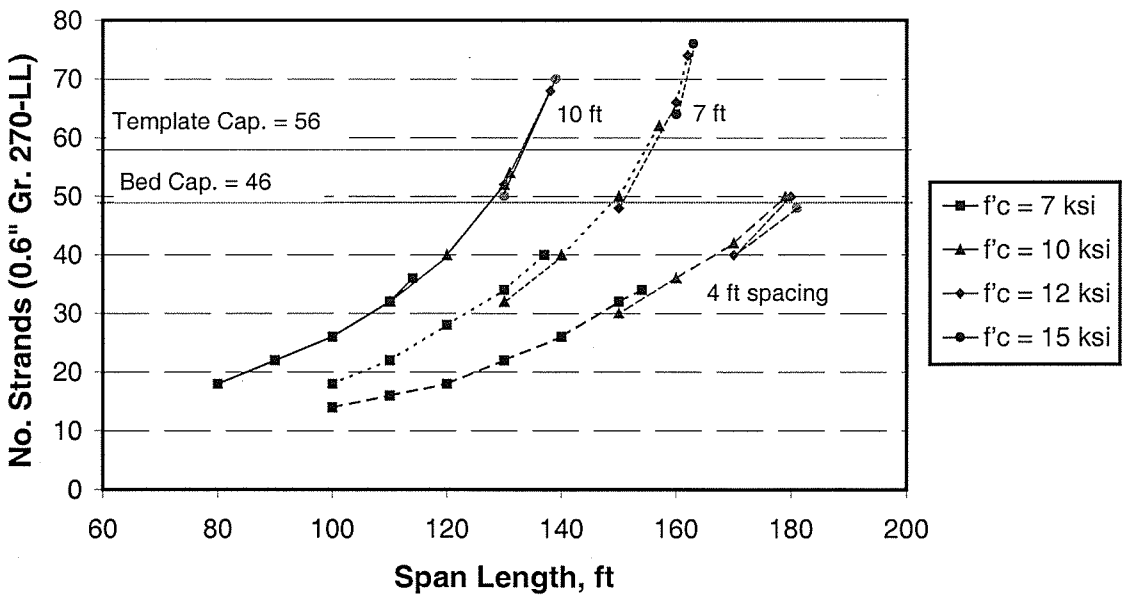

Figure 3.7d Effect of Concrete Strength on Transverse Girder Spacing, Mn/DOT 72I

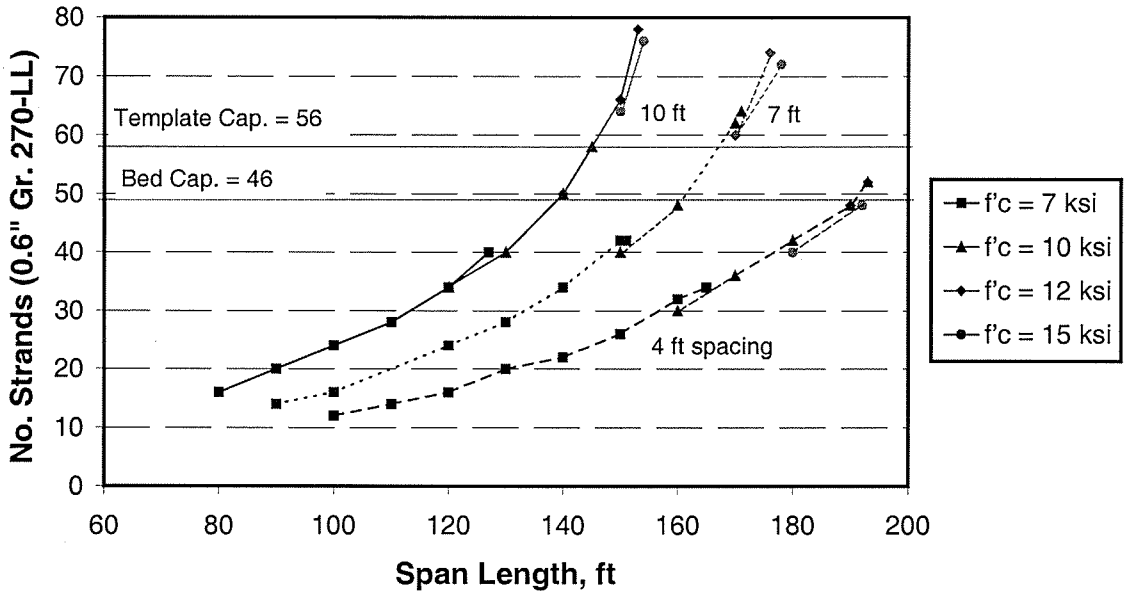

Figure 3.7e Effect of Concrete Strength on Transverse Girder Spacing, Mn/DOT 81I

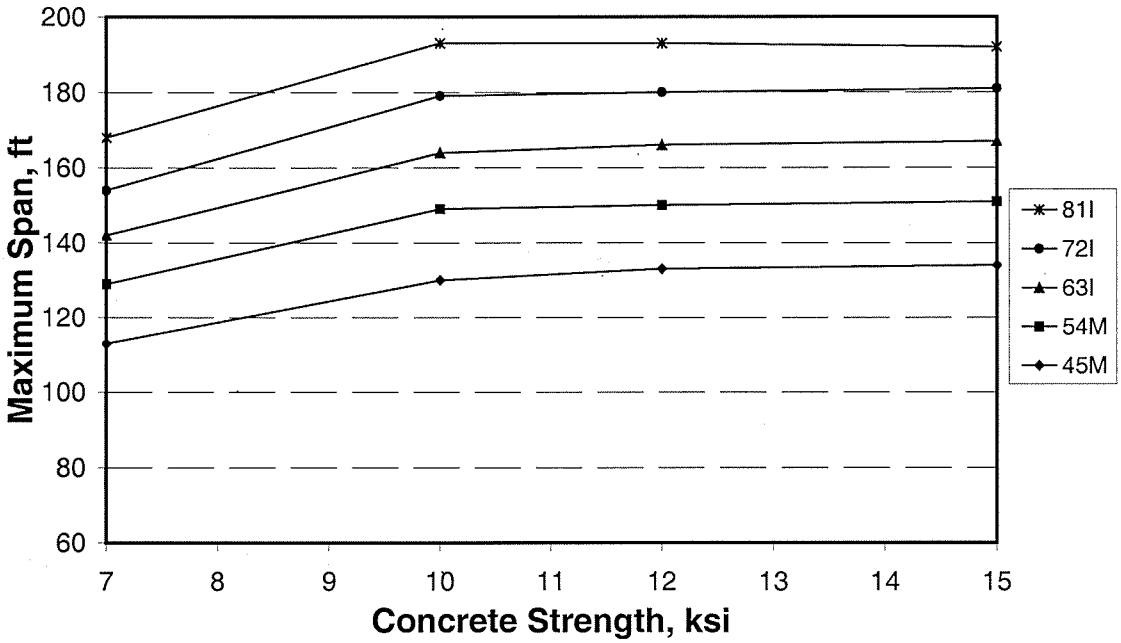

Figure 3.8a Maximum Span v. Concrete Strength, Girder Spacing = 4 ft.

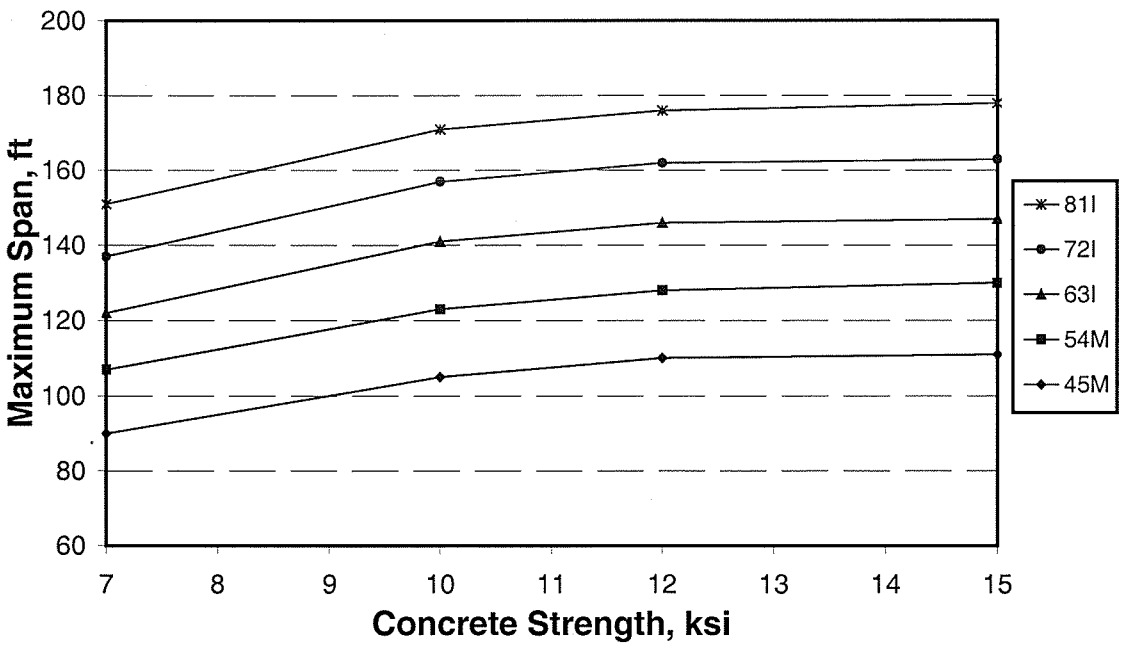

Figure 3.8b Maximum Span v. Concrete Strength, Girder Spacing = 7 ft.

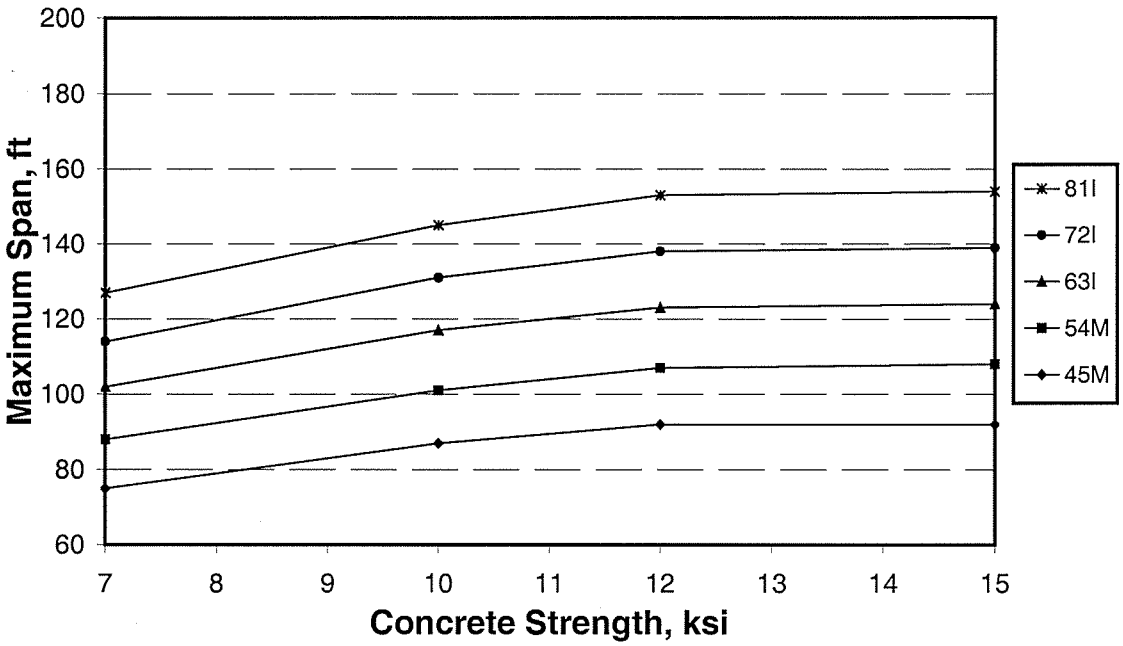

Figure 3.8c Maximum Span v. Concrete Strength, Girder Spacing = 10 ft.

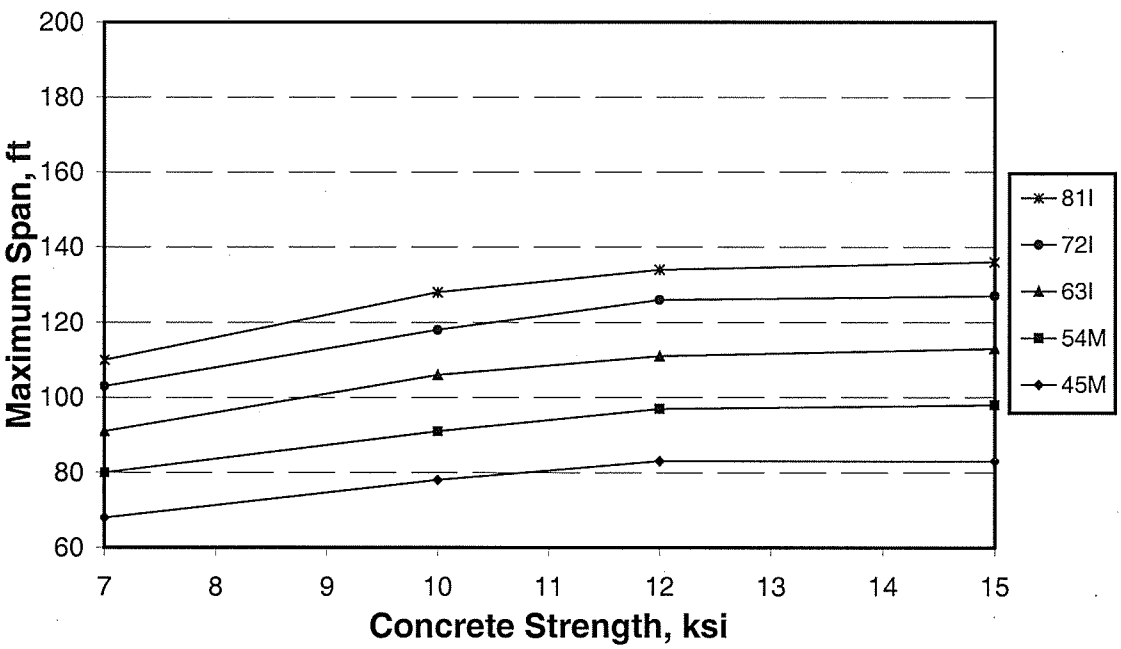

Figure 3.8d Maximum Span v. Concrete Strength, Girder Spacing = 12 ft.

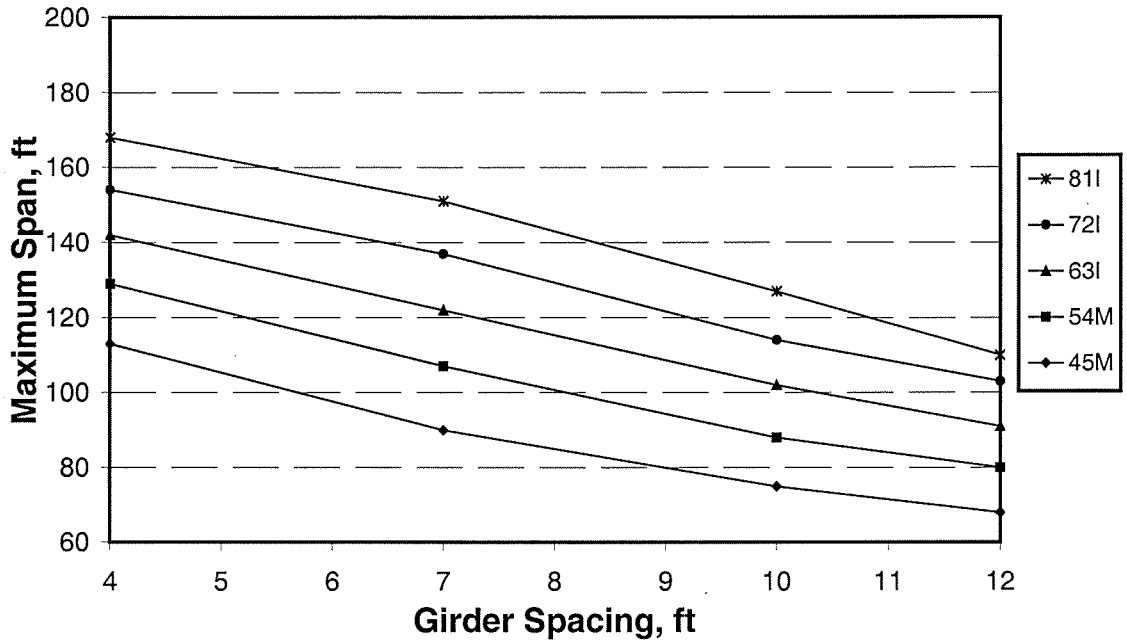

Figure 3.9a Maximum Span v. Girder Spacing, f'_c = 7 ksi

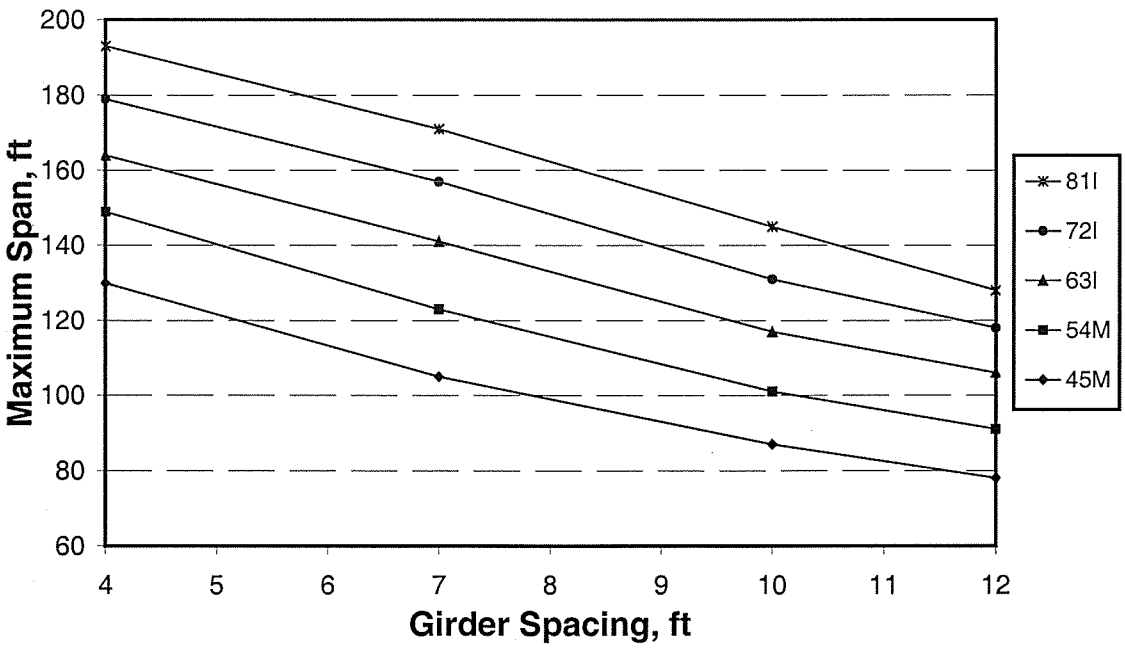

Figure 3.9b Maximum Span v. Girder Spacing, f'_c = 10 ksi

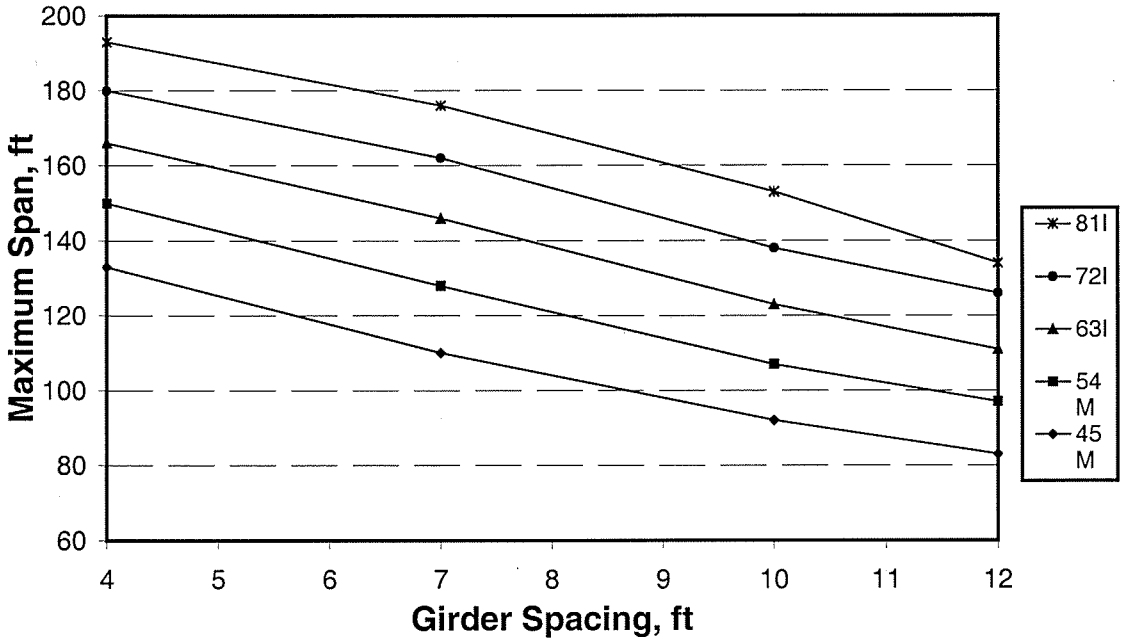

Figure 3.9c Maximum Span v. Girder Spacing, f'_c = 12 ksi

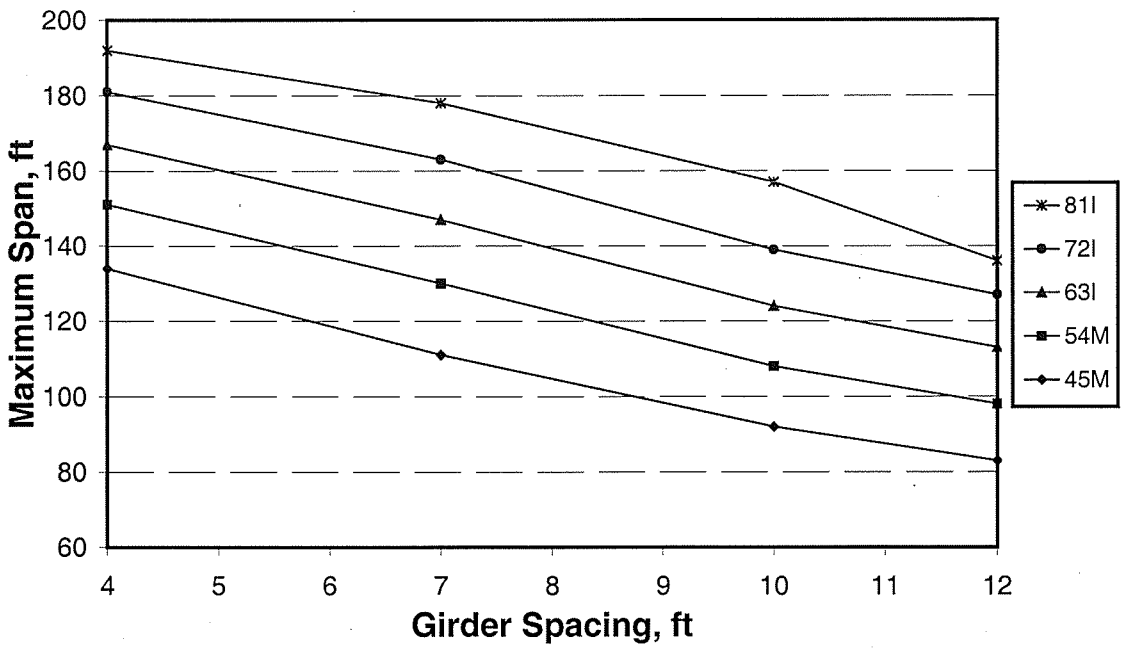

Figure 3.9d Maximum Span v. Girder Spacing, f'_c = 15 ksi

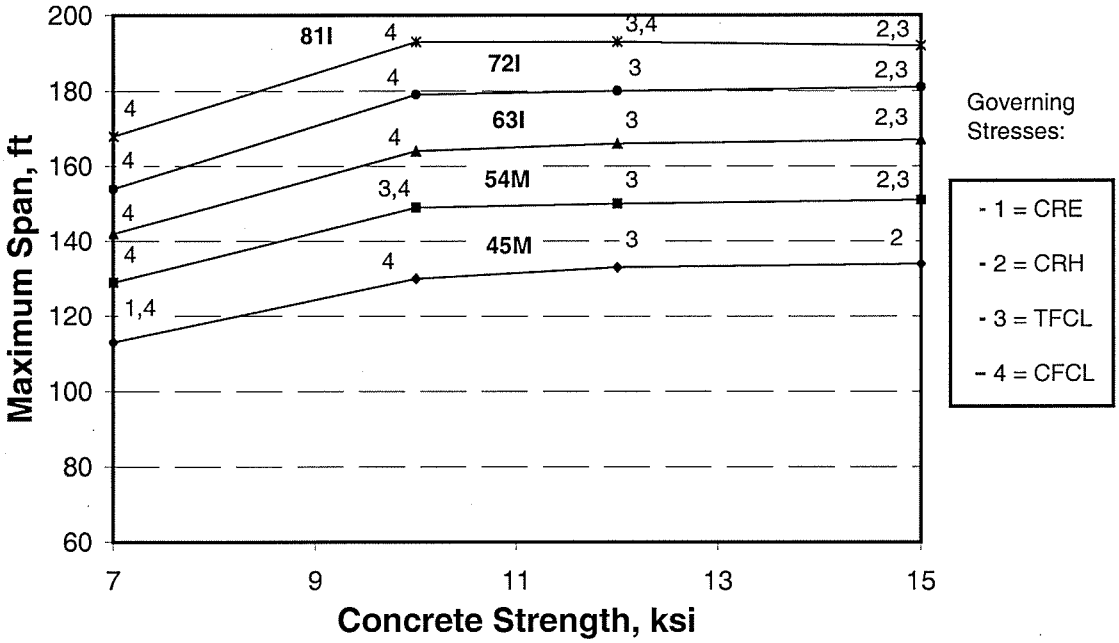

Figure 3.10a Governing Stresses at Maximum Span, Girder Spacing = 4 ft.

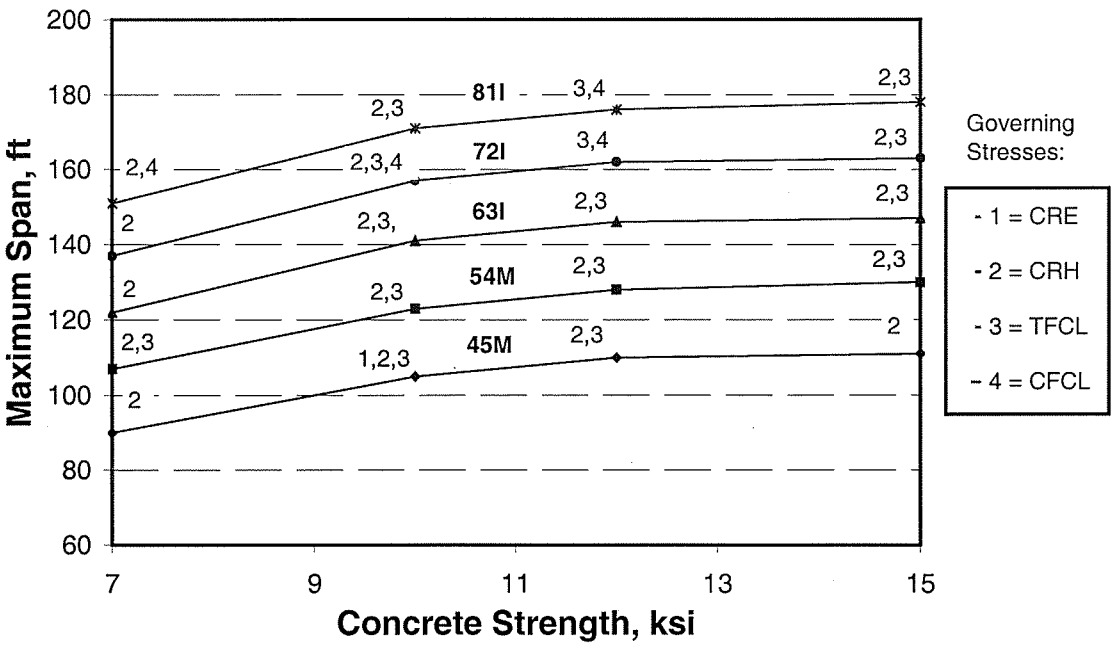

Figure 3.10b Governing Stresses at Maximum Span, Girder Spacing = 7 ft.

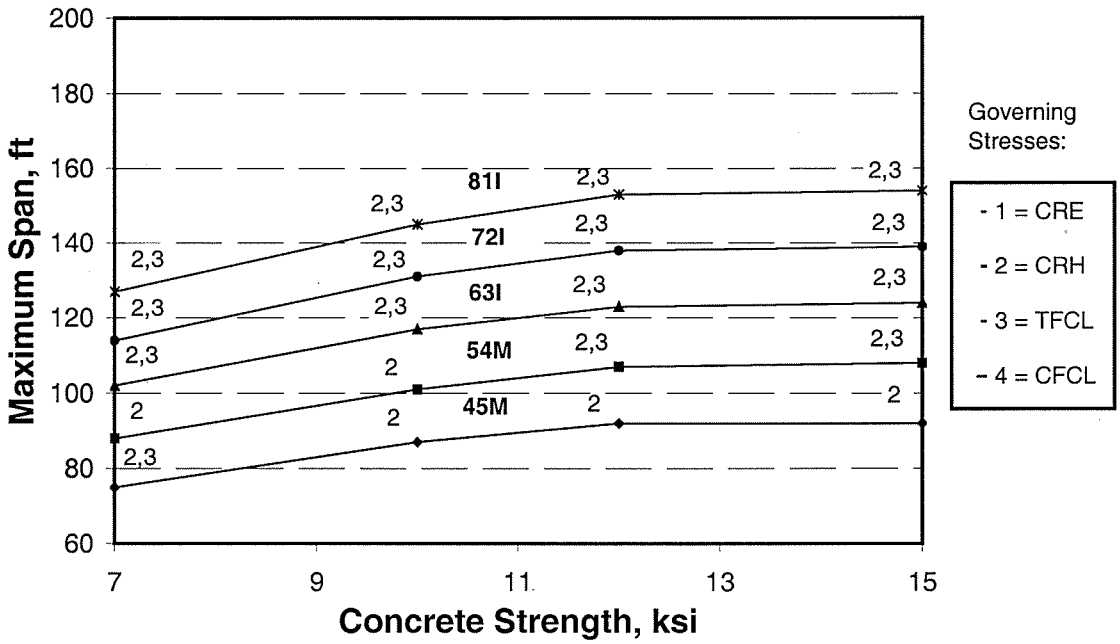

Figure 3.10c Governing Stresses at Maximum Span, Girder Spacing = 10 ft.

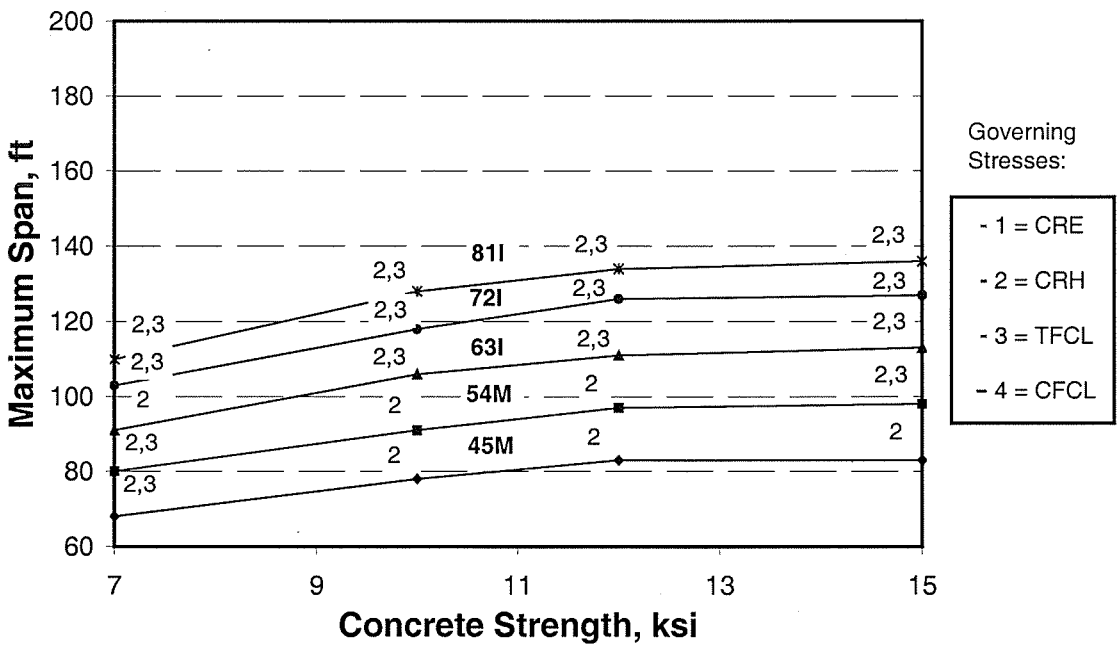

Figure 3.10d Governing Stresses at Maximum Span, Girder Spacing = 12 ft.

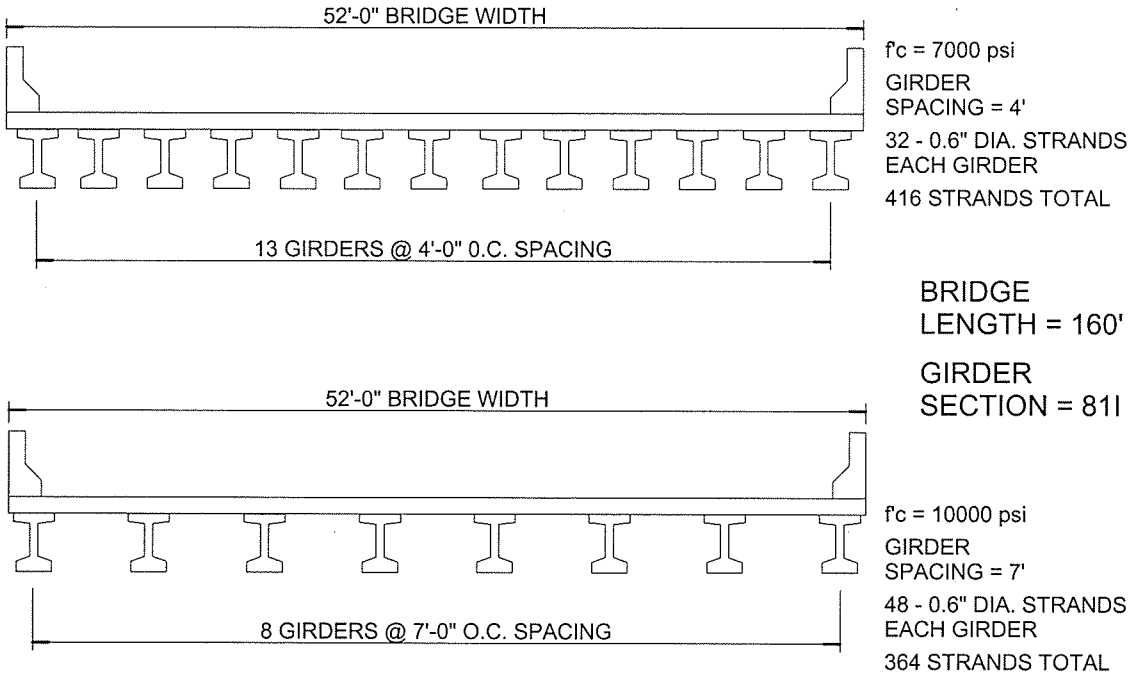

Figure 3.11 Comparison Design of a Bridge System

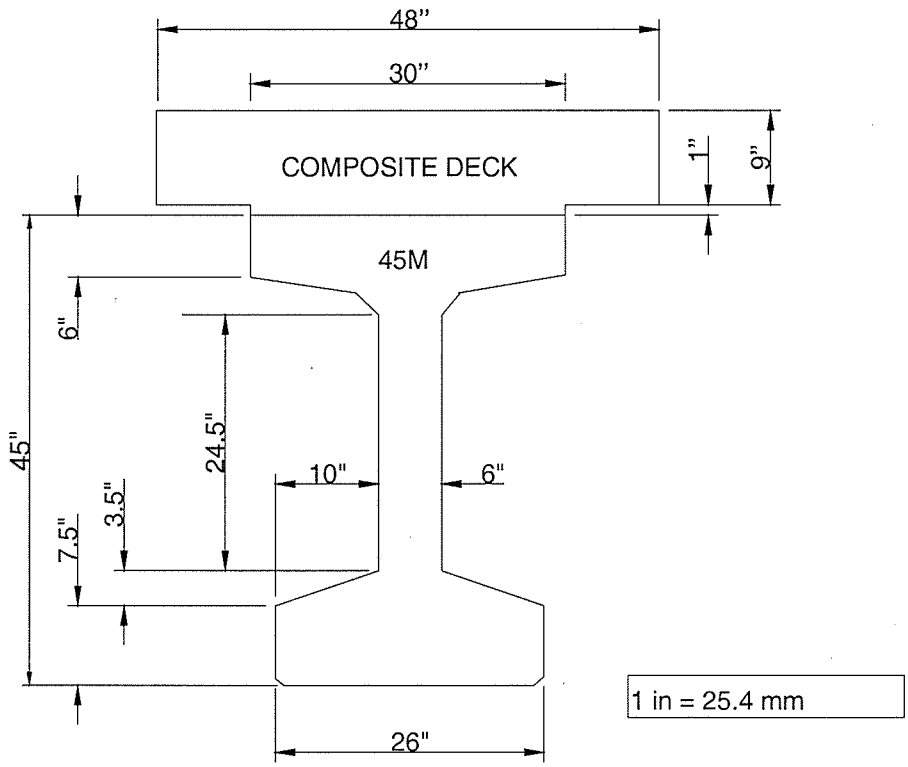

Figure 4.1 Composite Test Girder Dimensions

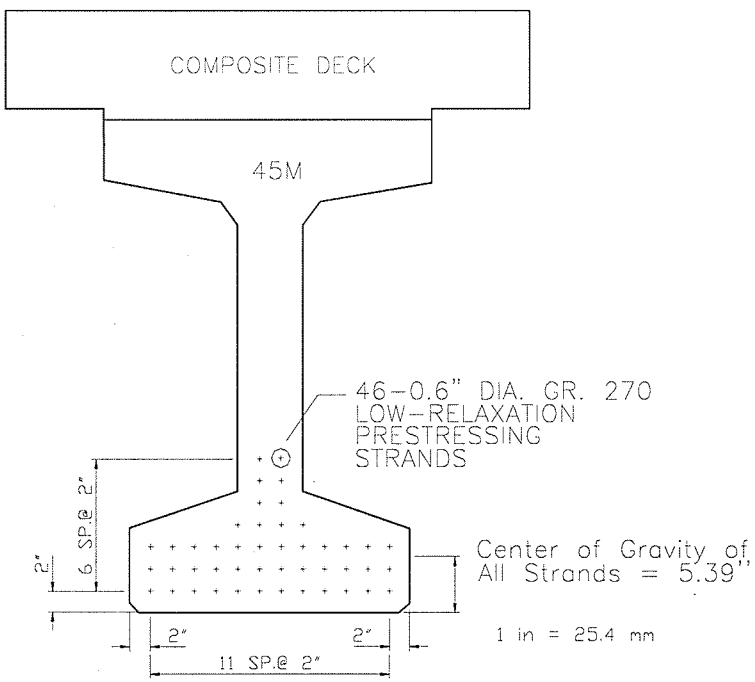

Figure 4.2 Strand Pattern at Midspan

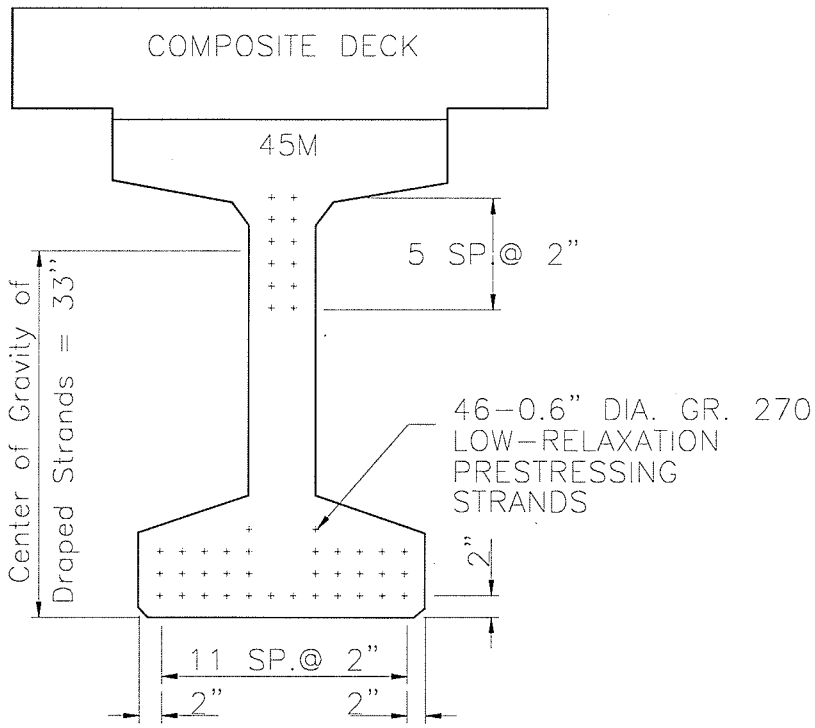

Figure 4.3 Strand Pattern at a Draped End

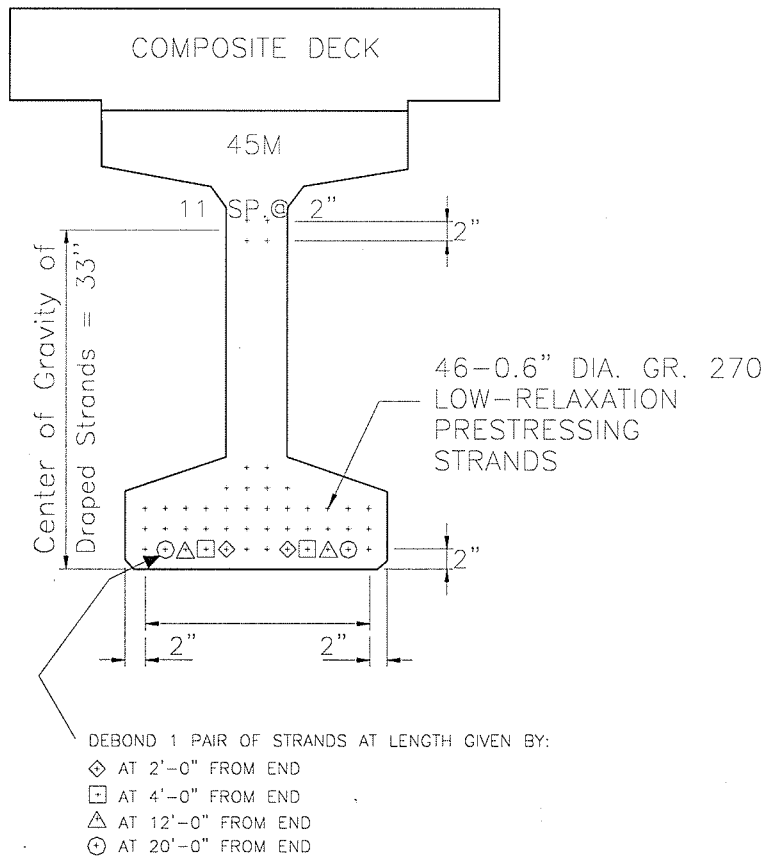

Figure 4.4 Strand Pattern at a Debonded End

BEAM CONFIGURATION TABLE					
BEAM	END	AGGREGATE FOR MIX	NO. STRANDS DRAPED	NO. STRANDS DEBONDED	END REGION STIRRUP CONFIGURATION
I	SOUTH	LIMESTONE	4	8	G402E
I	SOUTH	LIMESTONE	4	8	G408E
II	NORTH	GG w/ MS	4	8	G408E
II	NORTH	GG w/ MS	12	0	G408E

Y DISTANCES (in inches)			
	NO.	SPAN	END
DRAPED SECTION:			
STRAIGHT STRANDS	34	4.12"	
DRAPED STRANDS	12	9.00"	33.00"
TOTAL	46	5.39"	11.65"
DEBONDED SECTION:			
STRAIGHT STRANDS	42	4.67"	5.29"
DRAPED STRANDS	4	13.00"	33.00"
TOTAL	46	5.39"	

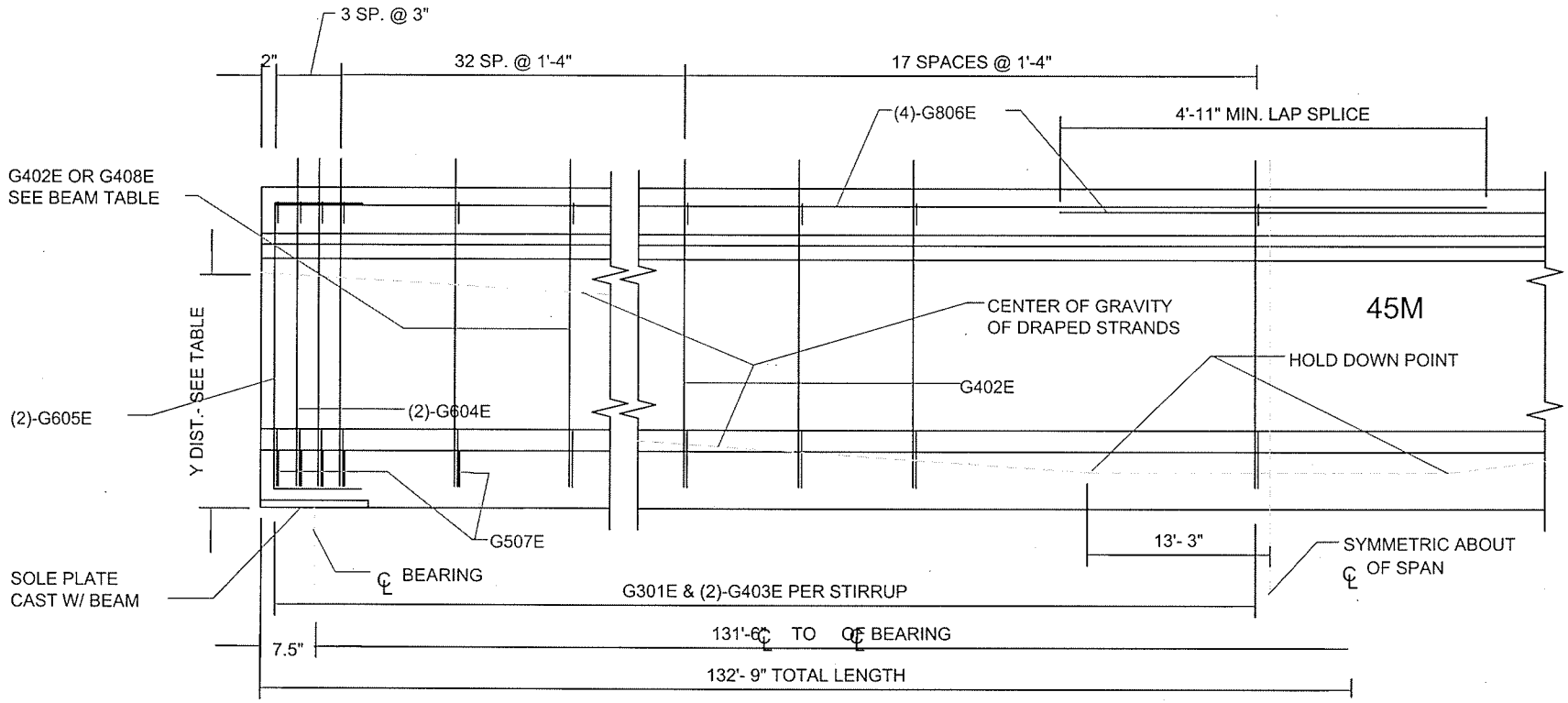

Figure 4.5 Test Girder Mild Steel Reinforcement, Elevation (reprinted from Kielb, 1994)

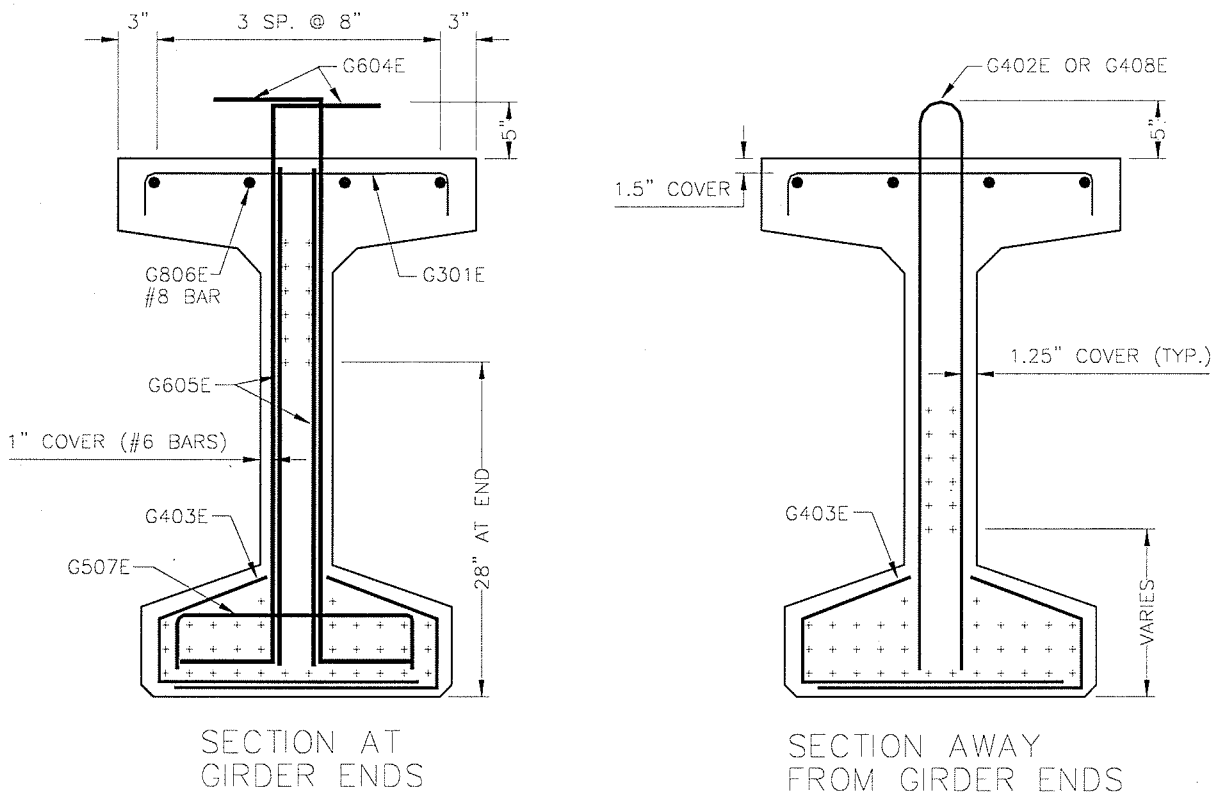

Figure 4.6 Test Girder Mild Steel Reinforcement, Cross Section
(Reprinted from Kielb, 1994)

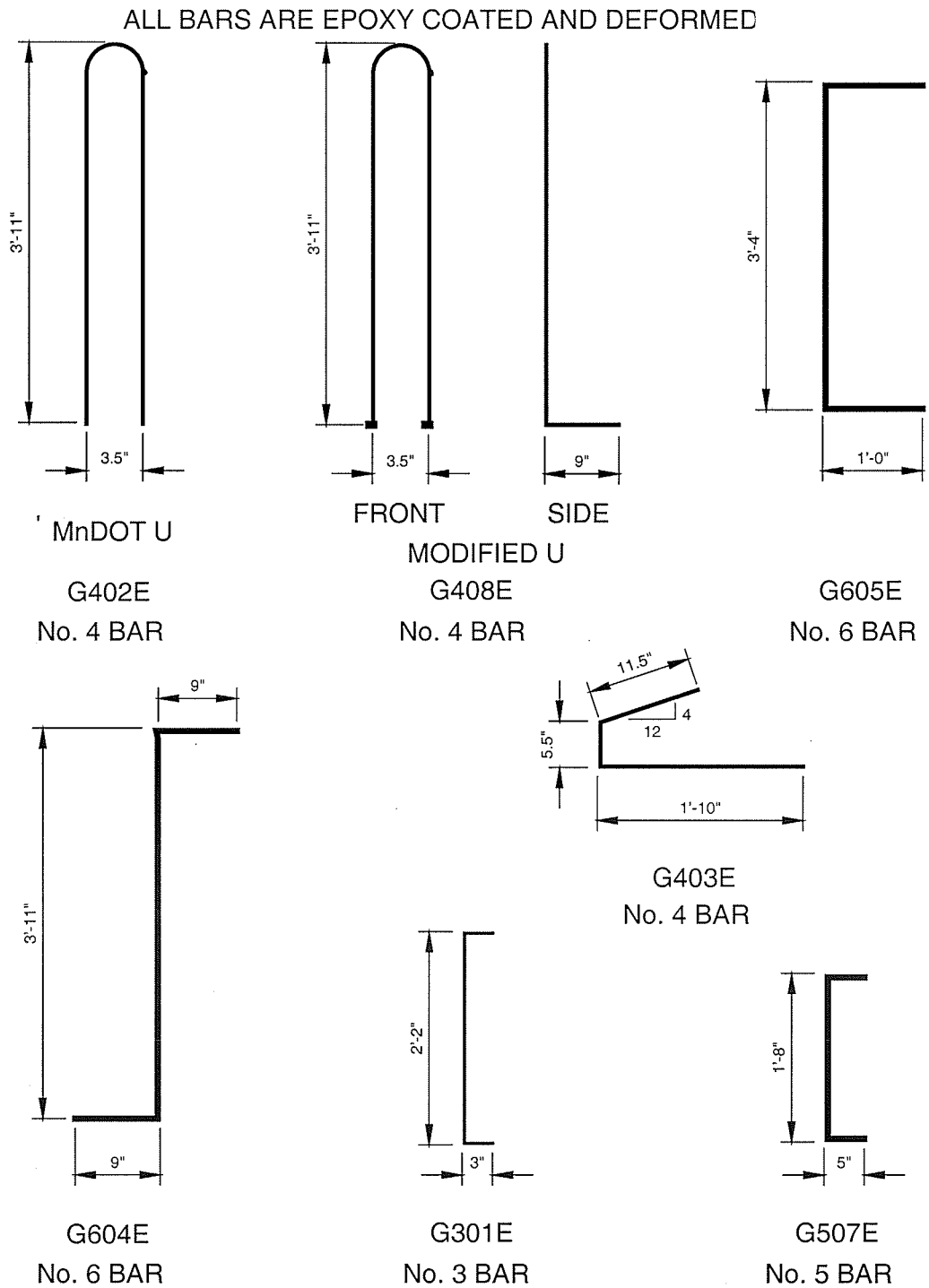

Figure 4.7 Mild Steel Reinforcing Details
(Reprinted from Kielb, 1994)

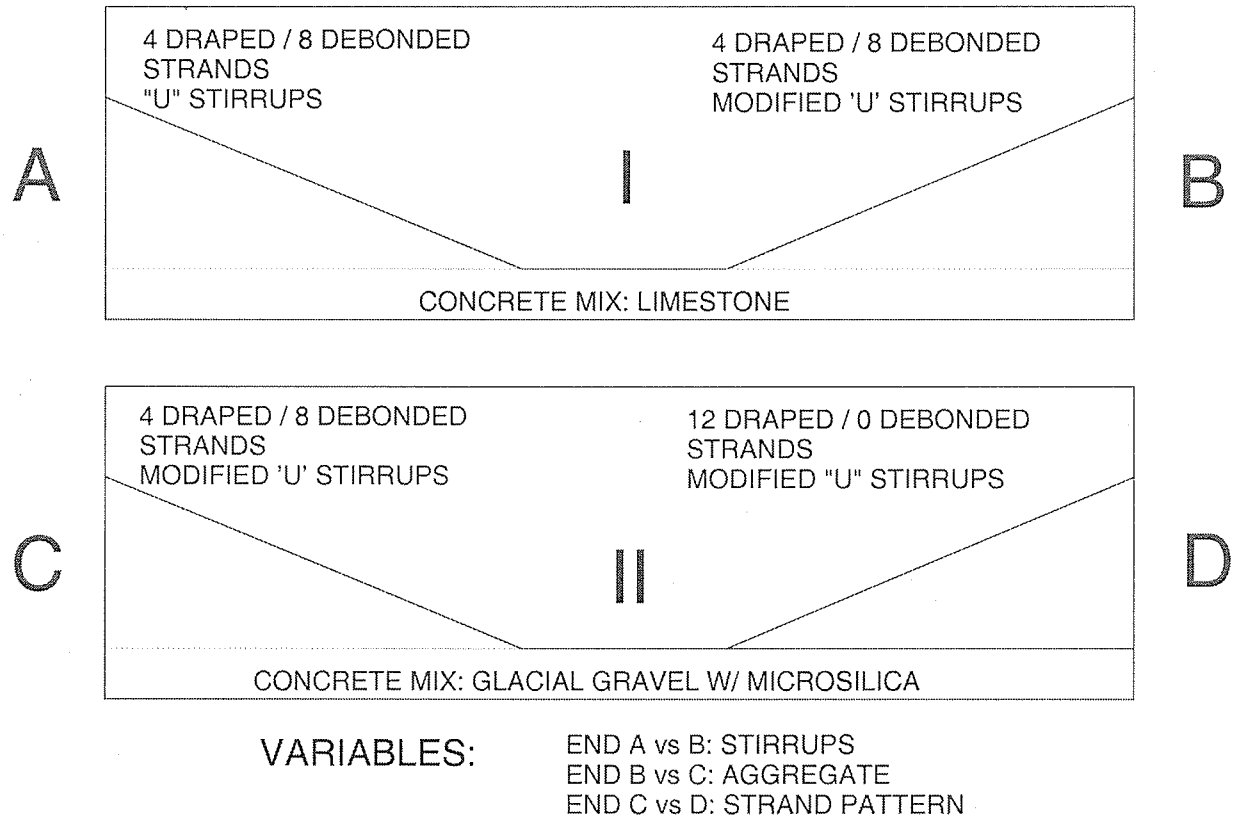

Figure 4.8 Summary of Girder Variables

CONCRETE DECK REINFORCEMENT

ALL SLAB BARS ARE EPOXY COATED,
DEFORMED No. 4 BARS

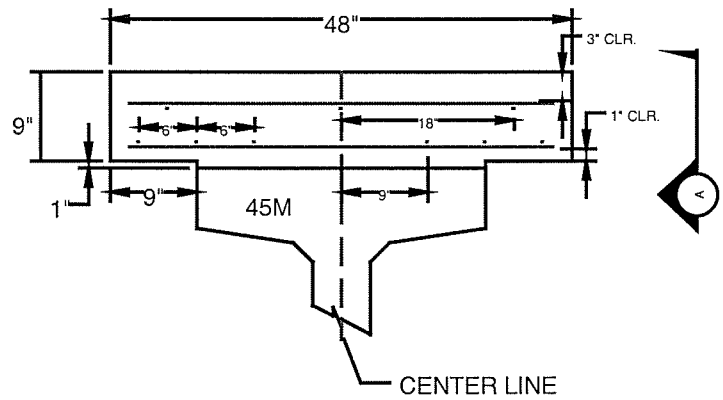

CONCRETE DECK SECTION

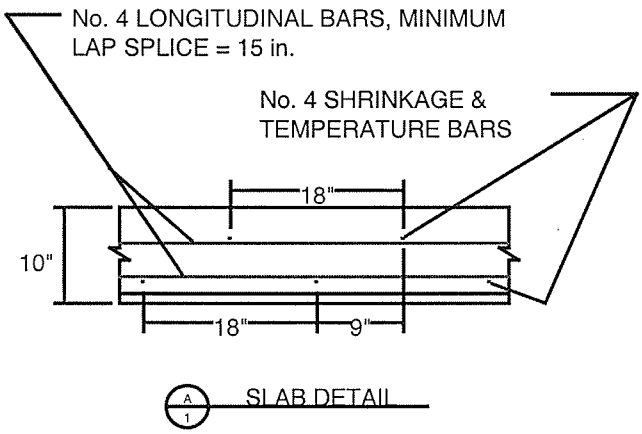

A/1 SLAB DETAIL

Figure 4.9 Concrete Deck Reinforcing Details, (reprinted from Kielb, 1994).

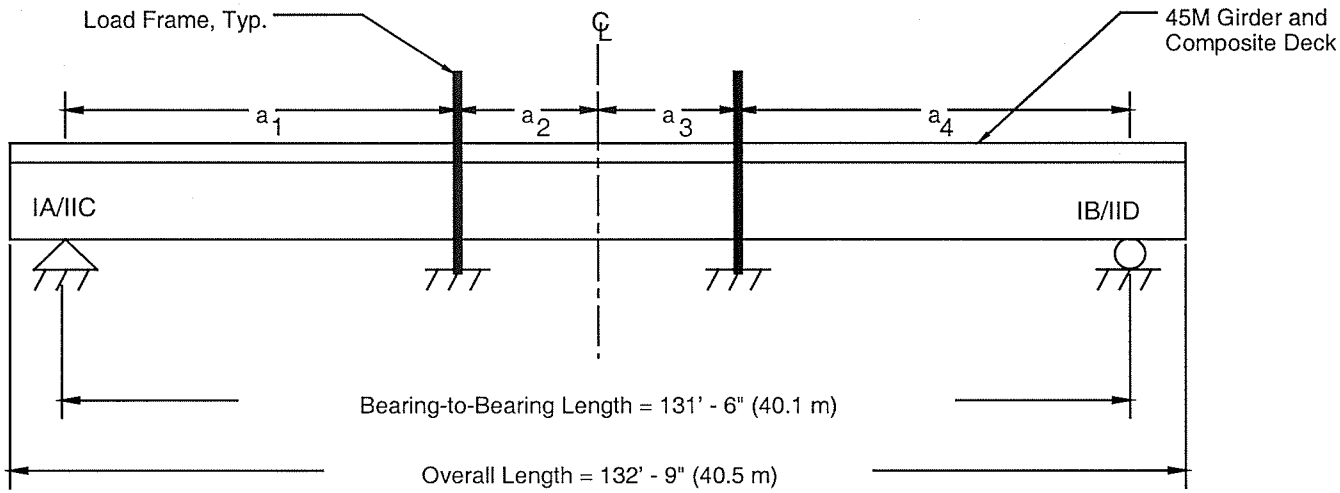

Girder:	I	II
a_1	627"	632"
a_2	162"	157"
a_3	157"	159"
a_4	632"	630"

Notes:
1. Not to Scale.
2. All phases of load testing utilized the same load point locations, independent of test type or girder tested.

Figure 5.1 Load Frame Locations During Load Testing

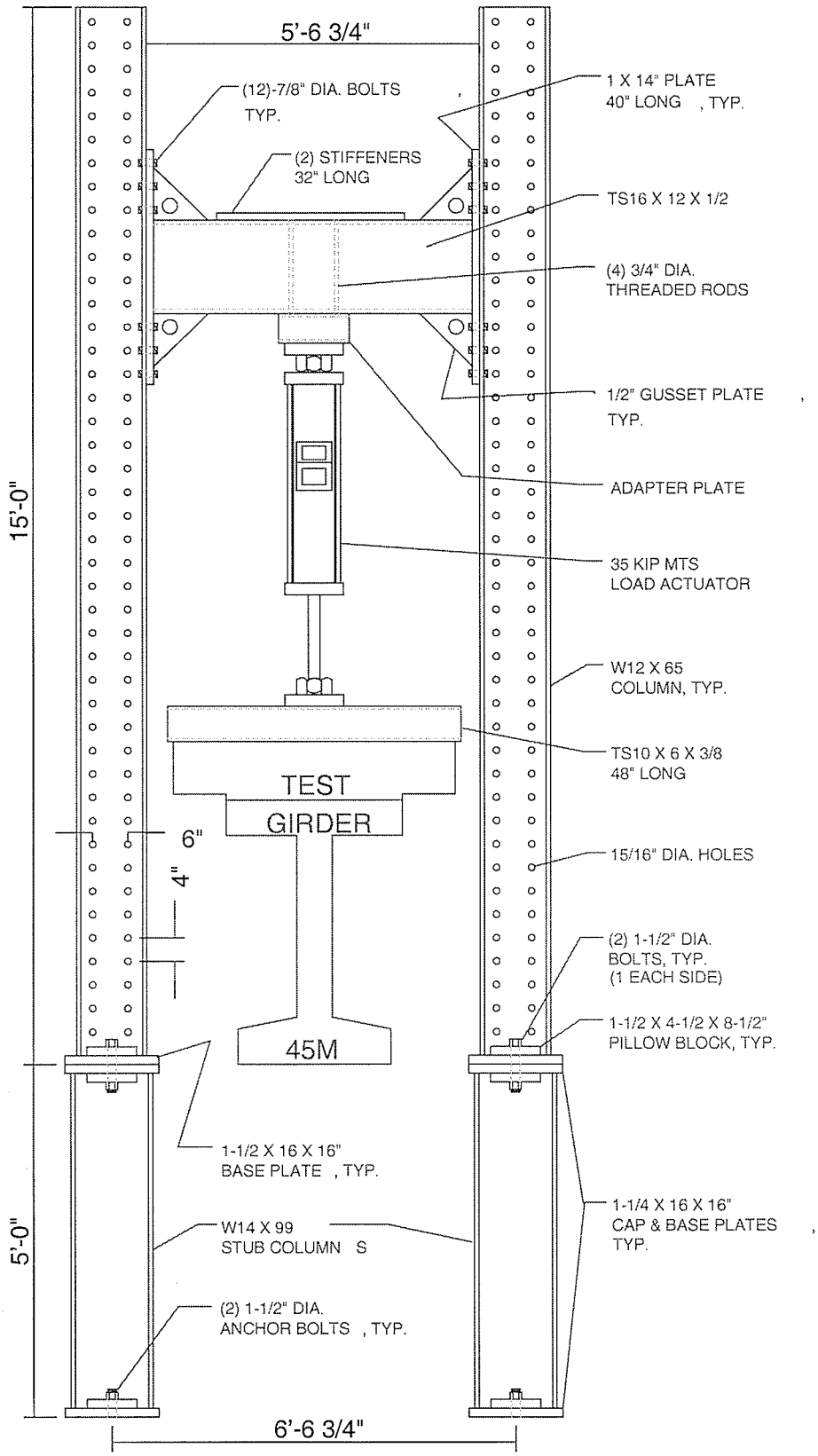

Figure 5.2 Load Frame Configuration for Static and Cyclic Load Testing

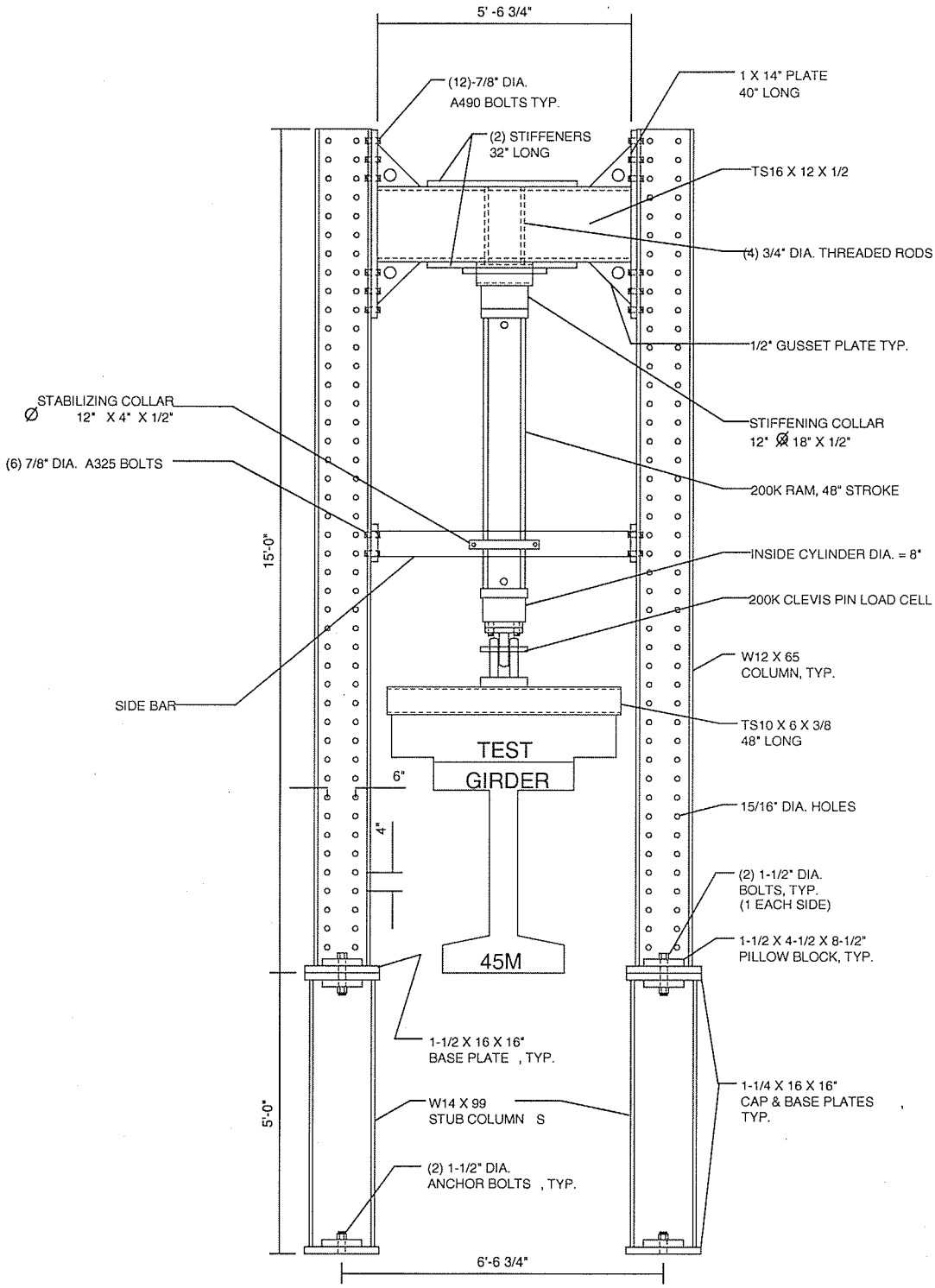

Figure 5.3 Load Frame Configuration for Ultimate Flexural Testing

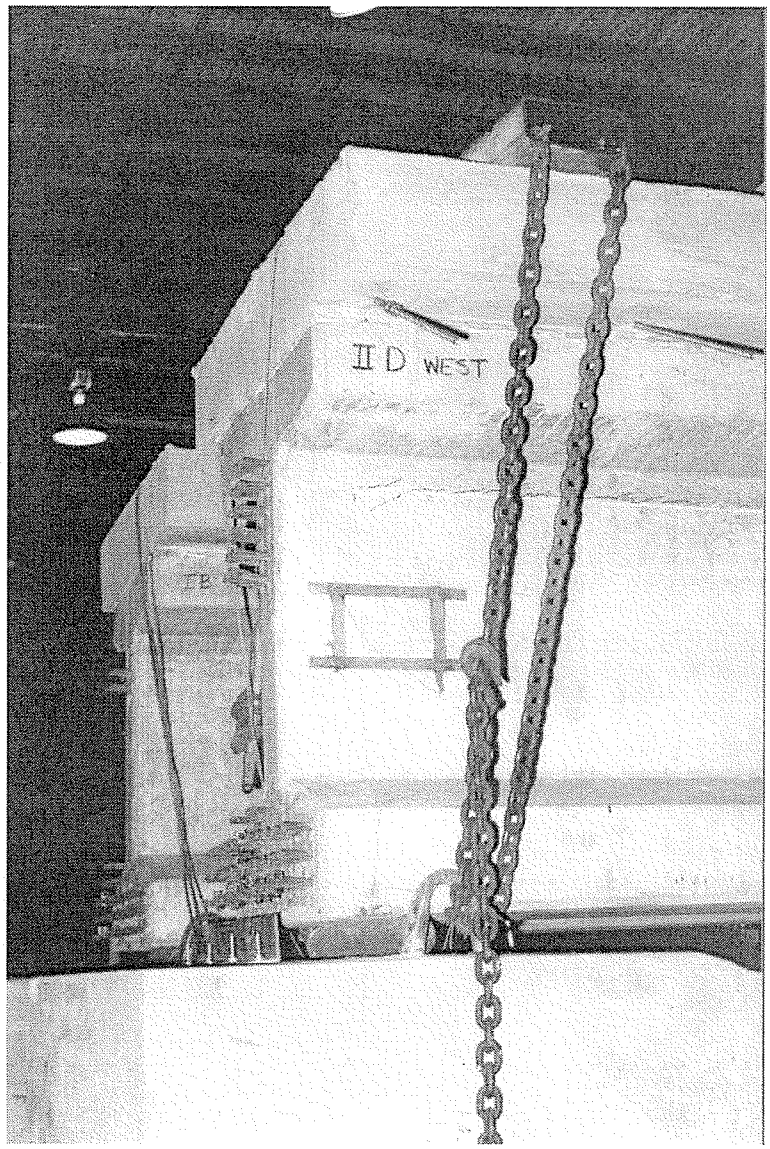

Figure 5.4 Chaining of Girder End to Reaction Block

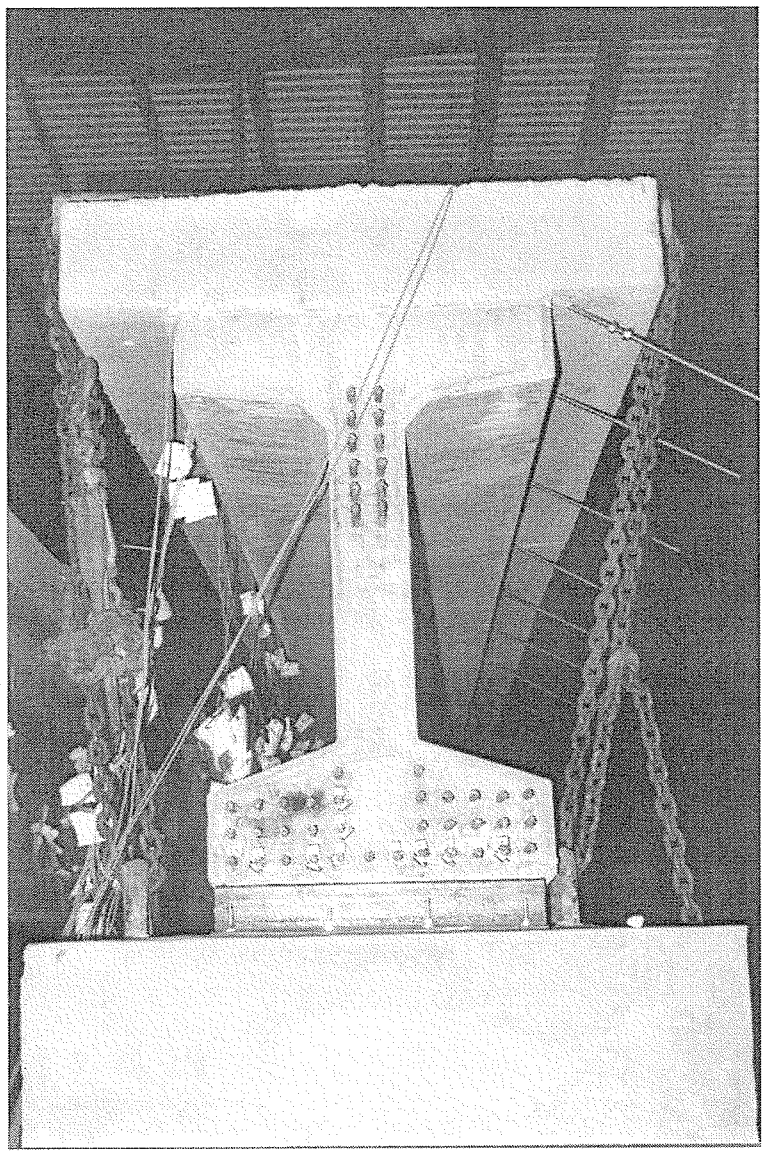

Figure 5.5 Chaining of Girder End to Reaction Block

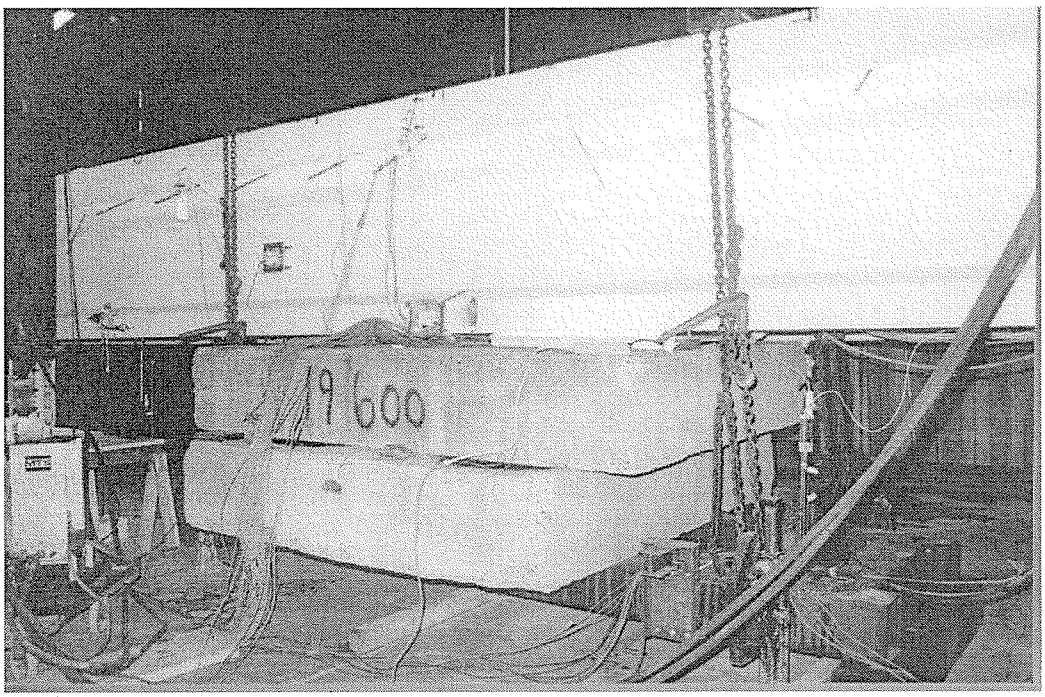

Figure 5.6 Hanging Dead Load used During Initial Crack Testing

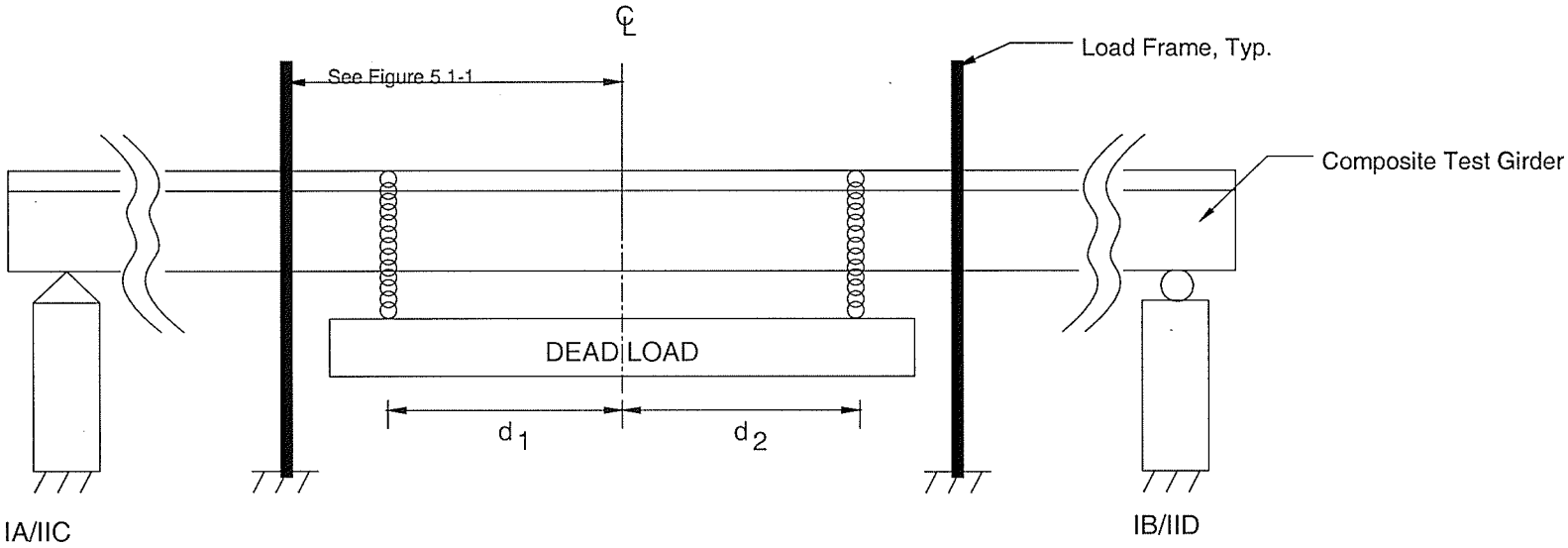

Notes: 1. Not to Scale
2. Total Dead Load = 35,020 lbs. (156 kN)
3. Bearing-to-Bearing Length = 131.5' (40.1 m)

Girder:	I	II
d_1	60" (1.5m)	78" (2.0m)
d_2	60" (1.5m)	66" (1.7m)

Figure 5.7 Dead Load Location for Initial Crack Testing

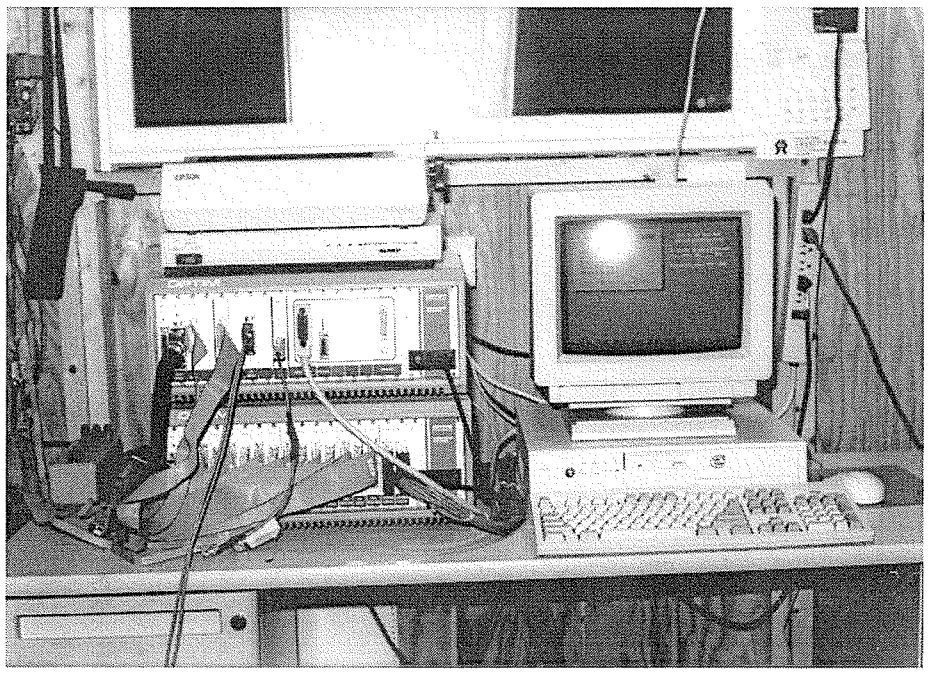

Figure 5.8 OPTIM Megadac Data Acquisition System

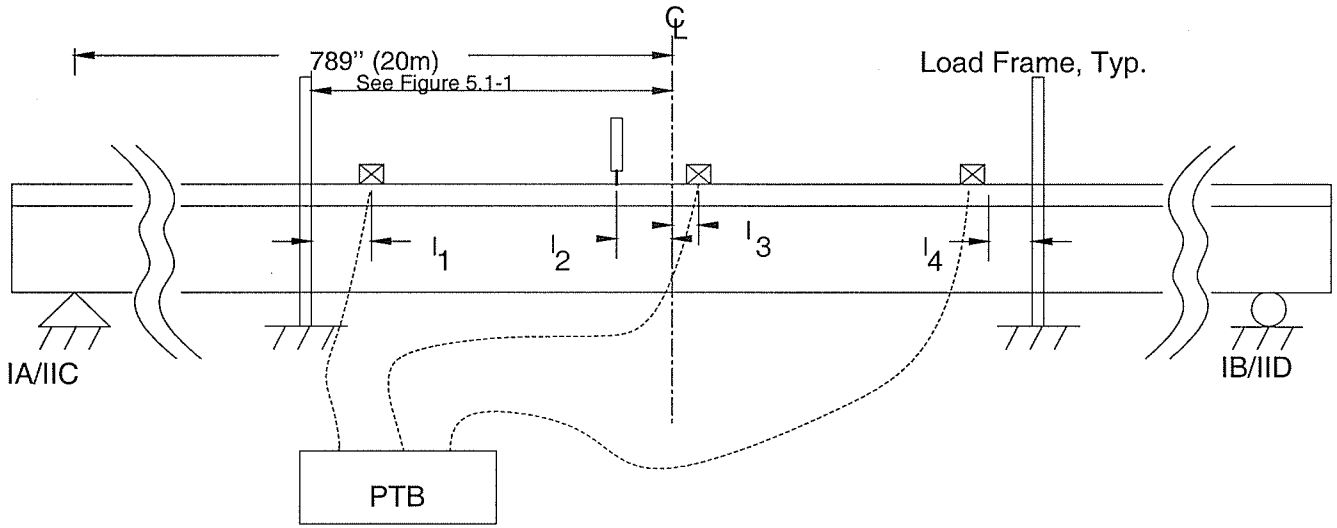

Girder:	I	II
l_1	22"	22"
l_2	10"	9"
l_3	2"	0"
l_4	21"	24"

℄ LVDT 10" Total Travel

Bucket - Placed on top of composite deck.

PTB Pressure transducers board loacted at approximately 6' (1.8m) below buckets. (one transducer per bucket)

Fluid line to pressure transducer

Figure 5.9 Placement of Deflection Devices - Ultimate Flexural Testing

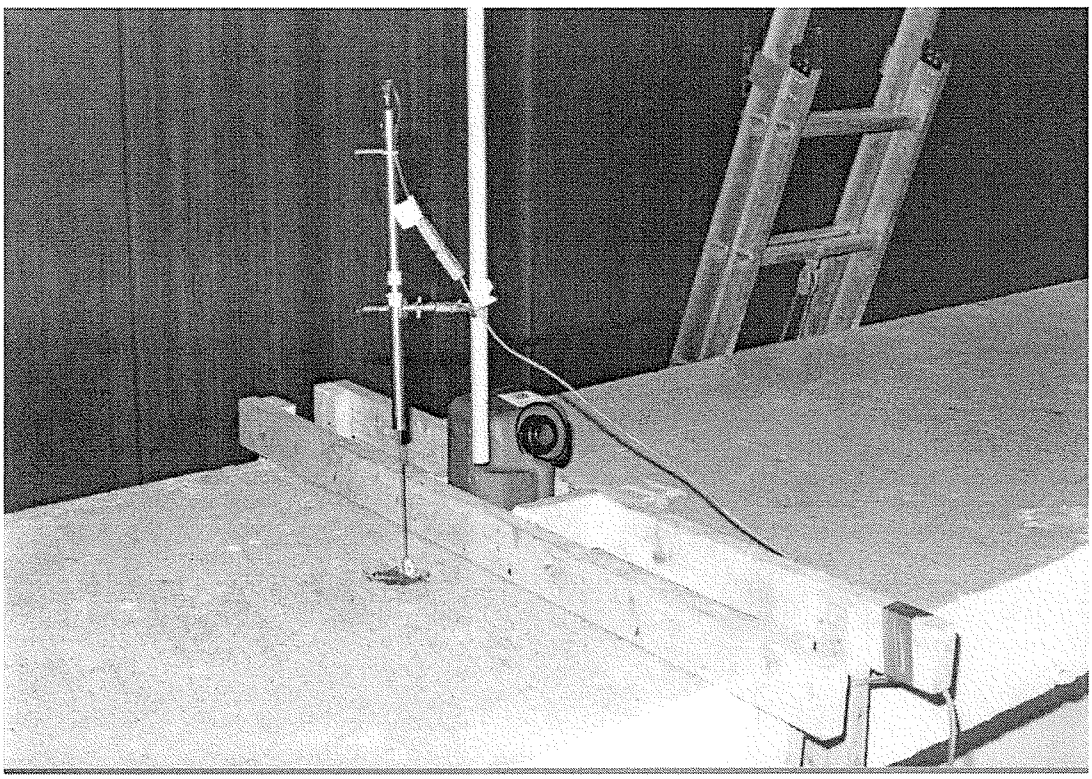

Figure 5.10 Deflection Devices at Midspan – Ultimate Flexural Testing

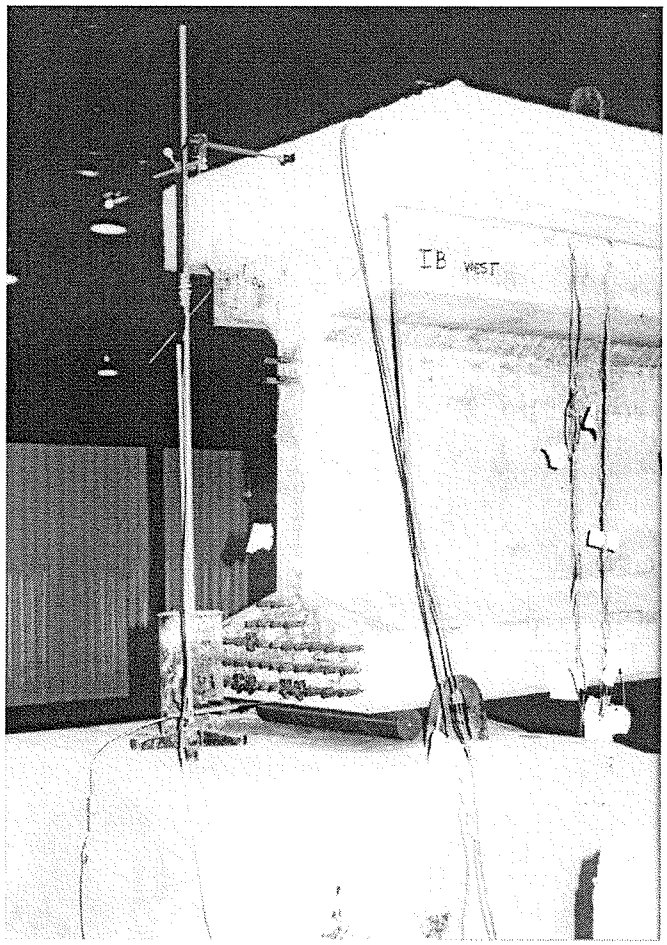

Figure 5.11 End Rotation Devices – Static Testing

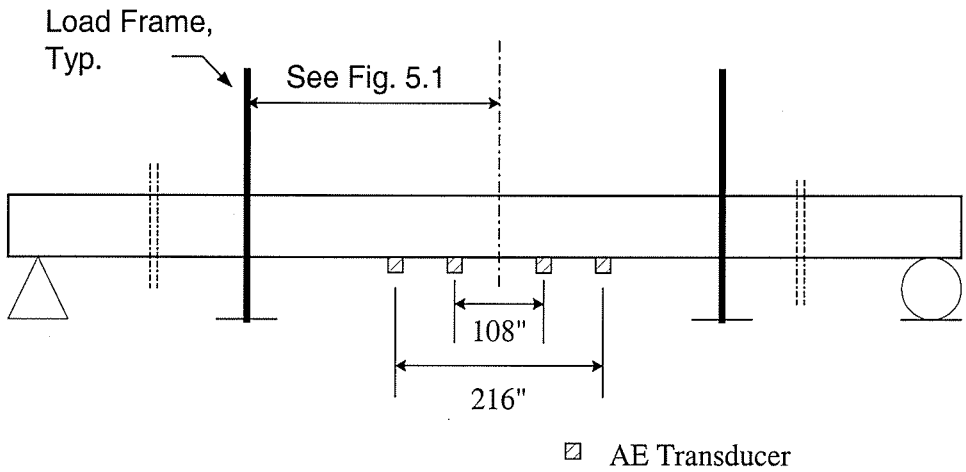

Figure 5.12 AE Transducer Locations

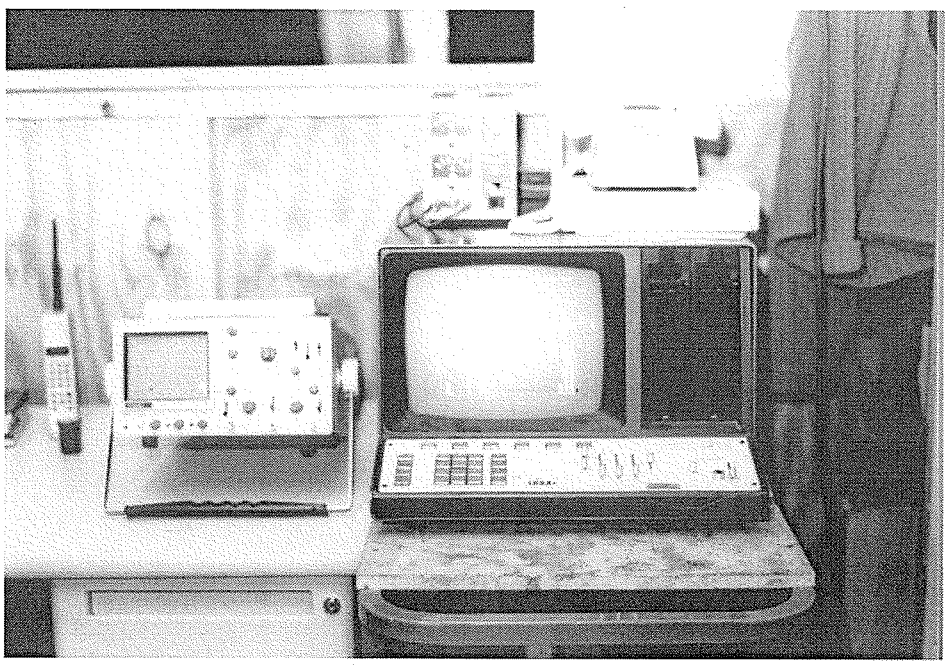

Figure 5.13 AE Data Acquisition System

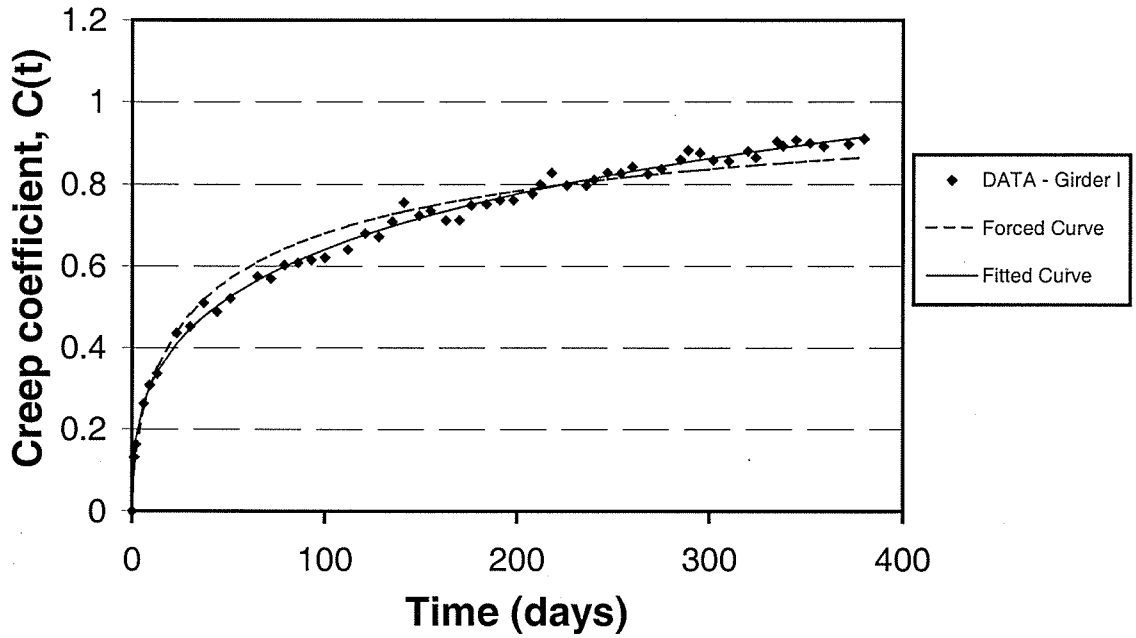

Figure 6.1 Concrete Creep Coefficient over Time – Girder I

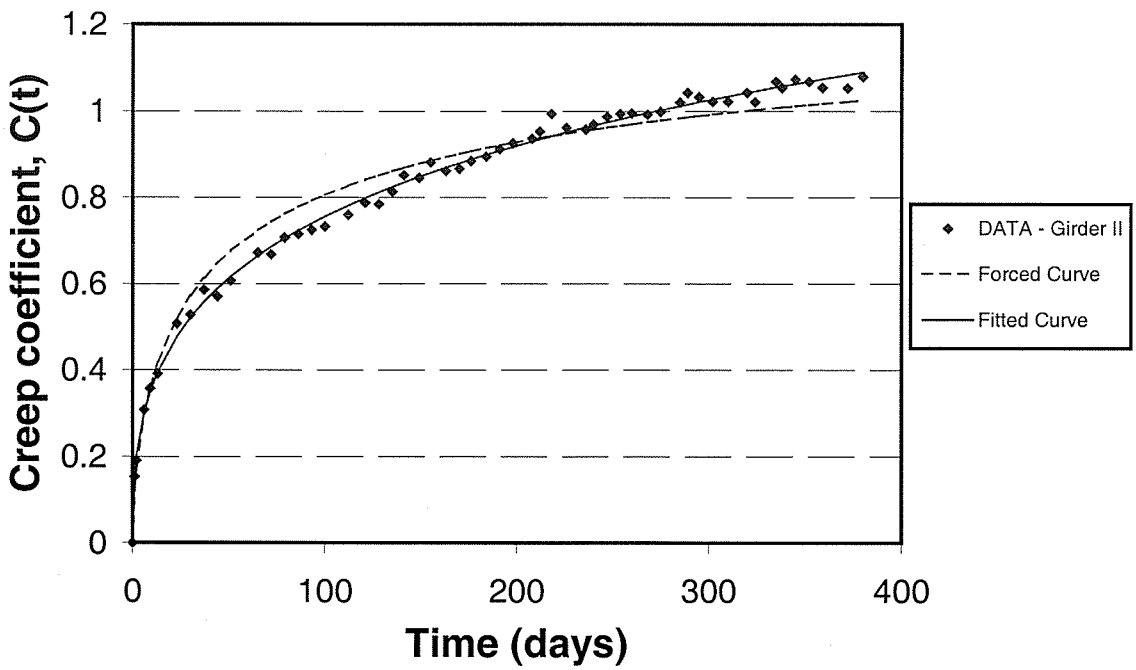

Figure 6.2 Concrete Creep Coefficient over Time – Girder II

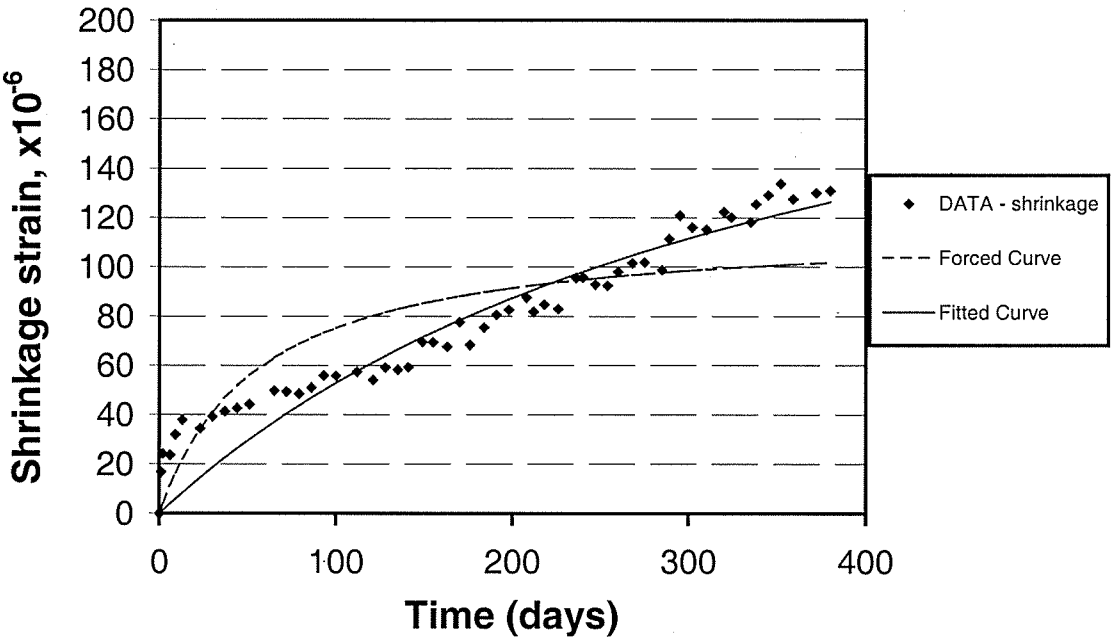

Figure 6.3 Concrete Shrinkage over Time – Girder I

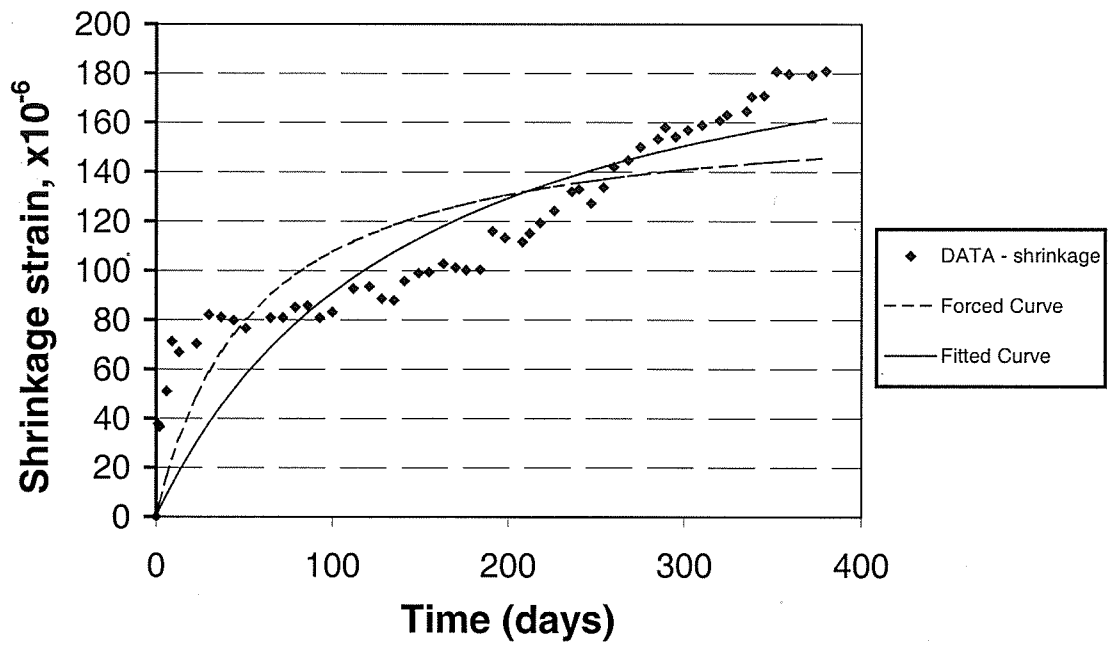

Figure 6.4 Concrete Shrinkage over Time – Girder II

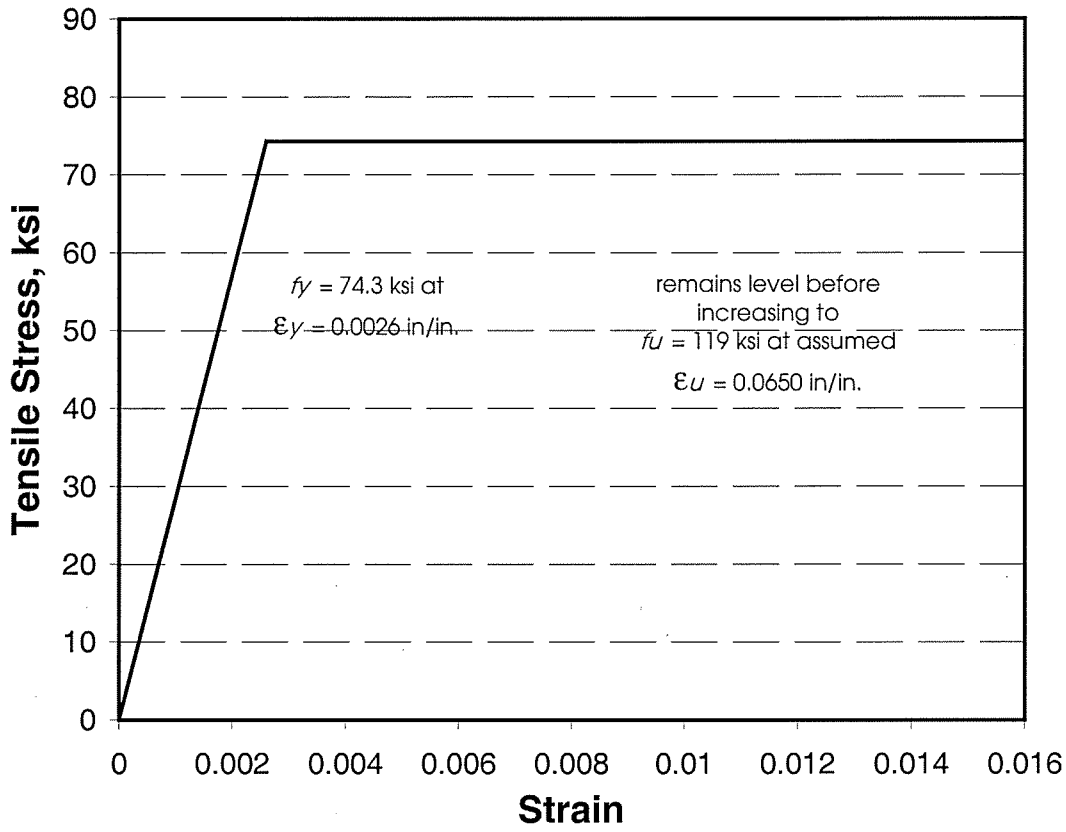

Figure 6.5 Generalized Stress-Strain Curve of Mild Steel Reinforcement

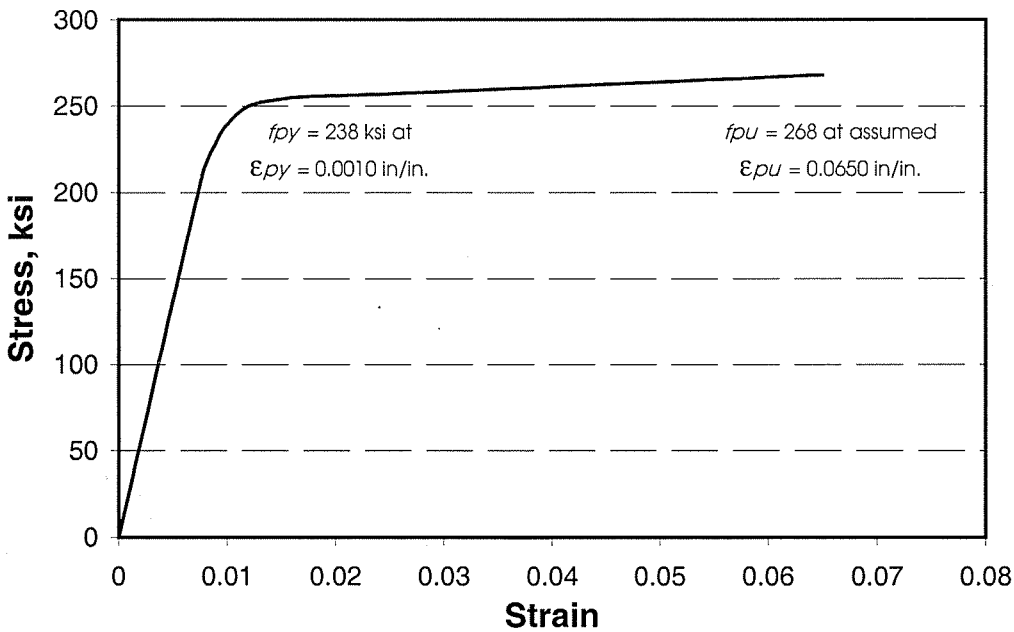

Figure 6.6 Generalized Stress-Strain Curve of Prestressing Steel

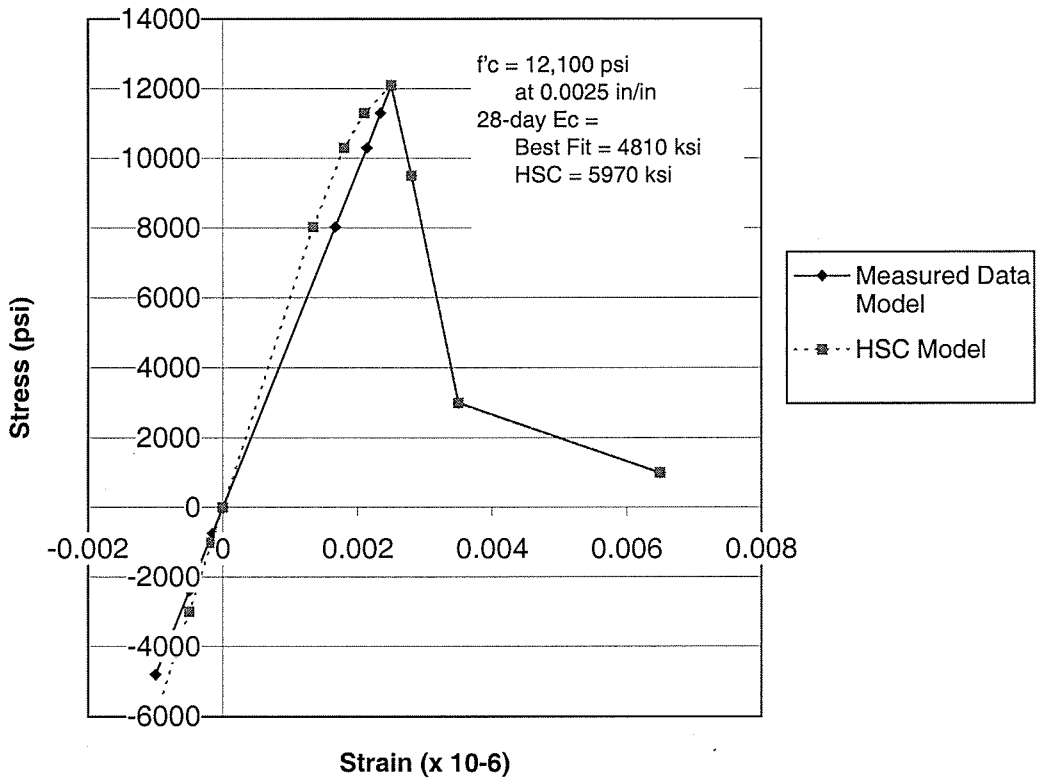

Figure 6.7 *Pbeam* Stress-Strain Model for Girder I Concrete

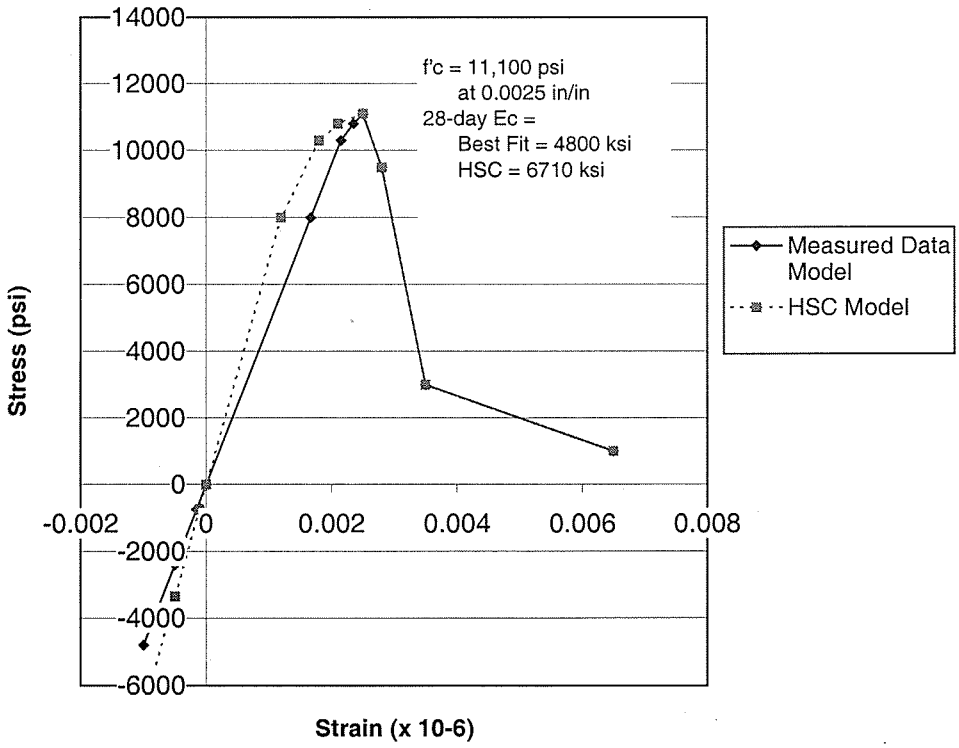

Figure 6.8 *Pbeam* Stress-Strain Model for Girder II Concrete

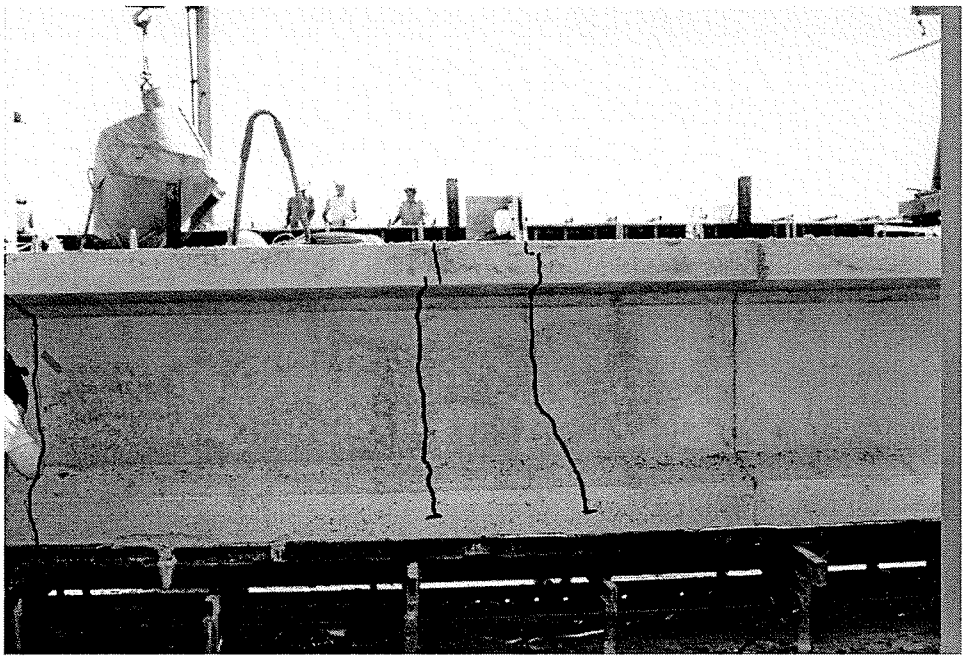

Figure 7.1 Pre-Release Cracks in Girder II

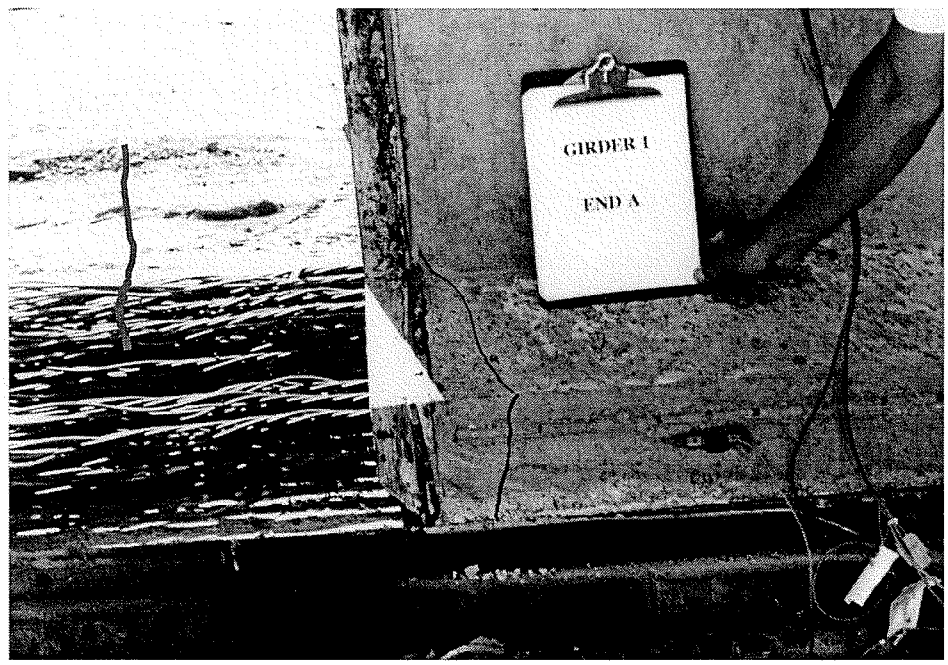

Figure 7.2 Typical End Cracking Due to Release, End I – A

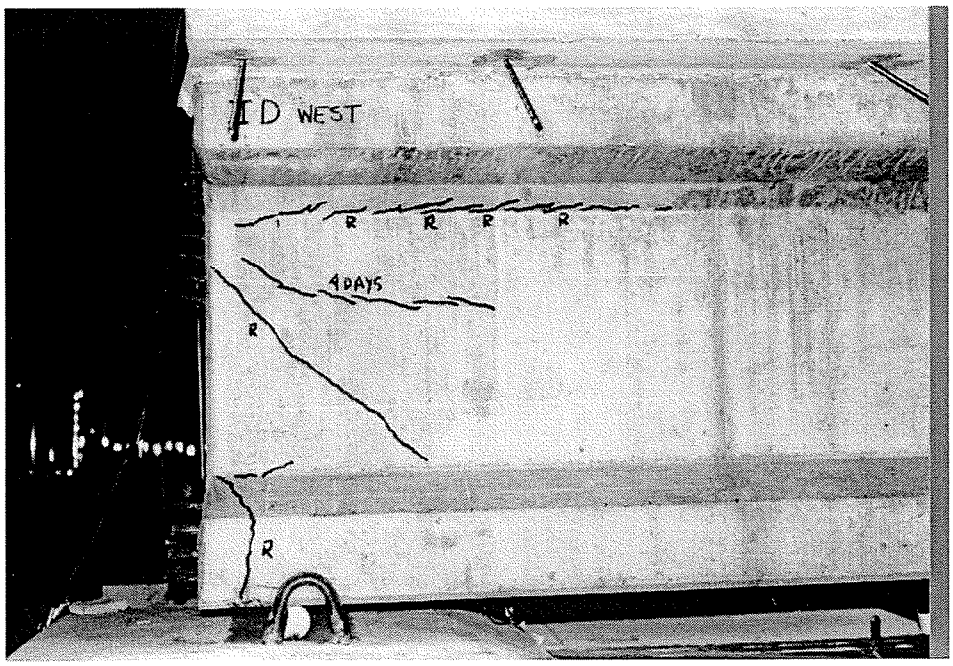

Figure 7.3 Web Cracking in End II - D

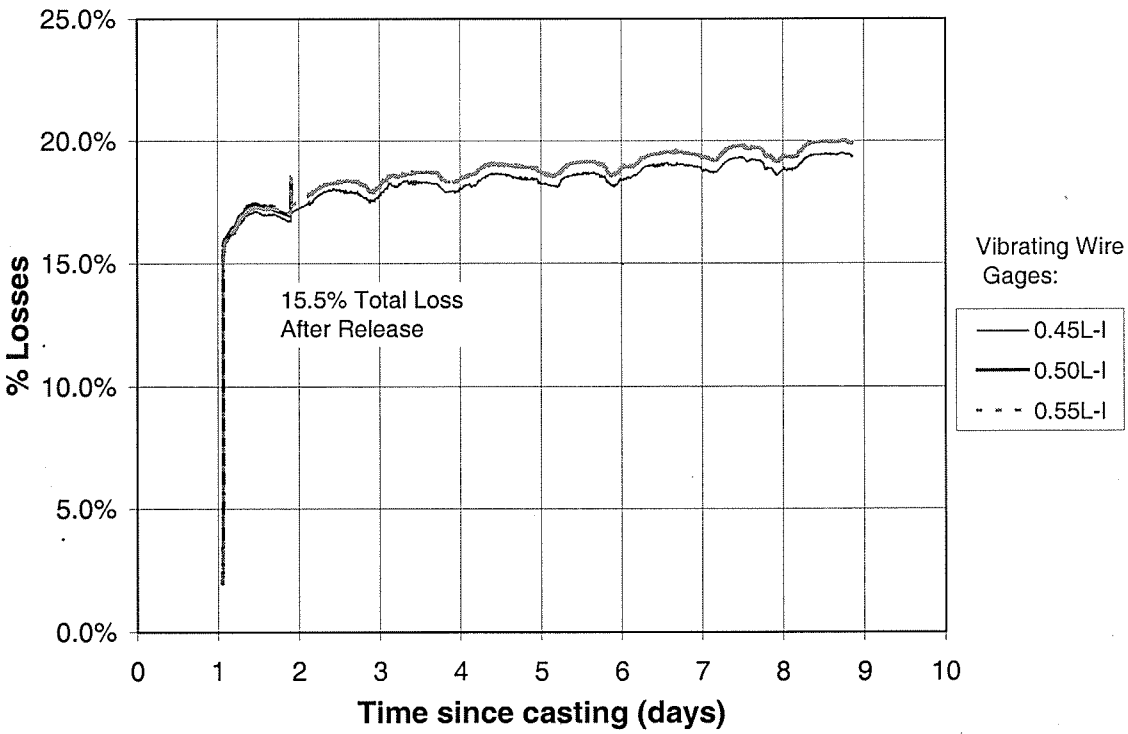

Figure 7.4 Initial Prestress Losses, Girder I

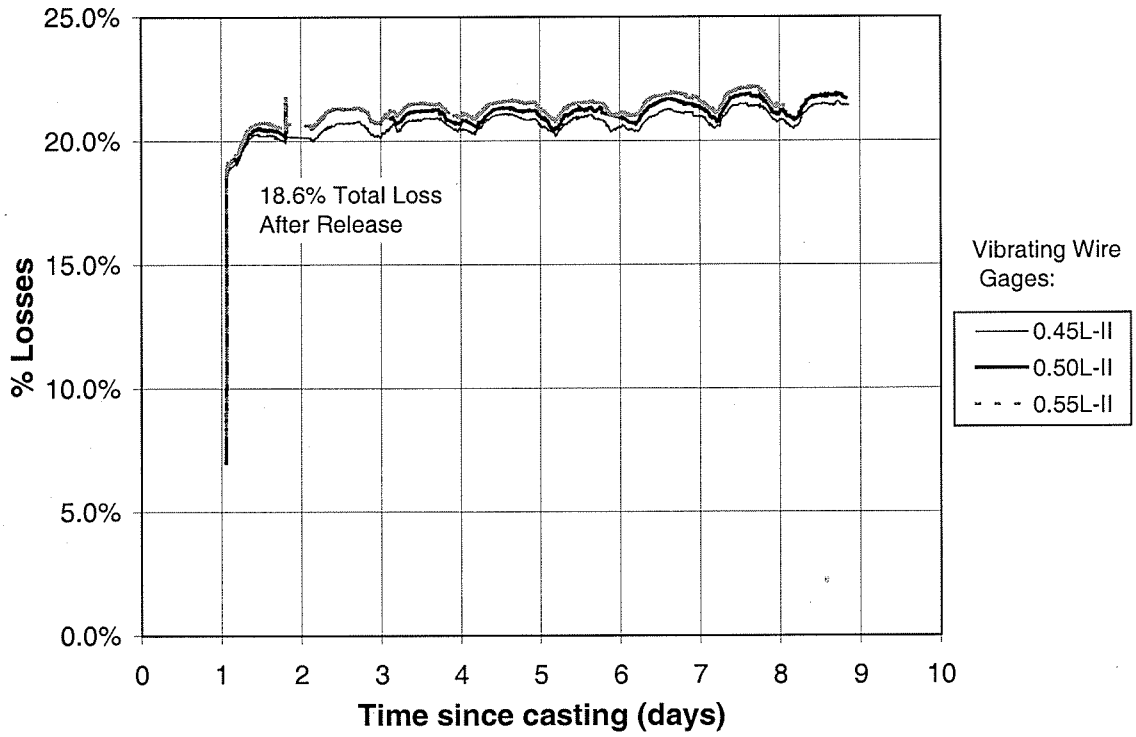

Figure 7.5 Initial Prestress Losses, Girder II

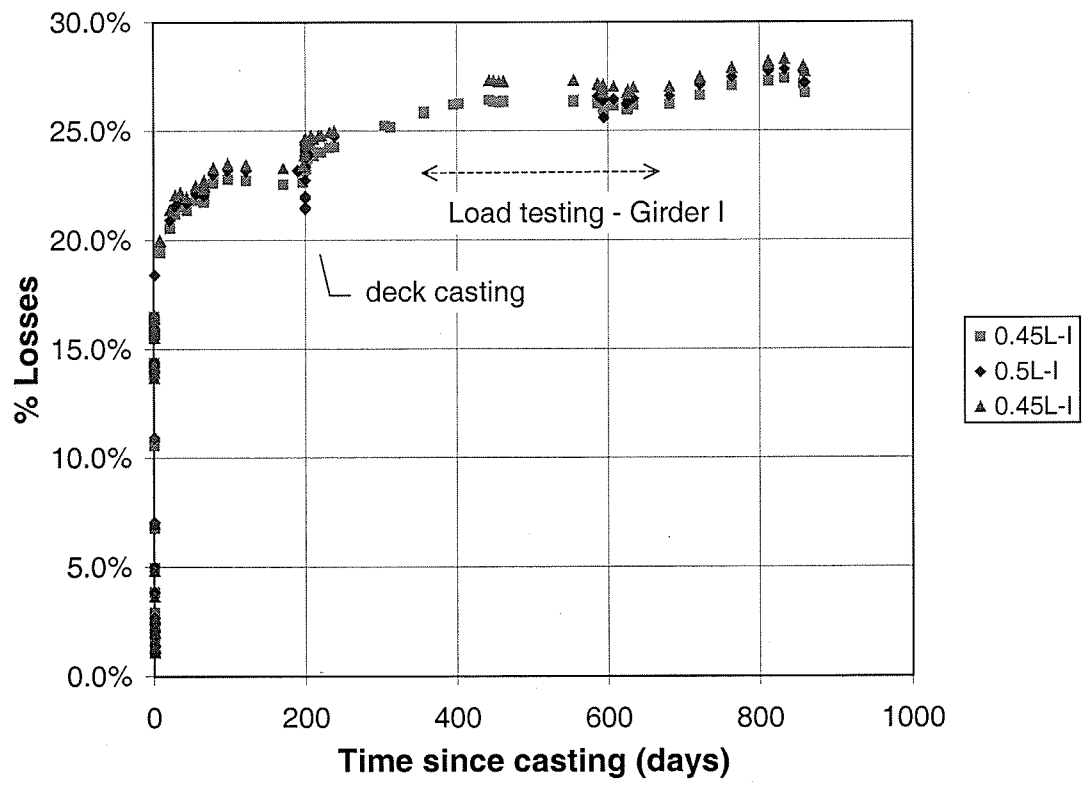

Figure 7.6 Long-term Prestress Losses, Girder I

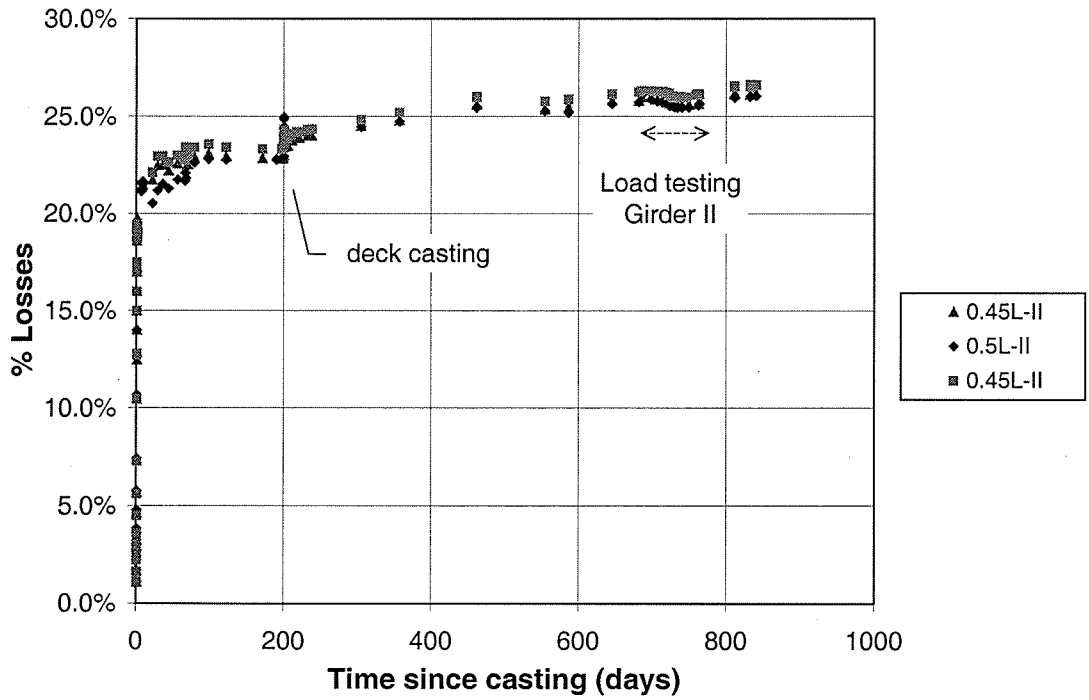

Figure 7.7 Long-term Prestress Losses, Girder II

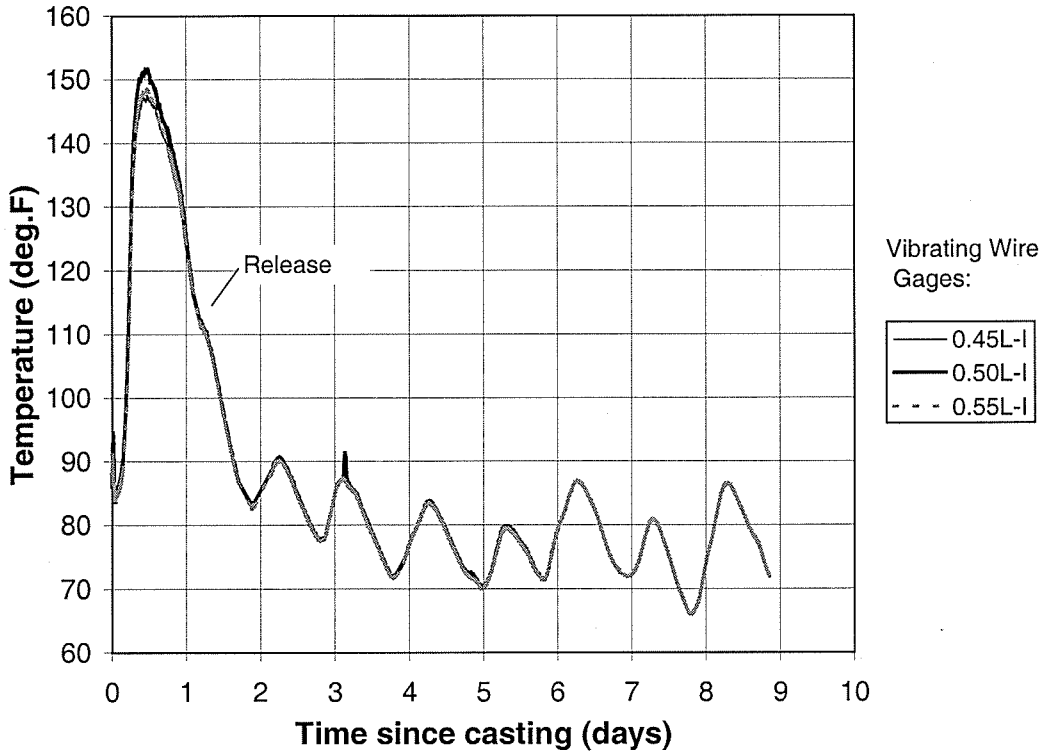

Figure 7.8 Daily Temperature Fluctuations in Girder I

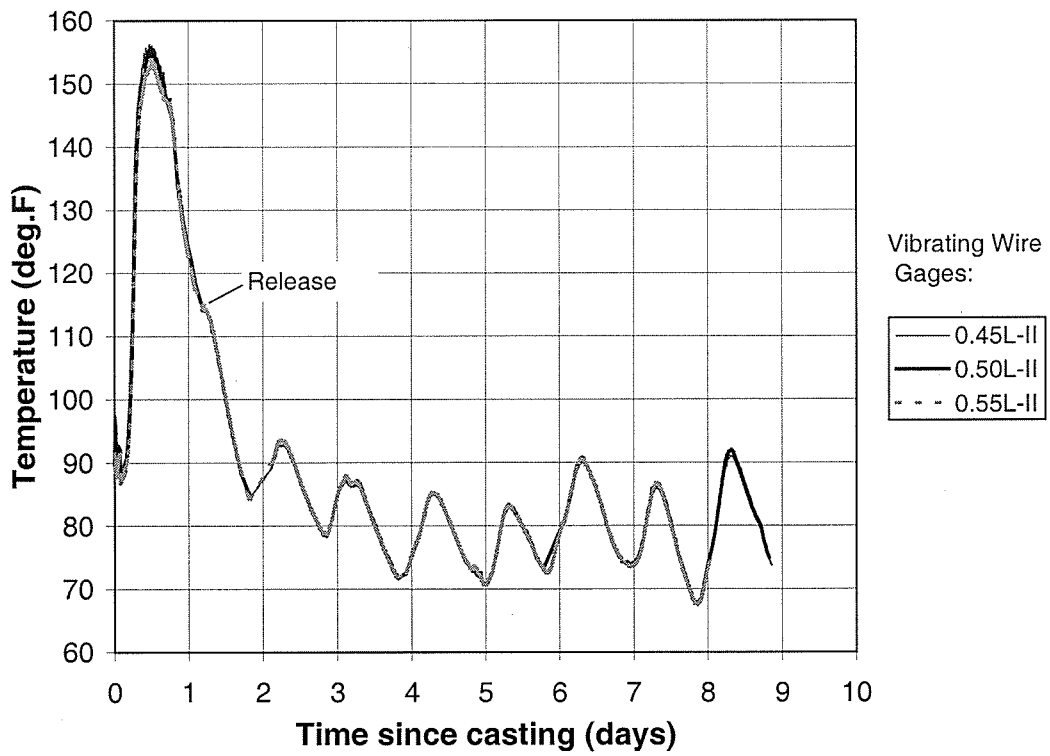

Figure 7.9 Daily Temperature Fluctuations in Girder II

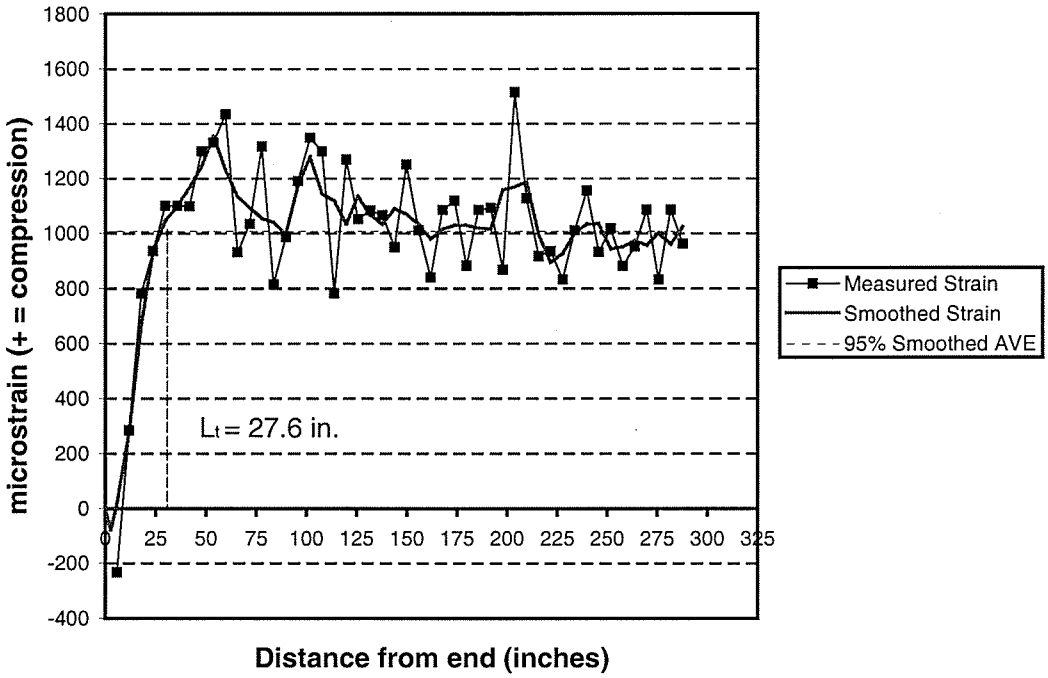

Figure 7.10a Transfer Length – 95% Average Maximum Strain Method, Girder I, End A

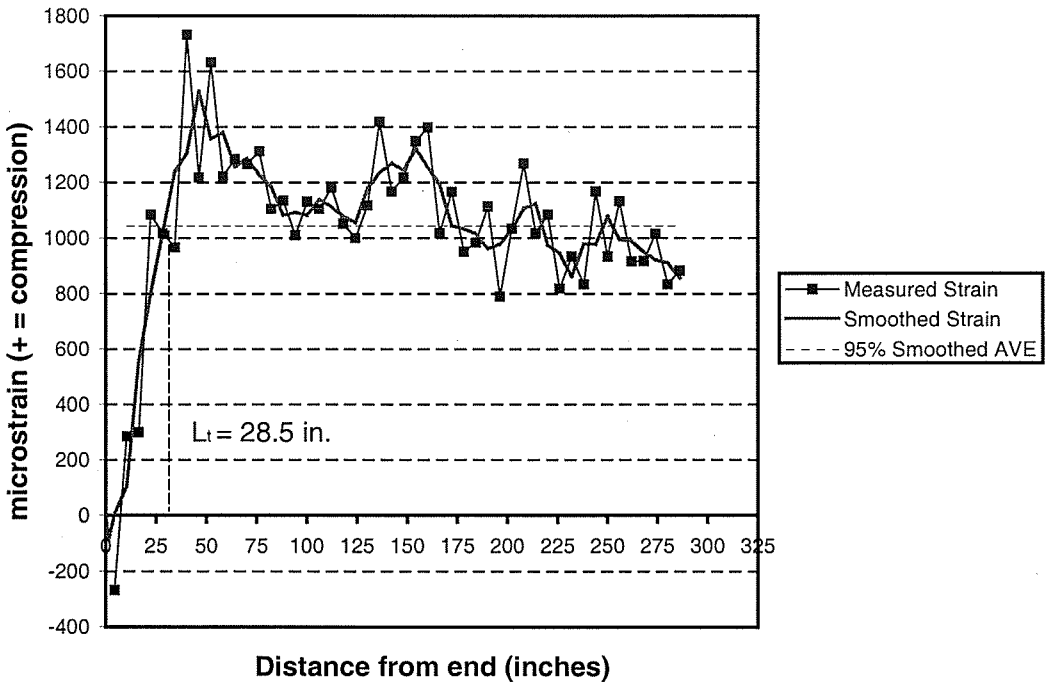

Figure 7.10b Transfer Length – 95% Average Maximum Strain Method, Girder I, End B

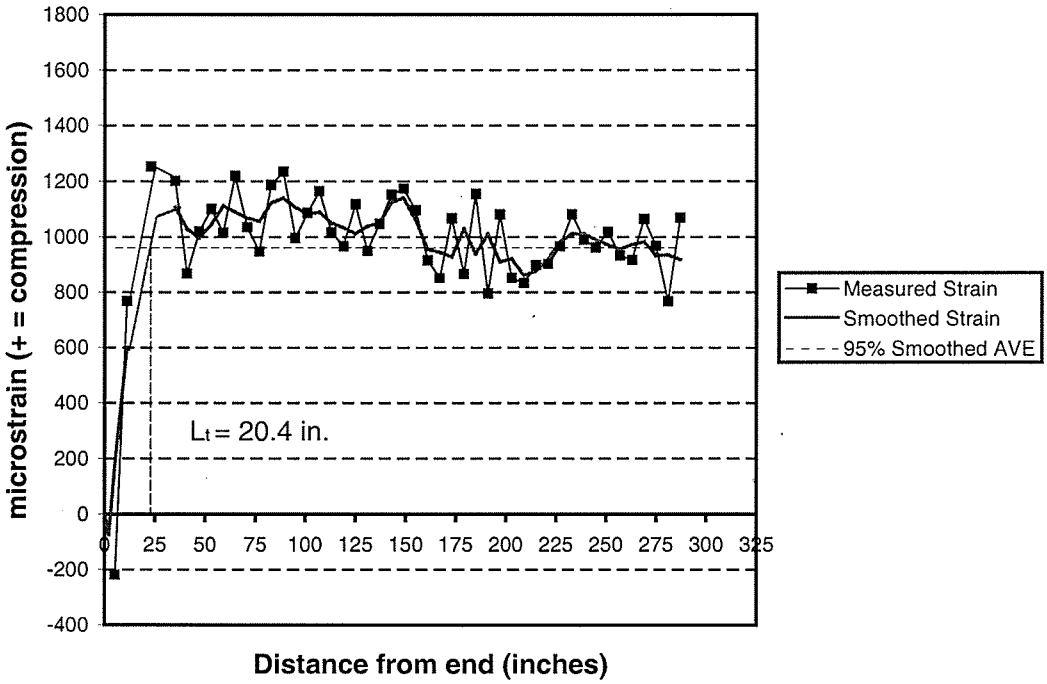

Figure 7.10c Transfer Length – 95% Average Maximum Strain Method, Girder II, End C

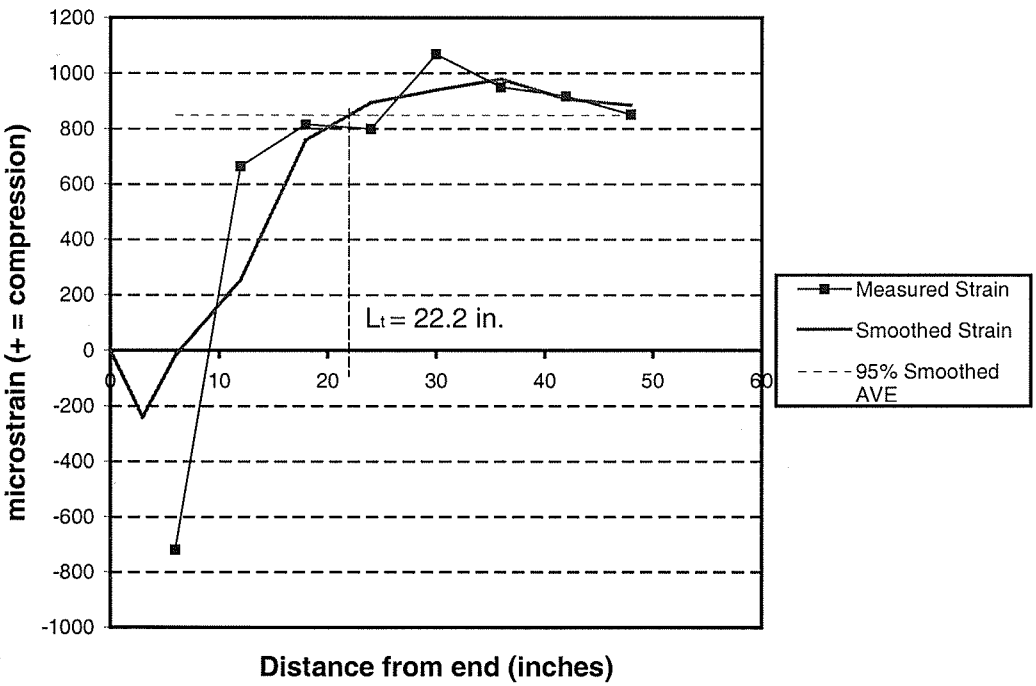

Figure 7.10d Transfer Length – 95% Average Maximum Strain Method, Girder II, End D

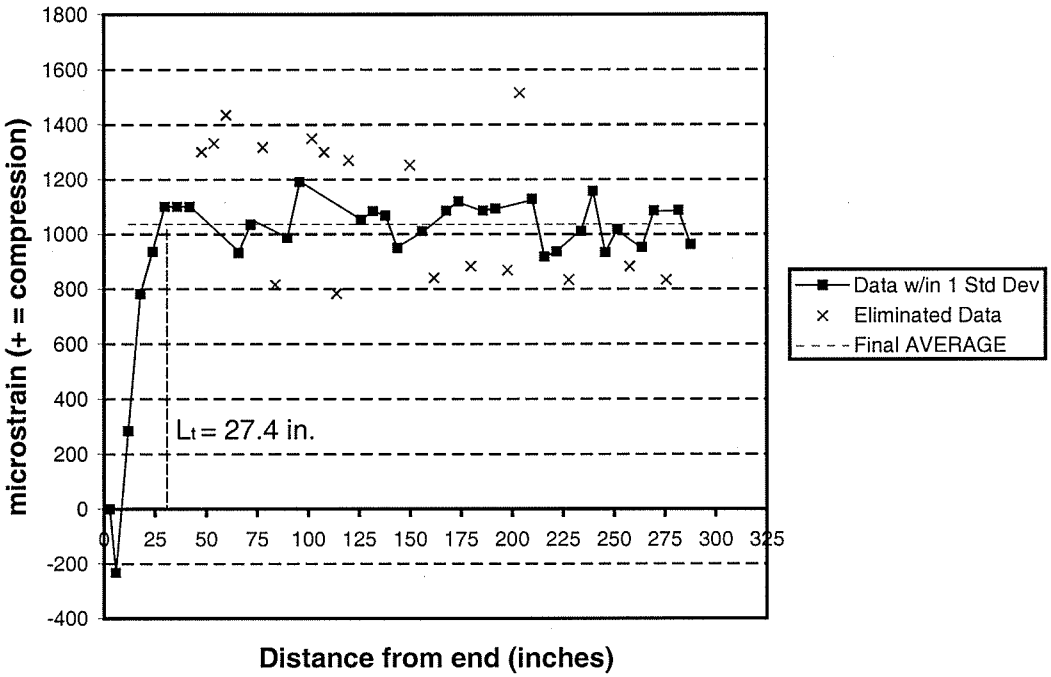

Figure 7.11a Transfer Length – Final Average Method, Girder I, End A

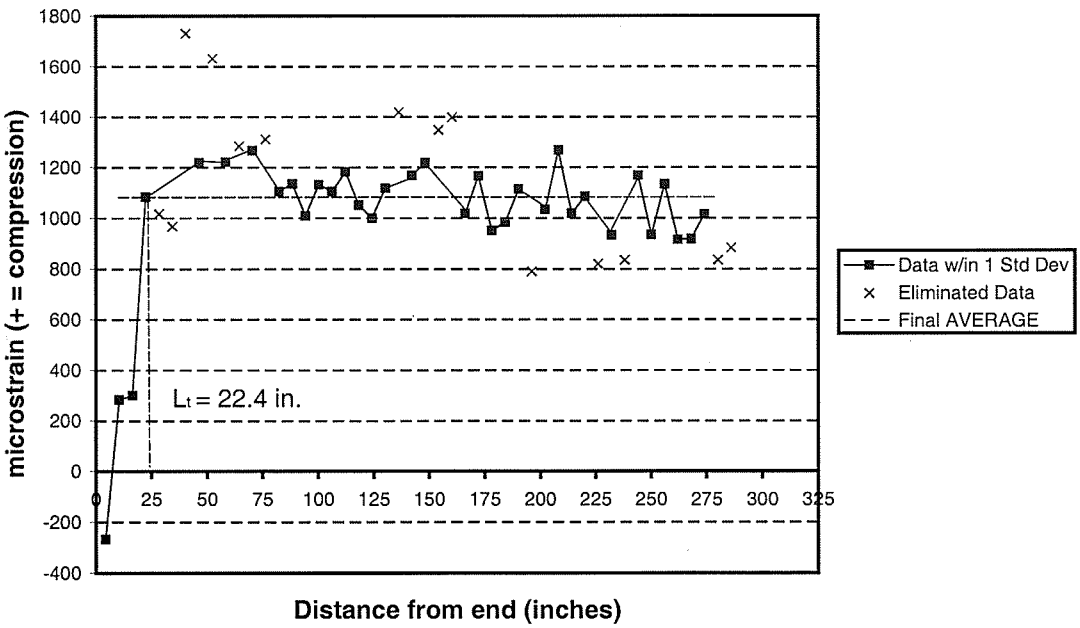

Figure 7.11b Transfer Length – Final Average Method, Girder I, End B

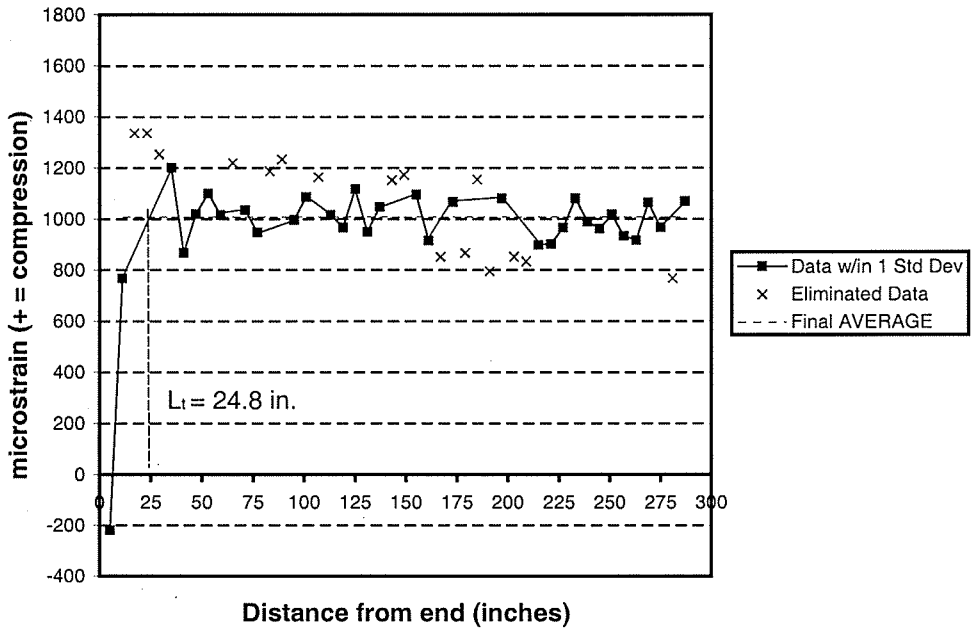

Figure 7.11c Transfer Length – Final Average Method, Girder II, End C

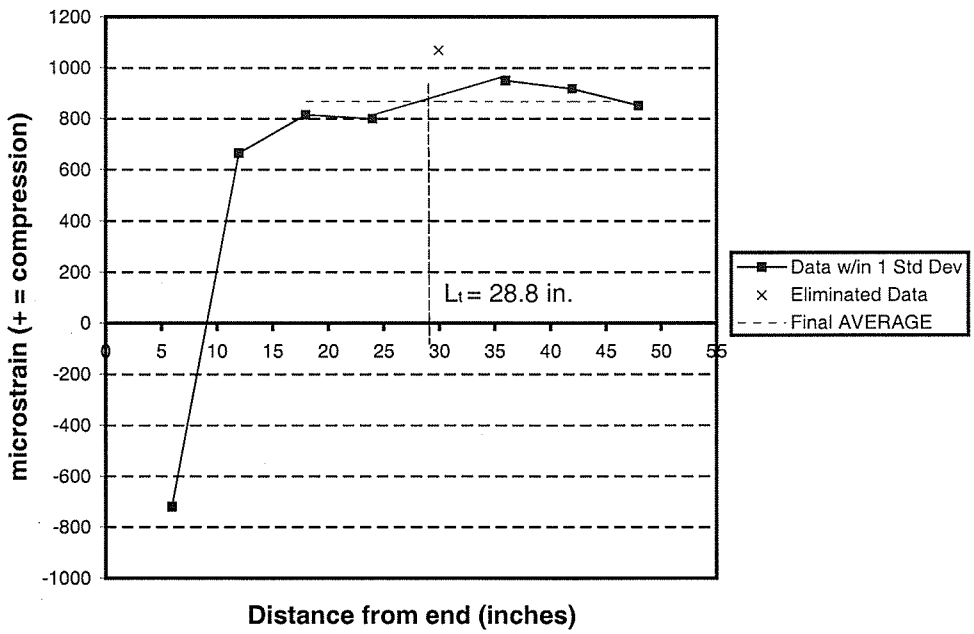

Figure 7.11d Transfer Length – Final Average Method, Girder II, End D

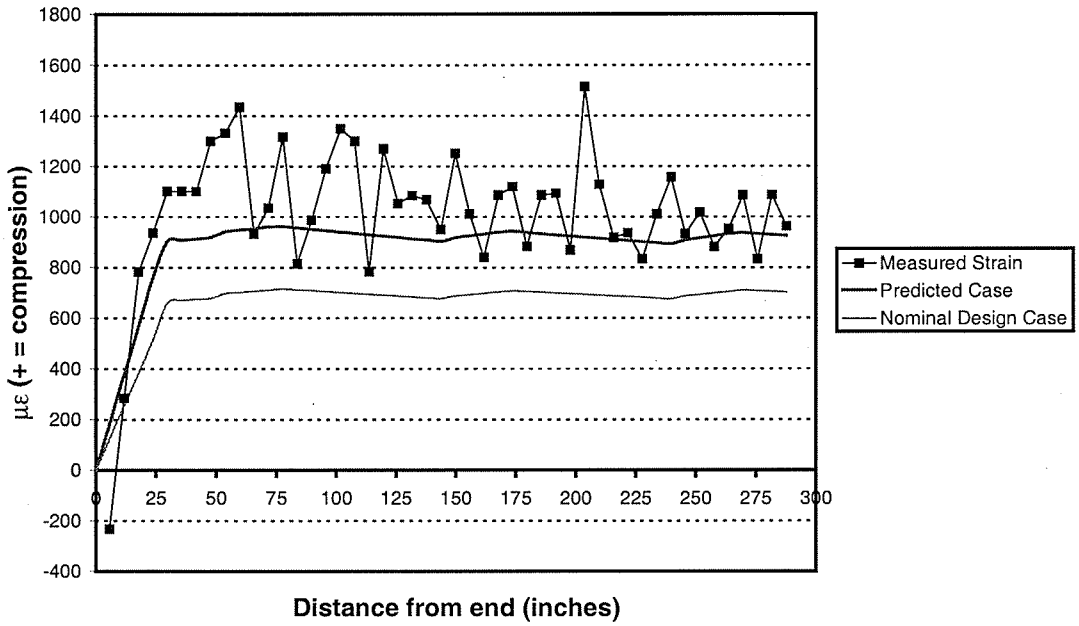

Figure 7.12a Strain Comparison for DEMEC Data, Girder I, End A

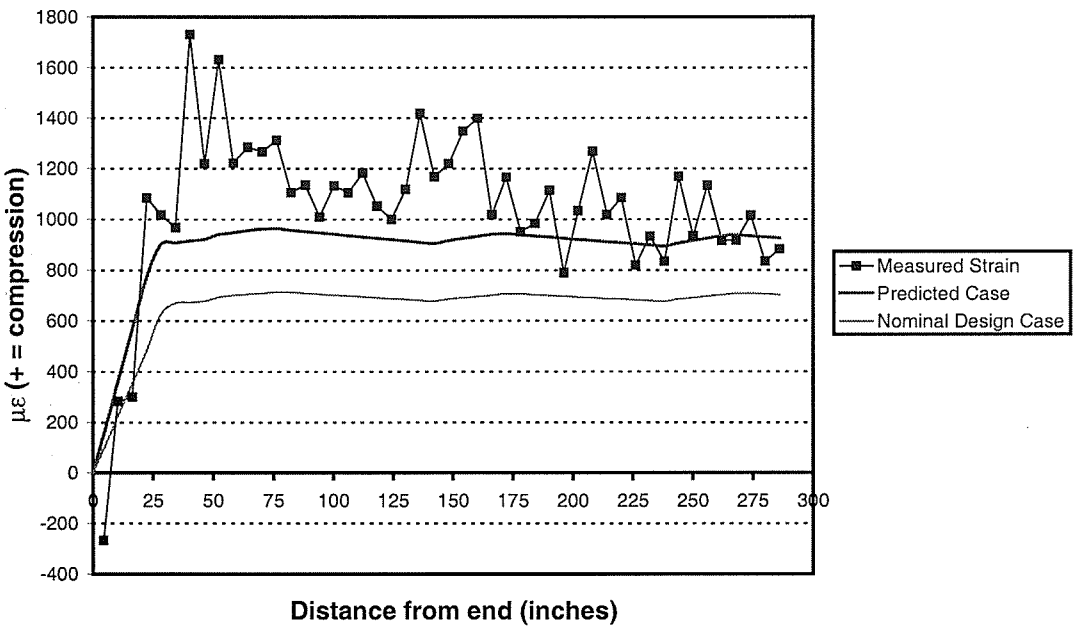

Figure 7.12b Strain Comparison for DEMEC Data, Girder I, End B

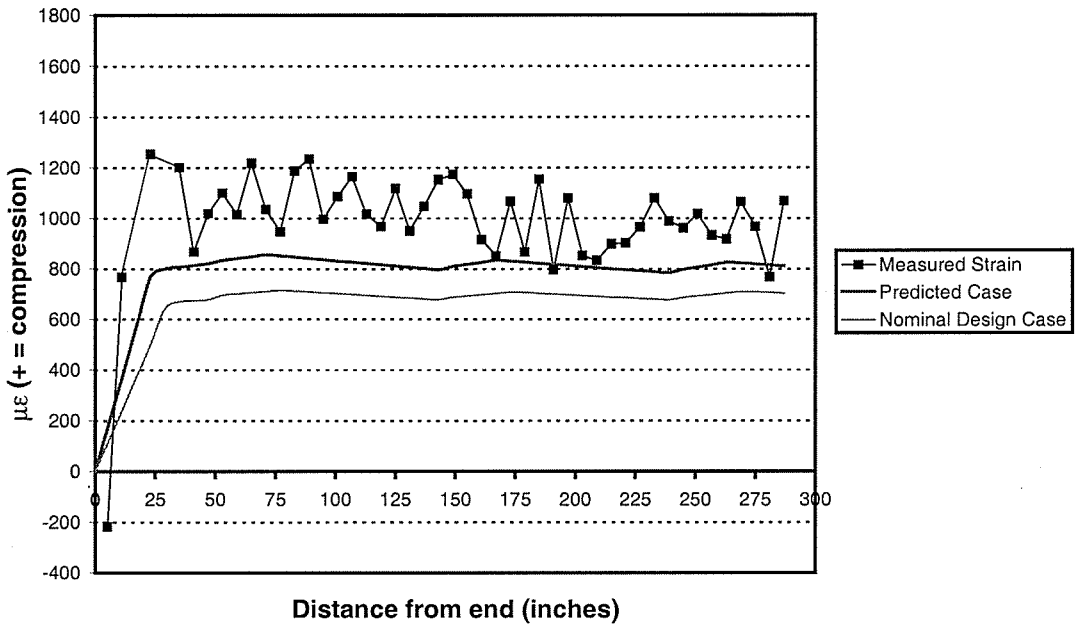

Figure 7.12c Strain Comparison for DEMEC Data, Girder II, End C

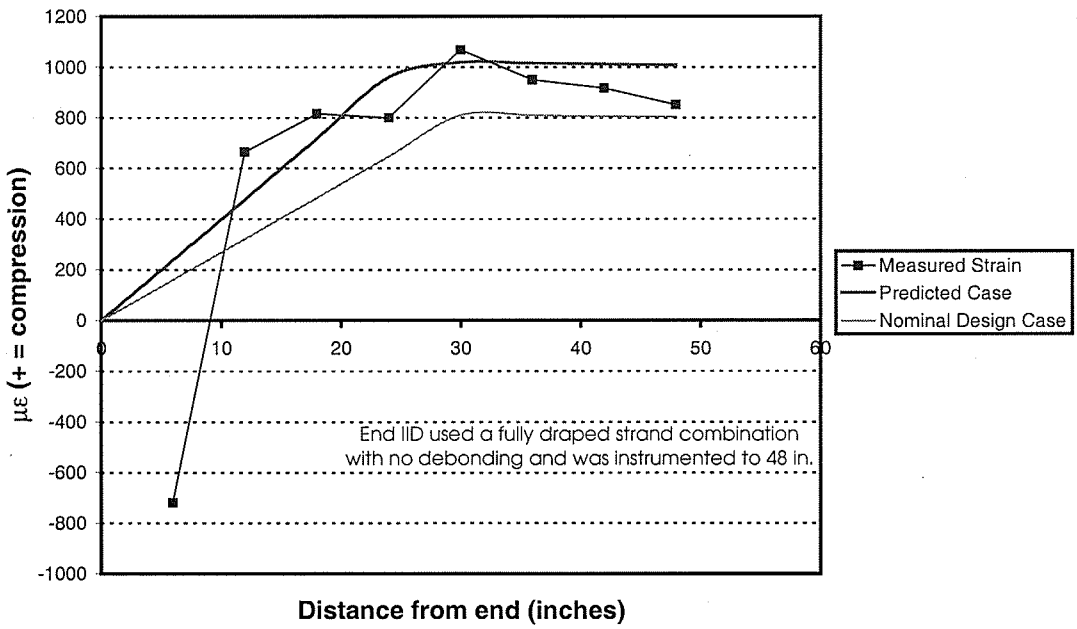

Figure 7.12d Strain Comparison for DEMEC Data, Girder II, End D

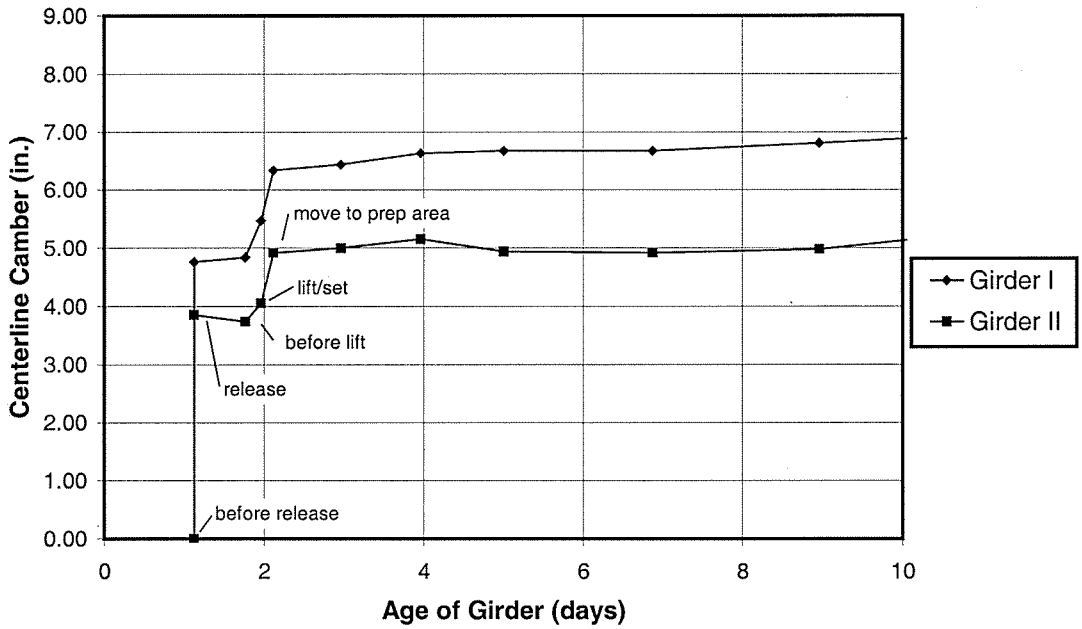

Figure 7.13 Initial Measured Camber of Test Girders

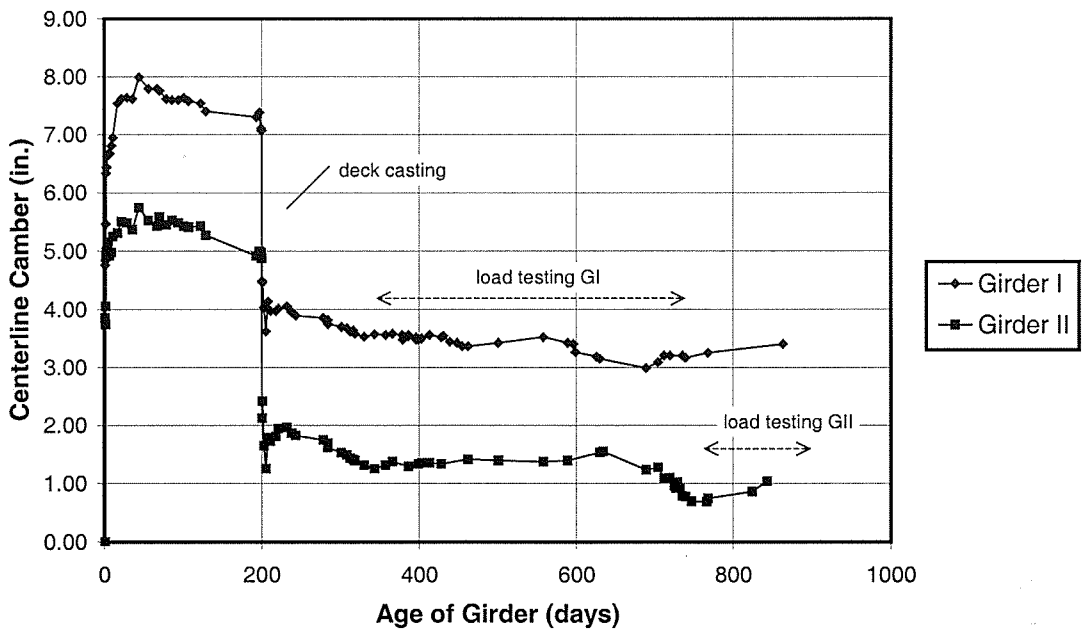

Figure 7.14 Long-term Measured Camber of Test Girders

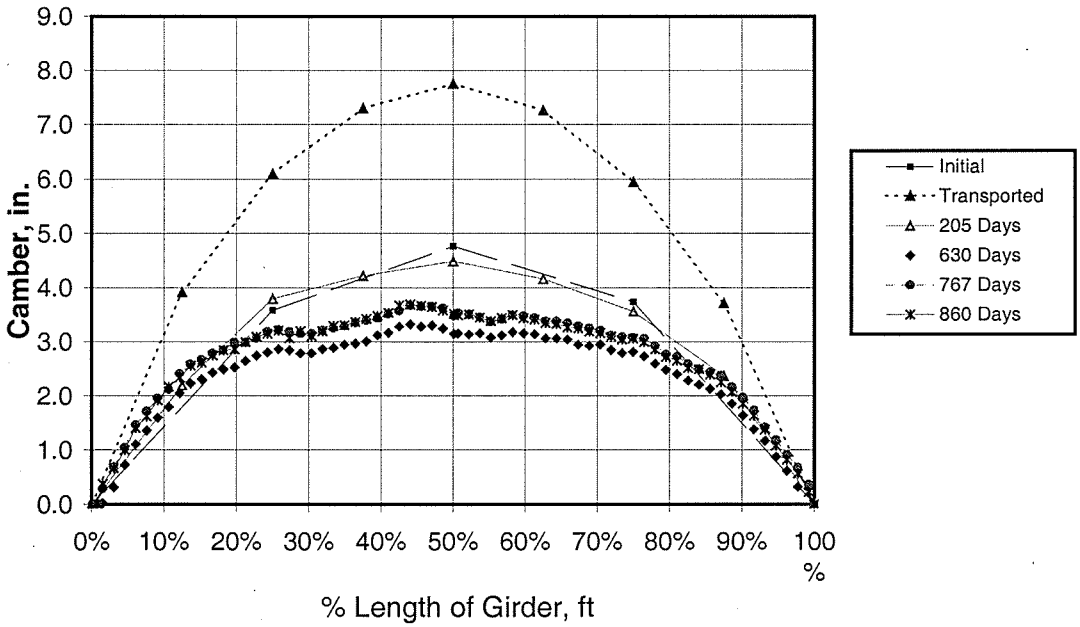

Figure 7.15 Measured Deflected Shape of Girder I

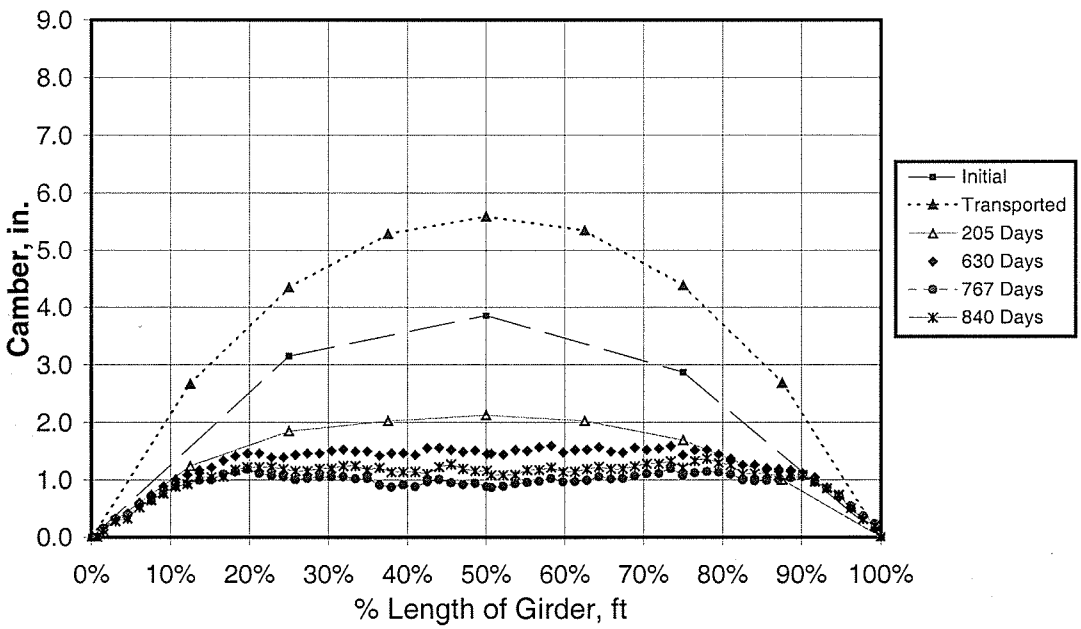

Figure 7.16 Measured Deflected Shape of Girder II

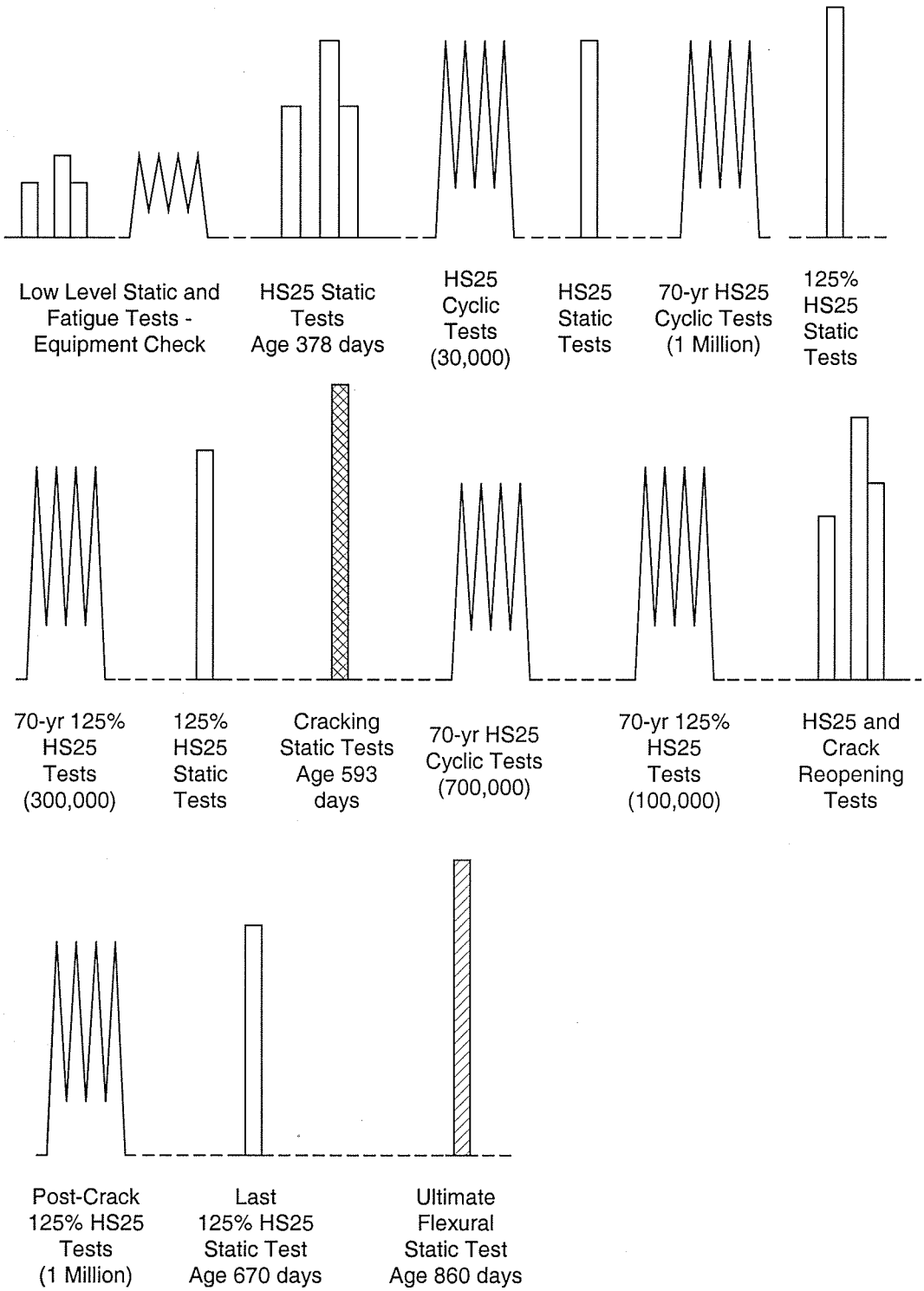

Figure 8.1 Load History Summary of Girder I

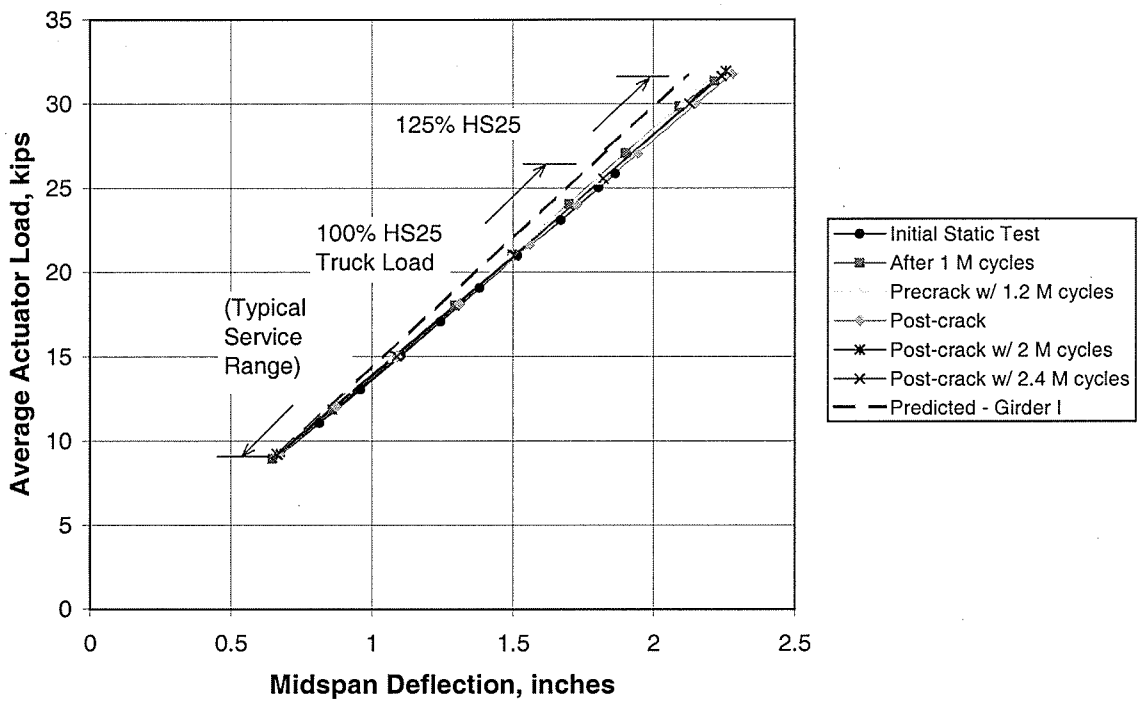

Figure 8.2 Load Deflection Response of Girder I

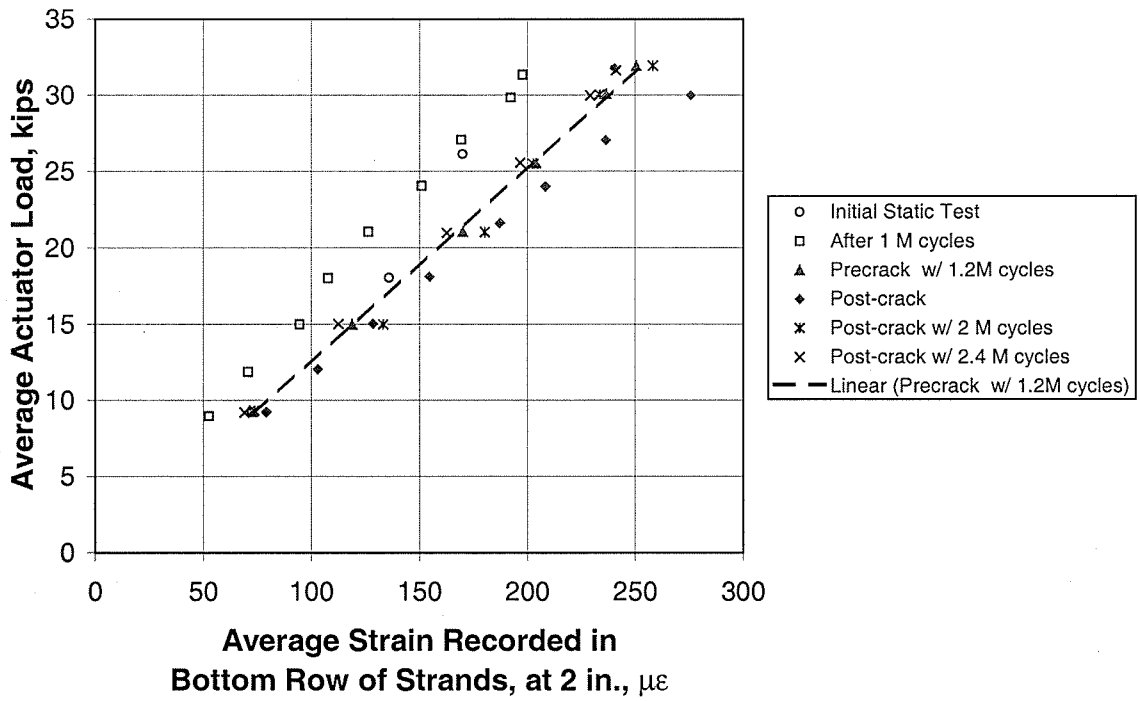

Figure 8.3 Load-Strain Behavior, Bottom Row of Strands – Girder I

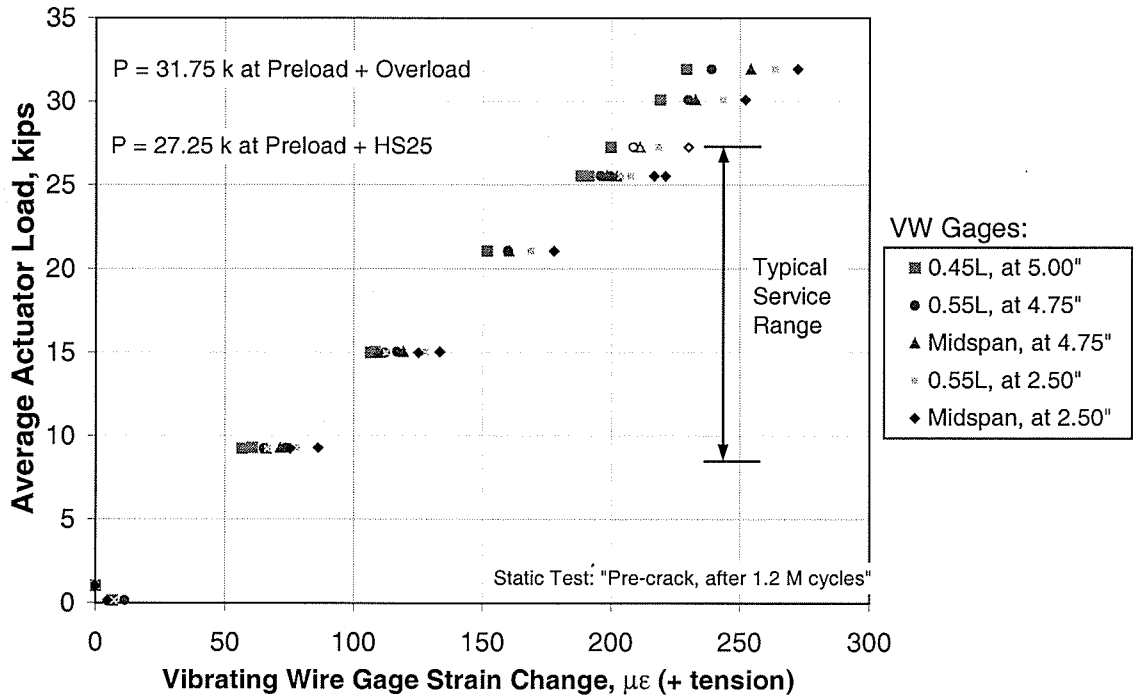

Figure 8.4 Load-Strain Behavior, Bottom Flange – Girder I

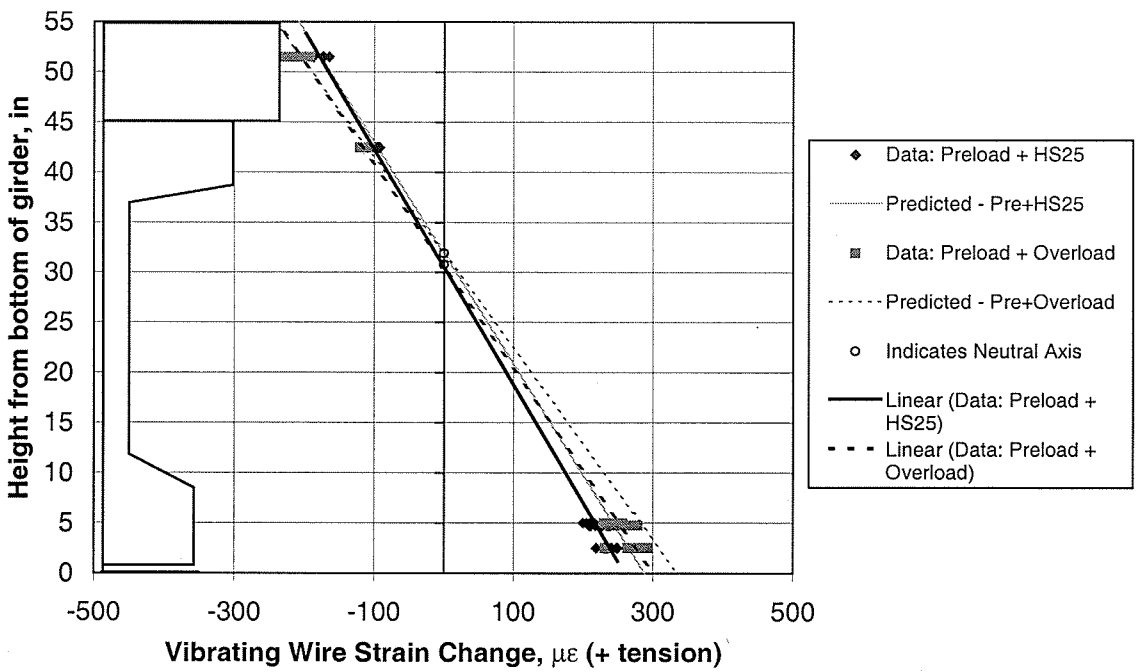

Figure 8.5 Strain Distribution versus Depth – VW Gages

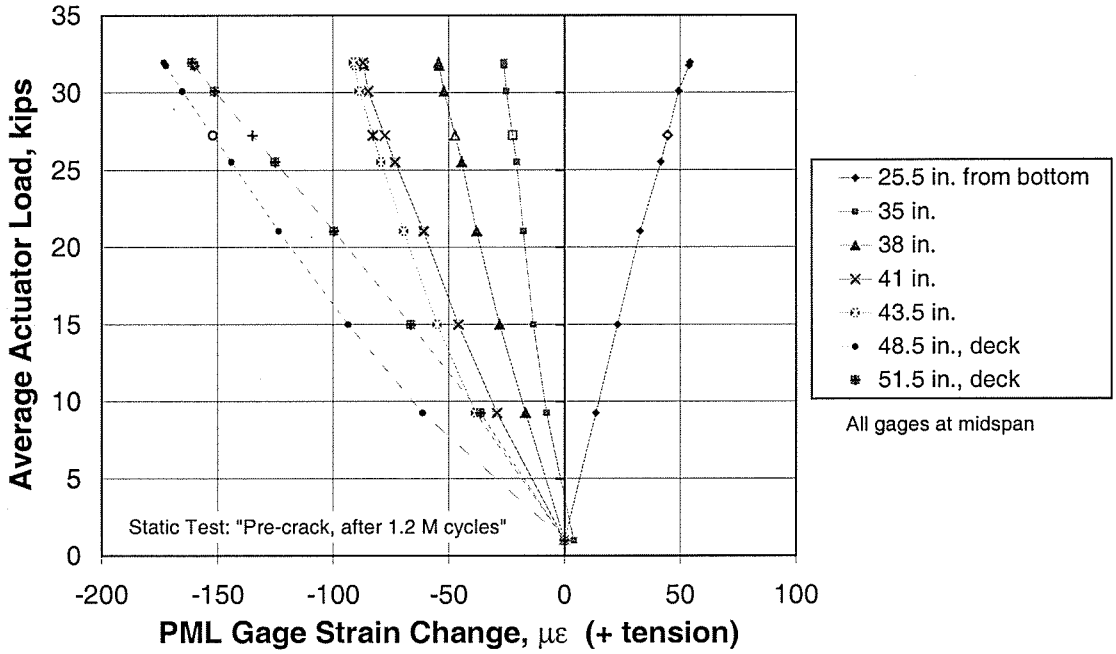

Figure 8.6 Load-Strain Behavior, Top Flange – Girder I

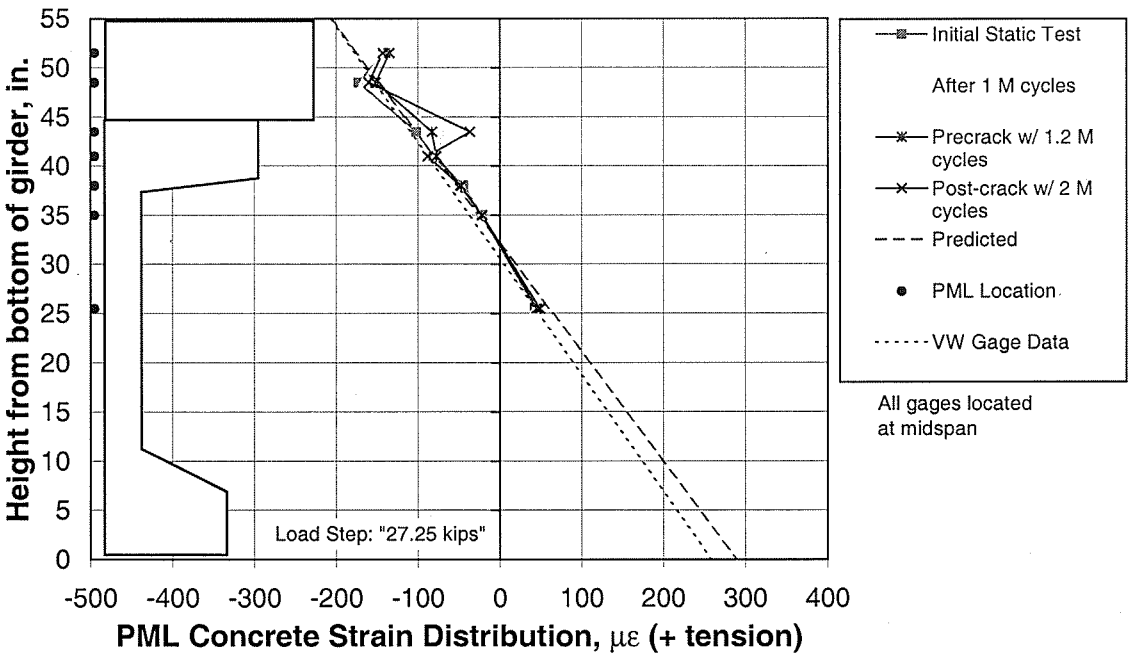

Figure 8.7 Strain Distribution versus Depth – PML Gages at HS25

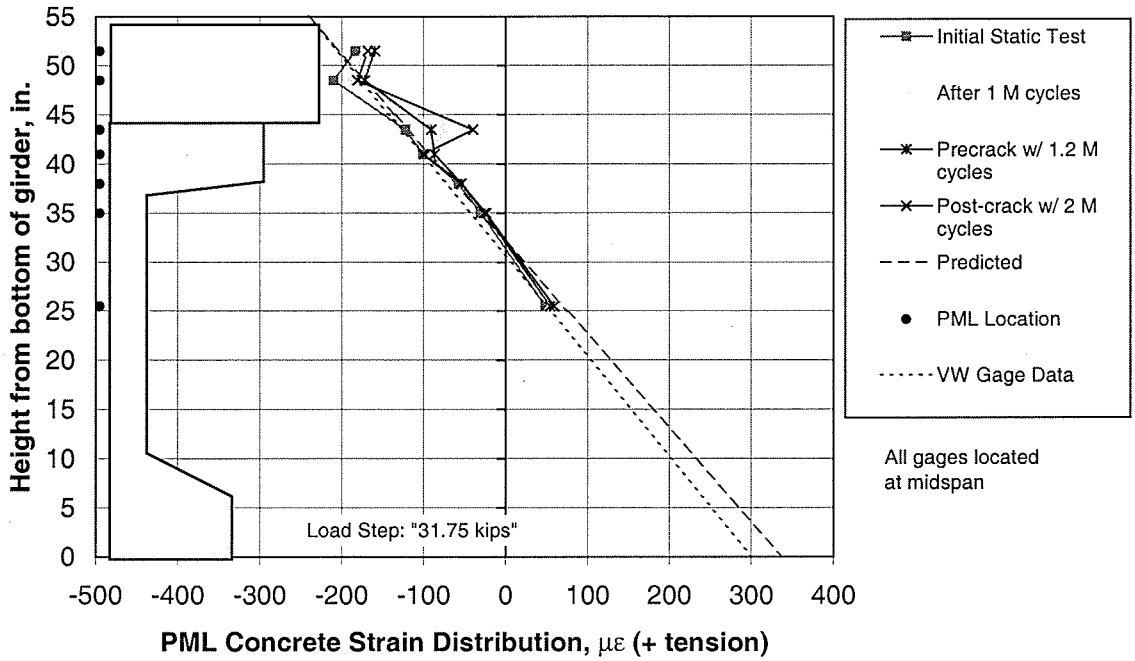

Figure 8.8 Strain Distribution versus Depth – PML Gages at Overload

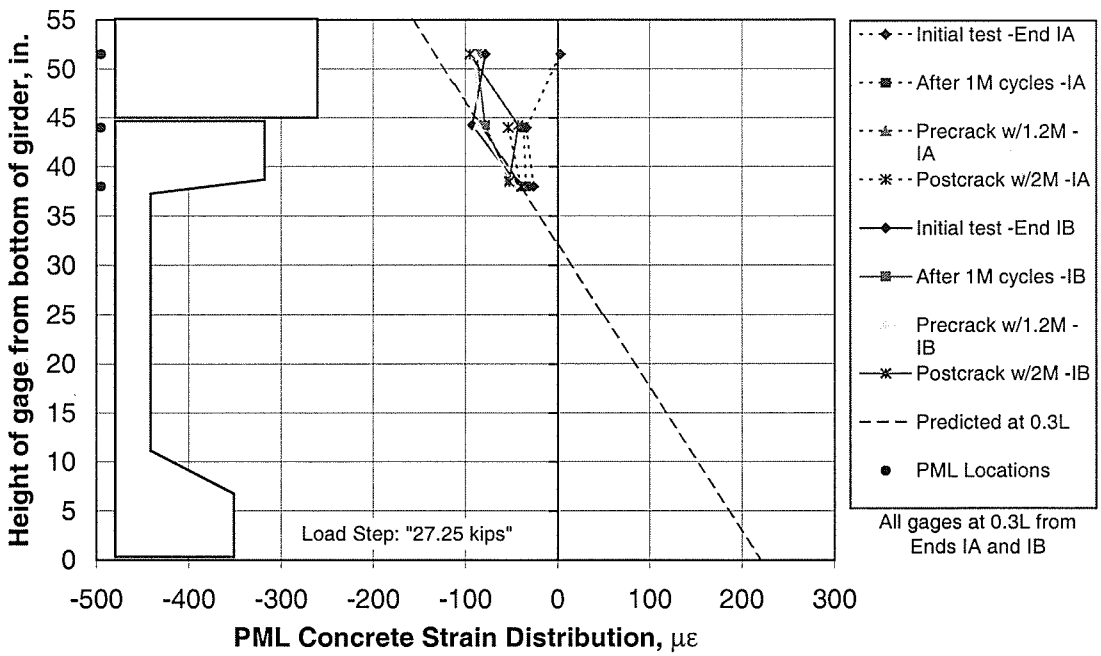

Figure 8.9 Strain Distribution versus Depth – PML Gages at HS25 – 0.3L

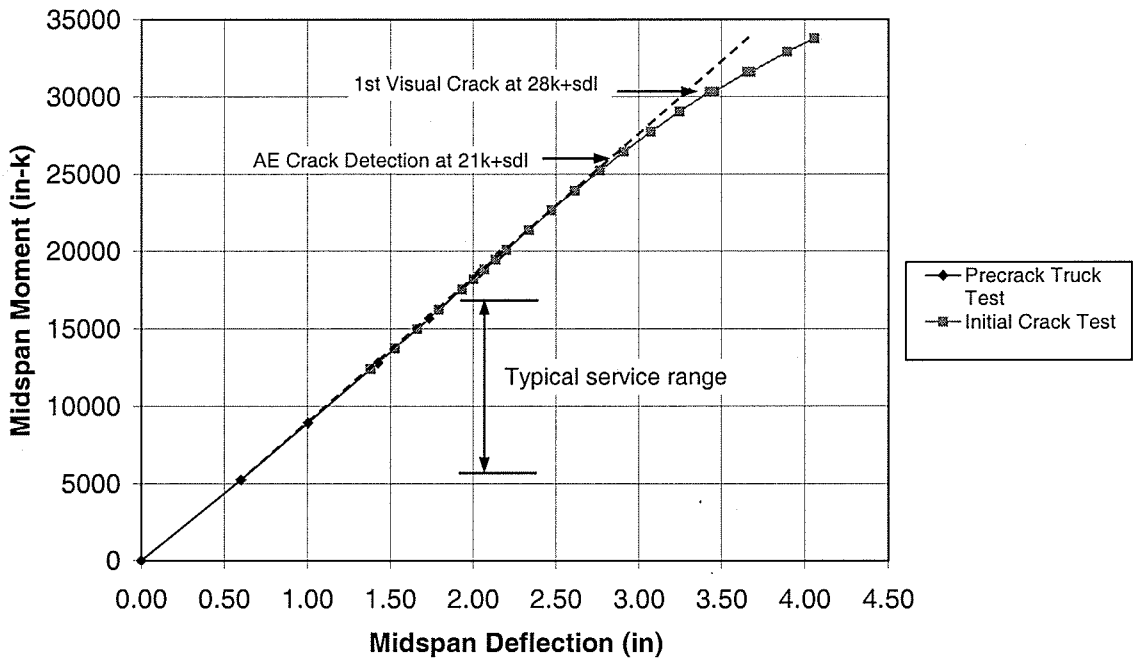

Figure 8.10 Moment-Deflection Response – Initial Crack Test

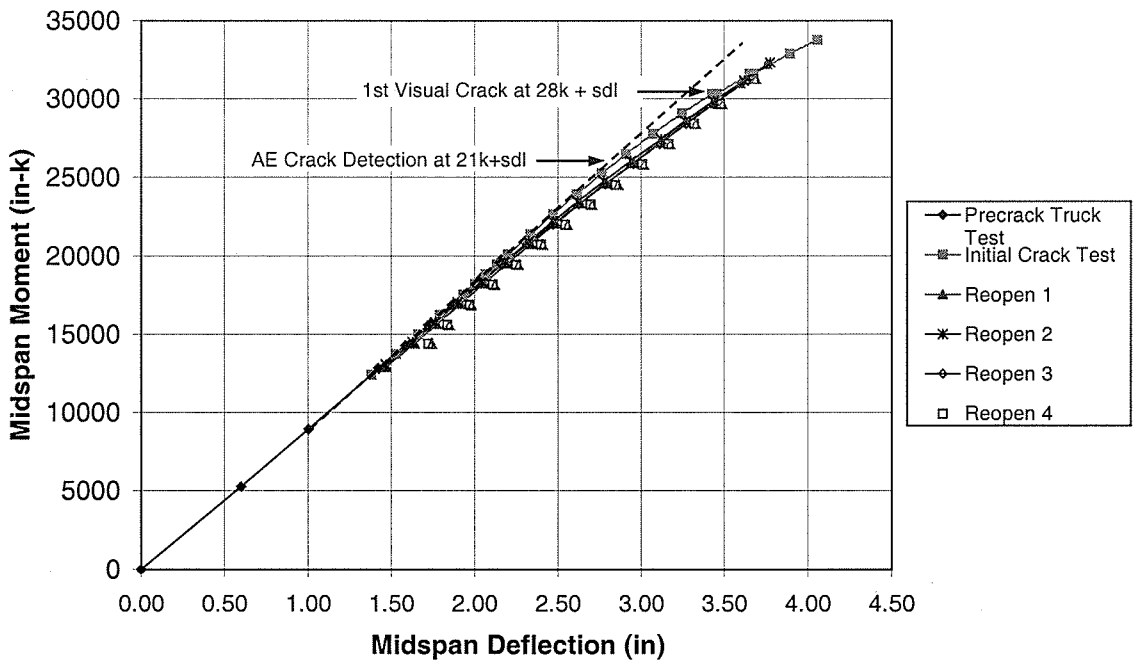

Figure 8.11 Moment-Deflection Response – Crack Reopening Tests

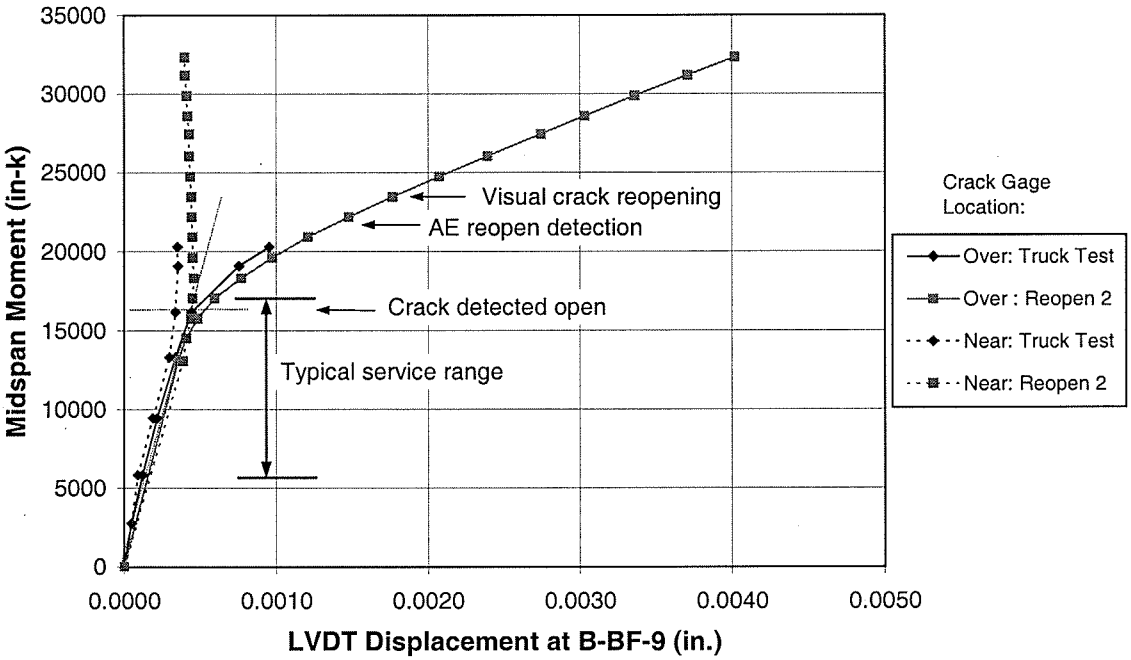

Figure 8.12 Moment versus LVDT Displacement, Initial Readings

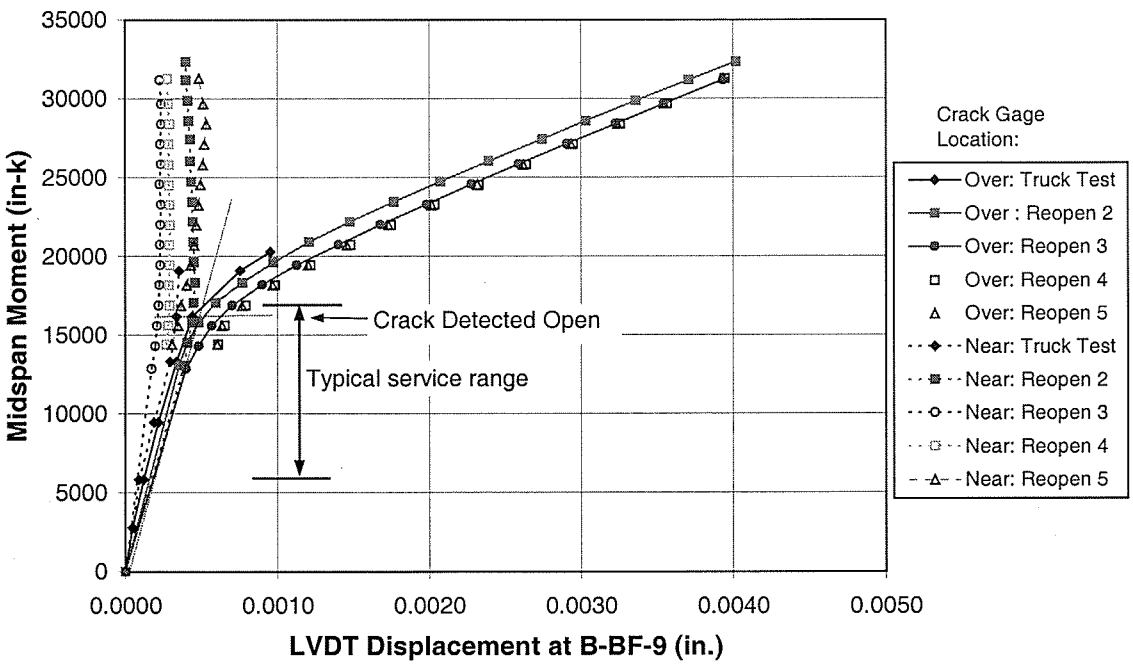

Figure 8.13 Moment versus LVDT Displacement, Reopen Tests

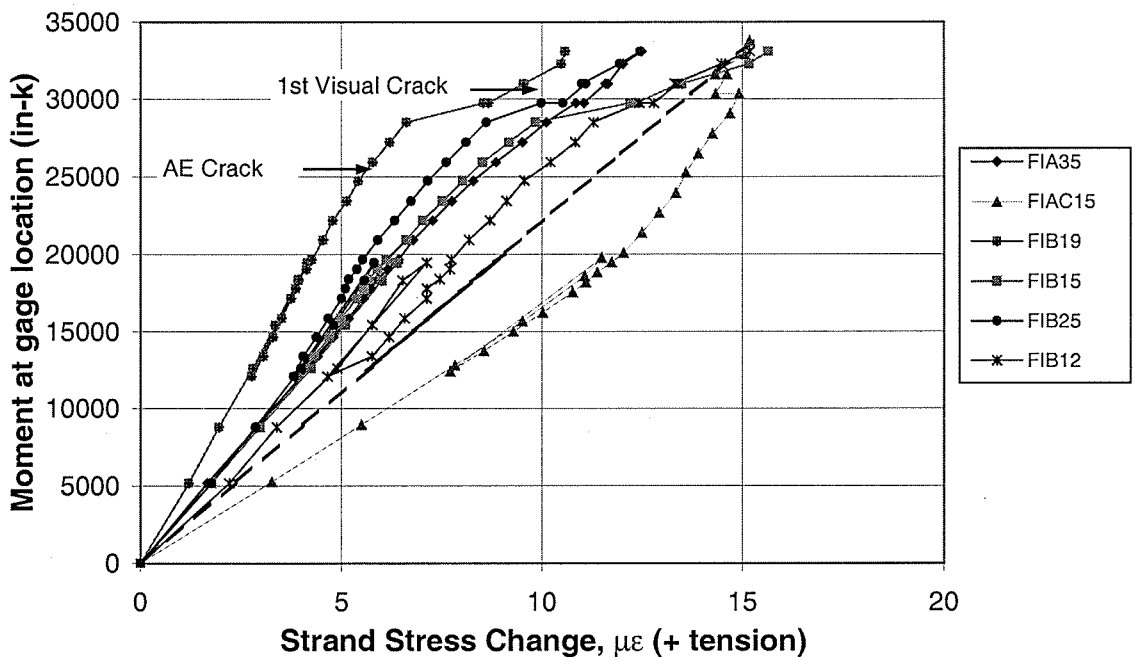

Figure 8.14 Moment-Stress Behavior of Strands, Initial Crack Test – Girder I

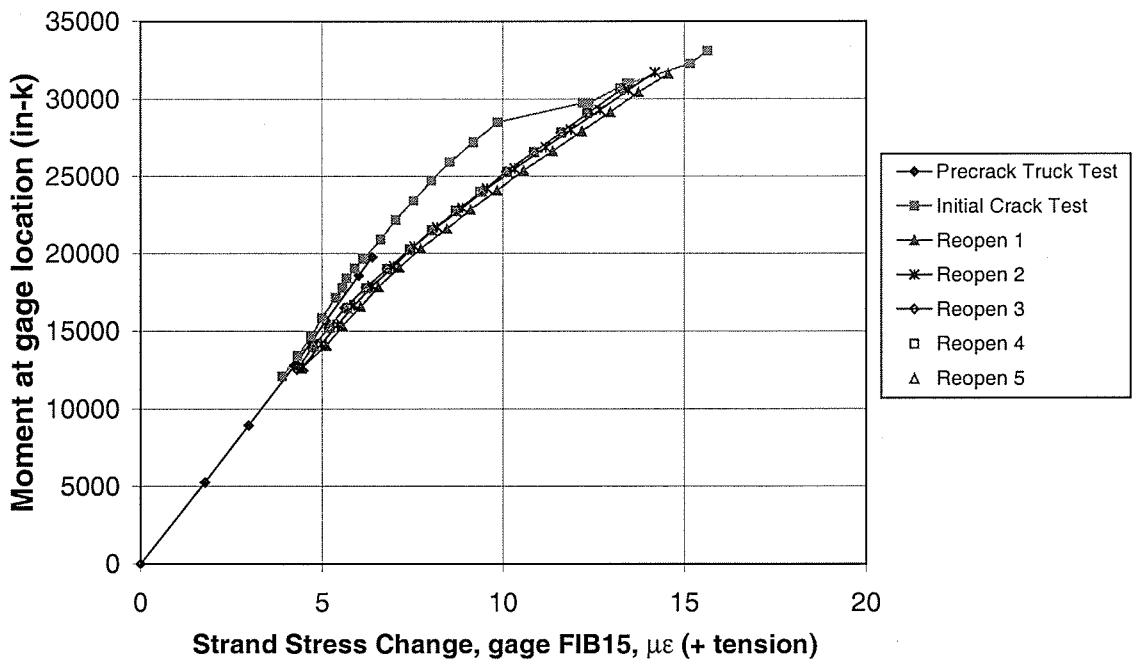

Figure 8.15 Moment-Stress Behavior of Strand FIB15, Crack Reopen Tests – Girder I

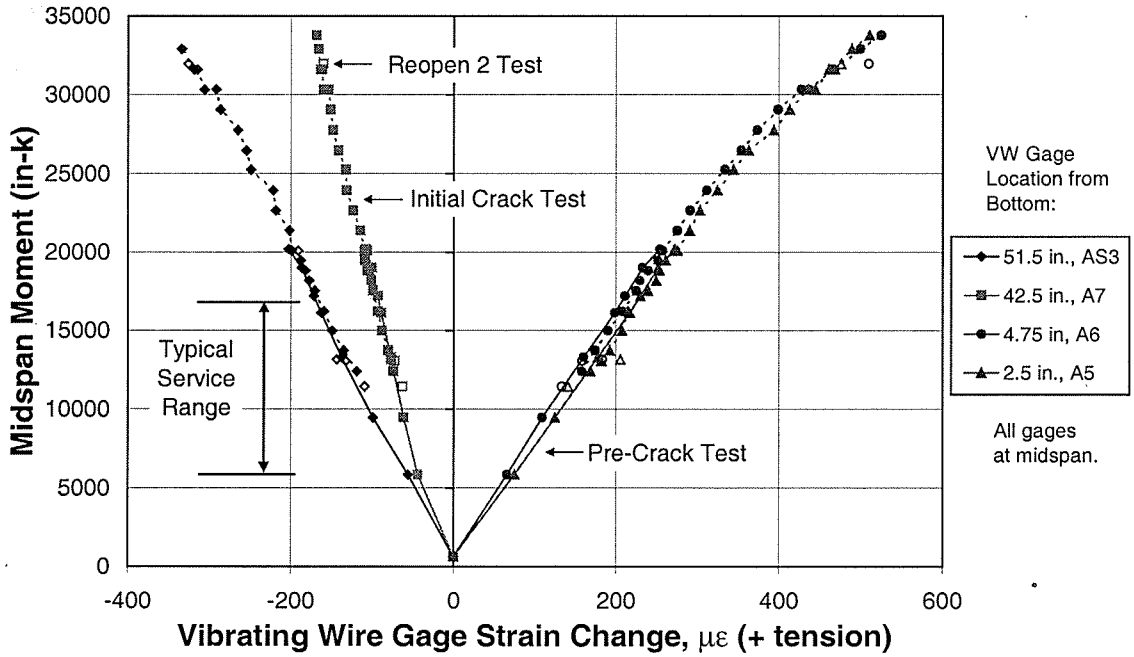

Figure 8.16 Moment-VW Strain Behavior of Concrete, Crack Load Testing – Girder I

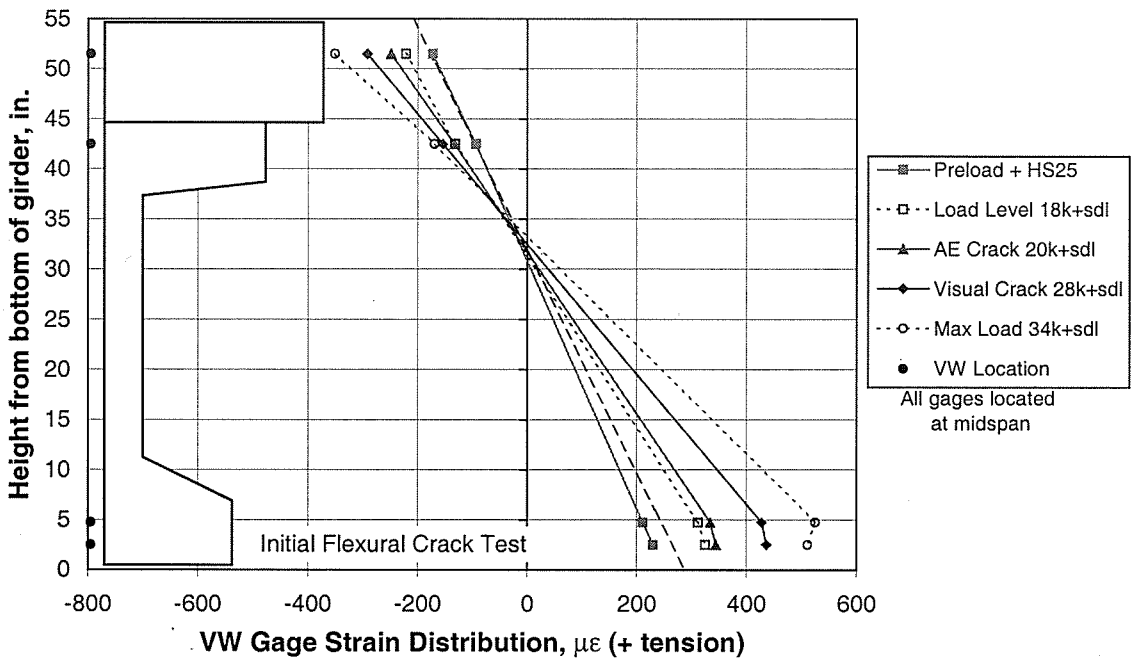

Figure 8.17 Strain Distribution versus Depth – VW Gages, Initial Crack Test

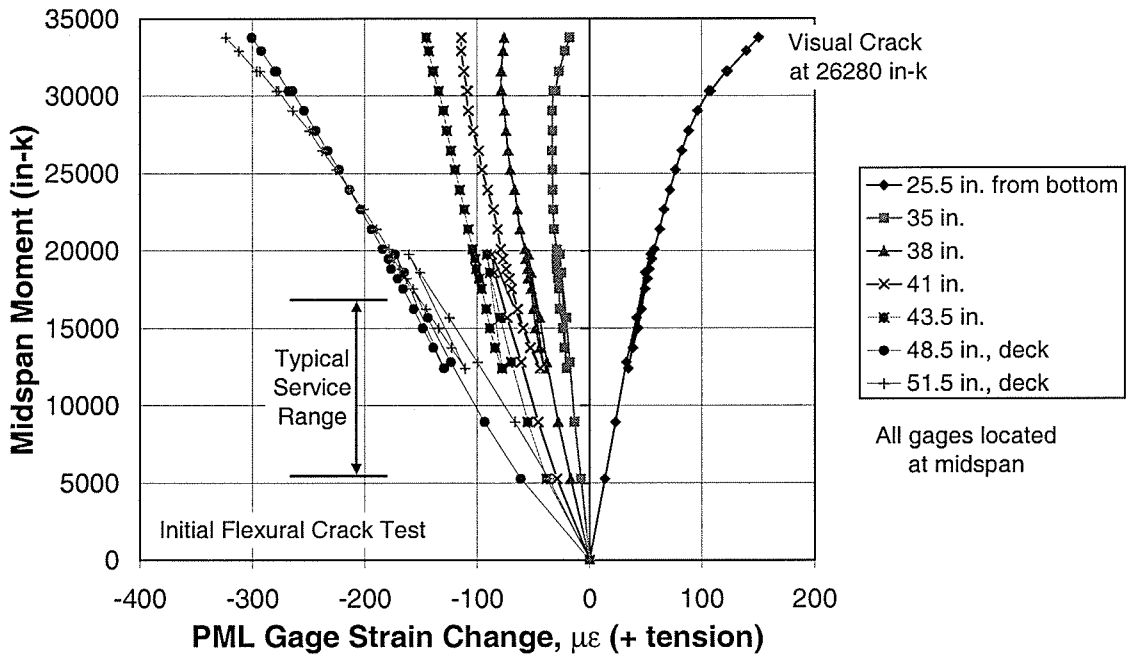

Figure 8.18 Moment-PML Strain Behavior of Concrete, Initial Crack Test – Girder I

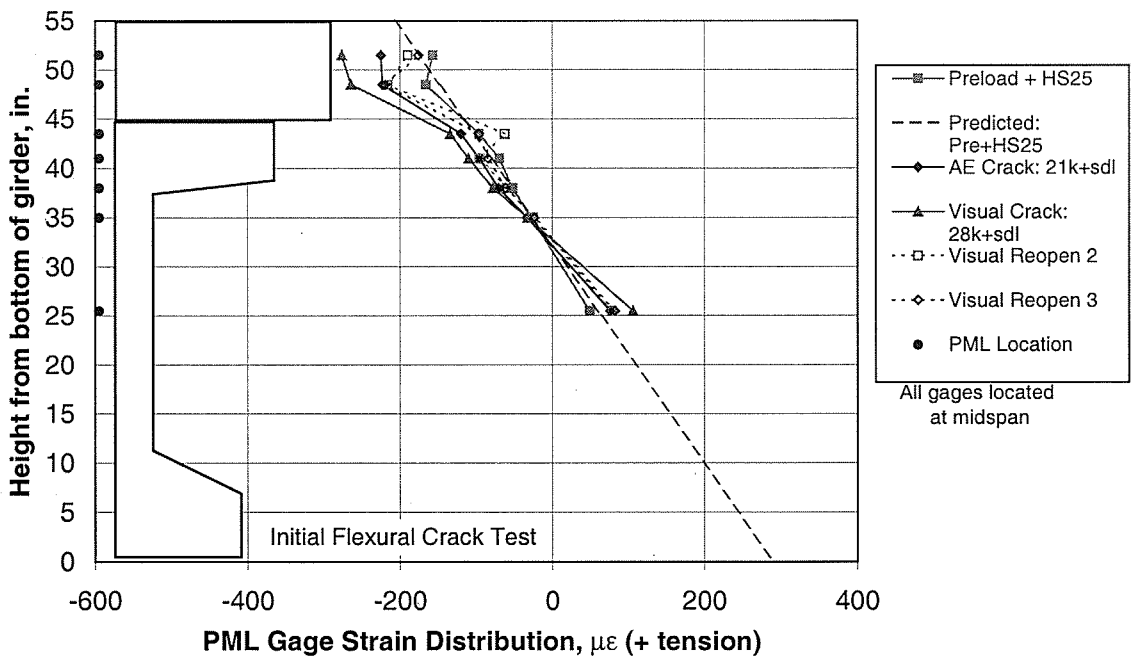

Figure 8.19 Strain Distribution versus Depth – PML Gages, Initial Crack Test

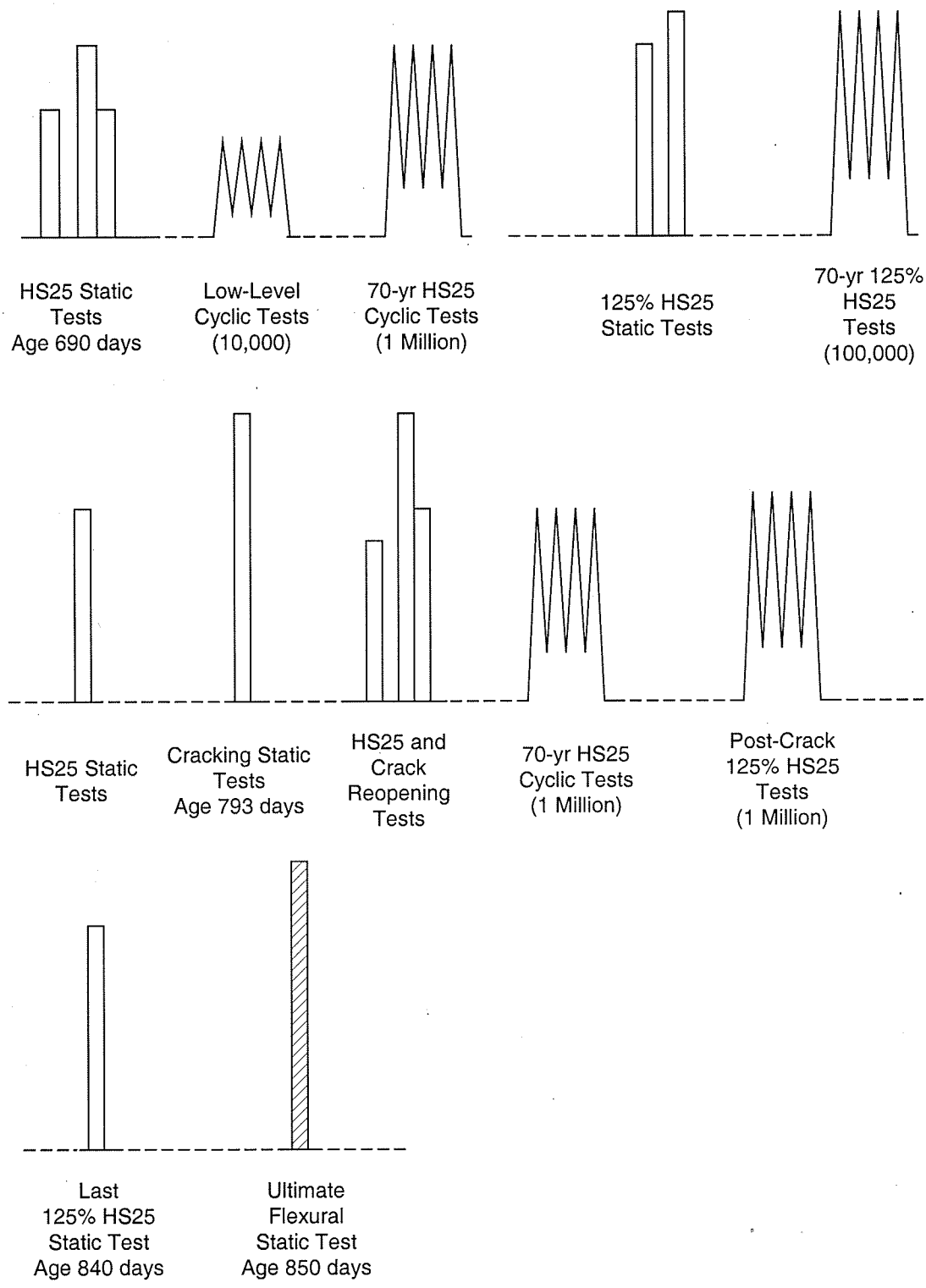

Figure 9.1 Load History Summary of Girder II

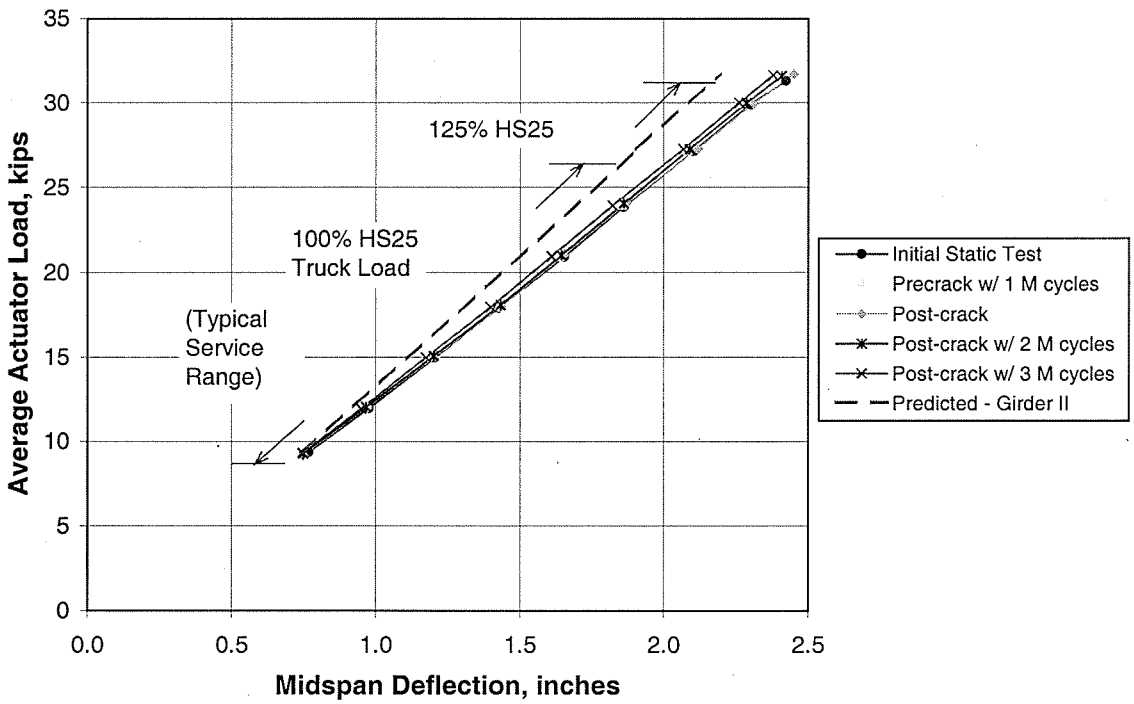

Figure 9.2 Load-Deflection Response of Girder II

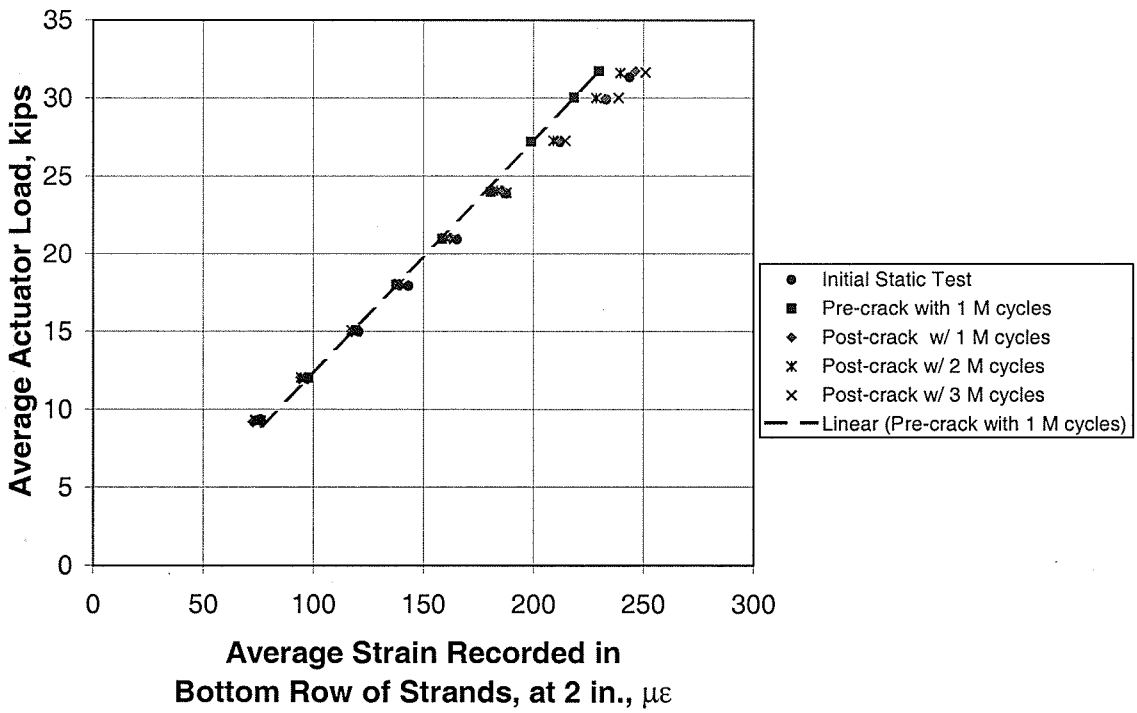

Figure 9.3 Load-Strain Behavior, Bottom Row of Strands – Girder II

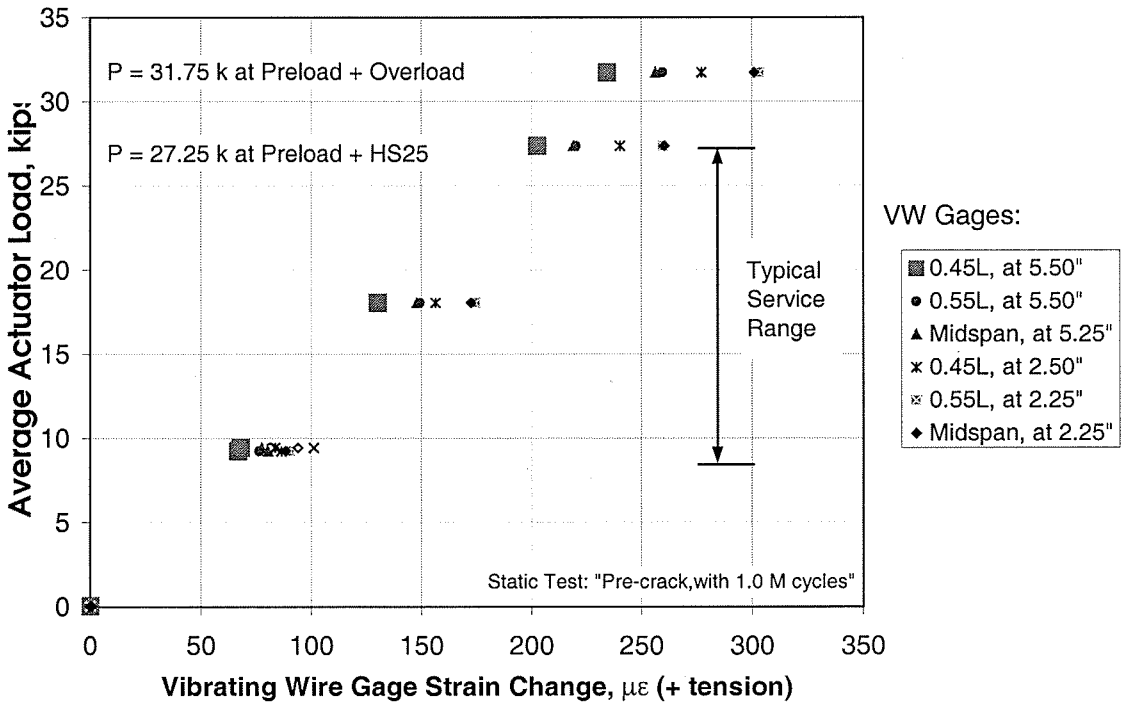

Figure 9.4 Load-Strain Behavior, Bottom Flange – Girder II

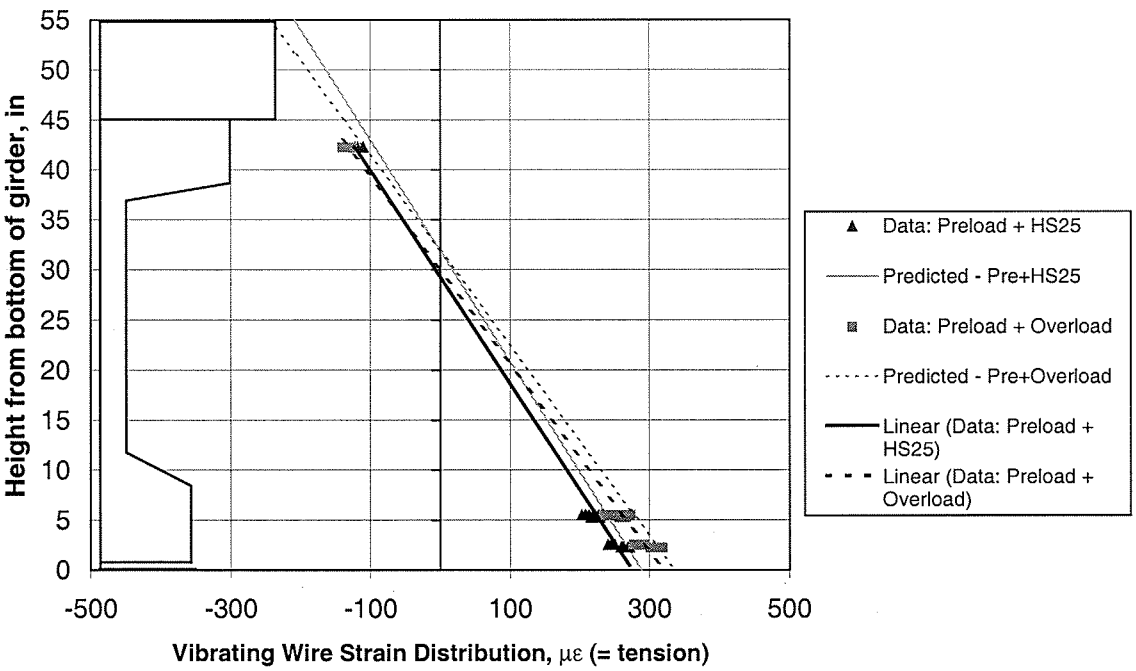

Figure 9.5 Strain Distribution versus Depth – VW Gages

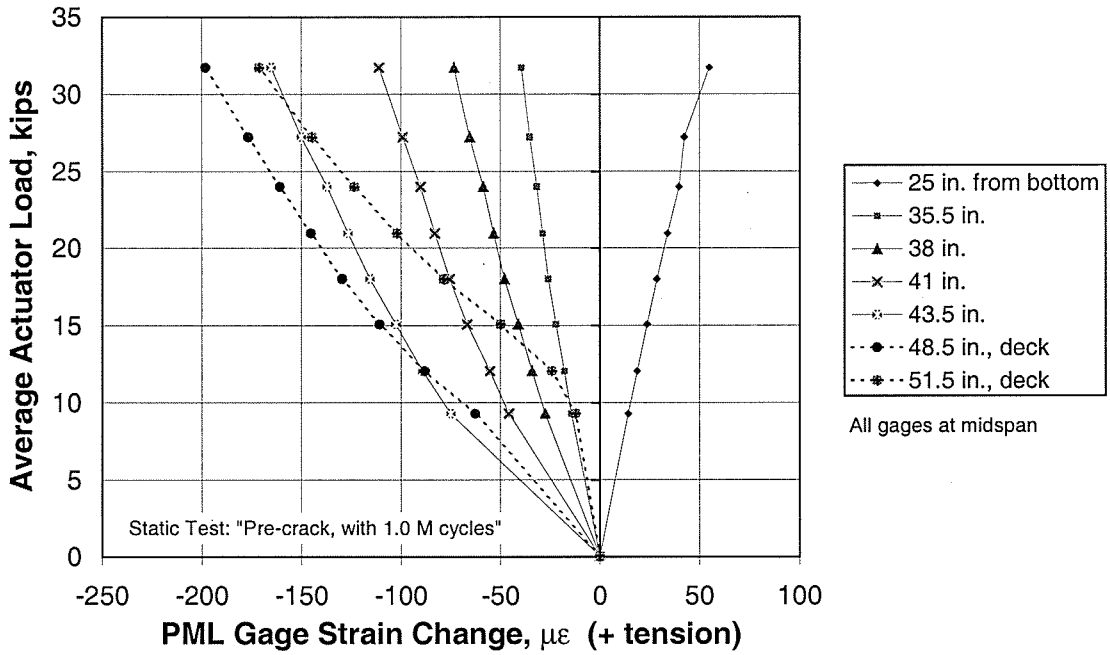

Figure 9.6 Load-Strain Behavior, Top Flange – Girder II

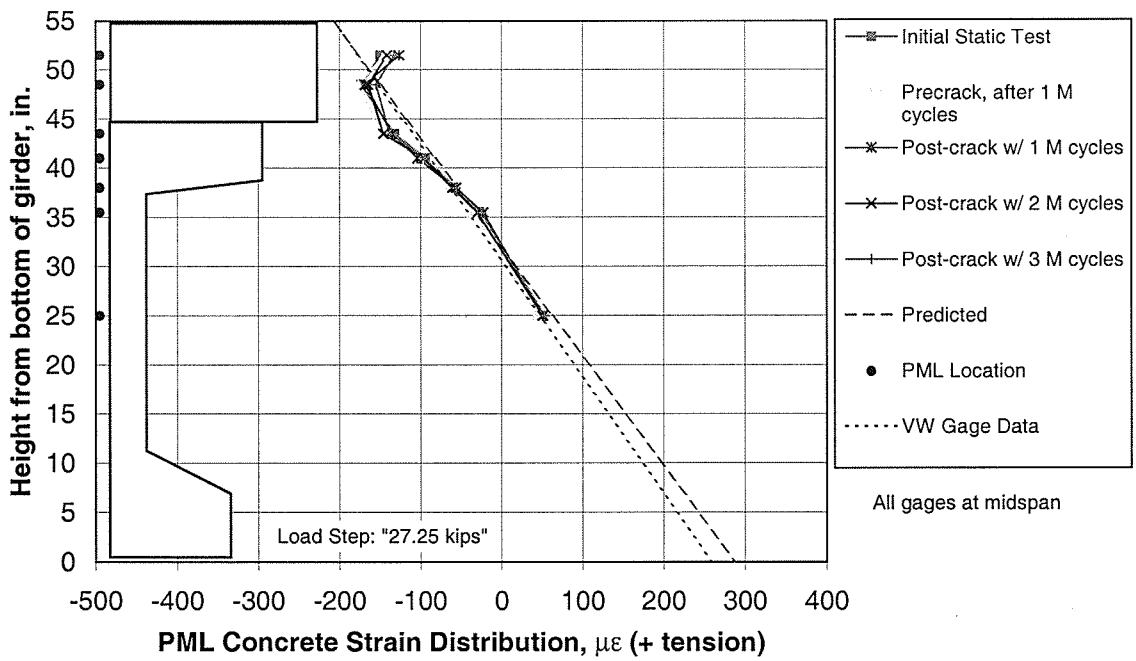

Figure 9.7 Strain Distribution versus Depth – PML Gages at HS25 – 0.3L

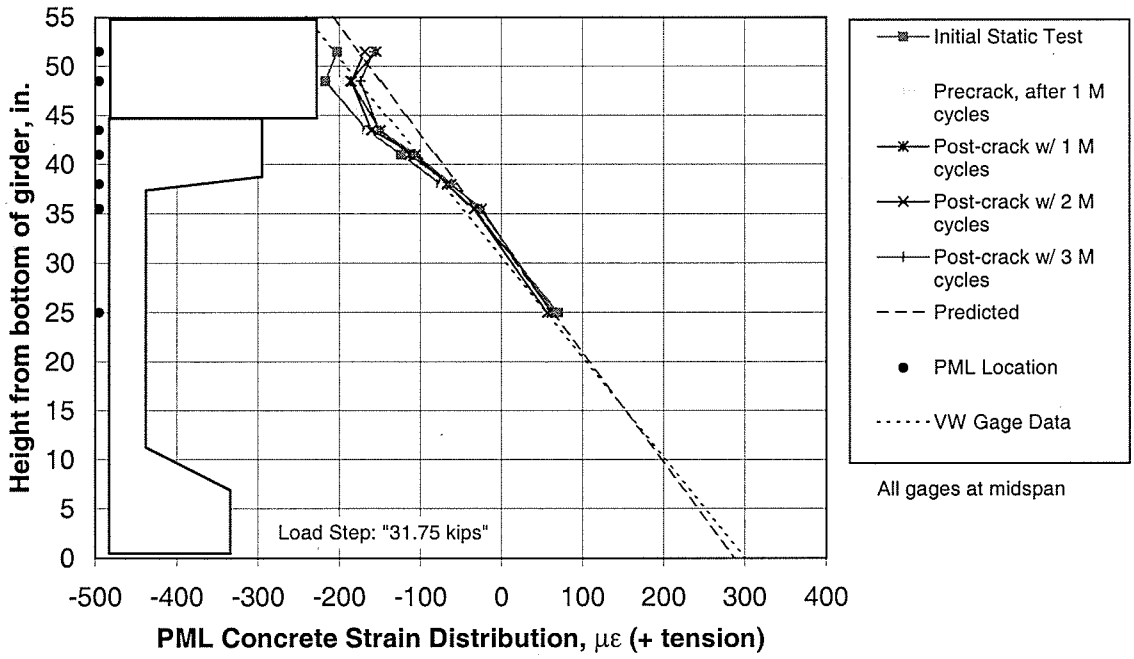

Figure 9.8 Strain Distribution versus Depth – PML Gages at Overload

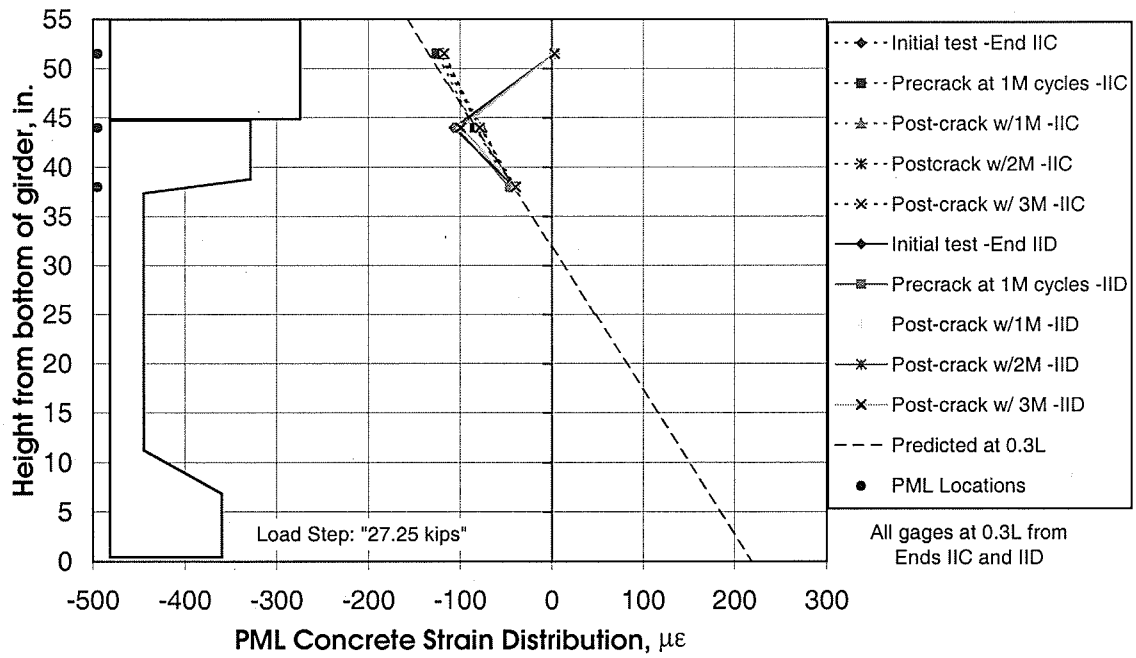

Figure 9.9 Strain Distribution versus Depth – PML Gages at HS25 – 0.3L

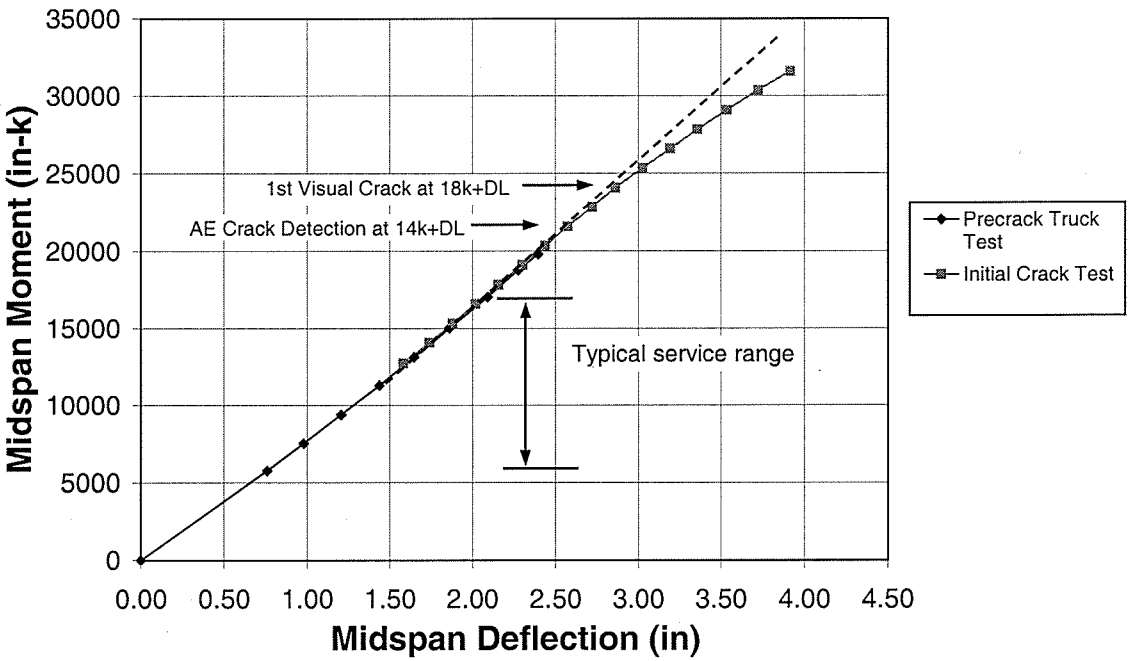

Figure 9.10 Moment-Deflection Response – Crack Reopening Tests

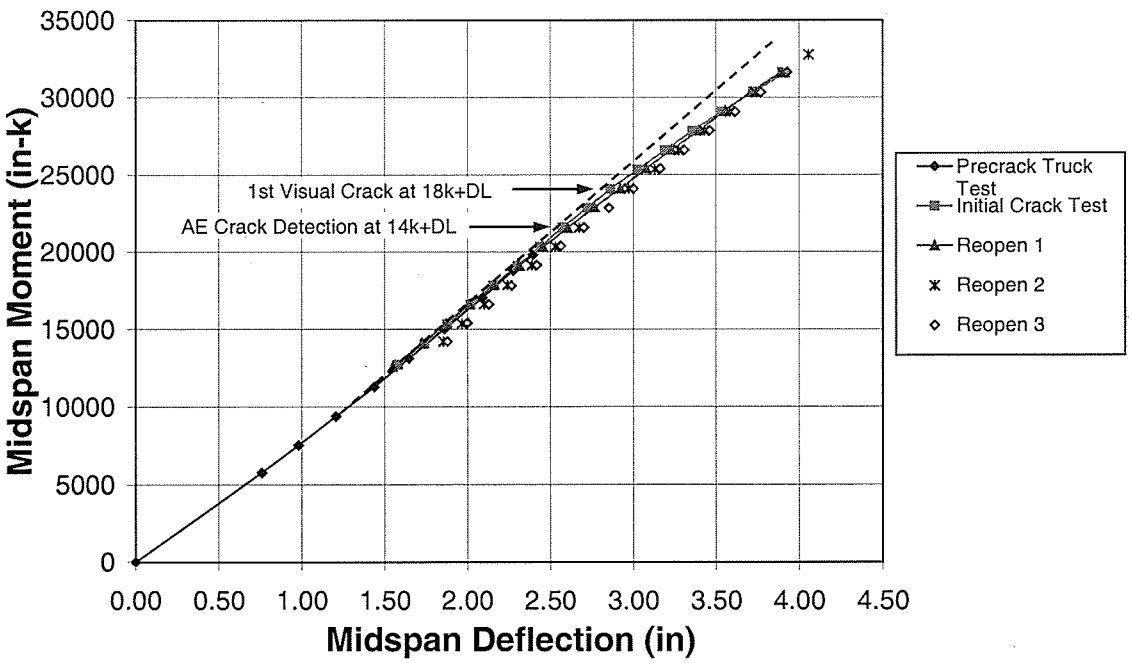

Figure 9.11 Moment-Deflection Response – Crack Reopening Tests

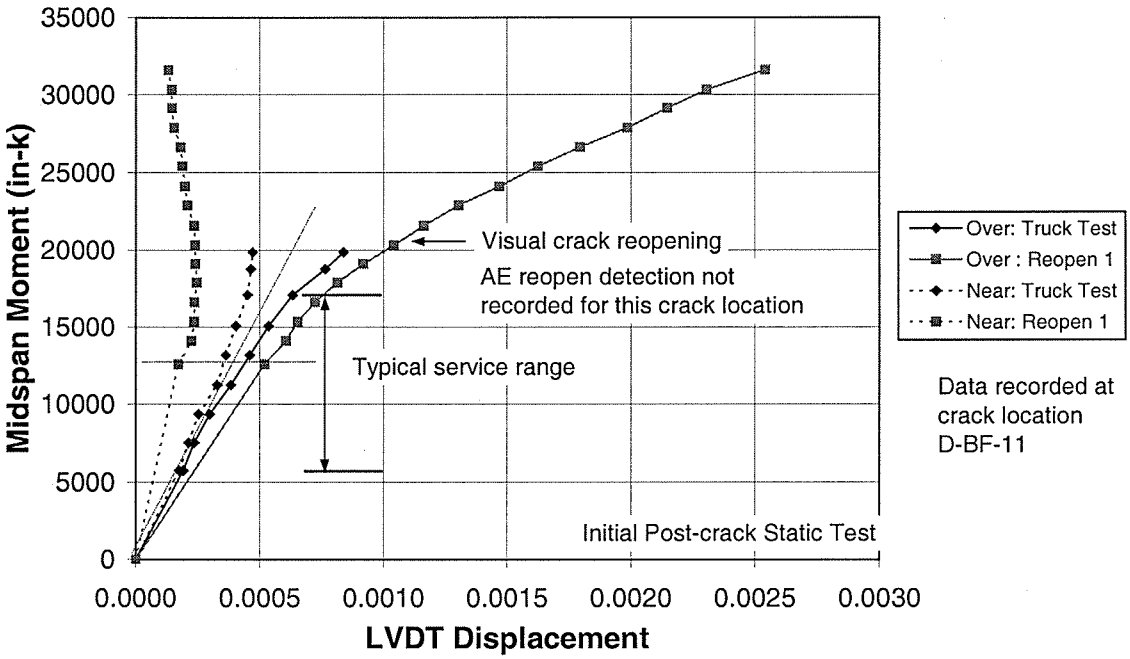

Figure 9.12 Moment versus LVDT Displacement, Initial Readings

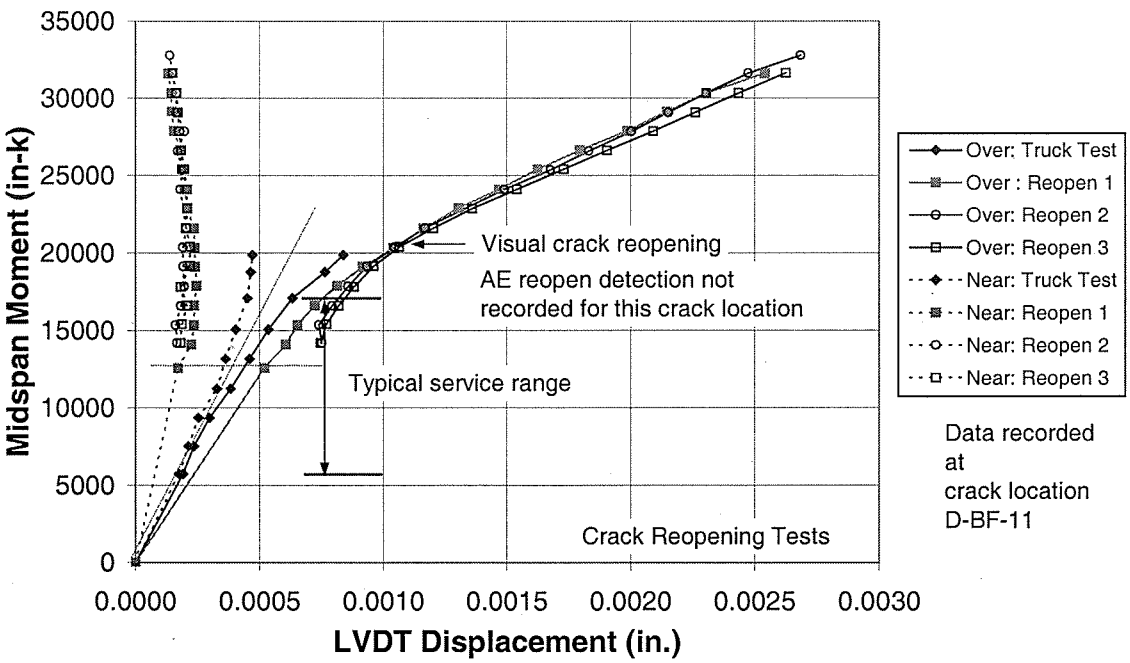

Figure 9.13 Moment versus LVDT Displacement, Reopen Tests

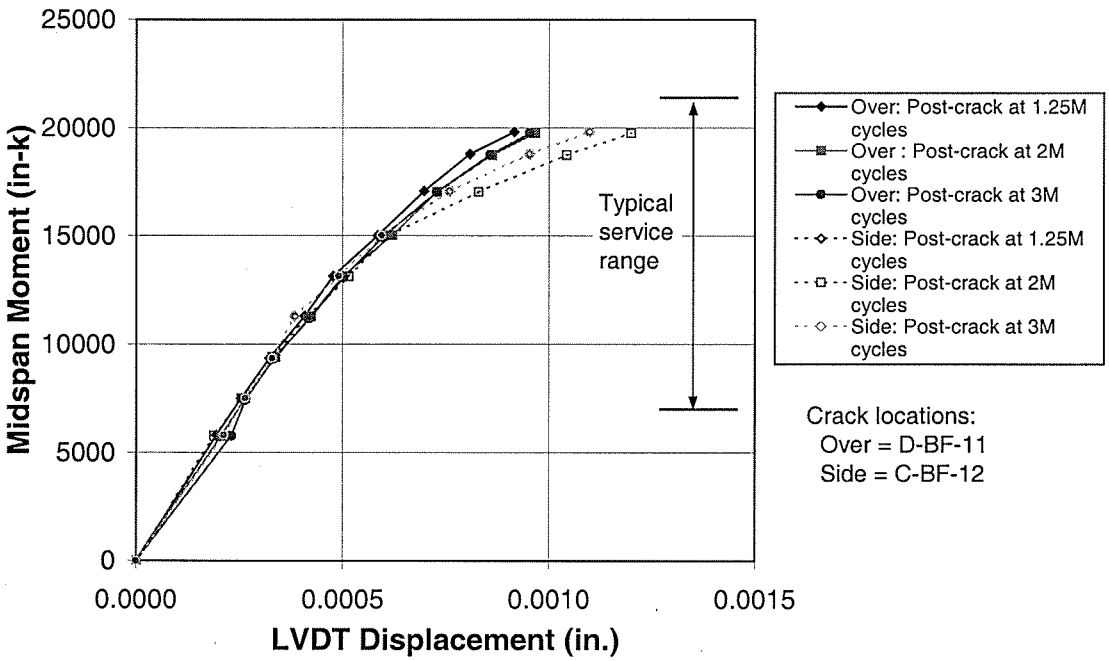

Figure 9.14 Moment versus LVDT Displacement, Bottom and Side Crack

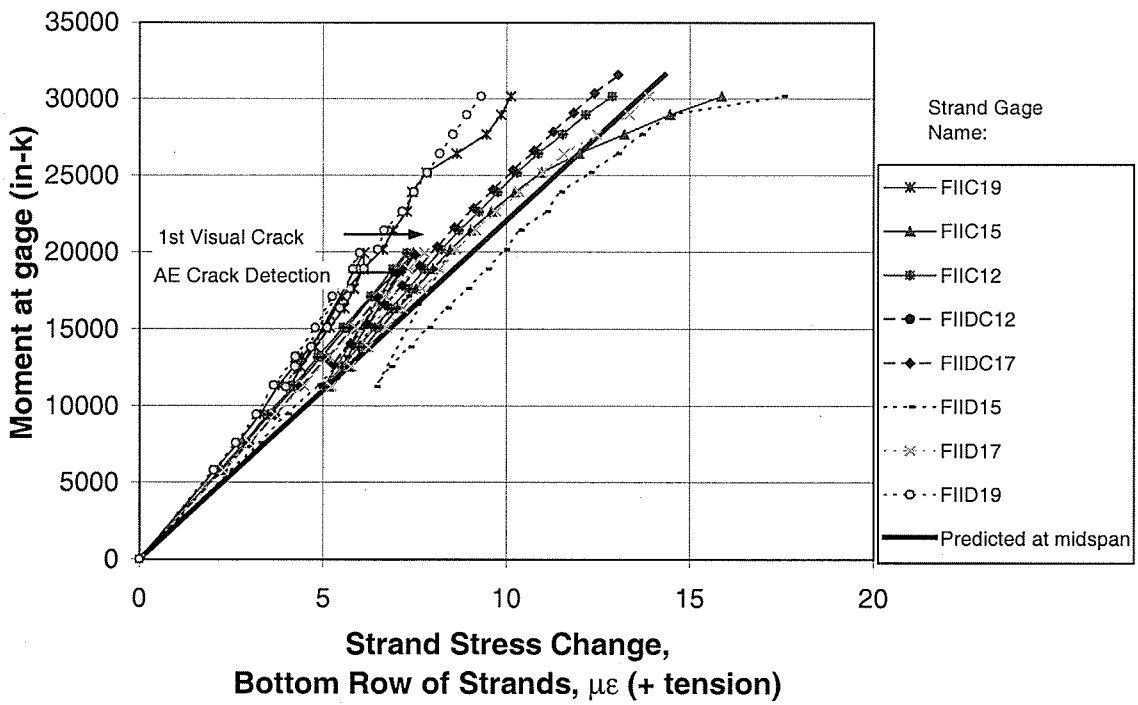

Figure 9.15 Moment-Stress Behavior of Strand Row 1, Initial Crack Test – Girder II

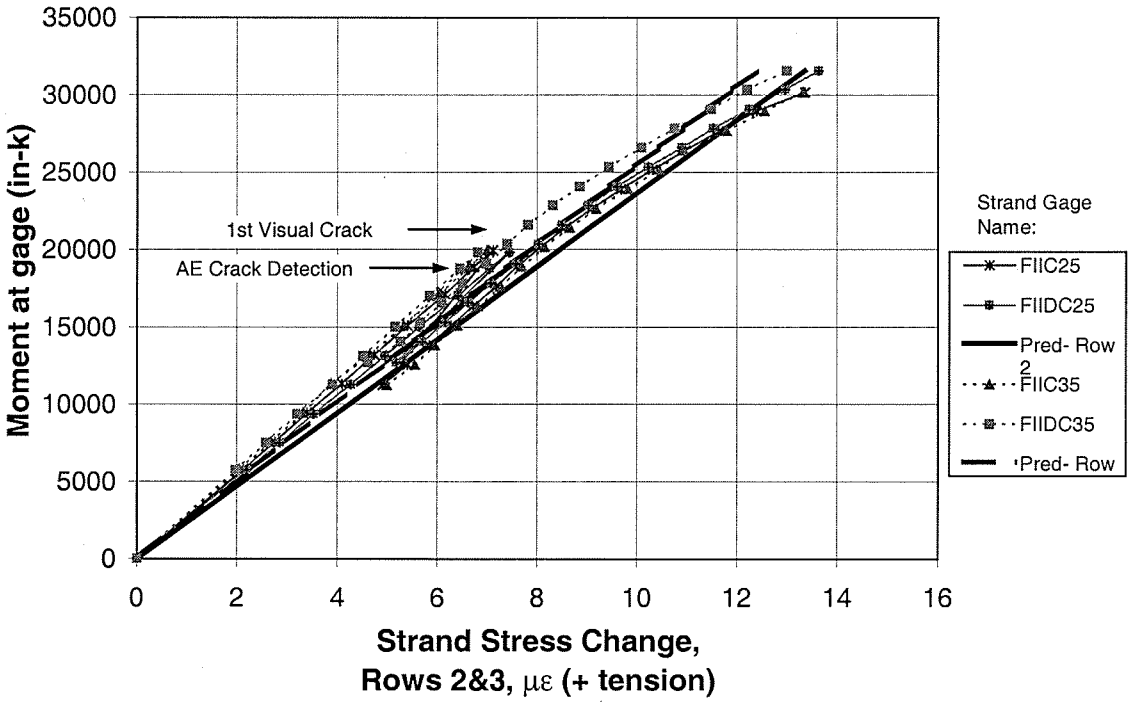

Figure 9.16 Moment-Stress Behavior of Strand Rows 2/3, Initial Crack Test – Girder II

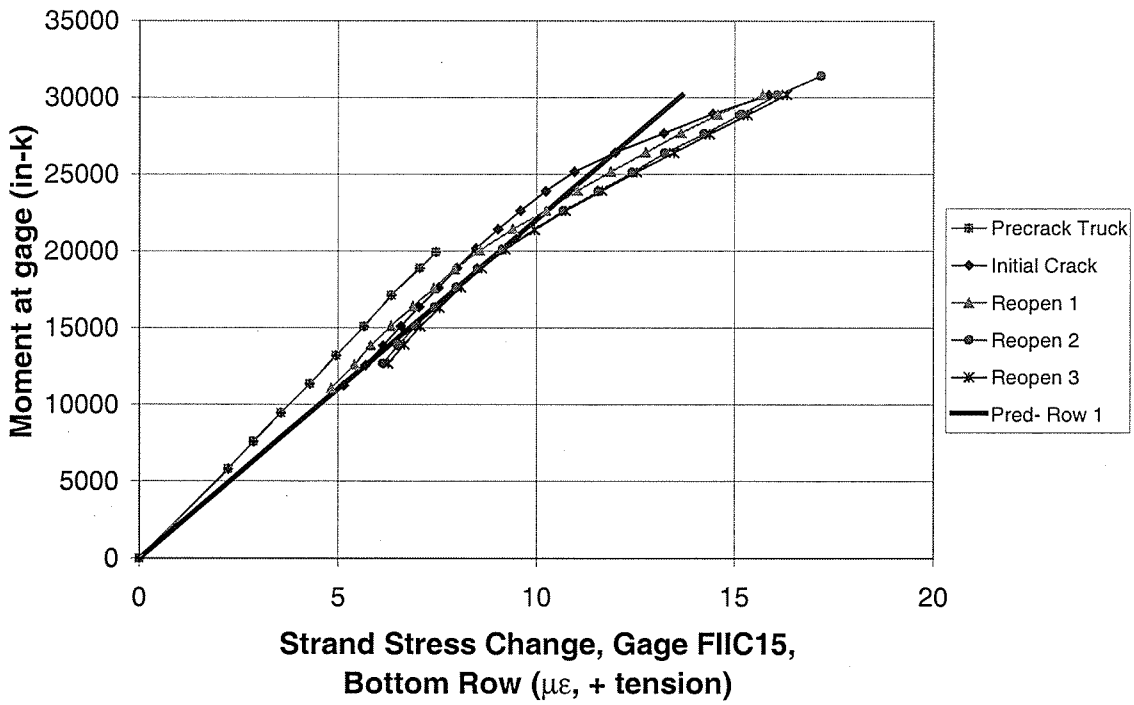

Figure 9.17 Moment-Stress Behavior of Strand FIIC15, Crack Reopen Tests – Girder II

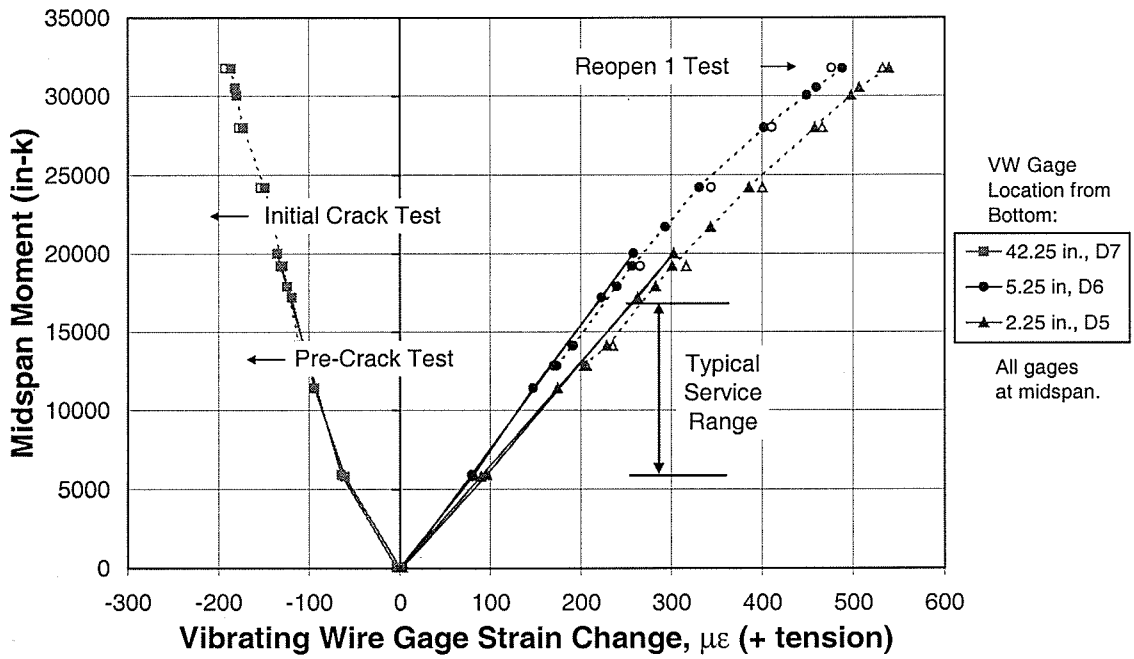

Figure 9.18 Moment-VW Strain Behavior of Concrete, Crack Load Testing – Girder II

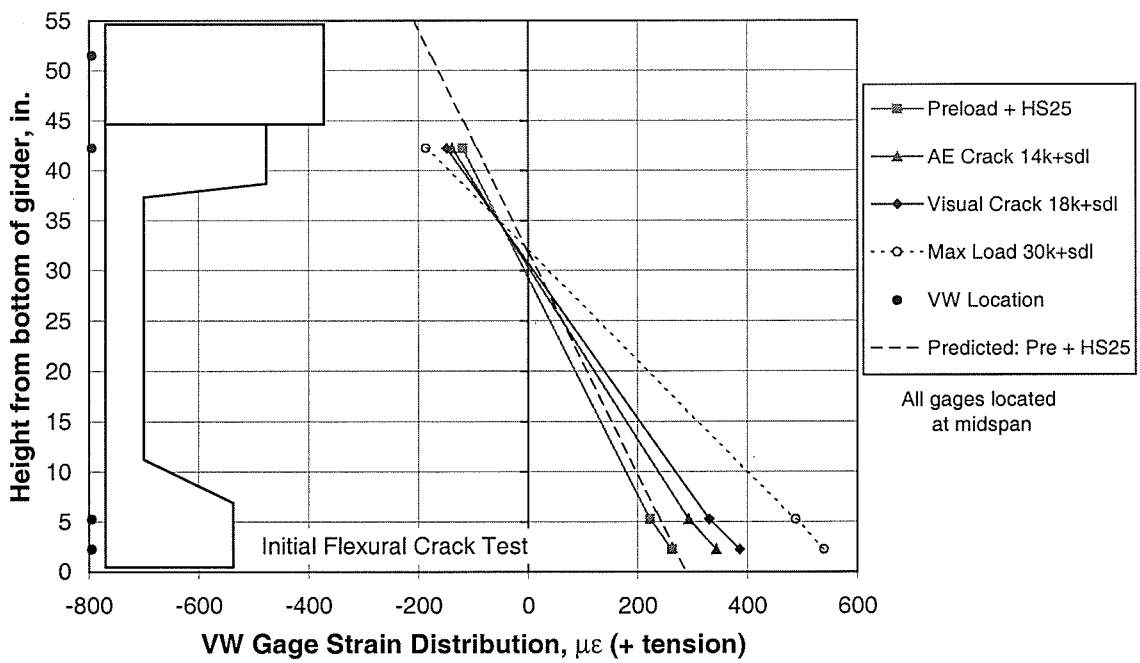

Figure 9.19 Strain Distribution versus Depth – VW Gages, Initial Crack Test

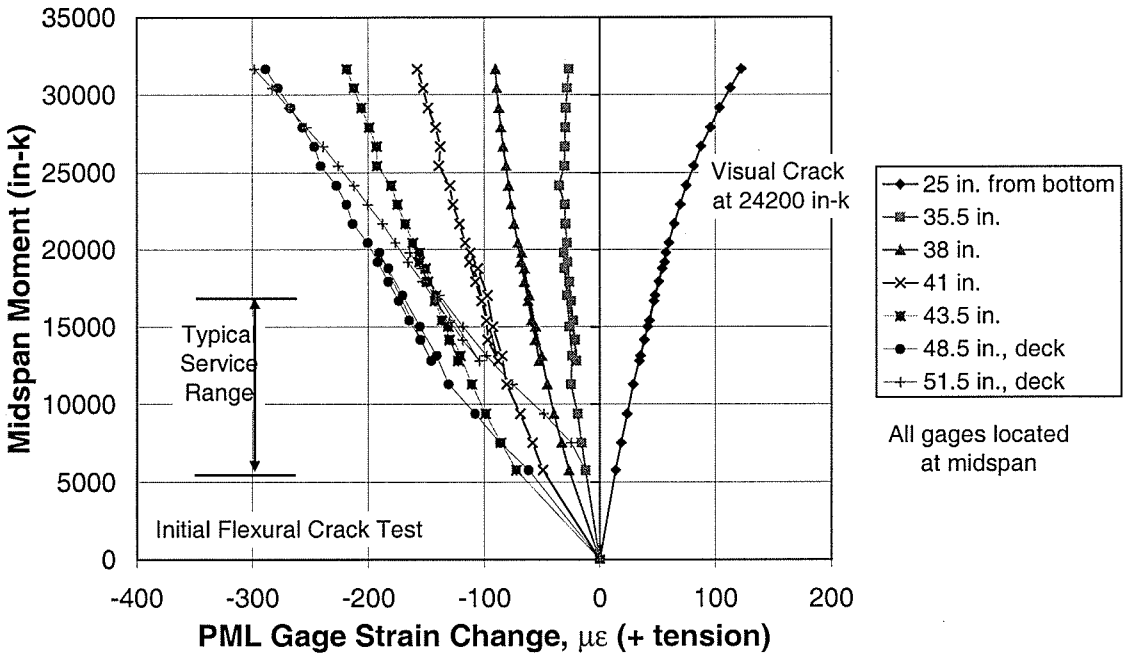

Figure 9.20 Moment-PML Strain Behavior of Concrete, Initial Crack Test – Girder II

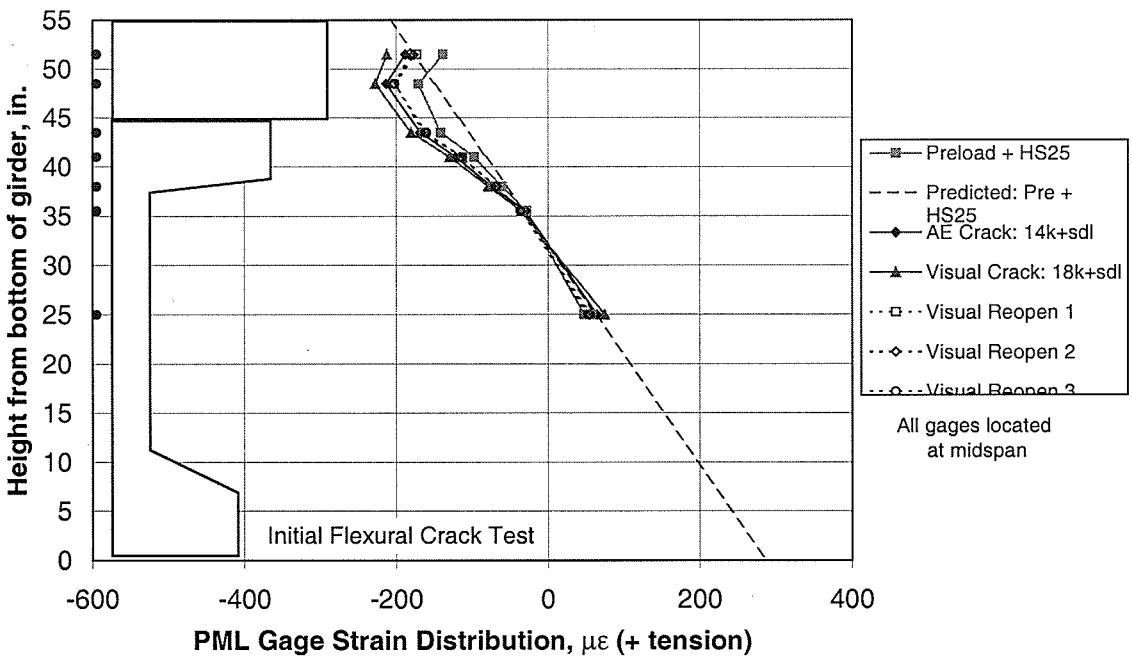

Figure 9.21 Strain Distribution versus Depth – PML Gages, Initial Crack Test

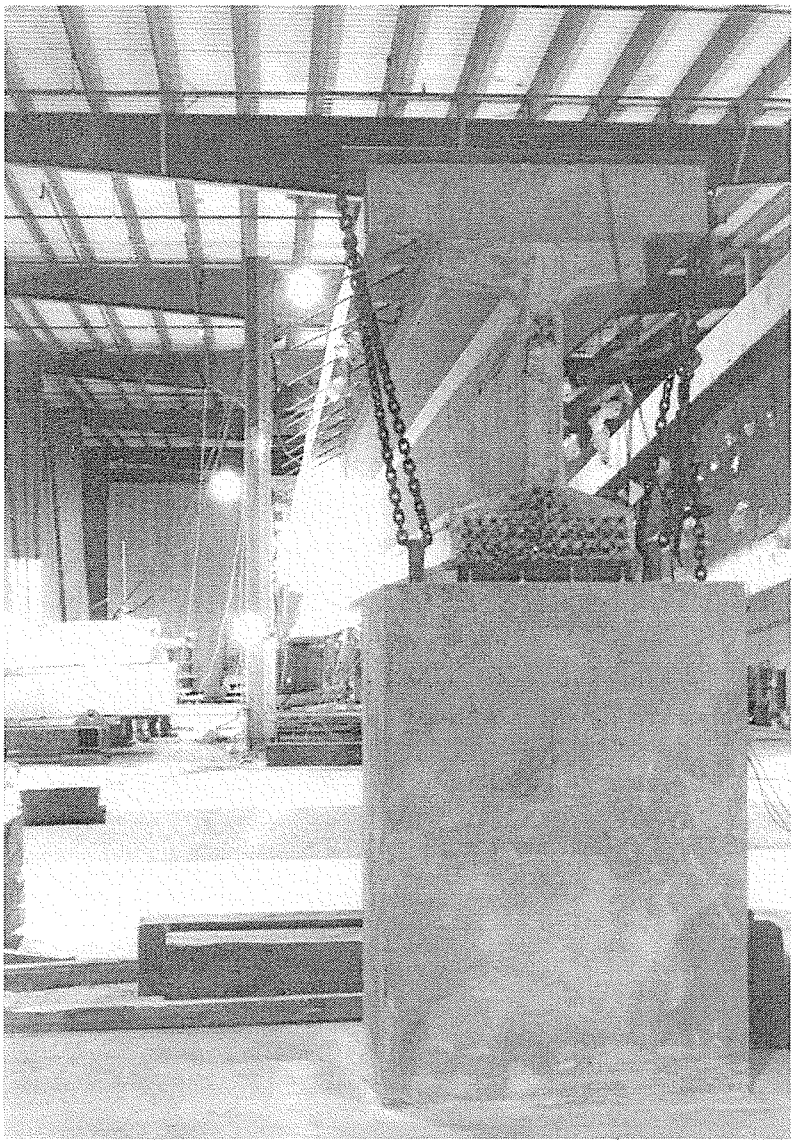

Figure 10.1 Girder I Prior to Ultimate Flexural Testing

Figure 10.2 Girder I During Ultimate Flexural Test, Before Deck Crushing

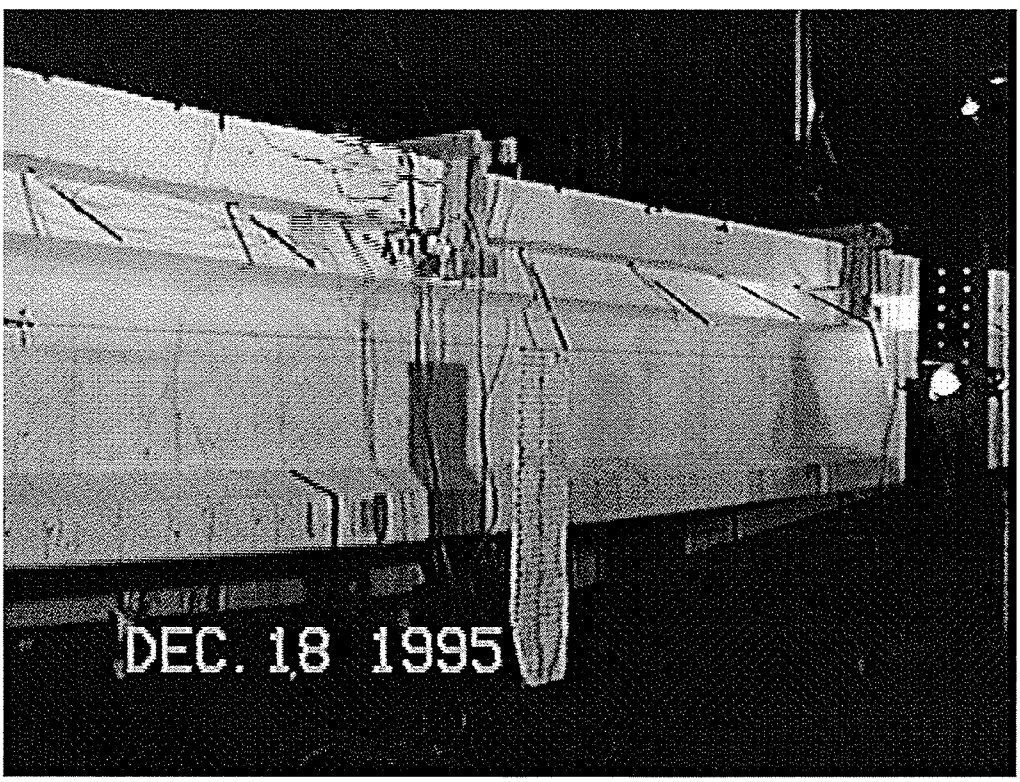

Figure 10.3 Girder I, Deck Crushing Begins

Figure 10.4 Girder I, Deck Failure, Web Failure Begins

Figure 10.5 Girder I, Deck and Web Failure

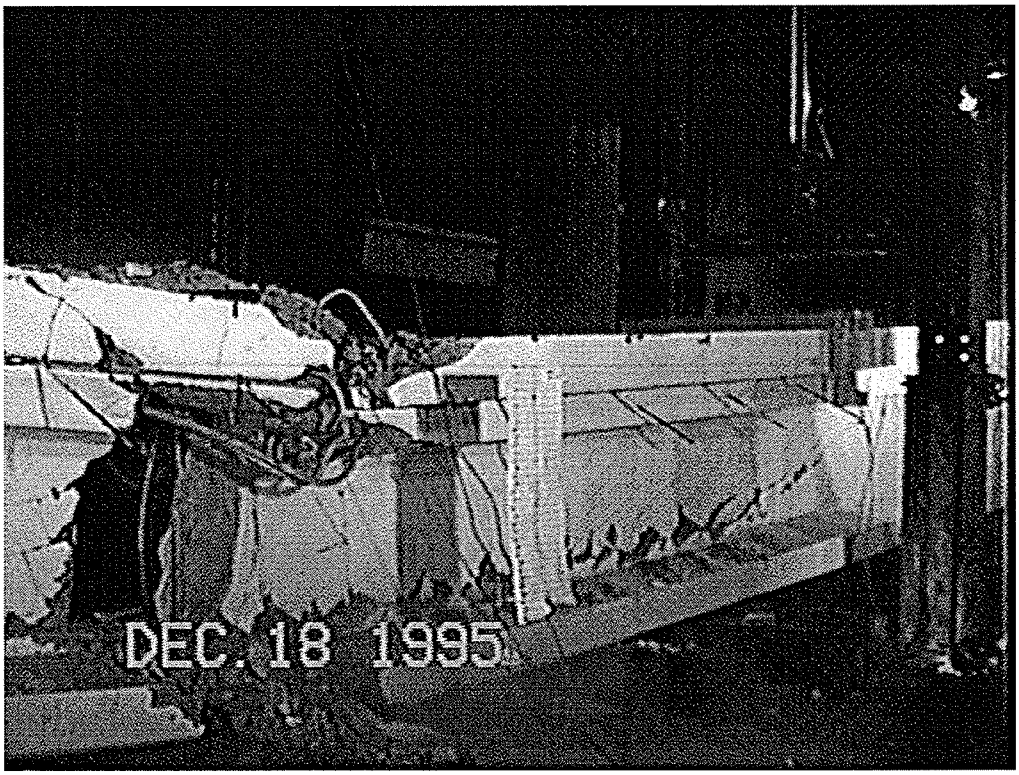

Figure 10.6 Girder I after Ultimate Collapse

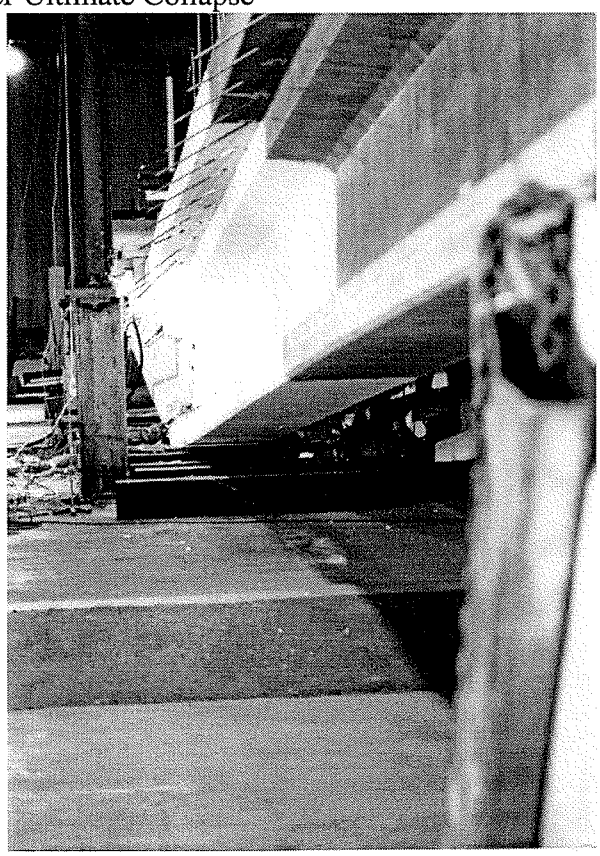

Figure 10.7 Ultimate Flexural Failure of Girder I

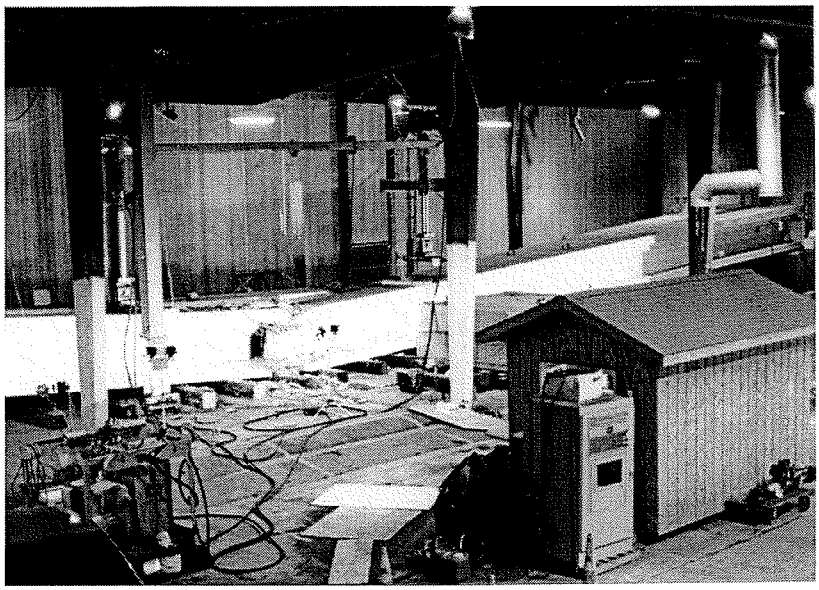

Figure 10.8 Overview of Girder I Failure

Figure 10.9 Heavily Damaged Region – Girder I

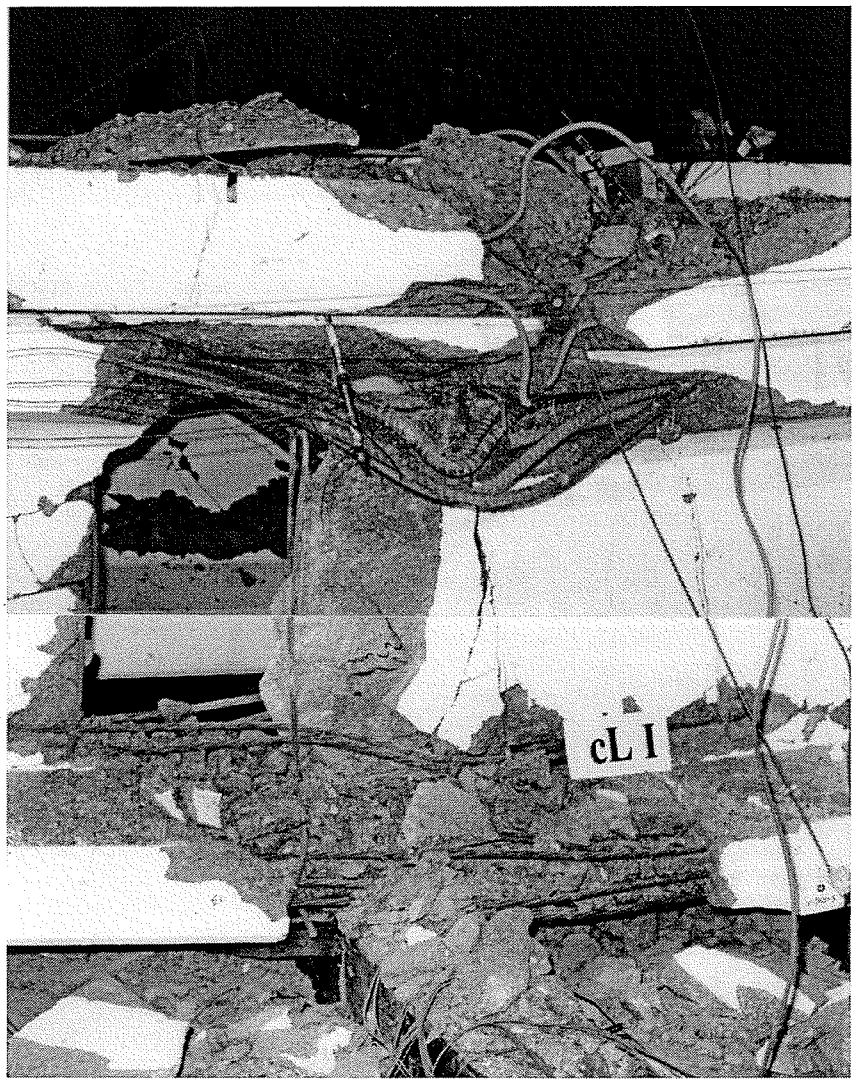

Figure 10.10 Close-up of Damaged Region – Girder I

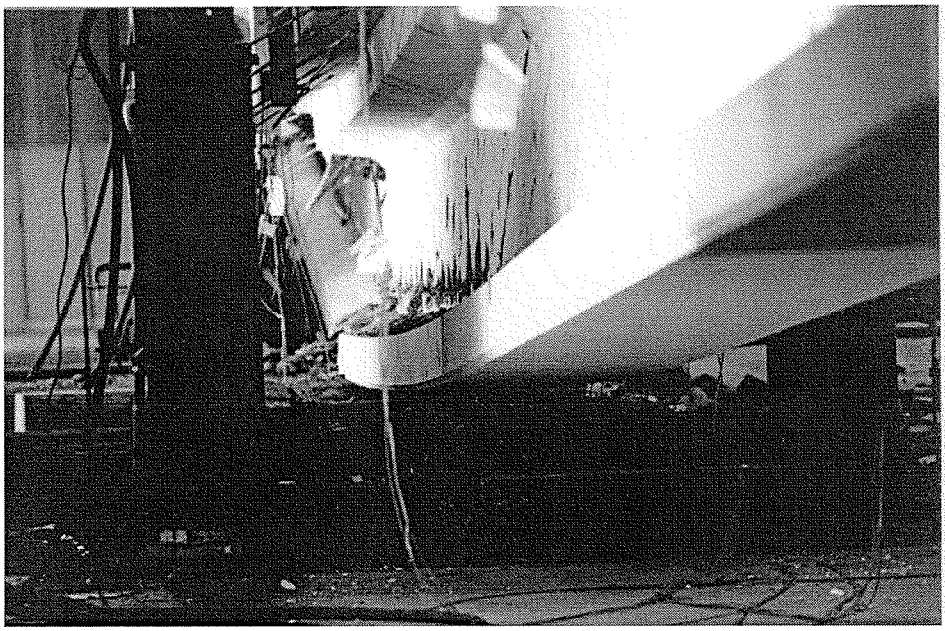

Figure 10.11 Ultimate Flexural Failure of Girder II

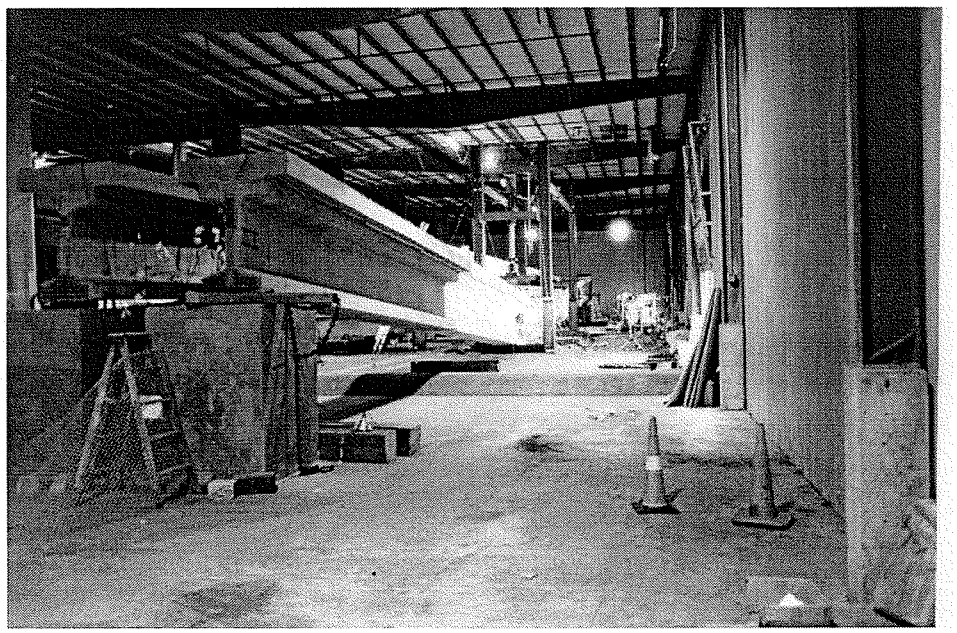

Figure 10.12 Overview of Girder II Failure

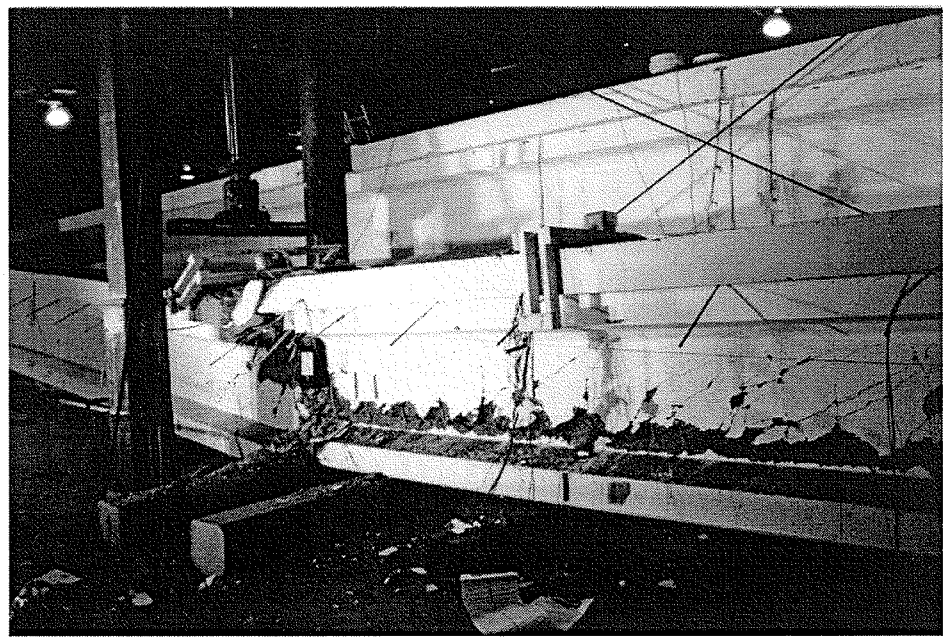

Figure 10.13 Damage of Midspan Region – Girder II

Figure 10.14 Heavily Damaged Region – Girder II at Load Point D

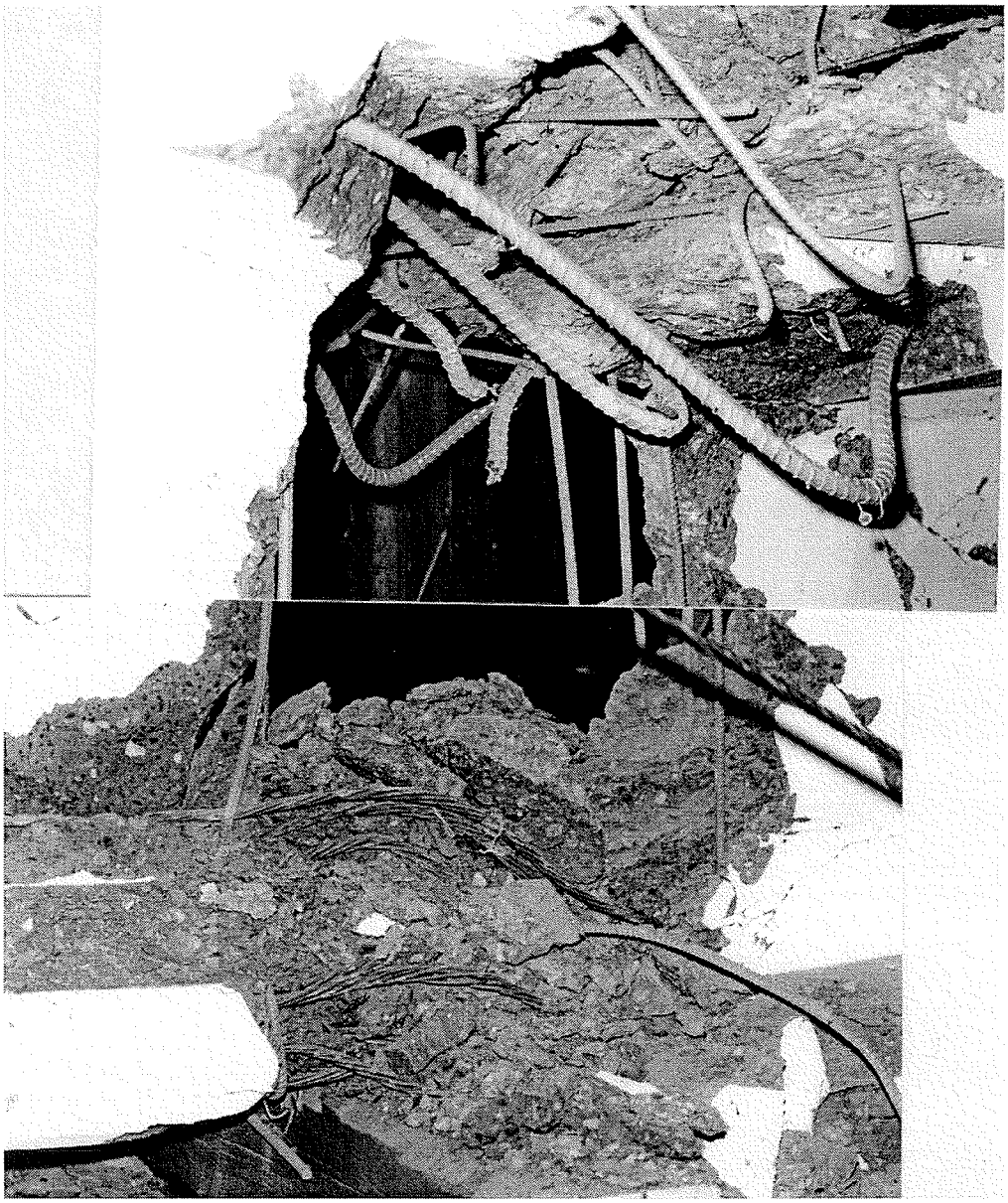

Figure 10.15 Close-up of Damaged Region – Girder II

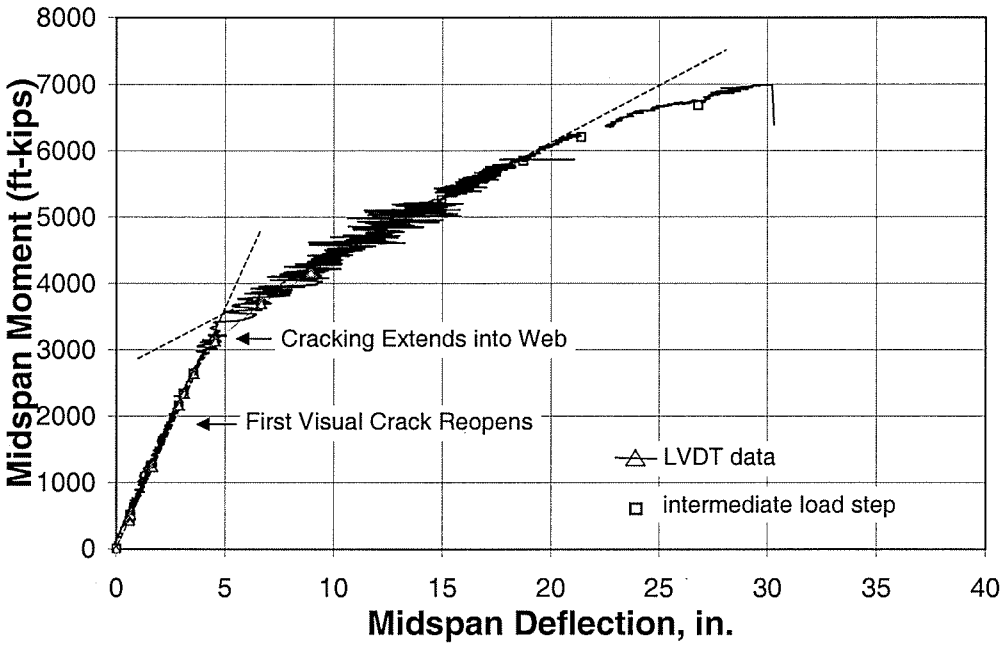

Figure 10.16 Moment-Deflection Response, Ultimate Flexural Test, Girder I

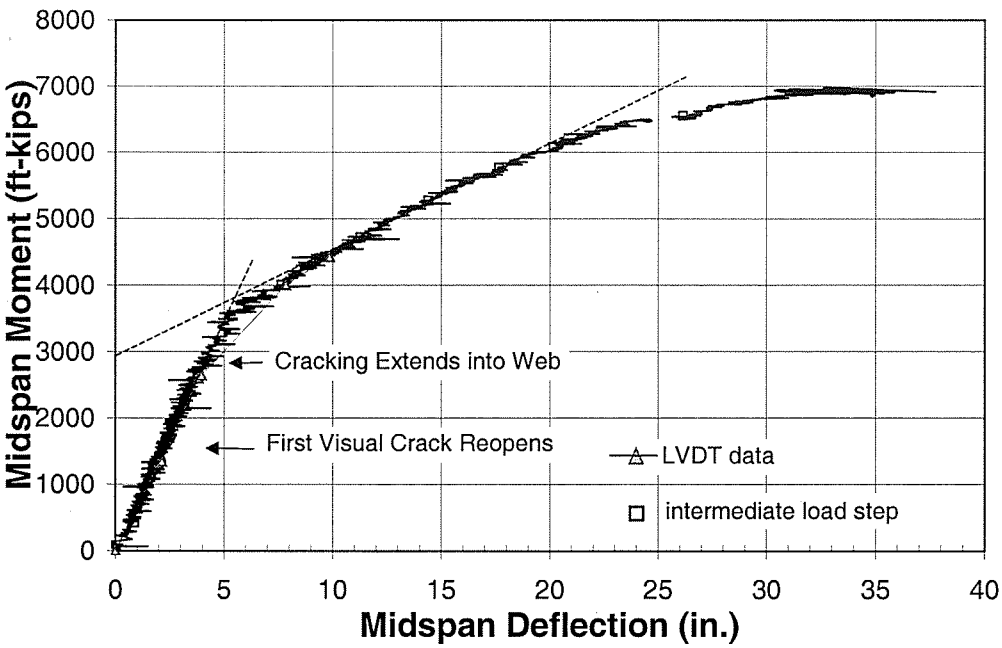

Figure 10.17 Moment-Deflection Response, Ultimate Flexural Test, Girder II

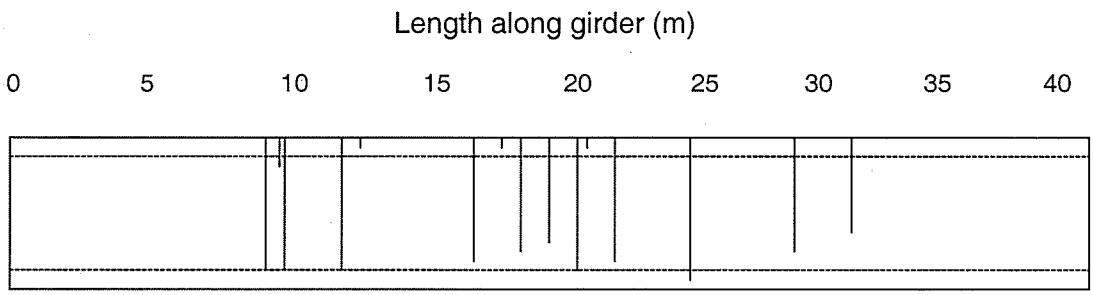

Figure 11.1 Pre-release Crack Pattern for Girder II (length of beam not to scale)

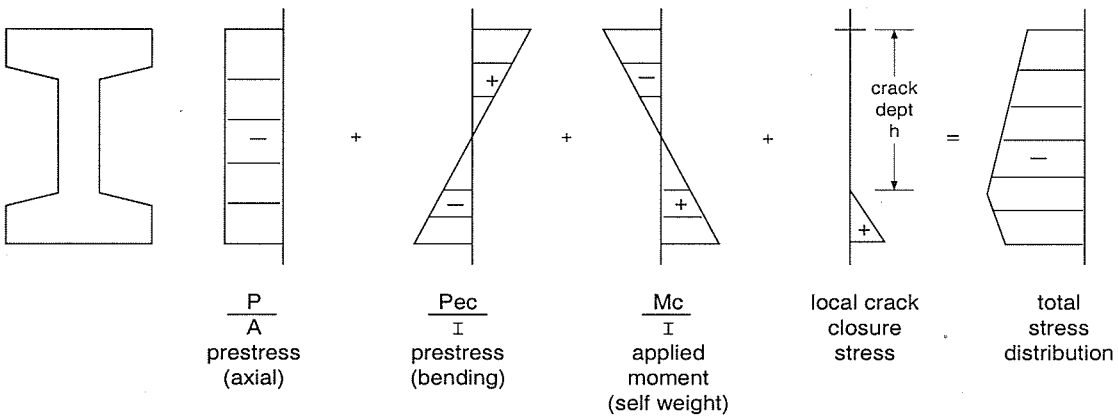

Figure 11.2 Concrete Stress Distribution at Release with Crack Closure

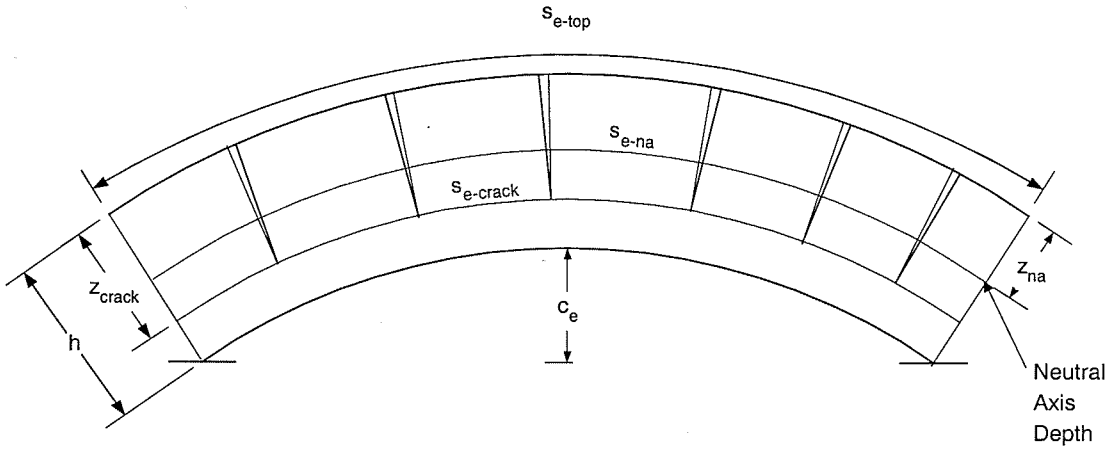

Figure 11.3 *Expected* Girder Shape

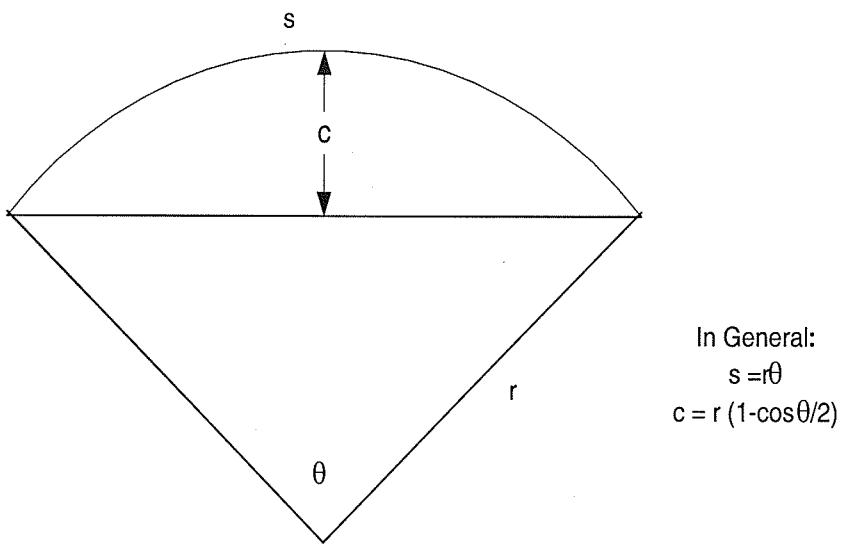

Figure 11.4 Geometry of a Sector and Segment of a Circle

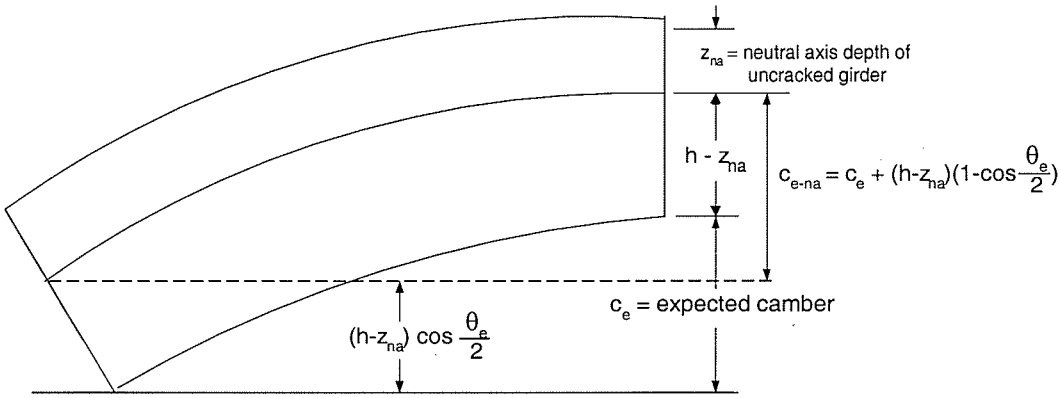

Figure 11.5 Segment Heights for Bottom and Top Girder Fibers

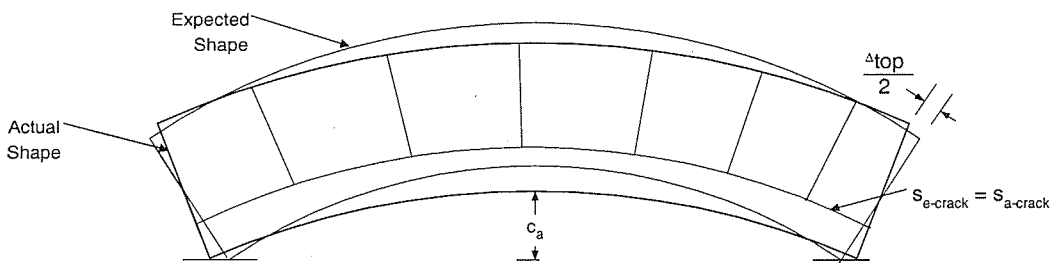

Figure 11.6 Girder Shape after Crack Closure

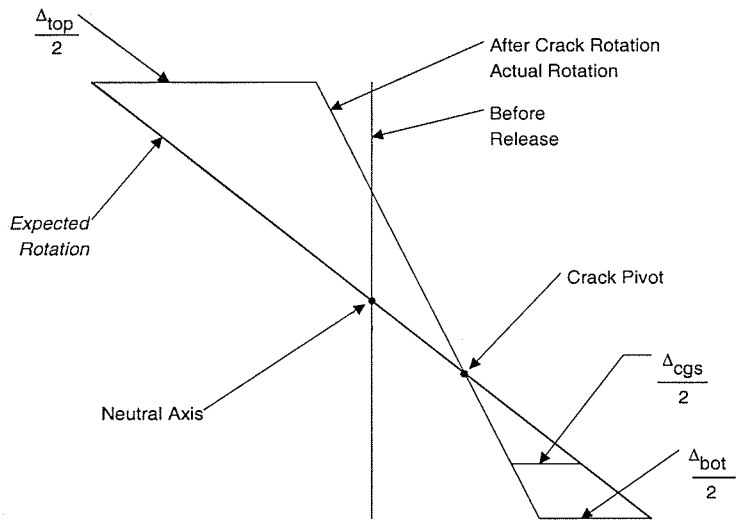

Figure 11.7 Left Girder End Rotation

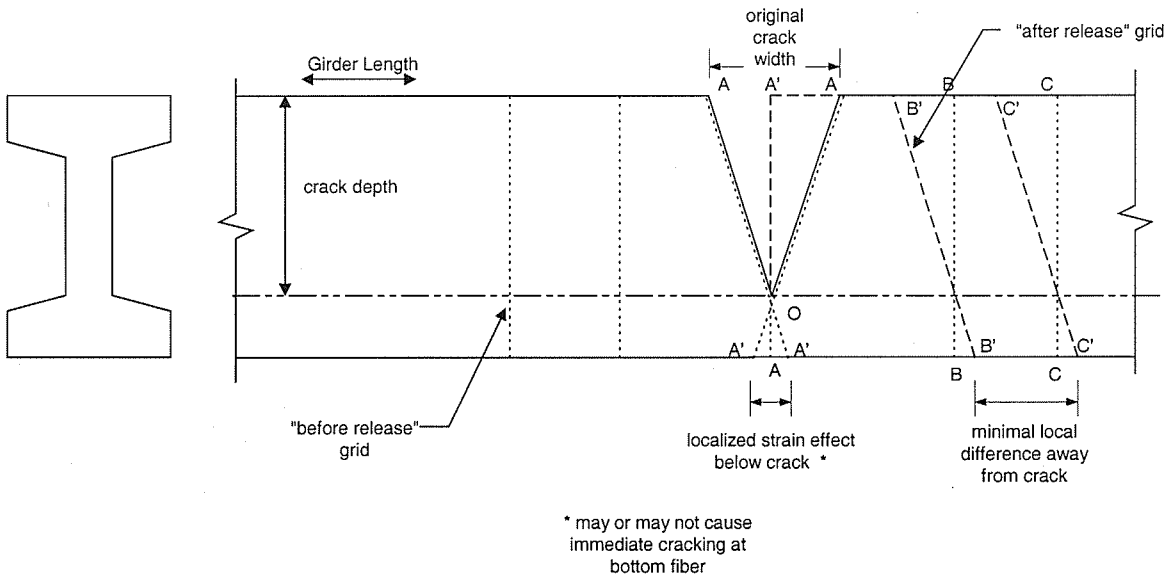

Figure 11.8 Localized Strain Effect at a Crack

APPENDIX A

Pbeam Input File for Girder I

```
UMN - HSC  g1am.dat
START    1 Problem #1, losses and load testing with cracking
   13    0    0    0    0    0    0    0    1    0    1    0
         7   18    8   42    0    3    0    1
   29    7 1.010e+00 1.825e+04                *Table 2: calc/print times*
 1.010e+00 2.010e+00 4.000e+00 7.010e+00 1.400e+01 2.800e+01 5.000e+01 1.000e+02
 1.500e+02 2.000e+02 2.010e+02 2.050e+02 2.070e+02 2.150e+02 2.280e+02 2.500e+02
 3.000e+02 4.000e+02 5.000e+02 5.930e+02 7.000e+02 8.000e+02 8.600e+02 9.000e+02
 1.000e+03 2.000e+03 4.000e+03 8.000e+03 1.825e+04
 1.010e+00 2.800e+01 2.000e+02 2.010e+02 5.930e+02 8.600e+02 1.825e+04
    5   20           1.000e+00 1.000e+00 1.000e+10 1.000e+10
    4                                     *Table 3A - no. material props*
    1    0    1    1    1    1  8.80e-02     *girder concrete props*
 1.000e+01 1.000e-06 1.980e-04-4.500e-03      cr on/sh on/age on
      0.21      0.99
      1.04      0.70
      0.60      10.0       1.0       0.0
 -2.26e-04     375.0
    2    0    2    1    1    1  8.51e-02     *deck concrete props*
 1.000e+01 1.000e-06 1.580e-04-5.000e-03      cr on/sh on/age off
      0.00      1.00
      2.35      0.70
      0.60      10.0       1.0       0.0
 -5.03e-04      55.0
    3    0    3    0    0    0  2.84e-01     *top flange rebar*
 1.000e+02 1.000e-05 6.530e-02-6.530e-02
    4    1    4    0    1    0  2.84e-01     *prestr strand* relax off
 1.000e+02 1.000e-04 6.530e-02-6.530e-02
 2.430e+05      45.0      0.55      0.60
    1    9           -100 -300 -950-1210-1130-1030 -802    0   96
*3B*
                    -6500-3500-2800-2500-2340-2140-1667    0  200
    2    1           -498 -293
                    -2200-3000
    3    3    1         0  743 743
                        0  256 5000
    4   11    1         0 2477 2500 2567 2600 2620 2643 2650 2683 2688 2692
                        0   86   90  100  110  120  140  150  300  400  600
   28      1.593e+03                                  *begin Table 4*
   17                                                 *number of subrectangles*
         1    6    1               0.01      1.01      1.01      *girder conc*
                26.0       7.5      3.75       0.0
         1    4    1               0.01      1.01      1.01
                16.2       3.5     9.250       0.0
         1   10    1               0.01      1.01      1.01
                 6.0      24.5     23.25       0.0
         1    4    1               0.01      1.01      1.01
                13.2       3.5     37.25       0.0
         1    6    1               0.01      1.01      1.01
                30.0       6.0     42.00       0.0
         3    1    1               0.01      1.01      1.01      *girder top rebar*
                3.16       1.0    42.625       0.0
         4    1    4               0.01      1.01      1.01      *str Layer 1 -
debonded*
 0.000e+00 1.520e+00 0.600e+00  2.00e+00 6.588e-03
 2.400e+02 4.560e+00 0.600e+00  2.00e+00 6.588e-03
 1.353e+03 4.560e+00 0.600e+00  2.00e+00 6.588e-03
 1.593e+03 1.520e+00 0.600e+00  2.00e+00 6.588e-03
         4    1    1               0.01      1.01      1.01      *str Layer 2*
                4.56       0.6       4.0 6.588e-03
         4    1    1               0.01      1.01      1.01      *str Layer 3*
                4.56       0.6      6.00 6.588e-03
         4    1    1               0.01      1.01      1.01      *str Layer 4*
                1.52       0.6      8.00 6.588e-03
         4    1    1               0.01      1.01      1.01      *str Layer 5*
                0.76       0.6     10.00 6.588e-03
```

```
         4    1    1                0.01      1.01      1.01      *Layer at cgs,
remainder of area*
                0.00       0.6      5.39 6.588e-03
         4    1    4                0.01      1.01      1.01      *Layers 6/7 draped*
 0.000e+00 1.520e+00 0.600e+00  3.30e+01 6.588e-03
 6.375e+02 1.520e+00 0.600e+00  1.30e+01 6.588e-03
 9.555e+02 1.520e+00 0.600e+00  1.30e+01 6.588e-03
 1.593e+03 1.520e+00 0.600e+00  3.30e+01 6.588e-03
         2    1    1               201.0     201.0     207.0      *deck haunch*
                30.0       1.0      45.5       0.0
         2    9    1               201.0     201.0     207.0      *deck concrete*
                48.0       9.0      50.5       0.0
         3    1    1               201.0     201.0     207.0      *deck bottom steel*
                2.40       0.5     47.75       0.0
         3    1    1               201.0     201.0     207.0      *deck top steel*
                1.20       0.5     51.25       0.0
         2                                                       *Table 5B restraints*
 0.000e+00                    -1.100e+30
 1.593e+03          -1.100e+30-1.100e+30
CEASE
```

APPENDIX B

Pbeam Input File for Girder II

```
UMN - HSC  g2am.dat
START    1 Problem #1, losses and load testing with cracking
   13    0    0    0    0    0    0    0    1    0    1    0
         7   18    8   47    0    3    0    1
   29    7 1.010e+00 1.825e+04              *Table 2: calc/print times*
 1.010e+00 2.010e+00 4.000e+00 7.010e+00 1.400e+01 2.800e+01 5.000e+01 1.000e+02
 1.500e+02 2.000e+02 2.010e+02 2.050e+02 2.070e+02 2.150e+02 2.280e+02 2.500e+02
 3.000e+02 4.000e+02 5.000e+02 5.930e+02 7.270e+02 8.000e+02 8.400e+02 9.000e+02
 1.000e+03 2.000e+03 4.000e+03 8.000e+03 1.825e+04
 1.010e+00 2.800e+01 2.000e+02 2.010e+02 7.270e+02 8.400e+02 1.825e+04
    5   20           1.000e+00 1.000e+00 1.000e+10 1.000e+10
    4                                    *Table 3A - no. material props*
    1    0    1    1    1    1  8.85e-02     *girder concrete props*
 1.000e+01 1.000e-06 1.560e-04-4.500e-03      cr on/sh on/age on
      0.02      1.00
      1.24      0.70
      0.60      10.0       1.0       0.0
 -2.02e-04     147.0
    2    0    2    1    1    1  8.51e-02     *deck concrete props*
 1.000e+01 1.000e-06 1.580e-04-5.000e-03      cr on/sh on/age off
      0.00      1.00
      2.35      0.70
      0.60      10.0       1.0       0.0
 -5.03e-04      55.0
    3    0    3    0    0    0  2.84e-01     *top flange rebar*
 1.000e+02 1.000e-05 6.530e-02-6.530e-02
    4    1    4    0    1    0  2.84e-01     *prestr strand* relax on
 1.000e+02 1.000e-04 6.530e-02-6.530e-02
 2.430e+05      45.0      0.55      0.60
    1    9           -100 -300 -950-1110-1080-1030 -800    0  240
*3B*
                    -6500-3500-2800-2500-2350-2150-1667    0  500
    2    1           -498 -293
                    -2200-3000
    3    3    1         0  743 743
                        0  256 5000
    4   11    1         0 2477 2500 2567 2600 2620 2643 2650 2683 2688 2692
                        0   86   90  100  110  120  140  150  300  400  600
   28      1.593e+03                                  *begin Table 4*
   18                                                 *number of subrectangles*
         1    6    1              0.01      1.01      1.01      *girder conc*
                26.0       7.5      3.75       0.0
         1    4    1              0.01      1.01      1.01
                16.2       3.5     9.250       0.0
         1   10    1              0.01      1.01      1.01
                 6.0      24.5     23.25       0.0
         1    4    1              0.01      1.01      1.01
                13.2       3.5     37.25       0.0
         1    6    1              0.01      1.01      1.01
                30.0       6.0     42.00       0.0
         3    1    1              0.01      1.01      1.01      *girder top rebar*
                3.16       1.0    42.625       0.0
         4    1    3              0.01      1.01      1.01      *str Layer 1 -
debonded*
 0.000e+00 1.520e+00 0.600e+00  2.00e+00 6.588e-03
 2.400e+02 4.560e+00 0.600e+00  2.00e+00 6.588e-03
 1.593e+03 4.560e+00 0.600e+00  2.00e+00 6.588e-03
         4    1    1              0.01      1.01      1.01      *str Layer 2*
                3.80       0.6       4.0 6.588e-03
         4    1    1              0.01      1.01      1.01      *str Layer 3*
                3.80       0.6       6.0 6.588e-03
         4    1    1              0.01      1.01      1.01      *str Layer 4*
                0.76       0.6       8.0 6.588e-03
         4    1    1              0.01      1.01      1.01      *Layer at cgs, no
area*
                0.00       0.6      5.39 6.588e-03
         4    1    3              0.01      1.01      1.01      *draped 2/3 *
```

```
 0.000e+00 1.520e+00 0.600e+00  0.50e+01 6.588e-03
 9.555e+02 1.520e+00 0.600e+00  0.50e+01 6.588e-03
 1.593e+03 1.520e+00 0.600e+00  2.90e+01 6.588e-03
         4    1    3                0.01      1.01       1.01       *draped 4/5 *
 0.000e+00 1.520e+00 0.600e+00  0.90e+01 6.588e-03
 9.555e+02 1.520e+00 0.600e+00  0.90e+01 6.588e-03
 1.593e+03 1.520e+00 0.600e+00  3.30e+01 6.588e-03
         4    1    4                0.01      1.01       1.01       *draped 6/7 - both
ends*
 0.000e+00 1.520e+00 0.600e+00  3.30e+01 6.588e-03
 6.375e+02 1.520e+00 0.600e+00  1.30e+01 6.588e-03
 9.555e+02 1.520e+00 0.600e+00  1.30e+01 6.588e-03
 1.593e+03 1.520e+00 0.600e+00  3.70e+01 6.588e-03
         2    1    1               201.0     201.0      207.0      *deck haunch*
                30.0       1.0      45.5       0.0
         2    9    1               201.0     201.0      207.0      *deck concrete*
                48.0       9.0      50.5       0.0
         3    1    1               201.0     201.0      207.0      *deck bottom steel*
                2.40       0.5      47.75      0.0
         3    1    1               201.0     201.0      207.0      *deck top steel*
                1.20       0.5      51.25      0.0
         2                                                        *Table 5B restraints*
 0.000e+00                    -1.100e+30
 1.593e+03          -1.100e+30-1.100e+30
CEASE
```

APPENDIX C

Load Testing History – Girder I

TEST SUMMARY of GIRDER I - Limestone								
Test Name	**Date**	**Type**	**Rate**	**TCS Test**	**Load Range**	**# cycles**	**Spreadsheet**	**Control**
TESTI0K	8/23/94	Static	35k/500sec.	STATIC1	2-10 k	1	TEST10K.wq1	M=DA
								M=DB
TESTI0K2	8/30/94	Static	35k/500sec.	STATIC1	2-10 k	1	TEST10K2.wq1	M=LdB
*bad column vibrations								SI=LdA
TEST10K3	8/30/94	Static	35k/1000sec.	STATIC1	2-10 k	1	TEST10K3.wq1	M=DB
(good)								SI=LdA
DYN100A	9/1/94	Fatigue	0.5Hz	DYN100	1-6 k	1000	DYN100A.wq1	M=DB
*bad- varied gain, 2nd mode?			1.0Hz					SI=LdA
DYN1002	9/2/94	Fatigue	1.0Hz	DYN1002	2.5-7k	1000	DYN1002.wq1	M=DB
*bad- load jagged, column vibs.								no-A
DYN6	9/8/94	Fatigue	0.1-1.0Hz	DYN601	2-6 k	1000	DYN6.wq1	no-B
				DYN603				M=LdA
				DYN605				
				DYN608				
TRUCK1	9/9/94	Static	10"/1000sec.	STATIC2	3-25.5 k	1	TRUCK1wq1	M=DB
								SI=LdA
TRUCK2	9/13/94	Static	10"/1000sec.	STAT50	3-27.9 k	1	TRUCK2.wq1	M=DB
*temp interlock at max								SI=LdA
TRUCK3	9/15/94	Static	10"/1000sec.	STAT50B	3-25.96 k	5	TRUCK3.wq1	M=DB
								SI=LdA
TRUCK4	9/16/94	Static	10"/1000sec.	STATIC3	9.25-25.5 k	1	TRUCK4.wq1	M=DB
								SI=LdA
DYN100B	9/20/94	Fatigue	0.1Hz	DYN100B	4-22 k	1000	DYN100B	M=LdA
								M=LdB
DYN300B	9/27/94	Fatigue	0.3-1.0Hz	DYN300B	4-22 k	1000	DYN300B	M=LdA
								M=LdB
DYN1000	10/11/94	Fatigue	1.0 Hz	DYN1000	4-22 k	1000	DYN1000	M=LdA
								M=LdB
09HZ75	10/13/94	Fatigue	0.9Hz	DLVDT1	4.5-20 k	5000	DLVDT1.wq1	M=LdA
				DSTR1	75% HS25	10000	DPMLCL	M=LdB
				DREBAR1			DPMLIAS	
				DREBAR2			DPMLIB	
				DPMLCL			DREBAR1	
				DPMLIB			DREBAR2	
				DPMLIAS			DSTR1	
075HZ100	10/18/94	Fatigue	0.75Hz	DLVDT1	100% HS25	100	2DLVDT1.wq1	M=LdA
				DSTR1	5-23k	5000	2DPMLCL	M=LdB
				DREBAR1		10000	2DPMLIAS	
				DREBAR2			2DPMLIB	
				DPMLCL			2DREBAR1	
				DPMLIB			2DREBAR2	
				DPMLIAS			2DSTR1	
			0.75 Hz		75% HS25	10000		
065HZ125	10/20/94	Fatigue	.065 Hz	DLVDT1	125% HS25	100	3DLVDT1.wq1	M=LdA
for 10000 cycles				DSTR1		5000	3DPMLCL	M=LdB

TEST SUMMARY of GIRDER I - Limestone								
Test Name	**Date**	**Type**	**Rate**	**TCS Test**	**Load Range**	**# cycles**	**Spreadsheet**	**Control**
				DREBAR1		10000	3DPMLIAS	
				DREBAR2			3DPMLIB	
				DPMLCL			3DREBAR1	
				DPMLIB			3DREBAR2	
				DPMLIAS			3DSTR1	
			0.65 Hz		100% HS25	10000		
			0.65 Hz		75% HS25	10000		
TRUCK5	10/26/94	Static	?	STATIC3	100% HS25			M=LdA
					8-23k			M=LdB
70YR	10/27/94	Fatigue	0.75 Hz	DLVDT1	100% HS25	100		M=LdA
				DSTR1	5-23k	10000	4DLVDT1.wq1	M=LdB
				DREBAR1		0	4DPMLIAS	
				DREBAR2		33000	4DPMLIB	
				DPMLCL		50000	4DREBAR1	
				DPMLIB		100000	4DREBAR2	
				DPMLIAS		250000	4DSTR1	
				DISPLTR		270000		
						TRUCK 6		
						400000		
						650000		
						750000	5DLVDT1.wq1	
						TRUCK 7	5DPMLIAS	
						900000	5DPMLIB	
						1010000	5DREBAR1	
						TRUCK 8	5DREBAR2	
							5DSTR1	
TRUCK 6	11/1/94	Static	1k/28.5sec.	? (STATIC3)	100% HS25	1	TRUCK 6	M=LdA
at 300000 cycles					to 26k			M=LdB
TRUCK 7	11/8/94	Static	1k/28.5sec.	?(STATIC3)	100% HS25	1	TRUCK 7	M=LdA
at 750000 cycles					to 26k			M=LdB
TRUCK 8	11/14/94	Static	1k/28.5sec.	STATTRK	125% HS25	1	TRK8LVDT	M=LdA
at post 1 million				VWTILT	9-32 k		TRK8PML	M=LdB
							TRK8REBR	
							TRK8STRD	
							TRK8VWT	
70YR125	11/15/94	Fatigue	0.5 Hz	DLVDT1	125% HS25			
				DSTR1	4-26.4k	100	6DLVDT1.wq1	M=LdA
				DREBAR1		80000	6DPMLIAS	M=LdB
				DREBAR2			6DPMLIB	
				DPMLCL			6DREBAR1	
				DPMLIB			6DREBAR2	
				DPMLIAS			6DSTR1	
70YR125B	11/17/94	Fatigue	0.65 Hz	DLVDT1	125% HS25	100	7DLVDT1.wq1	M=LdA
				DSTR1	6-27.5k	40000	7DPMLIAS	M=LdB
				DREBAR1			7DPMLIB	
				DREBAR2			7DREBAR1	
				DPMLCL			7DREBAR2	
				DPMLIB			7DSTR1	
				DPMLIAS				
TRUCK9		Static				1 loop	TRUCK9.wq1	M=LdA
bad test- jumpy loads and ground loop? start of problem								M=LdB

TEST SUMMARY of GIRDER I - Limestone								
Test Name	**Date**	**Type**	**Rate**	**TCS Test**	**Load Range**	**# cycles**	**Spreadsheet**	**Control**
TRUCK10	3/20/95	Static	1k/28.5sec.	VWTILT2	125% HS25	1 loop	TRK10VW	M=LdA
				STATRK3	9.25-31.9		TRUCK10.wq1	M=LdB
				DT2				
04HZ125	3/20/95	Fatigue	0.5Hz	DLVDT2	125% HS25	100		M=LdA
for 80000 cycles			?0.4Hz	DSTR2	9.2-31.7	23000		M=LdB
			?0.6Hz	DREB12		50000		
			rates	DREB22		80000		
			changed	DPMLC2				
				DPMLB2				
				DPMLA2				
TRUCK11	3/27/95	Static	1k/14.3sec.	STATRK3	125% HS25	1 loop	TRK11VW	M=LdA
*system ground before TRUCK11				VWTILT3	9.25-31.9		TRK11DT	M=LdB
				DT2			TRL11STR	
CRACK1	3/27/95	Static+	1k/28.5sec.	VWTILT3	DL+2 to DL+3	1load only	CRK1DT	M=LdA
		DL		STATR3		DL+2 to	CRK1ST	M=LdB
				DT2		DL+34	CRK1VW	
			no. diff. collection notes			incl Truck11	CRK1TOTL	
CRACK2	3/28/95	Static+	1k/28.5sec.	LOADDEF	9.25-30	(1)125% HS	CRK2VW.wq1	M=LdA
(*includes TRK load)		DL		VWTILT3	DL+2 to DL+3	(1)DL+2 to D	CRK2LD.wq1	M=LdB
						*incl Truck+	CRK2TOTL.wq1	
POSTCRK1	4/11/95	Fatigue	0.75 Hz	DLVDT2	100% HS25	100	10LVDT2.wq1	M=LdA
				DSTR2	9.25-27.3 k	88000	10STR2	M=LdB
				DREB12		136000	10REB12	
				DREB22		210000	10REB22	
				DPMLC2		380000	10PMLC2	
				DPMLB2		Truck12	10PMLB2	
				DPMLA2		381000	10PMLA2	
				DT2		500000	10DT2	
						650000		
					stopped at 700,000 cycles			
TRUCK12	4/17/95	Static	1k/14.3sec.	LOADDEF	125% HS25	2 loops	TRUCK12.wq1	M=LdA
@380000cycles					9-31+			M=LdB
POSTCRK2	4/24/95	Fatigue	0.5 Hz	DLVDT2	125% HS25	100	11LVDT2	M=LdA
				DREB12	9-31.8k	33000	11STR2.wq1	M=LdB
				DREB22		100000	11REB12	
				DPMLC2			11REB22	
				DPMLB2			11PMLC2	
				DPMLA2			11PMLB2	
				DT2			11PMLA2	
TRUCK13	4/27/95	Static	1k/14.3sec.	VWTILT3	125% HS25	2 loops	TRK13STR	M=LdA
	start small steps for DTs.			DT2	2-32		TRK13VW	M=LdB
				STATRK4			TRK13DT	
CRACK3	4/29/95	Static+	1k/28.5sec.	STATRK4	DL hang+100	1 load only	CRK30PEN	M=LdA
		DL hang		VWTILT3	DL+2 to DL+3	temp interloc	CRK3STR4	M=LdB
						for unload		
CRACK4	5/6/95	Static+	1k/28.5sec.	STATRK4(8se	DL hang+100	3 loops	CRK4LVDT	M=LdA
		DL hang		VWTILT3(3min	DL+2 to DL+28.5		CRK4STRD	M=LdB
							CRK4PML	

TEST SUMMARY of GIRDER I - Limestone								
Test Name	**Date**	**Type**	**Rate**	**TCS Test**	**Load Range**	**# cycles**	**Spreadsheet**	**Control**
							CRK4REBR	
							CRK4VW	
TRUCK14	5/8/95	Static	1k/14.3sec.	STATRK4	125%HS25	2 loops	TRK14STR	M=LdA
	*swap LVDT bottom flange, each loop				9.25-31.8			M=LdB
POSTCRK3	5/9/95	Fatigue	0.5Hz	DLVDT3	125% HS25	123000	12LVDT3	M=LdA
cont.from postcrk2				DSTR2	9.25-31.75	200000	12STR2	M=LdB
				DREB12			12REB12	
				DREB22	swap lvdt nea	200100	12REB22	
				DPMLC2	to lvdt over A	370000	12PMLC2	
				DPMLB2		500000	12PMLB2	
				DPMLA2		TRUCK 15	12PMLA2	
						800000		
						TRUCK 16		
						1000000		
						TRUCK 17		
TRUCK 15	5/25/95	Static	1k/14.3sec	STATRK5	125% HS25	2 Loops	TRUCK15	
TRUCK 16	6/1/95	Static	1k/14.3sec	STATRK5	125% HS25	2 Loops	TRUCK16	
TRUCK 17	6/5/95	Static	1k/14.3sec	STATRK5	125% HS25	2 Loops	TRUCK17	
Pre-ULT I	12/18/96	Static	1k/14.3sec		0-45k	1 Loop	FLYU1	
ULTIMATE I								
	12/18/96							

APPENDIX D

Load Testing History – Girder II

Test Name	Date	Type	Rate	TCS Test	Load Range	# cycles	Spreadsheet	Data sets included
TEST10K5	6/27/95	Static	1k/15 sec	SAMP2	0-10 K	3	10K5DATA.wq1	7--31
				VWTILT5			10K5VWT5.wq1	6--13
TRUCK20	6/28/95	Static	1k/15 sec	SAMP2	9.25-27.25K	2	T20DATA.wq1	32--52
				VWTILT5	100% HS25		T20VWT5.wq1	14--21
TRUCK21	7/10/95	Static	1k/15 sec	SAMP2	9.25-31.5K	2	T21DATA.wq1	54--80
				VWTILT5	125% HS25		T21VWT5.wq1	22--28
DYNAMP	7/11/95	Fatigue	0.1-1.0 HZ	F1LVDT	6-10K	1000 @ ea. freq	FALVDT.wq1	1--4
			VARIED	F1&2LVDT			FBLVDT.wq1	F1:5-6; F2:1-6
				F1STRCL			FASTRCL.wq1	1--4
				F1&2STRCL			FBSTRCL.wq1	F1:5-6; F2:1-5
				F1STRCD			FASTRCD.wq1	1--4
				F1&2STRCD			FBSTRCD.wq1	F1:5-6; F2:1-5
				F1REBAR			FAREBAR.wq1	1--4
				F1&2REBAR			FBREBAR.wq1	F1:5-6; F2:1-5
				F1PMLC			FAPMLC.wq1	1--4
				F1&2PMLC			FBPMLC.wq1	F1:5-6; F2:1-5
				F1PCL			FAPCL.wq1	1--4
				F1&2PCL			FBPCL.wq1	F1:5-6; F2:1-5
				F1PMLD			FAPMLD.wq1	1--4
				F1&2PMLD			FBPMLD.wq1	F1:5-6; F2:1-5
70YR100	7/12/95	Fatigue	0.75 HZ	F1LVDT	9.25-27.25K	0	FCLVDT.wq1	7--15
					100% HS25	50000	FDLVDT.wq1	16--19
				F1STRCL		125000	FCSTRCL.wq1	6--14
						260000	FDSTRCL.wq1	15-18
				F1STRCD		300000	FCSTRCD.wq1	6-14
						TRUCK22	FDSTRCD.wq1	15-18
				F1REBAR		380,000	FCREBAR.wq1	6--13
						455,000	FDREBAR.wq1	14--18
				F1PMLC		640,000	FCPMLC.wq1	6--14
						710,000	FDPMLC.wq1	15--18
				F1PCL		TRUCK23	FCPCL.wq1	6--13
						830,000	FDPCL.wq1	14--18
				F1PMLD		1,000,000	FCPMLD.wq1	6--14
						TRUCK 24	FDPMLD.wq1	15-18
TRUCK22	7/18/95	Static	1k/15 sec	SAMP2	9.25-31.5K	2	T22DATA.wq1	81--107
	@300,000 - 70YR100			VWTILT5	125% HS25		T22VWT5.wq1	29--35
TRUCK23	7/26/95	Static	1k/15 sec	SAMP2	9.25-31.5K	2	T23DATA.wq1	108--143
	@700,000 - 70YR100			VWTILT5	125% HS25		T23VWT5.wq1	36--42
TRUCK24	7/31/95	Static	1k/15 sec	SAMP2	9.25-31.5K	2	T24DATA.wq1	144--170
	@1,000,000 - 70YR100			VWTILT5	125% HS25		T24VWT5.wq1	43--49
70YR125	7/31/95	Fatigue	.65 hz	F1LVDT	9.25-31.75	100	FELVDT.wq1	20--23
				F1STRCL	125% HS25	50,000	FESTRCL.wq1	19--22
				F1STRCD		100,000	FESTRCD.wq1	19--22
				F1REBAR		TRUCK 25	FEREBAR.wq1	19--22
				F1PMLC			FEPMLC.wq1	19--22
				F1PCL			FEPCL.wq1	19--22
				F1PMLD			FEPMLD.wq1	19--22
TRUCK 25	8/2/95	Static	1K/15 sec	SAMP2	9.25-31.5K	2	T25DATA.WQ1	171--197
				VWTILT5	125% HS25		T25VWT5.WQ1	50--56
CRACK 20	8/3/95	Crack	1k/30 sec	SAMP2	DL+30 K	1	CR20DATA.WQ1	198--230
				VWTILT5			CR20VWT5.WQ1	57--70
CRACK21	8/4/95	Crack	1K/30 sec	SAMP3	DL+30K	2	CR21DATA.WQ1	1--91
				VWTILT5	DL+32K	1	CR21VWT5.WQ1	71--81
TRUCK26	8/7/95	Static	1k/15 sec	SAMP3	9.25-31.5K	2	T26DATA.WQ1	92--119
				VWTILT5	125% HS25		T26VWT5.WQ1	82--88

POSTCR20	8/7/95	Fatigue	.75 Hz	F3&4LVDT	9.25-27.25K	100	FFLVDT.WQ1	1--2; 1--4
					100% HS25	50,000	FGLVDT.WQ1	5--7
				F1STRCL		250,000	FFSTRCL.WQ1	23--24; 15--18
						TRUCK 27	FGSTRCL.WQ1	19--21
				F1STRCD		450,000	FFSTRCD.WQ1	23--24; 15--18
						500,000	FGSTRCD.WQ1	19--21
				F1REBAR		TRUCK 28	FFREBAR.WQ1	23--24; 15--18
						625,000	FGREBAR.WQ1	19--21
				F1PMLC		700,000	FFPMLC.WQ1	23--24; 15--18
						880,000	FGPMLC.WQ1	19--21
				F1PCL		1,000,000	FFPCL.WQ1	23--24; 15--18
						TRUCK 29	FGPCL.WQ1	19--21
				F1PMLD			FFPMLD.WQ1	23--24; 15--18
							FGPMLD.WQ1	19--21
TRUCK 27	8/11/95	Static	1k/15sec	SAMP4	9.25-31.5K	2	T27DATA.WQ1	1--27
	@ 250,000 CYCLES			VWTILT5	125% HS25		T27VWT5.WQ1	36--42
TRUCK 28	8/15/95	Static	1k/15sec	SAMP4	9.25-31.5K	2	T28DATA.WQ1	28--54
	@ 500,000 CYCLES			VWTILT5	125% HS25		T28VWT5.WQ1	43--49
TRUCK 29	8/23/95	Static	1k/15sec	SAMP4	9.25-31.5K	2	T29DATA.WQ1	55--81
	@ 1 M CYCLES			VWTILT5	125% HS25		T29VWT5.WQ1	50--56
POSTCR21	8/23/95	Fatigue	.65 Hz	F4LVDT	9.25-31.75K	100	FHLVDT.WQ1	8--14
					125% HS25	60,500	FILVDT.WQ1	15--18
				F1STRCL		280,000	FHSTRCL.WQ1	22-27
						440,000	FISTRCL.WQ1	28--31
				F1STRCD		TRUCK 30	FHSTRCD.WQ1	22-27
						500,000	FISTRCD.WQ1	28--31
				F1REBAR		700,000	FHREBAR.WQ1	22-27
						770,000	FIREBAR.WQ1	28--31
				F1PMLC		880,000	FHPMLC.WQ1	22-27
						1,100,000	FIPMLC.WQ1	28--31
				F1PCL		TRUCK 31	FHPCL.WQ1	22-27
							FIPCL.WQ1	28--31
				F1PMLD			FHPMLD.WQ1	22-27
							FIPMLD.WQ1	28--31
TRUCK 30	8/31/95	Static	1k/15sec	SAMP4	9.25-31.75K	2	T30DATA.WQ1	82--110
	@440,000 CYCLES			VWTILT5	125%HS25		T30VWT5.WQ1	57--63
TRUCK 31	9/12/95	Static	1k/15sec	SAMP4	9.25-31.75K	2	T31DATA.WQ1	111--137
	@1,100,000 CYCLES			VWTILT5	125%HS25		T31VWT5.WQ1	64--70
Pre-ult II	11/3/95	Static						
ULTIMATE II	11/29/95							